Kinetic Studies of the Gas Phase Reactions of Criegee Intermediates Relevant to Atmospheric Chemistry

Rachel Eloise Lade

Submitted in accordance with the requirements for the degree of Doctor of Philosophy

The University of Leeds

School of Chemistry

July 2024

Contributions to Published Work

I confirm that the work submitted is my own, except where work which has formed part of jointly authored publications has been included. My contribution and the other authors to this work has been explicitly indicated below. I confirm that appropriate credit has been given within the thesis where reference has been made to the work of others.

Chapter 4 of this thesis includes work which has appeared in the publication:

Onel, L., Lade, R., Mortiboy, J., Blitz, M. A., Seakins, P. W., Heard, D. E., Stone, D., Kinetics of the Gas Phase Reaction of the Criegee Intermediate CH_2OO with SO_2 as a Function of Temperature. *Physical Chemistry Chemical Physics*. 2021, 23, 19415-19423.

I performed experiments at temperatures of 298 K and above, processed the raw data for these experiments and carried out the analysis. The experiments at temperatures below 298 K and the theoretical calculations were performed by Dr Lavinia Onel. The manuscript was written by Dr Lavinia Onel and Dr Daniel Stone, with contributions from Dr Mark Blitz, Professor Paul Seakins and Professor Dwayne Heard.

Chapter 7 of this thesis includes work which has appeared in the publication:

Lade, R. E., Onel, L., Blitz, M. A., Seakins, P. W., Stone, D., Kinetics of the Gas-Phase Reactions of *syn*- and *anti*-CH_3CHOO Criegee Intermediate Conformers with SO_2 as a Function of Temperature and Pressure. *Journal of Physical Chemistry A.*, 2024, 128(14), 2815-2824.

I carried out all of the experiments and data analysis. The manuscript was written by myself and Dr Daniel Stone with contributions from Dr Lavinia Onel, Dr Mark Blitz and Professor Paul Seakins.

Acknowledgements

Firstly, I would like to express my gratitude to my supervisors, Dr Daniel Stone and Professor Paul Seakins, for providing me with the opportunity to join the Atmospheric and Planetary Chemistry research group at the University of Leeds. In particular, I would like to thank my primary supervisor, Dan, for his unwavering support and kindness throughout my years as a student, even before the PhD! I would also like to thank Dr Mark Blitz for his invaluable assistance within the lab over the years.

Next I would like to thank the members of the APC research group, with special appreciation for those in the Dainton office, for contributing to the memorable experiences of the past four years, I am truly grateful to have made some amazing friends.

To my friends outside of academia, particularly Maddy and Hope, and to Rob and his family, thank you for patiently listening to me talk about Chemistry and for keeping me sane throughout the process of writing this thesis – I couldn't have done it without you.

Finally, I would like to thank my family for their continuous love and support, especially my mother, whose words of encouragement made anything seem possible. To my Grandad, this one is for you.

Abstract

Air quality and climate change are influenced by atmospheric composition, which is controlled by both the emissions and chemistry of trace species. Criegee intermediates (CIs) are reactive zwitterionic species with the general formula R_1R_2COO that are produced in the atmosphere following the ozonolysis of unsaturated volatile organic compounds (VOCs). Bimolecular reactions of stabilised Criegee intermediates (SCIs) with NO_2, water vapour and SO_2 are of particular interest as they have the potential to impact atmospheric budgets of NO_x ($NO_x = NO + NO_2$), H_2SO_4, and secondary organic aerosols (SOA).

In this work, the reactions of CH_2OO with SO_2, NO_2 and water vapour, and the reactions of CH_3CHOO conformers with SO_2 have been investigated across a range of temperatures and pressures relevant to the troposphere using laser flash photolysis coupled to time-resolved broadband ultraviolet absorption spectroscopy.

At 298 K, results from this work indicate that the reactions of CH_2OO have rate coefficients of $k = (3.56 \pm 0.11) \times 10^{-11}$ cm^3 molecule^{-1} s^{-1} for the reaction with SO_2, $k = (1.24 \pm 0.16) \times 10^{-12}$ cm^3 molecule^{-1} s^{-1} for the reaction with NO_2, $k = (9.8 \pm 5.9) \times 10^{-16}$ cm^3 molecule^{-1} s^{-1} for the reaction with water monomers, and $k = (9.52 \pm 2.49) \times 10^{-12}$ cm^3 molecule^{-1} s^{-1} for the reaction with water dimers. No significant pressure dependence was observed for any of the CH_2OO reactions investigated. The reactions of CH_2OO with SO_2, NO_2, and water dimers exhibited negative temperature dependence, while the reaction of CH_2OO with water monomers exhibited a positive temperature dependence. Atmospheric modelling shows the reaction with water dimers dominates the atmospheric loss of CH_2OO under all conditions relevant to the troposphere, with sinks other than water representing less than 1 % of the overall loss of CH_2OO.

For the reaction of CH_3CHOO conformers with SO_2, results indicate a rate coefficient of $k = (4.80 \pm 0.46) \times 10^{-11}$ cm^3 molecule^{-1} s^{-1} for the reaction of *syn*-CH_3CHOO with SO_2 at 298 K and 760 Torr. Significant collisional stabilisation of the secondary ozonide formed in the reaction is expected under atmospheric conditions. Kinetics of *anti*-$CH_3CHOO + SO_2$ display no significant dependence on temperature or pressure over the ranges investigated, with a mean rate coefficient of $k = (1.18 \pm 0.21) \times 10^{-10}$ cm^3 molecule^{-1} s^{-1} over all conditions. Results indicate that the reaction of *syn*-CH_3CHOO with SO_2 is competitive with unimolecular decomposition and reaction with water vapour in areas of high SO_2 concentration and low humidity, particularly at lower temperatures. The atmospheric importance of the reaction between *anti*-CH_3CHOO and SO_2 remains uncertain due to the lack of literature regarding the reactions between *anti*-CH_3CHOO and water vapour, which should be the subject of future experimental studies into Criegee intermediates.

Table of Contents

Chapter 1 Introduction..... 1
1.1 The Earth's Atmosphere and Climate system..... 1
1.1.1 Air Quality..... 3
1.1.2 Climate Change..... 4
1.2 Atmospheric Oxidation Processes..... 5
1.2.1 OH-Initiated Oxidation..... 6
1.2.2 NO_3-Initiated Oxidation..... 7
1.2.3 O_3-Initiated Oxidation..... 8
1.3 Criegee Intermediates..... 9
1.3.1 Atmospheric Concentrations of Criegee Intermediates..... 11
1.3.2 Indirect Measurements of Criegee Intermediates..... 12
1.3.3 Direct Detection of Criegee Intermediates..... 13
1.4 Overview of this Thesis..... 17
1.5 References..... 18
Chapter 2 Theory of Gas Phase Kinetics and Photochemistry..... 24
2.1 Rate Theory of Gas Phase Kinetics..... 24
2.1.1 The Steady State Approximation..... 26
2.2 Theory of Temperature and Pressure Dependence..... 27
2.2.1 Temperature Dependence..... 27
2.2.1.1 Simple Collision Theory..... 28
2.2.1.2 Transition State Theory..... 31
2.2.1.3 Barrierless Reactions..... 35
2.2.1.3.1 Capture-Limited Rate Coefficients..... 36
2.2.2 Pressure Dependence..... 37
2.2.2.1 The Lindemann Mechanism..... 37
2.2.2.2 Chemical Activation..... 42
2.2.2.3 The Hinshelwood Theory..... 44
2.2.2.4 The Rice-Ramsperger-Kassel-Marcus Theory..... 44
2.2.2.5 The Troe Fall-off Form..... 45
2.2.3 Master Equation Calculations..... 46
2.3 Theory of Photochemistry..... 47
2.3.1 The Beer-Lambert Law..... 48
2.3.2 The Excitation of a Molecule..... 49
2.3.3 Fates of Excited Molecules..... 51
2.3.3.1 Photodissociation..... 52

2.4 Concluding Remarks..... 53
2.5 References..... 53
Chapter 3 Experimental Techniques to Investigate Criegee Intermediates..... 56
3.1 Kinetic Techniques..... 56
3.1.1 The Relative Rate Method..... 56
3.1.2 The Flow Method..... 57
3.1.3 Flash Photolysis..... 59
3.1.3.1 Excimer Lasers..... 59
3.1.3.2 Nd:YAG Lasers..... 61
3.2 Analytical Techniques..... 62
3.2.1 Mass Spectrometry..... 62
3.2.1.1 Photo-Ionisation Mass Spectrometry..... 62
3.2.2 Laser-Induced Fluorescence..... 63
3.2.3 Absorption Spectroscopy..... 66
3.2.3.1 Ultraviolet Absorption Spectroscopy..... 67
3.2.3.2 Cavity Ring-Down Spectroscopy..... 67
3.2.3.3 Cavity Enhanced Absorption Spectroscopy..... 68
3.2.3.4 Infrared Absorption Spectroscopy..... 69
3.2.3.4.1 Quantum Cascade Lasers..... 71
3.3 Experimental Technique and Data Analysis of This Work..... 72
3.3.1 Instrumental Arrangement..... 72
3.3.2 Charge Coupled Device..... 76
3.3.3 Spectral Fitting..... 79
3.3.4 Kinetic Analysis..... 82
3.3.4.1 Instrument Response Function..... 83
3.3.4.2 Mixed-Order Analysis..... 88
3.4 References..... 91
Chapter 4 Kinetics of the Reaction of CH_2OO with SO_2 as a Function of Temperature..... 96
4.1 Previous Direct Studies..... 96
4.2 Product Studies..... 103
4.3 Experimental..... 105
4.4 Results and Discussion..... 106
4.5 Concluding Remarks..... 119
4.6 References..... 119

Chapter 5 Kinetics of the Reaction Between CH_2OO and NO_2 as a Function of Temperature and Pressure..... 122
5.1 Previous Experimental Studies..... 122
5.2 Previous Theoretical Work..... 127
5.3 Experimental..... 128
5.4 Analysis of Absorbance Spectra..... 129
5.4.1 Limit of Detection for NO_3..... 138
5.5 Results and Discussion..... 140
5.5.1 Pressure Dependent Results..... 148
5.5.2 Temperature Dependent Results..... 149
5.5.3 Theoretical Calculations..... 154
5.5.4 Modelling of $O_2CH_2NO_2$..... 158
5.6 Concluding Remarks..... 159
5.7 References..... 160
Chapter 6 Kinetics of the Reactions of CH_2OO with Water as a Function of Temperature..... 163
6.1 Literature Studies..... 163
6.2 Experimental..... 166
6.3 Results and Discussion..... 167
6.4 Concluding Remarks..... 186
6.5 References..... 187
Chapter 7 Kinetics of *syn*- and *anti*-CH_3CHOO Conformers with SO_2 as a Function of Temperature and Pressure..... 192
7.1 Previous Direct Studies..... 192
7.2 Experimental..... 196
7.3 Analysis..... 197
7.3.1 Applying a Baseline Correction..... 203
7.3.2 Constraining the Change in CH_3CHI_2 Concentration..... 206
7.3.3 Averaging the Absorbance Data..... 212
7.3.4 Changing the Experimental Conditions..... 215
7.4 Results and Discussion..... 220
7.5 Concluding Remarks..... 236
7.6 References..... 236
Chapter 8 Atmospheric Implications..... 240
8.1 Atmospheric Implications..... 240
8.1.1 Model Simulations for CH_2OO Chemistry..... 240

8.1.2 Atmospheric Losses of CH_2OO..... 247
8.1.3 Atmospheric Losses of *syn*-CH_3CHOO..... 249
8.1.4 Atmospheric Losses of *anti*-CH_3CHOO..... 251
8.2 Summary..... 252
8.3 References..... 254
Chapter 9 Conclusions and Future work..... 258
Appendices..... 261
Appendix 1. Mass Flow Controller Calibrations..... 261
Appendix 2. Hygrometer Calibration and Measuring Potential Water Vapour Losses in the System..... 263
Appendix 3. Determination of the Reaction Temperature..... 264
Appendix 4. Calculating the Effective Pathlength..... 267
Appendix 5. Bimolecular Plots for the Reaction between CH_2OO and NO_2..... 269
Appendix 6. Experimental Data Obtained for the Reaction Between CH_2OO and NO_2..... 272
Appendix 7. MESMER Input for the Reaction between CH_2OO and NO_2..... 275
Appendix 8. Investigating the Potential for a Reaction between CH_2OO and Water Trimers..... 297
Appendix 9. Comparison of Pseudo-First-Order losses of CH_2OO in the Presence of Water Vapour with Literature..... 300
Appendix 10. Experimental data for the Reaction between CH_2OO and Water Vapour..... 303
Appendix 11. A Comparison between Fits to the Data Obtained for *syn*-CH_3CHOO with SO_2..... 306
Appendix 12. Experimental Data for the reaction between CH_3CHOO and SO_2..... 309

List of Figures

Chapter 1

Figure 1.1. Vertical temperature and pressure profile of the Earth's atmosphere ranging from 0 to 100 km in altitude..... 1

Figure 1.2. Bar chart for the radiative forcing / W m^{-2} for various species reported between 1750 and 2019..... 5

Figure 1.3. The ozonolysis mechanism for the production of Criegee intermediates..... 9

Figure 1.4. General resonance canonical structure for Criegee intermediates as well as the *syn*- and *anti*-conformers of the CH_3CHOO Criegee intermediate..... 10

Figure 1.5. Typical potential energy surface diagram for the ozonolysis of alkenes to produce Criegee intermediates..... 10

Figure 1.6. Global annual distributions of SCIs calculated using the ECHAM/MESSy atmospheric chemistry model, where a) is the concentration over 1 simulation year and b) shows the peak concentration of SCIs predicted within that year..... 12

Chapter 2

Figure 2.1. General schematic of a potential energy surface (PES) for a reaction described by transition state theory..... 31

Figure 2.2. General schematic representing a potential energy surface for a barrierless reaction..... 35

Figure 2.3. Schematic diagram of the rate coefficient, k_{obs}, as a function of pressure, [M], where k_{obs} is second-order at low pressures and first-order at high pressures..... 40

Figure 2.4. Schematic potential energy surface for a general reaction, A + B, to produce an excited complex, AB*, and the possible reaction pathways following excitation..... 42

Figure 2.5. Schematic of the Energy Grained Master Equation Model for an association reaction with two wells; C1 and C2..... 47

Figure 2.6. Jablonski diagram summarising the processes that may occur following excitation of a species. S_0 is the ground singlet electronic state, S_1 and S_2 are excited singlet electronic states and T_1, T_2 and T_3 are the triplet states. Solid lines represent radiative processes and dotted lines represent non-radiative processes..... 48

Figure 2.7. Schematic diagram showing transitions from the ground vibrational level in the electronic ground state to excited vibrational levels in a bound electronic excited state..... 50

Figure 2.8. Absolute UV absorption cross-sections for CH_2OO reported by Mir *et al.*. 50

Figure 2.9. Schematic showing the transition from the ground electronic state to an unbound electronic excited state..... 51

Chapter 3

Figure 3.1. Schematic of a typical experimental set-up for the microwave discharge flow method. MFC = mass flow controller..... 58

Figure 3.2. Schematic of an electronic transition from a bound upper electronic state to an unbound ground state that occurs in excimer lasers..... 60
Figure 3.3. Schematic diagram representing on-resonance fluorescence (left) and off-resonance fluorescence (right). v'' = 0 and v'' = 1 represent the ground and first vibrational energy levels of the ground electronic state and v' = 0 and v' = 1 represent the ground and first vibrational energy levels of the excited electronic state..... 64
Figure 3.4. Schematic diagram of the LFP-LIF experimental apparatus used to detect OH reactivity at the University of Leeds. FAGE = fluorescence assay gas expansion..... 65
Figure 3.5. Schematic showing the experimental set-up where CRDS is coupled to LFP..... 68
Figure 3.6. Schematic of the CEAS apparatus used in the literature to investigate the kinetics of Criegee intermediate reactions. CCD = charge coupled device..... 69
Figure 3.7. Comparison of the IR spectra obtained for the OO-stretching mode (ν_6) of CH_2OO at different resolutions between 880 and 932 cm^{-1}. (a) and (b) were obtained using step-scan FTIR spectroscopy with resolutions of 1.0 cm^{-1} and 0.25 cm^{-1} respectively and (c) obtained using a continuous wave QCL with a resolution of 0.0015 cm^{-1}..... 70
Figure 3.8. Schematic of an IR-QCL experimental set-up used to monitor the reaction of CH_2OO with SO_2..... 71
Figure 3.9. Diagram of a Quantum Cascade Laser..... 72
Figure 3.10. Schematic of the reaction cell used for these experiments..... 74
Figure 3.11. Schematic of the mirror mount containing 8 spectral mirrors, positioned outside the windows at each end of the reaction cell. The large rectangular hole is to allow for the excimer laser beam to pass through the mirror mount into the reaction cell..... 75
Figure 3.12. A diagram to outline how photo-charge is vertically shifted down the CCD array. The output from the spectrograph is focused onto an illuminated region and then shifted to a storage region (shown by the grey shading) at a given shift rate..... 77
Figure 3.13. A schematic outlining how photo-charge was vertically shifted through the CCD. The illuminated region was a region of 10 rows where charge accumulates. Once all 10 rows in the illuminated region were filled, the charge was shifted into the storage region..... 78
Figure 3.14. Flow chart summarising how the intensity data was collected throughout the experiments..... 79
Figure 3.15. Plots outlining how the experimental absorbance evolves as a function of time following the photolysis of CH_2I_2 at t = 0, 1, 3 and 4 ms. The black is the experimental absorbance, the blue is the CH_2OO reference spectra, red is CH_2I_2, purple is IO and orange is the overall fit. Experiments were conducted at 298 K and 85 Torr, with $[CH_2I_2] = 1.3 \times 10^{13}$ molecule cm^{-3} and $[SO_2] = 1.5 \times 10^{13}$ molecule cm^{-3}..... 81

Figure 3.16. Plots outlining how the experimental absorbance evolves as a function of time following the photolysis of CH_3CHI_2 at t = 0, 1, 2 and 3 ms. The experimental absorbance is shown in black, the CH_3CHI_2 reference spectra is shown in red, *syn*-CH_3CHOO in blue, *anti*-CH_3CHOO in green and IO in purple. The orange line represents the overall fit to the observed absorbance Experiments were conducted at 298 K and 50 Torr, with $[CH_2I_2] = 2.8 \times 10^{13}$ molecule cm^{-3} and $[SO_2] = 1.1 \times 10^{13}$ molecule cm^{-3}..... 82

Figure 3.17. Concentration – time profile for the reaction of CH_2OO with NO_2 at 298 K and 50 Torr where $[NO_2] = 9.7 \times 10^{14}$ molecule cm^{-3} and $[CH_2I_2] = 5.9 \times 10^{13}$ molecule cm^{-3}. The red solid line is fit using an equation for the convolution of the true decay with an instrument response function (Equation 3.18) and gave: k' = (1397 ± 47) s^{-1}, $[CH_2OO] = (1.73 \pm 0.15) \times 10^{12}$ molecule cm^{-3}, $t_c = -(5.6 \pm 0.2) \times 10^{-6}$ s and $w = (3.9 \pm 0.1) \times 10^{-5}$ s. The dashed blue line represents the fit to the data using an exponential decay (Equation 3.14) and gave: k' = (1389 ± 39) s^{-1} and $[CH_2OO] = (1.71 \pm 0.03) \times 10^{12}$ molecule cm^{-3}..... 85

Figure 3.18. Concentration – time profile for the reaction of CH_2OO with NO_2 at 298 K and 50 Torr where $[NO_2] = 6.7 \times 10^{14}$ molecule cm^{-3} and $[CH_2I_2] = 5.9 \times 10^{13}$ molecule cm^{-3}. The red solid line is fit using an equation for the convolution of the true decay with an instrument response function (Equation 3.18) and gave: k' = (1063 ± 30) s^{-1}, $[CH_2OO] = (1.90 \pm 0.21) \times 10^{12}$ molecule cm^{-3}, $t_c = -(5.6 \pm 0.2) \times 10^{-6}$ s and $w = (3.9 \pm 0.1) \times 10^{-5}$ s. The dashed blue line represents the fit to the data using an exponential decay (Equation 3.14) and gave: k' = (1067 ± 28) s^{-1} and $[CH_2OO] = (1.90 \pm 0.03) \times 10^{12}$ molecule cm^{-3}..... 86

Figure 3.19. (a) Pseudo-first-order losses for CH_2OO as a function of $[SO_2]$ for experiments at 298 K and 85 Torr: (b) Pseudo-first-order losses after k_x has been subtracted. The red lines represent an unweighted linear fit to the data and gave: (a) $k_{3.10} = (3.55 \pm 0.15) \times 10^{-11}$ cm^3 $molecule^{-1}$ s^{-1} with an intercept of k_x = (321 ± 42) s^{-1} and (b) $k_{3.10} = (3.55 \pm 0.15) \times 10^{-11}$ cm^3 $molecule^{-1}$ s^{-1} with an intercept of k_x = (0.1 ± 59) s^{-1}..... 87

Figure 3.20. Comparison of fits to the first-order rate equation (red, Equation 3.18) and the mixed-order rate equation (black, Equation 3.19) for CH_2OO in the presence of $[SO_2] = 8.8 \times 10^{12}$ molecule cm^{-3} at 85 Torr and 298 K. The solid red line gave: t_c = - (6.67 ± 0.26) × 10^{-5} s, w = (3.73 ± 0.15) × 10^{-5} s, $[CH_2OO]_0 = (1.24 \pm 0.18) \times 10^{12}$ molecule cm^{-3} and k' = (551 ± 6) s^{-1}. The dashed black line gave: $t_c = -(2.20 \pm 0.46) \times 10^{-5}$ s, $w = (1.01 \pm 0.39) \times 10^{-5}$ s, $[CH_2OO]_0 = (1.50 \pm 0.31) \times 10^{12}$ molecule cm^{-3}, $k'' = (1.09 \pm 0.02) \times 10^{10}$ cm^3 $molecule^{-1}$ s^{-1} and k' = (529 ± 8) s^{-1}..... 89

Figure 3.21. Comparison between first-order and mixed-order rate coefficients for the reaction of $CH_2OO + SO_2$ at 298 K and 85 Torr. The red line represents an unweighted linear fit to the data from the first-order fit, giving $k_{3.10} = (3.55 \pm 0.15) \times 10^{-11}$ cm^3 molecule^{-1} s^{-1} with an intercept of (321 ± 42) s^{-1} and the black line represents an unweighted linear fit to the data from the mixed-order fit, giving $k_{3.10} = (3.53 \pm 0.12) \times 10^{-11}$ cm^3 molecule^{-1} s^{-1} with an intercept of (275 ± 33) s^{-1}..... 90

Figure 3.22. Flow chart summarising the data analysis procedure used throughout this work..... 90

Chapter 4

Figure 4.1. Laser-induced fluorescence signals for OH, outlining an initial fast production of OH followed by a slower production. The three traces represent an increase in co-reagent concentration, and outline how the OH signal decreases as the concentration is increased..... 98

Figure 4.2. IR absorption spectra obtained upon the photolysis of a $CH_2I_2/N_2/O_2/SO_2$ mixture. Adapted from reference 17. The red circles show the absorption band at $\nu = 1391.5$ cm^{-1} which correspond to the stretching mode of SO_3..... 103

Figure 4.3. Typical absorbance measured following the photolysis of CH_2I_2, where the black line represents the observed absorbance, the blue is the CH_2OO reference spectra, red is CH_2I_2, purple is IO and orange is the overall fit. Experiments were conducted at 298 K and 85 Torr, with $[CH_2I_2] = 4.6 \times 10^{13}$ molecule cm^{-3} and $[SO_2] = 0$..... 106

Figure 4.4. Concentration-time profile for CH_2I_2 for an experiment at 85 Torr and 298 K. For these data, $[SO_2] = 0$, $[CH_2I_2] = 4.6 \times 10^{13}$ molecule cm^{-3} and $\Delta[CH_2I_2] = -3.7 \times 10^{12}$ molecule cm^{-3}..... 107

Figure 4.5. Concentration-time profile for CH_2OO for an experiment at 85 Torr and 298 K. For these data, $[SO_2] = 0$, $[CH_2I_2] = 4.6 \times 10^{13}$ molecule cm^{-3}..... 107

Figure 4.6. Concentration-time profile for IO for an experiment at 85 Torr and 298 K. For these data, $[SO_2] = 0$ and $[CH_2I_2] = 4.6 \times 10^{13}$ molecule cm^{-3}..... 108

Figure 4.7. Comparison between a first-order fit (red) and mixed-order fit (blue) for data at 298 K and 85 Torr. The first-order fit gave: $k' = (551 \pm 6)$ s^{-1}, $[CH_2OO]_0 = (1.24 \pm 0.12) \times 10^{12}$ molecule cm^{-3}, $t_c = -(6.7 \pm 0.3) \times 10^{-5}$ s and $w = (3.7 \pm 0.2) \times 10^{-5}$ s. The mixed-order fit gave: $k' = (529 \pm 8)$ s^{-1}, $k'' = (7.46 \pm 0.10) \times 10^{-11}$ cm^3 molecule^{-1} s^{-1}, $[CH_2OO]_0 = (1.30 \pm 0.22) \times 10^{12}$ molecule cm^{-3}, $t_c = -(7.1 \pm 0.7) \times 10^{-5}$ s and $w = (3.9 \pm 0.4) \times 10^{-5}$ s..... 109

Figure 4.8. Comparison between a first-order fit (red) and mixed-order fit (blue) for data at 298 K and 85 Torr. The first-order fit gave: $k' = (1425 \pm 23)$ s^{-1}, $[CH_2OO]_0 = (1.18 \pm 0.45) \times 10^{12}$ molecule cm^{-3}, $t_c = -(6.7 \pm 0.3) \times 10^{-5}$ s and $w = (3.7 \pm 0.2) \times 10^{-5}$ s. The mixed-order fit gave: $k' = (1385 \pm 33)$ s^{-1}, $k'' = (7.46 \pm 0.10) \times 10^{-11}$ cm^3 molecule^{-1} s^{-1}, $[CH_2OO]_0 = (1.15 \pm 0.22) \times 10^{12}$ molecule cm^{-3}, $t_c = -(7.1 \pm 0.7) \times 10^{-5}$ s and $w = (3.9 \pm 0.4) \times 10^{-5}$ s..... 109

Figure 4.9. Dependence of k' on $[SO_2]$ at 298 K and 85 Torr obtained for a first-order fit (red line) and a mixed-order fit (blue line). The first-order fit gave: $k_{4.1} = (3.55 \pm 0.15) \times 10^{-11}$ cm^3 molecule^{-1} s^{-1} with an intercept of $k_x = (321 \pm 42)$ s^{-1}. The mixed-order fit gave: $k_{4.1} = (3.53 \pm 0.12) \times 10^{-11}$ cm^3 molecule^{-1} s^{-1} with an intercept of $k_x = (275 \pm 33)$ s^{-1}..... 110

Figure 4.10. Concentration-time profiles showing how the CH_2OO decay changes with increasing $[SO_2]$ at 85 Torr and 298 K. For $[SO_2] = 0$, the fit gave $[CH_2OO]_0 = 1.44 \times 10^{12}$ molecule cm^{-3} and $k' = (369 \pm 4)$ s^{-1}, for $[SO_2] = 4.91 \times 10^{13}$ molecule cm^{-3}, the fit gave $[CH_2OO]_0 = 1.22 \times 10^{12}$ molecule cm^{-3} and $k' = (2054 \pm 42)$ s^{-1}, for $[SO_2] = 8.77 \times 10^{12}$ molecule cm^{-3}, the fit gave $[CH_2OO]_0 = 1.24 \times 10^{12}$ molecule cm^{-3} and $k' = (551 \pm 6)$ s^{-1} and for $[SO_2] = 1.96 \times 10^{13}$ molecule cm^{-3}, the fit gave $[CH_2OO]_0 = 1.20 \times 10^{12}$ molecule cm^{-3} and $k' = (1024 \pm 14)$ s^{-1}. The IRF parameters were: $t_c = -(6.7 \pm 0.3) \times 10^{-5}$ s and $w = (3.7 \pm 0.2) \times 10^{-5}$ s..... 111

Figure 4.11. Bimolecular plot for the reaction of $CH_2OO + SO_2$ at 298 K and 85 Torr, where the red line represents an unweighted linear fit to the data. The gradient is equal to $k_{4.1} = (3.56 \pm 0.11) \times 10^{-11}$ cm^3 molecule^{-1} s^{-1} and the intercept is equal to $k_x = (365 \pm 42)$ s^{-1}. The error bars represent the error in the exponential fit to Equation 4.1..... 112

Figure 4.12. Bimolecular plot for the reaction of $CH_2OO + SO_2$ at 324 K and 85 Torr, where the red line represents an unweighted linear fit to the data. The gradient is equal to $k_{4.1} = (3.56 \pm 0.15) \times 10^{-11}$ cm^3 molecule^{-1} s^{-1} and the intercept is equal to $k_x = (281 \pm 31)$ s^{-1}. The error bars represent the error in the exponential fit to Equation 4.1..... 113

Figure 4.13. Bimolecular plot for the reaction of $CH_2OO + SO_2$ at 331 K and 85 Torr, where the red line represents an unweighted linear fit to the data. The gradient is equal to $k_{4.1} = (3.39 \pm 0.13) \times 10^{-11}$ cm^3 molecule^{-1} s^{-1} and the intercept is equal to $k_x = (228 \pm 39)$ s^{-1}. The error bars represent the error in the exponential fit to Equation 4.1..... 113

Figure 4.14. Bimolecular plot for the reaction of $CH_2OO + SO_2$ at 340 K and 85 Torr, where the red line represents an unweighted linear fit to the data. The gradient is equal to $k_{4.1} = (2.15 \pm 0.12) \times 10^{-11}$ cm^3 molecule^{-1} s^{-1} and the intercept is equal to $k_x = (304 \pm 23)$ s^{-1}. The error bars represent the error in the exponential fit to Equation 4.1..... 114

Figure 4.15. A plot of the bimolecular rate coefficients for $CH_2OO + SO_2$ from this work (solid and open black circles) as a function of temperature between 242 and 353 K. The black line represents a fit to the equation $k_{4.1} = (7.85 \pm 1.95) \times 10^{-12} \times exp((476 \pm 68)/T)$ cm^3 molecule^{-1} s^{-1} with $R^2 = 0.80$ and the dashed blue line represents a fit to the equation $k_{4.1} = ((3.91 \pm 0.15) \times 10^{-11}) \times (T/298)^{-1.8 \pm 0.2}$ cm^3 molecule^{-1} s^{-1} with $R^2 = 0.82$. Previous literature studies are also shown. (PIMS = photo-ionisation mass spectrometry). The inset shows rate coefficients obtained between 293 and 300 K for clarity..... 116

Figure 4.16. Summary of the initial steps of the mechanism for the reaction between CH_2OO and SO_2, reported by Kuwata *et al*..... 117

Figure 4.17. PES for the reaction between CH_2OO and SO_2 showing the *endo* reaction pathway (light blue) and the *exo* reaction pathway (dark blue) copied from reference 3. Relative energies for 5a, 5b, TS-7a, TS-7b and $HCHO+SO_3$ were taken from reference 16 and relative energies for 3a, 3b, TS-4a and TS-4b were generated by MESMER calculations. Values for 3a, 3b, TS-4a and TS-4b shown in red were also taken from reference 16 for comparison. All energies are reported in kJ mol^{-1}. The notations for intermediates and transition states are the same as in the work of Kuwata *et al*..... 117

Figure 4.18. A plot of the rate coefficients obtained for the reaction between CH_2OO and SO_2 from this work (solid and open black circles) and from previous literature studies. (PIMS = photo-ionisation mass spectrometry). The red line represents the parameterisation of the MESMER result: $k_{4.1} = (3.72 \pm 0.01) \times 10^{-11} (T/298)^{(-1.89 \pm 0.02)}$..... 118

Chapter 5

Figure 5.1. Potential energy surface for the reaction of $CH_2OO + NO_2$ obtained from the work of Vereecken and Nguyen, calculated at the CCSD(T)/aug-cc-pVTZ/M06-2X level of theory. Energies marked with an asterisk used NEVPT2/aug-cc-pVTZ energy estimates..... 128

Figure 5.2. Absorbance spectra for the reaction of CH_2OO in the absence of NO_2 at T = 298 K, p = 100 Torr and t = 2 ms. The experimental absorbance is shown in black, CH_2OO is shown in blue, CH_2I_2 in pink, IO in purple, the total fit in orange and the residual of the fit is shown in grey. For these data: $[CH_2OO] = 9.19 \times 10^{11}$ molecule cm^{-3}, $\Delta[CH_2I_2] = -3.16 \times 10^{12}$ molecule cm^{-3}, $[IO] = 5.78 \times 10^{11}$ molecule cm^{-3}. The residual is offset by 0.0075 for clarity (as shown by the dark grey line)..... 129

Figure 5.3. Absorbance spectra obtained at a) 0.2 ms, b) 2 ms and c) 4ms post-photolysis in the presence of $[NO_2] = 4.0 \times 10^{14}$ molecule cm^{-3} at $T = 298$ K and $p = 100$ Torr. The experimental absorbance is shown in black, CH_2OO is shown in blue, CH_2I_2 in pink, IO in purple, the total fit in orange and the residual of the fit is shown in grey. The fit gave: a) $[CH_2OO] = 9.39 \times 10^{11}$ molecule cm^{-3}, $\Delta[CH_2I_2] = -2.61 \times 10^{12}$ molecule cm^{-3}, $[IO] = 2.12 \times 10^{11}$ molecule cm^{-3}, b) $[CH_2OO] = 3.78 \times 10^{11}$ molecule cm^{-3}, $\Delta[CH_2I_2] = -2.47 \times 10^{12}$ molecule cm^{-3}, $[IO] = 1.35 \times 10^{10}$ molecule cm^{-3} and c) $[CH_2OO] = 1.60 \times 10^{11}$ molecule cm^{-3}, $\Delta[CH_2I_2] = -2.59 \times 10^{12}$ molecule cm^{-3}, $[IO] = 7.66 \times 10^{9}$ molecule cm^{-3}..... 130

Figure 5.4. Absorbance spectra obtained at 2 ms post-photolysis in the presence of $[NO_2] = 4.0 \times 10^{14}$ molecule cm^{-3} at $T = 298$ K and $p = 100$ Torr. The experimental absorbance is shown in black, CH_2OO is shown in blue, CH_2I_2 in pink, IO in purple, $IONO_2$ in bright blue, the total fit in orange and the residual of the fit is shown in grey. For these data: $[CH_2OO] = 2.74 \times 10^{11}$ molecule cm^{-3}, $\Delta[CH_2I_2] = -3.20 \times 10^{12}$ molecule cm^{-3}, $[IO] = 1.47 \times 10^{10}$ molecule cm^{-3} and $[IONO_2] = 6.51 \times 10^{9}$ molecule cm^{-3}..... 131

Figure 5.5. Absorbance spectra obtained at 2 ms post-photolysis in the presence of $[NO_2] = 4.0 \times 10^{14}$ molecule cm^{-3} at $T = 298$ K and $p = 100$ Torr. The experimental absorbance is shown in black, CH_2OO is shown in blue, CH_2I_2 in pink, IO in purple, INO_2 in green, the total fit in orange and the residual of the fit is shown in grey. For these data: $[CH_2OO] = 3.42 \times 10^{11}$ molecule cm^{-3}, $\Delta[CH_2I_2] = -2.96 \times 10^{12}$ molecule cm^{-3}, $[IO] = 1.02 \times 10^{10}$ molecule cm^{-3}, $[INO_2] = 1.46 \times 10^{12}$ molecule cm^{-3}..... 132

Figure 5.6. Absorbance spectra obtained at 2 ms post-photolysis in the presence of $[NO_2] = 4.0 \times 10^{14}$ molecule cm^{-3} at $T = 298$ K and $p = 100$ Torr. The experimental absorbance is shown in black, CH_2OO is shown in blue, CH_2I_2 in pink, IO in purple, INO_2 in green, $IONO_2$ in bright blue the total fit in orange and the residual of the fit is shown in grey. For these data: $[CH_2OO] = 3.70 \times 10^{11}$ molecule cm^{-3}, $\Delta[CH_2I_2] = -2.81 \times 10^{12}$ molecule cm^{-3}, $[IO] = 1.74 \times 10^{10}$ molecule cm^{-3}, $[IONO_2] = 5.81 \times 10^{9}$ molecule cm^{-3}, $[INO_2] = 1.57 \times 10^{12}$ molecule cm^{-3}..... 133

Figure 5.7. Comparison between the UV absorption cross-sections for INO_2 reported by IUPAC and Bröske..... 134

Figure 5.8. Absorbance spectra obtained at 2 ms post-photolysis in the presence of $[NO_2] = 4.0 \times 10^{14}$ molecule cm^{-3} at $T = 298$ K and $p = 100$ Torr. The experimental absorbance is shown in black, CH_2OO is shown in blue, CH_2I_2 in pink, IO in purple, INO_2 in green, OIO in light blue, the total fit in orange and the residual of the fit is shown in grey. For these data: $[CH_2OO] = 3.85 \times 10^{11}$ molecule cm^{-3}, $\Delta[CH_2I_2] = -2.87 \times 10^{12}$ molecule cm^{-3}, $[IO] = 7.73 \times 10^{10}$ molecule cm^{-3}, $[INO_2] = 1.55 \times 10^{12}$ molecule cm^{-3}, $[OIO] = 5.33 \times 10^{11}$ molecule cm^{-3}..... 136

Figure 5.9. Absorbance spectra obtained at 2 ms post-photolysis in the presence of $[NO_2] = 4.0 \times 10^{14}$ molecule cm^{-3} at T = 298 K and p = 100 Torr. The experimental absorbance is shown in black, CH_2OO is shown in blue, CH_2I_2 in pink, IO in purple, INO_2 in green, I_2 in yellow, the total fit in orange and the residual of the fit is shown in grey. For these data: $[CH_2OO] = 3.80 \times 10^{11}$ molecule cm^{-3}, $\Delta[CH_2I_2] = -2.88 \times 10^{12}$ molecule cm^{-3}, $[IO] = 6.72 \times 10^{10}$ molecule cm^{-3}, $[INO_2] = 1.54 \times 10^{12}$ molecule cm^{-3}, $[I_2] = 9.10 \times 10^{11}$ molecule cm^{-3}..... 137

Figure 5.10. Absorbance spectra obtained at 2 ms post-photolysis in the presence of $[NO_2] = 4.0 \times 10^{14}$ molecule cm^{-3} at T = 298 K and p = 100 Torr. The experimental absorbance is shown in black, CH_2OO is shown in blue, CH_2I_2 in pink, IO in purple, INO_2 in green, I_2 in yellow, OIO in light blue, the total fit in orange and the residual of the fit is shown in grey. For these data: $[CH_2OO] = 3.81 \times 10^{11}$ molecule cm^{-3}, $\Delta[CH_2I_2] = -2.88 \times 10^{12}$ molecule cm^{-3}, $[IO] = 6.85 \times 10^{10}$ molecule cm^{-3}, $[INO_2] = 1.54 \times 10^{12}$ molecule cm^{-3}, $[I_2] = 8.54 \times 10^{11}$ molecule cm^{-3}, $[OIO] = 4.29 \times 10^{10}$ molecule cm^{-3}..... 138

Figure 5.11. Reference absorption cross-sections for NO_3 between 400 and 700 nm.... 139

Figure 5.12. Absorbance spectra obtained in the absence of NO_2 at 50 Torr and 298 K used to determine the limit of detection for NO_3..... 139

Figure 5.13. Typical observed absorbance (black) and total fit (red) obtained by fitting reference spectra for CH_2I_2 (pink), CH_2OO (blue), IO (purple), I_2 (orange) and INO_2 (green). Data shown were obtained at 0.3 ms after photolysis at p = 25 Torr and T = 298 K, with $[CH_2I_2] = 5.9 \times 10^{13}$ molecule cm^{-3}, $[O_2] = 4.0 \times 10^{17}$ molecule cm^{-3}, and $[NO_2] = 4.0 \times 10^{14}$ molecule cm^{-3}. The fit gave $\Delta[CH_2I_2] = -2.9 \times 10^{12}$ molecule cm^{-3}, $[CH_2OO] = 1.5 \times 10^{12}$ molecule cm^{-3}, $[IO] = 2.6 \times 10^{11}$ molecule cm^{-3}, $[I_2] = 0$ and $[INO_2] = 9.1 \times 10^{11}$ molecule cm^{-3}..... 140

Figure 5.14. Typical observed absorbance (black) and total fit (red) obtained by fitting reference spectra for CH_2I_2 (pink), CH_2OO (blue), IO (purple), I_2 (orange) and INO_2 (green). Data shown were obtained at 2 ms after photolysis at p = 25 Torr and T = 298 K, with $[CH_2I_2] = 5.9 \times 10^{13}$ molecule cm^{-3}, $[O_2] = 4.0 \times 10^{17}$ molecule cm^{-3}, and $[NO_2] = 4.0 \times 10^{14}$ molecule cm^{-3}. The fit gave $\Delta[CH_2I_2] = -3.0 \times 10^{12}$ molecule cm^{-3}, $[CH_2OO] = 4.7 \times 10^{11}$ molecule cm^{-3}, $[IO] = 6.4 \times 10^{10}$ molecule cm^{-3}, $[I_2] = 6.5 \times 10^{11}$ molecule cm^{-3} and $[INO_2] = 1.8 \times 10^{12}$ molecule cm^{-3}..... 141

Figure 5.15. Typical observed absorbance (black) and total fit (red) obtained by fitting reference spectra for CH_2I_2 (pink), CH_2OO (blue), IO (purple), I_2 (orange) and INO_2 (green). Data shown were obtained at 4 ms after photolysis at p = 25 Torr and T = 298 K, with $[CH_2I_2] = 5.9 \times 10^{13}$ molecule cm^{-3}, $[O_2] = 4.0 \times 10^{17}$ molecule cm^{-3}, and $[NO_2] = 4.0 \times 10^{14}$ molecule cm^{-3}. The fit gave $\Delta[CH_2I_2] = -3.1 \times 10^{12}$ molecule cm^{-3}, $[CH_2OO] = 1.7 \times 10^{11}$ molecule cm^{-3}, $[IO] = 6.5 \times 10^{9}$ molecule cm^{-3}, $[I_2] = 1.3 \times 10^{12}$ molecule cm^{-3} and $[INO_2] = 2.2 \times 10^{12}$ molecule cm^{-3}..... 141

Figure 5.16. Typical concentration-time profiles for a) CH_2OO, b) IO, c) INO_2 and d) I_2 obtained at p = 100 Torr and T = 298 K, with $[NO_2] = 9.8 \times 10^{14}$ molecule cm^{-3}..... 142

Figure 5.17. Concentration-time profile for IO at 298 K and 100 Torr, for $[NO_2]$ = 0 (black), $[NO_2] = 9.0 \times 10^{13}$ molecule cm^{-3} (pink), $[NO_2] = 1.5 \times 10^{14}$ molecule cm^{-3} (navy) and $[NO_2] = 6.5 \times 10^{14}$ molecule cm^{-3} (red), for an experiment with $[CH_2I_2] = 5.5 \times 10^{13}$ molecule cm^{-3}..... 143

Figure 5.18. Concentration-time profile for INO_2 at 298 K and 100 Torr for $[NO_2] = 9.0 \times 10^{13}$ molecule cm^{-3} (pink), $[NO_2] = 5.0 \times 10^{14}$ molecule cm^{-3} (green) and $[NO_2] = 1.1 \times 10^{15}$ molecule cm^{-3} (blue), for an experiment with $[CH_2I_2] = 5.5 \times 10^{13}$ molecule cm^{-3}..... 144

Figure 5.19. Concentration – time profiles showing the CH_2OO decay, in the presence of NO_2, at p = 100 Torr and T = 298 K. Solid lines represent an unweighted fit to Equation 5.1 convoluted with an instrument response function. For $[NO_2] = 9.0 \times 10^{13}$ molecule cm^{-3}, the fit gave $[CH_2OO]_0 = (1.50 \pm 0.13) \times 10^{12}$ molecule cm^{-3} and $k' = (666 \pm 18)$ s^{-1}; for $[NO_2] = 3.3 \times 10^{14}$ molecule cm^{-3}, the fit gave $[CH_2OO]_0 = (1.38 \pm 0.17) \times 10^{12}$ molecule cm^{-3} and $k' = (885 \pm 27)$ s^{-1}; for $[NO_2] = 6.5 \times 10^{14}$ molecule cm^{-3}, the fit gave $[CH_2OO]_0 = (1.37 \pm 0.24) \times 10^{12}$ molecule cm^{-3} and $k' = (1271 \pm 44)$ s^{-1}; and for $[NO_2] = 1.1 \times 10^{15}$ molecule cm^{-3}, the fit gave $[CH_2OO]_0 = (1.55 \pm 0.40) \times 10^{12}$ molecule cm^{-3} and $k' = (1853 \pm 70)$ s^{-1}. The IRF parameters were: $t_c = -(1.05 \pm 0.13) \times 10^{-5}$ s, $w = (4.05 \pm 0.90) \times 10^{-5}$ s. Uncertainties are 1σ..... 145

Figure 5.20. Bimolecular plot for the reaction of $CH_2OO + NO_2$ at 298 K and 100 Torr obtained by plotting the observed rate coefficient *vs* $[NO_2]$ where the red line represents an unweighted linear fit to the data. The slope of the fit is the bimolecular rate coefficient of $k_{5.1} = (1.24 \pm 0.07) \times 10^{-12}$ cm^{-3} $molecule^{-1}$ s^{-1} with an intercept of (531 ± 35) s^{-1}. Uncertainties are 1σ..... 146

Figure 5.21. Comparison of fits to the first-order equation (solid red line) and the mixed-order equation (dashed blue line) for CH_2OO in the presence of $[NO_2] = 6.5 \times 10^{14}$ molecule cm^{-3} at 100 Torr and 298 K. The solid red line gave: $t_c = -(1.05 \pm 0.13) \times 10^{-5}$ s, $w = (4.05 \pm 0.90) \times 10^{-5}$ s, $[CH_2OO]_0 = (1.37 \pm 0.24) \times 10^{12}$ molecule cm^{-3} and $k' = (1271 \pm 44)$ s^{-1}. The dashed blue line gave: $t_c = -(1.18 \pm 0.58) \times 10^{-5}$ s, $w = (3.27 \pm 0.32) \times 10^{-5}$ s, $[CH_2OO]_0 = (1.39 \pm 0.29) \times 10^{12}$ molecule cm^{-3}, $k'' = (9.99 \pm 0.25) \times 10^{11}$ cm^3 $molecule^{-1}$ s^{-1} and $k' = (1198 \pm 49)$ s^{-1}. Uncertainties are 1σ..... 147

Figure 5.22. Dependence of k' on $[NO_2]$ at T = 298 K and p = 100 Torr obtained for a first-order fit (solid red line) and mixed-order fit (solid blue line). The fits gave: $k_{5.1} = (1.24 \pm 0.07) \times 10^{-12}$ cm^3 $molecule^{-1}$ s^{-1} and $k_x = (531 \pm 35)$ s^{-1} for the first-order fit and $k_{5.1} = (1.30 \pm 0.07) \times 10^{-12}$ cm^3 $molecule^{-1}$ s^{-1} and $k_x = (412 \pm 38)$ s^{-1} for the mixed-order fit. Uncertainties are 1σ..... 148

Figure 5.23. A plot of $k_{5.1}$ as a function of pressure, the plot includes the results obtained in this work (black), the results of Stone *et al*. (blue), Luo *et al*. (green), Qiu and Tonokura (orange) and Welz *et al*. (red). Error bars for this work represent a combination of the statistical error and the systematic errors resulting from uncertainties in gas flow rates and in the concentration of NO_2..... 149

Figure 5.24. Pseudo-first-order rate coefficients as a function of NO_2 concentration for experiments carried out at temperatures between 242 and 353 K, where the solid lines represent an unweighted linear fit to the data..... 150

Figure 5.25. Left: Pseudo-first-order losses for CH_2OO as a function of NO_2 concentration for experiments carried out at 242 K. Right: Pseudo-first-order losses after the k_x values for each data set have been subtracted. The red line represents an unweighted linear fit to the data. 25 Torr (black): $k_{5.1} = (1.96 \pm 0.27) \times 10^{-12}$ cm^3 molecule^{-1} s^{-1}, $k_x = (981 \pm 160)$ s^{-1}, 50 Torr (pink): $k_{5.1} = (1.95 \pm 0.14) \times 10^{-12}$ cm^3 molecule^{-1} s^{-1}, $k_x = (787 \pm 76)$ s^{-1}, 200 Torr (blue): $k_{5.1} = (2.03 \pm 0.24) \times 10^{-12}$ cm^3 molecule^{-1} s^{-1}, $k_x = (605 \pm 141)$ s^{-1}, combined data: $k_{5.1} = (1.98 \pm 0.11) \times 10^{-12}$ cm^3 molecule^{-1} s^{-1}, $k_x = (-4 \pm 63)$ s^{-1}. Uncertainties are 1σ..... 151

Figure 5.26. Left: Pseudo-first-order losses for CH_2OO as a function of NO_2 concentration for experiments carried out at 254 K. Right: Pseudo-first-order losses after the k_x values for each data set have been subtracted. The red line represents an unweighted linear fit to the data. 25 Torr (black): $k_{5.1} = (1.65 \pm 0.17) \times 10^{-12}$ cm^3 molecule^{-1} s^{-1}, $k_x = (650 \pm 138)$ s^{-1}, 50 Torr (pink): $k_{5.1} = (1.70 \pm 0.10) \times 10^{-12}$ cm^3 molecule^{-1} s^{-1}, $k_x = (209 \pm 78)$ s^{-1}, 200 Torr (blue): $k_{5.1} = (1.75 \pm 0.10) \times 10^{-12}$ cm^3 molecule^{-1} s^{-1}, $k_x = (620 \pm 49)$ s^{-1}, combined data: $k_{5.1} = (1.66 \pm 0.06) \times 10^{-12}$ cm^3 molecule^{-1} s^{-1}, $k_x = (17 \pm 46)$ s^{-1}. Uncertainties are 1σ..... 151

Figure 5.27. A plot of the bimolecular rate coefficients for $CH_2OO + NO_2$ as a function of temperature for the results obtained in this work at pressures between 25 and 200 Torr and temperatures between 242 and 353 K. Errors represent a combination of the statistical error and the systematic errors resulting from uncertainties in gas flow rates and in the concentration of NO_2. The blue line represents a fit to the equation $k_{5.1} = ((1.07 \pm 0.02) \times 10^{-12}) \times (T/298)^{-2.9 \pm 0.2}$ cm^3 molecule^{-1} s^{-1} with $R^2 = 0.97$ and the red line represents a fit to the equation $k_{5.1} = ((7.71 \pm 2.08) \times 10^{-14}) \times exp(-784/T)$ cm^3 molecule^{-1} s^{-1} with $R^2 = 0.96$..... 153

Figure 5.28. A plot of $k_{5.1}$ as a function of temperature for the results obtained in this work and the theoretical results obtained in the work of Vereecken and Nguyen using the equation $k = 1.15 \times 10^{-11} exp(-298/T)$ cm^{-3} molecule^{-1} s^{-1}..... 154

Figure 5.29. Simplified potential energy surface for the reaction between CH_2OO + NO_2 based on the results reported by Vereecken and Nguyen. Solid lines and values in black show the surface reported by Vereecken and Nguyen. Dashed lines and values in red show the result obtained by fitting the barrier heights for TS1 and TS2 to the experimental observations made in this work using MESMER..... 155

Figure 5.30. Comparison of MESMER fit results and observed values for $k_{5.1}$. The best fit to the trend is given by $k_{5.1,MESMER} = (0.34 \pm 0.03) \times k_{5.1,experimental} + (6.90 \pm 0.45) \times 10^{-13}$ cm^3 molecule^{-1} s^{-1} ($r^2 = 0.87$) and is shown by the solid blue line. The 1:1 line is shown by the solid red line..... 156

Figure 5.31. k_{fit} / $k_{5.1}[NO_2]$ *vs* $k_{adduct\text{-}HCHO}$, where $[NO_2]$ is equal to either 1×10^{14} molecule cm^{-3} (black) or 1.5×10^{15} molecule cm^{-3} (blue). The red line represents a ratio of 0.67, which indicates the point where HCHO formation from the adduct is fast enough to give the correct CH_2OO + NO_2 kinetics from observations of HCHO..... 159

Chapter 6

Figure 6.1. Observed absorbance (black), total fit (orange) and individual contributions of CH_2OO, CH_2I_2 and IO obtained by performing a least squares fit of reference cross-sections to the observed absorbance at $t = 1$ ms after photolysis at $p = 760$ Torr, $T = 298$ K, and $[CH_2I_2]_0 = 4.1 \times 10^{13}$ molecule cm^{-3}. $[CH_2OO]_t = 6.4 \times 10^{11}$ molecule cm^{-3}, $\Delta[CH_2I_2]_t = - 3.8 \times 10^{12}$ molecule cm^{-3} and $[IO]_t = 7.3 \times 10^{11}$ molecule cm^{-3}..... 167

Figure 6.2. Concentration-time profile for CH_2I_2 for an experiment at 760 Torr and 298 K. For these data, $[H_2O] = 0$, $[CH_2I_2] = 4.1 \times 10^{13}$ molecule cm^{-3} and $\Delta[CH_2I_2] = -3.5 \times 10^{12}$ molecule cm^{-3}..... 168

Figure 6.3. Concentration-time profile for IO for an experiment at 760 Torr and 298 K. For these data, $[H_2O] = 0$ and $[CH_2I_2] = 4.1 \times 10^{13}$ molecule cm^{-3}..... 168

Figure 6.4. Concentration – time profiles showing the CH_2OO decay, in the presence and absence of water vapour, at p = 760 Torr and T = 298 K. Solid lines represent an unweighted fit to Equation 6.1 convoluted with the instrument response function. For $[H_2O] = 0$, the fit gave $[CH_2OO]_0 = 8.3 \times 10^{11}$ molecule cm^{-3} and $k' = (313 \pm 7)$ s^{-1}; for $[H_2O] = 2.0 \times 10^{17}$ molecule cm^{-3}, the fit gave $[CH_2OO]_0 = 6.6 \times 10^{11}$ molecule cm^{-3} and $k' = (1247 \pm 37)$ s^{-1}; for $[H_2O] = 3.9 \times 10^{17}$ molecule cm^{-3}, the fit gave $[CH_2OO]_0 = 5.8 \times 10^{11}$ molecule cm^{-3} and $k' = (2669 \pm 120)$ s^{-1} and for $[H_2O] = 4.4 \times 10^{17}$ molecule cm^{-3}, the fit gave $[CH_2OO]_0 = 5.7 \times 10^{11}$ molecule cm^{-3} and $k' = (3722 \pm 245)$ s^{-1}. Instrument response parameters were: $t_c = -(8.80 \pm 0.32) \times 10^{-5}$ s and $w = (2.85 \pm 0.45) \times 10^{-5}$ s..... 169

Figure 6.5. Comparison between a first-order fit (red) and mixed-order fit (blue) for data at 324 K and 760 Torr. The first-order fit gave: k' = (728 ± 14) s^{-1}, $[CH_2OO]_0$ = (7.05 ± 0.07) × 10^{11} molecule cm^{-3}, t_c = – (8.80 ± 0.32) × 10^{-5} s and w = (2.85 ± 0.45) × 10^{-5} s. The mixed-order fit gave: k' = (703 ± 10) s^{-1}, k'' = (9.18 ± 0.33) × 10^{-11} cm^3 $molecule^{-1}$ s^{-1}, $[CH_2OO]_0$ = (7.20 ± 0.22) × 10^{11} molecule cm^{-3}, t_c = – (1.10 ± 0.13) × 10^{-4} s and w = (3.30 ± 0.75) × 10^{-5} s..... 170

Figure 6.6. Pseudo-first-order rate coefficients as a function of water monomer concentration for experiments carried out at 298 K. The solid line represents an unweighted fit to Equation 6.8. The error bars represent the error in the exponential fit to Equation 6.1. The fit gave $k_{6.2}K_{eq}$ = (1.69 ± 0.07) × 10^{-32} cm^6 $molecule^{-2}$ s^{-1} and k_x = (51 ± 54) s^{-1}..... 171

Figure 6.7. Pseudo-first-order rate coefficients as a function of water dimer concentration for experiments carried out at 298 K. The solid line represents an unweighted fit to Equation 6.4. The error bars represent the error in the exponential fit to Equation 6.1. The fit gave $k_{6.2}$ = (8.09 ± 0.63) × 10^{-12} cm^3 $molecule^{-1}$ s^{-1} and k_x = (46 ± 148) s^{-1}..... 172

Figure 6.8. Pseudo-first-order rate coefficients as a function of water monomer concentration for experiments carried out at 760 Torr and temperatures between 262 and 353 K. The solid lines represent an unweighted fit to Equation 6.2, with $k_{6.3}$ set to zero. The error bars represent the error in the exponential fit to Equation 6.1. The inset shows data from experiments carried out at 262 K for clarity..... 175

Figure 6.9. Experimental (a and b) and theoretical (c) results obtained by Wu *et al*. The solid lines in (a) represent fits to Equation 6.2 and the solid lines in (b) represent fits to Equation 6.11..... 177

Figure 6.10. Dependence of $(k'-k_x)[H_2O]^{-2}$ on $[H_2O]$ for data obtained in this work at a) 262 K, b) 298 K and c) 353 K. The blue dashed lines represent Equation 6.11, where $k_{6.1}$, $k_{6.2}$ and $k_{6.3}$ were obtained from the work of Wu *et al*. Results at all other temperatures investigated in this work are shown in Appendix 8..... 178

Figure 6.11. $k_{6.1}$ as a function of temperature. The fit to results obtained in this work are shown by the solid black line, with uncertainties determined from a combination of the statistical error and the systematic errors resulting from uncertainties in gas flow rates and in the concentration of $[H_2O]$ shown by the shaded region. Stars represent the temperatures at which measurements were made. Results from previous studies are also included, where filled circles represent experimentally measured rate coefficients, hollow circles represent experimentally determined upper limits, and triangles represent rate coefficients calculated from theory. The solid grey line shows the data reported by Wu *et al.*, with the dashed grey line showing the extrapolation of the data reported by Wu *et al.* over the temperature range investigated in this work. The coral and light blue dashed lines are the parameterisations calculated by Lin *et al*. and Long *et al.*, respectively..... 179

Figure 6.12. $k_{6.2}K_{eq}$ as a function of temperature obtained in this work. The fit to results obtained in this work are shown by the solid black line, with uncertainties determined from a combination of the statistical error and the systematic errors resulting from uncertainties in gas flow rates and in the concentration of [H_2O] shown by the shaded region. Stars represent the temperatures at which measurements were made. The solid grey line shows the data reported by Wu *et al.*, with the dashed grey line showing the extrapolation of the data reported by Wu *et al.* over the temperature range investigated in this work. The red solid line represents a fit to the data reported by Smith *et al.*, with the dashed red line showing the extrapolation of the data reported by Smith *et al.* over the temperature range investigated in this work. The blue dotted line represents the current IUPAC recommendation, which is based on the data reported by Smith *et al*..... 181

Figure 6.13. Pseudo-first-order losses as a function of H_2O concentration for experiments at a) 262K, b) 298 K and c)353 K. Black points represent the experimental data, the green and blue solid lines represent losses due to reaction with the water monomer and the water dimer and the solid red line represents the total loss. The results of Wu *et al.* are also included in the plot, where the orange, pink and grey dashed lines represent reactions with the water monomer, dimer and trimer, and the purple dashed line represents the total loss. The light blue dotted line on b) represents [H_2O] = 4.8×10^{17} molecule cm^{-3}, the point at which Wu *et al.* report the reaction with the water trimer becomes significant at 298 K..... 183

Figure 6.14. Schematic potential energy surface for the reactions of CH_2OO with H_2O (blue) and $(H_2O)_2$ (red). PRC = pre-reaction complex, TS = transition state, HMHP = hydroxymethyl hydroperoxide..... 186

Chapter 7

Figure 7.1. Photo-ionisation spectrum for the *m/z* = 60 product following the reaction of CH_3CHI_2 + O_2 in the presence (black solid circles) and absence (open circles) of water. The addition of water preferentially removes signal corresponding to the *anti*-conformer (between 9.3 and 9.4 eV)..... 193

Figure 7.2. Plots outlining how the experimental absorbance evolves as the reaction progresses (shown for 1 ms, 2 ms, and 3 ms after photolysis). Observed absorbance (black), total fit (orange) and the individual contributions from *syn*-CH_3CHOO (blue), *anti*-CH_3CHOO (green), CH_3CHI_2 (red), and IO (purple)..... 198

Figure 7.3. Concentration-time profile for *syn*-CH_3CHOO at 298 K and 50 Torr. [CH_3CHI_2] = 1.9×10^{13} molecule cm^{-3}, [SO_2] = 3.01×10^{13} molecule cm^{-3}..... 199

Figure 7.4. Concentration-time profile for *anti*-CH_3CHOO at 298 K and 50 Torr. [CH_3CHI_2] = 1.9×10^{13} molecule cm^{-3}, [SO_2] = 3.01×10^{13} molecule cm^{-3}..... 199

Figure 7.5. Concentration-time profile for CH_3CHI_2 at 298 K and 50 Torr which exhibits a negative absorbance owing to depletion on photolysis. [CH_3CHI_2] = 1.9×10^{13} molecule cm^{-3}, [SO_2] = 3.01×10^{13} molecule cm^{-3}..... 200

Figure 7.6. Concentration-time profile for IO at 298 K and 50 Torr. $[CH_3CHI_2] = 1.9 \times 10^{13}$ molecule cm^{-3}, $[SO_2] = 3.01 \times 10^{13}$ molecule cm^{-3}..... 200

Figure 7.7. A plot of *syn*-$[CH_3CHOO]$ as a function of time for experiments at 298 K and 50 Torr, for $[CH_3CHI_2] = 1.9 \times 10^{13}$ molecule cm^{-3} and $[SO_2] = 3.01 \times 10^{13}$ molecule cm^{-3}. $k' = (1586 \pm 89)$ s^{-1}, $w = (4.09 \pm 0.86) \times 10^{-5}$ s, $t_c = -(1.53 \pm 0.05) \times 10^{-4}$ s, $[CH_3CHOO]_0 = (8.13 \pm 0.33) \times 10^{11}$ molecule cm^{-3}. The solid red line represents a fit to Equation 7.1 convoluted with the IRF. Uncertainties are 1σ..... 201

Figure 7.8. A plot of the observed rate coefficient k' as a function of $[SO_2]$ for *syn*-$[CH_3CHOO]$ at 298 K and 50 Torr, where the solid line represents an unweighted linear fit to the data, with a gradient of $(3.59 \pm 0.12) \times 10^{-11}$ cm^3 $molecule^{-1}$ s^{-1} and intercept of (401 ± 13) s^{-1} for $[CH_3CHI_2] = 1.9 \times 10^{13}$ molecule cm^{-3}. Uncertainties are 1σ..... 202

Figure 7.9. Example plots outlining how the baseline correction was applied to the *anti*-data. The gradient $-(8.1 \pm 0.4) \times 10^{12}$ molecule cm^{-3} s^{-1} and intercept $-(3.5 \pm 0.2) \times 10^{10}$ molecule cm^{-3} were subtracted from the overall *anti*-signal..... 203

Figure 7.10. A plot of *anti*-$[CH_3CHOO]$ as a function of time for $[SO_2] = 9.10 \times 10^{12}$ molecule cm^{-3} and $[CH_3CHI_2] = 1.9 \times 10^{13}$ molecule cm^{-3} at 298 K and 50 Torr. The black points represent the data before the baseline correction was applied and the red points represent the data after the baseline correction was applied..... 204

Figure 7.11. A plot of *anti*-$[CH_3CHOO]$ as a function of time for $[SO_2] = 9.10 \times 10^{12}$ molecule cm^{-3} and $[CH_3CHI_2] = 1.9 \times 10^{13}$ molecule cm^{-3} at 298 K and 50 Torr, after the baseline correction was applied. $k' = (1827 \pm 165)$ s^{-1}, *anti*-$[CH_3CHOO]_0 = (1.83 \pm 0.28) \times 10^{11}$ molecule cm^{-3}. Uncertainties are 1σ..... 204

Figure 7.12. A plot of the observed rate coefficient, k', as a function of SO_2 concentration for *anti*-CH_3CHOO at 298 K and 50 Torr, where the black line represents an unweighted linear fit to the data, giving a gradient of $(6.11 \pm 2.64) \times 10^{-11}$ cm^3 $molecule^{-1}$ s^{-1} and intercept of (779 ± 336) s^{-1}. Uncertainties are 1σ..... 205

Figure 7.13. Observed absorbance (black), total fit (orange), and the individual contributions from *syn*-CH_3CHOO, (blue) *anti*-CH_3CHOO, (green) CH_3CHI_2, (red) and IO (purple) determined by fitting reference spectra to the observed absorbance using the Beer-Lambert law. For these data, $T = 298$ K, $p = 50$ Torr, $t = 1$, 3 and 4 ms post-photolysis, $[CH_3CHI_2] = 1.7 \times 10^{13}$ molecule cm^{-3}..... 206

Figure 7.14. Concentration-time profile for *anti*-CH_3CHOO used to demonstrate a low signal for the *anti*-conformer. $[CH_3CHI_2] = 1.7 \times 10^{13}$ molecule cm^{-3} and $[SO_2] = 0$, at 298 K and 50 Torr..... 207

Figure 7.15. Concentration-time profile for CH_3CHI_2 following the photolysis of CH_3CHI_2. $[CH_3CHI_2] = 1.7 \times 10^{13}$ molecule cm^{-3} and $[SO_2] = 0$, at 298 K and 50 Torr..... 208

Figure 7.16. Concentration-time profile for CH_3CHI_2, where the black line represents the experimentally observed precursor concentration and the blue line represents the pre- and post-photolysis precursor concentrations that have been fixed. For these data, the change in concentration of CH_3CHI_2 was fixed to -1.92×10^{12} molecule cm^{-3}..... 208

Figure 7.17. Comparison of concentration-time profiles for *anti*-CH_3CHOO before the precursor concentration was fixed (a) and after the precursor concentration had been fixed (b) where the red line on the right plot represents a fit to Equation 7.1..... 209

Figure 7.18. A comparison of the bimolecular plots obtained for *anti*-CH_3CHOO + SO_2 at 298 K and 50 Torr for data before the precursor concentration was fixed (black) and after the precursor concentration was fixed (pink). The black line represents an unweighted linear fit to the data before the precursor was fixed, with a gradient of $(6.11 \pm 2.64) \times 10^{-10}$ cm^3 $molecule^{-1}$ s^{-1} and intercept of (779 ± 336) s^{-1} and the pink line represents an unweighted linear fit to the data, with a gradient of $(1.17 \pm 0.10) \times 10^{-10}$ cm^3 $molecule^{-1}$ s^{-1} and intercept of (1387 ± 153) s^{-1}. Uncertainties are 1σ..... 210

Figure 7.19. Comparison of the bimolecular plots for the reaction of *syn*-CH_3CHOO with SO_2 before and after the precursor had been fixed. The black points represent the values before the precursor was fixed, with a gradient of $(3.59 \pm 0.12) \times 10^{-11}$ cm^3 $molecule^{-1}$ s^{-1} and intercept of (401 ± 13) s^{-1} and the pink points represent the data after the precursor had been fixed, with a gradient of $(1.94 \pm 0.17) \times 10^{-11}$ cm^3 $molecule^{-1}$ s^{-1} and intercept of (387 ± 22) s^{-1}. Uncertainties are 1σ..... 211

Figure 7.20. Absorption signals obtained by Sheps *et al.*, where the data was averaged between 320 and 400 nm. The thick black line shows a fit to the two components in the model, which are outlined by the blue and pink shaded areas..... 212

Figure 7.21. Biexponential decay for an experiment at 298 K and 50 Torr for (a) $[SO_2] = 1.00 \times 10^{13}$ molecule cm^{-3} and (b) $[SO_2] = 2.00 \times 10^{13}$ molecule cm^{-3}, where the red line represents a fit to Equation 7.2 convoluted with the IRF. The fit gave: (a) $A_{0,syn} = (3.8 \pm 2.5) \times 10^{-6}$, $k'_{syn} = (629 \pm 65)$ s^{-1}, $A_{0,anti} = (4.6 \pm 0.8) \times 10^{-6}$, $k'_{anti} = (3432 \pm 771)$ s^{-1}, (b) $A_{0,syn} = (3.3 \pm 0.9) \times 10^{-6}$, $k'_{syn} = (788 \pm 135)$ s^{-1}, $A_{0,anti} = (4.6 \pm 3.2) \times 10^{-6}$, $k'_{anti} = (3706 \pm 838)$ s^{-1}. Uncertainties are 1σ..... 213

Figure 7.22. Bimolecular plot for *anti*-CH_3CHOO obtained after averaging the absorbance data between 340 and 400 nm. The blue line represents an unweighted linear fit to the data, with a gradient of $(1.21 \pm 0.23) \times 10^{-10}$ cm^3 $molecule^{-1}$ s^{-1} and intercept of (774 ± 402) s^{-1}. Uncertainties are 1σ..... 213

Figure 7.23. A comparison of the bimolecular plots obtained for *anti*-CH_3CHOO + SO_2 at 298 K and 50 Torr for data when the baseline correction was applied (black), after the precursor concentration was fixed (pink) and from averaging the absorbance data between 340 and 400 nm (blue). The black line represents an unweighted linear fit to the data before the precursor was fixed, with a gradient of $(6.11 \pm 2.64) \times 10^{-10}$ cm^3 $molecule^{-1}$ s^{-1} and intercept of (779 ± 336) s^{-1}, the pink line represents an unweighted linear fit to the data, with a gradient of $(1.17 \pm 0.10) \times 10^{-10}$ cm^3 $molecule^{-1}$ s^{-1} and intercept of (1387 ± 153) s^{-1} and the blue line represents an unweighted linear fit to the data, with a gradient of $(1.21 \pm 0.23) \times 10^{-10}$ cm^3 $molecule^{-1}$ s^{-1} and intercept of (774 ± 402) s^{-1}. Uncertainties are 1σ..... 214

Figure 7.24. Observed absorbance (black), total fit (orange), and the individual contributions from *syn*-CH_3CHOO (blue), *anti*-CH_3CHOO (green), CH_3CHI_2 (red), and IO (purple) determined by fitting reference spectra to the observed absorbance using the Beer-Lambert law. For these data, T = 353 K, p = 10 Torr, t = 1, 2 and 4 ms post-photolysis, $[CH_3CHI_2] = 6.0 \times 10^{13}$ molecule cm^{-3}..... 216

Figure 7.25. Concentration-time profile for CH_3CHI_2. T = 353 K, p = 10 Torr, $[CH_3CHI_2]_0 = 6.0 \times 10^{13}$ molecule cm^{-3} and $\Delta[CH_3CHI_2] = 5.5 \times 10^{12}$ molecule cm^{-3}..... 217

Figure 7.26. Concentration-time profile for CH_3CHI_2. T = 298 K, p = 10 Torr, $[CH_3CHI_2]_0 = 4.1 \times 10^{13}$ molecule cm^{-3} and $\Delta[CH_3CHI_2] = 2.8 \times 10^{12}$ molecule cm^{-3}..... 217

Figure 7.27. Time profiles for (a) *syn*-CH_3CHOO, (b) *anti*-CH_3CHOO and (c) the averaged absorbance signal between 340 and 400 nm for experiments at T = 289 K and p = 10 Torr. Solid red lines represent fits to Equation 7.1 convoluted with the IRF for (a) and (b) and Equation 7.2 convoluted with the IRF for (c). The fits to Equation 7.1 gave: (a) $k'_{syn} = (674 \pm 11)$ s^{-1}, (b) $k'_{anti} = (1532 \pm 63)$ s^{-1} and fits to Equation 7.2 gave: (c) $k'_{syn} = (708 \pm 66)$ s^{-1}, and $k'_{anti} = (2639 \pm 1135)$ s^{-1}..... 218

Figure 7.28. Pseudo-first-order rate coefficients as a function of SO_2 concentration obtained from experiments at T = 289 K and p = 10 Torr for (a) *syn*-CH_3CHOO and (b) *anti*-CH_3CHOO for the regular analysis (black) and the analysis where absorbance data is averaged between 340 – 400 nm (purple). Solid lines represent an unweighted linear fit to the data. For *syn*-CH_3CHOO, the regular analysis gave: $k_{7.1} = (3.02 \pm 0.12) \times 10^{-11}$ cm^3 $molecule^{-1}$ s^{-1} and $k_x = (332 \pm 21)$ s^{-1} and the averaging analysis gave: $k_{7.1} = (2.90 \pm 0.24) \times 10^{-11}$ cm^3 $molecule^{-1}$ s^{-1} and $k_x = (336 \pm 42)$ s^{-1}. For *anti*-CH_3CHOO, the regular analysis gave: $k_{7.2} = (1.04 \pm 0.08) \times 10^{-10}$ cm^3 $molecule^{-1}$ s^{-1} and $k_x = (721 \pm 135)$ s^{-1} and the averaging analysis gave: $k_{7.2} = (1.25 \pm 0.24) \times 10^{-10}$ cm^3 $molecule^{-1}$ s^{-1} and $k_x = (1205 \pm 157)$ s^{-1}..... 219

Figure 7.29. Observed concentration-time profiles for a) *syn*-CH_3CHOO and b) *anti*-CH_3CHOO. For these data, T = 298 K, p = 50 Torr, $[SO_2]$ = 1.1 × 10^{13} molecule cm^{-3} and $[CH_3CHI_2]$ = 2.8 × 10^{13} molecule cm^{-3}. The fits to Equation 7.1 (solid line) gave an initial concentration of (1.31 ± 0.03) × 10^{12} molecule cm^{-3} and k' = (765 ± 15) s^{-1} for *syn*-CH_3CHOO and an initial concentration of (3.39 ± 0.02) × 10^{11} molecule cm^{-3} and k' = (2280 ± 218) s^{-1} for *anti*-CH_3CHOO. Instrument response parameters were: w = (2.99 ± 0.10) × 10^{-5} s and t_c = – (4.80 ± 0.09) × 10^{-5} s for both conformers. Uncertainties are 1σ..... 220

Figure 7.30. Dependence of k' on $[SO_2]$ at T = 298 K and p = 50 Torr for a) *syn*-CH_3CHOO and b) *anti*-CH_3CHOO. Fits to the data gave $k_{7.1}$ = (3.67 ± 0.07) × 10^{-11} cm^3 $molecule^{-1}$ s^{-1}, with an intercept k_x of (326 ± 18) s^{-1}, and $k_{7.2}$ = (1.22 ± 0.10) × 10^{-10} cm^3 $molecule^{-1}$ s^{-1}, with an intercept k_x of (934 ± 70) s^{-1}. Uncertainties are 1σ..... 221

Figure 7.31. Comparison between first-order (solid red lines) and mixed-order (dashed black lines) for typical concentration-time profiles for a) *syn*-CH_3CHOO and b) *anti*-CH_3CHOO. The first-order fit to the *syn*-CH_3CHOO data gave k' = (765 ± 15) s^{-1} and $[CH_3CHOO]_0$ = (1.31 ± 0.03) × 10^{12} molecule cm^{-3} and the mixed-order fit gave k' = (754 ± 15) s^{-1}, k'' = (7.66 ± 0.34) × 10^{-11} cm^3 $molecule^{-1}$ s^{-1} and $[CH_3CHOO]_0$ = (1.35 ± 0.07) × 10^{12} molecule cm^{-3}. The first order fit to the *anti*-CH_3CHOO gave k' = (2280 ± 220) s^{-1} and $[CH_3CHOO]_0$ = (3.39 ± 0.02) × 10^{11} molecule cm^{-3} and the mixed-order fit gave k' = (2147 ± 93) s^{-1}, k'' = (2.55 ± 0.16) × 10^{-10} cm^3 $molecule^{-1}$ s^{-1} and $[CH_3CHOO]_0$ = (3.47 ± 0.04) × 10^{11} molecule cm^{-3}. Uncertainties are 1σ..... 223

Figure 7.32. Dependence of k' on $[SO_2]$ at T = 298 K and p = 50 Torr obtained for first-order fits (solid lines) and mixed-order fits (dashed lines) for a) *syn*-CH_3CHOO and b) *anti*-CH_3CHOO. Fits to the data for *syn*-CH_3CHOO gave $k_{7.1}$ (first-order, blue data) = (3.67 ± 0.07) × 10^{-11} cm^3 $molecule^{-1}$ s^{-1}, with an intercept k_x of (326 ± 18) s^{-1} and $k_{7.1}$ (mixed-order, black data) = (3.58 ± 0.07) × 10^{-11} cm^3 $molecule^{-1}$ s^{-1}, with an intercept k_x of (330 ± 9) s^{-1}. Fits to the data for *anti*-CH_3CHOO gave $k_{7.2}$ (first-order, green data) = (1.22 ± 0.10) × 10^{-10} cm^3 $molecule^{-1}$ s^{-1}, with an intercept k_x of (934 ± 70) s^{-1} and $k_{7.2}$ (mixed-order, black data) = (1.17 ± 0.06) × 10^{-10} cm^3 $molecule^{-1}$ s^{-1}, with an intercept k_x of (974 ± 67) s^{-1}. Uncertainties are 1σ..... 224

Figure 7.33. Schematic potential energy surface for the reaction between CH_3CHOO and SO_2 to produce excited $[CH_3CHOO\text{-}SO_2]$* and the possible reaction pathways following excitation. A further description of the chemical activation mechanism is given in Chapter 2, section 2.2.2.2..... 225

Figure 7.34. Comparison of the fit to Equations 7.3 and 7.4 for data at 298 K and pressures between 10 and 600 Torr. Results from previous studies at ~ 298 K are also shown.[1] [2] [3] [4] The fit result for Equation 7.3 gave: A_{int} = (2.35 ± 0.39) × 10^{-11} cm^3 $molecule^{-1}$ s^{-1}, n_{int} = (0.61 ± 0.79), A_0 = (3.29 ± 1.30) × 10^{-29} cm^3 $molecule^{-1}$ s^{-1}, n_0 = -(9.52 ± 1.78), A_∞ = (4.95 ± 0.51) × 10^{-11} cm^3 $molecule^{-1}$ s^{-1}, n_∞ = -(2.52 ± 0.29) and the fit result for Equation 7.4 gave: A_{int} = (2.39 ± 0.28) × 10^{-11} cm^3 $molecule^{-1}$ s^{-1}, n_{int} = (0.19 ± 0.72), A_0 = (6.07 ± 4.74) × 10^{-29} cm^3 $molecule^{-1}$ s^{-1}, n_0 = -(10.13 ± 1.81), A_∞ = (8.98 ± 7.22) × 10^{-11} cm^3 $molecule^{-1}$ s^{-1}, n_∞ = -(3.34 ± 0.71)..... 226

Figure 7.35. Effects of pressure on $k_{7.1}$ at (a) 298 K and (b) all temperatures studied in this work. Previous reports for $k_{7.1}$ are also shown. Solid lines represent a fit to Equation 7.3. Error bars represent a combination of the statistical error and the systematic errors resulting from uncertainties in gas flow rates and in the concentration of SO_2..... 227

Figure 7.36. The structures of the secondary ozonide (SOZ) and the transition state (TS) formed in the reaction between *syn*-CH_3CHOO and SO_2..... 227

Figure 7.37. The yield of the SOZ and CH_3CHO + SO_3 as a function of pressure, calculated using Equations 7.3 and 7.5-7.7..... 228

Figure 7.38. Comparison of rate coefficients as a function of temperature for a) CH_2OO + SO_2 reported by Manonmani *et al.* and Onel *et al.*, b) *syn*-CH_3CHOO + SO_2 reported by Manonmani *et al.* and the results of this work and c) $(CH_3)_2CHOO$ + SO_2 reported by Manonmani *et al.* and the IUPAC recommended parameterisation. The solid lines represent the experimental temperature range investigated in each study and the dotted lines are an extrapolation of the data to temperatures between 200 and 400 K..... 229

Figure 7.39. Effects of pressure on $k_{7.2}$ at 298 K. The solid line shows the mean value for $k_{7.2}$ at 298 K ((1.15 ± 0.16) × 10^{-10} cm^3 $molecule^{-1}$ s^{-1}). Previous results reported for $k_{7.2}$ are also shown. Error bars represent a combination of the statistical error and the systematic errors resulting from uncertainties in gas flow rates and in the concentration of SO_2..... 231

Figure 7.40. Effect of pressure on $k_{7.2}$ at each temperature, where solid lines represent the average value for the rate coefficient across each temperature. a) T = 242 K, $k_{7.2}$ = (1.12 ± 0.19) × 10^{-10} cm^3 $molecule^{-1}$ s^{-1}; b) T = 254 K, $k_{7.2}$ = (0.98 ± 0.16) × 10^{-10} cm^3 $molecule^{-1}$ s^{-1}; c) T = 273 K, $k_{7.2}$ = (1.47 ± 0.20) × 10^{-10} cm^3 $molecule^{-1}$ s^{-1}; d) T = 298 K, $k_{7.2}$ = (1.15 ± 0.16) × 10^{-10} cm^3 $molecule^{-1}$ s^{-1}; e) T = 318 K, $k_{7.2}$ = (1.23 ± 0.20) × 10^{-10} cm^3 $molecule^{-1}$ s^{-1} and f) T = 353 K, $k_{7.2}$ = (1.16 ± 0.20) × 10^{-10} cm^3 $molecule^{-1}$ s^{-1}..... 232

Figure 7.41. Mean value for $k_{7.2}$ determined at each temperature. The solid line represents the mean value for $k_{7.2}$ over all conditions investigated in this work is $(1.18 \pm 0.21) \times 10^{-10}$ cm^3 molecule^{-1} s^{-1}. Previous results reported for $k_{7.2}$ and rate coefficients calculated using collision theory (k_{col}, red dashed line) and capture theory (k_{capt}, blue dashed line) are also shown. Error bars represent a combination of the statistical error and the systematic errors resulting from uncertainties in gas flow rates and in the concentration of SO_2..... 234

Chapter 8

Figure 8.1. Comparison of rate coefficients used in GEOS-Chem for reactions of CH_2OO with (a) the water monomer and (b) the water dimer at temperatures between 200 and 400 K. Parameterisations are given in Table 8.1..... 241

Figure 8.2. Impacts of changes made in the first set of GEOS-Chem updates, compared to the base model run, on annual mean surface layer concentrations for CH_2OO and several key atmospheric species. The first set of model updates incorporate current IUPAC recommendations for $k_{6.1}$ and $k_{6.2}K_{eq}$, as well as updates to rate coefficients for reactions of CH_2OO with O_3, SO_2, and NO_2 (see Table 8.1 for details)..... 244

Figure 8.3. Impacts of changes made in the second set of GEOS-Chem updates, compared to the results obtained with the first set of updates, on annual mean surface layer concentrations for CH_2OO and several key atmospheric species. The second set of model updates make use of the results obtained in this work for $k_{6.1}$ and $k_{6.2}K_{eq}$ (see Table 8.1 for details)..... 245

Figure 8.4. Temperature profile of the surface layer..... 246

Figure 8.5. Concentrations of a) water monomers, b) water dimers, c) SO_2 and d) NO_2 in the surface layer..... 247

Figure 8.6. Percentage losses of CH_2OO via reaction with a) water monomers and dimers combined, b) water monomers, c) water dimers, d) SO_2 e) NO_2 and f) thermal decomposition..... 248

Figure 8.7. CH_2OO surface and zonal distributions (top panel) and lifetime (bottom panel) for GEOS-Chem simulations using the second set of model updates, which make used of results obtained in this work for $k_{6.1}$ and $k_{6.2}K_{eq}$ (see Table 8.1 for details). The black dotted line represents the tropopause..... 249

Figure 8.8. Percentage losses of *syn*-CH_3CHOO via reaction with a) water monomers b) SO_2 c) NO_2 and d) thermal decomposition..... 250

Figure 8.9. Percentage losses of *anti*-CH_3CHOO via reaction with a) water monomers and dimers combined, b) water monomers, c) water dimers, d) SO_2 e) NO_2 and f) thermal decomposition..... 251

Appendices

Figure A.1. MFC calibration data for MFC 1 (a) – MFC 5 (e). Each fit gave: a) intercept = (157.793 ± 10.469), gradient = (3.231 ± 0.016), R^2 = 0.9998. b) Intercept = - (0.046 ± 0.400), gradient = (0.112 ± 0.006), R^2 = 0.9997. c) Intercept = (14.279 ± 3.512), gradient = (1.025 ± 0.006), R^2 = 0.9997. d) Intercept = (0.114 ± 0.150), gradient = (0.075 ± 0.002), R^2 = 0.9999. e) Intercept = - (154.556 ± 22.194), gradient = (12.085 ± 0.096), R^2 = 0.9994..... 261

Figure A.2. Calibration plot of the relative humidity (RH) measured with the RH probe used for experiments against the RH measured using a dew point hygrometer. The red line represents a linear fit to the data and gave: gradient = 0.801 ± 0.005, intercept = 3.959 ± 0.307 and R2 = 0.999..... 263

Figure A.3. An example plot of the thermocouple position / cm against the measured temperature from the thermocouple / ^{o}C for measurements taken at 328 ^{o}C and 85 Torr. A position of 0 cm corresponds to the end of the cell where the gas enters through an inlet tube..... 264

Figure A.4. A typical profile of $\Delta[CH2I2] \times l$ as a function of time for $[CH_2I_2]_0 = 8.1 \times 10^{13}$ molecule cm^{-3} at 298 K and 50 Torr. The data points at t<0 correspond to pre-photolysis data points..... 268

Figure A.5. Bimolecular plot for the reaction between CH_2OO and NO_2 at 277 K and 50 Torr. The solid line represents an unweighted linear fit and gives $k_{5.1} = (1.31 \pm 0.14) \times 10^{-12}$ cm^3 molecule^{-1} s^{-1} and an intercept of $k_x = (600 \pm 97)$ s^{-1}. Uncertainties are 1σ..... 269

Figure A.6. Bimolecular plot for the reaction between CH_2OO and NO_2 at 298 K and 50 Torr. The solid line represents an unweighted linear fit and gives $k_{5.1} = (1.11 \pm 0.09) \times 10^{-12}$ cm^3 molecule^{-1} s^{-1} and an intercept of $k_x = (324 \pm 82)$ s^{-1}. Uncertainties are 1σ..... 269

Figure A.7. Bimolecular plot for the reaction between CH_2OO and NO_2 at 318 K and 50 Torr. The solid line represents an unweighted linear fit and gives $k_{5.1} = (9.39 \pm 0.96) \times 10^{-13}$ cm^3 molecule^{-1} s^{-1} and an intercept of $k_x = (545 \pm 73)$ s^{-1}. Uncertainties are 1σ..... 270

Figure A.8. Bimolecular plot for the reaction between CH_2OO and NO_2 at 334 K and 50 Torr. The solid line represents an unweighted linear fit and gives $k_{5.1} = (7.66 \pm 0.67) \times 10^{-13}$ cm^3 molecule^{-1} s^{-1} and an intercept of $k_x = (639 \pm 32)$ s^{-1}. Uncertainties are 1σ..... 270

Figure A.9. Bimolecular plot for the reaction between CH_2OO and NO_2 at 353 K and 50 Torr. The solid line represents an unweighted linear fit and gives $k_{5.1} = (5.78 \pm 0.60) \times 10^{-13}$ cm^3 molecule^{-1} s^{-1} and an intercept of $k_x = (521 \pm 25)$ s^{-1}. Uncertainties are 1σ..... 271

Figure A.10. Dependence of $(k'-k_x)[H_2O]^{-2}$ on $[H_2O]$ for data obtained in this work at temperatures between 270 and 343 K. The blue dashed line represents the equation $(k' - k_x)[H_2O]^{-2} = k_{6.1}[H_2O]^{-1} + k_{6.2} + k_{6.3}[H_2O]$, where $k_{6.1}$, $k_{6.2}$ and $k_{6.3}$ were obtained from the work of Wu *et al.* Results at 262, 298 and 353 K are shown in Chapter 6..... 297

Figure A.11. Pseudo-first-order losses as a function of H_2O concentration for experiments at 262 - 353 K. Black points represent the experimental data, the green and blue solid lines represent losses due to reaction with the water monomer and the water dimer and the solid red line represents the total loss. The results of Wu et al. are also included in the plot, where the orange, pink and grey dashed lines represent reactions with the water monomer, dimer and trimer, and the purple dashed line represents the total loss. Comparisons for data at 262, 298 and 353 K are shown in Chapter 6..... 300

Figure A.12. Comparison of the fit to Equations 7.9 and 7.13 for $k_{7.1}$ at T = 242 - 353 K and p = 10 - 600 Torr. Both equations were fit globally to each temperature and pressure investigated. Results from previous studies at ~ 298 K are also shown. The fit result for Equation 7.9 gave: A_{int} = (2.35 ± 0.39) × 10^{-11} cm^3 $molecule^{-1}$ s^{-1}, n_{int} = (0.61 ± 0.79), A_0 = (3.29 ± 1.30) × 10^{-29} cm^3 $molecule^{-1}$ s^{-1}, n_0 = -(9.52 ± 1.78), A_∞ = (4.95 ± 0.51) × 10^{-11} cm^3 $molecule^{-1}$ s^{-1}, n_∞ = -(2.52 ± 0.29) and the fit result for Equation 7.13 gave: A_{int} = (2.39 ± 0.28) × 10^{-11} cm^3 $molecule^{-1}$ s^{-1}, n_{int} = (0.19 ± 0.72), A_0 = (6.07 ± 4.74) × 10^{-29} cm^3 $molecule^{-1}$ s^{-1}, n_0 = -(10.13 ± 1.81), A_∞ = (8.98 ± 7.22) × 10^{-11} cm^3 $molecule^{-1}$ s^{-1}, n_∞ = -(3.34 ± 0.71)..... 306

List of Tables

Chapter 3

Table 3.1. Typical species mixtures used in excimer lasers, the exciplex formed and the corresponding wavelength..... 61

Chapter 4

Table 4.1. Summary of the reactions and rate coefficients used by Howes *et al*. to simulate the data of Chhantyal-Pun *et al*. All rate coefficients were obtained from the report of Chhantyal-Pun *et al*. except the CH_2OO self-reaction which is the IUPAC recommended value..... 100

Table 4.2. Values for the rate coefficient for $CH_2OO + SO_2$ determined in previous experiments, utilising a range of techniques. LFP = laser flash photolysis, PIMS = photo-ionisation mass spectrometry, LIF = laser-induced fluorescence and CRDS = cavity ring down spectroscopy..... 102

Table 4.3. Summary table of the rate coefficients obtained in these experiments for R4.1 at temperatures between 298 and 340 K at 85 Torr..... 114

Table 4.4. Summary of the rate coefficients / 10^{-11} cm^3 $molecule^{-1}$ s^{-1} for the reaction of CH_2OO and SO_2 for temperatures between 223–344 K at 85 Torr where (a) represents the high temperature data obtained as part of this thesis and (b) represents the measurements by Dr Lavinia Onel..... 115

Chapter 5

Table 5.1. Summary table of the previous kinetic data reported for R5.1. LFP = laser flash photolysis, PIMS = photo-ionisation mass spectrometry, LIF = laser-induced fluorescence and IR abs = infrared absorption..... 126

Table 5.2. Calculations of the total iodine species in the system for experiments at $t = 298$ K and $p = 100$ Torr and the comparison between the INO_2 concentrations obtained from fits where the UV absorption cross-sections were obtained from IUPAC and from Bröske..... 135

Table 5.3. Bimolecular rate coefficients obtained for R5.1 at 298 K and pressures between 25 and 300 Torr. The uncertainties represent a combination of the statistical error and the systematic errors resulting from uncertainties in gas flow rates and in the concentration of NO_2..... 148

Table 5.4. Bimolecular rate coefficients for R5.1 obtained in this work at pressures between 25 and 300 Torr and temperatures between 242 and 353 K. The uncertainties represent a combination of the statistical error and the systematic errors resulting from uncertainties in gas flow rates and in the concentration of NO_2..... 152

Chapter 6

Table 6.1. A comparison of the Equilibrium constant, K_{eq}, values reported by Scribano *et al*. and Ruscic *et al.* for water dimer formation at 262, 298 and 353 K, and impacts on calculated water dimer concentrations and pseudo-first-order losses for CH_2OO resulting from reaction with water dimers when described explicitly in terms of water dimer concentrations (i.e. $k' = k_{6.2}[(H_2O)_2]$, using values for $k_{6.2}$ determined at each temperature in this work)..... 174

Table 6.2. Comparison between $k_{6.1}$ values obtained at room temperature in this work and in previous literature. LFP = laser flash photolysis, PIMS = photo-ionisation mass spectrometry, CI-APi-TOF-MS = Chemical ionisation-atmospheric pressure interface-time-of-flight mass spectrometry, RR = relative rate study..... 180

Table 6.3. Comparison between the $k_{6.2}$ values obtained at room temperature in this work and in previous literature. LFP = laser flash photolysis, IfT-LFT = Institute for Tropospheric Research – Laminar Flow Tube, RR = relative rate study. $k_{6.2}K_{eq}$ have been calculated using the K_{eq} values reported by Ruscic *et al*..... 182

Table 6.4. Theoretical calculations of the PES for R6.1 and R6.2 and, where available, calculations of the reaction kinetics. Where multiple reaction pathways for R6.1 and R6.2 were given, the lowest energy pathway was chosen. PRC = pre-reaction complex, TS = transition state, CTST = conventional transition state theory, VTST = variational transition state theory, VPT2 = vibrational second order perturbation theory, MP-CVT/SCT = Multipath variational transition state theory with small-curvature tunneling, CUS = canonical unified statistical theory. [a] Level of theory used to optimise geometries and energies for reactant, PRCs, and products. [b] Level of theory used to optimise geometries and energies for transition state..... 185

Chapter 7

Table 7.1. Summary of literature results for $k_{7.1}$ and $k_{7.2}$. LFP = Laser flash photolysis, PIMS = Photo-ionisation mass spectrometry, UV abs = Ultraviolet absorption..... 195

Table 7.2. Results obtained in this work for $k_{7.1}$ and $k_{7.2}$ at each temperature and pressure..... 235

Chapter 8

Table 8.1. Summary of reactions, products, rate coefficients and percentage losses for CH_2OO reactions used in the three model simulations..... 242

Appendices

Table A.1. A summary table of the results obtained from the temperature calibration experiments..... 265

Table A.2. Experimental data obtained for experiments to investigate the kinetics of CH_2OO and NO_2 between 25 and 200 Torr and 242 and 353 K..... 272
Table A.3. Experimental data obtained in this work. All experiments were carried out at a total pressure of 760 Torr..... 303
Table A.4. Experimental data obtained for experiments to investigate the kinetics of CH_3CHOO and SO_2 between 10 and 600 Torr and 242 and 353 K..... 309

Chapter 1

Introduction

Throughout modern society, poor air quality and climate change have been widely accepted to be important environmental and societal problems. Both air quality and climate change are impacted by atmospheric composition, which is controlled by both the emissions and chemistry of trace species, including nitrogen oxides (NO_x = NO + NO_2), volatile organic compounds (VOCs) and sulfur dioxide (SO_2). Understanding the chemistry that governs each aspect of climate change and air quality is therefore crucial in overcoming today's environmental crisis, allowing for the development of accurate atmospheric models to inform legislative measurements and policies.

1.1 The Earth's Atmosphere and Climate System

The Earth's atmosphere can be divided into distinct vertical layers: the lowest of which is the troposphere, followed by the stratosphere, mesosphere and thermosphere. The position of each layer is shown in Figure 1.1, with each layer being described by its characteristic temperature profile.[1] The temperature throughout Earth's atmosphere varies by less than a factor of 2 but shows a rather complex temperature profile, while the pressure changes by nearly 6 orders of magnitude,[2] but decreases exponentially with increasing altitude.

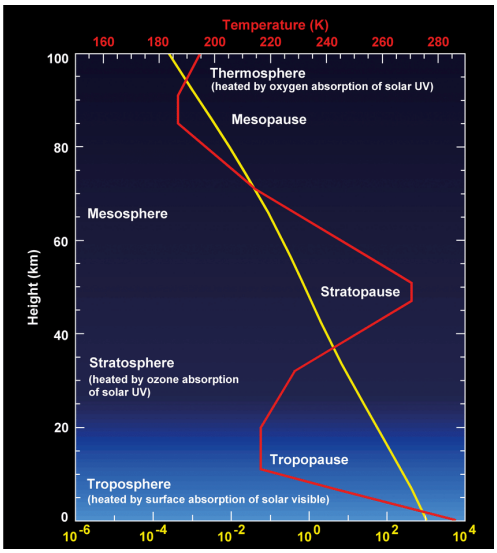

Figure 1.1. Vertical temperature and pressure profile of the Earth's atmosphere ranging from 0 to 100 km in altitude. Copied from reference 3.[3]

The lowest layer of the atmosphere is the troposphere, which extends from the Earth's surface up to the tropopause at an altitude of approximately 15 km (depending on latitude). There is a negative temperature gradient with increasing altitude in the troposphere as its primary heat

source is energy transfer from the Earth's surface. The negative temperature profile promotes the rapid vertical movement of gases throughout the layer, and, with nearly all of the atmospheric water vapour residing within this region, it is where most of the Earth's weather occurs.[1] While the troposphere only extends to 15 km in altitude, it contains ~ 80 % of the atmosphere's mass,[2] and can be divided into distinct sub-layers. The atmospheric boundary layer (ABL) is the lowest region of the troposphere, extending up to approximately 2 km in altitude, and is in direct contact with the Earth's surface. During the day, the ABL is well mixed as a result of direct heat transfer from the Earth's surface to the surface layer, followed by the vertical transfer of heat. The region above the ABL is known as the free troposphere, where the negative temperature gradient is decreased compared to the boundary layer due to less significant interactions with the Earth's surface. The presence of this stable layer above the ABL can prevent further vertical mixing,[4] resulting in pollutants becoming trapped. During the night, the Earth's surface cools down and minimises heat transfer and thus mixing in the boundary layer, reducing its height and confining pollutants to the surface layer.

The region above the troposphere is the stratosphere, which extends to approximately 50 km in altitude. While the pressure continues to decrease throughout this region, the temperature profile changes, with temperature increasing with increasing altitude. This temperature gradient is a result of the absorption of solar ultraviolet (UV) light by molecular oxygen (O_2) and ozone (O_3),[1] in what is known as the Chapman cycle (R1.1-R1.4), resulting in a steady-state concentration of stratospheric ozone.

$$O_2 + h\nu\ (\lambda < 242\ \text{nm}) \rightarrow 2O \qquad \text{(R1.1)}$$

$$O + O_2 + M \rightarrow O_3 + M \qquad \text{(R1.2)}$$

$$O + O_3 \rightarrow 2O_2 \qquad \text{(R1.3)}$$

$$O_3 + h\nu \rightarrow O + O_2 \qquad \text{(R1.4)}$$

The majority of stratospheric ozone resides within the ozone layer, which is essential to human health as it absorbs UV radiation at wavelengths below 290 nm, providing protection from harmful solar UV radiation.[5] There is little mixing in the stratosphere due to the temperature profile, which is a result of the ozone layer, and relatively no scavenging of pollutants by precipitation[1] and therefore large influxes of particles into the stratosphere, such as the eruption of a volcano, may result in layers of particles throughout the stratosphere. The mesosphere is the region above the stratosphere which again, is characterised by a negative temperature gradient, resulting in rapid vertical mixing. The temperature decreases to below 200 K at an altitude of ~ 85 km, which is due to decreasing O_3 concentrations with increasing altitude. Above the mesosphere is the thermosphere, a region where the positive temperature

gradient is solely due to the absorption of solar radiation by N_2, O_2 and O at wavelengths below 200 nm.[1]

It should be noted that most of the chemistry described within this chapter, and the work presented throughout this thesis, is concerned with the chemical processes taking place within the troposphere.

1.1.1 Air Quality

The quality of air refers to the level of pollution in the air at a given time and in a particular area. Pollutants such as O_3, particulate matter, carbon monoxide (CO), SO_2 and NO_2 are present in the atmosphere as a result of direct emissions and the chemical processing of emissions derived from both anthropogenic sources, such as the production of CO from the incomplete combustion of hydrocarbons,[6] and from biogenic sources, such as the production from plants and phytoplankton/algae. Pollutants can also be released into the atmosphere via natural sources, for example the emission of SO_2 into the atmosphere from volcanoes.[7] Volatile organic compounds (VOCs) can directly impact the quality of air through introduction to the atmosphere from both biogenic and anthropogenic sources[8] and play a major role in atmospheric chemistry and so the mechanisms behind their reactions are at the forefront of current atmospheric research. Large quantities of VOCs directly impact air quality and climate change due to their likelihood to become oxidised in the atmosphere and result in the formation of secondary pollutants, including O_3 and secondary organic aerosol (SOA).[9, 10] VOCs may also pose a significant threat to human health as some VOCs may be carcinogenic in character, and so some VOCs require government regulations to be put in place to reduce the health risk.

A significant number of studies have been carried out in order to determine the full effect air pollution can have on human health, with many links being made between poor air quality and a number of diseases, including dementia, respiratory illnesses and cardiovascular disease.[11, 12] The European Environment Agency (EEA) report that there were ~21,400 premature deaths as a result of enhanced ozone levels in 2000 across Europe.[13] Another study reported that air pollution has the ability to decrease the average global life expectancy by approximately 2 years.[14] It is thus of the utmost importance that governments are supplied with up to date, accurate data on the emission rates, concentrations and chemistry of pollutants, which will enable the preparation of well-informed air quality regulations in an effort to reduce the number of premature deaths globally.

1.1.2 Climate Change

Climate change refers to a long-term change of the climate's regular temperature and weather patterns and can occur on both a regional and global scale. Climate change is understood to lead to the unnatural, gradual warming of the Earth's atmosphere due to the 'greenhouse effect'. The greenhouse effect refers to the increasing temperature of the Earth's surface as a result of high levels of radiatively active gases, such as carbon dioxide (CO_2), water vapour (H_2O), and methane (CH_4), which are often described as greenhouse gases. Such species absorb a fraction of the IR radiation emitted from the Earth's surface and become vibrationally excited. Following excitation, energy can be released as thermal energy, with some of this radiation becoming trapped within the atmosphere and creating a 'heating effect' at the Earth's surface.[15] The natural greenhouse effect is a result of the heating of the Earth's atmosphere due to naturally occurring greenhouse gases, which results in an average global temperature of around 15 ^{o}C.[16] Without the natural greenhouse effect (i.e. if the atmosphere were comprised solely of oxygen and nitrogen) the average surface temperature would be below 0 ^{o}C, making Earth uninhabitable as we know it.[16] The enhanced greenhouse effect results in further heating of the atmosphere due to increased concentrations of greenhouse gases resulting from human activity, such as the burning of fossil fuels. Large concentrations of such gases in the atmosphere could have detrimental effects on the quality of the air, and lead to more rapid climate change.

Carbon dioxide plays a major role in climate change due to the significant increase in its concentration since the industrial revolution, and a vast amount of research has been conducted to map the patterns in changes to atmospheric CO_2 concentrations over the past 650,000 years through the analysis of the air bubbles present in ice cores obtained in Antarctica.[17] It is important to note that an increase in concentration of pollutants in the atmosphere has the ability to alter the climate in ways other than increasing atmospheric temperature, including heavy precipitation, drought and tropical cyclone activity.

The Intergovernmental Panel on Climate Change (IPCC) reports how changes in the concentration of various greenhouse gases and aerosols influence the overall radiative forcing in the atmosphere and hence how they influence climate change (Figure 1.2).[18] Radiative forcing measures the energy imbalance of the Earth-atmosphere system when an imposed change takes place, such as a change in the concentration of a greenhouse gas, and allows comparisons of the climate response to be made, such as changes to the mean global temperature.[18] A positive radiative forcing arises from species such as CO_2 and CH_4 absorbing a fraction of the IR radiation emitted from the Earth's surface, which in turn creates an overall

warming effect of the atmosphere. Conversely, a negative radiative forcing occurs as a result of the Earth reflecting large amounts of radiation, creating an overall cooling effect.

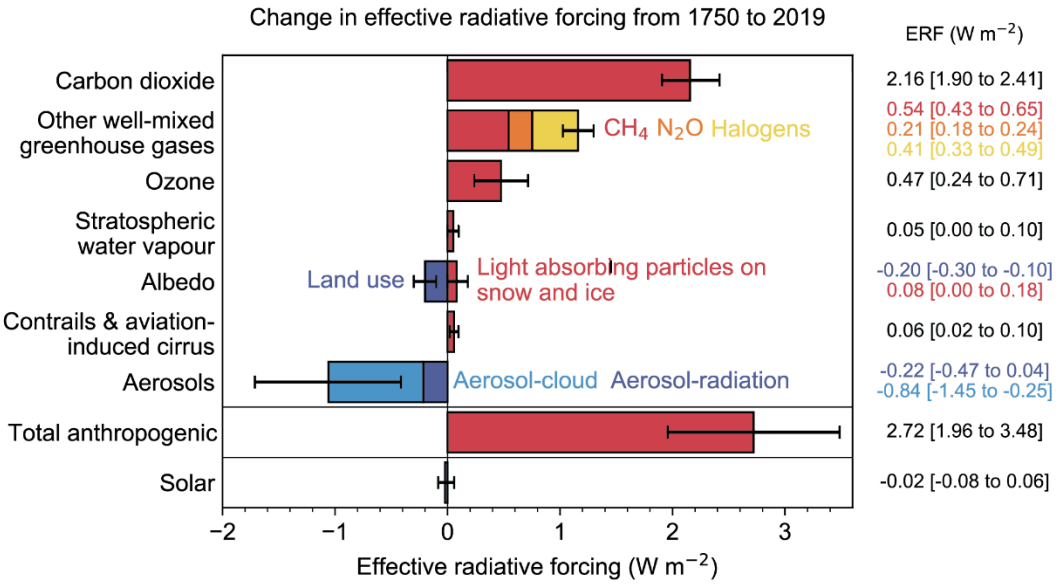

Figure 1.2. Bar chart for the radiative forcing / W m^{-2} for various species reported between 1750 and 2019. Copied from reference 19.[19]

From the plot shown in Figure 1.2, it is evident that greenhouse gases, such as CO_2, N_2O and CH_4, have an overall large positive radiative forcing, whereas aerosol interactions have a largely negative radiative forcing. The plot contains large error bars for the radiative forcing of each of the species previously mentioned, which demonstrates the need to understand the effects of these species at a fundamental level and the processes controlling their atmospheric concentrations. To reduce the error associated with radiative forcing, the mechanisms for the oxidation chemistry taking place within the troposphere, which impacts the concentrations of greenhouse gases and the concentrations and nature of aerosol particles, need to be studied.

1.2 Atmospheric Oxidation Processes

The chemistry of the troposphere is dominated by oxidation processes, which can be initiated by a number of oxidants, including hydroxyl radicals (OH), nitrate radicals (NO_3) and O_3. The significance of each oxidant varies with location, time of day and season, with each oxidant initiating a cascade of reactions that lead to the removal of primary pollutants from the atmosphere, whilst potentially leading to the production of secondary pollutants.

1.2.1 OH-Initiated Oxidation

The hydroxyl radical (OH) is responsible for the removal of many trace gases from the atmosphere, including VOCs. OH reacts rapidly following its formation[20] and is the dominant tropospheric oxidising species.[21] As a result of the high reactivity of OH, the atmospheric lifetime of OH is short (less than 1 second), particularly in polluted environments and so its concentration within the troposphere is relatively low (~10^6 molecule cm^{-3}).[22]

OH radicals primarily are produced in the troposphere through the solar photolysis of ozone. This produces an excited oxygen atom ($O(^1D)$) with the release of molecular oxygen (R1.4). The excited oxygen atom can react with water vapour in the troposphere to produce two hydroxyl radicals (R1.5).[21]

$O_3 + h\nu\ (\lambda \leq 340\ nm) \rightarrow O_2 + O\ (^1D)$ (R1.4)

$O\ (^1D) + H_2O \rightarrow 2OH$ (R1.5)

As the above mechanism suggests, the production of OH will be highest during the day due to its need for solar radiation, with limited production at night-time, when there is no sunlight. Due to the competition between the reaction of $O(^1D)$ with water vapour or its stabilisation to $O(^3P)$, higher concentrations of OH will be produced in areas with a higher water vapour content.

The hydroxyl radical can react with carbon monoxide (CO) (R1.6) and volatile organic compounds (VOCs) (R1.9) to produce peroxy radicals HO_2 and RO_2. HO_2 is produced via the reaction between OH and CO in the presence of O_2 (R1.6-R1.7). The HO_2 is then able to reform the OH through its reaction with O_3 (R1.8). HO_x collectively refers to OH and the hydroperoxy radical (HO_2) as these species are closely coupled, $HO_x = OH + HO_2$.[21]

$OH + CO \rightarrow H + CO_2$ (R1.6)

$H + O_2 + M \rightarrow HO_2 + M$ (R1.7)

$HO_2 + O_3 \rightarrow OH + 2O_2$ (R1.8)

Organic peroxy radicals (RO_2) are formed when OH reacts with VOCs, with the mechanism involving the abstraction of a hydrogen atom from the organic species (RH) to produce an alkyl radical (R) (R1.9) followed by the reaction between the alkyl radical and O_2 (R1.10).

$OH + RH \rightarrow R + H_2O$ (R1.9)

$R + O_2 + M \rightarrow RO_2 + M$ (R1.10)

The removal mechanism of peroxy radicals in the atmosphere largely depends on the level of pollution within a region. In regions with high concentrations of NO, HO_2 and RO_2 removal will be dominated through reactions R1.11 and R1.12, leading to the production of NO_2 and, subsequently O_3 (R1.14 and R1.2).[21]

$HO_2 + NO \rightarrow OH + NO_2$ (R1.11)

$RO_2 + NO \rightarrow RO + NO_2$ (R1.12)

$RO + O_2 \rightarrow R'CHO + HO_2$ (R1.13)

$NO_2 + h\nu\ (\lambda \leq 400\ nm) \rightarrow O + NO$ (R1.14)

$O + O_2 + M \rightarrow O_3 + M$ (R1.2)

In less polluted environments, the removal of peroxy radicals from the atmosphere tends to be dominated by radical termination reactions involving the HO_2 self-reaction (R1.15) and HO_2 + RO_2 cross-reactions (R1.16).

$HO_2 + HO_2\ (+M) \rightarrow H_2O_2 + O_2\ (+M)$ (R1.15)

$HO_2 + RO_2 \rightarrow ROOH + O_2$ (R1.16)

1.2.2 NO_3-Initiated Oxidation

During the night, when levels of solar radiation are low, atmospheric concentrations of OH are typically low. However, concentrations of the nitrate radical (NO_3) can be significant (typically ranging between 0.01 and 10 ppt in the United Kingdom[23]), and oxidation by NO_3 can become important. NO_3 is produced by the reaction between NO_2 and O_3 (R1.17), which is rapidly followed by reaction with NO_2 (R1.18) (k = ~2 × 10^{-12} cm^3 $molecule^{-1}$ s^{-1} at 298 K and 760 Torr[24]) to establish an equilibrium between NO_3 and dinitrogen pentoxide (N_2O_5). During the day, the nitrate radical is rapidly photolysed (~ 0.2 s^{-1} during the summer at midday)[25] (R1.19) and so its concentration remains low.

$NO_2 + O_3 \rightarrow NO_3 + O_2$ (R1.17)

$NO_3 + NO_2 + M \rightarrow N_2O_5 + M$ (R1.18)

$NO_3 + h\nu\ (\lambda \leq 590\ nm) \rightarrow NO_2 + O$ (R1.19a)

$(\lambda \leq 400\ nm) \rightarrow NO + O_2$ (R1.19b)

At night, when concentrations of NO_3 are not limited by removal through solar photolysis, NO_3 radicals can be important oxidants for unsaturated VOCs, such as alkenes. NO_3 typically reacts via an addition mechanism in which NO_3 adds to C=C double bonds to create a carbon-

centred radical (R1.20) which reacts rapidly with O_2 to produce a peroxy radical bearing a nitrate group (R1.21):

$NO_3 + C_2H_4 \rightarrow H_2C(ONO_2)C^{\cdot}H_2$ (R1.20)

$H_2C(ONO_2)C^{\cdot}H_2 + O_2 \rightarrow H_2C(ONO_2)CH_2OO^{\cdot}$ (R1.21)

The peroxy radicals formed in this way can then follow similar chemistry to that described above for RO_2 radicals produced via OH-initiated oxidation, but they can also lead to the formation of organic nitrates which contribute to the formation of secondary organic aerosols. The formation of RO_2 radicals via NO_3-initiated oxidation can also provide a pathway to the production of HO_2 and OH at night (R1.22 – R1.25).

$RO_2 + NO_3 \rightarrow RO + NO_2 + O_2$ (R1.22)

$RO + O_2 \rightarrow R'CHO + HO_2$ (R1.13)

$HO_2 + O_3 \rightarrow OH + 2O_2$ (R1.8)

$HO_2 + NO_3 \rightarrow OH + NO + O_2$ (R1.23)

1.2.3 O_3-Initiated Oxidation

Ozone is an important atmospheric oxidant that acts as an electrophilic agent, meaning it has a high affinity for electron-rich compounds, and as such, O_3 will oxidise unsaturated VOCs that have been introduced to the atmosphere through both biogenic and anthropogenic routes. Oxidation by O_3 represents a significant sink for monoterpenes and is responsible for approximately 10 % of the global removal of isoprene (C_5H_8, 2-methyl-1,3-butadiene), the dominant non-methane hydrocarbon emitted into the atmosphere.[26] In contrast to OH or NO_3, oxidation by O_3 is significant during the day and night, and when solar radiation levels, and thus OH concentrations, are low, the oxidation of unsaturated VOCs by O_3 can take precedence.[27]

The reactions of ozone with unsaturated VOCs, which are referred to as ozonolysis reactions, involve a mechanism in the gas phase in which ozone adds across the carbon-carbon double bond to produce a five–membered ring intermediate, known as a primary ozonide (POZ), which rapidly decomposes into a carbonyl product (RC(O)R) and a carbonyl oxide (R_2COO), which is commonly referred to as a Criegee intermediate[28] (Figure 1.3).

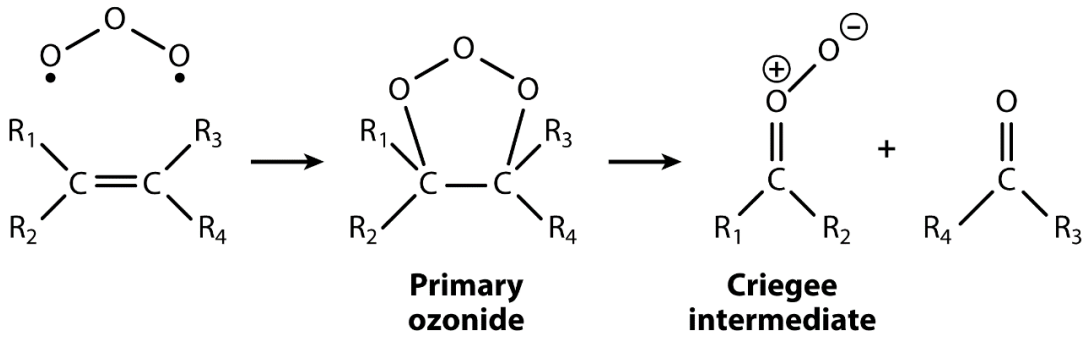

Figure 1.3. The ozonolysis mechanism for the production of Criegee intermediates.[29] Copied from reference 30.[30]

1.3 Criegee Intermediates

Criegee intermediates are reactive species with the general formula R_1R_2COO, and are currently the focus of many laboratory kinetic studies. Early studies suggested that Criegee intermediates are best represented as biradical species.[31] However, more recently it was concluded that the UV and infrared absorption spectra for Criegee intermediates are more consistent with a zwitterionic structure.[32] Figure 1.4 shows the general resonance canonical structures for a Criegee intermediate. For asymmetrically substituted Criegee intermediates, there is the possibility of the existence of *E/Z* isomers or *syn/anti* conformers depending on the orientation of the carbonyl substituent to that of the terminal oxygen atom since there is restricted rotation around the C-O Criegee bond owing to its double bond nature.[33] Figure 1.4 shows the structures for the *syn*- and *anti*-conformers of the Criegee intermediate CH_3CHOO, which have been shown to have a barrier to interconversion of ~160 kJ mol^{-1} [34] and so can be considered as distinct species under ambient atmospheric conditions.

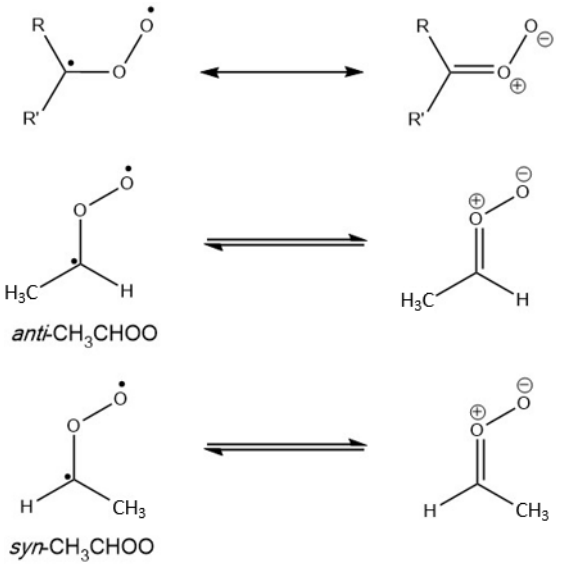

Figure 1.4. General resonance canonical structure for Criegee intermediates as well as the *syn*- and *anti*-conformers of the CH_3CHOO Criegee intermediate. Adapted from reference 31.[31]

Figure 1.5 shows a typical potential energy surface for an ozonolysis reaction. The initial reaction releases large amounts of energy (~250-300 kJ mol^{-1}),[31] with the exothermicity of this reaction leading to the production of Criegee intermediates with high internal energies.

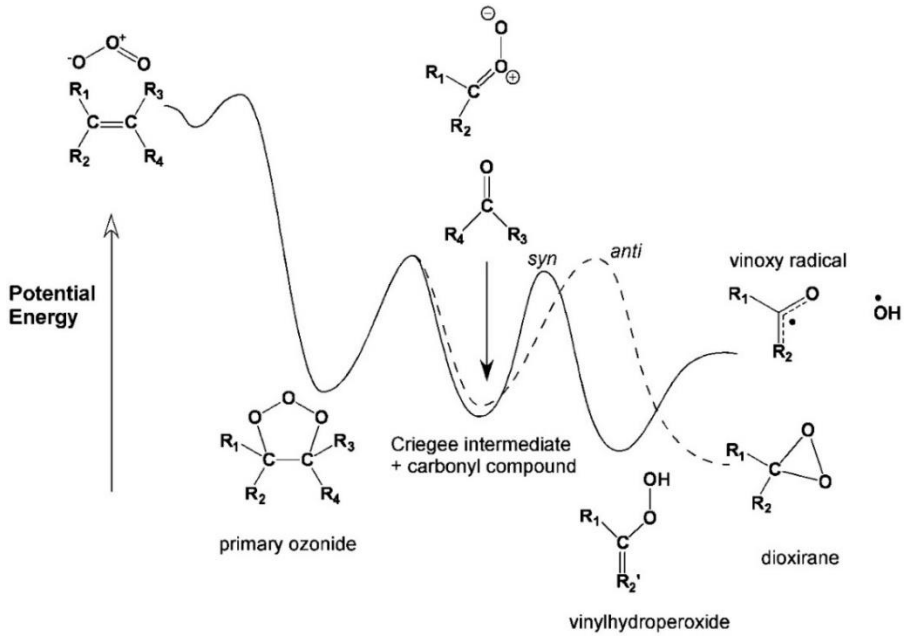

Figure 1.5. Typical potential energy surface diagram for the ozonolysis of alkenes to produce Criegee intermediates. Copied from reference 35.[35]

The atmospheric fate of a Criegee intermediate is largely governed by the distribution of its internal energy. The nascent excited Criegee intermediate can undergo unimolecular decomposition to form important trace species such as OH, CO and HO_2,[36] and can represent

a significant source of HO_x in the winter and during the night, when the intensity of solar radiation is low.[28] Prior to the PUMA (Pollution of the Urban Midlands Atmosphere) campaigns held in 1999 & 2000, the oxidising capacity of the troposphere in winter was still largely unknown, with few measurements of OH during the winter. Measurements from this campaign showed that the concentrations of OH only decrease by a factor of 2 during the winter, despite the OH production from the solar photolysis of ozone being reduced by a factor of 15. After reproducing the high OH concentrations for the winter period using a detailed box model, it was concluded that the production of radicals, such as OH, RO_2 and HO_2 are sustained during the winter by their production from the decomposition of excited Criegee intermediates following reactions between unsaturated VOCs and ozone.[28]

Excited Criegee intermediates may also undergo collisional stabilisation with species such as N_2 and O_2, which removes some of the excess internal energy to produce a stabilised Criegee intermediate (SCI). This is more likely to occur at higher pressures where the concentration of bath gas species is much higher, and so the frequency of collisions is greater.[36] As the internal energies of SCIs are much lower than those associated with nascent excited Criegee intermediates, they have longer atmospheric lifetimes and as a result are able to participate in a wider range of chemical reactions. SCIs can undergo unimolecular decomposition but this is in competition with bimolecular reactions with other atmospheric species such as water and water dimers,[37,38] SO_2[39,40] and NO_2.[39,41]

1.3.1 Atmospheric Concentrations of Criegee Intermediates

The atmospheric concentration of Criegee intermediates is controlled by a combination of the processes by which they are formed (see above) as well as the mechanisms by which they are removed. The rate coefficients for ozonolysis reactions are typically low (10^{-17} - 10^{-18} cm^3 $molecule^{-1}$ s^{-1}),[42] whereas the bimolecular rate coefficients for Criegee intermediates with atmospheric species, such as $(H_2O)_2$ and SO_2, are often much higher (as outlined in subsequent Chapters of this report). The slow formation rate, combined with the fast removal rate, results in a relatively low atmospheric concentration of SCIs, which translates to difficulties in directly measuring CIs in the atmosphere, as well as in ozonolysis studies carried out in atmospheric simulation chambers. Estimates for atmospheric SCI concentrations are in the range of 10^2 - 10^5 molecule cm^{-3}, which come from atmospheric measurements of O_3 and VOCs alongside extensive atmospheric modelling[43] as well as theoretical examinations of CIs to determine structure-activity relationships for dominant CI reaction pathways.[44] Figure 1.6 shows a plot of the modelled global annual mean distribution of SCIs at the Earth's surface using a numerical chemistry and climate system simulation which describes tropospheric and middle atmosphere processes and their interactions with

land, oceans and human influences.[44] The plots suggest that the annual mean concentration of SCIs never exceeds ~ 7×10^3 molecule cm^{-3}, with the highest concentrations being found over forested regions, and the highest predicted peak concentration of SCIs being below 1×10^5 molecule cm^{-3}.

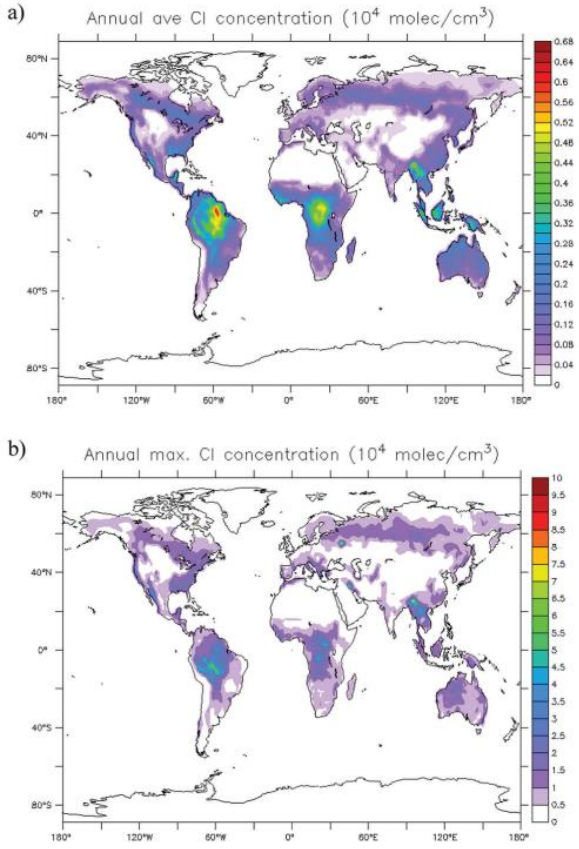

Figure 1.6. Global annual distributions of SCIs calculated using the ECHAM/MESSy atmospheric chemistry model, where a) is the concentration over 1 simulation year and b) shows the peak concentration of SCIs predicted within that year. Taken from reference 44.[44]

To fully assess the atmospheric impact of SCI reactions, both the concentration of Criegee intermediates and the rate of their bimolecular reactions need to be considered. This report provides further details regarding the different bimolecular channels of Criegee intermediates, their rate coefficients and hence relative importance in the atmosphere.

1.3.2 Indirect Measurements of Criegee Intermediates

Although the chemistry of Criegee intermediates in the troposphere has been of interest to atmospheric scientists for decades, significant uncertainties exist in the mechanisms and rate coefficients for Criegee intermediates owing to their high reactivity, and consequently short lifetimes, which represent significant experimental challenges. Until recently, studies of Criegee chemistry required the use of indirect methods that relied on the interpretation of

observations of stable products in ozonolysis reactions which could be produced by multiple pathways.[31] Various chamber experiments have been conducted where the focus was to investigate how the products of ozonolysis reactions will change upon the addition of different reagents. To interpret the results of such systems, extensive modelling of the ozonolysis reaction was required which involved the need for the production, stabilisation and reactions of the Criegee intermediates to be modelled in order to acquire accurate results. In ozonolysis reactions, there are often multiple pathways to produce the same product, so determining the relative contribution of each reaction pathway is challenging, which led to large uncertainties in Criegee intermediate kinetics.[45]

1.3.3 Direct Detection of Criegee Intermediates

Recent advances have led to an improved understanding of Criegee intermediates and the realisation of a more significant role for SCIs in the atmosphere than previously expected. These advances have resulted from developments that enabled the direct production of Criegee intermediates in the laboratory using photolytic sources.

The simplest Criegee intermediate (formaldehyde oxide, CH_2OO) was first observed in the gas phase in a study by Taatjes *et al.*[46] using the photolysis of $(COCl)_2/(CH_3)_2SO/O_2$ mixtures to generate the Criegee intermediate (R1.24-R1.26) combined with tuneable synchrotron photo-ionisation mass spectrometry (PIMS).

$$(COCl)_2 + h\nu\ (\lambda = 248\ \text{nm}) \rightarrow COCl + CO + Cl \qquad \text{(R1.24)}$$

$$(CH_3)_2SO + Cl \rightarrow CH_3SOCH_2 + HCl \qquad \text{(R1.25)}$$

$$CH_3SOCH_2 + O_2 \rightarrow CH_2OO + CH_3SO \qquad \text{(R1.26)}$$

The PIMS technique employed by Taatjes *et al.* enabled identification of the *m/z* signal corresponding to CH_2OO as the Criegee intermediate through use of its photo-ionisation efficiency (PIE) spectrum. However, the method used to generate CH_2OO resulted in significant secondary chemistry, resulting in the production of many by-products which complicated the analysis of the experimental data. Yields of CH_2OO were also low, and the analysis of the $m/z = 46$ peak for CH_2OO was complicated by the presence of large amounts of CH_2S produced in the system, which precluded further analysis beyond the identification of the presence of the Criegee intermediate.

Subsequent work by the same group identified alternative methods to generate Criegee intermediates using the photolysis of di-iodo precursors. Welz *et al.*[45] used the photolysis of diiodomethane at a low pressure (4 Torr) to produce the simplest Criegee, CH_2OO, via reactions (R1.27) and (R1.28).

$CH_2I_2 + h\nu$ (λ = 248 nm) → $CH_2I + I$ (R1.27)

$CH_2I + O_2 \rightarrow CH_2OO + I$ (R1.28a)

Welz *et al.* used the PIMS technique to confirm that the peak seen at *m/z* = 46 arises from the Criegee intermediate and not any other isomers of CH_2OO such as formic acid (HCOOH) or dioxirane (CH_2O_2). Photolysis of CH_2I_2/O_2 gas mixtures enabled the production of CH_2OO in sufficient concentration to make the first direct measurements of the kinetics of a number of CH_2OO reactions, representing the first direct measurements of any Criegee intermediate kinetics. Reactions of CH_2OO with SO_2 and NO_2 were found to be approximately 1000 times faster than previous indirect estimates had suggested,[39] indicating a more important role for Criegee intermediates than previously assumed.

The reaction for the formation of CH_2OO following the photolysis of CH_2I_2/O_2 proceeds via the production of an excited intermediate species, CH_2IOO^* (R1.28b), which either decomposes to produce the Criegee intermediate and an iodine atom (R1.29a), or is collisionally stabilised by a bath gas, such as N_2, to produce the stabilised peroxy radical CH_2IO_2 (R1.29b) and the yield of CH_2OO therefore has a dependence on pressure.

$CH_2I + O_2 \rightarrow CH_2IOO^*$ (R1.28b)

$CH_2IOO^* \rightarrow CH_2OO + I$ (R1.29a)

$CH_2IOO^* + M \rightarrow CH_2IO_2 + M$ (R1.29b)

Huang *et al.*[47] reported the yield of CH_2OO as a function of pressure (3 – 80 Torr) for N_2, He and O_2 buffer at 298 K using infrared (IR) absorption spectroscopy to determine I atom yields. The group identified a rapid production of I atoms, as a result of CH_2I_2 photolysis, followed by a slower production of I atoms, which was attributed to the reaction of CH_2I with O_2 (R1.28b-R1.29a), the slow production of I atoms can therefore be directly correlated to CH_2OO yields. Huang *et al.* reported that the yield of CH_2OO decreases with increasing pressure, as a result of increased stabilisation of the peroxy radical (R1.29b) and initially reported a yield of ~ 4 % at 760 Torr and found that the collision efficiency of O_2 was approximately 13 times greater than N_2. However, subsequent studies[48, 49] disagreed with the large collision efficiency of O_2 and Huang *et al.* later disregarded this finding as a result of incorrect data processing. After reviewing their data, Huang *et al.* reported a new yield for CH_2OO of ~ 15 % at 760 Torr.

Stone *et al.*[48] investigated the yield of CH_2OO between 25 and 450 Torr at 295 K using a combination of resonance fluorescence to measure the yields of the iodine atoms produced in reactions R1.27 and R1.28 and laser-induced fluorescence (LIF) to measure the yields of

formaldehyde (HCHO) produced by reactions of CH_2OO and CH_2IO_2. Results indicated a yield of CH_2OO of ~18 % at atmospheric pressure, in agreement with the revised work of Huang *et al.*[47]

Ting *et al.*[49] employed broadband UV absorption spectroscopy to obtain temporal profiles of CH_2OO, CH_2I_2, CH_2I and IO following the photolysis of CH_2I_2/O_2 mixtures at 295 K and pressures between 7.6 and 779 Torr. A detailed mechanism was used to model the observed temporal profiles which used a value of (R1.28a + R1.28b) = 1.5×10^{-12} cm^3 $molecule^{-1}$ s^{-1} (taken as the average of previous literature values). Rate coefficients for R1.28a and R1.28b were determined using: R1.28a = y(R1.28a + R1.28b) and R1.28b = (1-y)(R1.28a + R1.28b), where y is equal to the yield of CH_2OO. The CH_2OO yield was equal to $[CH_2OO]_0$ / $[CH_2I]_0$, where $[CH_2OO]_0$ was determined from the temporal profile of CH_2OO extrapolated back to t=0, and $[CH_2I]_0$ was equal to $-\Delta[CH_2I_2]$. Ting *et al*. report a yield for CH_2OO of ~ 30 % at atmospheric pressure, which is approximately twice the yields reported in previous studies.[47, 48] The discrepancy in results between Ting *et al.* and previous studies may be a result of the difference in methods used to determine the yields. Ting *et al*. used a less direct method to determine the CH_2OO yield than those used by both Stone *et al*. and Huang *et al*., where Ting *et al*. relied on fits to time profiles of the different species, which requires absorption cross-sections to be well known, and also requires rate coefficients for other reactions taking place to be known.

Taatjes *et al.*[34] extended the technique used by Welz *et al.*[45] to successfully produce the larger Criegee intermediate acetaldehyde oxide (CH_3CHOO) using flash photolysis of 1,1-diiodoethane (CH_3CHI_2) in the presence of O_2 at 298 K and 4 Torr (R1.30-R1.32c).

$CH_3CHI_2 + h\nu\ (\lambda = 248\ nm) \rightarrow CH_3CHI + I$ (R1.30)

$CH_3CHI + O_2 \rightarrow CH_3CHIOO^*$ (R1.31)

$CH_3CHIOO^* + M \rightarrow CH_3CHIO_2 + M$ (R1.32a)

$CH_3CHIOO^* \rightarrow$ *syn*-$CH_3CHOO + I$ (R1.32b)

$CH_3CHIOO^* \rightarrow$ *anti*-$CH_3CHOO + I$ (R1.32c)

Using the PIMS technique, Taatjes *et al.* were able to identify the *syn*- and *anti*-conformers of CH_3CHOO from their individual photo-ionisation spectra, with the measurements showing that the two conformers display significant differences in reactivity. Similar to the results of Welz *et al.* for CH_2OO,[45] the direct measurements performed by Taatjes *et al.* demonstrated that the reactions of *syn*-CH_3CHOO and *anti*-CH_3CHOO with SO_2 were more rapid than previously expected, with the *anti*-conformer reacting more rapidly than the *syn*-conformer.

The gas phase oxidation of SO_2 by Criegee intermediates is of particular interest as it has the potential to influence atmospheric composition and climate if the reactions involve the production of sulfur trioxide (SO_3), since SO_3 can subsequently generate H_2SO_4 (R1.33) and sulfate aerosol. Prior to the recent direct measurements of the kinetics of Criegee intermediate reactions with SO_2 it was thought that the only gas phase oxidation mechanism for SO_2 in the atmosphere involved the reaction with OH (R1.34 and R1.35).

$$SO_3 + H_2O + M \rightarrow H_2SO_4 + M \quad \text{(R1.33)}$$

$$SO_2 + OH + M \rightarrow HOSO_2 + M \quad \text{(R1.34)}$$

$$HOSO_2 + O_2 \rightarrow SO_3 + HO_2 \quad \text{(R1.35)}$$

However, the rate coefficient for the reaction between OH and SO_2 is relatively low ($\sim 10^{-12}$ cm^3 $molecule^{-1}$ s^{-1} [50]) and in areas of low sunlight or throughout the night, this route to the production of SO_3 is limited owing to low concentrations of OH. The recent direct measurements of Criegee intermediate kinetics, made possible through the discovery of photolytic sources for use in the laboratory, have led to the suggestion that Criegee intermediates provide additional important pathways for the atmospheric oxidation of SO_2.

Field measurements have also suggested the presence of oxidants of SO_2 other than OH, with the measurements indicating an important role for Criegee intermediates. Mauldin *et al.*[51] measured OH and H_2SO_4 concentrations at the SMEAR II station in a boreal forest in Finland. The measurements showed typical diurnal behaviour for OH, but also showed profiles for an unidentified oxidant with the capability of oxidising SO_2 to H_2SO_4 in the gas phase, similar to OH. The concentration-time profiles for the unknown species showed no significant diurnal cycle and that concentrations were typically higher than those of OH (i.e. exceeding 10^6 molecule cm^{-3}).[51] The concentration of the unknown species and H_2SO_4 appeared to remain high during the night and periods of low light, suggesting that this species is a non-photolytic source of H_2SO_4. It was concluded that the H_2SO_4 produced through this non-OH pathway could account for up to 50% of the total H_2SO_4 formed.[51] Mauldin *et al.* suggested that the non-OH species is likely to be linked with surface emissions and subsequent ozone chemistry.[51] To determine the identity of the unknown species, laboratory experiments were conducted using chemical ionisation mass spectrometry (CIMS) where SO_2 was combined with different mixtures of ozone and an alkene, in the presence and absence of an OH scavenger molecule. Observations showed that the production of H_2SO_4 was much greater when the alkene used was a monoterpene. As the reaction between alkenes and ozone is known to produce Criegee intermediates, and Criegee intermediates were shown to oxidise SO_2,[52] Mauldin *et al.* concluded that the unknown species is likely to be a Criegee intermediate produced from the ozonolysis of alkenes, such as monoterpenes.[51]

The field measurements of OH and H_2SO_4, combined with the recent awareness of rapid reactions of Criegee intermediates with SO_2 have indicated a potentially important role for Criegee intermediates in the oxidation of SO_2. Other recent direct studies have shown that the reactions of Criegee intermediates with water and water dimers potentially dominate the atmospheric chemistry of many Criegee intermediates, including CH_2OO and *anti*-CH_3CHOO,[38, 53, 54] while decomposition reactions are also important for some Criegee intermediates such as *syn*-CH_3CHOO[55] and $(CH_3)_2COO$.[56]

As a result of being able to produce Criegee intermediates directly from photolytic sources, there have been a number of studies investigating the kinetics of the reactions that take place between Criegee intermediates and atmospherically relevant species. These studies have utilised a wide range of methods to monitor both the Criegee intermediate as well as the reaction products, including laser-induced fluorescence (LIF),[39, 57] photo-ionisation mass spectrometry (PIMS)[40, 58] and ultra-violet and infrared absorption spectroscopy.[40, 59] However, a number of uncertainties within the kinetics of these reactions remain, particularly regarding the temperature and pressure dependence of SCI reaction kinetics.

There is still a need for temperature-dependent studies and further product analysis studies of the reactions between Criegee intermediates and SO_2, NO_2 and water/water dimers to allow for a greater understanding of the reaction mechanisms and their roles in the atmosphere. As the concentration of water vapour in the atmosphere is significantly greater than that of other trace species such as SO_2 and NO_2, understanding the kinetics of Criegee reactions with each of these species under atmospheric conditions is crucial in determining which reactions may dominate.

1.4 Overview of this Thesis

This thesis provides an overview of Criegee intermediate reactions and discusses how they influence atmospheric chemistry, therefore impacting air quality and climate change. The kinetics of the simplest Criegee intermediate, CH_2OO, with SO_2, NO_2 and water vapour have been investigated across a wide range of temperatures and pressures relevant to the troposphere, and the results, along with atmospheric implications, will be summarised in subsequent chapters. The kinetics of both the *syn*- and *anti*-conformers of the second largest Criegee intermediate, CH_3CHOO, with SO_2 have also been measured as a function of temperature and pressure, showing a distinct conformer-dependence. Each reaction was investigated using laser flash photolysis at $\lambda = 248$ nm combined with time resolved broadband ultraviolet absorption spectroscopy, details of which are provided in Chapter 3.

The Chapters presented in this thesis are as follows:

Chapter 2 provides an overview of the main theories used to explain the dependence of reaction rates on temperature and pressure and also discusses the subject of photochemistry.

Chapter 3 summarises the main experimental techniques used within the literature to investigate the kinetics of Criegee intermediate reactions and also describes the experimental set-up and analysis procedure used to obtain the results presented within this thesis.

Chapter 4 gives details of previous investigations into the kinetics of the reaction between CH_2OO and SO_2 and discusses the kinetics of this reaction as determined in this work as a function of temperature and pressure.

Chapter 5 gives details of previous investigations into the kinetics of the reaction between CH_2OO and NO_2 and discusses the kinetics of this reaction as determined in this work as a function of temperature and pressure.

Chapter 6 gives details of previous investigations into the kinetics of the reaction between CH_2OO and water vapour and discusses the kinetics of this reaction as determined in this work as a function of temperature.

Chapter 7 gives details of previous investigations into the kinetics of the reaction between CH_3CHOO conformers and SO_2 and discusses the kinetics of this reaction as determined in this work as a function of temperature and pressure.

Chapter 8 summarises the results presented throughout this thesis, discusses the atmospheric implications of the results and outlines possible areas for future work.

1.5 References

1. Barbara J. Finlayson-Pitts, J.N.P., Jr. *Chemistry of the Upper and Lower Atmosphere: Theory, Experiments and Applications.* San Diego, California: Academic Press, 1999.
2. John H. Seinfeld, S.N.P. *Atmospheric Chemistry and Physics: From Air Pollution to Climate Change.* New Jersey, USA: John Wiley & Sons, Incorporated, 2016.
3. Burrows, J.P., Goede, A.P.H., Muller, C. and Bovensmann, H. SCIAMACHY – The Need for Atmospheric Research from Space. In: Gottwald, M. and Bovensmann, H. eds. *SCIAMACHY - Exploring the Changing Earth's Atmosphere*. Dordrecht: Springer Netherlands, 2011, pp.1-17.
4. Garratt, J.R. Review: the atmospheric boundary layer. *Earth-Science Reviews.* 1994, **37**(1), pp.89-134.
5. Van Der Leun, J.C. The ozone layer. *Photodermatology, Photoimmunology & Photomedicine.* 2004, **20**(4), pp.159-162.

6. Gatts, T., Liu, S., Liew, C., Ralston, B., Bell, C. and Li, H. An experimental investigation of incomplete combustion of gaseous fuels of a heavy-duty diesel engine supplemented with hydrogen and natural gas. *International Journal of Hydrogen Energy.* 2012, **37**(9), pp.7848-7859.
7. Rodríguez, L.A., Watson, I.M., Rose, W.I., Branan, Y.K., Bluth, G.J.S., Chigna, G., Matías, O., Escobar, D., Carn, S.A. and Fischer, T.P. SO_2 emissions to the atmosphere from active volcanoes in Guatemala and El Salvador, 1999–2002. *Journal of Volcanology and Geothermal Research.* 2004, **138**(3), pp.325-344.
8. Regina Montero-Montoya, R.L.-V., Omar Arellano-Aguilar. Volatile Organic Compounds in Air: Sources, Distribution, Exposure and Associated Illness in Children. *Annals of Global Health.* 2018, **84**(2), pp.225-238.
9. Koppmann, R. *Volatile Organic Compounds in the Atmosphere.* 1st ed. Blackwell Publishing Ltd, 2007.
10. Theloke, J. and Friedrich, R. Compilation of a database on the composition of anthropogenic VOC emissions for atmospheric modeling in Europe. *Atmospheric Environment.* 2007, **41**(19), pp.4148-4160.
11. Carey, I.M., Anderson, H.R., Atkinson, R.W., Beevers, S.D., Cook, D.G., Strachan, D.P., Dajnak, D., Gulliver, J. and Kelly, F.J. Are noise and air pollution related to the incidence of dementia? A cohort study in London, England. *BMJ Open.* 2018, **8**(9), p.e022404.
12. Franklin, B.A., Brook, R. and Arden Pope, C. Air Pollution and Cardiovascular Disease. *Current Problems in Cardiology.* 2015, **40**(5), pp.207-238.
13. (EEA), E.E.A. Air pollution in Europe 1990-2004. 2007, (2), p.29.
14. Michael Greenstone, C.Q.F. Twelve Facts about Particulate Air Pollution, Human Health and Global Policy. *Energy Policy Institute at the University of Chicago.* 2018, p.3.
15. *The Greenhouse effect.* [Online]. [Accessed 30th December]. Available from: https://scied.ucar.edu/learning-zone/how-climate-works/greenhouse-effect
16. Houghton, J. Global warming. *Reports on Progress in Physics.* 2005, **68**(6), pp.1343-1403.
17. Lüthi, D., Le Floch, M., Bereiter, B., Blunier, T., Barnola, J.-M., Siegenthaler, U., Raynaud, D., Jouzel, J., Fischer, H., Kawamura, K. and Stocker, T.F. High-resolution carbon dioxide concentration record 650,000–800,000 years before present. *Nature.* 2008, **453**(7193), pp.379-382.
18. Myhre, G., D. Shindell, F.-M. Breon, W. Collins, J.Fuglestvedt, J. Huang, D.Koch, J.-F. Lamarque, D. Lee, B. Mendoza, T. Nakajima, A. Robock, G. Stephens, T.

Takemura and H. Zhang. *Anthropogenic and Natural Radiative Forcing* Cambridge University Press 2013.

19. The Earth's Energy Budget, Climate Feedbacks and Climate Sensitivity. In: Intergovernmental Panel on Climate, C. ed. *Climate Change 2021 – The Physical Science Basis: Working Group I Contribution to the Sixth Assessment Report of the Intergovernmental Panel on Climate Change*. Cambridge: Cambridge University Press, 2023, pp.923-1054.
20. Gligorovski, S., Strekowski, R., Barbati, S. and Vione, D. Environmental Implications of Hydroxyl Radicals (•OH). *Chemical Reviews.* 2015, **115**(24), pp.13051-13092.
21. Stone, D., Whalley, L.K. and Heard, D.E. Tropospheric OH and HO_2 radicals: field measurements and model comparisons. *Chemical Society Reviews.* 2012, **41**(19), pp.6348-6404.
22. Pilling, M.J., Seakins, P.W. *Reaction Kinetics.* Oxford University Press Inc, 1995.
23. Khan, M.A.H., Ashfold, M.J., Nickless, G., Martin, D., Watson, L.A., Hamer, P.D., Wayne, R.P., Canosa-Mas, C.E. and Shallcross, D.E. Night-time NO_3 and OH radical concentrations in the United Kingdom inferred from hydrocarbon measurements. *Atmospheric Science Letters.* 2008, **9**(3), pp.140-146.
24. Atkinson, R., Baulch, D.L., Cox, R.A., Crowley, J.N., Hampson, R.F., Hynes, R.G., Jenkin, M.E., Rossi, M.J. and Troe, J. Evaluated kinetic and photochemical data for atmospheric chemistry: Volume I - gas phase reactions of Ox, HOx, NOx and SOx species. *Atmospheric Chemistry and Physics.* 2004, **4**(6), pp.1461-1738.
25. Brown, S.S., Osthoff, H.D., Stark, H., Dubé, W.P., Ryerson, T.B., Warneke, C., de Gouw, J.A., Wollny, A.G., Parrish, D.D., Fehsenfeld, F.C. and Ravishankara, A.R. Aircraft observations of daytime NO_3 and N_2O_5 and their implications for tropospheric chemistry. *Journal of Photochemistry and Photobiology A: Chemistry.* 2005, **176**(1), pp.270-278.
26. Nguyen, T.B., Tyndall, G.S., Crounse, J.D., Teng, A.P., Bates, K.H., Schwantes, R.H., Coggon, M.M., Zhang, L., Feiner, P., Milller, D.O., Skog, K.M., Rivera-Rios, J.C., Dorris, M., Olson, K.F., Koss, A., Wild, R.J., Brown, S.S., Goldstein, A.H., de Gouw, J.A., Brune, W.H., Keutsch, F.N., Seinfeld, J.H. and Wennberg, P.O. Atmospheric fates of Criegee intermediates in the ozonolysis of isoprene. *Physical Chemistry Chemical Physics.* 2016, **18**(15), pp.10241-10254.
27. Gutbrod, R., Kraka, E., Schindler, R.N. and Cremer, D. Kinetic and Theoretical Investigation of the Gas-Phase Ozonolysis of Isoprene: Carbonyl Oxides as an Important Source for OH Radicals in the Atmosphere. *Journal of the American Chemical Society.* 1997, **119**(31), pp.7330-7342.

28. Heard, D.E., Carpenter, L.J., Creasey, D.J., Hopkins, J.R., Lee, J.D., Lewis, A.C., Pilling, M.J., Seakins, P.W., Carslaw, N. and Emmerson, K.M. High levels of the hydroxyl radical in the winter urban troposphere. *Geophysical Research Letters.* 2004, **31**(18).
29. Criegee, R. Mechanism of Ozonolysis. *Angewandte Chemie International Edition in English.* 1975, **14**(11), pp.745-752.
30. Osborn, D.L. Reaction Mechanisms on Multiwell Potential Energy Surfaces in Combustion (and Atmospheric) Chemistry. *Annual Review of Physical Chemistry.* 2017, **68**(1), pp.233-260.
31. Johnson, D. and Marston, G. The gas-phase ozonolysis of unsaturated volatile organic compounds in the troposphere. *Chemical Society Reviews.* 2008, **37**(4), pp.699-716.
32. Su, Y.-T., Huang, Y.-H., Witek, H.A. and Lee, Y.-P. Infrared Absorption Spectrum of the Simplest Criegee Intermediate CH_2OO. *Science.* 2013, **340**(6129), p.174.
33. Novelli, A., Vereecken, L., Lelieveld, J. and Harder, H. Direct observation of OH formation from stabilised Criegee intermediates. *Physical Chemistry Chemical Physics.* 2014, **16**(37), pp.19941-19951.
34. Taatjes, C.A., Welz, O., Eskola, A.J., Savee, J.D., Scheer, A.M., Shallcross, D.E., Rotavera, B., Lee, E.P.F., Dyke, J.M., Mok, D.K.W., Osborn, D.L. and Percival, C.J. Direct Measurements of Conformer-Dependent Reactivity of the Criegee Intermediate CH_3CHOO. *Science.* 2013, **340**(6129), p.177.
35. Osborn, D.L. and Taatjes, C.A. The physical chemistry of Criegee intermediates in the gas phase. *International Reviews in Physical Chemistry.* 2015, **34**(3), pp.309-360.
36. Stone, D., Au, K., Sime, S., Medeiros, D.J., Blitz, M., Seakins, P.W., Decker, Z. and Sheps, L. Unimolecular decomposition kinetics of the stabilised Criegee intermediates CH_2OO and CD_2OO. *Physical Chemistry Chemical Physics.* 2018, **20**(38), pp.24940-24954.
37. Berndt, T., Kaethner, R., Voigtländer, J., Stratmann, F., Pfeifle, M., Reichle, P., Sipilä, M., Kulmala, M. and Olzmann, M. Kinetics of the unimolecular reaction of CH_2OO and the bimolecular reactions with the water monomer, acetaldehyde and acetone under atmospheric conditions. *Physical Chemistry Chemical Physics.* 2015, **17**(30), pp.19862-19873.
38. Lewis, T.R., Blitz, M.A., Heard, D.E. and Seakins, P.W. Direct evidence for a substantive reaction between the Criegee intermediate, CH_2OO, and the water vapour dimer. *Physical Chemistry Chemical Physics.* 2015, **17**(7), pp.4859-4863.
39. Stone, D., Blitz, M., Daubney, L., Howes, N.U.M. and Seakins, P. Kinetics of CH_2OO reactions with SO_2, NO_2, NO, H_2O and CH_3CHO as a function of pressure. *Physical Chemistry Chemical Physics.* 2014, **16**(3), pp.1139-1149.

40. Howes, N.U.M., Mir, Z.S., Blitz, M.A., Hardman, S., Lewis, T.R., Stone, D. and Seakins, P.W. Kinetic studies of C1 and C2 Criegee intermediates with SO_2 using laser flash photolysis coupled with photoionization mass spectrometry and time resolved UV absorption spectroscopy. *Physical Chemistry Chemical Physics.* 2018, **20**(34), pp.22218-22227.

41. Caravan, R.L., Khan, M.A.H., Rotavera, B., Papajak, E., Antonov, I.O., Chen, M.-W., Au, K., Chao, W., Osborn, D.L., Lin, J.J.-M., Percival, C.J., Shallcross, D.E. and Taatjes, C.A. Products of Criegee intermediate reactions with NO_2: experimental measurements and tropospheric implications. *Faraday Discussions.* 2017, **200**(0), pp.313-330.

42. *IUPAC Task Group on Atmospheric Chemical Kinetic Data Evaluation.* [Online database].

43. Pierce, J.R., Evans, M.J., Scott, C.E., D'Andrea, S.D., Farmer, D.K., Swietlicki, E. and Spracklen, D.V. Weak global sensitivity of cloud condensation nuclei and the aerosol indirect effect to Criegee + SO_2 chemistry. *Atmos. Chem. Phys.* 2013, **13**(6), pp.3163-3176.

44. Vereecken, L., Novelli, A. and Taraborrelli, D. Unimolecular decay strongly limits the atmospheric impact of Criegee intermediates. *Physical Chemistry Chemical Physics.* 2017, **19**(47), pp.31599-31612.

45. Welz, O., Savee, J.D., Osborn, D.L., Vasu, S.S., Percival, C.J., Shallcross, D.E. and Taatjes, C.A. Direct Kinetic Measurements of Criegee Intermediate (CH_2OO) Formed by Reaction of CH_2I with O_2. *Science.* 2012, **335**(6065), p.204.

46. Taatjes, C.A., Meloni, G., Selby, T.M., Trevitt, A.J., Osborn, D.L., Percival, C.J. and Shallcross, D.E. Direct Observation of the Gas-Phase Criegee Intermediate (CH_2OO). *Journal of the American Chemical Society.* 2008, **130**(36), pp.11883-11885.

47. Huang, H., Eskola, A.J. and Taatjes, C.A. Pressure-Dependent I-Atom Yield in the Reaction of CH_2I with O_2 Shows a Remarkable Apparent Third-Body Efficiency for O_2. *The Journal of Physical Chemistry Letters.* 2012, **3**(22), pp.3399-3403.

48. Stone, D., Blitz, M., Daubney, L., Ingham, T. and Seakins, P. CH_2OO Criegee biradical yields following photolysis of CH_2I_2 in O_2. *Physical Chemistry Chemical Physics.* 2013, **15**(44), pp.19119-19124.

49. Ting, W.-L., Chang, C.-H., Lee, Y.-F., Matsui, H., Lee, Y.-P. and Lin, J.J.-M. Detailed mechanism of the $CH_2I + O_2$ reaction: Yield and self-reaction of the simplest Criegee intermediate CH_2OO. *The Journal of Chemical Physics.* 2014, **141**(10), p.104308.

50. Blitz, M.A., Hughes, K.J. and Pilling, M.J. Determination of the High-Pressure Limiting Rate Coefficient and the Enthalpy of Reaction for $OH + SO_2$. *The Journal of Physical Chemistry A.* 2003, **107**(12), pp.1971-1978.

51. Mauldin Iii, R.L., Berndt, T., Sipilä, M., Paasonen, P., Petäjä, T., Kim, S., Kurtén, T., Stratmann, F., Kerminen, V.M. and Kulmala, M. A new atmospherically relevant oxidant of sulphur dioxide. *Nature.* 2012, **488**(7410), pp.193-196.

52. Johnson, D., Lewin, A.G. and Marston, G. The Effect of Criegee-Intermediate Scavengers on the OH Yield from the Reaction of Ozone with 2-methylbut-2-ene. *The Journal of Physical Chemistry A.* 2001, **105**(13), pp.2933-2935.

53. Anglada, J.M., González, J. and Torrent-Sucarrat, M. Effects of the substituents on the reactivity of carbonyl oxides. A theoretical study on the reaction of substituted carbonyl oxides with water. *Physical Chemistry Chemical Physics.* 2011, **13**(28), pp.13034-13045.

54. Chao, W., Hsieh, J.-T., Chang, C.-H. and Lin, J.J.-M. Direct kinetic measurement of the reaction of the simplest Criegee intermediate with water vapor. *Science.* 2015, **347**(6223), p.751.

55. Robinson, C., Onel, L., Newman, J., Lade, R., Au, K., Sheps, L., Heard, D.E., Seakins, P.W., Blitz, M.A. and Stone, D. Unimolecular Kinetics of Stabilized CH_3CHOO Criegee Intermediates: syn-CH_3CHOO Decomposition and anti-CH_3CHOO Isomerization. *The Journal of Physical Chemistry A.* 2022, **126**(39), pp.6984-6994.

56. Taatjes, C.A., Liu, F., Rotavera, B., Kumar, M., Caravan, R., Osborn, D.L., Thompson, W.H. and Lester, M.I. Hydroxyacetone Production From C3 Criegee Intermediates. *The Journal of Physical Chemistry A.* 2017, **121**(1), pp.16-23.

57. Liu, Y., Bayes, K.D. and Sander, S.P. Measuring Rate Constants for Reactions of the Simplest Criegee Intermediate (CH_2OO) by Monitoring the OH Radical. *The Journal of Physical Chemistry A.* 2014, **118**(4), pp.741-747.

58. Chhantyal-Pun, R., Davey, A., Shallcross, D.E., Percival, C.J. and Orr-Ewing, A.J. A kinetic study of the CH_2OO Criegee intermediate self-reaction, reaction with SO_2 and unimolecular reaction using cavity ring-down spectroscopy. *Physical Chemistry Chemical Physics.* 2015, **17**(5), pp.3617-3626.

59. Sheps, L. Absolute Ultraviolet Absorption Spectrum of a Criegee Intermediate CH_2OO. *The Journal of Physical Chemistry Letters.* 2013, **4**(24), pp.4201-4205.

Chapter 2

Theory of Gas Phase Kinetics and Photochemistry

The study of reaction kinetics refers to measuring and understanding the rate at which reactions occur. Kinetics also provides information about the mechanisms of complex reactions, which take place via a series of elementary processes to give the overall reaction. This chapter provides an overview of the main theories used to explain the dependence of reaction rates on temperature and pressure, such as those of Criegee intermediates that form the basis of this thesis. The subject of photochemistry is also discussed within this chapter, which studies the absorption of radiation and the subsequent processes that follow.

2.1 Rate Theory of Gas Phase Kinetics

A general chemical reaction can be described as:

$$a\mathrm{A} + b\mathrm{B} \rightarrow c\mathrm{C} + d\mathrm{D} \qquad \text{(R2.1)}$$

where A, B, C and D are the chemical species and *a*, *b*, *c* and *d* are the stoichiometric coefficients for each species.

The rate of reaction, *r*, is defined as the change in concentration of a species as a function of time, either the decrease of a reactant $r = -\frac{1}{a}\frac{d[\mathrm{A}]}{dt}$ or the increase of a product, $r = +\frac{1}{c}\frac{d[\mathrm{C}]}{dt}$.

For the general reaction given above, the rate of reaction can be written as:

$$r = -\frac{1}{a}\frac{d[\mathrm{A}]}{dt} = k[\mathrm{A}]^{\alpha}[\mathrm{B}]^{\beta} \qquad \text{(Equation 2.1)}$$

where *k* is the rate coefficient, [A] and [B] are the concentrations of reactants A and B and α and β represent the orders of the reaction with respect to A and B, which describe how the rate of a reaction is dependent on the concentration of each reactant, with the overall order of a reaction given by the sum of the individual orders.

The molecularity of an elementary reaction, a chemical reaction that occurs in a single step, is determined by the number of species that are involved in the collision that subsequently leads to a reaction.[1] A unimolecular reaction involves a single reactant which may undergo rearrangement or dissociation, a bimolecular reaction involves two species, and a termolecular reaction involves three species. The order of an elementary reaction is equivalent to its stoichiometry i.e. the number of species involved in the reaction and is therefore equivalent to

its molecularity, a unimolecular reaction is first-order, a bimolecular reaction is second-order and a termolecular reaction is third-order.

The rate equation provides information about the rate of a reaction at a given instant during the course of the reaction, whereas the integrated rate equation allows us to determine the composition of a reacting mixture at a given time throughout the reaction.

For an elementary first-order reaction, A → B, the rate equation is written as Equation 2.2 and integrated to give Equation 2.4.

$$Rate = k[\mathrm{A}] = -\frac{d[\mathrm{A}]}{dt} \qquad \text{(Equation 2.2)}$$

$$\int_0^t \frac{d[\mathrm{A}]}{[\mathrm{A}]} = \int_0^t -k dt \qquad \text{(Equation 2.3)}$$

$$[\mathrm{A}]_t = [\mathrm{A}]_0 \, exp^{-kt} \qquad \text{(Equation 2.4)}$$

For an elementary second-order reaction, A + A → B, the rate equation is written as Equation 2.5 and integrated to give Equation 2.7.

$$Rate = -\frac{1}{2}\frac{d[\mathrm{A}]}{dt} = k[\mathrm{A}]^2 \qquad \text{(Equation 2.5)}$$

$$\int_{[A]_0}^{[A]_t} \frac{d[\mathrm{A}]}{[\mathrm{A}]^2} = \int_0^t -2k dt \qquad \text{(Equation 2.6)}$$

$$\frac{1}{[\mathrm{A}]_t} = \frac{1}{[\mathrm{A}]_0} + 2kt \qquad \text{(Equation 2.7)}$$

For an overall reaction that consists of an elementary first-order reaction and an elementary second-order reaction, the rate equation can be written as a mixed-order rate equation (Equation 2.8), which includes a first-order loss of reactant A and a second-order loss of reactant A.

$$Rate = -\frac{d[\mathrm{A}]}{dt} = k'[\mathrm{A}] + 2k''[\mathrm{A}]^2 \qquad \text{(Equation 2.8)}$$

where k' is the first-order rate coefficient and k'' is the second-order rate coefficient.

Equation 2.8 can be integrated to give Equation 2.9:

$$[\mathrm{A}]_t = \frac{[\mathrm{A}]_0 k'}{k' \, exp(k't) - 2k''[\mathrm{A}]_0 + 2k''[\mathrm{A}]_0 \, exp(k't)} \qquad \text{(Equation 2.9)}$$

A large number of reactions have more complex mechanisms occurring across multiple steps, where the rate law is no longer reflected by the stoichiometry of the reaction. In the study of kinetics, these reactions are termed 'complex reactions', which simply means the mechanism is made up from more than one elementary step. Consecutive reactions are an example of complex reactions and play an important role in kinetics and proceed via a mechanism that involves the formation of intermediates. The reactions of Criegee intermediates presented throughout this thesis are examples of complex reactions, which often proceed via the formation of an intermediate addition product before forming the overall reaction products.

2.1.1 The Steady State Approximation

Most complex reactions are often more complicated than those described in the previous section and therefore deriving the overall rate equations are more challenging. An approximation for the rate equations can be made using the steady state approximation (SSA). SSA assumes that, after an initial period of production of a reactive intermediate (C), its concentration reaches a low and constant level and we can therefore approximate that the rate of change of C is equal to zero:

$$\frac{d[\mathrm{C}]}{dt} \approx 0 \qquad \text{(Equation 2.10)}$$

For a reaction consisting of the following elementary reactions:

$\mathrm{A} + \mathrm{B} \rightarrow \mathrm{C}$ (R2.2)

$\mathrm{C} \rightarrow \mathrm{A} + \mathrm{B}$ (R2.3)

$\mathrm{C} \rightarrow \mathrm{D}$ (R2.4)

The overall rate of product formation is given by:

$$+\frac{d[\mathrm{D}]}{dt} = k_{2.4}[\mathrm{C}] \qquad \text{(Equation 2.11)}$$

C is the reactive intermediate, and using SSA we set the rate of change of C to zero.

$$+\frac{d[\mathrm{C}]}{dt} = k_{2.2}[\mathrm{A}][\mathrm{B}] - (k_{2.3}[\mathrm{C}] + k_{2.4}[\mathrm{C}]) \quad \text{(Equation 2.12)}$$

$$+\frac{d[\mathrm{C}]}{dt} = k_{2.2}[\mathrm{A}][\mathrm{B}] - [\mathrm{C}]\,(k_{2.3} + k_{2.4}) \approx 0 \quad \text{(Equation 2.13)}$$

The rate of production of the reactive intermediate is equal to the rate of its loss:

$$k_{2.2}[\mathrm{A}][\mathrm{B}] = [\mathrm{C}]\,(k_{2.3} + k_{2.4}) \quad \text{(Equation 2.14)}$$

This is then rearranged for the steady-state concentration of C:

$$[\mathrm{C}]_{ss} = \frac{k_{2.2}[\mathrm{A}][\mathrm{B}]}{k_{2.3} + k_{2.4}} \quad \text{(Equation 2.15)}$$

Substituting into the equation for the overall rate of product formation gives:

$$+\frac{d[\mathrm{D}]}{dt} = k_{2.4}[\mathrm{C}] = \frac{k_{2.4}k_{2.2}[\mathrm{A}][\mathrm{B}]}{k_{2.3} + k_{2.4}} \quad \text{(Equation 2.16)}$$

Application of the SSA is beneficial as it allows data analysis to be simplified and enables concentrations of reactive intermediates to be determined and expressions for rate laws to be obtained.

2.2 Theory of Temperature and Pressure Dependence

The rate coefficients of many reactions, particularly those that take place in the atmosphere, often show a dependence on the temperature and/or pressure of the system, examples of these reactions are shown in Chapters 4-7 and are the focus of this thesis. While experiments presented throughout this work span a wide range of temperatures and pressures, it is not always possible to reach the conditions of interest experimentally and so theoretical approaches are required to determine rate coefficients. The following section provides an overview of the methods used to quantitatively rationalise temperature and pressure dependent reactions.

2.2.1 Temperature Dependence

In 1889, Arrhenius suggested that the rate coefficient increases as the temperature is increased for the majority of reactions,[2] and that the positive temperature dependence can be described using the Arrhenius equation:

$$k = A\,exp^{\left(-\frac{E_a}{RT}\right)} \quad \text{(Equation 2.17)}$$

where *A* is the pre-exponential factor, which represents the frequency of successful collisions that lead to a reaction and E_a is the activation energy, which represents the minimum amount of energy required to overcome the reaction barrier, *R* is the gas constant and *T* is the temperature.

The exponential term increases with temperature and therefore the rate of reaction will increase as the temperature increases, for a reaction that exhibits typical Arrhenius behaviour.

Simple Collision Theory and Transition State Theory have been developed to rationalise the effects of temperature on reaction rates, and are described below.

2.2.1.1 Simple Collision Theory

Simple collision theory (SCT) is built upon the idea that elementary bimolecular reactions can be considered as collisional processes and assumes that the reacting species behave as hard spheres, which undergo elastic collisions, and that a reaction can only take place upon/during a collision. When reactant species collide, only a portion of the collisions result in a reaction, named successful collisions. These successful collisions must have enough energy to overcome the energy barrier to the reaction (the activation energy). The overall rate of reaction can be increased by either increasing the concentration of the reactant species, or increasing the temperature of the system. Increasing the concentration increases the number of collisions while increasing the temperature increases the kinetic energy of the reactant species and therefore are more likely to have enough energy to overcome the barrier to reaction (E_a).

SCT states that the rate of reaction, *r*, is equal to the collision frequency between the reactants, Z_{AB}, multiplied by the fraction of molecules that have sufficient energy to react upon collision, *F*.

$$r = Z_{\mathrm{AB}} F \qquad \text{(Equation 2.18)}$$

where the collision frequency is given by:

$$Z_{AB} = V_{col}[\mathrm{A}][\mathrm{B}] \qquad \text{(Equation 2.19)}$$

where V_{col} is the collision volume, which is the volume swept out by a moving molecule in unit time, and [A] and [B] are the molecular concentrations of A and B respectively.

The collision volume is determined by the product of the collision cross-section, σ_{AB}, and the mean relative speed of A and B, $\overline{c}_{\mathrm{rel}}$.

$$V_{col} = \sigma_{AB}\bar{c}_{\text{rel}} = \sigma_{AB}\left(\frac{8k_BT}{\pi\mu_{AB}}\right)^{\frac{1}{2}} \quad \text{(Equation 2.20)}$$

where k_B is the Boltzmann constant, T, is the temperature and μ_{AB} is the reduced mass of species A and B.

The collision cross-section is calculated using:

$$\sigma_{AB} = \pi(r_A + r_B)^2 \quad \text{(Equation 2.21)}$$

where r_A and r_B are the radii of species A and B.

The reduced mass is calculated using:

$$\mu_{AB} = \frac{m_A m_B}{m_A + m_B} \quad \text{(Equation 2.22)}$$

where m_A and m_B are the masses of species A and B.

Substituting Equation 2.20 into Equation 2.19 gives:

$$\mathrm{Z}_{AB} = \sigma_{AB}\left(\frac{8k_BT}{\pi\mu_{AB}}\right)^{\frac{1}{2}}[\mathrm{A}][\mathrm{B}] \quad \text{(Equation 2.23)}$$

The fraction of collisions with sufficient energy to overcome an energy barrier, F, is given by the fraction of species with a kinetic energy above a certain critical value, ε, within a Boltzmann distribution of kinetic energies, $f(E)$.

$$f(E) = \frac{1}{k_BT}exp^{\left(-\frac{E}{k_BT}\right)} \quad \text{(Equation 2.24)}$$

Integrating the distribution of kinetic energies between the critical energy of the reaction, ε, and infinity, ∞, gives the fraction of species with sufficient energy to overcome the reaction barrier, F.

$$F = f(E \geq E_a) = \int_{E_a}^{\infty} \frac{1}{k_BT}exp^{\left(-\frac{E}{k_BT}\right)}\,dE \quad \text{(Equation 2.25)}$$

$$= \frac{1}{k_BT}\int_{E_a}^{\infty} exp^{\left(-\frac{E}{k_BT}\right)}\,dE \quad \text{(Equation 2.26)}$$

$$= exp^{\left(-\frac{E_a}{k_BT}\right)} \quad \text{(Equation 2.27)}$$

The rate of a reaction can therefore be estimated from SCT using:

$$r = \sigma_{AB}\left(\frac{8k_BT}{\pi\mu_{AB}}\right)^{\frac{1}{2}}[\mathrm{A}][\mathrm{B}]\,exp^{\left(-\frac{E_a}{k_BT}\right)} \qquad \text{(Equation 2.28)}$$

Considering an elementary reaction, SCT predicts the rate coefficient, *k*, is given by Equation 2.29, which compares well with the experimentally determined Arrhenius equation (Equation 2.17).

$$k = \sigma_{AB}\left(\frac{8k_BT}{\pi\mu_{AB}}\right)^{\frac{1}{2}}\,exp^{\left(-\frac{E_a}{k_BT}\right)} \qquad \text{(Equation 2.29)}$$

Equation 2.29 can be used to calculate the hard-sphere collision limit of a reaction, that is, the maximum rate at which a reaction can occur, by assuming 100 % of the collisions have sufficient energy to overcome the barrier to reaction. Equation 2.29 is thus simplified to:

$$k = \sigma_{AB}\left(\frac{8k_BT}{\pi\mu_{AB}}\right)^{\frac{1}{2}} \qquad \text{(Equation 2.30)}$$

The use of Equation 2.30 to obtain the collision-limited rate coefficient at different temperatures is shown in Chapter 7.

When comparing calculated rate coefficients from SCT to experimentally determined rate coefficients, SCT often overestimates the pre-exponential factor and therefore, the rate coefficient. An explanation for this is that SCT assumes that all collisions between reacting species will lead to a reaction and is therefore independent of the orientation of the reacting molecules. The inclusion of a steric factor, *P*, is used to rectify the discrepancy between calculated and observed rate coefficients, which is defined as the ratio between the experimentally determined value for *A* and the calculated collision frequency.

$$P = \frac{A_{experimental}}{Z_{AB,calculated}} \qquad \text{(Equation 2.31)}$$

The assumptions made by SCT, which ignore the significance of the structure of the reactant molecule as well as the potential role of molecular forces (such as attraction and repulsion), can result in a poor agreement between calculated and experimentally determined rate coefficients. The orientation at which collisions occur will influence whether the collision leads to a reaction as there are certain steric requirements that need to be met for a reaction to take place i.e. the reactive sites of the molecule need to be involved in the collision. SCT also assumes that collisions are instantaneous when in reality, following a successful collision,

there is a change in the distribution of energy between molecules and a transient complex is formed. A theory that considers the structure of the reacting molecules as well as intermolecular forces is required to accurately characterise the temperature dependence exhibited by reactions.

2.2.1.2 Transition State Theory

Transition State Theory (TST) builds on SCT and considers the reaction taking place as a trajectory across a potential energy surface (PES) (Figure 2.1). As two reactant molecules approach one another, their potential energy increases and reaches a maximum. This maximum energy corresponds to an activated complex, which can be described as a cluster of atoms that may proceed to produce the reaction products, or fall apart back to the reactants. The peak in potential energy produces a cluster of atoms with a structure where any further distortion will lead to product formation – this is termed the transition state. TST assumes the activated complex is in quasi-equilibrium with the reactants and once the transition state has been reached, it is impossible to re-form reactants and so will proceed towards the formation of products.

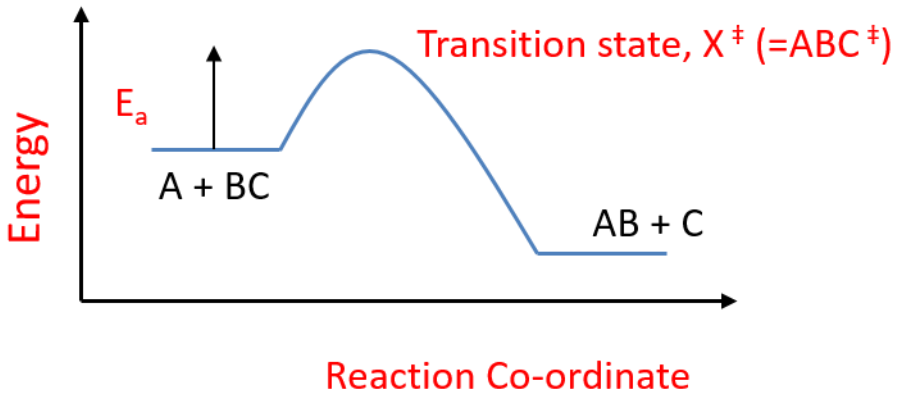

Figure 2.1. General schematic of a potential energy surface (PES) for a reaction described by transition state theory.

For an overall reaction:

$$A + BC \rightarrow AB + C \qquad \text{(R2.5)}$$

We can apply TST and incorporate the presence of a transition state, $ABC^{\ddagger}$:

$$A + BC \rightarrow ABC^{\ddagger} \qquad \text{(R2.6)}$$

$$ABC^{\ddagger} \rightarrow A + BC \qquad \text{(R2.7)}$$

$$ABC^{\ddagger} \rightarrow AB + C \qquad \text{(R2.8)}$$

The rate equations for the loss of reactants ($r_{2.6}$) and the formation of products ($r_{2.8}$) can be written as:

$$r_{2.6} = -\frac{d[\mathrm{A}]}{dt} = -\frac{d[\mathrm{BC}]}{dt} = k_{2.6}[\mathrm{A}][\mathrm{BC}] \qquad \text{(Equation 2.32)}$$

$$r_{2.8} = +\frac{d[\mathrm{AB}]}{dt} = +\frac{d[\mathrm{C}]}{dt} = k_{2.8}^{\ddagger}[\mathrm{ABC}^{\ddagger}] \qquad \text{(Equation 2.33)}$$

where $k_{2.8}^{\ddagger}$ is the rate coefficient for the formation of the transition state.

The equilibrium constant for the quasi-equilibrium between reactants and the intermediate can be defined as:

$$K^{\ddagger} = \frac{[\mathrm{ABC}^{\ddagger}]}{[\mathrm{A}][\mathrm{BC}]} \qquad \text{(Equation 2.34)}$$

where $K^{\ddagger}$ is the equilibrium constant.

Rearranging to give the concentration of the transition state, $\mathrm{ABC}^{\ddagger}$:

$$[\mathrm{ABC}^{\ddagger}] = K^{\ddagger}[\mathrm{A}][\mathrm{BC}] \qquad \text{(Equation 2.35)}$$

Substituting into the equation for overall product formation:

$$rate = k^{\ddagger}[\mathrm{ABC}^{\ddagger}] = k^{\ddagger}K^{\ddagger}[\mathrm{A}][\mathrm{BC}] = k[\mathrm{A}][\mathrm{BC}] \qquad \text{(Equation 2.36)}$$

To obtain the overall rate coefficient, the equilibrium constant for the formation of the transition state, $K^{\ddagger}$, and the rate coefficient for the formation of products from the transition state, $k^{\ddagger}$, need to be defined. Using statistical thermodynamics, $K^{\ddagger}$ can be calculated as:

$$K^{\ddagger} = \frac{q_{\mathrm{ABC}^{\ddagger}}}{q_A q_B}\, exp^{\left(\frac{-\varepsilon}{k_B T}\right)} \qquad \text{(Equation 2.37)}$$

where q represents the molecular partition functions of each species, made up of translational, rotational, vibrational and electronic partition functions of each species ($q_{tot} = q_{trans} \times q_{rot} \times q_{vib} \times q_{elec}$). A second assumption of TST is that it is a single vibration, the dissociation mode, that is independent from all other vibrations and rotations in the transition state, responsible for product formation. We can therefore separate this single partition function:

$$q_{ABC,tot}^{\ddagger} = q_{ABC}^{\ddagger} \times q_{diss} \qquad \text{(Equation 2.38)}$$

where q_{diss} represents the partition function for dissociation and is equal to:

$$q_{diss} = \frac{k_B T}{h\nu} \quad \text{(Equation 2.39)}$$

$$q^{\ddagger}_{ABC,tot} = q^{\ddagger}_{ABC} \times \frac{k_B T}{h\nu} \quad \text{(Equation 2.40)}$$

$$K^{\ddagger} = \frac{q^{\ddagger}_{ABC,tot}}{q_A q_B}\, exp^{\left(\frac{-\varepsilon}{K_B T}\right)} = \frac{k_B T}{h\nu}\frac{q^{\ddagger}_{ABC}}{q_A q_B}\, exp^{\left(\frac{-\varepsilon}{k_B T}\right)} \quad \text{(Equation 2.41)}$$

The rate coefficient, $k^{\ddagger}$, is equal to the imaginary frequency of the vibrational mode responsible for converting the activated complex to products, *v*:

$$k^{\ddagger} = \nu \quad \text{(Equation 2.42)}$$

Substitution gives the overall rate coefficient, *k*:

$$k = \frac{k_B T}{h}\frac{q_{\mathrm{ABC}^{\ddagger}}}{q_A q_B}\, exp^{\left(\frac{-\varepsilon}{k_B T}\right)} \quad \text{(Equation 2.43)}$$

The calculation of partition functions can be difficult as the structure and vibrational frequencies of the transition state are often not well known.

For a system at equilibrium, the change in Gibbs free energy is:

$$\Delta G^{\ddagger} = -RT\ln K^{\ddagger} \quad \text{(Equation 2.44)}$$

Equation 2.44 can be rearranged to give an expression for $K^{\ddagger}$:

$$K^{\ddagger} = exp^{\left(-\frac{\Delta G^{\ddagger}}{RT}\right)} \quad \text{(Equation 2.45)}$$

where $\Delta G^{\ddagger}$ can be defined as

$$\Delta G^{\ddagger} = \Delta H^{\ddagger} - T\Delta S^{\ddagger} \quad \text{(Equation 2.46)}$$

where $\Delta H^{\ddagger}$ is the change in the enthalpy of transition state formation, relating to the amount of heat absorbed or released and $\Delta S^{\ddagger}$ is the change in the entropy upon formation of the transition state, describing the disorder of the system.

Substitution then gives:

$$K^{\ddagger} = exp^{\left(\frac{-\Delta H^{\ddagger}}{RT}\right)} exp^{\left(\frac{\Delta S^{\ddagger}}{R}\right)} \quad \text{(Equation 2.47)}$$

The rate coefficient can therefore be described by:

$$k = \frac{k_B T}{h} exp^{\left(\frac{-\Delta H^{\ddagger}}{RT}\right)} exp^{\left(\frac{\Delta S^{\ddagger}}{R}\right)} \quad \text{(Equation 2.48)}$$

The enthalpy, $\Delta H^{\ddagger}$, and entropy, $\Delta S^{\ddagger}$, of the formation of the transition state complex can be related to the activation energy, E_a, and the pre-exponential factor, A, in the Arrhenius equation. The more negative the entropy, the more ordered the system and the smaller the value for the steric factor, P.

When comparing to experimental observations, TST often gives rate coefficients that are too low for reactions involving light atoms, particularly at low temperatures, as it ignores the possibility of tunnelling. Quantum mechanics states that there is a non-zero possibility of a particle appearing on the other side of the reaction barrier, even if its energy is less than that of the barrier height, which is referred to as tunnelling.[1] At ambient temperatures, the 'classical' rate of a reaction is likely to be much greater than the tunnelling rate, and tunnelling is therefore often insignificant. As the temperature of the system is lowered, the amount of energised particles is reduced and the classical rate becomes comparable to the tunnelling rate, resulting in the rate of reaction proceeding much faster than that expected classically.

TST also assumes the rate of reaction corresponds to the rate of passage through the 'bottleneck' region, which is the lowest energy point on the PES. While this assumption may be valid at lower temperatures, TST often fails to accurately predict the rate coefficient at higher temperatures. This is because at higher temperatures, higher vibrational energy levels can be reached within the transition state as the average energy of molecules is much higher. This means that the harmonic oscillator approximation, used to calculate the vibrational partition function, q_{vib}, is poor and more complex expressions are needed.

TST also works under the approximation that the reactants are in thermal equilibrium i.e. the energy distribution is given by the Boltzmann distribution and therefore the concentration of the activated complex can be calculated using the equilibrium constant (Equation 2.45). This theory assumes that the activated complex has a long enough lifetime to reach equilibrium, which is not always the case. More detailed versions of TST, such as variational transition state theory (VTST) and canonical transition state theory (CTST) have been developed to account for the limitations of TST and improve the comparison with experimentally observed rate coefficients.

2.2.1.3 Barrierless Reactions

SCT and TST both assume the presence of an energy barrier to reaction. For a chemical reaction involving a barrier, the species within the system need sufficient translational energy (equal to or in excess of the activation energy) for the reaction to proceed. As the temperature is increased, the number of species with sufficient energy to react will increase thus increasing the rate of reaction.

However, some reactions may exhibit a negative temperature dependence, where the rate of reaction will decrease as the temperature is increased, examples of which are shown throughout this thesis. When fit with an Arrhenius expression, the activation energy of these reactions will be negative due to the lack of energy barrier (i.e. no bonds need to be broken for the reaction to occur). These reactions are named barrierless reactions and a general potential energy surface (PES) schematic is shown in Figure 2.2.

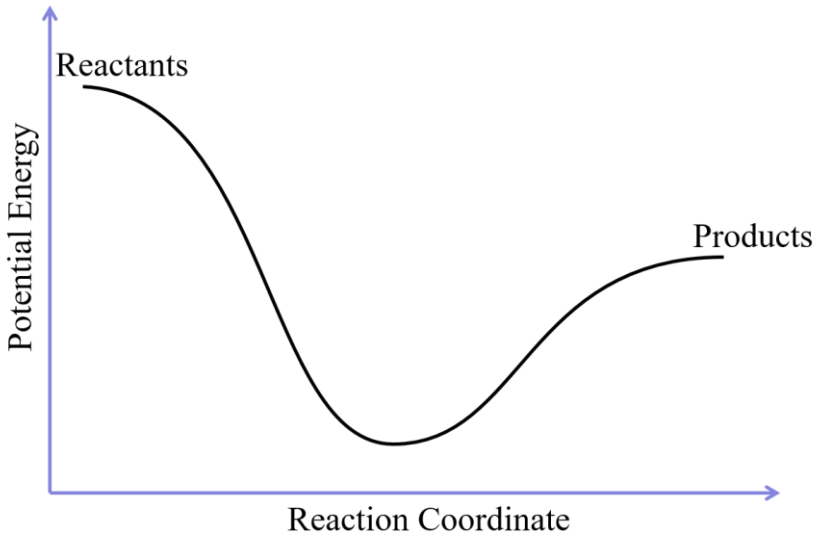

Figure 2.2. General schematic representing a potential energy surface for a barrierless reaction.

Barrierless reactions are often addition reactions, where the total potential energy is reduced as the two reactants come together as there are no bonds to be broken. At lower temperatures, the addition product has less vibrational energy and a longer lifetime, which provides more opportunity to go on to produce the reaction products rather than re-dissociate back to reactants. At higher temperatures, there are more vibrationally active modes within the addition product, reducing its lifetime and making it more likely to dissociate back to the reactants.

TST assumes that a transition state in a reaction is only crossed once, which may be a sufficient prediction for reactions where the energy of the system is significantly lower than that of the

activation energy. However, for barrierless reactions, or where the activation energy is small, it is possible for the species to cross the transition state and turn around, or cross multiple times, but only react once. Variational TST (VTST) is used to identify the position of the transition state on the PES that leads to a successful reaction– for a barrierless reaction, the transition state is determined from entropy rather than enthalpy as the enthalpy term is related to activation energy (see Section 2.2.1.2) which becomes negligible for a barrierless reaction.

Reactions with large activation barriers may also demonstrate a negative temperature dependence as a result of quantum mechanical tunnelling (QMT) – a species such as hydrogen can penetrate through a reaction barrier that is higher in energy than the species own kinetic energy.

2.2.1.3.1 Capture-Limited Rate Coefficients

Barrierless reactions are of particular importance within atmospheric chemistry because of the type of reactions that occur without a barrier, i.e. radical-radical reactions, and their large rate coefficients. When a reaction is governed by long-range attractive forces between two reactant species, there is no reaction barrier, and the rate coefficient is described by the rate of capture between reactants. A transient association complex is formed in an attractive potential energy well, which can be either short-lived and subsequently form reaction products, or long-lived. Capture theory assumes that, once the association complex is formed, the system can no longer revert back to reactant species.[3] Capture theory was first proposed in the 1970s and 1980s[4, 5, 6, 7] as a way to describe processes that did not follow simple Arrhenius behaviour, by taking into account long-range interactions between reactant molecules.

Quantum capture theories take into account the contributions of individual rotational states to determine the likelihood of a reaction occurring. Georgievskii and Klippenstein[8] modelled long-range interactions using variational TST (VTST). This approach implemented the conservation of total angular momentum and total energy, which had previously been disregarded by canonical TST (C-VTST) and microcanonical TST (μ-VTST), to yield μJ-VTST. In this approach, only the reaction co-ordinate that is defined by the separation between the centres of mass of the two reactants is considered and quantum effects are incorporated by treating the rotations of each reactant quantum mechanically. The result of μJ-VTST is a description of the capture rate coefficient with a power-law dependence on the distance between the two reactants:

$$k_{\text{capt}} = C\sqrt{\frac{\pi}{\mu}}(d_1 d_2)^{\frac{2}{3}}(k_B T)^{-\frac{1}{6}} \quad \text{(Equation 2.49)}$$

where C is a constant that is specific for each type of interaction[8] (C = 4.08 for the case of isotropic capture[9]), μ is the reduced mass, d_1 and d_2 represent the dipole moments of reactant 1 and 2, k_B is the Boltzmann constant and T is the temperature.

Equation 2.49 is used in Chapter 7, alongside values obtained for the collision-limited rate coefficient (Equation 2.30) to discuss the kinetics of the reaction between *anti*-CH_3CHOO and SO_2. It should be noted that capture-limited rate coefficients work under the assumption that once the reactants are 'captured' and the association complex is formed, there is no possibility for the complex to dissociate back to the reactants. The theory also ignores any influence of short-range interactions that can influence the possibility of the reaction proceeding and as a result, are often treated as upper limits rather than absolute values.[3]

2.2.2 Pressure Dependence

As two atoms come together to form a new bond (association), an amount of energy is released that is equal to the dissociation energy of that new bond. The reaction exothermicity is contained within the newly formed bond and it is possible that the nascent molecule will dissociate back to the reactants. However, the nascent molecule may also become stabilised through collision with a bath gas molecule, M, where some of the reaction exothermicity is transferred to translational excitation of the bath gas species, this process is known as stabilisation and will depend on the concentration of M and thus pressure.

2.2.2.1 The Lindemann Mechanism

At high pressures, there are a number of reactions that follow first-order kinetics, such that their rate of reaction is dependent only on a single reactant. The rate coefficient increased with increasing temperature, suggesting the presence of an activation barrier, but the first-order kinetics seemed to prevent collisional activation.

The Lindemann mechanism, first proposed in the 1920's, provides the first model to describe the pressure dependence of reactions and predicted that the rate coefficient should decrease with decreasing pressure, and the reaction will eventually become second-order overall.

The overall unimolecular dissociation reaction (R2.9) can be split into elementary reactions (R2.10-R2.12).

$A \rightarrow P$ (R2.9)

$A + M \rightarrow A^* + M$ (R2.10)

$A^* + M \rightarrow A + M$ (R2.11)

$A^* \rightarrow P$ (R2.12)

The first step involves a collision between A and M (usually a bath gas) where energy is transferred from M to the reactants to produced energised A* (excitation). This energised A* can either undergo deactivation (the reverse of the first step) to reform the reactant A, or it may undergo a reaction to produce the products.

The rate of formation of reaction products is described as:

$$Rate = +\frac{d[P]}{dt} = k_{2.12}[A^*]$$ (Equation 2.50)

The steady state approximation states that after a period of time, the production and removal of A* will become equal, and therefore A* reaches a steady state concentration (see Section 2.1.1 for further details):

Rate of production of A*:

$$Rate = +\frac{d[A^*]}{dt} = k_{2.10}[A][M]$$ (Equation 2.51)

Rate of loss of A*:

$$Rate = -\frac{d[A^*]}{dt} = k_{2.11}[A^*][M] + k_{2.12}[A^*]$$ (Equation 2.52)

The rate of formation of A* is equal to the rate of loss of A*:

$$k_{2.10}[A][M] = k_{2.11}[A^*][M] + k_{2.12}[A^*]$$ (Equation 2.53)

Equation 2.53 can be rearranged for A*:

$$[A^*] = \frac{k_{2.10}[A][M]}{k_{2.11}[M] + k_{2.12}}$$ (Equation 2.54)

Substituting back into the equation for the formation of reaction products gives:

$$Rate = +\frac{d[P]}{dt} = k_{2.12}[A^*] = \frac{k_{2.12}k_{2.10}[A][M]}{k_{2.11}[M] + k_{2.12}}$$ (Equation 2.55)

When reactions are occurring at lower pressures, the rate of collisional deactivation is slow compared to the unimolecular reaction and $k_{2.11}[\mathrm{M}] << k_{2.12}$, and the rate of product formation is simplified from Equation 2.55 to Equation 2.57:

$$Rate = \frac{k_{2.12}k_{2.10}[\mathrm{A}][\mathrm{M}]}{k_{2.12}} \quad \text{(Equation 2.56)}$$

$$Rate = k_{2.10}[\mathrm{A}][\mathrm{M}] \quad \text{(Equation 2.57)}$$

At low pressure, the observed rate coefficient, k_{obs}, can be described as:

$$k_{obs} = k_0 = k_{2.10}[\mathrm{A}][\mathrm{M}] \quad \text{(Equation 2.58)}$$

where k_0 describes the low pressure limiting rate coefficient.

Kinetics are now described as being second-order as the rate is dependent on the concentrations of both [A] and [M]. For the low-pressure regime, the rate coefficient increases as the pressure is increased since k_{obs} is directly proportional to [M].

When reactions take place at higher pressures, i.e. high [M], collisional deactivation is fast, and the unimolecular reaction is relatively slow and therefore the rate determining step. Since $k_{2.12} << k_{2.11}[\mathrm{M}]$, the rate or product formation is simplified from Equation 2.55 to Equation 2.60:

$$Rate = \frac{k_{2.12}k_{2.10}[\mathrm{A}][\mathrm{M}]}{k_{2.11}[\mathrm{M}]} \quad \text{(Equation 2.59)}$$

$$Rate = \frac{k_{2.12}k_{2.10}}{k_{2.11}}[\mathrm{A}] \quad \text{(Equation 2.60)}$$

The observed rate coefficient, k_{obs}, can be described as:

$$k_{obs} = k_\infty = \frac{k_{2.12}k_{2.10}}{k_{2.11}} \quad \text{(Equation 2.61)}$$

where k_∞ is the high pressure limiting rate coefficient.

The rate coefficient therefore becomes independent of total pressure, [M], and the kinetics are first-order as the rate is only dependent on the concentration of [A]. The region in which the observed rate coefficient, k_{obs}, transitions from the low-pressure regime to the high-pressure regime is called the fall-off region, and it shown schematically in Figure 2.3.

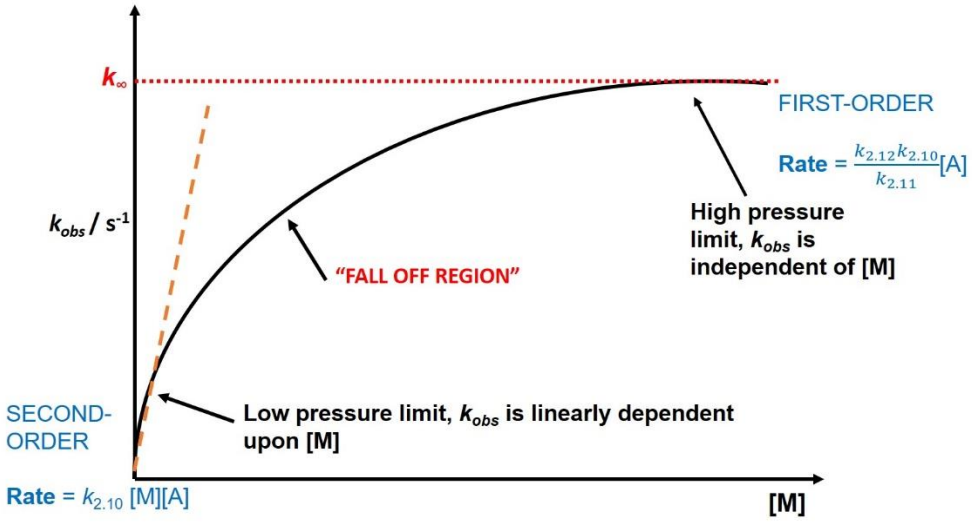

Figure 2.3. Schematic diagram of the rate coefficient, k_{obs}, as a function of pressure, [M], where k_{obs} is second-order at low pressures and first-order at high pressures. Adapted from reference 10.[10]

The unimolecular rate coefficient, k_{obs}, at any pressure can be defined in terms of both k_0 and k_∞:

$$k_{obs} = \frac{k_0[\mathrm{M}]k_\infty}{k_0[\mathrm{M}] + k_\infty} \qquad \text{(Equation 2.62)}$$

A similar mechanism to the one outlined above can be used to explain pressure dependence in termolecular reactions, where two reactants, A+B, are excited by a bath gas molecule to produce AB*, which can then dissociate back to reactants as before or produce a single reaction product AB. For a generic termolecular reaction:

$$\mathrm{A + B + M \rightarrow AB + M} \qquad \text{(R2.13)}$$

The elementary reactions are given as:

$$\mathrm{A + B \rightarrow AB^*} \qquad \text{(R2.14)}$$

$$\mathrm{AB^* \rightarrow A + B} \qquad \text{(R2.15)}$$

$$\mathrm{AB^* + M \rightarrow AB + M} \qquad \text{(R2.16)}$$

Application of the steady state approximation gives:

$$+\frac{d[\mathrm{AB}]}{dt} = k_{2.16}[\mathrm{AB^*}][\mathrm{M}] = \frac{k_{2.16}k_{2.14}[\mathrm{A}][\mathrm{B}][\mathrm{M}]}{k_{2.15} + k_{2.16}[\mathrm{M}]} \qquad \text{(Equation 2.63)}$$

The experimentally observed termolecular rate coefficient k_{termol} is given by:

$$+\frac{d[\mathrm{AB}]}{dt} = k_{termol}[\mathrm{A}][\mathrm{B}] \quad \text{(Equation 2.64)}$$

where:

$$k_{termol} = \frac{k_{2.16}k_{2.14}[\mathrm{M}]}{k_{2.16}[\mathrm{M}] + k_{2.15}} \quad \text{(Equation 2.65)}$$

In the same way as for unimolecular reactions, at low pressures, since $k_{2.16}[\mathrm{M}] << k_{2.15}$ the rate of formation of AB can be simplified to:

$$+\frac{d[AB]}{dt} = \frac{k_{2.16}k_{2.14}}{k_{2.15}}[\mathrm{A}][\mathrm{B}][\mathrm{M}] = k_0[\mathrm{A}][\mathrm{B}][\mathrm{M}] \quad \text{(Equation 2.66)}$$

Resulting in a third-order rate equation where:

$$k_0 = \frac{k_{2.16}k_{2.14}}{k_{2.15}} \quad \text{(Equation 2.67)}$$

At high pressures where $k_{2.16}[\mathrm{M}] >> k_{2.15}$ the rate of product formation is given by:

$$+\frac{d[\mathrm{AB}]}{dt} = k_{2.15}[\mathrm{A}][\mathrm{B}] = k_\infty[\mathrm{A}][\mathrm{B}] \quad \text{(Equation 2.68)}$$

Resulting in a second-order rate equation where:

$$k_\infty = k_{2.14} \quad \text{(Equation 2.69)}$$

When comparing the Lindemann mechanism to experimentally observed results for both unimolecular and termolecular reactions, it provides a qualitative analysis of the kinetics, such that it can explain the occurrence of the fall-off region. However, it predicts that k_{obs} decreases with pressure and that its reciprocal is a linear function of the reciprocal of pressure, but this is often observed to be a curved plot rather than linear.

There are two major failures of the Lindemann mechanism which explain why its predictions do not align with experimental observations. These failures have been addressed by extensions of the theory and are summarised in Sections 2.2.2.3 and 2.2.2.4.

2.2.2.2 Chemical Activation

It will be seen in later chapters of this thesis that there may be competition between association/dissociation reactions and chemical activation, where chemical activation is the process by which reaction products are formed from the excited complex rather than becoming stabilised through collisions with M or dissociating back to the reactants.

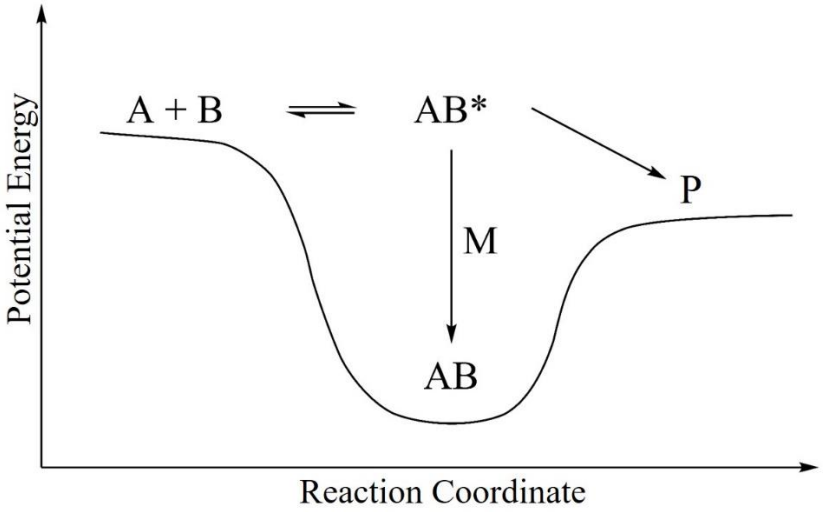

Figure 2.4. Schematic potential energy surface for a general reaction, A + B, to produce an excited complex, AB*, and the possible reaction pathways following excitation.

For the general reaction:

A+ B → P (R2.17)

The elementary reactions can be written as:

A + B → AB* (R2.18)

AB* → A + B (R2.19)

AB* + M → AB + M (R2.20)

AB* → P (R2.21)

The rate of formation for the two different product channels, association ($k_{2.20}$) and chemical activation ($k_{2.21}$) can be defined as:

$$+\frac{d[\mathrm{AB}]}{dt} = k_{2.20}[\mathrm{AB^*}][\mathrm{M}] \quad \text{(Equation 2.70)}$$

$$+\frac{d[\mathrm{P}]}{dt} = k_{2.21}[\mathrm{AB^*}] \quad \text{(Equation 2.71)}$$

Applying the steady state approximation for an expression for [AB*] gives:

$$k_{2.18}[\mathrm{A}][\mathrm{B}] = [\mathrm{AB}^*](k_{2.19} + k_{2.20}[\mathrm{M}] + k_{2.21}) \quad \text{(Equation 2.72)}$$

$$[\mathrm{AB}^*] = \frac{k_{2.18}[\mathrm{A}][\mathrm{B}]}{k_{2.19} + k_{2.20}[\mathrm{M}] + k_{2.21}} \quad \text{(Equation 2.73)}$$

Substituting back in for the expressions for association and chemical activation gives:

$$+\frac{d[\mathrm{AB}]}{dt} = k_{2.20}[\mathrm{AB}^*][\mathrm{M}] = \frac{k_{2.18}k_{2.20}[\mathrm{A}][\mathrm{B}][\mathrm{M}]}{k_{2.19} + k_{2.20}[\mathrm{M}] + k_{2.21}} \quad \text{(Equation 2.74)}$$

$$+\frac{d[\mathrm{P}]}{dt} = k_{2.21}[\mathrm{AB}^*] = \frac{k_{2.18}k_{2.21}[\mathrm{A}][\mathrm{B}]}{k_{2.19} + k_{2.20}[\mathrm{M}] + k_{2.21}} \quad \text{(Equation 2.75)}$$

The observed rate coefficient, k_{obs}, will be a combination of association and chemical activation:

$$k_{obs} = \frac{k_{2.18}k_{2.20}[\mathrm{M}]}{k_{2.19} + k_{2.20}[\mathrm{M}] + k_{2.21}} + \frac{k_{2.18}k_{2.21}}{k_{2.19} + k_{2.20}[\mathrm{M}] + k_{2.21}} \quad \text{(Equation 2.76)}$$

$$k_{obs} = \frac{k_{2.18}k_{2.20}[\mathrm{M}] + k_{2.18}k_{2.21}}{k_{2.19} + k_{2.20}[\mathrm{M}] + k_{2.21}} \quad \text{(Equation 2.77)}$$

At any pressure, the observed rate coefficient can be described in terms of k_0, k_∞ and k_{int}, where k_{int} represents the rate coefficient at zero pressure:

$$k_{obs} = k_{int} + \frac{(k_\infty - k_{int}) + k_0[\mathrm{M}]}{k_0[\mathrm{M}] + k_\infty} \quad \text{(Equation 2.78)}$$

where:

$$k_\infty = k_{2.18} \quad \text{(Equation 2.79)}$$

$$k_0 = \frac{k_{2.18}k_{2.20}[\mathrm{M}]}{k_{2.19} + k_{2.21}} \quad \text{(Equation 2.80)}$$

$$k_{int} = \frac{k_{2.18}k_{2.21}}{k_{2.19} + k_{2.21}} \quad \text{(Equation 2.81)}$$

This mechanism has been used to explain the pressure dependence of the reaction between *syn*-CH_3CHOO and SO_2 and determine the yield of the association product (CH_3CHOO-SO_2)

and the activation products ($CH_3CHO + SO_3$) as a function of pressure. More details are given in Chapter 7.

2.2.2.3 The Hinshelwood Theory

The first failure of the Lindemann mechanism is that the description of the rates of activation and deactivation are too simplistic and assumes they can be calculated directly from collision theory and therefore neglects the internal degrees of freedom of the reactant species. Hinshelwood theorised that excess energy can be stored within a number of combinations of states within the excited molecule, A*, and that the number of states increases with energy. The rate of excitation of A to A* will therefore increase as the number of states increases.

2.2.2.4 The Rice-Ramsperger-Kassel-Marcus Theory

The second failure of the Lindemann mechanism is that this mechanism assumes that the unimolecular step is not energy dependent since it takes no account for the fact that a unimolecular reaction specifically involves one particular form of molecular motion. A minimum amount of energy must be in this form of motion i.e. rotation, for a reaction to occur. Rice and Ramsperger,[11] Kassel[12] and Marcus[13] developed RRKM theory by considering the conversion of the excited molecule, A*, to a molecule that has sufficient energy localised within a particular motion, $A^{\ddagger}$:

$$A + M \rightarrow A^* + M \qquad \text{(R2.22)}$$

$$A^* + M \rightarrow A + M \qquad \text{(R2.23)}$$

$$A^* \rightarrow A^{\ddagger} \qquad \text{(R2.24)}$$

$$A^{\ddagger} \rightarrow P \qquad \text{(R2.25)}$$

The reaction is now thought to proceed via $A^{\ddagger}$, which contains the same amount of energy as A* but with an amount of energy stored within a specific reactive mode, whereas the energy in A* is considered to be randomised. As the size of the reacting molecule is increased, the number of modes will increase, which will decrease the probability of the energy being localised within a specific mode, decreasing the rate coefficient for overall product formation.

2.2.2.5 The Troe Fall-off Form

Troe[14] theorised a general description for fall-off curves by introducing a broadening factor, F, to reflect the pressure dependence of experimentally determined rate coefficients, k_{obs}:

$$k_{obs} = \frac{k_0[\mathrm{M}]k_\infty}{k_0[\mathrm{M}] + k_\infty} F \qquad \text{(Equation 2.82)}$$

where

$$\log F = \frac{\log F_c}{1 + \left[\frac{\log\left(\frac{k_0[M]}{k_\infty}\right)}{N}\right]^2} \qquad \text{(Equation 2.83)}$$

where N is given by:

$$N = 0.75 - 1.27 \times \log F_C \qquad \text{(Equation 2.84)}$$

F_c depends on the reaction being investigated but the NASA/JPL[15] and IUPAC[16] panels identified that using a value of 0.6 provides an accurate description for most atmospheric reactions. The following equations provide a description of the broadening factor, which may be suitable for reactions with broad fall-off curves.[14]

$$F = \frac{\left(1 + \frac{k_0[\mathrm{M}]}{k_\infty}\right)}{\left[1 + \left(\frac{k_0[\mathrm{M}]}{k_\infty}\right)^n\right]^{1/n}} \qquad \text{(Equation 2.85)}$$

where

$$n = \left(\frac{\ln(2)}{\ln\left(\frac{2}{F_c}\right)}\right)\left[0.8 + 0.2\left(\frac{k_0[\mathrm{M}]}{k_\infty}\right)^q\right] \qquad \text{(Equation 2.86)}$$

where

$$q = \frac{(F_c - 1)}{\ln\left(\frac{F_c}{10}\right)} \qquad \text{(Equation 2.87)}$$

2.2.3 Master Equation Calculations

Kinetic modelling is of particular interest as many reactions relevant to both industry and the atmosphere take place under conditions that cannot be easily replicated within laboratories, such as reactions relevant to combustion chemistry or atmospheric chemistry that occurs at extreme temperatures.

The master equation (ME) is a theoretical tool that allows for the extrapolation of kinetics obtained within the laboratory to predict kinetics under these extreme conditions. The master equation is described by Equation 2.88:

$$\frac{dn_i}{dt} = \boldsymbol{M}i \qquad \text{(Equation 2.88)}$$

where n_i is the population of species i and $\boldsymbol{M}$ is the transition matrix, which describes the change in population as a function of time as a result of collisional energy transfer and reactions.

A number of chemical reactions occur with non-Boltzmann energy distributions, where the kinetics cannot be accurately described using equilibrium thermodynamics. In this regime, thermal relaxation time scales are competitive with kinetic time scales. One theoretical approach uses an energy grained master equation (EGME) to treat the competition between the relaxation and kinetic time scales. The EGME partitions rovibrational energy states for all species in the reaction (reactants, transition states, intermediates and products) into grains of a defined number of states.[17] Grains that correspond to the reactants are assigned populations based on a Boltzmann distribution, with other species given a population of zero. The population distribution can change through two processes. The first process is through transformation of one species to another, which is controlled by the microcanonical rate coefficients in the system and are described by RRKM theory. The second process is through collisional energy transfer via interactions with a bath gas, a process which is described by an exponential down model. The energy transfer from one grain to another upon collision is determined by the parameter $\langle \Delta E \rangle_{\mathrm{down}}$. The temperature and pressure dependent kinetics of the system can be described by the energy barriers, well depths and $\langle \Delta E \rangle_{\mathrm{down}}$. Figure 2.5 shows a schematic of the EGME for a typical association reaction.

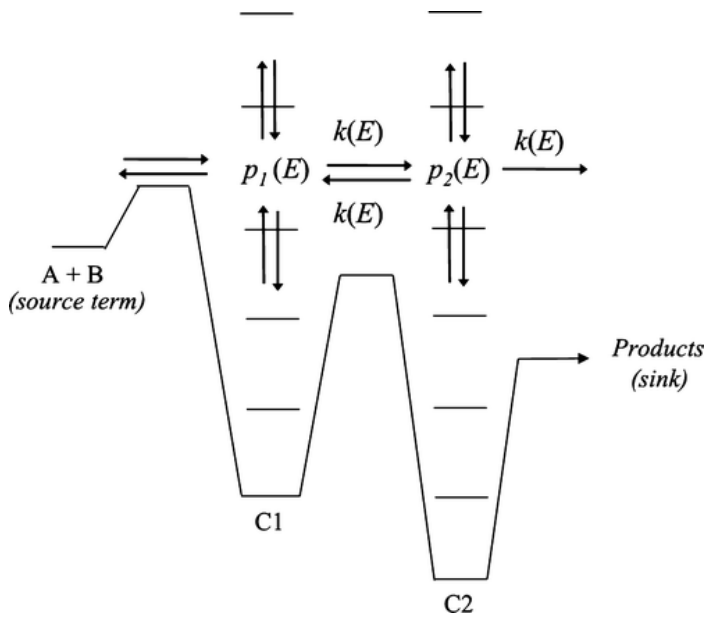

Figure 2.5. Schematic of the Energy Grained Master Equation Model for an association reaction with two wells; C1 and C2. Copied from reference 18.[18]

The Master Equation Solver for Multi-Energy well Reactions (MESMER), developed at the University of Leeds, uses a one-dimensional form of the EGME where the total rovibrational energy of the system, *E*, is the independent variable.[18] MESMER uses $\langle \Delta E \rangle_{\text{down}}$ and defined potential energy surfaces to calculate rate coefficients but also allows potential energy surfaces to be optimised by fitting barrier heights and $\langle \Delta E \rangle_{\text{down}}$ to observed experimental data.

2.3 Theory of Photochemistry

Photochemistry is a process initiated by the absorption of radiation and follows the chemistry of excited species or dissociation products. As described throughout Chapter 1, absorption of the sun's radiation by a multitude of species forms the basis of nearly all atmospheric processes,[1] therefore controlling atmospheric composition and thus air quality. This section will describe the process by which excited atoms and molecules are produced (absorption) as well as summarise some of the processes that take place following excitation, as outlined in Figure 2.6.

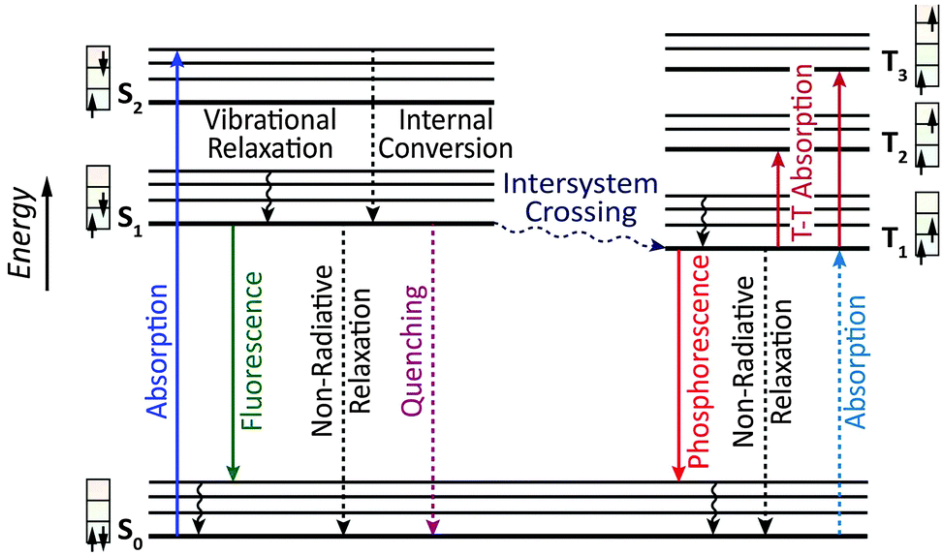

Figure 2.6. Jablonski diagram summarising the processes that may occur following excitation of a species. S_0 is the ground singlet electronic state, S_1 and S_2 are excited singlet electronic states and T_1, T_2 and T_3 are the triplet states. Solid lines represent radiative processes and dotted lines represent non-radiative processes. Copied from reference 19.[19]

2.3.1. The Beer-Lambert Law

The Beer-Lambert law (Equation 2.89) is used to define the absorbance of light at a particular wavelength, λ, and is defined as the natural logarithm of the ratio between the incident (I_0) and transmitted (I_t) radiation.

$$A_\lambda = \ln\left(\frac{I_0}{I_t}\right) \qquad \text{(Equation 2.89)}$$

where A_λ is the absorbance at a particular wavelength, I_0 is the light intensity prior to its interaction with the species at wavelength λ and I_t is the light intensity once it has passed through the sample, at wavelength λ.

The total absorbance is also related to the concentration of the species [C], the absorption cross-section of the species at a particular wavelength, σ_λ, and the total distance travelled by the light, l, as shown in Equation 2.90.

$$A_\lambda = \sum_{i=1}^{i=n} \sigma_{i,\lambda}[C]_i l \qquad \text{(Equation 2.90)}$$

Determining the concentrations of atmospherically important species can therefore be achieved using absorption spectroscopy, providing the absorption cross-section is known, which is particularly important within the field of atmospheric chemistry. Further details about

how absorption spectroscopy can be utilised for measurements of the atmospheric concentrations of reactive species and provide information about their reactions are provided in subsequent chapters of this report.

2.3.2 The Excitation of a Molecule

When species absorb electromagnetic radiation, there is a transition of the molecule from one quantum state to another. The energy of a photon can be calculated by:

$$E = h\nu = \frac{hc}{\lambda} = hc\tilde{\nu} \qquad \text{(Equation 2.91)}$$

where ν is the frequency of the radiation, h is Planck's constant, c is the speed of light, λ is the wavelength of light and $\tilde{\nu}$ is wavenumber. Since molecules have quantised energy levels, there can only be discrete values of absorption/emission. To absorb a photon of light, the molecule needs to have an allowed transition that is equal to the energy of the photon.

After a molecule has absorbed a photon of light, one of three types of excitation will occur, which corresponds to transitions involving changes in either electronic, vibrational or rotational energy levels, with $\Delta E_{elec} >> \Delta E_{vib} >> \Delta E_{rot}$. Vibronic transitions involve the simultaneous change in electronic and vibrational energy levels within a molecule, and correspond to the UV/Visible region of the electromagnetic spectrum. Ro-vibrational transitions involve changes in both the rotational and vibrational states in a molecule and correspond to the IR region of the electromagnetic spectrum. Since $\Delta E_{vib} >> \Delta E_{rot}$, changes in the rotational state gives fine structure to the vibrational spectrum.

For electronic transitions, a new electronic state with higher energy is populated, with the fate of this state depending on whether it is bound – the molecule is confined to a potential well with quantised energies, or whether it is unbound – where there is a continuum of energies with no quantisation. Electronic transitions to a bound state are ro-vibronic transitions, such that there are changes to the electronic, vibrational and rotational states within the molecule. Following an electronic transition to a bound state (Figure 2.7), the excited molecule will relax back to the ground state via energy transfer processes outlined below. Transitions to a bound electronic state occur at lower energies (longer wavelengths), with the discrete energy levels resulting in vibronic structure. The Frank-Condon principle states that, for an electronic transition, the probability of a transition between vibrational energy levels in the ground and the upper state increases with the overlap between the two vibrational wavefunctions and therefore the intensity of the vibronic lines in the spectra are governed by this overlap.[20] The vibrational energy levels within a molecule become closer together at higher potential energies until they become a continuum, the energy at which the continuum occurs is the dissociation

limit (red lines on Figure 2.7). Transitions that occur at higher energies (shorter wavelengths) may be above the dissociation limit, resulting in broad and featureless spectra. An example of this is shown in Figure 2.8 for the UV cross-sections of CH_2OO determined in the literature.[21] Clear structure is observed at wavelengths greater than 360 nm whereas below 350 nm, the spectrum is featureless.

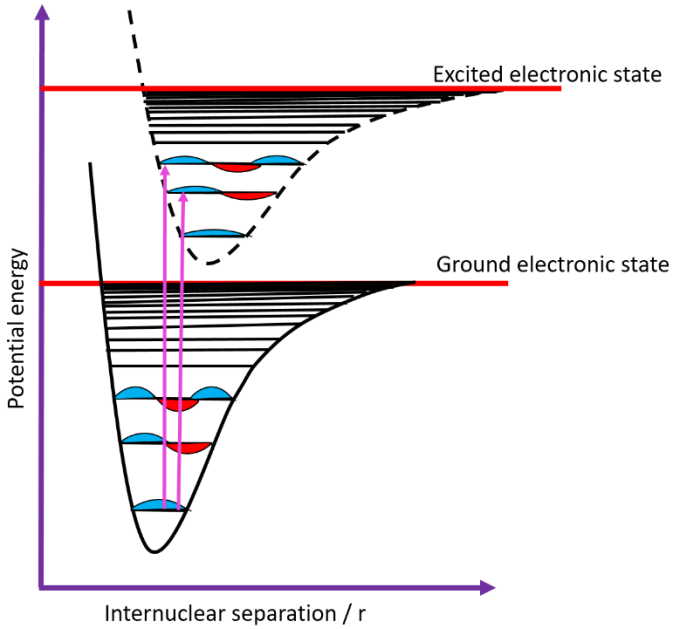

Figure 2.7. Schematic diagram showing transitions from the ground vibrational level in the electronic ground state to excited vibrational levels in a bound electronic excited state.

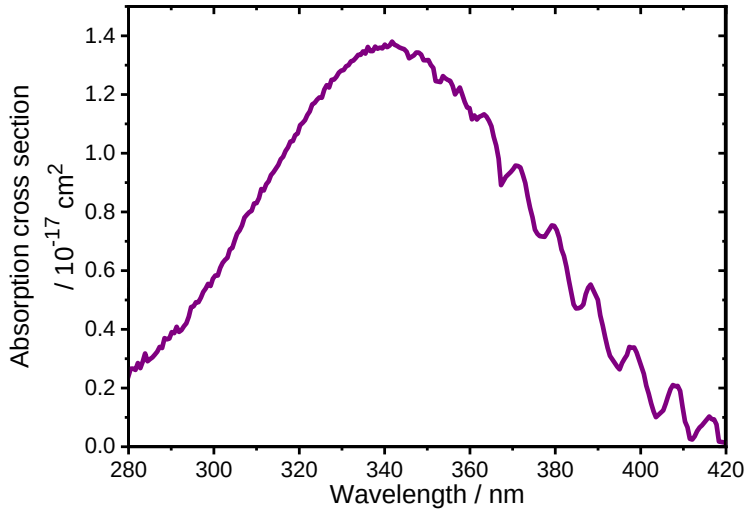

Figure 2.8. Absolute UV absorption cross-sections for CH_2OO reported by Mir *et al.*[21]

When excitation occurs to an unbound state (Figure 2.9), at all wavelengths the excited molecule will travel along the trajectory of the potential energy surface to form reaction products, the structure of the molecule changes throughout this process often resulting in dissociation of the molecule to two or more atoms/molecules. Excitation to an upper unbound state result in broad and featureless absorbance spectra.

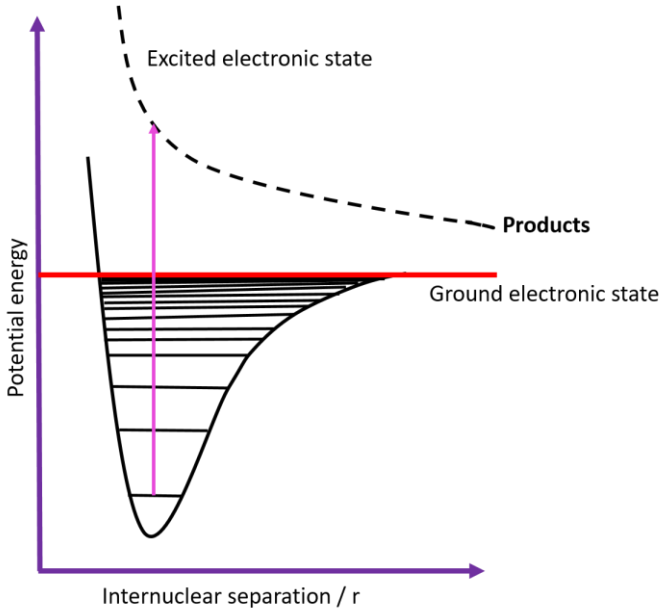

Figure 2.9. Schematic showing the transition from the ground electronic state to an unbound electronic excited state.

2.3.3 Fates of Excited Molecules

There are a number of processes that can occur following the excitation of a molecule from a ground electronic state (S_0 in Figure 2.6) to an excited electronic singlet state (S_1 or S_2 in Figure 2.6). The emission of a photon may occur via fluorescence, where the molecule relaxes down to its ground state either directly or via internal conversion to a lower lying singlet state i.e. $S_1 \rightarrow S_0$ or by phosphorescence, where relaxation occurs via intersystem crossing to an excited triplet state followed by relaxation to the ground state i.e. $T_1 \rightarrow S_0$. If emission is the only process occurring, then it is first-order and can be described as:

$$\frac{d[A^*]}{dt} = -k'[A^*] \qquad \text{(Equation 2.92)}$$

where A* represents the excited molecule and k' is the first-order rate coefficient.

Emission via fluorescence and phosphorescence are both spontaneous processes and are represented as:

$A^* \rightarrow A + h\nu$ (R2.26)

There is however, a second process known as stimulated emission. This is where the emission of a photon is triggered by another photon:

$A^* + h\nu \rightarrow A + 2h\nu$ (R2.27)

This process is particularly important for experimental studies since laser action depends on stimulated emission (further details given in Chapter 3).

Relaxation may also occur via quenching, also known as collisional energy transfer, where a molecule in an excited electronic state collides with a bath gas molecule, such as O_2 or N_2, and transfers its excess energy into the vibrational modes of the bath gas. Collisional energy transfer occurs throughout atmospheric chemistry with many examples given in Chapter 1.

2.3.3.1 Photodissociation

Photodissociation is of particular interest within atmospheric chemistry as it is the driving force behind many important processes occurring in both the troposphere and stratosphere, such as the photodissociation of molecular oxygen and ozone in the Chapman cycle, or the photodissociation of NO_2 to NO (outlined in Chapter 1).

Photodissociation occurs when the total energy of the absorbed photon(s) is greater than the bond energy within a molecule, causing it to fall apart. Photodissociation may occur directly, where the molecule is excited into a repulsive state. Alternatively, the molecule may be excited to a bound upper state and undergo internal conversion to a lower state. If the energy of the lower electronic state is greater than the bond dissociation energy of the molecule then it may dissociate.

The rate coefficient for photodissociation, J, at wavelength, λ, can be calculated from Equation 2.93:

$$J_\lambda = \int_{\lambda_2}^{\lambda_1} F_\lambda \, \sigma_\lambda \, \phi_\lambda \, d\lambda \qquad \text{(Equation 2.93)}$$

where F_λ is the actinic flux (the amount of available light) at wavelength λ, σ_λ is the absorption cross-section at wavelength λ, and ϕ_λ is the quantum yield for dissociation at wavelength λ.

2.4 Concluding Remarks

This chapter has provided a brief overview of the theoretical explanations to gas phase kinetics, i.e. the rationale behind temperature and pressure dependent reactions and the theory of photochemistry, providing explanations of the processes that occur both during and following the absorption of radiation. Experimental observations are crucial for testing the validity of theoretical explanations, and this chapter has demonstrated that there are often discrepancies between theory and experiment. The following chapter outlines some of the experimental approaches used in the study of gas phase kinetics as well as the experimental and data analysis method used throughout the work presented in this thesis.

2.5 References

1. Michael J. Pilling, P.W.S. *Reaction Kinetics.* Oxford University Press Inc, 1995.
2. Arrhenius, S. Influence of temperature on the rate of inversion of sucrose. *Physical Chemistry*. 1889, **4**, p.226.
3. Tsikritea, A., Diprose, J.A., Softley, T.P. and Heazlewood, B.R. Capture theory models: An overview of their development, experimental verification, and applications to ion–molecule reactions. *The Journal of Chemical Physics.* 2022, **157**(6), p.060901.
4. Su, T. and Bowers, M.T. Theory of ion-polar molecule collisions. Comparison with experimental charge transfer reactions of rare gas ions to geometric isomers of difluorobenzene and dichloroethylene. *The Journal of Chemical Physics*. 1973, **58**(7), pp.3027-3037.
5. Su, T. and Bowers, M.T. Parameterization of the average dipole orientation theory: temperature dependence. *International Journal of Mass Spectrometry and Ion Physics*. 1975, **17**(2), pp.211-212.
6. Su, T. and Chesnavich, W.J. Parametrization of the ion–polar molecule collision rate constant by trajectory calculations. *The Journal of Chemical Physics.* 1982, **76**(10), pp.5183-5185.
7. Clary, D.C. Calculations of rate constants for ion-molecule reactions using a combined capture and centrifugal sudden approximation. *Molecular Physics.* 1985, **54**(3), pp.605-618.

8. Georgievskii, Y. and Klippenstein, S.J. Long-range transition state theory. *The Journal of Chemical Physics.* 2005, **122**(19), p.194103.

9. Maergoiz, A.I., Nikitin, E.E., Troe, J. and Ushakov, V.G. Classical trajectory and adiabatic channel study of the transition from adiabatic to sudden capture dynamics. III. Dipole–dipole capture. *The Journal of Chemical Physics.* 1996, **105**(15), pp.6277-6284.

10. Oref, I. General expression for unimolecular rate coefficients in the falloff region. *The Journal of Physical Chemistry.* 1989, **93**(9), pp.3465-3469.

11. Rice, O.K., Ramsperger, Herman C Theories of unimolecular gas reactions at low pressures. *Journal of the American Chemical Society.* 1927, **49**(7), pp.1617-1629.

12. Kassel, L.S. Studies in homogeneous gas reactions. I. *The Journal of Physical Chemistry.* 1928, **32**(2), pp.225-242.

13. Marcus, R.A. Unimolecular Dissociations and Free Radical Recombination Reactions. *The Journal of Chemical Physics.* 1952, **20**(3), pp.359-364.

14. Troe, J. Theory of thermal unimolecular reactions at low pressures. I. Solutions of the master equation. *The Journal of Chemical Physics.* 1977, **66**(11), pp.4745-4757.

15. Sander, S., Friedl, R., Golden, D., Kurylo, M., Moortgat, G., Wine, P., Ravishankara, A., Kolb, C., Molina, M. and Finlyason-Pitts, B. *Chemical kinetics and photochemical data for use in atmospheric studies: evaluation number 15.* Pasadena, CA: Jet Propulsion Laboratory, California Institute of Technology, 2010.

16. Atkinson, R., Baulch, D.L., Cox, R.A., Hampson, R.F., Jr., Kerr, J.A., Rossi, M.J. and Troe, J. Evaluated Kinetic and Photochemical Data for Atmospheric Chemistry: Supplement VI. IUPAC Subcommittee on Gas Kinetic Data Evaluation for Atmospheric Chemistry. *Journal of Physical and Chemical Reference Data.* 1997, **26**(6), pp.1329-1499.

17. Robinson, C., Onel, L., Newman, J., Lade, R., Au, K., Sheps, L., Heard, D.E., Seakins, P.W., Blitz, M.A. and Stone, D. Unimolecular Kinetics of Stabilized CH_3CHOO Criegee Intermediates: syn-CH_3CHOO Decomposition and anti-CH_3CHOO Isomerization. *The Journal of Physical Chemistry A.* 2022, **126**(39), pp.6984-6994.

18. Glowacki, D.R., Liang, C.-H., Morley, C., Pilling, M.J. and Robertson, S.H. MESMER: An Open-Source Master Equation Solver for Multi-Energy Well Reactions. *The Journal of Physical Chemistry A.* 2012, **116**(38), pp.9545-9560.

19. Xu, H., Chen, R., Sun, Q., Lai, W., Su, Q., Huang, W. and Liu, X. Recent progress in metal–organic complexes for optoelectronic applications. *Chemical Society Reviews.* 2014, **43**(10), pp.3259-3302.

20. Thompson, M.J. and Messina, M. A Quantitative Explanation of the Dynamics Underlying the Franck–Condon Principle: A Mostly Classical Viewpoint. *Journal of Chemical Education.* 2019, **96**(6), pp.1171-1177.

21. Mir, Z.S., Lewis, T.R., Onel, L., Blitz, M.A., Seakins, P.W. and Stone, D. CH_2OO Criegee intermediate UV absorption cross-sections and kinetics of CH_2OO + CH_2OO and CH_2OO + I as a function of pressure. *Physical Chemistry Chemical Physics.* 2020, **22**(17), pp.9448-9459.

Chapter 3

Experimental Techniques for the Investigation of Criegee Intermediates

This chapter provides an overview of the main experimental techniques used in laboratory studies of gas phase kinetics relevant to the field of atmospheric chemistry. More specifically, techniques that have previously been used for the detection of, and investigation into, Criegee intermediates. A description of the experimental procedure and method of data analysis used throughout the work presented in this thesis is also given. General information regarding the experimental conditions will be given in this Chapter, with more details given in the experimental sections of Chapters relevant to a single reaction.

3.1 Kinetic Techniques

The rate of a chemical reaction can either be measured in relation to a reaction where the kinetics have already been well characterised, known as the relative rate method, or they can be investigated independently via absolute methods. This section provides an overview of the relative rate method along with an overview of flow and pump-probe methods, both of which allow absolute kinetics to be obtained.

3.1.1 The Relative Rate Method

The relative rate method measures the loss of a reactant (A, R3.1) relative to a second reactant (B, R3.2) in the presence of a reactive species (X).[1] Reactants A and B are added to a reaction chamber or cell, and the concentrations of A and B subsequently decrease as they react with X. The concentration of each reactant is measured at varying times after the mixing has occurred, enabling a time-profile to be constructed.

$X + A \rightarrow$ Products (R3.1)

$X + B \rightarrow$ Products (R3.2)

With knowledge of the rate coefficient for the reactive species with reactant B, $k_{3.2}$, the rate coefficient for the reactive species with A, $k_{3.1}$, can be determined.

The rate equations can be written as follows:

$$-\frac{d[\mathrm{A}]}{dt} = k_{3.1}[\mathrm{X}][\mathrm{A}] = k'_{3.1}[\mathrm{A}] \qquad \text{(Equation 3.1)}$$

$$-\frac{d[\mathrm{B}]}{dt} = k_{3.2}[\mathrm{X}][\mathrm{B}] = k'_{3.2}[\mathrm{B}] \qquad \text{(Equation 3.2)}$$

where $k'_{3.1} = k_{3.1}[\mathrm{X}]$ and $k'_{3.2} = k_{3.2}[\mathrm{X}]$

The rate equations can be integrated over time to give:

$$\ln\left(\frac{[\mathrm{A}]_t}{[\mathrm{A}]_0}\right) = k'_{3.1}t \qquad \text{(Equation 3.3)}$$

$$\ln\left(\frac{[\mathrm{B}]_t}{[\mathrm{B}]_0}\right) = k'_{3.2}t \qquad \text{(Equation 3.4)}$$

Equations 3.3 and 3.4 can then be combined to give:

$$\ln\left(\frac{[\mathrm{A}]_0}{[\mathrm{A}]_t}\right) = \frac{k_{3.1}}{k_{3.2}}\ln\left(\frac{[\mathrm{B}]_0}{[\mathrm{B}]_t}\right) \qquad \text{(Equation 3.5)}$$

A plot of $\ln\left(\frac{[\mathrm{A}]_0}{[\mathrm{A}]_t}\right)$ *vs* $\ln\left(\frac{[\mathrm{B}]_0}{[\mathrm{B}]_t}\right)$ will therefore produce a straight line where the gradient is equal to $\frac{k_{3.1}}{k_{3.2}}$.[2] Knowledge of the absolute rate coefficient for $k_{3.2}$ allows an absolute value for $k_{3.1}$ to be determined.[1]

A disadvantage of the relative rate method is the requirement of a well-known reference rate coefficient, which relies on other experimental techniques. The relative rate method does not require absolute concentrations to be known and is therefore advantageous for reactions where the concentration of one or more reactants are difficult to measure and also proves to be beneficial in situations where real-time analysis of a single reaction is not possible. Reactive species are often present in low concentrations throughout the reaction, increasing their lifetime and thus the overall reaction time, allowing detection techniques with relatively poor time resolution to be utilised alongside this method. For reactions that occur over shorter timescales, such as those discussed throughout this thesis, techniques with faster time resolution are required, some of which are summarised below.

3.1.2 The Flow method

In the discharge flow method, the reactive species, typically generated through use of microwave discharges,[3] are introduced into a flow tube. At a known point along the length of the flow tube, the co-reactant is introduced to the system using a moveable injector. A schematic showing the typical experimental set-up for microwave discharge is shown in Figure 3.1. The point of reaction initiation is the tip of the moveable injector, where the reactive species and co-reagent begin mixing, with detection occurring downstream from this

point. The time taken between initiation and detection (t) can be calculated using Equation 3.6, where X is the distance between initiation and detection and V is the linear flow velocity of the gas mixture.[4]

$$t = X / V \qquad \text{(Equation 3.6)}$$

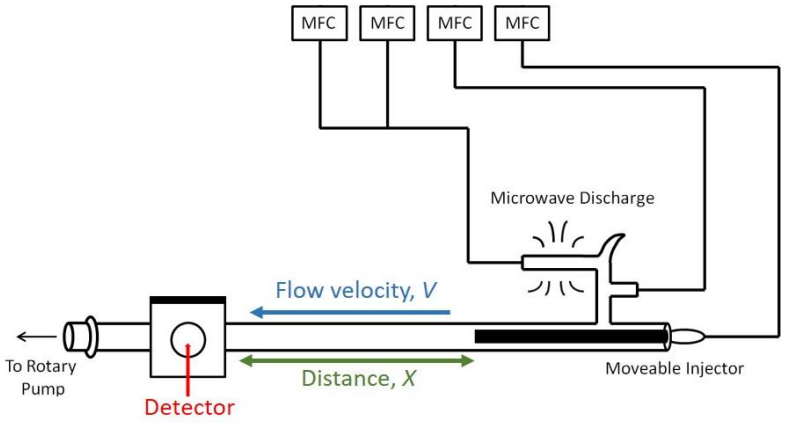

Figure 3.1. Schematic of a typical experimental set-up for the microwave discharge flow method. MFC = mass flow controller. Adapted from reference 4.[4]

Varying the position of the moveable injector allows the composition of the gas mixture to be measured at different time points after the reaction has been initiated, allowing a concentration-time profile to be constructed and kinetic parameters to be obtained.

A major limitation of the discharge flow method is the time it takes for mixing to occur between the reactant gases (typically a fraction of a millisecond at 1×10^2 Pa),[4] meaning a uniform concentration will not be reached until downstream of the tip of the sliding injector. Therefore, the timescale of reactions studied using the discharge flow method is limited to the millisecond range. A second limitation of the traditional discharge flow method is that experiments are generally restricted to low pressure conditions (below 10^3 Pa) in order to maintain a uniform flow velocity throughout the flow tube.[4] However, advances have been made to show that, by incorporating turbulent flow conditions, the pressure range achieved using the flow tube method can be greatly extended (60 – 760 Torr).[5,6]

The main advantage of the discharge flow technique is that it is widely applicable as it can be coupled to a variety of sensitive detection techniques, such as laser-induced fluorescence (LIF) and mass spectrometry. This advantage is a result of the time-resolution being achieved by varying the distance between injection and detection using the sliding injector, and so detection techniques do not need to have fast response times.

3.1.3 Flash Photolysis

The limitations of flow systems are overcome by the kinetic technique of flash photolysis, developed by Norrish and Porter in the late 1940s.[7] In this technique, precursor and reactant gases are pre-mixed and then flowed into the photolysis cell under the desired experimental conditions. A short pulse of light from either a flash lamp or laser (the pump) is used to initiate the chemistry within the photolysis cell via production of an atom, radical or excited state.

The majority of flash photolysis experiments use lasers, such as excimer or Nd:YAG lasers, to generate the desired reactive species and initiate a reaction. The reactive species can be produced either directly by photolysis or as a result of further chemistry, such as the method to produce Criegee intermediates from di-iodo precursors outlined in Chapter 1. The use of lasers to produce the reactive species is particularly advantageous as they have high pulse energies (typically millijoules to joules), high repetition rates and well-defined wavelength outputs. A high pulse energy is particularly advantageous as it allows the transient species to be produced from low precursor concentrations, reducing the potential for unwanted side reactions taking place within the reaction cell and simplifying the overall kinetics. The reactive species must be produced on a timescale that is shorter than the reaction of interest, which must be taken into consideration when selecting an appropriate precursor to the reactive species. Providing suitable precursors have been selected, lasers have the advantage of being highly specific as they can be tuned to specific wavelengths to only photolyse the target molecule. The timescale for flash photolysis experiments is dependent on the pulse duration of the flash. Early flash photolysis experiments used a gas flash lamp, where the flash duration was on the order of milliseconds however, the pulse duration of excimer and Nd:YAG lasers is typically between 5 and 20 nanoseconds. The rapid production of the reactants can therefore be separated from the kinetics describing the subsequent reactions which has enabled flash photolysis experiments to investigate reactions on timescales between milliseconds and nanoseconds.[4, 8]

Reactants and/or products can be monitored as they are removed/formed within the reaction cell through the use of various detection techniques. The main detection techniques used in the study of kinetics are outlined in Section 3.2.

3.1.3.1 Excimer Lasers

Lasing action can only take place if there is a population inversion within the active medium where stimulated emission can occur and if there is an optical cavity to amplify the emitted light.[4] Within the lasing medium, a photon of a specific energy is absorbed and promoted to an excited state, which subsequently relaxes to the ground state via spontaneous emission. Stimulated emission also occurs as a result of interactions between electrons in the excited

state and the incoming photon, resulting in a second photon that is in phase with and propagates in the same direction as the incoming photon.[4]

Excimer lasers are commonly used in flash photolysis experiments and are based upon the formation of an active medium, known as an excited diatomic complex or exciplex. Electric discharge is pulsed through the gas mixture (e.g. $Kr/F_2/He$) producing ions that combine to give electronically excited species (e.g. KrF^*), which undergo stimulated emission as relaxation back to the ground state occurs, resulting in the emission of a photon. A population inversion is achieved in excimer lasers since the excited species have bound upper electronic states, but unbound ground states (Figure 3.2), meaning any population within the ground state is removed via dissociation.[4]

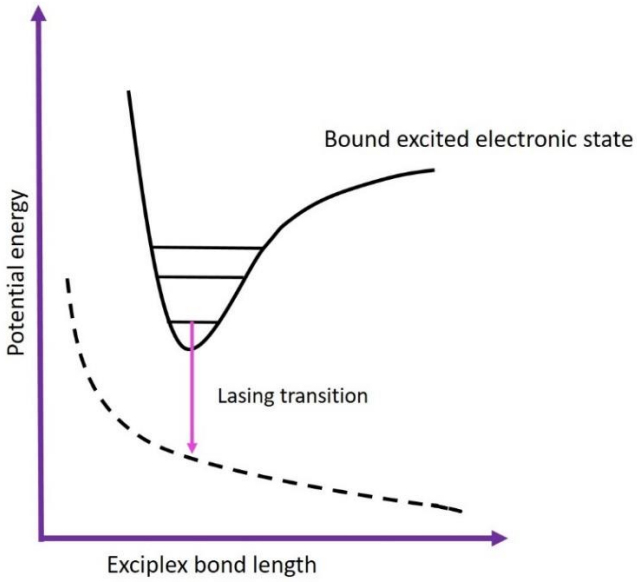

Figure 3.2. Schematic of an electronic transition from a bound upper electronic state to an unbound ground state that occurs in excimer lasers. Reproduced from reference 4.[4]

The wavelength of the laser depends on the exciplex formed, since the energy separation between the ground and upper electronic states will vary between species. Table 3.1 summarises the typical gas mixtures used in excimer lasers.[4]

Species mixture	Exciplex	Output / nm
$Ar/F_2/He$	ArF	193
Kr/HCl/He	KrCl	222
$Kr/F_2/He$	KrF	248
Xe/HCl/He	XeCl	308
$Xe/F_2/He$	XeF	351

Table 3.1. Typical species mixtures used in excimer lasers, the exciplex formed and the corresponding wavelength.[4]

3.1.3.2 Nd:YAG Lasers

The lasing source of an Nd:YAG laser is a crystal made of yttrium aluminium garnet doped with neodymium ($Nd:Y_3Al_5O_{12}$).[9] Broadband light, typically from a flash lamp, enters the laser medium and a small fraction is absorbed by Nd^{3+} ions that become electronically excited and rapidly relax to the ground state.[10] Stimulated emission occurs as the ions relax back down to the ground state releasing photons, which results in lasing action if the photon passing through the crystal is of the same frequency as the lasing transition. Short pulses of high intensity laser light can be achieved using a Q-switch. The Q stands for quality factor (or Q-factor), which is a measure of how well the cavity can store energy. A high Q-factor corresponds to the cavity storing energy efficiently and a low Q-factor corresponds to significant energy loss. The inclusion of a shutter prevents the laser cavity emitting a laser beam, resulting in a build-up of energy within the cavity, creating a significant population inversion. As the shutter is opened, the stored energy is released as a short, high energy pulse.

The system involves two mirrors at each end of the lasing medium, one of which has a partially reflective surface, allowing a portion of the light to pass through. The Nd:YAG crystal gives this laser a characteristic wavelength of 1064 nm however, a phenomenon known as frequency mixing means that the laser is also able to emit wavelengths of 532 nm, 355 nm (via frequency mixing of 1064 nm + 532 nm) and 266 nm (via frequency mixing of 1064 nm + 355 nm) as the second, third and fourth harmonics respectively.[11] This is achieved by passing the 1064 nm laser light through non-linear optical crystals. The second harmonic, achieved by frequency doubling, involves two photons of frequency ν being absorbed by a molecule in its ground state, resulting in the emission of a photon of frequency 2ν, generating a wavelength of 532 nm. The same process occurs for the third and fourth harmonics, but with the emission of photons with frequency 3ν and 4ν respectively.

3.2 Analytical Techniques

The following sections will provide an overview for some of the most common techniques used to detect reactive species once they have been produced, namely mass spectrometry (MS), laser-induced fluorescence (LIF), and absorption spectroscopy.

3.2.1 Mass Spectrometry

Mass spectrometry is an analytical technique that is used to identify and quantify molecules based on the mass-to-charge ratio of charged particles.[12] The process by which a mass spectrum is produced involves four stages; ionisation, acceleration, separation and detection. Ionisation can occur using a variety of methods, including photo-ionisation, electron impact, or proton transfer.[4, 13] Ionisation may result in significant fragmentation leading to complicated spectra, and therefore samples that contain mixtures of large or complex species may require soft ionisation techniques, such as photo-ionisation, which result in less fragmentation. After the ions are produced, they are accelerated towards the detector using an electric field so that each ion has similar kinetic energy. The ions are then separated based on their mass-to-charge (*m/z*) ratio, with the two most common methods to separate the ions are by use of either a quadrupole mass analyser or a time-of-flight (ToF) mass analyser. The quadrupole mass analyser only detects ions of a certain mass by applying a radio frequency voltage across two pairs of metal rods. Only ions of a specific *m/z* will have a stable trajectory across the rods and reach the detector, while the rest of the ions will be lost through collisions with the rods. The ToF mass analyser is able to detect multiple species at once as the velocities at which the ions are accelerated through the electric field will be dependent on their *m/z* ratio and so they can be separated by the time taken for them to reach the detector.[13] The ions are maintained under a high vacuum to reduce the potential for collisions between ions, limiting the potential for fragmentation.[12]

3.2.1.1 Photo-Ionisation Mass Spectrometry

Photo-ionisation mass spectrometry (PIMS) is an example of soft ionisation, which reduces complications in both detection and analysis relating to fragmentation. The method involves tuning the wavelength of the photo-ionisation source, such as a dye laser or synchrotron radiation, to match the photo-ionisation energy (PIE) of the species of interest, such that only one isomer is ionised, increasing the specificity of the method. The first study in which Criegee intermediates were directly produced in the laboratory utilised photo-ionisation mass spectrometry (PIMS) as a method to identify the production of CH_2OO from a mixture of $(COCl)_2/(CH_3)_2SO/O_2$[14] and later used by the same group to confirm the production of

CH_2OO, and not any other isomer, from a di-iodo precursor.[15] The PIMS technique was then subsequently used to identify the production of both the *syn*- and *anti*- conformers of CH_3CHOO based on their individual photo-ionisation spectra.[16] The use of this technique has thus paved the way for subsequent laboratory studies of Criegee intermediates, which have identified their reactions to be much more atmospherically relevant than had been previously predicted (further details are given in Chapter 1).

3.2.2 Laser-Induced Fluorescence

Laser-induced fluorescence (LIF) spectroscopy is often used in conjunction with LFP and operates by electronically exciting the target species, which subsequently relaxes back down to its ground state via fluorescence. Dye lasers are commonly used as the light source as their wavelength can be tuned to match a particular transition, meaning this is a very selective detection technique.[4] Relaxation can occur through several processes, such as emission, collisional stabilisation or dissociation, which are discussed in more detail in Chapter 2.

In a LIF experiment, photons emitted via fluorescence are detected. A photolysis laser (such as an excimer or Nd:YAG laser) is first used to produce the radical species and setting time $t = 0$. At a known time after the photolysis pulse, the dye laser excites the radical species. Following excitation, emission occurs via fluorescence, where the molecule relaxes down to its ground state either directly or via internal conversion to a lower lying singlet state (more details given in Chapter 2). The emitted photon may be of the same energy and thus wavelength as the excitation photon, termed on-resonance fluorescence, or the excited species may initially lose some of its vibrational energy via relaxation in the upper electronic state and therefore the emitted photon will be at a lower energy and longer wavelength than the excitation photon, termed off-resonance fluorescence[4] (Figure 3.3).

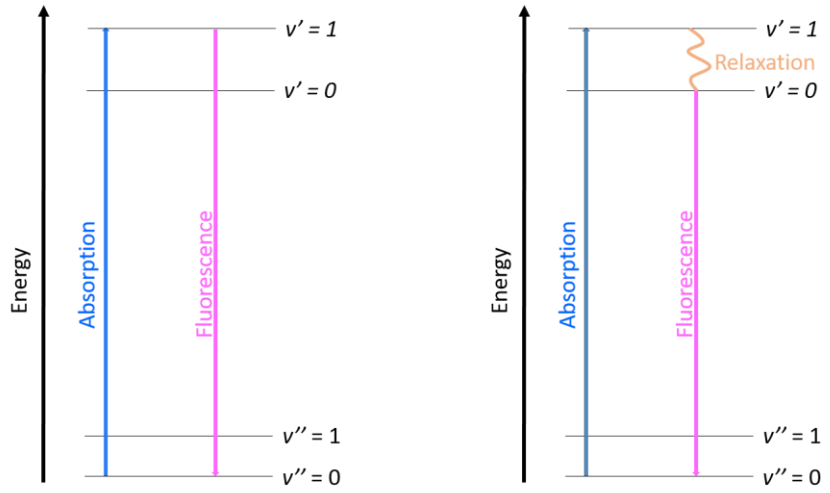

Figure 3.3. Schematic diagram representing on-resonance fluorescence (left) and off-resonance fluorescence (right). v'' = 0 and v'' = 1 represent the ground and first vibrational energy levels of the ground electronic state and v' = 0 and v' = 1 represent the ground and first vibrational energy levels of the excited electronic state. Edited from reference 17.[17]

A time profile can be constructed by altering the time between the photolysis laser and the dye laser firing, and the magnitude of the fluorescence signal at that time is proportional to the concentration of the radical species. LIF provides a relative measure of the concentration of the species of interest, whereas other methods, such as absorption spectroscopy, are able to provide absolute concentrations, but may be less sensitive. The fluorescence signal in a LIF experiment is detected using a photomultiplier tube (PMT) for example, and care needs to be taken when arranging the experimental apparatus to minimise the amount of laser light detected by the PMT, as the intensity of laser light will be significantly higher than the fluorescence.[4] This is often achieved by placing the probe laser orthogonal to the PMT or by introducing a filter to minimise the intensity of scattered laser light. Figure 3.4 shows a schematic diagram of the LFP-LIF apparatus used to measure OH reactivity at the University of Leeds.[18] When performing on-resonance fluorescence studies, as with the field work carried out at the University of Leeds, rapid gating is used to separate the laser light and the OH fluorescence signal. Using the fluorescence assay gas expansion (FAGE) technique increases the fluorescence lifetime of OH, enabling the OH signal to be more easily separated from the laser light.

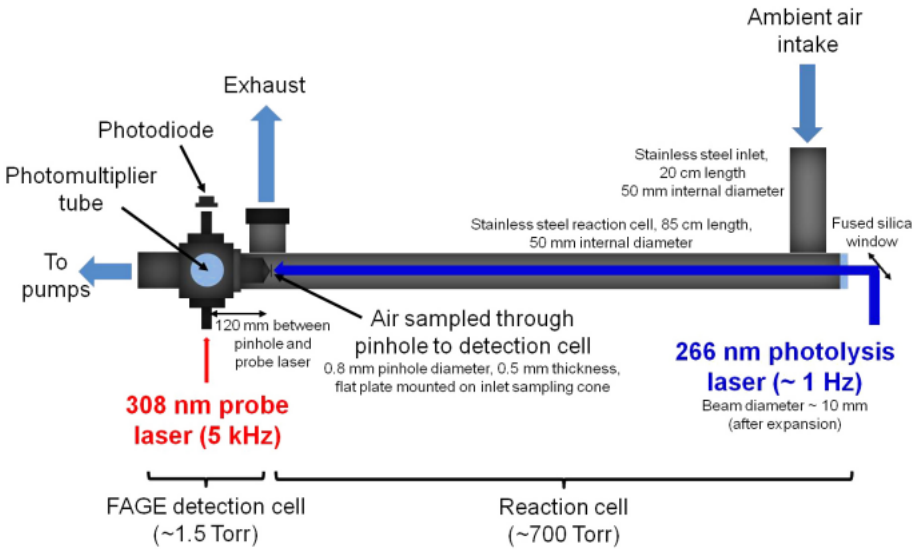

Figure 3.4. Schematic diagram of the LFP-LIF experimental apparatus used to detect OH reactivity at the University of Leeds. FAGE = fluorescence assay gas expansion. Copied from reference 18.[18]

The use of LIF in atmospheric field measurements is particularly beneficial as it is a highly selective technique, meaning possible interferences from species other than the one of interest will not affect results. The sensitivity also means it is a suitable technique for monitoring species that are often present in lower concentrations than what may be used in the laboratory. There is also the advantage of having a wide range of dyes available for the dye lasers used in LIF experiments, with output ranging between 200 nm and 1 μm,[19] meaning this technique can be employed to monitor a range of atmospheric species. However, experiments are often carried out under low pressure conditions to avoid competition with quenching, which may limit its experimental applications. Research carried out at the University of Leeds has coupled LFP to LIF for both field[18] and laboratory[20, 21] measurements of reactive species.

While Criegee intermediates themselves cannot be directly monitored using LIF as they do not fluoresce,[4] LIF has previously been used to report the kinetics of CH_2OO by monitoring the production of OH,[22, 23] which occurs as a result of the decomposition of excited CH_2OO (further details given in Chapter 4). LIF has also been used to report the kinetics of CH_2OO with SO_2, NO_2 and CH_3CHO by monitoring the formation of HCHO,[20] which can be produced from the reactions of CH_2OO and CH_2IO_2 with I or as a direct reaction product (further details are given in Chapter 5).

3.2.3 Absorption Spectroscopy

Absorption spectroscopy operates by measuring the absorbance of light by the species of interest at a given wavelength or over a range of wavelengths and is commonly used to measure fast reactions.[4] The amount of light absorbed by the species of interest is directly proportional to the concentration, as defined by the Beer-Lambert Law (Equation 3.7).

$$A_\lambda = \ln\left(\frac{I_{0,\lambda}}{I_{t,\lambda}}\right) = \sum_{i=1}^{i=n} \sigma_{i,\lambda}\,[\mathrm{C}]_{i,t}\,l \qquad \text{(Equation 3.7)}$$

where A_λ is the absorbance of light at wavelength λ, $I_{0,\lambda}$ is the incident light intensity at wavelength λ, $I_{t,\lambda}$ is the light intensity at time t after photolysis at wavelength λ, $\sigma_{i,\lambda}$ is the absorption cross section of species i at wavelength λ, $[\mathrm{C}]_{i,t}$ is the concentration of species i at time t and l is the pathlength of light.

Upon production of the reactive species, the absorption of light will appear to increase instantaneously on the timescale of the experiment, and then decrease as the reactive species reacts. The absorption of light at a wavelength corresponding to a product of the reaction may increase as the absorption owing to the reactive species decreases, allowing the formation of reaction products to be monitored. The ratio of light before (I_0) and after (I_t) the photolysis laser pulse allows the absorbance to be calculated (Equation 3.7) and from this a time profile can be produced.

An advantage of the absorption technique is that it allows for direct measurements of the concentration of the absorbing species, providing the pathlength (l) and the absorption cross-section (σ) are known (Equation 3.7). The concentrations of reactive species are often kept relatively low to decrease the effects of unwanted side reactions, which in turn results in a lower absorbance signal, increasing experimental difficulty. To overcome this, the absorbance can be increased by increasing the pathlength (Equation 3.7).

Complications can arise when the reaction being studied contains more than one species absorbing in the wavelength region of interest, particularly if the absorbance spectrum of one or more of the species is broad and/or featureless. Improving the signal-to-noise ratio by averaging multiple decay traces may allow for better separation of the absorbance spectra of different species. The difficulties of separating the absorbance spectra for different species within the same wavelength region are described in further detail in Chapter 7.

3.2.3.1 Ultraviolet Absorption Spectroscopy

A multitude of species of interest within atmospheric chemistry absorb light in the ultraviolet (UV) region of the electromagnetic spectrum and may undergo vibronic transitions, in which electronic and vibrational transitions are coupled, where excitation occurs between vibrational levels of the lower and upper electronic states (discussed in further detail in Chapter 2). The major benefit of using UV absorption spectroscopy is that UV absorption cross-sections are known for many species, making it a widely applicable technique and an ideal method for monitoring reactions within atmospheric chemistry. However, UV absorption spectra are often broad and contain minimal structure, making it harder to distinguish between species when they absorb within the same wavelength region, a disadvantage which is highlighted in Chapter 7.

The simplest Criegee intermediate, CH_2OO, has relatively large absorption cross-sections, with recent work at the University of Leeds reporting a peak absorption cross-section of $(1.37 \pm 0.29) \times 10^{-17}$ cm^2 at 340 nm.[24] The absorption spectrum of CH_2OO also shows characteristic vibronic structure at wavelengths between 360 and 400 nm, making it easily identifiable. Similarly, large absorption cross-sections have been reported for the conformers of the larger Criegee intermediate, CH_3CHOO.[25,26] As a result of these large cross-sections, UV absorption spectroscopy has been widely used to investigate the reactions of Criegee intermediates, [27,28,29] particularly at the University of Leeds [30,31,32] and is also the method used to measure the kinetics of the reactions presented in this thesis.

3.2.3.2 Cavity Ring-Down Spectroscopy

Cavity ring-down spectroscopy (CRDS) is a technique that has been used to measure the kinetics of reactions relevant to the atmosphere due to its high sensitivity. The apparatus consists of an optical cavity containing two highly reflective mirrors (R = >99.99%).[33] A short pulse of the probe light (e.g. from a dye laser) is introduced into the cavity through one of the mirrors and reflected back and forth between the mirrors resulting in large effective pathlengths, often kilometres. A small amount of light (less than 0.01%) is transmitted at each mirror, which is detected after it leaves the cavity. As light is transmitted, the intensity will decay exponentially with a lifetime, τ, known as the ring-down time. CRDS experiments typically use LFP to initiate the reaction and produce the species of interest. After photolysis, the reactive species will absorb a fraction of the probe light and so its intensity will decay at a faster rate than when there is no absorbing species (before photolysis). The concentration of the absorbing species is determined by measuring the ring-down time without the photolysis laser τ_{off} and with the photolysis laser τ_{on} (Equation 3.8) and a concentration-time profile can

be obtained by varying the time delay between the probe and the photolysis pulses. Figure 3.5. shows a schematic of an experimental set-up where CRDS is coupled to LFP.[34]

$$\alpha = \sigma_\lambda [\mathrm{C}] = c\left(\frac{1}{\tau_{on}} - \frac{1}{\tau_{off}}\right) \qquad \text{(Equation 3.8)}$$

where α is the absorption coefficient, σ_λ is the absorption cross-section of the species at wavelength λ, [C] is the concentration of the species, c is the speed of light and τ_{on} and τ_{off} are the ring-down times with and without the photolysis laser.

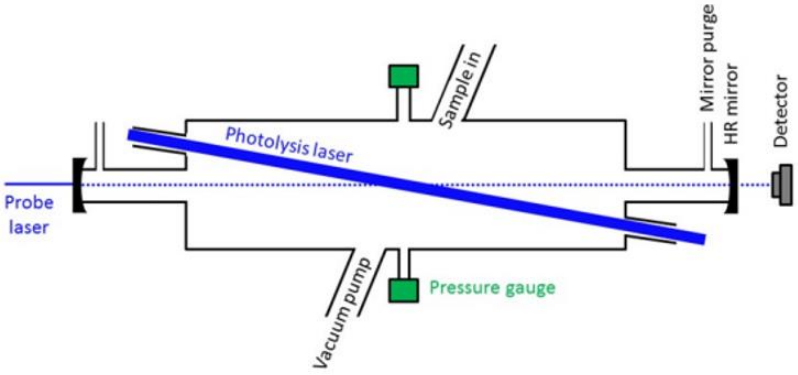

Figure 3.5. Schematic showing the experimental set-up where CRDS is coupled to LFP. Copied from reference 34.[34]

CRDS has been shown to be a useful technique in studying the kinetics of CH_2OO[34] and $(CH_3)_2COO$[35] as it is highly sensitive due to the large pathlength which means experiments can be conducted under low precursor concentrations, reducing the risk of possible secondary chemistry taking place. A disadvantage of this technique is that it operates at a single wavelength, or across a very small range of wavelengths, only. This is because the reflectivity of the mirrors is reduced significantly outside of their centre wavelength, meaning they cannot be used in broadband absorption experiments. Complications may arise if there are more than one species absorbing at the wavelength of interest, which means CRDS would not be a suitable technique for studying asymmetric Criegee intermediates, such as CH_3CHOO, as it would not be able to distinguish between the two conformers that absorb within the same wavelength region.

3.2.3.3 Cavity Enhanced Absorption Spectroscopy

Cavity enhanced absorption spectroscopy (CEAS) is an experimental technique that is also used to increase the effective pathlength of light and thus absorbance, to improve the sensitivity. CEAS consists of an off-axis arrangement of the optical cavity, with the probe light repeatedly reflected back and forth by highly reflective broadband optical cavity

mirrors.[33] The probe light sources for CEAS experiments are continuous, such as a continuous-wave laser or broadband incoherent sources such as Xe arc lamps, and as with CRDS, a small fraction of light is transmitted out of the cavity and can be detected. In CEAS experiments, it is the intensity of light that is measured and used to determine the absorbance rather than a decay time, as with CRDS. CEAS is again often coupled to LFP and the absorption of light is measured before and after the photolysis pulse, and the concentration of the absorbing species is calculated using the Beer-Lambert law, as with conventional absorption spectroscopy. A schematic of the CEAS apparatus used in experiments to investigate the kinetics of Criegee intermediates[27,25,36] is shown in Figure 3.6. In the experimental set-up shown in Figure 3.6, the cavity output is wavelength resolved by a ruled optical grating and focussed onto a charge coupled device (CCD) detector. There is also a rotating mirror that sweeps the cavity output vertically across the CCD, enabling both spectral and temporal information to be mapped across the CCD.

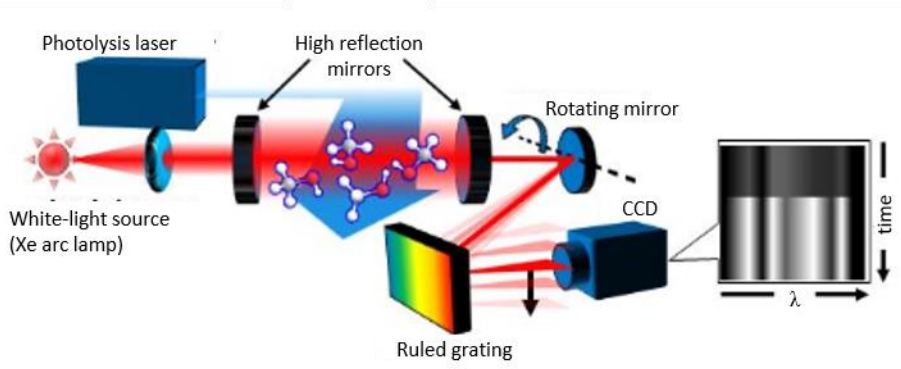

Figure 3.6. Schematic of the CEAS apparatus used in the literature to investigate the kinetics of Criegee intermediate reactions. CCD = charge coupled device. Copied from reference 37.[37]

The number of passes of light in a CEAS system depends on the reflectivity of the mirrors which will vary significantly as a function of wavelength for broadband light sources. This means that the pathlength is wavelength dependent and will need to be calibrated prior to experiments. Despite the large pathlengths in CEAS experiments, the sensitivity may be reduced due to the low intensity of the probe light reaching the detector. If the probe intensity is low, it may be difficult to identify small changes in the absorbance.

3.2.3.4 Infrared Absorption Spectroscopy

There are also many relevant species that absorb light in the infrared (IR) region of the electromagnetic spectrum, which involve transitions between the rotational levels within the ground electronic state (Chapter 2). The ro-vibrational features present in many IR spectra make this technique highly selective, particularly when compared to the more broad and featureless UV spectra.

Step-scan Fourier transform infrared (FTIR) spectroscopy allows time-resolved IR spectra to be obtained and has been employed by both Su *et al.*[38] and Huang *et al.*[39] to obtain the IR spectrum of CH_2OO at resolutions of 1.0 cm^{-1} and 0.25 cm^{-1} respectively. Luo *et al.*[40] utilised a quantum cascade laser (QCL) to measure the IR absorption spectra of CH_2OO at an improved resolution of 0.0015 cm^{-1} allowing the ro-vibrational lines of CH_2OO to be resolved. A comparison between the IR spectra of CH_2OO obtained at different spectral resolutions can be seen in Figure 3.7.

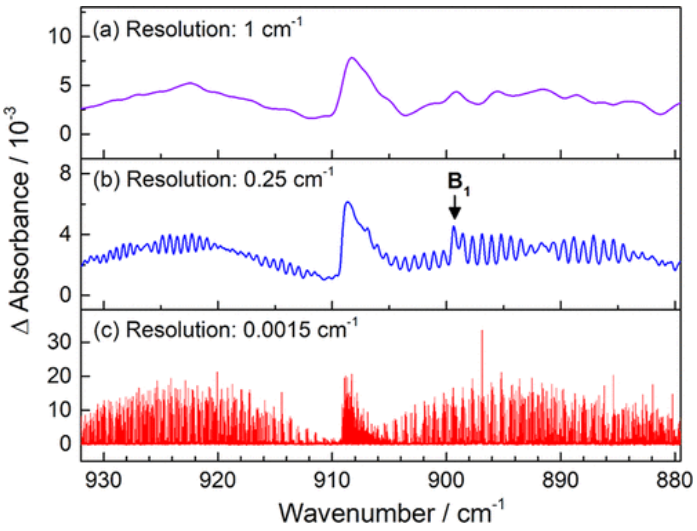

Figure 3.7. Comparison of the IR spectra obtained for the OO-stretching mode (ν_6) of CH_2OO at different resolutions between 880 and 932 cm^{-1}. (a) and (b) were obtained using step-scan FTIR spectroscopy with resolutions of 1.0 cm^{-1} [38] and 0.25 cm^{-1} [39] respectively and (c) obtained using a continuous wave QCL with a resolution of 0.0015 cm^{-1}.[40]

The reaction products of many Criegee intermediate reactions often have small UV absorption cross-sections, making them difficult to detect in many UV systems. For example, SO_3, a product of the reaction between Criegee intermediates and SO_2, cannot be detected using UV absorption. However, as SO_3 exhibits absorption within the IR range of the electromagnetic spectrum, IR absorption spectroscopy is a suitable technique for its detection. Wang *et al.*[41] employed step-scan FTIR spectroscopy with a resolution of 4 cm^{-1} to monitor the reaction between CH_2OO and SO_2 and were able to monitor the formation of SO_3 at 1391.5 cm^{-1}. More recently, Mir *et al.*[42] employed LFP coupled with mid-infrared QCL absorption spectroscopy with a resolution of <0.004 cm^{-1} to measure the IR spectrum of CH_2OO as well as report kinetics and product yields for the reaction between CH_2OO and SO_2. Mir *et al.* were able to monitor the production of SO_3 at ~ 1388.7 cm^{-1}, demonstrating that SO_3 is a direct product from the reaction between CH_2OO and SO_2. A schematic of the experimental apparatus used by Mir *et al.* is shown in Figure 3.8. The experimental setup used by Mir *et al.* is similar to that used in the experiments presented throughout this thesis (described in detail in subsequent

sections) where the probe beam is a multi-pass arrangement to increase the total pathlength and sensitivity.

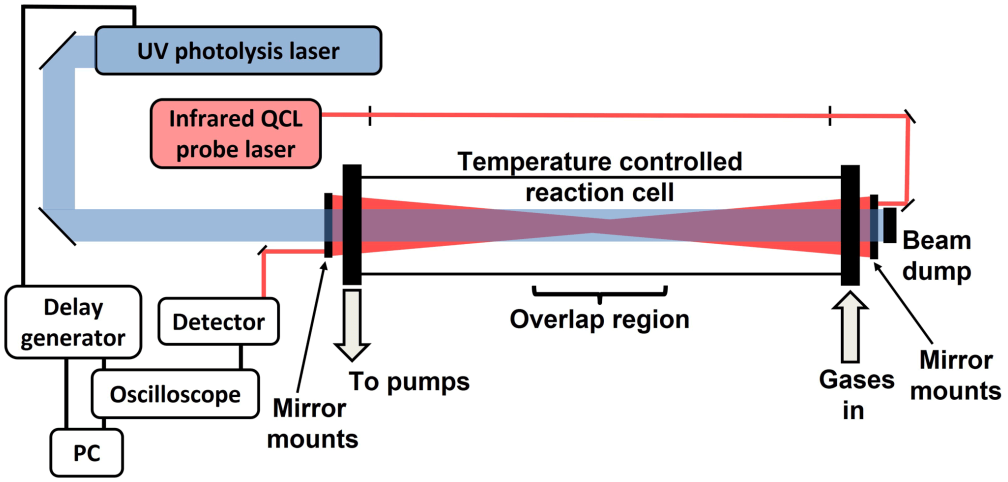

Figure 3.8. Schematic of an IR-QCL experimental set-up used to monitor the reaction of CH_2OO with SO_2. Copied from reference 42.[42]

3.2.3.4.1 Quantum Cascade Lasers

Quantum cascade lasers (QCLs) are a tunable source of IR light invented in 1994[43] and have been rapidly developing within infrared spectroscopy research. QCLs are made from alternating layers of semiconductor material that create quantum wells, the thickness of the layer will determine the depth of the quantum well and thus the energy of the photon emitted. Each stage in the QCL is comprised of an active region alternated with a doped electron region (Figure 3.9), and these stages give rise to an energy staircase, resulting in the cascading emission of photons.[44] The active region contains three energy states (1, 2 and 3 in Figure 3.9) with the energy difference between stages 2 and 3 defining the output of the laser. As stated earlier, for lasing action to occur, a population inversion is required. In QCLs this is achieved by the lifetime of level 3 being much longer than that of level 2, which results from the energy separation between levels 3 and 2 being larger than that of levels 2 and 1. When a current is applied, electrons are injected into the upper level of the active region by a process known as resonant tunnelling, which ensures highly selective injection. The electrons release photons as they relax from level 3 to level 2 and then from level 2 to level 1 and travel from one stage to another via tunnelling from level 1 in the active region, across the injector region. The process of tunnelling from level 3 directly across the injector region needs to be suppressed as this will reduce the population inversion between levels 3 and 2. This is done by designing the adjacent injector such that there is a region of low density of states at an energy corresponding to E_3 and then a dense manifold of states adjacent to level 1 and 2 (grey shaded regions in Figure 3.9).[44]

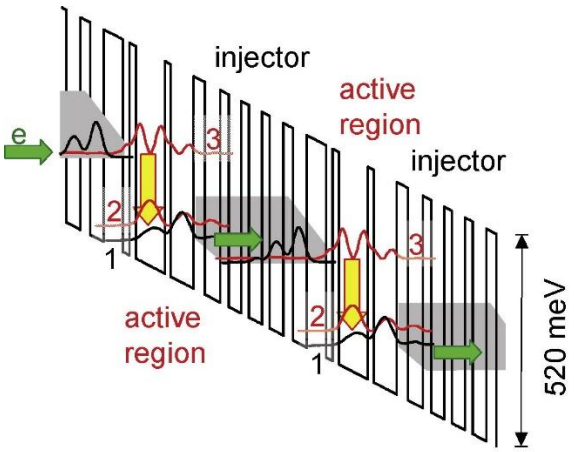

Figure 3.9. Diagram of a Quantum Cascade Laser, copied from reference 44.[44]

The output of the QCL is determined by the semi-conductor material used, and various QCLs enable different spectral outputs to be attained. External cavity (EC) QCLs can be used to obtain broadband emission, typically over several hundred cm^{-1}, or Fabry-Perót (FP) QCLs to achieve a range of ~ 50 cm^{-1}. Work carried out by Mir *et al.*[45] at the University of Leeds employed a distributed feedback (DFB) QCL to achieve single mode emission. In the mid-IR, DFB QCLs can be operated at room temperature, and control of the temperature of the semi-conductor material and the applied current results in fine tuning the laser output within ~ 5 cm^{-1}.

The earlier Sections of this Chapter have summarised various experimental techniques used for the production and monitoring of reactive species within the field of atmospheric chemistry, each with their own advantages and limitations. Since the development of the flash photolysis technique, significant advances have been made in both optics and lasers which have transformed the study of highly reactive species that otherwise could not be easily produced within the laboratory. Flash photolysis has been pivotal in the study of Criegee intermediates and has been coupled to PIMS,[15,16] LIF [20,22] and absorption spectroscopy [28,34,27,30] to report the kinetics of their reactions. In this work, LFP has been coupled to time-resolved broadband UV absorption spectroscopy to report the kinetics of CH_2OO and CH_3CHOO reactions, and is described in more detail in the following sections.

3.3 Experimental Technique and Data Analysis of This Work

3.3.1 Instrumental Arrangement

The kinetics of the reactions between CH_2OO with SO_2, NO_2 and water/water dimers and CH_3CHOO conformers with SO_2 were studied using laser flash photolysis of either $CH_2I_2/O_2/N_2/X$ or $CH_3CHI_2/O_2/N_2/SO_2$ gas mixtures coupled with time-resolved broadband UV absorption spectroscopy, where X = SO_2, NO_2 or H_2O.

Known quantities of precursor gases (N_2 (BOC, 99.998 %), O_2 (BOC, 99.5 %), and SO_2 or NO_2 (Sigma Aldrich 99.9 %, prepared at known dilute concentrations in N_2 and stored in glass bulbs)) were introduced into a mixing chamber using calibrated mass flow controllers (Appendix 1) and then passed into the reaction cell. For $CH_2OO + H_2O$ experiments, water vapour was added to the system by passing a known flow of N_2 gas through a bubbler containing deionised water held in a water bath at 70 ^oC. The concentration of water vapour was measured at the exit of the reaction cell by a relative humidity (RH) probe (Michell Instruments PCMini52) that was calibrated against a dew point hygrometer (Buck Research Instruments, CR-4 chilled mirror hygrometer) (Appendix 2). Liquid precursors (i.e. CH_2I_2 (Alfa Aesar 99 %) or CH_3CHI_2 (Sigma-Aldrich 98 %, SynHet 95 %)) were introduced into the reaction cell by flowing a small quantity of the gas mixture through a bubbler containing the liquid at a fixed temperature in an ice bath. The concentration of the precursor could be altered by a needle valve placed before the bubbler and was determined experimentally by measuring the UV intensity transmitted through the cell in experiments with and without the precursor flowing through the cell. All experiments were performed under pseudo-first-order conditions, with SO_2, NO_2 or water vapour present in excess over the Criegee intermediate. Specific details of initial concentrations are given in chapters corresponding to each reaction. Gases and chemicals were used as supplied (i.e. no further purification).

The reaction cell was a 100 cm long jacketed glass tube with an inner diameter of 3 cm and fused silica windows at both ends. A diagram of the experimental set-up is given in Figure 3.10. The total pressure of the cell was controlled by throttling the exit of the cell to the pump and measured by a capacitance manometer (MKS instruments). Experiments were carried out at temperatures between 242 and 353 K with the temperature of the system controlled by circulating a thermofluid (HUBE6479 DW-THERM) from a thermoregulator (Huber Unistat 360) through the outer jacket of the cell. Details of temperature calibrations are given in Appendix 3. Specific details of flow rates and residence times are given in Sections 4.3, 5.3, 6.2 and 7.2.

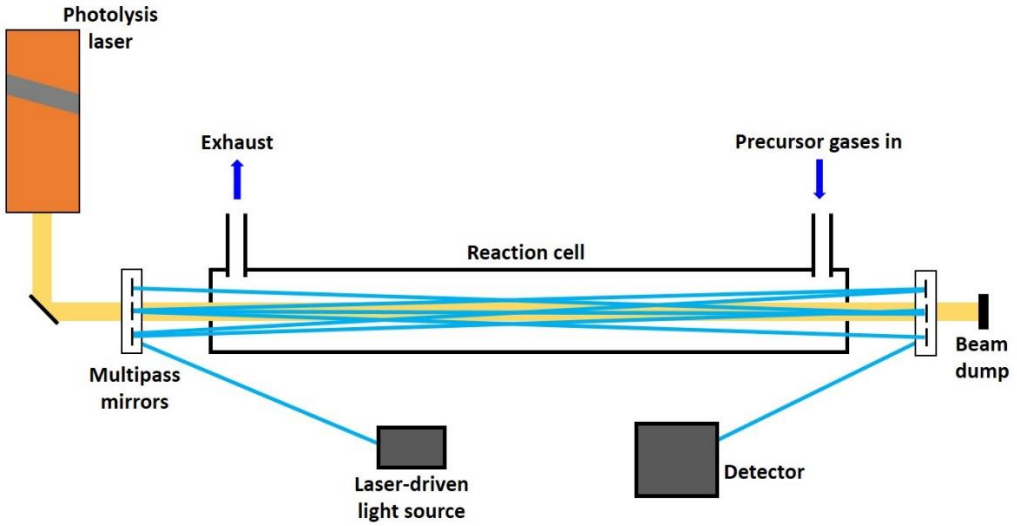

Figure 3.10. Schematic of the reaction cell used for these experiments. Adapted from Lewis *et al.*[46]

Reactions R3.3-R3.5 or R3.6-R3.8 were initiated within the reaction cell using an excimer laser (KrF, Lambda-Physik CompEx 210) operating at a wavelength of λ = 248 nm with a laser fluence of 20 – 60 mJ cm^{-2}. The laser was aligned along the length of the cell using a dichroic turning mirror (Edmund Optics). The pulse repetition rate was set to ensure there was enough time for a fresh gas mixture to be introduced to the reaction cell before the laser fired again – eliminating the risk of unwanted photolysis of the reaction products.

$CH_2I_2 + h\nu\ (\lambda = 248\ nm) \rightarrow CH_2I + I$ (R3.3)

$CH_2I + O_2 \rightarrow CH_2IOO^*$ (R3.4)

$CH_2IOO^* \rightarrow CH_2OO + I$ (R3.5a)

$CH_2IOO^* + M \rightarrow CH_2IO_2 + M$ (R3.5b)

$CH_3CHI_2 + h\nu\ (\lambda = 248\ nm) \rightarrow CH_3CHI + I$ (R3.6)

$CH_3CHI + O_2 \rightarrow CH_3CHIOO^*$ (R3.7)

$CH_3CHIOO^* + M \rightarrow CH_3CHIO_2 + M$ (R3.8a)

$CH_3CHIOO^* \rightarrow$ *syn*-$CH_3CHOO + I$ (R3.8b)

$CH_3CHIOO^* \rightarrow$ *anti*-$CH_3CHOO + I$ (R3.8c)

Absorption of UV light was measured using a laser-driven light source (LDLS, Energetiq EQ-99X) that provided ~10 mW cm^{-2} of light at wavelengths between 200 and 800 nm. The light was collimated using an off-axis parabolic mirror (ThorLabs MPD129-F01 UV enhanced

aluminium) and multi-passed 7 or 9 times through the reaction cell by 8 or 10 Al mirrors (reflectivity > 85 % in the UV), each of 12 mm diameter (Figure 3.11), which were positioned outside the windows of the cell as shown in Figure 3.10 (above). Figure 3.11 shows a schematic of the mirror mount for experiments where 8 mirrors were used (enabling the light to be multi-passed 7 times through the cell), which enables the photolysis beam to pass through the mirror mount and the centre of the reaction cell, with the mirrors for the mulitpass probe arrangement positioned around the central hole for the photolysis beam. Each mirror in the multipass arrangement could be adjusted to align the probe beam such that there is maximum overlap with the 248 nm excimer beam, giving a total effective pathlength of $l = (471 \pm 50)$ cm[30] for the 7 pass arrangement or $l = (595 \pm 53)$ cm for the 9 pass arrangement (details for measuring the effective pathlength are given in Appendix 4).

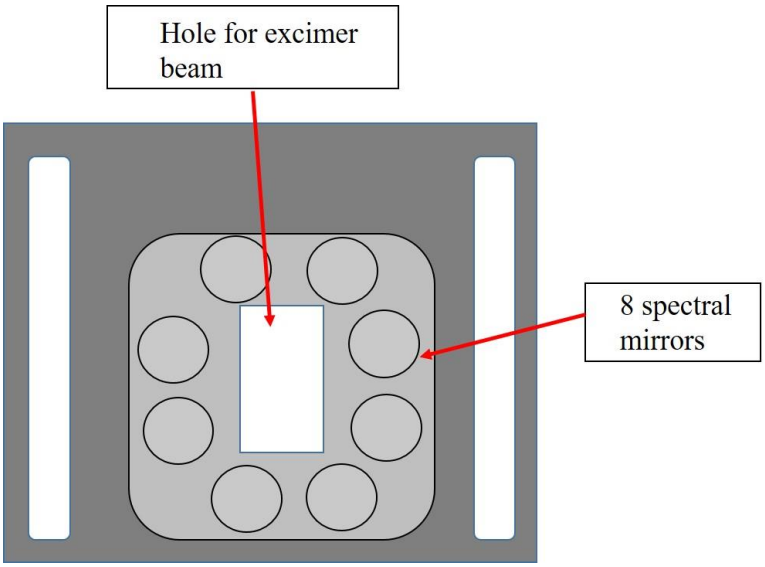

Figure 3.11. Schematic of the mirror mount containing 8 spectral mirrors (enabling the light to be multi-passed 7 times through the cell), positioned outside the windows at each end of the reaction cell. The large rectangular hole is to allow for the excimer laser beam to pass through the mirror mount into the reaction cell.[46]

In order to reduce scattered light from the photolysis laser reaching the detector, the beam exiting the cell was passed through a sharp cut-on filter (RazorEdge ultrasteep long-pass edge filter 248 nm), which effectively blocks light at wavelengths below 250 nm, and focussed onto a fibre optic. The fibre optic directed light through either a 25 or 100 μm slit onto a spectrograph with a diffraction grating of 300 (Princeton Instruments, FER-GRT-29.5-575) or 600 (Princeton Instruments, FER-GRT-060-500) grooves / mm which imaged the light onto a charge-coupled device (CCD) detector with a spectral resolution (full width half maximum (FWHM)) of ~1 nm. Using a diffraction grating with a greater number of grooves / mm offers the advantage of a higher dispersion of the incoming light, increasing the angular spread of

light and enabling more spectral features to be distinguished from one another, thus increasing the resolution of the detector. However, as the size of the detector is finite, increasing the dispersion of light will decrease the spectral range of the detector, as less wavelengths are able to fit onto the detector. Therefore, there is a trade-off in experiments between spectral resolution and spectral range. In some experiments, reaction products that absorb light at a higher wavelength (>600 nm) than the Criegee intermediates may also be monitored. In this case, it would be beneficial to use a grating with fewer grooves / mm to increase the spectral range so that all species can be monitored simultaneously. As the spectral resolution is also dependent on the size of the slit that light travels through to get to the spectrograph, decreasing the slit width would overcome the decrease in resolution associated with using a grating with fewer grooves / mm. A brief description of how photo-charge is passed through the CCD is outlined below.

3.3.2 Charge Coupled Device (CCD)

The detector used in these experiments was a Charge Coupled Device (CCD). CCDs are arrays of light-sensitive pixels that convert incident radiation to charge – where the charge relates to the number of photons on a given pixel after it has been exposed to a light source for a set period of time. The camera used throughout the experiments was the FERGIE^{TM} spectroscopy camera (Princeton Instruments, FER-SCI-1024BRX), which is an integrated diffraction grating/spectrometer and CCD detector.

The pixels in the CCD are arranged in a 2D array and the wavelength-resolved light exiting the spectrograph is imaged across an illuminated region at the top of the CCD. The photo-charge is shifted from the illuminated region of the CCD into a region shielded from the light exiting the spectrograph (termed the storage region) at specified rates. Thus one dimension of the CCD represents wavelength and the other represents time, as depicted schematically in Figure 3.12. The CCD used in this work consisted of 1024 columns along the wavelength axis and 265 rows in the time axis.

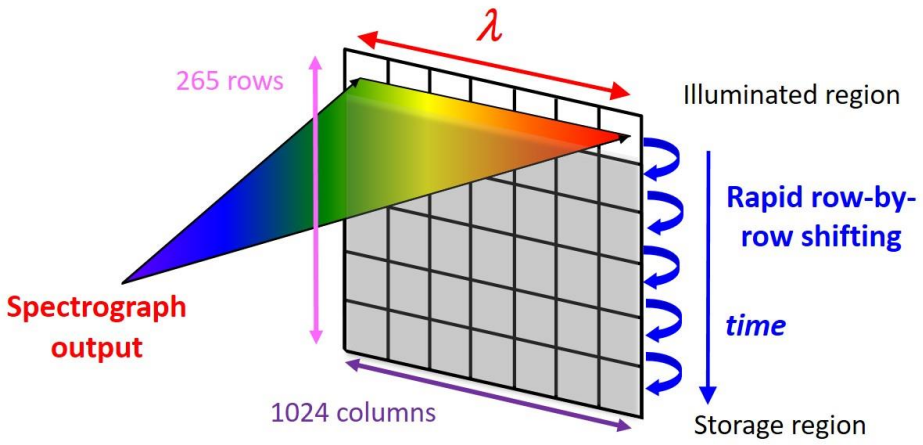

Figure 3.12. A diagram to outline how photo-charge is vertically shifted down the CCD array. The output from the spectrograph is focused onto an illuminated region and then shifted to a storage region (shown by the grey shading) at a given shift rate.

The CCD consisted of all 1024 columns on the wavelength axis (calibrated by measurements of the well-known Hg emission spectrum) and 265 rows on the time axis, with the illuminated region consisting of 10 rows. For measurements where time resolution was not required (i.e. for measurements of the light intensity transmitted through stable gas mixtures, as is the case for measurements of precursor gas concentrations), the CCD was simply exposed for a set period of time before data are transferred to the PC for analysis. For time-resolved measurements, the illuminated region of the CCD was exposed to incoming radiation for a set time typically between 10 and 100 µs, after which photo-charge was shifted vertically down the illuminated region of the CCD row-by-row at shift rates between 5.6 µs per row and 35 µs per row into the storage region. As the photo-charge was shifted from the illuminated region to the storage region, the photo-charge from all 10 rows of the illuminated region was binned and summed, and shifted vertically into the adjacent row in the storage region at the same shift rate at which the photo-charge was shifted in the illuminated region. This process was repeated throughout the experiment until the storage region was full and is depicted in Figure 3.13. Each row in the storage region therefore contained photo-charge from 10 illuminated rows, impacting the time resolution of the experiments. The time resolution is given by a combination of the number of rows exposed in the illuminated region and the shift rate of the CCD, with typical time resolutions for the experiments reported in this work ranging between 70 and 485 µs.

The time delay between the operation of the camera and the firing of the excimer laser was controlled by a delay generator (SRS model DG 535) allowing the intensity data to be collected before (I_o) and after (I_t) photolysis, which enabled determination of the absorbance and thus concentration from the Beer-Lambert law before, during, and after a reaction.

Once all 265 frames in the storage region are filled with photo-charge, the output from the 2D array was transferred to the PC for analysis.

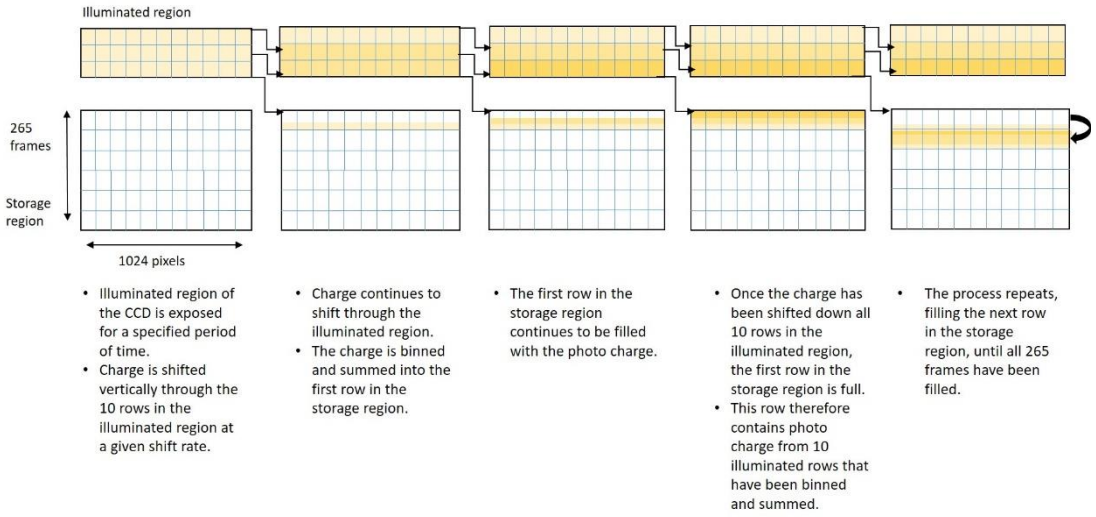

Figure 3.13. A schematic outlining how photo-charge was vertically shifted through the CCD. The illuminated region was a region of 10 rows where charge accumulates. Once all 10 rows in the illuminated region were filled, the charge was shifted into the storage region.

The CCD detector can also generate charge owing to thermal excitation, which generates 'dark current' on the CCD. In order to minimise such effects, the camera was cooled to -45 ^{o}C by a Peltier device to reduce the amount of residual current within the CCD when there is no illumination. Prior to the start of experiments, a background spectrum was also measured to account for any remaining dark current on the device.

Figure 3.14 shows a flow chart summarising the experimental procedure and how the intensity data was collected by the CCD.

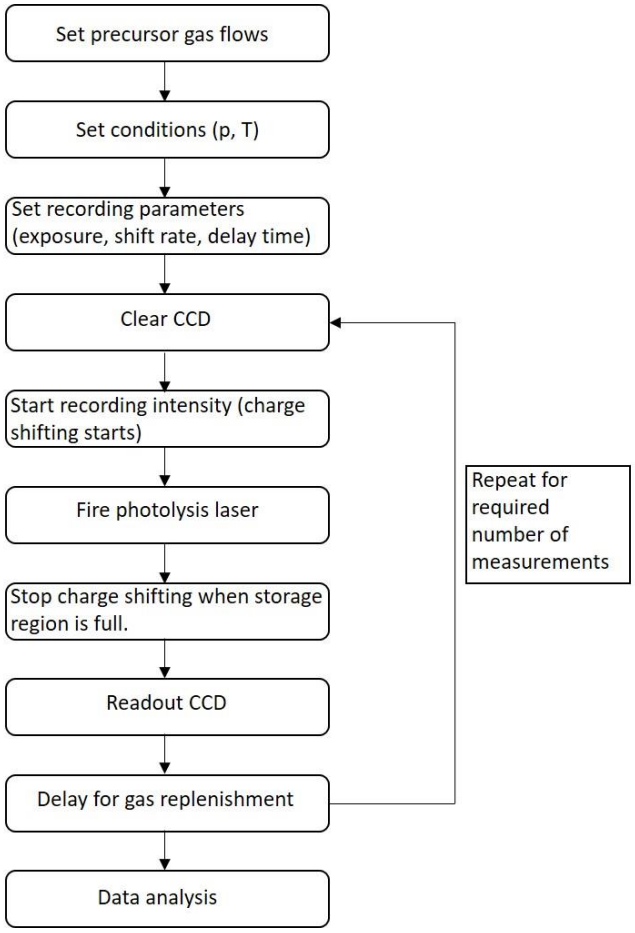

Figure 3.14. Flow chart summarising how the intensity data was collected throughout the experiments.

3.3.3 Spectral Fitting

The raw data output from these experiments were 2D arrays of 265 time points with light intensities recorded over 1024 wavelengths. The absorbance, $A_{\lambda,t}$, was determined for each wavelength λ and time point t from the measured intensities using the Beer-Lambert Law (Equation 3.7), where the incident light intensity, $I_{0,\lambda}$, was defined by averaging the absorbance spectra obtained at time points before the photolysis laser fired.

For experiments involving the CH_2OO Criegee intermediate, the absorbance in the wavelength region of interest (290 – 450 nm) contained contributions from the Criegee intermediate, the CH_2I_2 precursor (which exhibits a negative absorbance owing to depletion on photolysis), and iodine monoxide (IO) radicals which are produced in the system as a result of secondary chemistry. For the species present in experiments involving CH_2OO, the absorbance was thus given by:

$$A_{\lambda,t} = (\sigma_{\mathrm{CH_2I_2},\lambda} \times [\mathrm{CH_2I_2}]_{\lambda,t} \times l) + (\sigma_{\mathrm{CH_2OO},\lambda} \times [\mathrm{CH_2OO}]_{\lambda,t} \times l) + (\sigma_{\mathrm{IO},\lambda} \times [\mathrm{IO}]_{\lambda,t} \times l) \quad \text{(Equation 3.9)}$$

where $\sigma_{\mathrm{CH_2I_2},\lambda}$ is the cross-section of CH_2I_2[47] at wavelength λ, $[CH_2I_2]_{\lambda,t}$ is the concentration of CH_2I_2 at wavelength λ and time t, $\sigma_{\mathrm{CH_2OO},\lambda}$ is the cross-section of CH_2OO[24] at wavelength λ, $[CH_2OO]_{\lambda,t}$ is the concentration of CH_2OO at wavelength λ and time t, $\sigma_{\mathrm{IO},\lambda}$ is the cross-section of IO[48] at wavelength λ and $[IO]_{\lambda,t}$ is the concentration of IO at wavelength λ and time t.

The total absorbance in experiments involving CH_3CHOO Criegee intermediates was similarly determined from contributions of *syn*-CH_3CHOO, *anti*-CH_3CHOO, the CH_3CHI_2 precursor, and IO.

In order to determine the concentration of each species in the reaction mixture at each time point throughout the reaction, reference spectra for the absorbing species were interpolated onto the experimental wavelength grid and a least squares fit of the reference spectra to the total observed absorbance was performed for each time point. Figures 3.15 and 3.16 show example fits which output the product of the concentration of each species with the effective pathlength for each time point, which can be converted to concentration through knowledge of the effective pathlength. However it is worth noting that for experiments described in this work, which were performed under pseudo-first-order conditions, knowledge of the pathlength is not strictly required and uncertainties in the determination of the pathlength do not contribute to uncertainties in the kinetics reported (details for determining the effective pathlength are given in Appendix 4).

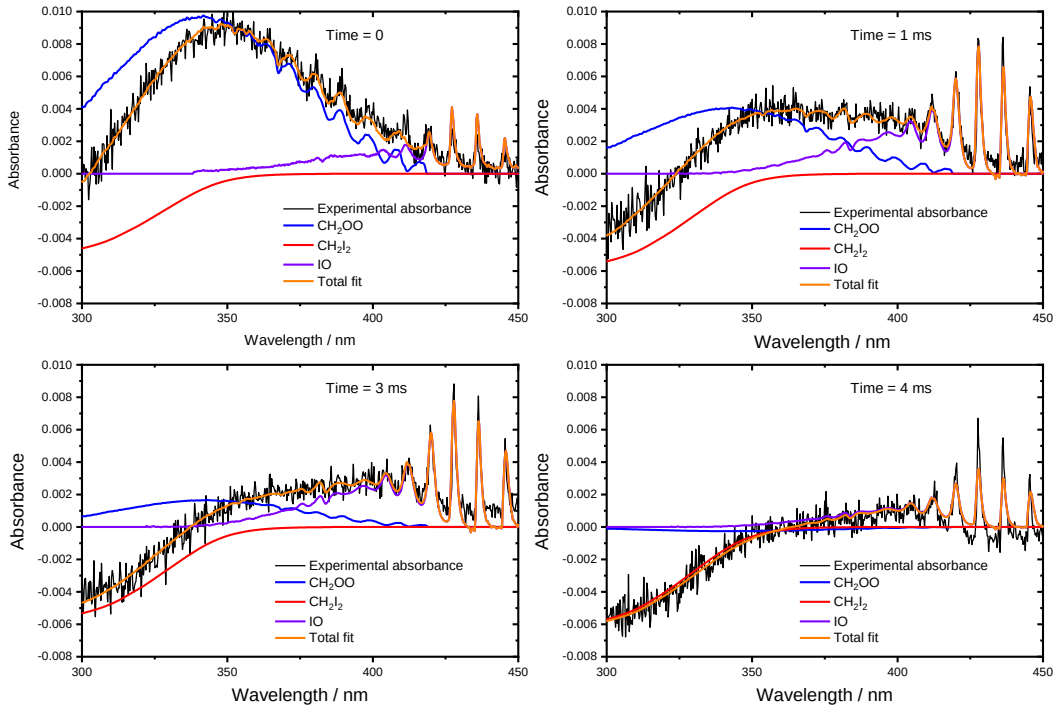

Figure 3.15. Plots outlining how the experimental absorbance evolves as a function of time following the photolysis of CH_2I_2 at t = 0, 1, 3 and 4 ms. The black is the experimental absorbance, the blue is the CH_2OO reference spectra,[24] red is CH_2I_2,[47] purple is IO[48] and orange is the overall fit. Experiments were conducted at 298 K and 85 Torr, with $[CH_2I_2]_0 = 1.3 \times 10^{13}$ molecule cm^{-3} and $[SO_2] = 1.5 \times 10^{13}$ molecule cm^{-3}.

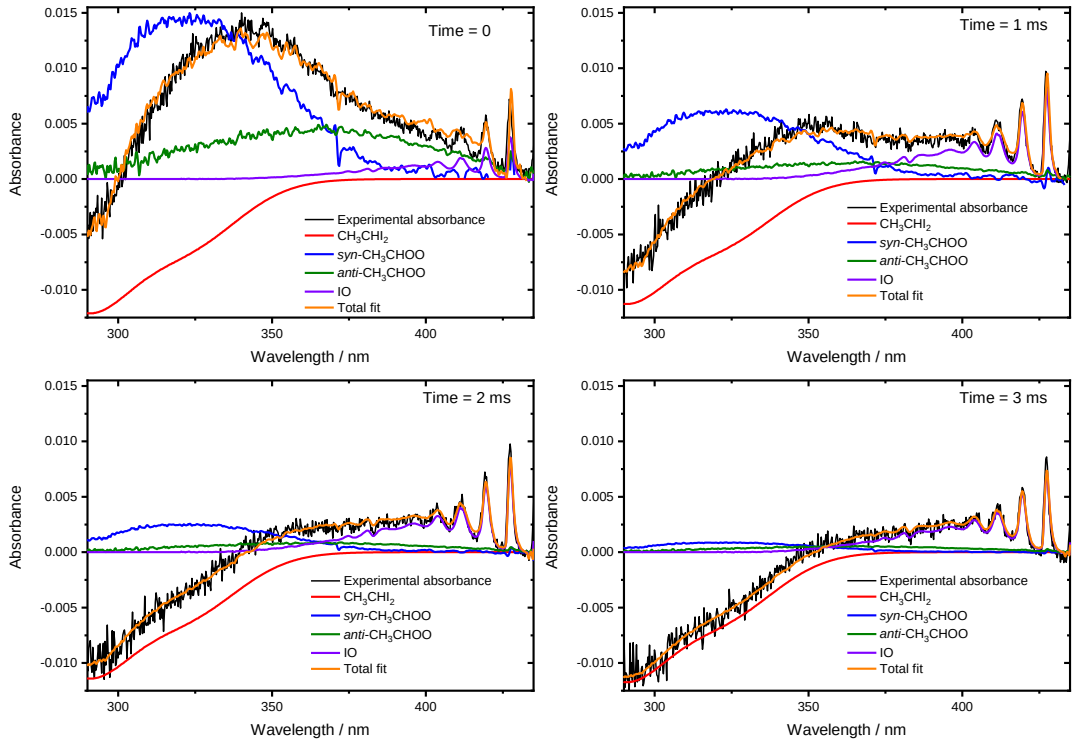

Figure 3.16. Plots outlining how the experimental absorbance evolves as a function of time following the photolysis of CH_3CHI_2 at t = 0, 1, 2 and 3 ms. The experimental absorbance is shown in black, the CH_3CHI_2 reference spectra is shown in red,[49] *syn*-CH_3CHOO in blue,[25] *anti*-CH_3CHOO in green[25] and IO in purple.[48] The orange line represents the overall fit to the observed absorbance. Experiments were conducted at 298 K and 50 Torr, with $[CH_2I_2]_0 = 2.8 \times 10^{13}$ molecule cm^{-3} and $[SO_2] = 1.1 \times 10^{13}$ molecule cm^{-3}.

3.3.4 Kinetic Analysis

The reactions presented throughout this thesis were all studied under pseudo-first-order conditions, where the concentration of the reactant, SO_2, NO_2 or water vapour were used in large excess over either CH_2OO or CH_3CHOO. For the general reaction:

$$A + B \rightarrow \text{Products} \qquad \text{(R3.9)}$$

Using [B] in large excess over [A] allows the rate coefficient to be simplified from Equation 3.10 to Equation 3.11.

$$rate = k[A][B] \qquad \text{(Equation 3.10)}$$

$$rate = k'[A] \qquad \text{(Equation 3.11)}$$

where k' is an effective rate coefficient termed the pseudo-first-order rate coefficient:

$$k' = k[\mathrm{B}] \qquad \text{(Equation 3.12)}$$

The rate equation can now be integrated in the same way as the first-order rate equation (given in Chapter 2) to give Equation 3.13:

$$[\mathrm{A}]_t = [\mathrm{A}]_0 \, exp^{-k't} \qquad \text{(Equation 3.13)}$$

For the reaction of CH_2OO with SO_2, the loss of CH_2OO in the system occurs as a result of several processes:

$CH_2OO + SO_2 \rightarrow HCHO + SO_3$ (R3.10)

$CH_2OO + X \rightarrow$ Products (R3.11)

$CH_2OO \rightarrow$ Products (R3.12)

where X = CH_2OO, I, IO.

The change in concentration of the Criegee intermediate can thus be described by Equation 3.14:

$$[\mathrm{CH_2OO}]_\mathrm{t} = [\mathrm{CH_2OO}]_0 \left(exp^{-k't}\right) \qquad \text{(Equation 3.14)}$$

where $[CH_2OO]_t$ is the concentration of CH_2OO at time t, $[CH_2OO]_0$ is the initial Criegee intermediate concentration and k' is the observed rate coefficient, which incorporates the rate coefficient for the Criegee intermediate decay when there is no SO_2 in the system ($k_x = k_{3.11} + k_{3.12}$) and the pseudo-first-order rate constant for the reaction between the Criegee intermediates and SO_2 ($k'_{3.10}$).

$$k' = k_x + k'_{3.10} \qquad \text{(Equation 3.15)}$$

where

$$k'_{3.10} = k_{3.10}[SO_2] \qquad \text{(Equation 3.16)}$$

3.3.4.1 Instrument Response Function

Concentration-time profiles observed in this work are given by a convolution of the 'true' kinetic decay with an instrument response function (IRF) which results from the simultaneous illumination of multiple rows on the CCD detector (section 3.2) and the row-by-row shifting of photo-charge from the illuminated region of the CCD to a storage region. The IRF can be

described by a Gaussian function with peak height *a* centred at t_c and with width *w* (Equation 3.17):

$$f(t) = a\ exp\left(-\frac{(t-t_c)^2}{2w^2}\right) \qquad \text{(Equation 3.17)}$$

Convolution of the IRF (Equation 3.17) with the first-order (or pseudo-first-order) kinetic decay (Equation 3.14) gives Equation 3.18:

$$[CH_2OO]_t = \frac{[CH_2OO]_0}{2}\ exp\left\{\frac{(k'w)^2}{2} - k'(t-t_c)\right\} \times \left\{1 + \text{erf}\left(\frac{t - t_c - k'w^2}{\sqrt{2}w}\right)\right\} \qquad \text{(Equation 3.18)}$$

where erf is the error function obtained in the integration of the normalised form of the Gaussian function.

Figures 3.17 and 3.18 show a comparison between fitting the data with Equation 3.14 (dashed blue line) and Equation 3.18 (solid red line).

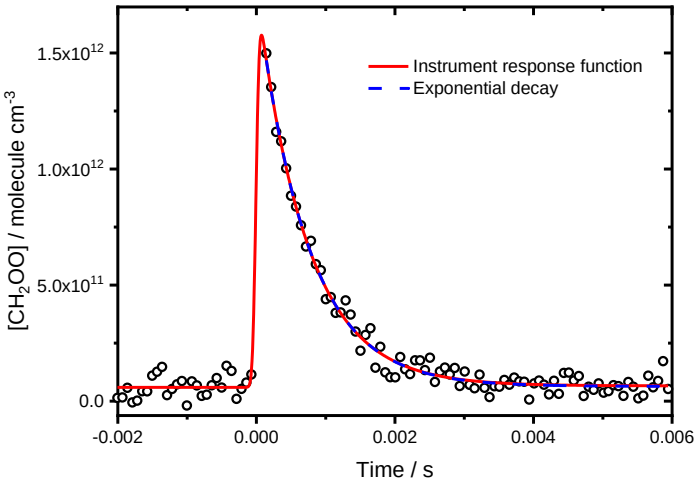

Figure 3.17. Concentration – time profile for the reaction of CH_2OO with NO_2 at 298 K and 50 Torr where $[NO_2] = 9.7 \times 10^{14}$ molecule cm^{-3} and $[CH_2I_2]_0 = 5.9 \times 10^{13}$ molecule cm^{-3}. The red solid line is fit using an equation for the convolution of the true decay with an instrument response function (Equation 3.18) and gave: k' = (1397 ± 47) s^{-1}, $[CH_2OO]_0 = (1.73 \pm 0.15) \times 10^{12}$ molecule cm^{-3}, t_c = -(5.6 ± 0.2) × 10^{-6} s and $w = (3.9 \pm 0.1) \times 10^{-5}$ s. The dashed blue line represents the fit to the data using an exponential decay (Equation 3.14) and gave: k' = (1389 ± 39) s^{-1} and $[CH_2OO]_0 = (1.71 \pm 0.03) \times 10^{12}$ molecule cm^{-3}. Uncertainties are 1σ.

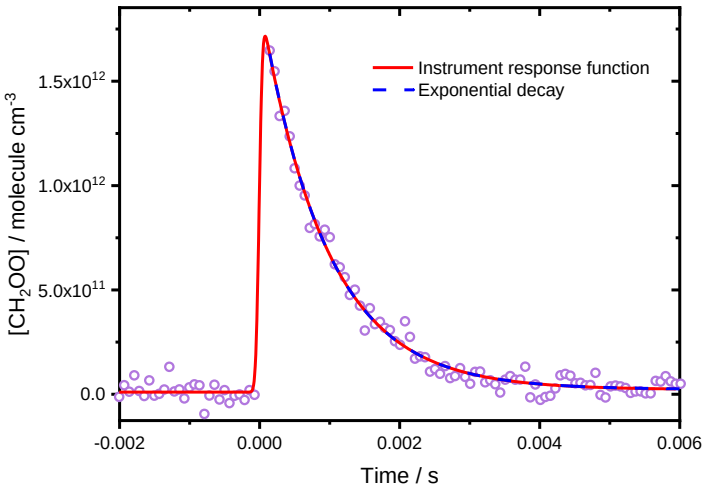

Figure 3.18. Concentration – time profile for the reaction of CH_2OO with NO_2 at 298 K and 50 Torr where $[NO_2] = 6.7 \times 10^{14}$ molecule cm^{-3} and $[CH_2I_2]_0 = 5.9 \times 10^{13}$ molecule cm^{-3}. The red solid line is fit using an equation for the convolution of the true decay with an instrument response function (Equation 3.18) and gave: k' = (1063 ± 30) s^{-1}, $[CH_2OO]_0 = (1.90 \pm 0.21) \times 10^{12}$ molecule cm^{-3}, t_c = -(5.6 ± 0.2) × 10^{-6} s and $w = (3.9 \pm 0.1) \times 10^{-5}$ s. The dashed blue line represents the fit to the data using an exponential decay (Equation 3.14) and gave: k' = (1067 ± 28) s^{-1} and $[CH_2OO]_0 = (1.90 \pm 0.03) \times 10^{12}$ molecule cm^{-3}. Uncertainties are 1σ.

To obtain values for bimolecular rate coefficients, the pseudo-first-order rate coefficients, obtained from fits of Equation 3.18 to concentration-time profiles, were plot as a function of SO_2 concentration, where the intercept of such plot describes k_x and $k_{3.10}$ is given by the gradient. Figure 3.19 shows a comparison of a bimolecular plot for the reaction of CH_2OO + SO_2 at 298 K where the value for k_x is included and where it has been subtracted from k'.

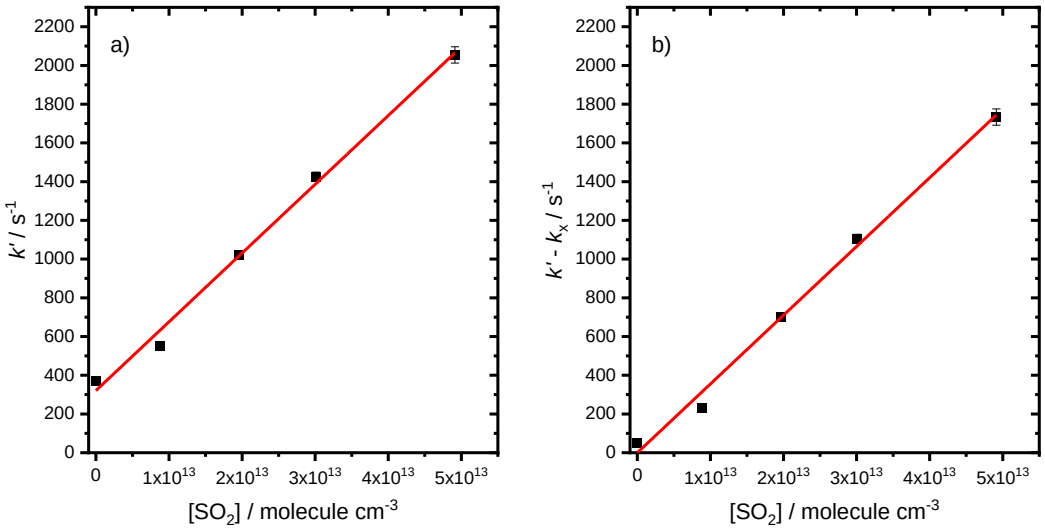

Figure 3.19. (a) Pseudo-first-order losses for CH_2OO as a function of $[SO_2]$ for experiments at 298 K and 85 Torr: (b) Pseudo-first-order losses after k_x has been subtracted. The red lines represent an unweighted linear fit to the data and gave: (a) $k_{3.10} = (3.55 \pm 0.15) \times 10^{-11}$ cm^3 molecule^{-1} s^{-1} with an intercept of $k_x = (321 \pm 42)$ s^{-1} and (b) $k_{3.10} = (3.55 \pm 0.15) \times 10^{-11}$ cm^3 molecule^{-1} s^{-1} with an intercept of $k_x = (0.1 \pm 59)$ s^{-1}. Uncertainties are 1σ.

After subtracting the value for k_x from k', the fit gave a new k_x value of (0.1 ± 59) s^{-1}. The value for k_x cannot be negative and is effectively zero however, there are some experimental errors associated with its value.

The data from experiments of CH_2OO with NO_2 and water/water dimers, as well as from experiments involving the larger Criegee intermediate, CH_3CHOO, can be described in a similar manner.

The rate coefficient k_x is dominated by the CH_2OO self-reaction[24] and reactions with IO[32] or iodine atoms.[24] Under the experimental conditions used in this work, the concentration of the Criegee intermediate remains low enough to minimise the effects of unwanted side reactions, and the concentration of the co-reactant is always in excess of the Criegee intermediate. As a result of these two factors, k_x is approximated to be first-order in this analysis. This has been shown to be a valid approximation in a number of literature studies to investigate the reactions of Criegee intermediates under conditions similar to those used in this work.[50,28,51] To investigate the potential for mixed first- and second-order behaviour, and the validity of k_x being approximated to be a first-order loss process, the kinetic decays obtained in this work were also fit using a mixed first- and second-order rate equation (Equation 3.19). Comparisons

between the first-order and mixed-order fits for each reaction investigated in this work are given in the Chapter relevant to that reaction.

$$[CH_2OO]_t = \frac{[CH_2OO]k'}{k'\,exp(k't) - 2k''[CH_2OO]_0 + 2k''[CH_2OO]_0\,exp(k't)} \qquad \text{(Equation 3.19)}$$

where $[CH_2OO]_t$ is the concentration of CH_2OO at time t, $[CH_2OO]_0$ is the initial concentration of CH_2OO, k' represents the first-order (or pseudo-first-order) losses of the Criegee intermediate and k'' represents the second-order losses of the Criegee intermediate.

3.3.4.2 Mixed-Order Analysis

The potential for mixed first- and second-order behaviour described above was also investigated, in which case the 'true' kinetic decays are described by Equation 3.19.

Convolution of the IRF (Equation 3.17) with the mixed first- and second-order kinetic decay (Equation 3.19) gives Equation 3.20:

$$[CH_2OO]_t = \left\{\frac{1}{\left(\frac{1}{[CH_2OO]_0} + \frac{2k''}{k'}\right)}\right\} \exp\left\{\frac{(k'w)^2}{2} - k'\,(t - t_c) + \frac{2k''}{k'}\right\} \times \frac{\left\{1 + \text{erf}\left(\frac{t - t_c - k'w^2}{\sqrt{2}\,w}\right)\right\}}{2} \qquad \text{(Equation 3.20)}$$

where $[CH_2OO]_t$ is the concentration of the CH_2OO at time t, $[CH_2OO]_0$ is the initial concentration of CH_2OO, k' is the pseudo-first-order rate coefficient describing the loss of the Criegee intermediate, k'' represents the second-order losses of the Criegee intermediate and t_c and w are the centre time and width of the Gaussian function respectively.

Figure 3.20 shows a comparison between the first-order and mixed-order fits to typical concentration-time profiles for CH_2OO, which indicates there were no significant differences between the first-order component obtained when describing the kinetics using a first-order model and when describing the kinetics using a mixed-order model. For fits to the mixed-order equation, the second-order component (k'' in Equations 3.19 and 3.20) was treated as a global parameter for each conformer at each temperature and pressure.

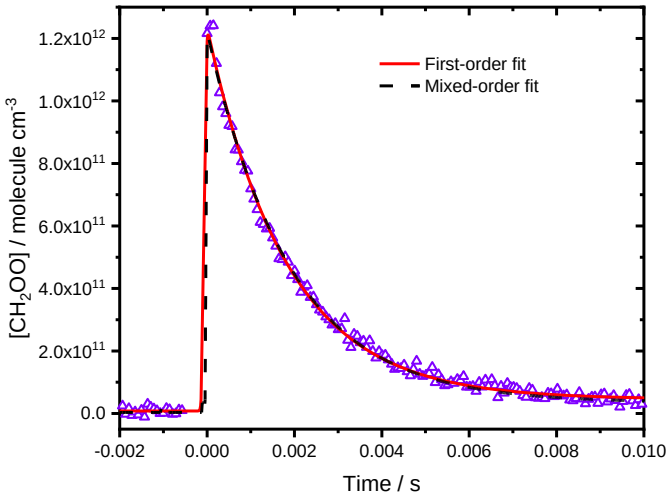

Figure 3.20. Comparison of fits to the first-order rate equation (red, Equation 3.18) and the mixed-order rate equation (black, Equation 3.19) for CH_2OO in the presence of $[SO_2] = 8.8 \times 10^{12}$ molecule cm^{-3} at 85 Torr and 298 K. The solid red line gave: $t_c = -(6.67 \pm 0.26) \times 10^{-5}$ s, $w = (3.73 \pm 0.15) \times 10^{-5}$ s, $[CH_2OO]_0 = (1.24 \pm 0.18) \times 10^{12}$ molecule cm^{-3} and $k' = (551 \pm 6)$ s^{-1}. The dashed black line gave: $t_c = -(2.20 \pm 0.46) \times 10^{-5}$ s, $w = (1.01 \pm 0.39) \times 10^{-5}$ s, $[CH_2OO]_0 = (1.50 \pm 0.31) \times 10^{12}$ molecule cm^{-3}, $k'' = (1.09 \pm 0.02) \times 10^{10}$ cm^3 $molecule^{-1}$ s^{-1} and $k' = (529 \pm 8)$ s^{-1}. Uncertainties are 1σ.

Figure 3.21 compares rate coefficients for the reaction of CH_2OO with SO_2 obtained from the first-order fits to those obtained from the mixed-order fits. Results show less than 5 % difference between the rate coefficients obtained when kinetics were described using the first-order and mixed-order models and values obtained for the intercept, k_x, between the two fits within their error limits. We therefore conclude that data are well described by pseudo-first-order kinetics.

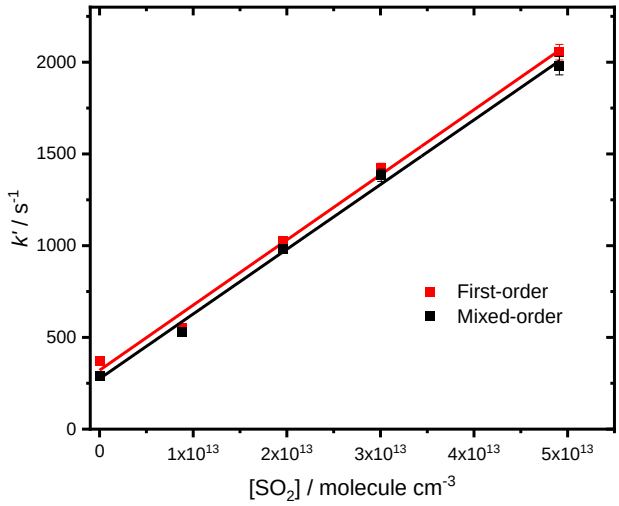

Figure 3.21. Comparison between first-order and mixed-order rate coefficients for the reaction of $CH_2OO + SO_2$ at 298 K and 85 Torr. The red line represents an unweighted linear fit to the data from the first-order fit, giving $k_{3.10} = (3.55 \pm 0.15) \times 10^{-11}$ cm^3 molecule^{-1} s^{-1} with an intercept of (321 ± 42) s^{-1} and the black line represents an unweighted linear fit to the data from the mixed-order fit, giving $k_{3.10} = (3.53 \pm 0.12) \times 10^{-11}$ cm^3 molecule^{-1} s^{-1} with an intercept of (275 ± 33) s^{-1}. Uncertainties are 1σ.

A summary of the data analysis procedure used throughout this work is given in Figure 3.22 below.

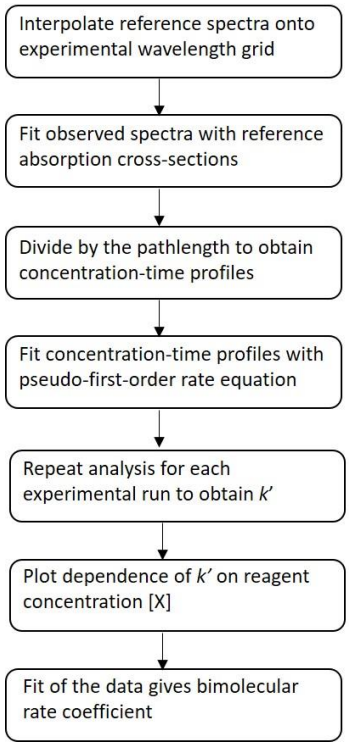

Figure 3.22. Flow chart summarising the data analysis procedure used throughout this work.

3.4 References

1. Brauers, T. and Finlayson-Pitts, B.J. Analysis of relative rate measurements. *International Journal of Chemical Kinetics.* 1997, **29**(9), pp.665-672.
2. King, M.J.E.E.B. The relative-rate technique for deter-mining rate constants. 2016, pp.25-26.
3. Howard, C.J.J.J.o.P.C. Kinetic measurements using flow tubes. 1979, **83**(1), pp.3-9.
4. Michael J. Pilling, P.W.S. *Reaction Kinetics.* Oxford University Press Inc, 1995.
5. Seeley, J.V., Jayne, J.T. and Molina, M.J. High pressure fast-flow technique for gas phase kinetics studies. *International Journal of Chemical Kinetics.* 1993, **25**(7), pp.571-594.
6. Percival, C.J., Shallcross, D.E., Canosa-Mas, C.E. and Dyke, J.M. Recent advances in the application of discharge-flow to the determination of gas-phase rate coefficients at pressures and temperatures of relevance to the Earth's atmosphere. *Journal of Photochemistry and Photobiology A: Chemistry.* 2005, **176**(1), pp.250-259.
7. Norrish, R.G.W. and Porter, G. Chemical Reactions Produced by Very High Light Intensities. *Nature.* 1949, **164**(4172), pp.658-658.
8. Wayne, R.P. *Principles and applications of photochemistry.* Oxford University Press: Oxford, UK, 1988.
9. Geusic, J.E., Marcos, H.M. and Van Uitert, L.G. LASER OSCILLATIONS IN Nd-DOPED YTTRIUM ALUMINUM, YTTRIUM GALLIUM AND GADOLINIUM GARNETS. *Applied Physics Letters.* 2004, **4**(10), pp.182-184.
10. Thomason, L.P. *Nd:YAG lasers: Technology and applications.* Nova science Publishers Inc: New York, USA, 2019.
11. Cremers D.A., R., L. J. *Handbook of Laser-Induced Breakdown Spectroscopy* John Wiley & Sons: Hoboken, New Jersey, 2013.
12. Dass, C. *Fundamentals of Contemporary Mass Spectrometry.* Hoboken, New Jersey: John Wiley & Sons 2007.
13. Gross, J.H. *Mass Spectrometry: A textbook.* Switzerland: Springer International Publishing AG, 2017.
14. Taatjes, C.A., Meloni, G., Selby, T.M., Trevitt, A.J., Osborn, D.L., Percival, C.J. and Shallcross, D.E. Direct Observation of the Gas-Phase Criegee Intermediate (CH_2OO). *Journal of the American Chemical Society.* 2008, **130**(36), pp.11883-11885.
15. Welz, O., Savee, J.D., Osborn, D.L., Vasu, S.S., Percival, C.J., Shallcross, D.E. and Taatjes, C.A. Direct Kinetic Measurements of Criegee Intermediate (CH_2OO) Formed by Reaction of CH_2I with O_2. *Science.* 2012, **335**(6065), p.204.

16. Taatjes, C.A., Welz, O., Eskola, A.J., Savee, J.D., Scheer, A.M., Shallcross, D.E., Rotavera, B., Lee, E.P.F., Dyke, J.M., Mok, D.K.W., Osborn, D.L. and Percival, C.J. Direct Measurements of Conformer-Dependent Reactivity of the Criegee Intermediate CH_3CHOO. *Science.* 2013, **340**(6129), p.177.

17. Heard, D.E. ATMOSPHERIC FIELD MEASUREMENTS OF THE HYDROXYL RADICAL USING LASER-INDUCED FLUORESCENCE SPECTROSCOPY. *Annual Review of Physical Chemistry.* 2006, **57**(1), pp.191-216.

18. Stone, D., Whalley, L.K., Ingham, T., Edwards, P.M., Cryer, D.R., Brumby, C.A., Seakins, P.W. and Heard, D.E. Measurement of OH reactivity by laser flash photolysis coupled with laser-induced fluorescence spectroscopy. *Atmospheric Measurement Techniques.* 2016, **9**(7), pp.2827-2844.

19. Filinski, I. and Skettrup, T. Incoherent Light Source With Radiance Comparable With Laser Radiances. In: *Proc.SPIE*, 1987, pp.282-286.

20. Stone, D., Blitz, M., Daubney, L., Howes, N.U.M. and Seakins, P. Kinetics of CH_2OO reactions with SO_2, NO_2, NO, H_2O and CH_3CHO as a function of pressure. *Physical Chemistry Chemical Physics.* 2014, **16**(3), pp.1139-1149.

21. Stone, D., Au, K., Sime, S., Medeiros, D.J., Blitz, M., Seakins, P.W., Decker, Z. and Sheps, L. Unimolecular decomposition kinetics of the stabilised Criegee intermediates CH_2OO and CD_2OO. *Physical Chemistry Chemical Physics.* 2018, **20**(38), pp.24940-24954.

22. Liu, Y., Bayes, K.D. and Sander, S.P. Measuring Rate Constants for Reactions of the Simplest Criegee Intermediate (CH_2OO) by Monitoring the OH Radical. *The Journal of Physical Chemistry A.* 2014, **118**(4), pp.741-747.

23. Liu, Y., Liu, F., Liu, S., Dai, D., Dong, W. and Yang, X. A kinetic study of the CH_2OO Criegee intermediate reaction with SO_2, $(H_2O)_2$, CH_2I_2 and I atoms using OH laser induced fluorescence. *Physical Chemistry Chemical Physics.* 2017, **19**(31), pp.20786-20794.

24. Mir, Z.S., Lewis, T.R., Onel, L., Blitz, M.A., Seakins, P.W. and Stone, D. CH_2OO Criegee intermediate UV absorption cross-sections and kinetics of CH_2OO + CH_2OO and CH_2OO + I as a function of pressure. *Physical Chemistry Chemical Physics.* 2020, **22**(17), pp.9448-9459.

25. Sheps, L., Scully, A.M. and Au, K. UV absorption probing of the conformer-dependent reactivity of a Criegee intermediate CH_3CHOO. *Physical Chemistry Chemical Physics.* 2014, **16**(48), pp.26701-26706.

26. Smith, M.C., Ting, W.-L., Chang, C.-H., Takahashi, K., Boering, K.A. and Lin, J.J.-M. UV absorption spectrum of the C2 Criegee intermediate CH_3CHOO. *The Journal of Chemical Physics.* 2014, **141**(7), p.074302.

27. Sheps, L. Absolute Ultraviolet Absorption Spectrum of a Criegee Intermediate CH_2OO. *The Journal of Physical Chemistry Letters.* 2013, **4**(24), pp.4201-4205.

28. Chao, W., Hsieh, J.-T., Chang, C.-H. and Lin, J.J.-M. Direct kinetic measurement of the reaction of the simplest Criegee intermediate with water vapor. *Science.* 2015, **347**(6223), p.751.

29. Huang, H.-L., Chao, W. and Lin, J.J.-M. Kinetics of a Criegee intermediate that would survive high humidity and may oxidize atmospheric SO_2. *Proceedings of the National Academy of Sciences.* 2015, **112**(35), pp.10857-10862.

30. Onel, L., Lade, R., Mortiboy, J., Blitz, M.A., Seakins, P.W., Heard, D.E. and Stone, D. Kinetics of the gas phase reaction of the Criegee intermediate CH_2OO with SO_2 as a function of temperature. *Physical Chemistry Chemical Physics.* 2021, **23**(35), pp.19415-19423.

31. Robinson, C., Onel, L., Newman, J., Lade, R., Au, K., Sheps, L., Heard, D.E., Seakins, P.W., Blitz, M.A. and Stone, D. Unimolecular Kinetics of Stabilized CH_3CHOO Criegee Intermediates: syn-CH_3CHOO Decomposition and anti-CH_3CHOO Isomerization. *The Journal of Physical Chemistry A.* 2022, **126**(39), pp.6984-6994.

32. Onel, L., Blitz, M., Seakins, P., Heard, D. and Stone, D. Kinetics of the Gas Phase Reactions of the Criegee Intermediate CH_2OO with O_3 and IO. *The Journal of Physical Chemistry A.* 2020, **124**(31), pp.6287-6293.

33. Nowakowski, M., Wojtas, J., Bielecki, Z. and Mikołajczyk, J. Cavity enhanced absorption spectroscopy sensor. *Acta Physica Polonica A.* 2009, **116**(3), pp.363-367.

34. Chhantyal-Pun, R., Davey, A., Shallcross, D.E., Percival, C.J. and Orr-Ewing, A.J. A kinetic study of the CH_2OO Criegee intermediate self-reaction, reaction with SO_2 and unimolecular reaction using cavity ring-down spectroscopy. *Physical Chemistry Chemical Physics.* 2015, **17**(5), pp.3617-3626.

35. Chhantyal-Pun, R., Welz, O., Savee, J.D., Eskola, A.J., Lee, E.P.F., Blacker, L., Hill, H.R., Ashcroft, M., Khan, M.A.H., Lloyd-Jones, G.C., Evans, L., Rotavera, B., Huang, H., Osborn, D.L., Mok, D.K.W., Dyke, J.M., Shallcross, D.E., Percival, C.J., Orr-Ewing, A.J. and Taatjes, C.A. Direct Measurements of Unimolecular and Bimolecular Reaction Kinetics of the Criegee Intermediate $(CH_3)_2COO$. *The Journal of Physical Chemistry A.* 2017, **121**(1), pp.4-15.

36. Sheps, L., Rotavera, B., Eskola, A.J., Osborn, D.L., Taatjes, C.A., Au, K., Shallcross, D.E., Khan, M.A.H. and Percival, C.J. The reaction of Criegee intermediate CH_2OO with water dimer: primary products and atmospheric impact. *Physical Chemistry Chemical Physics.* 2017, **19**(33), pp.21970-21979.

37. Sheps, L. and Chandler, D.W. *Time-resolved broadband cavity-enhanced absorption spectroscopy for chemical kinetics.* Sandia National Lab.(SNL-CA), Livermore, CA (United States), 2013.

38. Su, Y.-T., Huang, Y.-H., Witek, H.A. and Lee, Y.-P. Infrared Absorption Spectrum of the Simplest Criegee Intermediate CH_2OO. *Science.* 2013, **340**(6129), p.174.

39. Huang, Y.-H., Li, J., Guo, H. and Lee, Y.-P. Infrared spectrum of the simplest Criegee intermediate CH_2OO at resolution 0.25 cm^{-1} and new assignments of bands $2\nu_9$ and ν_5. *The Journal of Chemical Physics.* 2015, **142**(21), p.214301.

40. Luo, P.-L., Endo, Y. and Lee, Y.-P. Identification and Self-Reaction Kinetics of Criegee Intermediates *syn*-CH_3CHOO and CH_2OO via High-Resolution Infrared Spectra with a Quantum-Cascade Laser. *The Journal of Physical Chemistry Letters.* 2018, **9**(15), pp.4391-4395.

41. Wang, Y.-Y., Dash, M.R., Chung, C.-Y. and Lee, Y.-P. Detection of transient infrared absorption of SO_3 and 1,3,2-dioxathietane-2,2-dioxide [cyc-$(CH_2)O(SO_2)O$] in the reaction CH_2OO+SO_2. *The Journal of Chemical Physics.* 2018, **148**(6), p.064301.

42. Mir, Z.S., Jamieson, M., Greenall, N.R., Seakins, P.W., Blitz, M.A. and Stone, D. Identification, monitoring, and reaction kinetics of reactive trace species using time-resolved mid-infrared quantum cascade laser absorption spectroscopy: development, characterisation, and initial results for the CH_2OO Criegee intermediate. *Atmospheric Measurement Techniques.* 2022, **15**(9), pp.2875-2887.

43. Faist, J., Capasso, F., Sivco, D.L., Sirtori, C., Hutchinson, A.L. and Cho, A.Y. Quantum Cascade Laser. *Science.* 1994, **264**(5158), pp.553-556.

44. Curl, R.F., Capasso, F., Gmachl, C., Kosterev, A.A., McManus, B., Lewicki, R., Pusharsky, M., Wysocki, G. and Tittel, F.K. Quantum cascade lasers in chemical physics. *Chemical Physics Letters.* 2010, **487**(1), pp.1-18.

45. Mir, Z.S., Jamieson, M., Greenall, N.R., Seakins, P.W., Blitz, M.A. and Stone, D. Identification, monitoring, and reaction kinetics of reactive trace species using time-resolved mid-infrared quantum cascade laser absorption spectroscopy: development, characterisation, and initial results for the CH_2OO Criegee intermediate. *Atmospheric Measurement Techniques.* 2022, **15**(9), pp.2875-2887.

46. Lewis, T., Heard, D.E. and Blitz, M.A. A novel multiplex absorption spectrometer for time-resolved studies. *Review of Scientific Instruments.* 2018, **89**(2), p.024101.

47. Atkinson, R., Baulch, D.L., Cox, R.A., Crowley, J.N., Hampson, R.F., Hynes, R.G., Jenkin, M.E., Rossi, M.J., Troe, J. and Wallington, T.J. Evaluated kinetic and photochemical data for atmospheric chemistry: Volume IV – gas phase reactions of organic halogen species. *Atmos. Chem. Phys.* 2008, **8**(15), pp.4141-4496.

48. Harwood, M.H., Burkholder, J.B., Hunter, M., Fox, R.W. and Ravishankara, A.R. Absorption Cross Sections and Self-Reaction Kinetics of the IO Radical. *The Journal of Physical Chemistry A.* 1997, **101**(5), pp.853-863.

49. S.P. Sander, J.A., J.R. Burkholder. R.R. Freidl, D.M. Golden, R.E. Huie, C.E. Kolb, M.J. Kurylo, G.K. Moortgat, V.L. Orkin, P.H. Wine. Chemical Kinetics and Photochemical Data for Use in Atmospheric Studies, Evaluation Number 17. *Jet Propulsion Laboratory publication 10-6.* 2011.

50. Howes, N.U.M., Mir, Z.S., Blitz, M.A., Hardman, S., Lewis, T.R., Stone, D. and Seakins, P.W. Kinetic studies of C1 and C2 Criegee intermediates with SO_2 using laser flash photolysis coupled with photoionization mass spectrometry and time resolved UV absorption spectroscopy. *Physical Chemistry Chemical Physics.* 2018, **20**(34), pp.22218-22227.

51. Smith, M.C., Chang, C.-H., Chao, W., Lin, L.-C., Takahashi, K., Boering, K.A. and Lin, J.J.-M. Strong Negative Temperature Dependence of the Simplest Criegee Intermediate CH_2OO Reaction with Water Dimer. *The Journal of Physical Chemistry Letters.* 2015, **6**(14), pp.2708-2713.

Chapter 4

Kinetics of the Reaction of CH_2OO with SO_2 as a Function of Temperature

Direct studies, made possible as a result of developments in photolytic Criegee sources for laboratory studies, have revealed significantly faster kinetics for the reaction of CH_2OO with SO_2 than have been indicated by previous indirect studies,[1, 2] suggesting a potentially important role for Criegee intermediates in the atmospheric oxidation of SO_2. This chapter provides an overview of previous direct studies of the kinetics of CH_2OO and SO_2, as well as studies to investigate the products of the reaction and outlines the areas in which uncertainties remain. Results are provided for a study of the temperature dependence of the reaction between CH_2OO and SO_2, which are required in order to determine the competition between CH_2OO and SO_2 and other atmospherically important reactions.

The results shown throughout this chapter formed part of a larger study to investigate the temperature dependence of the reaction of $CH_2OO + SO_2$ and have been published in *Physical Chemistry Chemical Physics*: Onel, L., Lade, R., Mortiboy, J., Blitz, M.A., Seakins, P.W., Heard, D.E. and Stone, D. Kinetics of the gas phase reaction of the Criegee intermediate CH_2OO with SO_2 as a function of temperature. *Physical Chemistry Chemical Physics.* 2021, **23**(35), pp.19415-19423.[3]

4.1 Previous Direct Studies

Welz *et al.*[4] performed the first direct study of the kinetics of the reaction between CH_2OO and SO_2 (R4.1) using the photolysis of CH_2I_2/O_2 coupled with PIMS at 298 K and a total pressure of 4 Torr in He.

$$CH_2OO + SO_2 \rightarrow HCHO + SO_3 \qquad (R4.1)$$

Welz *et al.*[4] reported a rate coefficient for R4.1 of $k_{4.1} = (3.9 \pm 0.7) \times 10^{-11}$ cm^3 molecule^{-1} s^{-1}, a value which is significantly larger than the upper limit reported by Johnson *et al.* (4×10^{-15} cm^3 molecule^{-1} s^{-1}, based on measurements of OH yields from the ozonolysis reactions in the presence of SO_2).[1] Welz *et al.* identified that, if the rate coefficients for the reactions of larger Criegee intermediates, such as acetaldehyde oxide (CH_3CHOO), with SO_2 were of similar magnitude, these reactions could be just as important in the oxidation of SO_2 as that involving OH,[4] which has been discussed in more detail in Chapter 1. Since Welz *et al.* demonstrated that Criegee intermediates could be produced in sufficiently high concentrations and in relative isolation under controlled conditions in the laboratory using the photolysis of

CH_2I_2/O_2, many direct experimental measurements of the reactions of Criegee intermediates with SO_2 have been conducted using a range of different detection techniques.

Sheps *et al.*[5] utilised broadband UV absorption spectroscopy to investigate both the CH_2OO UV absorption spectrum and the kinetics of $CH_2OO + SO_2$, and reported a rate coefficient of $k_{4.1} = (4.1 \pm 0.3) \times 10^{-11}$ cm^3 molecule^{-1} s^{-1} at 295 K and pressures between 2.7 and 7.1 Torr, in agreement with the value of $k_{4.1} = (3.9 \pm 0.7) \times 10^{-11}$ cm^3 molecule^{-1} s^{-1} reported by Welz *et al.*[4]

A study carried out by Stone *et al.*[6] investigated the pressure dependence of $CH_2OO + SO_2$ kinetics between 1.5 and 450 Torr at 295 K, using a combination of PIMS to monitor CH_2OO (for the experiments at 1.5 Torr) and laser-induced fluorescence (LIF) spectroscopy to monitor the HCHO product of the reaction (for experiments between 50 and 450 Torr). For the PIMS experiments, CH_2OO was photo-ionised using vacuum ultraviolet radiation at a wavelength of 118 nm generated by frequency tripling the 355 nm output from the third harmonic of an Nd:YAG laser, in contrast to the PIMS experiments reported by Welz *et al.*[4] which used a tuneable synchrotron VUV source. Stone *et al.* monitored the CH_2OO ion signal at different time delays following the photolysis of CH_2I_2, with results giving a rate coefficient of $k_{4.1} = (3.6 \pm 0.5) \times 10^{-11}$ cm^3 molecule^{-1} s^{-1}. The HCHO LIF experiments between 50 and 450 Torr gave an average rate coefficient of $k_{4.1} = (3.40 \pm 0.40) \times 10^{-11}$ cm^3 molecule^{-1} s^{-1}, with the combined average of the PIMS and LIF experiments giving $k_{4.1} = (3.42 \pm 0.42) \times 10^{-11}$ cm^3 molecule^{-1} s^{-1}, agreeing with the rate coefficient reported by Welz *et al.*[4] and indicating that there is no significant pressure dependence in the kinetics of $CH_2OO + SO_2$ under atmospheric conditions.

LIF experiments to measure the kinetics of $CH_2OO + SO_2$ have also been performed by Liu *et al.*[7] at 295 K and pressures between 50 and 200 Torr, using observations of the hydroxyl radical (λ = 308 nm). Liu *et al.* observed the formation of OH through two different processes, separated by their time dependence. They reported an initial rapid formation of OH, which was attributed to high energy CH_2I^* radicals reacting with O_2 to directly produce OH (R4.2) and a slower formation of OH which was attributed to the decomposition of CH_2OO (R4.3).

$$CH_2I^* + O_2 \rightarrow OH + HCO + I \qquad \text{(R4.2)}$$

$$CH_2OO + M \rightarrow OH + \text{Products} \qquad \text{(R4.3)}$$

An example plot showing the formation and loss of OH signal in experiments conducted by Liu *et al.* is shown in Figure 4.1. Liu *et al.* suggest that, if CH_2OO were to retain the excess energy of CH_2I^*, it is possible that the decomposition of CH_2OO may result in the production of OH + HCO, a process which has a reaction barrier ~ 40 kJ mol^{-1} higher than its

decomposition to dioxirane.[8] Rate coefficients were obtained by introducing reactants known to react with CH_2OO, such as SO_2, which will increase the decay rate of the OH signal. Liu *et al.* reported a rate coefficient for R4.1 of $k_{4.1} = (3.53 \pm 0.29) \times 10^{-11}$ cm^3 molecule^{-1} s^{-1},[7] which is in agreement with the values obtained in previous work.[4, 6] The measurements by Liu *et al.* also indicated that there were no effects of pressure on the kinetics, in agreement with the pressure independent results of Stone *et al.*[6]

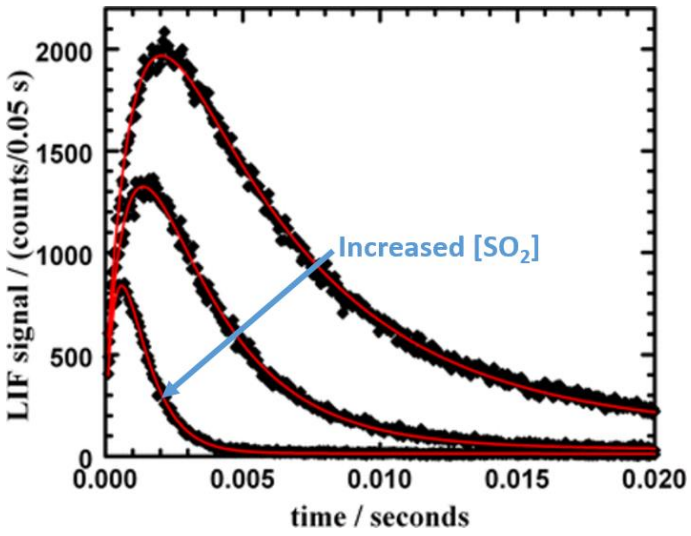

Figure 4.1. Laser-induced fluorescence signals for OH, outlining an initial fast production of OH followed by a slower production. The three traces represent an increase in co-reagent concentration, and outline how the OH signal decreases as the concentration is increased. Adapted from reference 7.[7]

Cavity ring-down spectroscopy (CRDS) has been used by Chhantyal-Pun *et al.*[9] to investigate the kinetics of the reaction between CH_2OO and SO_2 at 293 K and low pressure conditions between 7 and 30 Torr. Photolysis of $CH_2I_2/N_2/O_2$ gas mixtures was used to initiate the chemistry, followed by the use of CRDS to probe temporal profiles of the Criegee intermediate signal at 355 nm.[9] Chhantyal-Pun *et al.* identified the importance of considering the CH_2OO self-reaction to obtain accurate rate coefficients for the reaction between CH_2OO and SO_2 at low concentrations of SO_2. Chhantyal-Pun *et al.* suggested that the decay of CH_2OO in the presence of SO_2 includes contributions from both first- and second-order loss processes, where the first-order loss processes were related to the pseudo-first-order reaction between CH_2OO and SO_2 (R4.1), where the concentration of SO_2 is in excess of the concentration of CH_2OO, as well as CH_2OO losses as a result of diffusion within the reaction cell. The second-order loss mechanisms resulted from the bimolecular reactions of CH_2OO, including the reaction between CH_2OO and I atoms (R4.4) as well as the contribution from the rapid CH_2OO self-

reaction (R4.5). Under high concentrations of SO_2 ($2.0 – 21.6 \times 10^{13}$ molecule cm^{-3}) Chhantyal-Pun *et al.* reported a pressure independent rate coefficient of $k_{4.1} = (3.80 \pm 0.04) \times 10^{-11}$ cm^3 $molecule^{-1}$ s^{-1} for the reaction of CH_2OO and SO_2, which is in agreement with the previously reported values.

$CH_2OO + I \rightarrow$ Products (R4.4)

$CH_2OO + CH_2OO \rightarrow 2\ HCHO + O_2$ (R4.5)

Chhantyal-Pun *et al.*[9] reported that, at low SO_2 concentrations ($1.08 – 6.48 \times 10^{12}$ molecule cm^{-3}), where the loss of CH_2OO is described by mixed first- and second-order kinetics, an enhanced removal of CH_2OO was observed compared to the expected removal based on the rate coefficient obtained at higher SO_2 concentrations ($(3.80 \pm 0.04) \times 10^{-11}$ cm^3 $molecule^{-1}$ s^{-1}) and the CH_2OO self-reaction (R4.5). A rate coefficient of $k_{4.1} = (7.46 \pm 0.29) \times 10^{-11}$ cm^3 $molecule^{-1}$ s^{-1} was reported for experiments carried out under low SO_2 concentrations, suggesting a different reaction mechanism may be contributing at lower concentrations of SO_2. Chhantyal-Pun *et al.* suggested a mechanism by which isomerisation or intersystem crossing (ISC) of the CH_2OO is catalysed by the addition of lower concentrations of SO_2, which is in competition with the formation of $HCHO + SO_3$ (R4.1). The group concluded that the bimolecular rate coefficient obtained at higher SO_2 concentrations can be attributed to the reaction between CH_2OO and SO_2, but the loss processes shown by the intercept of the bimolecular plot includes contributions from an unidentified intermediate isomer whose formation is likely to occur at lower SO_2 concentrations.

In subsequent experiments, Howes *et al.*[10] employed both PIMS and time-resolved broadband UV absorption spectroscopy techniques to investigate the kinetics of the reaction between CH_2OO and SO_2 for different SO_2 concentration ranges to investigate the effects reported by Chhantyal-Pun *et al.*[9] The chemistry was initiated using LFP of $CH_2I_2/N_2/O_2/SO_2$ gas mixtures, with the concentration of SO_2 maintained high enough to ensure pseudo-first-order conditions. Both sets of data were analysed using the first-order rate equation (given in Chapter 3) and gave bimolecular rate coefficients of $k_{4.1} = (3.87 \pm 0.22) \times 10^{-11}$ cm^3 $molecule^{-1}$ s^{-1} for the time-resolved broadband UV absorption experiments and $k_{4.1} = (3.73 \pm 0.13) \times 10^{-11}$ cm^3 $molecule^{-1}$ s^{-1} for the PIMS experiments.

As the concentration of sulfur dioxide in the atmosphere is similar to the concentrations used in the low SO_2 region of the study from Chhantyal-Pun *et al.*, Howes *et al.*[10] conducted PIMS experiments at low concentrations of SO_2 ($0.5 - 7.5 \times 10^{13}$ molecule cm^{-3}) to investigate the formation of an intermediate product through isomerisation or ISC. Howes *et al.* reported a bimolecular rate coefficient of $k_{4.1} = (3.73 \pm 0.13) \times 10^{-11}$ cm^3 $molecule^{-1}$ s^{-1}, which is in good

agreement with that of previous literature and report no variation in the rate coefficient with SO_2 concentration. Howes *et al.*[10] reported a mean pressure independent value for R4.1 of $k_{4.1} = (3.76 \pm 0.14) \times 10^{-11}$ cm^3 molecule^{-1} s^{-1} at 295 K.

To reconcile the difference in the rate coefficients obtained for the low and high SO_2 regimes reported by Chhantyal-Pun *et al.*,[9] Howes *et al.*[10] used a model to simulate variations in the CH_2OO decay as a function of SO_2 concentration using the data reported by Chhantyal-Pun *et al.*[9] Table 4.1 below summarises the reactions and the rate coefficients used in the model by Howes *et al.*[10] All rate coefficients used were obtained from the report by Chhantyal-Pun *et al.*, except for the CH_2OO self-reaction where the IUPAC recommended value was used.[11]

Reaction	Rate coefficient
$CH_2I + O_2 \rightarrow CH_2OO + I$	1.82×10^{-12} cm^3 molecule^{-1} s^{-1}
$CH_2OO + CH_2OO \rightarrow 2HCHO + O_2$	$(7.35 \pm 0.63) \times 10^{-11}$ cm^3 molecule^{-1} s^{-1}
$CH_2OO + I \rightarrow$ Products	1.00×10^{-11} cm^3 molecule^{-1} s^{-1}
$CH_2OO + SO_2 \rightarrow$ Products	$(7.46 \pm 0.29) \times 10^{-11}$ cm^3 molecule^{-1} s^{-1}
	$(3.80 \pm 0.04) \times 10^{-11}$ cm^3 molecule^{-1} s^{-1}
$CH_2OO \rightarrow$ Products	11.6 ± 8 s^{-1}

Table 4.1. Summary of the reactions and rate coefficients used by Howes *et al.*[10] to simulate the data of Chhantyal-Pun *et al.* All rate coefficients were obtained from the report of Chhantyal-Pun *et al.*[9] except for the reaction between CH_2I and O_2, which was taken from Sheps *et al.*[5] The rate coefficient for $CH_2OO + I$ is an upper limited estimated by Chhantyal-Pun *et al.* and no error value was provided.

Howes *et al.*[10] ran the model with no SO_2 and then with an SO_2 concentration of 1×10^{12} molecule cm^{-3} and found that the concentration of CH_2OO changed by less than 7 % upon the addition of SO_2, and only exceeds a change of ~ 15 % at longer times, where most of the initial CH_2OO has been consumed and the loss is dominated by secondary chemistry. The CH_2OO decay was then simulated for the two rate coefficients for $CH_2OO + SO_2$ reported by Chhantyal-Pun *et al.* [9] ($(7.46 \pm 0.29) \times 10^{-11}$ cm^3 molecule^{-1} s^{-1} and $(3.80 \pm 0.04) \times 10^{-11}$ cm^3 molecule^{-1} s^{-1}) with the concentration of SO_2 varied within a range that covered $1 - 5 \times 10^{12}$ molecule cm^{-3}. Howes *et al.*[10] reported that the simulation suggested that pseudo-first-order conditions were maintained down to an SO_2 concentration of 4.5×10^{12} molecule cm^{-3} and that the change in the concentration of CH_2OO observed as a result of the reaction between $CH_2OO + SO_2$ was relatively small for the majority of the decay and so the loss of CH_2OO at low SO_2 concentrations can be attributed to the Criegee self-reaction (R4.5) and under these conditions, the study is insensitive to the reaction taking place between CH_2OO and SO_2.[10]

Liu *et al.*[12] also performed experiments at relatively low concentrations of SO_2 ($0.5 – 2.5 \times 10^{13}$ molecule cm^{-3}) at 300 K and a total pressure of 10 Torr, using measurements of OH to determine CH_2OO kinetics, similar to the previous study by Liu *et al.*[7] The reduction in the OH signal with increasing SO_2 concentration was attributed to R4.1 as well as other first-order loss processes that occur within the system, such as diffusion and unimolecular decomposition. The data were fit using a rate equation that accounted for both the first- and second-order loss processes of CH_2OO following from the report of Chhantyal-Pun *et al.*[9] that suggested second-order processes should be accounted for within the analysis. A value of $k_{4.1} = (3.88 \pm 0.13) \times 10^{-11}$ cm^3 $molecule^{-1}$ s^{-1} for the bimolecular rate coefficient was reported, which agrees with the previous literature. In contrast to the report from Chhantyal-Pun *et al.*,[9] Liu *et al.* found no evidence to support the theory of a competing isomerisation or ISC reaction at low concentrations of SO_2.

More recently, Qiu and Tonokura[13] reported the detection of CH_2OO with a mid-infrared continuous-wave quantum cascade laser (cw-QCL) coupled with LFP, to investigate the reaction between CH_2OO and SO_2. The group first measured the infrared absorption spectrum of CH_2OO in the region $\nu = 1273.0 – 1277.5$ cm^{-1} which was in agreement with a simulated spectra also reported within the same study. Qiu and Tonokura[13] then measured the rate coefficient for the reaction between CH_2OO by monitoring the concentration of CH_2OO as a function of time upon the addition of varying concentrations of SO_2 ($0.4 – 4.2 \times 10^{14}$ molecule cm^{-3}) and obtained a rate coefficient of $k_{4.1} = (3.6 \pm 0.1) \times 10^{-11}$ cm^3 $molecule^{-1}$ s^{-1} at 295 K and 10.4 Torr, which is in good agreement with previous literature. A summary of previous results is given in Table 4.2.

	Technique	Photolysis λ / nm	T / K	p / Torr	$[CH_2I_2]$ / molecule cm^{-3}	$[SO_2]$ / 10^{13} molecule cm^{-3}	$k_{4.1}$ / 10^{-11} cm^3 $molecule^{-1}$ s^{-1}
Welz *et al.*[4]	LFP / PIMS	248	298	4	5.7×10^{12}	0.4 – 4.5	(3.9 ± 0.7)
Sheps *et al.*[5]	LFP / UV absorption	266	295	2.7 – 7.1		0.5 – 3.0	(4.1 ± 0.3)
Liu *et al.*[7]	LFP / LIF OH	351	295	50 – 200	3.85×10^{14}	0.1 – 0.9	(3.53 ± 0.29)
Stone *et al.*[6]	LFP / LIF HCHO	355	295	50 – 450		20 – 120	(3.42 ± 0.42)
Chhantyal-Pun *et al.*[9]	LFP / CRDS	355	293	30		2 – 12	(3.80 ± 0.04)
Liu *et al.*[12]	LFP / LIF OH	355	300	10	6.32×10^{14}	0.5 – 2.5	(3.88 ± 0.13)
Howes *et al.*[10]	LFP / PIMS	248	295	2	1×10^{13}	0.5 – 17	(3.74 ± 0.43)
	LFP / UV absorption	248	295	50		0.1 – 1.1	(3.87 ± 0.45)
Qiu and Tonokura.[13]	LFP / IR absorption	266	295	10.4	$1\text{-}10 \times 10^{14}$	4.2 – 42.0	(3.6 ± 0.1)

Table 4.2. Values for the rate coefficient for $CH_2OO + SO_2$ determined in previous experiments, utilising a range of techniques. LFP = laser flash photolysis, PIMS = photo-ionisation mass spectrometry, LIF = laser-induced fluorescence and CRDS = cavity ring-down spectroscopy.

4.2 Product Studies

The products of R4.1 have been investigated in a number of studies. Theoretical studies have predicted the production of HCHO + SO_3,[14, 15] with the LIF measurements by Stone *et al.*[6] confirming the production of HCHO in ~ 100 % yield. The co-production of SO_3 has been demonstrated by Wang *et al.*[16] using infrared (IR) absorption spectroscopy to identify that the formation of SO_3 from the reaction between CH_2OO and SO_2 is the dominant product channel. A step-scan Fourier Transform IR spectrometer was coupled to a multi-pass absorption cell to record the evolution of the IR spectra during the reaction. Figure 4.2 shows the observed IR spectra obtained following the photolysis of a $CH_2I_2/N_2/O_2/SO_2$ gas mixture at 308 nm.

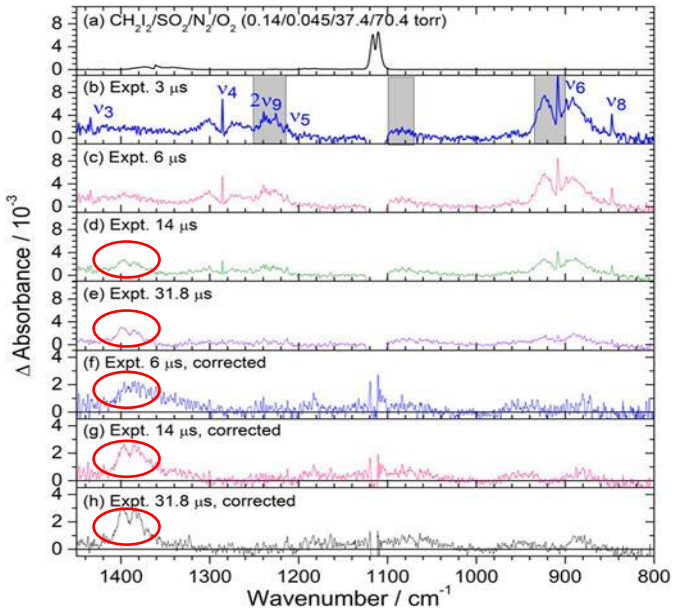

Figure 4.2. IR absorption spectra obtained upon the photolysis of a $CH_2I_2/N_2/O_2/SO_2$ mixture. Adapted from reference 16.[16] The red circles show the absorption band at ν = 1391.5 cm^{-1} which correspond to the stretching mode of SO_3.

The spectra show an intense absorption band at ν = ~ 1114 cm^{-1} corresponding to CH_2I_2 as well as a weaker band at ν = 1361 cm^{-1} corresponding to SO_2. The SO_2 absorption peak is much weaker as the concentration of SO_2 used throughout the experiments remained low enough to ensure SO_3 could be identified with little interference from SO_2. Figure (4.2b) indicates the initial formation of bands at ν = 1435, 1286, 1234, 1213, 908 and 848 cm^{-1}, owing to the formation of CH_2OO as well as weaker bands at ν = 1234, 1224, 1087 and 923 cm^{-1} owing to the formation of CH_2IOO. The CH_2IOO bands are represented as grey areas on the spectra as they overlap with both the CH_2I_2 and CH_2OO bands. The disappearance of the CH_2OO bands was accompanied by the formation of an intense band at ν = 1391.5 cm^{-1} that increased as the reaction progresses, as seen in Figure 4.2c-e. Figures 4.2f-h show the spectra after the CH_2OO and HCHO bands were removed and the CH_2I_2 band had been added, the

band at 1391.5 cm^{-1} is illustrated to be the most prominent band and is associated with the stretching-mode of SO_3.

The band at ν =1391.5 cm^{-1} agrees well with the literature,[17] but to further confirm that this corresponds to SO_3, Wang *et al.*[16] compared the observed spectra with the line spectrum of the stretching mode of SO_3 compiled in the HITRAN database[18] and were able to conclude that the dominant product of the reaction between CH_2OO and SO_2 is SO_3 as shown by the absorption band at ν = 1391.5 cm^{-1}.

More recently, the kinetics of the production of SO_3 from R4.1 were investigated by Mir *et al.*[19] using mid-infrared quantum cascade laser (QCL) absorption spectroscopy at a wavenumber of ~ 1390 cm^{-1}. The absorbance of SO_3 obtained in these experiments was well described by a pseudo-first-order growth combined with a first-order loss. A bimolecular rate coefficient of $k_{4.1}$ = (3.55 ± 0.35) × 10^{-11} cm^3 $molecule^{-1}$ s^{-1} was obtained for R4.1 at 50 Torr from a plot of the pseudo-first-order growth of SO_3 as a function of SO_2 concentration, in excellent agreement with rate coefficients obtained by directly monitoring the loss of CH_2OO (described above), providing further evidence for the direct production of SO_3 from R4.1.

The room temperature kinetics of the reaction between CH_2OO and SO_2 have now been well established with a rate coefficient of $k_{4.1} = \left(3.7^{+0.45}_{-0.40}\right) \times 10^{-11}$ cm^3 $molecule^{-1}$ s^{-1} as the current IUPAC recommendation at 298 K[11] and has been shown to be independent of pressure. However, there has been no previous study into the temperature dependence of this reaction, which is required to gain a complete understanding of its atmospheric implications.

The major competitor for this reaction is that of Criegee intermediates with water dimers due to large concentrations of water vapour in the atmosphere. Understanding how the reaction with SO_2 changes with temperature will allow the major reaction route to be determined for areas of both low and high humidity.

The remainder of this chapter will summarise the results of the investigation of the kinetics of CH_2OO with SO_2 as a function of temperature.

4.3 Experimental

The kinetics of R4.1 were measured at 85 Torr and temperatures between 298 and 340 K using the experimental set-up described in Chapter 3, where reactions R4.1, R4.4, R4.5 and R4.7 – R4.9 were initiated within the reaction cell using LFP and the concentration of CH_2OO monitored using time-resolved broadband ultraviolet absorption spectroscopy.

$CH_2I_2 + h\nu$ (λ = 248 nm) → $CH_2I + I$ (R4.6)

$CH_2I + O_2 \rightarrow CH_2IOO^*$ (R4.7)

$CH_2IOO^* \rightarrow CH_2OO + I$ (R4.8a)

$CH_2IOO^* + M \rightarrow CH_2IO_2 + M$ (R4.8b)

$CH_2OO + SO_2 \rightarrow HCHO + SO_3$ (R4.1)

$CH_2OO + I \rightarrow$ Products (R4.4)

$CH_2OO + CH_2OO \rightarrow 2HCHO + O_2$ (R4.5)

$CH_2OO \rightarrow$ Products (R4.9)

Experiments were carried out under pseudo-first-order conditions with SO_2 in excess over CH_2OO. Typical initial concentrations used for these experiments were as follows: $[SO_2] = (0.7 – 5) \times 10^{13}$ molecule cm^{-3}, $[CH_2I_2] = (1.0 - 8.0) \times 10^{13}$ molecule cm^{-3} and $[O_2] = 3.0 \times 10^{17}$ molecule cm^{-3}. The total flow rate remained at 2000 standard cm^3 per minute (sccm) for a residence time within the cell of ~ 3 s. The pulse repetition rate was fixed at 0.33 Hz to ensure a fresh gas mixture entered the reaction cell after each laser pulse, to avoid any unwanted secondary chemistry, with intensity data typically averaged over 300 laser shots. The effective pathlength for these experiments was (471 ± 50) cm. More details of the experimental procedure are given in Chapter 3.

The measurements presented throughout this chapter at temperatures between 298 and 340 K were carried out as part of this thesis, and formed part of a larger study to investigate the temperature dependence of R4.1 between 223 and 344 K at 85 Torr. Results for measurements made at 223-296 K, 316 K and 344 K were carried out by Dr Lavinia Onel and are also shown within this chapter. The experiments by Dr Onel were conducted under similar experimental conditions to those described above, with: $[SO_2] = (0.6 – 5.6) \times 10^{13}$ molecule cm^{-3}, $[CH_2I_2] = (1.0 – 7.4) \times 10^{13}$ molecule cm^{-3} and $[O_2] = 7.5 \times 10^{17}$ molecule cm^{-3}. A more detailed description regarding the experimental conditions used for measurements made by Dr Onel can be found in reference 3.[3]

4.4 Results and Discussion

As described in Chapter 3, the absorbance in the wavelength region of interest (290 – 450 nm for these experiments) contains contributions from CH_2OO, CH_2I_2 and IO. Concentrations for each species were determined from a least squares fit of reference absorption cross-sections to the total observed absorbance at each time point (more details given in Chapter 3). Figure 4.3 shows the typical absorbance measured following the photolysis of CH_2I_2 and concentration – time profiles for CH_2I_2, CH_2OO and IO are shown in Figures 4.4 – 4.6.

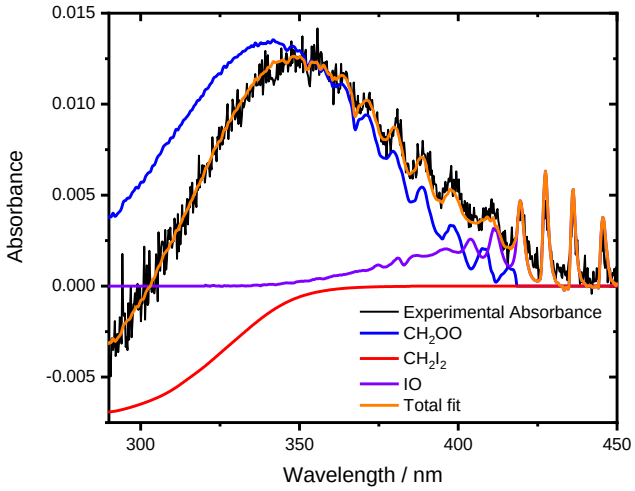

Figure 4.3. Typical absorbance measured following the photolysis of CH_2I_2, where the black line represents the observed absorbance, the blue is the CH_2OO reference spectra,[20] red is CH_2I_2,[21] purple is IO[22] and orange is the overall fit. Experiments were conducted at 298 K and 85 Torr, with $[CH_2I_2]_0 = 4.6 \times 10^{13}$ molecule cm^{-3} and $[SO_2] = 0$.

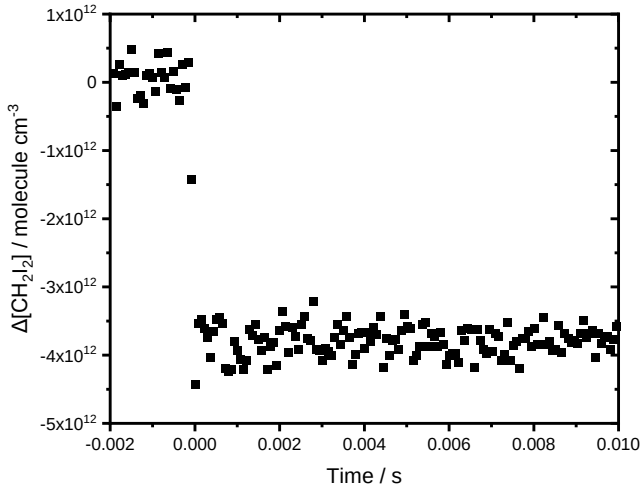

Figure 4.4. Concentration-time profile for CH_2I_2 for an experiment at 85 Torr and 298 K. For these data, $[SO_2] = 0$, $[CH_2I_2]_0 = 4.6 \times 10^{13}$ molecule cm^{-3} and $\Delta[CH_2I_2] = -3.7 \times 10^{12}$ molecule cm^{-3}.

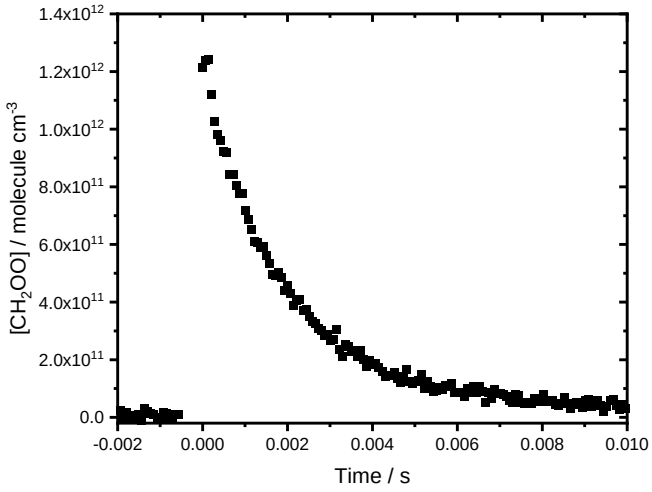

Figure 4.5. Concentration-time profile for CH_2OO for an experiment at 85 Torr and 298 K. For these data, $[SO_2] = 0$, $[CH_2I_2]_0 = 4.6 \times 10^{13}$ molecule cm^{-3}.

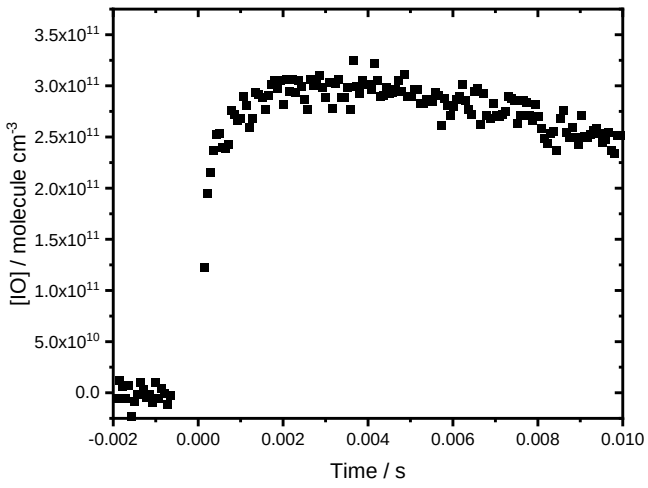

Figure 4.6. Concentration-time profile for IO for an experiment at 85 Torr and 298 K. For these data, $[SO_2] = 0$ and $[CH_2I_2]_0 = 4.6 \times 10^{13}$ molecule cm^{-3}.

As experiments were conducted under pseudo-first-order conditions with SO_2 present in excess, the change in the concentration of CH_2OO can be described using Equation 4.1.

$$[CH_2OO]_t = [CH_2OO]_0 \times \left(exp^{-k' \times t}\right) \quad \text{(Equation 4.1)}$$

where $[CH_2OO]_t$ is the concentration of CH_2OO at time t, $[CH_2OO]_0$ is the initial Criegee intermediate concentration and k' is the observed rate coefficient, which incorporates the rate coefficient for the Criegee intermediate decay when there is no SO_2 in the system (k_x, R4.4, R4.5 and R4.9) and the pseudo-first-order rate coefficient for the reaction between the Criegee intermediate and SO_2 ($k'_{4.1} = k_{4.1}[SO_2]$), i.e. $k' = k_x + k'_{4.1}$.

The data were fit with Equation 4.1 convoluted with an instrument response function (IRF) to account for the simultaneous illumination of multiple rows on the CCD followed by row-by row shifting (further details regarding the IRF are provided in Chapter 3).

The potential for the contribution of second-order behaviour was also investigated, where the decay of CH_2OO is described by a mixed first- and second-order model (further details given in Chapter 3).

Figures 4.7 and 4.8 compare fitting typical concentration-time profiles for CH_2OO with the first-order model and the mixed first- and second-order model.

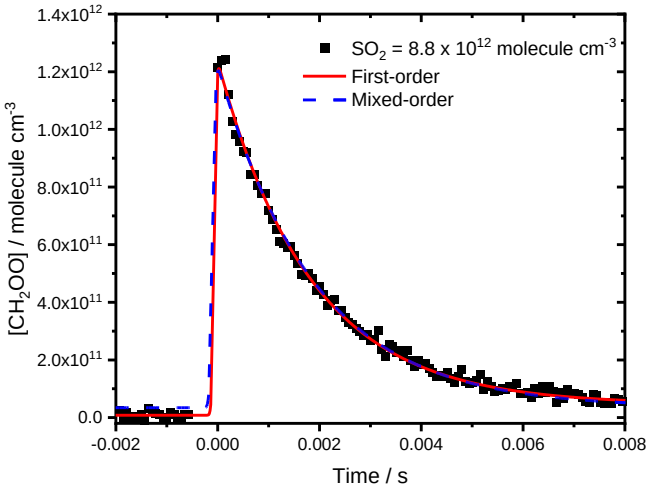

Figure 4.7. Comparison between a first-order fit (red) and mixed-order fit (blue) for data at 298 K and 85 Torr. The first-order fit gave: k' = (551 ± 6) s^{-1}, $[CH_2OO]_0$ = (1.24 ± 0.12) × 10^{12} molecule cm^{-3}, t_c = - (6.7 ± 0.3) × 10^{-5} s and w = (3.7 ± 0.2) × 10^{-5} s. The mixed-order fit gave: k' = (529 ± 8) s^{-1}, k'' = (7.46 ± 0.10) × 10^{-11} cm^3 $molecule^{-1}$ s^{-1}, $[CH_2OO]_0$ = (1.30 ± 0.22) × 10^{12} molecule cm^{-3}, t_c = -(7.1 ± 0.7) × 10^{-5} s and w = (3.9 ± 0.4) × 10^{-5} s. Uncertainties are 1σ.

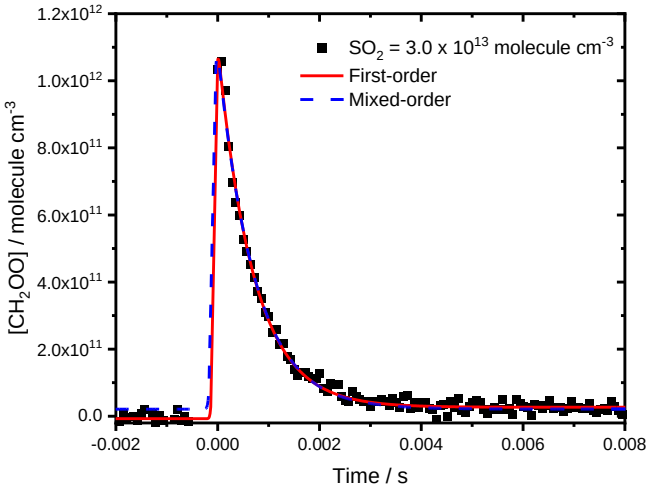

Figure 4.8. Comparison between a first-order fit (red) and mixed-order fit (blue) for data at 298 K and 85 Torr. The first-order fit gave: k' = (1425 ± 23) s^{-1}, $[CH_2OO]_0$ = (1.18 ± 0.45) × 10^{12} molecule cm^{-3}, t_c = -(6.7 ± 0.3) × 10^{-5} s and w = (3.7 ± 0.2) × 10^{-5} s. The mixed-order fit gave: k' = (1385 ± 33) s^{-1}, k'' = (7.46 ± 0.10) × 10^{-11} cm^3 $molecule^{-1}$ s^{-1}, $[CH_2OO]_0$ = (1.15 ± 0.22) × 10^{12} molecule cm^{-3}, t_c = -(7.1 ± 0.7) × 10^{-5} s and w = (3.9 ± 0.4) × 10^{-5} s. Uncertainties are 1σ.

Figure 4.9 shows an example of results obtained for the pseudo-first-order losses of CH_2OO obtained from the fits to the first-order and mixed first- and second-order models, with results showing that the data are well described by pseudo-first-order kinetics.

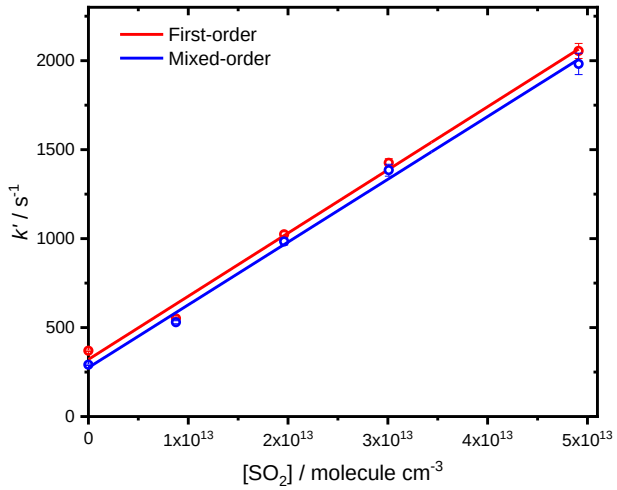

Figure 4.9. Dependence of k' on $[SO_2]$ at 298 K and 85 Torr obtained for a first-order fit (red line) and a mixed-order fit (blue line). The first-order fit gave: $k_{4.1} = (3.55 \pm 0.15) \times 10^{-11}$ cm^3 molecule^{-1} s^{-1} with an intercept of $k_x = (321 \pm 42)$ s^{-1}. The mixed-order fit gave: $k_{4.1} = (3.53 \pm 0.12) \times 10^{-11}$ cm^3 molecule^{-1} s^{-1} with an intercept of $k_x = (275 \pm 33)$ s^{-1}. Uncertainties are 1σ.

Figure 4.10 shows concentration-time profiles for CH_2OO, fit with Equation 4.1 convoluted with the IRF, where it is evident the decay of CH_2OO becomes more rapid as the concentration of SO_2 is increased.

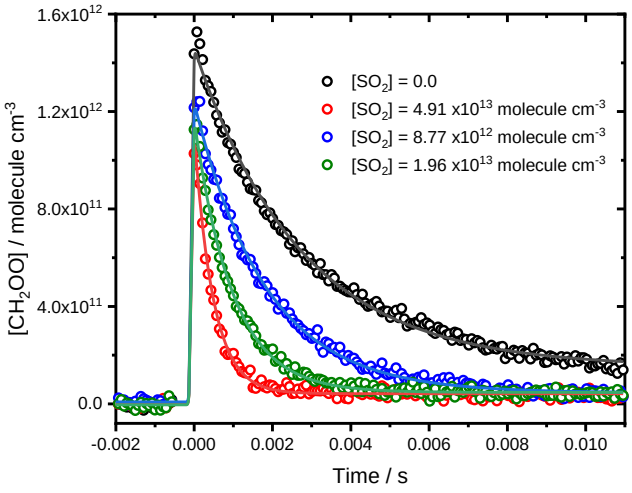

Figure 4.10. Concentration-time profiles showing how the CH_2OO decay changes with increasing $[SO_2]$ at 85 Torr and 298 K. For $[SO_2]$ = 0, the fit gave $[CH_2OO]_0 = 1.44 \times 10^{12}$ molecule cm^{-3} and $k' = (369 \pm 4)$ s^{-1}, for $[SO_2] = 4.91 \times 10^{13}$ molecule cm^{-3}, the fit gave $[CH_2OO]_0 = 1.22 \times 10^{12}$ molecule cm^{-3} and $k' = (2054 \pm 42)$ s^{-1}, for $[SO_2] = 8.77 \times 10^{12}$ molecule cm^{-3}, the fit gave $[CH_2OO]_0 = 1.24 \times 10^{12}$ molecule cm^{-3} and $k' = (551 \pm 6)$ s^{-1} and for $[SO_2] = 1.96 \times 10^{13}$ molecule cm^{-3}, the fit gave $[CH_2OO]_0 = 1.20 \times 10^{12}$ molecule cm^{-3} and $k' = (1024 \pm 14)$ s^{-1}. The IRF parameters were: $t_c = -(6.7 \pm 0.3) \times 10^{-5}$ s and $w = (3.7 \pm 0.2) \times 10^{-5}$ s. Uncertainties are 1σ.

A value for the bimolecular rate coefficient, $k_{4.1}$, was obtained by plotting the pseudo-first-order rate coefficients, obtained from the concentration-time profiles, against the concentration of SO_2. An example bimolecular plot is shown in Figure 4.11, where the gradient is equivalent to $k_{4.1}$ and the intercept describes k_x (the parameter describing other loss processes of the Criegee intermediate, described in Chapter 3).

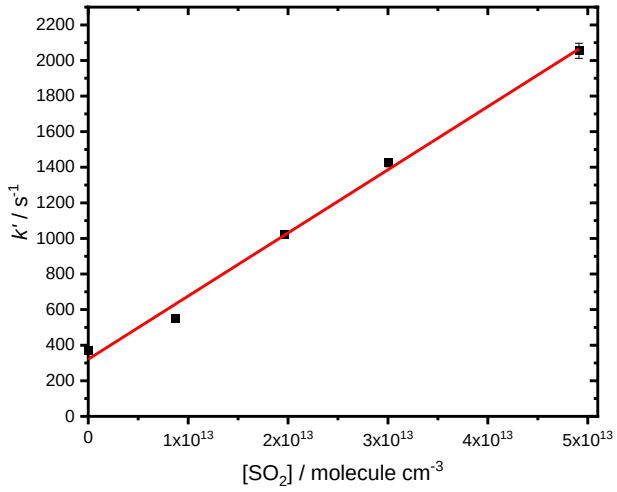

Figure 4.11. Bimolecular plot for the reaction of CH_2OO + SO_2 at 298 K and 85 Torr, where the red line represents an unweighted linear fit to the data. The gradient is equal to $k_{4.1}$ = (3.56 ± 0.11) × 10^{-11} cm^3 $molecule^{-1}$ s^{-1} and the intercept is equal to k_x = (365 ± 42) s^{-1}. The error bars represent the error in the exponential fit to Equation 4.1. Uncertainties are 1σ.

The reaction between CH_2OO and SO_2 was investigated as a function of temperature (324 – 340 K) at 85 Torr, with all other reaction conditions remaining the same as experiments carried out at 298 K. The data were analysed in the same way as described above. Bimolecular plots obtained for experiments at 324 K, 331 K and 340 K are shown in Figures 4.12-4.14, with results summarised in Table 4.3.

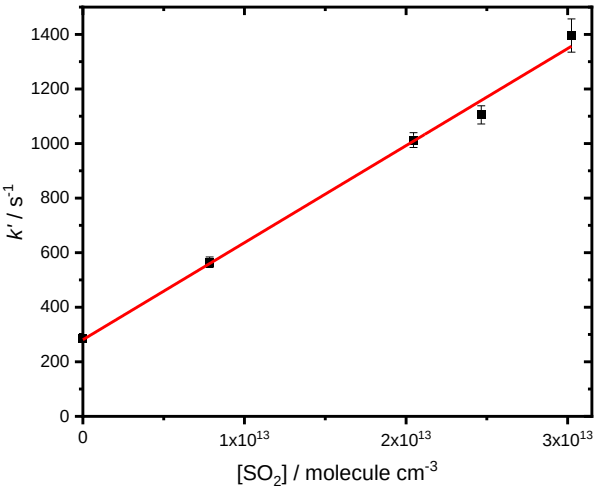

Figure 4.12. Bimolecular plot for the reaction of $CH_2OO + SO_2$ at 324 K and 85 Torr, where the red line represents an unweighted linear fit to the data. The gradient is equal to $k_{4.1} = (3.56 \pm 0.15) \times 10^{-11}$ cm^3 molecule^{-1} s^{-1} and the intercept is equal to $k_x = (281 \pm 31)$ s^{-1}. The error bars represent the error in the exponential fit to Equation 4.1. Uncertainties are 1σ.

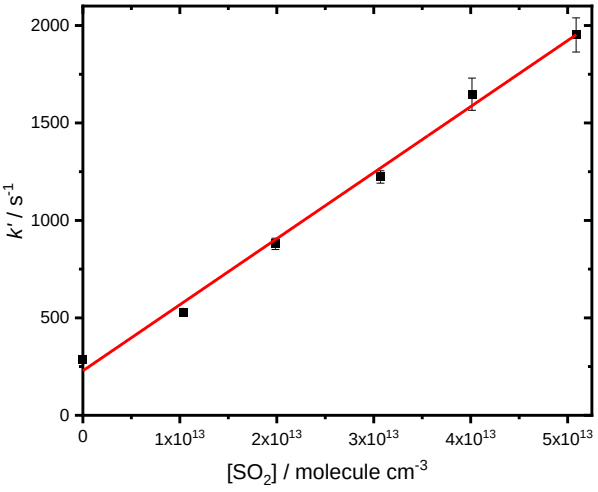

Figure 4.13. Bimolecular plot for the reaction of $CH_2OO + SO_2$ at 331 K and 85 Torr, where the red line represents an unweighted linear fit to the data. The gradient is equal to $k_{4.1} = (3.39 \pm 0.13) \times 10^{-11}$ cm^3 molecule^{-1} s^{-1} and the intercept is equal to $k_x = (228 \pm 39)$ s^{-1}. The error bars represent the error in the exponential fit to Equation 4.1. Uncertainties are 1σ.

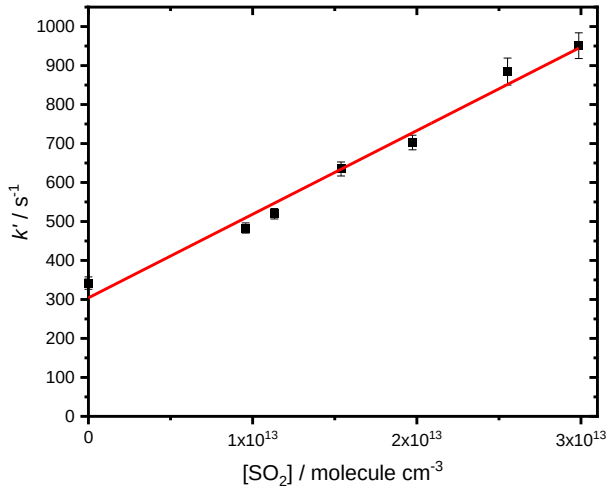

Figure 4.14. Bimolecular plot for the reaction of CH_2OO + SO_2 at 340 K and 85 Torr, where the red line represents an unweighted linear fit to the data. The gradient is equal to $k_{4.1}$ = (2.15 ± 0.12) × 10^{-11} cm^3 $molecule^{-1}$ s^{-1} and the intercept is equal to k_x = (304 ± 23) s^{-1}. The error bars represent the error in the exponential fit to Equation 4.1. Uncertainties are 1σ.

Temperature / K	$k_{4.1}$ / 10^{-11} cm^3 $molecule^{-1}$ s^{-1}
298	3.6 ± 0.1
324	3.6 ± 0.2
331	3.4 ± 0.1
340	2.2 ± 0.1

Table 4.3. Summary table of the rate coefficients obtained in these experiments for R4.1 at temperatures between 298 and 340 K at 85 Torr.

The bimolecular rate coefficient for the reaction between CH_2OO and SO_2 was determined to be $k_{4.1}$ = (3.56 ± 0.11) × 10^{-11} cm^3 $molecule^{-1}$ s^{-1} at 298 K and 85 Torr, which is in agreement with previous reports of the rate coefficient by Welz *et al.*,[4] Stone *et al.*[6] and Howes *et al.*,[10] with results showing the reaction exhibits a negative temperature dependence between 298 K and 340 K.

The values for the rate coefficients for R4.1 at temperatures above 298 K formed part of a larger study to investigate the temperature dependence of R4.1 between 223 and 344 K. Table 4.4 summaries the rate coefficients obtained in the work presented here at temperatures between 298 and 340 K and the work carried out by Dr Lavinia Onel at temperatures of 223-296 K, 316 K and 344 K, all rate coefficients are reported in Onel *et al.*[3]

Temperature / K	$k_{4.1}$ / 10^{-11} cm^3 $molecule^{-1}$ s^{-1}
223[b]	6.4 ± 0.3
259[b]	5.5 ± 0.3
266[b]	4.4 ± 0.3
270[b]	5.3 ± 0.3
275[b]	4.1 ± 0.5
281[b]	4.1 ± 0.1
296[b]	4.0 ± 0.1
298[a]	3.6 ± 0.1
316[b]	4.2 ± 0.1
324[a]	3.6 ± 0.2
331[a]	3.4 ± 0.1
340[a]	2.2 ± 0.1
344[b]	3.3 ± 0.1

Table 4.4. Summary of the rate coefficients / 10^{-11} cm^3 $molecule^{-1}$ s^{-1} for the reaction of CH_2OO and SO_2 for temperatures between 223–344 K at 85 Torr where (a) represents the high temperature data obtained as part of this thesis and (b) represents the measurements by Dr Lavinia Onel.

Results show that the reaction between CH_2OO and SO_2 exhibits a negative temperature dependence between 223 and 344 K. Figure 4.15 compares fitting all of the data with the Arrhenius equation (further details in Chapter 2) and fitting the data using the power law form, AT^n, where A is a constant, T is the temperature and n is an empirical exponent.

Figure 4.15 also shows a comparison between the temperature dependent rate expressions obtained by only fitting to the data obtained by myself at temperatures between 298 and 340 K and fitting to all of the data obtained by myself and Dr. Onel at temperatures between 223 and 344 K (as described in Table 4.4).

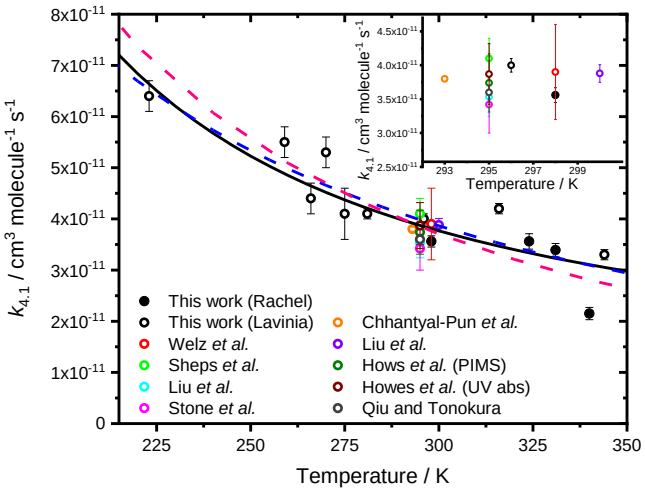

Figure 4.15. A plot of the bimolecular rate coefficients for $CH_2OO + SO_2$ from this work (solid and open black circles) as a function of temperature between 223 and 344 K. The black line represents a fit to the equation $k_{4.1} = (7.85 \pm 1.95) \times 10^{-12} \times exp((476 \pm 68)/T)$ cm^3 molecule^{-1} s^{-1} with $R^2 = 0.80$ and the dashed blue line represents a fit to the equation $k_{4.1} = (3.91 \pm 0.15) \times 10^{-11} \times (T/298)^{-(1.8 \pm 0.2)}$ cm^3 molecule^{-1} s^{-1} with $R^2 = 0.82$. The dashed pink line represents a fit to the data obtained by myself at temperatures between 298 and 340 K and gave: $k_{4.1} = (3.76 \pm 0.63) \times 10^{-11} \times (T/298)^{-(2.2 \pm 1.9)}$ cm^3 molecule^{-1} s^{-1} with $R^2 = 0.40$. Previous literature studies are also shown.[4-7, 9, 10, 12, 13] (PIMS = photo-ionisation mass spectrometry). The inset shows rate coefficients obtained between 293 and 300 K for clarity.

The fit to the data using the Arrhenius equation gave: $k_{4.1} = (7.85 \pm 1.95) \times 10^{-12} \times exp((476 \pm 68)/T)$ cm^3 molecule^{-1} s^{-1} with $R^2 = 0.80$ and the fit using AT^n gave $k_{4.1} = (3.91 \pm 0.15) \times 10^{-11} \times (T/298)^{-(1.8 \pm 0.2)}$ cm^3 molecule^{-1} s^{-1} with $R^2 = 0.82$. As shown in Figure 4.15, there were only minor differences between the two fits to the data however, the fit using AT^n gave an R^2 value closer to 1 and so it was concluded that this was the best description of the data. Fitting only the data obtained by myself between 298 and 340 K using the AT^n expression gave: $k_{4.1} = (3.76 \pm 0.63) \times 10^{-11} \times (T/298)^{-(2.2 \pm 1.9)}$ cm^3 molecule^{-1} s^{-1} with $R^2 = 0.40$. Values for A and n obtained from the fit to only the data between 298 and 340 K are within the error range of the values obtained when fitting to all data points however, the lower R^2 value obtained when fitting only to the data obtained by myself at temperatures between 298 and 340 K suggests that this fit is of poorer quality when compared to fitting to all of the data. This is likely due to the fact that there are only four data points contributing to this fit making it less accurate compared to the fit that includes 13 data points.

The negative temperature dependence is indicative of the barrierless addition of SO_2 to the Criegee intermediate, producing a secondary ozonide (SOZ). The most recent computational

study of R4.1, by Kuwata *et al.*,[15] provided a detailed description of the potential energy surface (PES) for R4.1 and predicted that ~ 90-91 % of the reaction occurs via a closed-shell transition structure to form HCHO + SO_3 with a small contribution (~ 6 - 7 %) from an open-shell mechanism leading to HCHO + SO_3.

Figure 4.16 shows a summary of the initial steps of the reaction mechanism reported by Kuwata *et al.*[15] The reaction proceeds via the formation of a dipole-dipole pre-reaction complex that can exist as either an *endo* or *exo* conformer (Figure 4.16, structure 3a or 3b), which is determined by the position of the oxo-substituent. The mechanism then follows a cycloaddition of the Criegee intermediate 1,3 dipole across the sulfur-oxygen bond, resulting in a cyclic transition state (Figure 4.16, structure TS-4a or TS-4b), which subsequently leads to the formation of a SOZ (Figure 4.16, structure 5a or 5b), which can again exist as either an *endo* (5a) or *exo* (5b) conformer. The SOZ then decomposes to produce HCHO + SO_3.

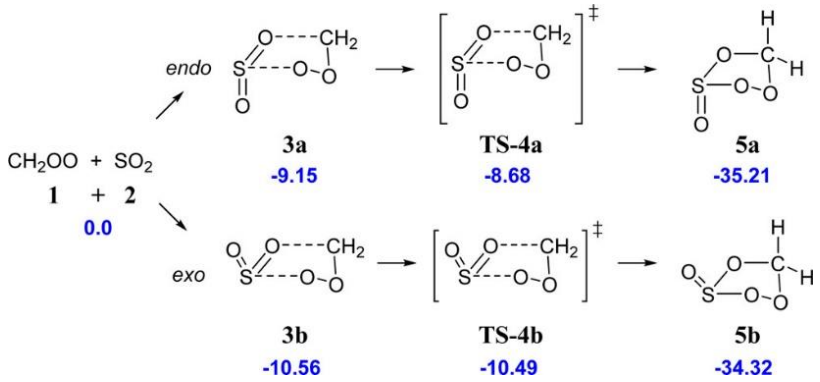

Figure 4.16. Summary of the initial steps of the mechanism for the reaction between CH_2OO and SO_2, reported by Kuwata *et al.* copied from reference 15.[15]

Figure 4.17 shows the PES for R4.1 obtained by reducing the PES determined by Kuwata *et al.* to the closed-shell mechanism, which proceeds through either *endo* or *exo* conformers, described above.

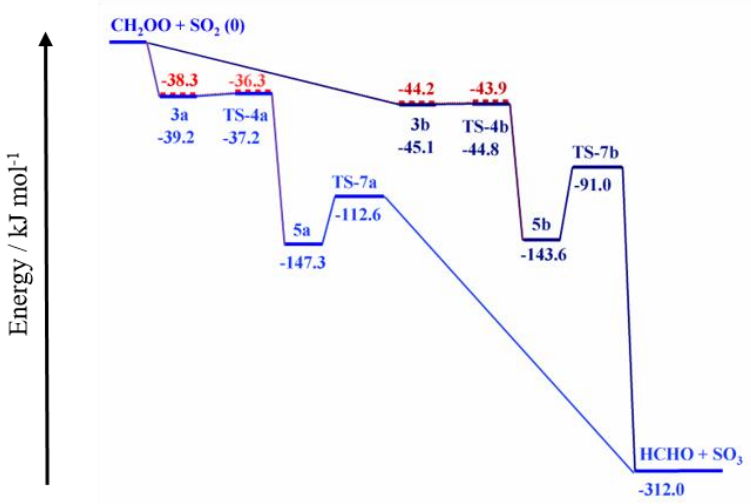

Figure 4.17. PES for the reaction between CH_2OO and SO_2 showing the *endo* reaction pathway (light blue) and the *exo* reaction pathway (dark blue) copied from reference 3.[3] Relative energies for 5a, 5b, TS-7a, TS-7b and HCHO+SO_3 were taken from reference 15[15] and relative energies for 3a, 3b, TS-4a and TS-4b were generated by MESMER calculations.[3] Values for 3a, 3b, TS-4a and TS-4b shown in red were also taken from reference 15[15] for comparison. All energies are reported in kJ mol^{-1}. The notations for intermediates and transition states are the same as in the work of Kuwata *et al.*[15]

MESMER (described in Chapter 2) was used by Onel *et al.*[3] to fit the potential energy surface (shown in Figure 4.17) to the experimentally determined rate coefficients obtained in this work for R4.1 at T = 223 – 344 K and p = 85 Torr and the IUPAC recommendation for R4.1 of $k_{4.1} = \left(3.7^{+0.45}_{-0.40}\right) \times 10^{-11}$ cm^3 $molecule^{-1}$ s^{-1} at T = 298 K and p = 2-760 Torr. The energies of the pre-reaction complexes, (3a and 3b) were linked to the energies of the transition states (TS-4a and TS-4b) to ensure the same relative differences as those reported by Kuwata *et al.* The relative energies of 3a, 3b, TS-4a and TS-4b were floated during simulations and the energies used for 5a, 5b, TS-7a, TS-7b and HCHO + SO_3 were obtained from the work of Kuwata *et al.*[15] Values for of 3a, 3b, TS-4a and TS-4b from the MESMER fit are included in Figure 4.17, which show an agreement of ~ 98 % with the energies predicted by Kuwata *et al.*[15] The observed negative temperature dependence is characteristic of the barrierless formation of the pre-reaction complexes (3a or 3b), which subsequently leads to the formation of secondary ozonides (SOZ) (5a or 5b) through low energy barriers.

The fit result for $k_{4.1}$ is parameterised by $k_{4.1} = (3.72 \pm 0.01) \times 10^{-11} (T/298)^{(-2.05 \pm 0.02)}$ cm^3 $molecule^{-1}$ s^{-1} and is shown in Figure 4.18 along with the experimental results obtained throughout this study.[3]

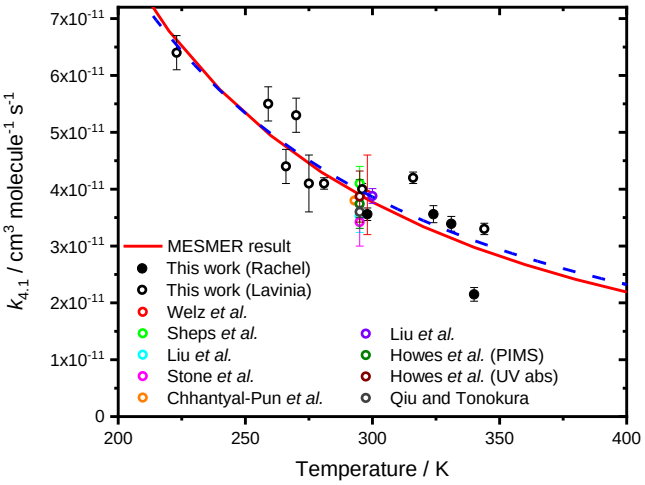

Figure 4.18. A plot of the rate coefficients obtained for the reaction between CH_2OO and SO_2 from this work (solid and open black circles) and from previous literature studies.[4-7, 9, 10, 12, 13] (PIMS = photo-ionisation mass spectrometry). The dashed blue line represents a fit to the equation $k_{4.1} = (3.91 \pm 0.15) \times 10^{-11} \times (T/298)^{-1.8 \pm 0.2}$ cm^3 molecule^{-1} s^{-1} with $R^2 = 0.82$ and the red line represents the parameterisation of the MESMER result: $k_{4.1} = (3.72 \pm 0.01) \times 10^{-11} (T/298)^{(-1.89 \pm 0.02)}$ cm^3 molecule^{-1} s^{-1}.[3]

The final fit to the data is given by the parameterisation of the MESMER result: $k_{4.1} = (3.72 \pm 0.01) \times 10^{-11} (T/298)^{(-1.89 \pm 0.02)}$ cm^3 molecule^{-1} s^{-1}. Using MESMER to obtain a description of the negative temperature dependence results in a fit that can be more reliably extrapolated to temperatures beyond those used within experiments as the fit is based on a potential energy surface.

4.5 Concluding Remarks

The kinetics of the reaction between $CH_2OO + SO_2$ have now been well established with an IUPAC recommended value of $k_{4.1} = \left(3.7^{+0.45}_{-0.40}\right) \times 10^{-11}$ cm^3 molecule^{-1} s^{-1} at 298 K.[11] Previous studies have shown that the reaction exerts no pressure dependence between 1.5 and 450 Torr[6] with the results of this report showing that the reaction exerts a negative temperature dependence that is well described by $k_{4.1} = (3.72 \pm 0.01) \times 10^{-11} (T/298)^{(2.05 \pm 0.02)}$ cm^3 molecule^{-1} s^{-1}. The atmospheric implications of this result will be discussed in Chapter 8.

4.6 References

1. Johnson, D., Lewin, A.G. and Marston, G. The Effect of Criegee-Intermediate Scavengers on the OH Yield from the Reaction of Ozone with 2-methylbut-2-ene. *The Journal of Physical Chemistry A.* 2001, **105**(13), pp.2933-2935.

2. Johnson, D. and Marston, G. The gas-phase ozonolysis of unsaturated volatile organic compounds in the troposphere. *Chemical Society Reviews.* 2008, **37**(4), pp.699-716.
3. Onel, L., Lade, R., Mortiboy, J., Blitz, M.A., Seakins, P.W., Heard, D.E. and Stone, D. Kinetics of the gas phase reaction of the Criegee intermediate CH_2OO with SO_2 as a function of temperature. *Physical Chemistry Chemical Physics.* 2021, **23**(35), pp.19415-19423.
4. Welz, O., Savee, J.D., Osborn, D.L., Vasu, S.S., Percival, C.J., Shallcross, D.E. and Taatjes, C.A. Direct Kinetic Measurements of Criegee Intermediate (CH_2OO) Formed by Reaction of CH_2I with O_2. *Science.* 2012, **335**(6065), p.204.
5. Sheps, L. Absolute Ultraviolet Absorption Spectrum of a Criegee Intermediate CH_2OO. *The Journal of Physical Chemistry Letters.* 2013, **4**(24), pp.4201-4205.
6. Stone, D., Blitz, M., Daubney, L., Howes, N.U.M. and Seakins, P. Kinetics of CH_2OO reactions with SO_2, NO_2, NO, H_2O and CH_3CHO as a function of pressure. *Physical Chemistry Chemical Physics.* 2014, **16**(3), pp.1139-1149.
7. Liu, Y., Bayes, K.D. and Sander, S.P. Measuring Rate Constants for Reactions of the Simplest Criegee Intermediate (CH_2OO) by Monitoring the OH Radical. *The Journal of Physical Chemistry A.* 2014, **118**(4), pp.741-747.
8. Vereecken, L. and Francisco, J.S. Theoretical studies of atmospheric reaction mechanisms in the troposphere. *Chemical Society Reviews.* 2012, **41**(19), pp.6259-6293.
9. Chhantyal-Pun, R., Davey, A., Shallcross, D.E., Percival, C.J. and Orr-Ewing, A.J. A kinetic study of the CH_2OO Criegee intermediate self-reaction, reaction with SO_2 and unimolecular reaction using cavity ring-down spectroscopy. *Physical Chemistry Chemical Physics.* 2015, **17**(5), pp.3617-3626.
10. Howes, N.U.M., Mir, Z.S., Blitz, M.A., Hardman, S., Lewis, T.R., Stone, D. and Seakins, P.W. Kinetic studies of C1 and C2 Criegee intermediates with SO_2 using laser flash photolysis coupled with photoionization mass spectrometry and time resolved UV absorption spectroscopy. *Physical Chemistry Chemical Physics.* 2018, **20**(34), pp.22218-22227.
11. Cox, R.A., Ammann, M., Crowley, J.N., Herrmann, H., Jenkin, M.E., McNeill, V.F., Mellouki, A., Troe, J. and Wallington, T.J. Evaluated kinetic and photochemical data for atmospheric chemistry: Volume VII – Criegee intermediates. *Atmospheric Chemistry and Physics.* 2020, **20**(21), pp.13497-13519.
12. Liu, Y., Liu, F., Liu, S., Dai, D., Dong, W. and Yang, X. A kinetic study of the CH_2OO Criegee intermediate reaction with SO_2, $(H_2O)_2$, CH_2I_2 and I atoms using OH laser induced fluorescence. *Physical Chemistry Chemical Physics.* 2017, **19**(31), pp.20786-20794.

13. Qiu, J. and Tonokura, K. Detection of the simplest Criegee intermediate CH_2OO in the ν4 band using a continuous wave quantum cascade laser and its kinetics with SO_2 and NO_2. *Chemical Physics Letters: X.* 2019, **2**, p.100019.

14. Vereecken, L., Harder, H. and Novelli, A. The reaction of Criegee intermediates with NO, RO_2, and SO_2, and their fate in the atmosphere. *Physical Chemistry Chemical Physics.* 2012, **14**(42), pp.14682-14695.

15. Kuwata, K.T., Guinn, E.J., Hermes, M.R., Fernandez, J.A., Mathison, J.M. and Huang, K. A Computational Re-examination of the Criegee Intermediate–Sulfur Dioxide Reaction. *The Journal of Physical Chemistry A.* 2015, **119**(41), pp.10316-10335.

16. Wang, Y.-Y., Dash, M.R., Chung, C.-Y. and Lee, Y.-P. Detection of transient infrared absorption of SO_3 and 1,3,2-dioxathietane-2,2-dioxide [cyc-$(CH_2)O(SO_2)O$] in the reaction CH_2OO+SO_2. *The Journal of Chemical Physics.* 2018, **148**(6), p.064301.

17. Shimanouchi, T. Tables of molecular vibrational frequencies. Consolidated volume II. *Journal of Physical and Chemical Reference Data.* 1977, **6**(3), pp.993-1102.

18. Hill, C., Gordon, I.E., Kochanov, R.V., Barrett, L., Wilzewski, J.S. and Rothman, L.S. HITRANonline: An online interface and the flexible representation of spectroscopic data in the HITRAN database. *Journal of Quantitative Spectroscopy and Radiative Transfer.* 2016, **177**, pp.4-14.

19. Mir, Z.S., Jamieson, M., Greenall, N.R., Seakins, P.W., Blitz, M.A. and Stone, D. Identification, monitoring, and reaction kinetics of reactive trace species using time-resolved mid-infrared quantum cascade laser absorption spectroscopy: development, characterisation, and initial results for the CH_2OO Criegee intermediate. *Atmospheric Measurement Techniques.* 2022, **15**(9), pp.2875-2887.

20. Mir, Z.S., Lewis, T.R., Onel, L., Blitz, M.A., Seakins, P.W. and Stone, D. CH_2OO Criegee intermediate UV absorption cross-sections and kinetics of CH_2OO + CH_2OO and CH_2OO + I as a function of pressure. *Physical Chemistry Chemical Physics.* 2020, **22**(17), pp.9448-9459.

21. Atkinson, R., Baulch, D.L., Cox, R.A., Crowley, J.N., Hampson, R.F., Hynes, R.G., Jenkin, M.E., Rossi, M.J., Troe, J. and Wallington, T.J. Evaluated kinetic and photochemical data for atmospheric chemistry: Volume IV – gas phase reactions of organic halogen species. *Atmospheric Chemistry and Physics.* 2008, **8**(15), pp.4141-4496.

22. Harwood, M.H., Burkholder, J.B., Hunter, M., Fox, R.W. and Ravishankara, A.R. Absorption Cross Sections and Self-Reaction Kinetics of the IO Radical. *The Journal of Physical Chemistry A.* 1997, **101**(5), pp.853-863.

Chapter 5

Kinetics of the Reaction of CH_2OO with NO_2 as a Function of Temperature and Pressure

The reaction of CH_2OO with NO_2 has been the subject of a number of studies, but there are significant discrepancies in the kinetics at room temperature, uncertainties relating to the nature of products, and thus far there have been no experimental measurements of the temperature dependence of the kinetics. This chapter provides an overview of previous direct studies of the kinetics of the reaction between CH_2OO and NO_2 at room temperature and highlights the areas in which uncertainties remain. Results are provided for a study of the temperature and pressure dependence of $CH_2OO + NO_2$ kinetics, which are required in order to determine the competition between the reaction of CH_2OO with NO_2 and other atmospherically important reactions, such as $CH_2OO + SO_2$ and CH_2OO + water/water dimers.

5.1 Previous Experimental Studies

The first direct measurements of the reaction between CH_2OO and NO_2 (R5.1) were made by Welz *et al.*[1] at 4 Torr and 298 K using laser flash photolysis of CH_2I_2 in the presence of O_2 to generate CH_2OO, with detection of the Criegee intermediate using tunable VUV synchrotron PIMS. Experiments were performed using $^{13}CH_2OO$ to enable separation of the CH_2OO signal from that of $^{14}NO_2$. Welz *et al.* reported a rate coefficient of $k_{5.1} = (7^{+3}_{-2}) \times 10^{-12}$ cm^3 molecule^{-1} s^{-1}, a value that is an order of magnitude greater than previous estimates (7.0×10^{-13} cm^3 molecule^{-1} s^{-1} [2]) based on investigations of the products of ozonolysis reactions.

$CH_2OO + NO_2 \rightarrow$ Products (R5.1)

Following the work of Welz *et al.*, there have been a limited number of studies to investigate the kinetics of R5.1 at room temperature, which all utilise the same Criegee production technique of Welz *et al.* (outlined in Chapter 1) but differ in the techniques used to monitor the kinetics.

The potential for pressure dependence of $k_{5.1}$ was investigated by Stone *et al.*[3] at 295 K and pressures between 25 and 300 Torr. The kinetics of R5.1 were determined using LIF spectroscopy to monitor HCHO production in the system, which was produced from both CH_2OO and CH_2IO_2 in the absence of NO_2. In the presence of NO_2, HCHO was produced in a yield that was consistent with ~ 100 % production from CH_2OO only, with inhibition of

HCHO production from CH_2IO_2 attributed to production of the peroxy nitrate $CH_2IO_2NO_2$. Experiments gave a mean value of $k_{5.1} = (1.5 \pm 0.5) \times 10^{-12}$ cm^3 molecule^{-1} s^{-1} which displayed no significant dependence on pressure over the range investigated, and yields of CH_2OO and CH_2IO_2 from R5.3 determined from measurements of HCHO in experiments using $CH_2I_2/O_2/N_2/NO_2$ were in agreement with those determined via other methods.

More recently, Qiu and Tonokura[4] utilised LFP coupled with mid-IR absorption spectroscopy at $\nu = 1273.0 – 1277.5$ cm^{-1} to monitor the loss of CH_2OO occurring due to R5.1 and reported a rate coefficient for R5.1 of $k_{5.1} = (4.4 \pm 0.2) \times 10^{-12}$ cm^3 molecule^{-1} s^{-1} at 10.4 Torr and 295 K, a value that is of the same order of magnitude than previous measurements.[1, 3] Qiu and Tonokura reported a detection limit for the Criegee intermediate of approximately 2×10^{12} molecule cm^{-3} and highlight that their experimental set-up only used a single pass of the probe beam through the reaction cell, resulting in a pathlength of 40 cm. As a result of the relatively poor sensitivity, experiments were carried out at initial CH_2OO concentrations of ~ 10^{13} molecule cm^{-3} (approximately 10 times greater than that used by Stone *et al.*) leading to intercepts greater than 2000 s^{-1} on their bimolecular plots. The fit quality to the decay profiles of CH_2OO also look relatively poor in the work of Qiu and Tonokura, suggesting that there is a missing second-order component that should be included in their fits to the data. As a result of this, Criegee intermediate loss processes other than R5.1 may be significant under the conditions studied in their work.

Similar to the work of Qiu and Tonokura, Luo *et al.*[5] monitored R5.1 using LFP coupled with IR absorption spectroscopy of CH_2OO at $\nu = 880 – 932$ cm^{-1}. In contrast to the work of Qiu and Tonokura, the experimental set-up utilised by Luo *et al.* had an optical pathlength of 16.2 m, leading to greater sensitivity and a much lower limit of detection for the Criegee intermediate ($1 – 5 \times 10^{10}$ molecule cm^{-3}). The greater sensitivity allowed the group to perform experiments at a lower initial concentration of CH_2OO (~10^{12} molecule cm^{-3}), resulting in smaller intercepts on their bimolecular plots (~ 105 s^{-1} compared with ~ 2000 s^{-1} from Qiu and Tonokura) and therefore less influence from secondary chemistry. Luo *et al.* reported a rate coefficient of $k_{5.1} = (1.0 \pm 0.2) \times 10^{-12}$ cm^3 molecule^{-1} s^{-1} at a total pressure of 5.7 - 9.7 Torr at 298 K, which is approximately one-seventh the value reported by Welz *et al.*[1] but lies within the error range of that reported by Stone *et al.*[3]

The reaction between CH_2OO and NO_2 is not well characterised, with discrepancies of a factor of seven in the kinetics reported from direct studies and inconsistencies remaining in the literature regarding the reaction products. It was previously suggested that NO_3 could be a major product of R5.1, formed via terminal oxygen atom transfer from the Criegee

intermediate to NO_2,[6] which would influence the oxidising capacity of the troposphere at night-time and periods of low sunlight.

The formation of the NO_3 radical following R5.1 has only been observed in the work of Ouyang *et al.*[7] at 760 Torr and 297 K. CH_2OO was produced via LFP of CH_2I_2 in the presence of O_2 and the production of NO_3 and the sum of NO_3 and N_2O_5 (produced by R5.2) were measured using a dual channel broadband cavity enhanced absorption spectrometer between 652 and 672 nm. Experiments were performed under pseudo-first-order conditions with respect to NO_2, resulting in the rapid production of N_2O_5 by R5.2.

$$NO_2 + NO_3 + M \rightarrow N_2O_5 + M \qquad (R5.2)$$

The sum of NO_3 and N_2O_5 was determined by heating the detection cell to 358 K in order to promote thermal dissociation of N_2O_5 to NO_3, which allowed the total optical absorption due to NO_3 to be obtained. The group performed multiple experiments under varying reaction conditions to confirm the precursor to the NO_3 signal was the Criegee intermediate. However, due to the nature of the experimental apparatus used, the time resolution of the experiments was on the order of seconds, and it is possible that the NO_3 observed may be a result of secondary iodine chemistry (R5.3) rather than a direct product of R5.1.[8]

$$INO_2 + IONO_2 \rightarrow I_2 + NO_3 + NO_2 \qquad (R5.3)$$

Caravan *et al.*[9] carried out experiments using multiplexed photo-ionisation mass spectrometry (MPIMS) at 10 and 40 Torr and 298 K, and reported that, following the reaction of CH_2OO with NO_2, no signal corresponding to NO_3 was observed, but do however, report the presence of a signal at $m/z = 92$ that is dependent on the concentration of NO_2, which they attribute to the formation of a CH_2OO-NO_2 adduct. Using the rate coefficient obtained in their study for the reaction of acetaldehyde oxide (CH_3CHOO) with NO_2 ($(1.7 \pm 0.3) \times 10^{-12}$ cm^3 $molecule^{-1}$ s^{-1}) and the acetaldehyde signal obtained when no NO_2 is present, Caravan *et al.*[9] estimated an upper limit of ~ 30% for the production of NO_3 and HCHO from R5.1. The group estimated that, under their reaction conditions, the limit of detection for NO_3 is approximately 3×10^{11} molecule cm^{-3}, which is comparable to the 30 % yield suggested, however, they note that NO_3 may elude detection as a result of secondary chemistry taking place within the reaction cell, significantly reducing the concentration of NO_3 formed. Following the report of Ouyang *et al.*,[7] Caravan *et al.* also investigated the presence of N_2O_5 as a reaction product however, no time-resolved signal was observed. To further explore the potential secondary products of NO_3, Caravan *et al.* monitored the production of IO in both the presence and absence of NO_2. A previous study by Chambers *et al.*[10] reported that the reaction of NO_3 with I occurs rapidly (4.5×10^{-10} cm^3 $molecule^{-1}$ s^{-1}) to produce IO + NO_2 and so an increase in the IO signal with NO_2 concentration

may be indicative of the presence of NO_3. However, Caravan *et al.* reported a decrease in IO concentration with increasing NO_2 and highlight that as a result of other sources of IO in the system (i.e. R5.4, measured by Mir *et al.*[11]), an increase in IO signal with increasing NO_2 would not be sufficient evidence for the formation of NO_3.

$$CH_2OO + I \rightarrow HCHO + IO \qquad \text{(R5.4)}$$

A summary of previous studies of the kinetics of R5.1 is shown in Table 5.1.

Reference	Technique	Photolysis λ / nm	Temperature / K	Pressure / Torr	Bath gas	$[CH_2OO]_0$ / molecule cm^{-3}	$k_{5.1}$ / 10^{-12} cm^3 $molecule^{-1}$ s^{-1}
Welz *et al.*[1]	LFP / PIMS	248	298	4	He	~10^{12}	7^{+3}_{-2}
Stone *et al.*[3]	LFP / LIF	248	295	25 - 300	N_2	~10^{12}	1.5 ± 0.5
Qiu & Tonokura [4]	LFP / IR abs	266	295	10.4	N_2	~ 10^{13}	4.4 ± 0.2
Luo *et al.* [5]	LFP / IR abs	248	298	5.9 – 9.7	N_2	2.8 – 9.6 × 10^{12}	1.0 ± 0.2

Table 5.1. Summary table of the previous kinetic data reported for R5.1. LFP = laser flash photolysis, PIMS = photo-ionisation mass spectrometry and LIF = laser-induced fluorescence.

5.2 Previous Theoretical Work

To date, there is currently only one theoretical study to investigate the reaction between CH_2OO and NO_2, reported by Vereecken and Nguyen.[12] The authors utilised quantum chemical and theoretical kinetic methodologies to obtain a rate coefficient for R5.1 of $k_{5.1} = 4.4 \times 10^{-12}$ cm^3 molecule^{-1} s^{-1} at 298 K at the high-pressure limit, in excellent agreement with the rate coefficient reported by Qiu and Tonokura.[13] The potential energy surface produced by Vereecken and Nguyen (Figure 5.1) suggests that the two most likely reaction pathways for R5.1 proceed via the production of a Criegee-NO_2 adduct, via the addition of either the nitrogen atom or the oxygen atom to the Criegee intermediate chain, denoted as INT1 and INT2 respectively on the potential energy surface shown in Figure 5.1. Their calculations found no low-lying isomerisation channel or dissociation transition state for INT1, suggesting that this reaction pathway produces a stable radical species that would follow RO_2-type chemistry in the atmosphere. They predict multiple reaction pathways from INT2, with the lowest energy pathway leading to the production of HCHO, O_2 and NO. However, Vereecken and Nguyen state that characterising the entrance transition states for this reaction is extremely difficult owing to multi-reference effects (where the molecule cannot be described by a single electronic configuration) and predicted that the reported barrier heights may be overestimated by more than 20 kJ mol^{-1}. The reaction was also predicted to exhibit a positive temperature dependence between 200 – 400 K that can be characterised by $k(T) = 1.15 \times 10^{-11} \exp(-298/T)$ cm^3 molecule^{-1} s^{-1}. However, there have been no experimental studies of the temperature dependence of R5.1.

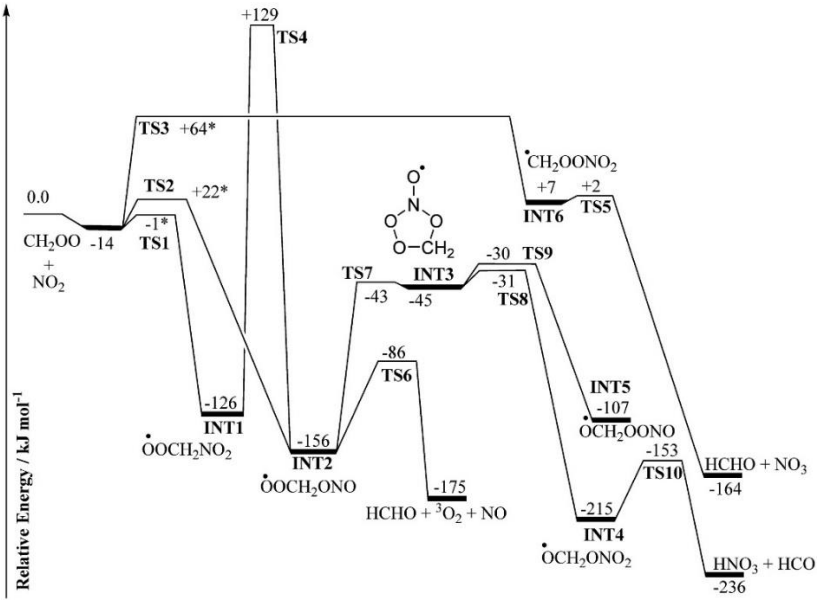

Figure 5.1. Potential energy surface for the reaction of $CH_2OO + NO_2$ obtained from the work of Vereecken and Nguyen,[12] calculated at the CCSD(T)/aug-cc-pVTZ/M06-2X level of theory. Energies marked with an asterisk used NEVPT2/aug-cc-pVTZ energy estimates.

5.3 Experimental

The kinetics of the reaction between CH_2OO and NO_2 were studied as a function of temperature (242 – 353 K) and pressure (25 – 300 Torr) using the experimental set-up described in Chapter 3.

Experiments were performed under pseudo-first-order conditions, with NO_2 present in large excess over CH_2OO. The initial concentrations were: $[NO_2] = (0.09– 1.5) \times 10^{15}$ molecule cm^{-3}, $[CH_2I_2] = (4 – 7.5) \times 10^{13}$ molecule cm^{-3}, and $[O_2] = (0.4 – 1.5) \times 10^{18}$ molecule cm^{-3}. The chemistry was initiated within the cell using an excimer laser operating at a wavelength of λ = 248 nm with an average laser fluence of 20 – 30 mJ cm^{-2}. For experiments performed at 50 Torr, the total flow rate in the cell was 1200 standard cm^3 per minute (sccm), giving a residence time in the cell of ~ 3 s. The total flow rate was adjusted with pressure to maintain a constant residence time. The pulse repetition rate was fixed at 0.27 Hz to ensure a fresh gas mixture entered the reaction cell after each laser pulse, to avoid any unwanted secondary chemistry, with intensity data typically averaged over 300 laser shots. The effective pathlength for these experiments was determined to be (471 ± 50) cm. More details of the experimental procedure are given in Chapter 3.

5.4 Analysis of Absorbance Spectra

Absorbance spectra were obtained in the same way as described in Chapter 3. Figure 5.2 shows an example absorbance spectrum obtained for experiments performed in the presence of NO_2.

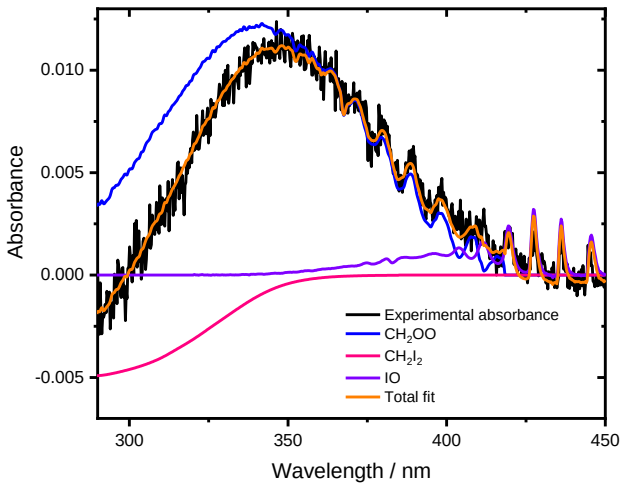

Figure 5.2. Absorbance spectra obtained at 0.3 ms post-photolysis in the presence of $[NO_2] = 4.0 \times 10^{14}$ molecule cm^{-3} at $T = 298$ K and $p = 100$ Torr. The experimental absorbance is shown in black, CH_2OO is shown in blue,[11] CH_2I_2 in pink,[2] IO in purple[14] and the total fit in orange. For these data: $[CH_2OO]_t = 1.89 \times 10^{12}$ molecule cm^{-3}, $\Delta[CH_2I_2] = -2.74 \times 10^{12}$ molecule cm^{-3} and $[IO]_t = 3.22 \times 10^{11}$ molecule cm^{-3}.

Lewis *et al.*[8] suggested the possibility of secondary iodine chemistry from the reaction between CH_2OO and NO_2, which included the potential formation of $IONO_2$, INO_2, and I_2, and if both iodine and oxygen atoms are present, then the formation of OIO would also be possible. Figure 5.3 shows example absorbance spectra obtained following the addition of NO_2 at various time points after photolysis, along with reference spectra for CH_2OO, CH_2I_2 and IO. Immediately following photolysis, the residual shows a good fit between the observed absorbance and the total fit. However, as the reaction progressed, the characteristic structure belonging to IO was no longer observed and two unknown novel peaks appeared in the ranges of 280-295 nm and 465-530 nm.

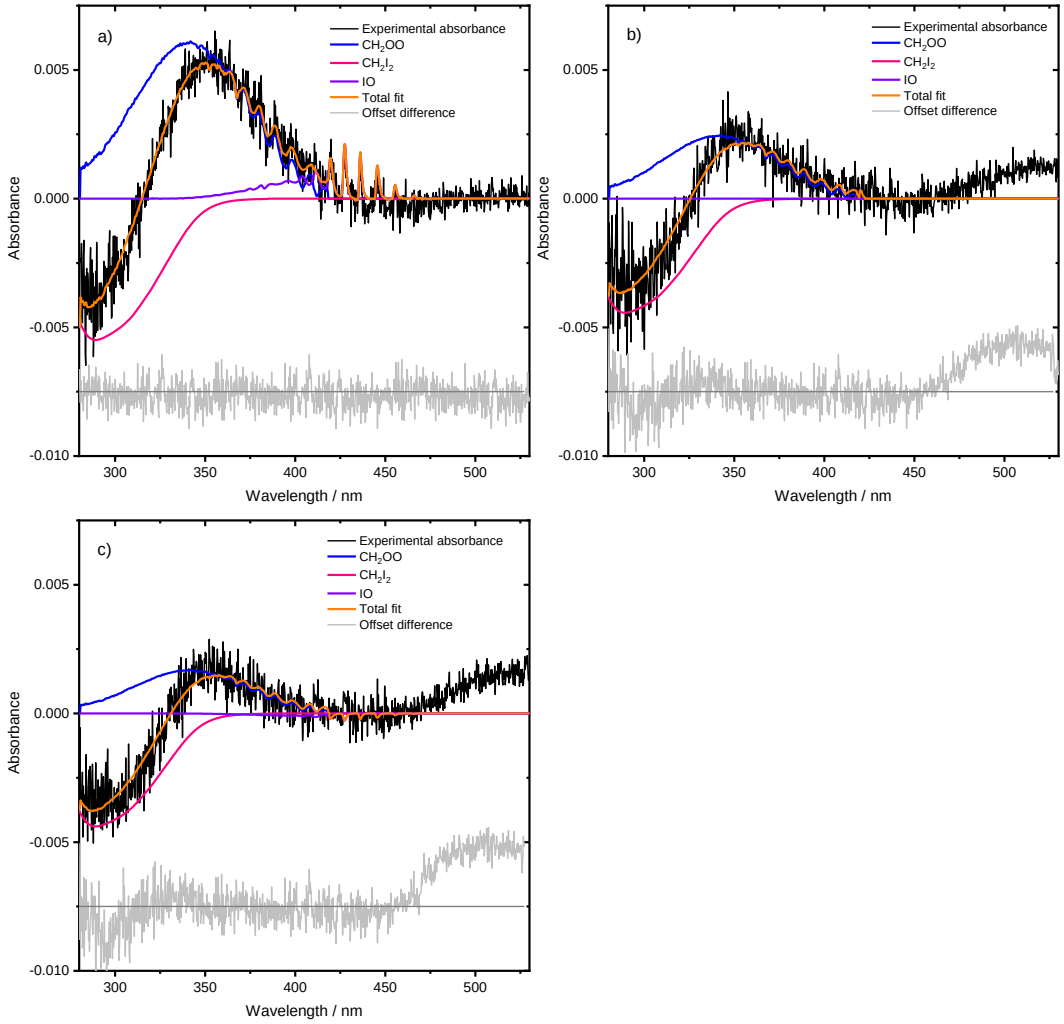

Figure 5.3. Absorbance spectra obtained at a) 0.2 ms, b) 2 ms and c) 4 ms post-photolysis in the presence of $[NO_2]$ = 4.0 × 10^{14} molecule cm^{-3} at T = 298 K and p = 100 Torr. The experimental absorbance is shown in black, CH_2OO is shown in blue,[11] CH_2I_2 in pink,[2] IO in purple,[14] the total fit in orange and the residual of the fit is shown in grey. The fit gave: a) $[CH_2OO]_t$ = 9.39 × 10^{11} molecule cm^{-3}, $\Delta[CH_2I_2]$ = -2.61 × 10^{12} molecule cm^{-3}, $[IO]_t$ = 2.12 × 10^{11} molecule cm^{-3}, b) $[CH_2OO]_t$ = 3.78 × 10^{11} molecule cm^{-3}, $\Delta[CH_2I_2]$ = -2.47 × 10^{12} molecule cm^{-3}, $[IO]_t$ = 1.35 × 10^{10} molecule cm^{-3} and c) $[CH_2OO]_t$ = 1.60 × 10^{11} molecule cm^{-3}, $\Delta[CH_2I_2]$ = -2.59 × 10^{12} molecule cm^{-3}, $[IO]_t$ = 7.66 × 10^9 molecule cm^{-3}.

To determine which species were present, modelled absorbance spectra were constructed using the Beer-Lambert law, which included a combination of reference absorption cross-sections for CH_2I_2,[2] CH_2OO,[11] INO_2,[15] $IONO_2$,[15] IO,[14] OIO[16] and I_2.[17] Least-squares fits were performed between the experimentally observed absorbance and the modelled absorbance to obtain the residual of the fit.

The wavelength region of 280 – 430 nm was first probed for the potential presence of $IONO_2$ and INO_2. Absorbance spectra shown throughout the remainder of this section were taken at 2 ms post-photolysis. At this time point, the formation of the two novel peaks could be clearly observed and peaks corresponding to CH_2OO, CH_2I_2 and IO can still be seen.

Figure 5.4 shows a fit to the observed absorbance using reference absorption cross-sections for CH_2OO, CH_2I_2, IO and $IONO_2$. The residual of the plot between 280 and 300 nm showed no significant improvement compared to the corresponding time point in the fit where $IONO_2$ was not included (Figure 5.3 b), indicating that $IONO_2$ was not significantly contributing to the absorbance seen within this region.

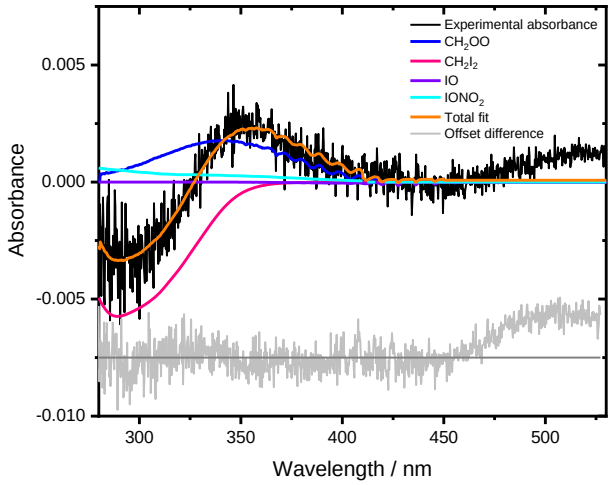

Figure 5.4. Absorbance spectra obtained at 2 ms post-photolysis in the presence of $[NO_2] = 4.0 \times 10^{14}$ molecule cm^{-3} at $T = 298$ K and $p = 100$ Torr. The experimental absorbance is shown in black, CH_2OO is shown in blue,[11] CH_2I_2 in pink,[2] IO in purple,[14] $IONO_2$ in bright blue,[15] the total fit in orange and the residual of the fit is shown in grey. For these data: $[CH_2OO]_t = 2.74 \times 10^{11}$ molecule cm^{-3}, $\Delta[CH_2I_2] = -3.20 \times 10^{12}$ molecule cm^{-3}, $[IO]_t = 1.47 \times 10^{10}$ molecule cm^{-3} and $[IONO_2]_t = 6.51 \times 10^{9}$ molecule cm^{-3}.

The data were then analysed in the same way as above with INO_2. Figure 5.5 shows a fit to the observed absorbance using reference absorption cross-sections for CH_2OO, CH_2I_2, IO and INO_2. The residual of the fit between 280 and 300 nm shows noticeable improvement when compared to the fits with no additional reference spectra (Figure 5.3 b) and from the fit where $IONO_2$ was included (Figure 5.4). We therefore concluded that INO_2 is responsible for the absorbance seen at wavelengths below 300 nm for experiments carried out in the presence of NO_2.

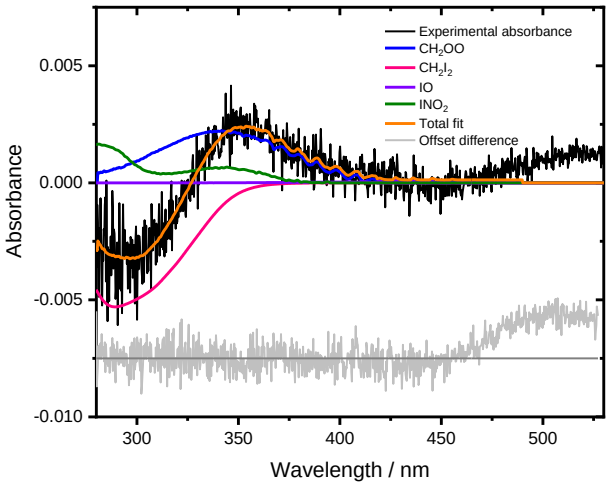

Figure 5.5. Absorbance spectra obtained at 2 ms post-photolysis in the presence of $[NO_2] = 4.0 \times 10^{14}$ molecule cm^{-3} at $T = 298$ K and $p = 100$ Torr. The experimental absorbance is shown in black, CH_2OO is shown in blue,[11] CH_2I_2 in pink,[2] IO in purple,[14] INO_2 in green,[18] the total fit in orange and the residual of the fit is shown in grey. For these data: $[CH_2OO]_t = 3.42 \times 10^{11}$ molecule cm^{-3}, $\Delta[CH_2I_2] = -2.96 \times 10^{12}$ molecule cm^{-3}, $[IO]_t = 1.02 \times 10^{10}$ molecule cm^{-3}, $[INO_2]_t = 1.46 \times 10^{12}$ molecule cm^{-3}.

To assess whether $IONO_2$ should also be included in the analysis, the modelled absorbance was constructed which included both $IONO_2$ and INO_2, as shown in Figure 5.6. The addition of $IONO_2$ showed no improvement in the residual fit, with the fit also suggestion that $IONO_2$ was present in significantly lower concentrations than that of INO_2 (10^9 molecule cm^{-3} for $IONO_2$ compared to 10^{12} molecule cm^{-3} for INO_2). As a result of this, we concluded that $IONO_2$ was not produced in significant concentrations under the conditions studied in this work and therefore not included within the analysis.

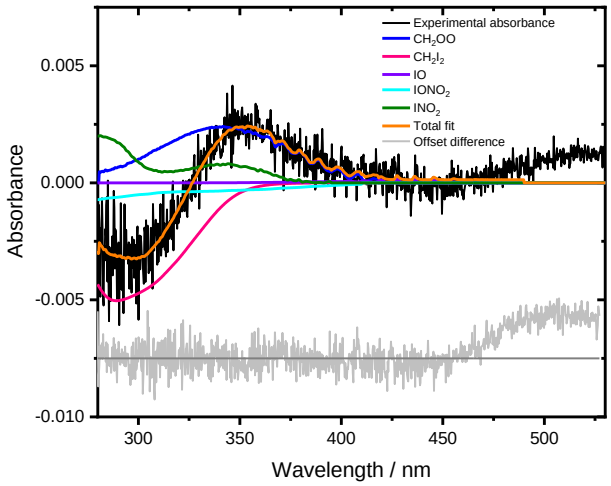

Figure 5.6. Absorbance spectra obtained at 2 ms post-photolysis in the presence of $[NO_2] = 4.0 \times 10^{14}$ molecule cm^{-3} at $T = 298$ K and $p = 100$ Torr. The experimental absorbance is shown in black, CH_2OO is shown in blue,[11] CH_2I_2 in pink,[2] IO in purple,[14] INO_2 in green,[18] $IONO_2$ in bright blue,[15] the total fit in orange and the residual of the fit is shown in grey. For these data: $[CH_2OO]_t = 3.70 \times 10^{11}$ molecule cm^{-3}, $\Delta[CH_2I_2] = -2.81 \times 10^{12}$ molecule cm^{-3}, $[IO]_t = 1.74 \times 10^{10}$ molecule cm^{-3}, $[IONO_2]_t = 5.81 \times 10^{9}$ molecule cm^{-3}, $[INO_2]_t = 1.57 \times 10^{12}$ molecule cm^{-3}.

There are only two literature sources for the UV cross-sections of INO_2, which give significantly different values. The Bröske[18] reference spectrum are upper limits with a maximum value of 1.04×10^{-17} cm^2 $molecule^{-1}$ at 240 nm. In these experiments, INO_2 was prepared from the photolysis of NO_2/I_2 gas mixtures with visible light at 298 K and the spectra were recorded using a diode array. The IUPAC[15] reference spectrum for INO_2 has a maximum absorption cross-section of 4.22×10^{-18} cm^2 $molecule^{-1}$ at 240 nm. The values reported by IUPAC are lower limits, based on the measurements of Bröske and assuming stoichiometric conversion of NO_2 into INO_2. A comparison between the two reference spectra is shown in Figure 5.7.

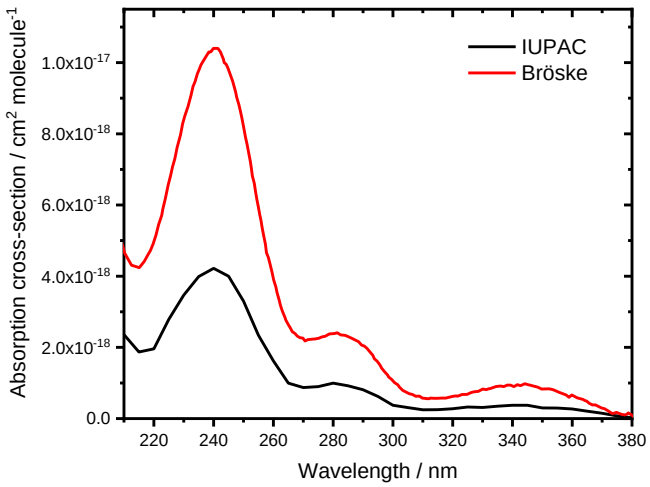

Figure 5.7. Comparison between the UV absorption cross-sections for INO_2 reported by IUPAC (lower limits)[15] and Bröske (upper limits).[18]

Using the yield of CH_2OO at 100 Torr (0.58) and the initial concentration of CH_2OO, initial concentrations of CH_2IO_2 and I were determined from Equations 5.1 – 5.4.

$$\frac{0.58}{0.42} = 1.40 \qquad \text{(Equation 5.1)}$$

$$[CH_2IO_2]_0 = \frac{[CH_2OO]_0}{1.40} \qquad \text{(Equation 5.2)}$$

$$[CH_2I]_0 = \frac{[CH_2OO]_0}{0.58} \qquad \text{(Equation 5.3)}$$

$$[I]_0 = [CH_2I]_0 \times (1 + 0.58) \qquad \text{(Equation 5.4)}$$

The sum of the initial concentrations of CH_2IO_2 and I gives the total amount of iodine that can be released into the system. The data were fit with both reference spectra between 280 and 450 nm and the ratio of INO_2:total iodine was determined. Results from the calculations are shown in Table 5.2, where it is clear that fitting the data with the IUPAC reference spectra suggests a concentration of INO_2 that is greater than the total amount of iodine present in the system. Combining all of the iodine species using the IUPAC reference spectra for INO_2 gave a total value of 1.89, whereas the total using the Bröske reference spectra was 0.85. Following this analysis, the observed absorbance spectra were fit using the INO_2 reference spectra reported by Bröske.[18]

$[NO_2]$ / 10^{14} molecule cm^{-3}	$[CH_2OO]$ / 10^{11} molecule cm^{-3}	$[CH_2I]_0$ / 10^{12} molecule cm^{-3}	$[I]_0$ / 10^{12} molecule cm^{-3}	Total iodine / 10^{12} molecule cm^{-3}	$[INO_2]$ / 10^{12} molecule cm^{-3} (IUPAC[15])	$[INO_2]$ / Total iodine (IUPAC[15])	$[INO_2]$ / 10^{12} cm^{-3} (Bröske[18])	$[INO_2]$ / Total iodine (Bröske[18])
9.76	10.2	1.74	2.76	3.48	8.52	2.44	3.16	0.91
8.42	10.0	1.72	2.73	3.45	6.06	1.76	2.27	0.66
7.06	9.6	1.65	2.61	3.30	6.24	1.89	2.27	0.69
5.68	8.6	1.48	2.35	2.96	4.59	1.55	1.70	0.57
4.28	9.8	1.68	2.65	3.35	4.80	1.43	1.84	0.55
2.86	10.2	1.75	2.77	3.50	3.00	0.86	1.10	0.31

Table 5.2. Calculations of the total iodine species in the system for experiments at T = 298 K and p = 100 Torr and the comparison between the INO_2 concentrations obtained from fits where the UV absorption cross-sections were obtained from IUPAC[15] and from Bröske.[18] The cross-sections taken from Bröske are upper limits and the cross-sections from IUPAC are lower limits based on the work of Bröske and assuming stoichiometric conversion of NO_2 into INO_2. While results suggest that the cross-sections from IUPAC are too low, we are unable to determine if the cross-sections reported by Bröske are the correct values.

The absorbance spectra at wavelengths between 465 and 530 nm were analysed in the same way as above using reference absorption cross-sections for I_2[17] and OIO.[19] Figure 5.8 shows an absorbance spectra with the addition of OIO. The residual of the plot has been improved when compared to plots without any additional reference spectra at longer wavelengths (Figures 5.3-5.6) however, the structure shown by the residual between 480 and 530 nm suggests that OIO is not present in significant concentrations within this region and therefore not responsible for the observed absorbance within this region.

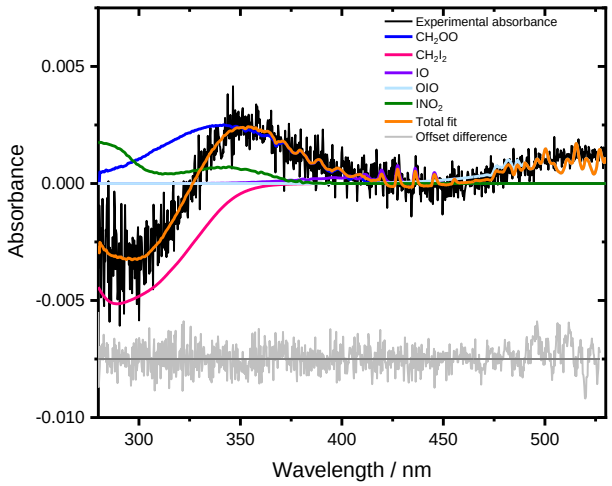

Figure 5.8. Absorbance spectra obtained at 2 ms post-photolysis in the presence of $[NO_2] = 4.0 \times 10^{14}$ molecule cm^{-3} at $T = 298$ K and $p = 100$ Torr. The experimental absorbance is shown in black, CH_2OO is shown in blue,[11] CH_2I_2 in pink,[2] IO in purple,[14] INO_2 in green,[18] OIO in light blue,[16] the total fit in orange and the residual of the fit is shown in grey. For these data: $[CH_2OO]_t = 3.85 \times 10^{11}$ molecule cm^{-3}, $\Delta[CH_2I_2] = -2.87 \times 10^{12}$ molecule cm^{-3}, $[IO]_t = 7.73 \times 10^{10}$ molecule cm^{-3}, $[INO_2]_t = 1.55 \times 10^{12}$ molecule cm^{-3}, $[OIO]_t = 5.33 \times 10^{11}$ molecule cm^{-3}.

Figure 5.9 shows the absorbance spectra with only the I_2 reference spectra included. This fit resulted in the residual of the fit being flat indicating a good fit between the observed and modelled absorbance. We therefore concluded that I_2 was responsible for the peak observed at longer wavelengths.

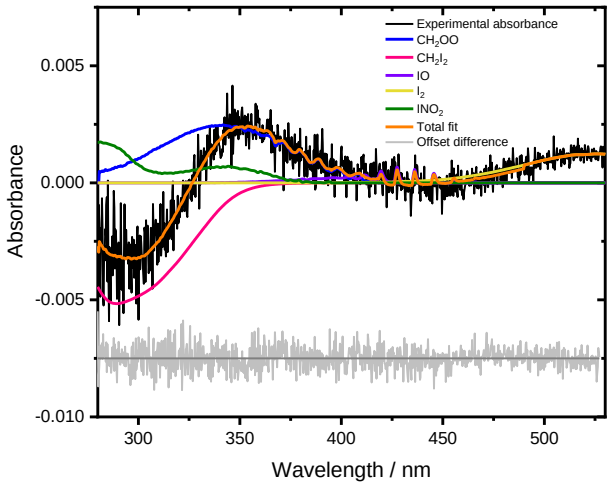

Figure 5.9. Absorbance spectra obtained at 2 ms post-photolysis in the presence of $[NO_2] = 4.0 \times 10^{14}$ molecule cm^{-3} at $T = 298$ K and $p = 100$ Torr. The experimental absorbance is shown in black, CH_2OO is shown in blue,[11] CH_2I_2 in pink,[2] IO in purple,[14] INO_2 in green,[18] I_2 in yellow,[17] the total fit in orange and the residual of the fit is shown in grey. For these data: $[CH_2OO]_t = 3.80 \times 10^{11}$ molecule cm^{-3}, $\Delta[CH_2I_2] = -2.88 \times 10^{12}$ molecule cm^{-3}, $[IO]_t = 6.72 \times 10^{10}$ molecule cm^{-3}, $[INO_2]_t = 1.54 \times 10^{12}$ molecule cm^{-3}, $[I_2]_t = 9.10 \times 10^{11}$ molecule cm^{-3}.

To assess whether OIO should also be included in the analysis, a modelled absorbance was constructed which included both I_2 and OIO, as shown in Figure 5.10. The residual of the fit showed no significant improvement compared to the fit with just I_2 included, with the fit result suggesting that I_2 was present at a concentration approximately 15 times greater than that of OIO.

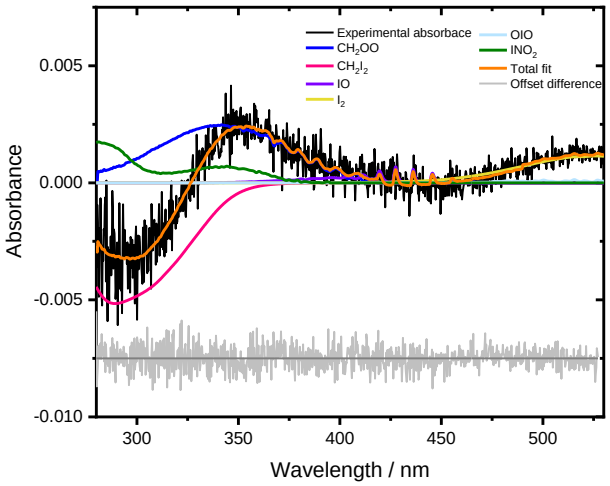

Figure 5.10. Absorbance spectra obtained at 2 ms post-photolysis in the presence of $[NO_2] = 4.0 \times 10^{14}$ molecule cm^{-3} at $T = 298$ K and $p = 100$ Torr. The experimental absorbance is shown in black, CH_2OO is shown in blue,[11] CH_2I_2 in pink,[2] IO in purple,[14] INO_2 in green,[18] I_2 in yellow,[17] OIO in light blue,[16] the total fit in orange and the residual of the fit is shown in grey. For these data: $[CH_2OO]_t = 3.81 \times 10^{11}$ molecule cm^{-3}, $\Delta[CH_2I_2] = -2.88 \times 10^{12}$ molecule cm^{-3}, $[IO]_t = 6.85 \times 10^{10}$ molecule cm^{-3}, $[INO_2]_t = 1.54 \times 10^{12}$ molecule cm^{-3}, $[I_2]_t = 8.54 \times 10^{11}$ molecule cm^{-3}, $[OIO]_t = 4.29 \times 10^{10}$ molecule cm^{-3}.

5.4.1 Limit of Detection for NO_3

Previous work[7] had suggested the possible formation of NO_3 as a product of the reaction between CH_2OO and NO_2. Reference absorption cross-sections for NO_3 between 400 and 700 nm are shown in Figure 5.11, which show two large peaks at ~ 625 and 660 nm. The absorbance observed in this work was between 280 and 540 nm and so we would be unable to see the formation of NO_3 from our kinetic experiments. To investigate the potential formation of NO_3, the centre wavelength of the CCD was shifted upwards enabling any absorbance up to ~ 700 nm to be observed.

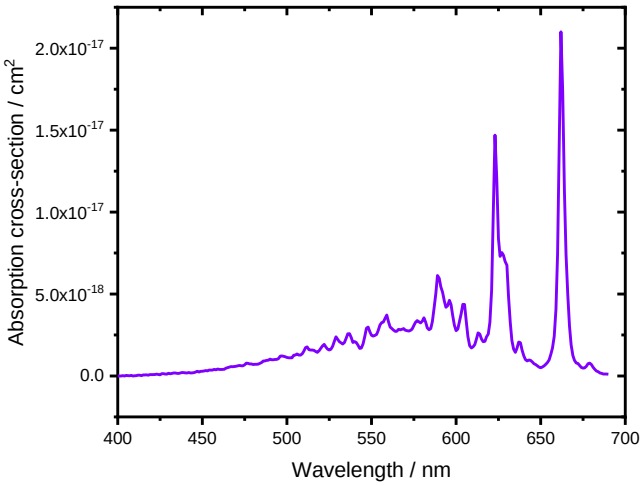

Figure 5.11. Reference absorption cross-sections for NO_3 between 400 and 700 nm.[20]

The limit of detection (LOD) for NO_3 was first determined by calculating the standard deviation of the signal-to-noise ratio of the absorbance from a reaction without NO_2 at 298 K and 50 Torr. Figure 5.12 shows an absorbance spectra obtained for these experiments, as there was no absorbance between 465 and 539 nm, this region was used to determine the LOD.

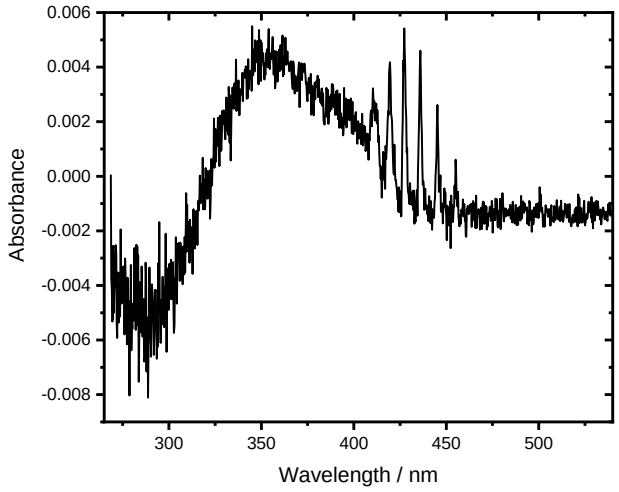

Figure 5.12. Absorbance spectra obtained in the absence of NO_2 at 50 Torr and 298 K used to determine the limit of detection for NO_3.

From these experiments, the LOD was determined to be 2.96×10^{10} molecule cm^{-3}. The initial concentration of CH_2OO in these experiments was ~1.6×10^{12} molecule cm^{-3}, and therefore an upper limit of 2 % was placed on the yield of NO_3.

5.5 Results and Discussion

Figures 5.13-5.15 show typical absorbance spectra at different time points following photolysis. From these spectra it is clear that as time progresses, the signals corresponding to CH_2OO and IO decrease while the signals corresponding to INO_2 and I_2 increase. The spectra showed no evidence for the contribution of OIO under these conditions, and the addition of the OIO reference spectrum did not improve the fit and so it was not included. It should be noted that, to determine the kinetics of R5.1, the data were fit between 290 – 450 nm, where only CH_2I_2, CH_2OO, INO_2 and IO contribute to the total fit.

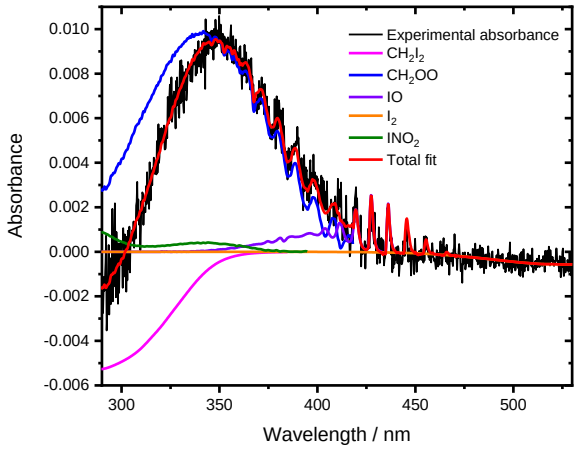

Figure 5.13. Typical observed absorbance (black) and total fit (red) obtained by fitting reference spectra for CH_2I_2 (pink),[2] CH_2OO (blue),[11] IO (purple),[14] I_2 (orange)[17] and INO_2 (green).[18] Data shown were obtained at 0.3 ms after photolysis at p = 25 Torr and T = 298 K, with $[CH_2I_2]_0 = 5.9 \times 10^{13}$ molecule cm^{-3}, $[O_2] = 4.0 \times 10^{17}$ molecule cm^{-3}, and $[NO_2] = 4.0 \times 10^{14}$ molecule cm^{-3}. The fit gave $\Delta[CH_2I_2] = -2.9 \times 10^{12}$ molecule cm^{-3}, $[CH_2OO]_t = 1.5 \times 10^{12}$ molecule cm^{-3}, $[IO]_t = 2.6 \times 10^{11}$ molecule cm^{-3}, $[I_2]_t = 0$ and $[INO_2]_t = 9.1 \times 10^{11}$ molecule cm^{-3}.

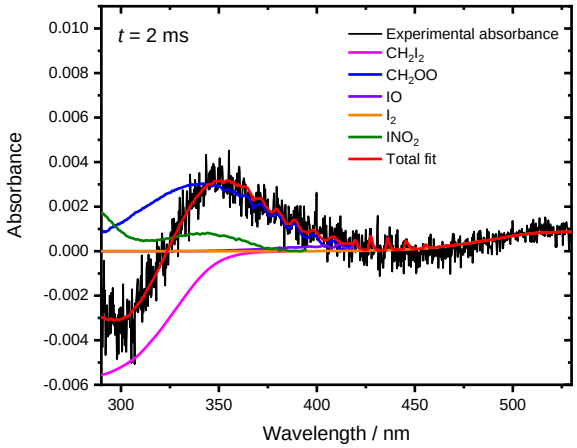

Figure 5.14. Typical observed absorbance (black) and total fit (red) obtained by fitting reference spectra for CH_2I_2 (pink),[2] CH_2OO (blue),[11] IO (purple),[14] I_2 (orange)[17] and INO_2 (green).[18] Data shown were obtained at 2 ms after photolysis at p = 25 Torr and T = 298 K, with $[CH_2I_2]_0 = 5.9 \times 10^{13}$ molecule cm^{-3}, $[O_2] = 4.0 \times 10^{17}$ molecule cm^{-3}, and $[NO_2] = 4.0 \times 10^{14}$ molecule cm^{-3}. The fit gave $\Delta[CH_2I_2] = -3.0 \times 10^{12}$ molecule cm^{-3}, $[CH_2OO]_t = 4.7 \times 10^{11}$ molecule cm^{-3}, $[IO]_t = 6.4 \times 10^{10}$ molecule cm^{-3}, $[I_2]_t = 6.5 \times 10^{11}$ molecule cm^{-3} and $[INO_2]_t = 1.8 \times 10^{12}$ molecule cm^{-3}.

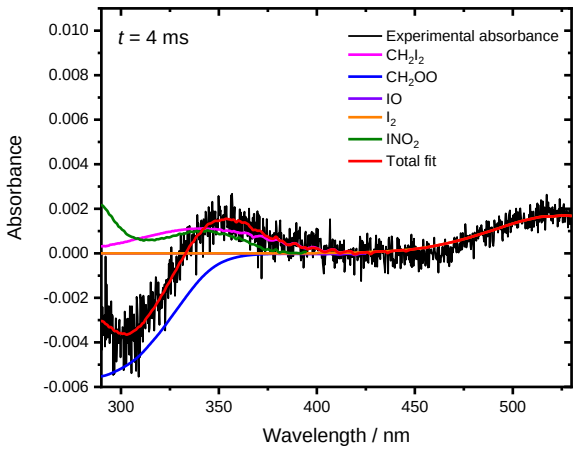

Figure 5.15. Typical observed absorbance (black) and total fit (red) obtained by fitting reference spectra for CH_2I_2[2] (pink), CH_2OO[11] (blue), IO[14] (purple), I_2[17] (orange) and INO_2[18] (green). Data shown were obtained at 4 ms after photolysis at p = 25 Torr and T = 298 K, with $[CH_2I_2]_0 = 5.9 \times 10^{13}$ molecule cm^{-3}, $[O_2] = 4.0 \times 10^{17}$ molecule cm^{-3}, and $[NO_2] = 4.0 \times 10^{14}$ molecule cm^{-3}. The fit gave $\Delta[CH_2I_2] = -3.1 \times 10^{12}$ molecule cm^{-3}, $[CH_2OO]_t = 1.7 \times 10^{11}$ molecule cm^{-3}, $[IO]_t = 6.5 \times 10^{9}$ molecule cm^{-3}, $[I_2]_t = 1.3 \times 10^{12}$ molecule cm^{-3} and $[INO_2]_t = 2.2 \times 10^{12}$ molecule cm^{-3}.

Concentration-time profiles were obtained for each species present between 290 and 550 nm, with typical results shown in Figure 5.16.

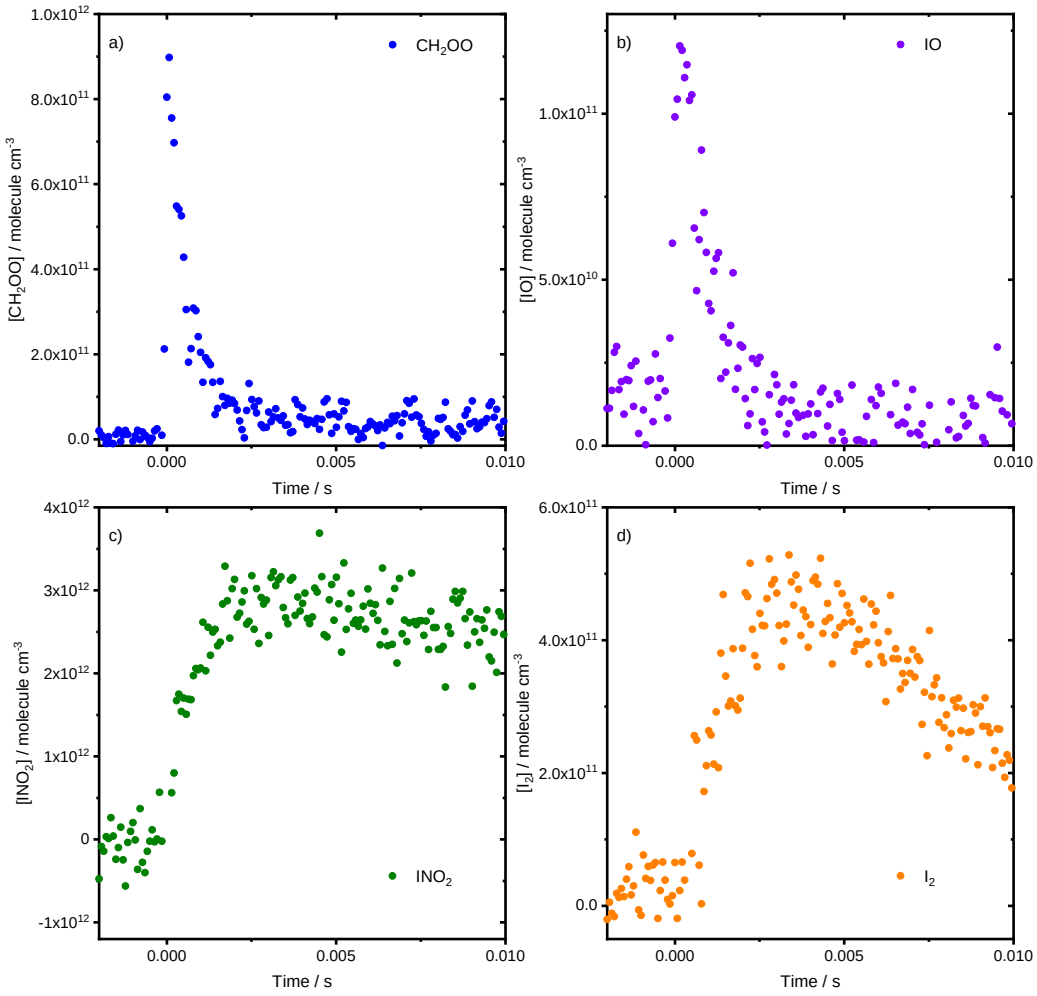

Figure 5.16. Typical concentration-time profiles for a) CH_2OO, b) IO, c) INO_2 and d) I_2 obtained at p = 100 Torr and T = 298 K, with $[NO_2] = 9.8 \times 10^{14}$ molecule cm^{-3}.

As described above, the signal corresponding to IO decreases upon the addition of NO_2 as a result of the formation of INO_2 (R5.9). Figure 5.17 compares concentration-time profiles for IO in the presence and absence of NO_2, which shows a more rapid decrease in the concentration of IO when higher concentrations of NO_2 are introduced to the system.

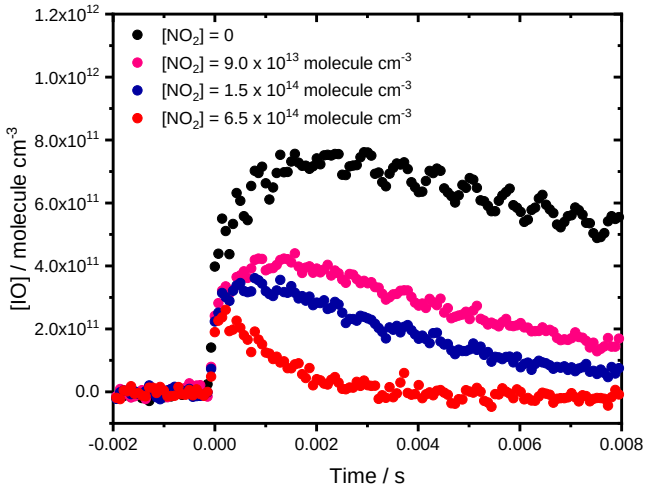

Figure 5.17. Concentration-time profile for IO at 298 K and 100 Torr, for $[NO_2] = 0$ (black), $[NO_2] = 9.0 \times 10^{13}$ molecule cm^{-3} (pink), $[NO_2] = 1.5 \times 10^{14}$ molecule cm^{-3} (navy) and $[NO_2] = 6.5 \times 10^{14}$ molecule cm^{-3} (red), for an experiment with $[CH_2I_2]_0 = 5.5 \times 10^{13}$ molecule cm^{-3}. The repeating oscillation seen in the $[NO_2] = 0$ trace is likely a result of vibrations within the laboratory causing the probe beam to move on and off of the probe mirrors.

Figure 5.18 shows example concentration-time profiles for INO_2 in the presence of different concentrations of NO_2. The data obtained for INO_2 shows more scatter than data typically obtained for the other species present, this is because INO_2 absorbs at lower wavelengths than CH_2OO and IO where there is less light available and so the signal-to-noise ratio is reduced. However, it is still evident that a higher concentration of INO_2 is produced under higher NO_2 concentrations.

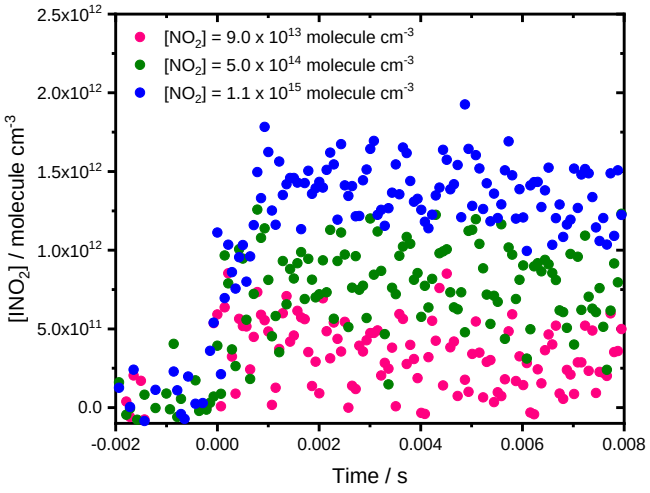

Figure 5.18. Concentration-time profile for INO_2 at 298 K and 100 Torr for $[NO_2] = 9.0 \times 10^{13}$ molecule cm^{-3} (pink), $[NO_2] = 5.0 \times 10^{14}$ molecule cm^{-3} (green) and $[NO_2] = 1.1 \times 10^{15}$ molecule cm^{-3} (blue), for an experiment with $[CH_2I_2]_0 = 5.5 \times 10^{13}$ molecule cm^{-3}.

As experiments were conducted under pseudo-first-order conditions, where the concentration of NO_2 is in excess of CH_2OO, the change in the concentration of CH_2OO can be described using Equation 5.5.

$$[CH_2OO]_t = [CH_2OO]_0 \times \left(exp^{-k' \times t}\right) \qquad \text{(Equation 5.5)}$$

where $[CH_2OO]_t$ is the concentration of CH_2OO at time t, $[CH_2OO]_0$ is the initial Criegee intermediate concentration and k' is the observed rate coefficient, which incorporates the rate coefficient for the Criegee intermediate decay when there is no NO_2 in the system (k_x) and the pseudo-first-order rate constant for the reaction between the Criegee intermediates and NO_2 ($k'_{5.1} = k_{5.1}[NO_2]$), i.e. $k' = k_x + k'_{5.1}$.

The data were fit with an equation that incorporates an instrument response function (IRF) in Equation 5.5, to account for the simultaneous illumination of multiple rows on the CCD followed by row-by-row shifting (further details regarding the IRF are provided in Chapter 3).

Figure 5.19 shows how the decay of CH_2OO increases as the concentration of NO_2 added to the reaction cell is increased.

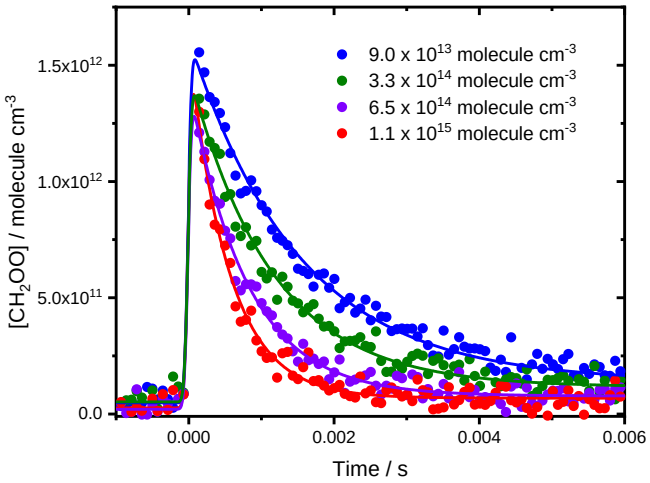

Figure 5.19. Concentration – time profiles showing the CH_2OO decay, in the presence of NO_2, at p = 100 Torr and T = 298 K. Solid lines represent an unweighted fit to Equation 5.5 convoluted with an instrument response function. For $[NO_2] = 9.0 \times 10^{13}$ molecule cm^{-3}, the fit gave $[CH_2OO]_0 = (1.50 \pm 0.13) \times 10^{12}$ molecule cm^{-3} and $k' = (666 \pm 18)$ s^{-1}; for $[NO_2] = 3.3 \times 10^{14}$ molecule cm^{-3}, the fit gave $[CH_2OO]_0 = (1.38 \pm 0.17) \times 10^{12}$ molecule cm^{-3} and $k' = (885 \pm 27)$ s^{-1}; for $[NO_2] = 6.5 \times 10^{14}$ molecule cm^{-3}, the fit gave $[CH_2OO]_0 = (1.37 \pm 0.24) \times 10^{12}$ molecule cm^{-3} and $k' = (1271 \pm 44)$ s^{-1}; and for $[NO_2] = 1.1 \times 10^{15}$ molecule cm^{-3}, the fit gave $[CH_2OO]_0 = (1.55 \pm 0.40) \times 10^{12}$ molecule cm^{-3} and $k' = (1853 \pm 70)$ s^{-1}. The IRF parameters were: $t_c = -(1.05 \pm 0.13) \times 10^{-5}$ s, $w = (4.05 \pm 0.90) \times 10^{-5}$ s. Uncertainties are 1σ.

Bimolecular rate coefficients were obtained by plotting pseudo-first-order rate coefficients against NO_2 concentrations, as shown in Figure 5.20.

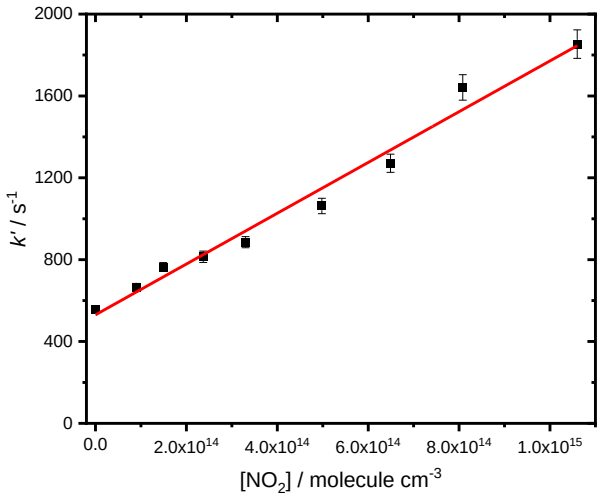

Figure 5.20. Bimolecular plot for the reaction of CH_2OO + NO_2 at 298 K and 100 Torr obtained by plotting the observed rate coefficient *vs* [NO_2] where the red line represents an unweighted linear fit to the data. The slope of the fit is the bimolecular rate coefficient of $k_{5.1}$ = (1.24 ± 0.07) × 10^{-12} cm^{-3} $molecule^{-1}$ s^{-1} with an intercept of (531 ± 35) s^{-1}. Uncertainties are 1σ.

The potential for the contribution of second-order behaviour was also investigated, where the decay of CH_2OO is described by a mixed first- and second-order model (further details given in Chapter 3). Figure 5.21 compares fits obtained for a typical concentration-time profile for CH_2OO using the first-order model and the mixed first- and second-order model.

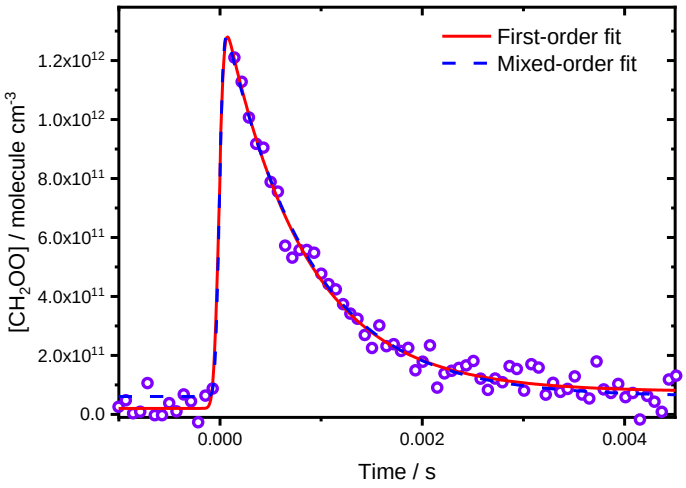

Figure 5.21. Comparison of fits to the first-order equation (solid red line) and the mixed-order equation (dashed blue line) for CH_2OO in the presence of $[NO_2] = 6.5 \times 10^{14}$ molecule cm^{-3} at 100 Torr and 298 K. The solid red line gave: $t_c = -(1.05 \pm 0.13) \times 10^{-5}$ s, $w = (4.05 \pm 0.90) \times 10^{-5}$ s, $[CH_2OO]_0 = (1.37 \pm 0.24) \times 10^{12}$ molecule cm^{-3} and $k' = (1271 \pm 44)\ s^{-1}$. The dashed blue line gave: $t_c = -(1.18 \pm 0.58) \times 10^{-5}$ s, $w = (3.27 \pm 0.32) \times 10^{-5}$ s, $[CH_2OO]_0 = (1.39 \pm 0.29) \times 10^{12}$ molecule cm^{-3}, $k'' = (9.99 \pm 0.25) \times 10^{11}\ cm^3$ molecule^{-1} s^{-1} and $k' = (1198 \pm 49)\ s^{-1}$. Uncertainties are 1σ.

Figure 5.22 compares rate coefficients for CH_2OO with NO_2 obtained from the first-order fits to those obtained from the mixed-order fits. Results show less than 5 % difference between the rate coefficients obtained when kinetics were described using the first-order and mixed-order models. We therefore conclude that data are well described by pseudo-first-order kinetics.

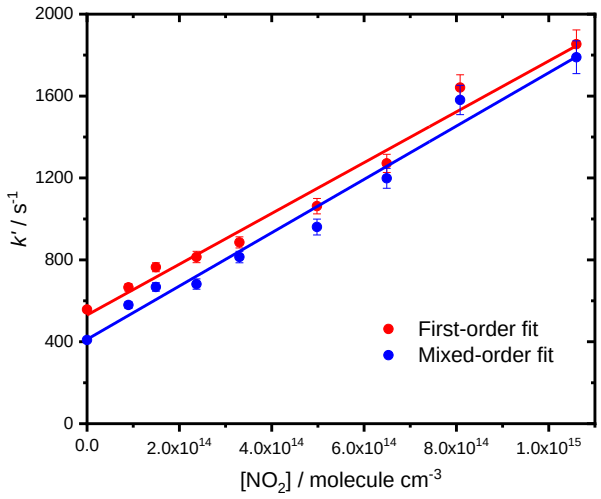

Figure 5.22. Dependence of k' on [NO_2] at T = 298 K and p = 100 Torr obtained for a first-order fit (solid red line) and mixed-order fit (solid blue line). The fits gave: $k_{5.1}$ = (1.24 ± 0.07) × 10^{-12} cm^3 $molecule^{-1}$ s^{-1} and k_x = (531 ± 35) s^{-1} for the first-order fit and $k_{5.1}$ = (1.30 ± 0.07) × 10^{-12} cm^3 $molecule^{-1}$ s^{-1} and k_x = (412 ± 38) s^{-1} for the mixed-order fit. Uncertainties are 1σ.

5.5.1 Pressure Dependent Results

Experiments were performed at pressures between 25 and 300 Torr at 298 K with rate coefficients for each pressure summarised in Table 5.3, where the uncertainties represent a combination of the statistical error and the systematic errors resulting from uncertainties in gas flow rates and in the concentration of NO_2. Figure 5.23 shows a plot of the bimolecular rate coefficients as a function of pressure for the results obtained in this work, as well as the results of previous literature.[1, 3-5]

Pressure / Torr	$k_{5.1}$ / 10^{-12} cm^3 $molecule^{-1}$ s^{-1}
25	1.19 ± 0.14
50	1.11 ± 0.14
100	1.24 ± 0.15
200	1.39 ± 0.15
300	1.28 ± 0.15

Table 5.3. Bimolecular rate coefficients obtained for R5.1 at 298 K and pressures between 25 and 300 Torr. The uncertainties represent a combination of the statistical error and the systematic errors resulting from uncertainties in gas flow rates and in the concentration of NO_2.

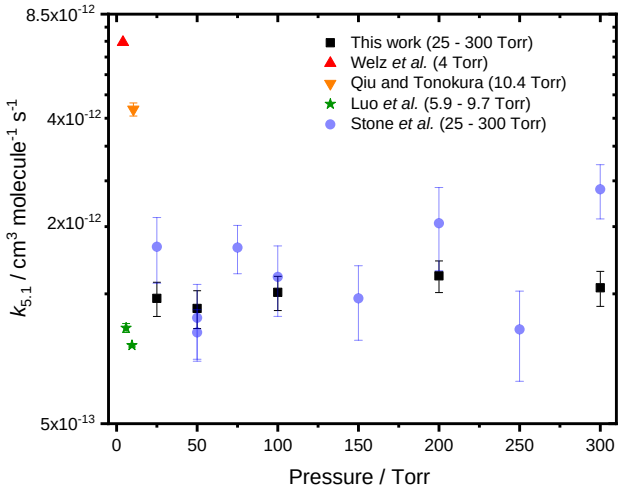

Figure 5.23. A plot of $k_{5.1}$ as a function of pressure, the plot includes the results obtained in this work (black), the results of Stone *et al*. (blue),[3] Luo *et al*. (green),[5] Qiu and Tonokura (orange)[13] and Welz *et al*. (red).[1] Error bars for this work represent a combination of the statistical error and the systematic errors resulting from uncertainties in gas flow rates and in the concentration of NO_2.

The reaction between CH_2OO and NO_2 was found to be independent of pressure with a rate coefficient of $k_{5.1} = (1.24 \pm 0.16) \times 10^{-12}$ cm^3 molecule^{-1} s^{-1} at 298 K. This value is in good agreement with the rate coefficients reported by Luo *et al.*[5] at 5.9 and 9.7 Torr ($(1.0 \pm 0.2) \times 10^{-12}$ cm^3 molecule^{-1} s^{-1} at 295 K) as well as the pressure independent values reported by Stone *et al.*[3] between 25 – 300 Torr ($(1.5 \pm 0.5) \times 10^{-12}$ cm^3 molecule^{-1} s^{-1} at 298 K). This value is approximately one seventh of the value reported in the earliest kinetic study by Welz *et al.*[1] who reported a rate coefficient of $k_{5.1} = (7.0^{+3}_{-2}) \times 10^{-12}$ cm^3 molecule^{-1} s^{-1} at 298 K and 4 Torr. This value is also not in agreement with the work by Qiu and Tonokura,[13] who report a rate coefficient of $k_{5.1} = (4.4 \pm 0.2) \times 10^{-12}$ cm^3 molecule^{-1} s^{-1} at 10.4 Torr and 295 K, although this difference can potentially be attributed to the poor sensitivity of their experimental apparatus which in-turn led to the use of much higher initial Criegee concentrations (~ 10^{13} molecule cm^{-3}), which may have promoted secondary chemistry.

5.5.2 Temperature Dependent Results

The reaction between CH_2OO and NO_2 was investigated as a function of temperature (242 – 353 K) at 50 Torr, using the same method as described above. Bimolecular plots obtained at each temperature are shown in Figure 5.24. Values for the intercept, k_x, have been subtracted from the pseudo-first-order rate coefficients for clarity.

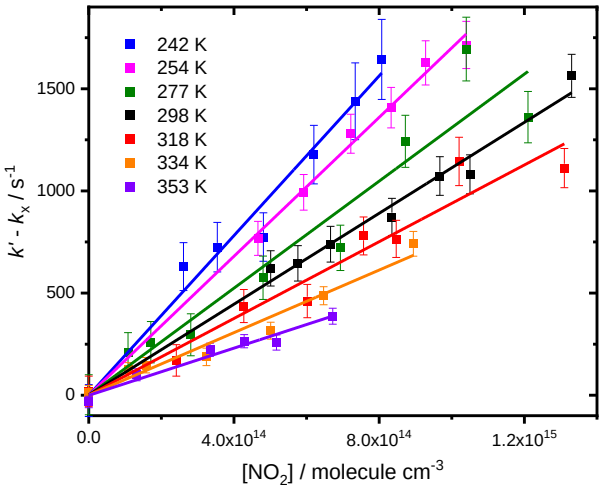

Figure 5.24. Pseudo-first-order rate coefficients as a function of NO_2 concentration for experiments carried out at temperatures between 242 and 353 K, where the solid lines represent an unweighted linear fit to the data. Error bars for this work represent a combination of the statistical error and the systematic errors resulting from uncertainties in gas flow rates and in the concentration of NO_2.

The pressure dependence was again investigated at the two lowest temperatures (242 and 254 K) between 25 and 200 Torr, with results showing that R5.1 remained independent of pressure at these low temperatures. Figures 5.25 and 5.26 show the data obtained for the pressure dependence at 242 and 254 K, along with the combined bimolecular plot for these temperatures after the intercept, k_x, has been subtracted for clarity.

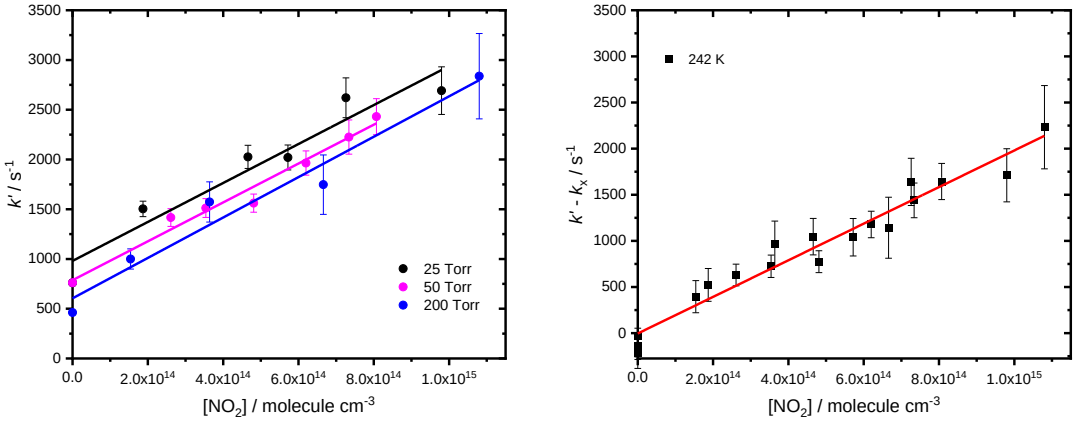

Figure 5.25. Left: Pseudo-first-order losses for CH_2OO as a function of NO_2 concentration for experiments carried out at 242 K. Right: Pseudo-first-order losses after the k_x values for each data set have been subtracted. The red line represents an unweighted linear fit to the data. 25 Torr (black): $k_{5.1} = (1.96 \pm 0.27) \times 10^{-12}$ cm^3 molecule^{-1} s^{-1}, $k_x = (981 \pm 160)$ s^{-1}, 50 Torr (pink): $k_{5.1} = (1.95 \pm 0.14) \times 10^{-12}$ cm^3 molecule^{-1} s^{-1}, $k_x = (787 \pm 76)$ s^{-1}, 200 Torr (blue): $k_{5.1} = (2.03 \pm 0.24) \times 10^{-12}$ cm^3 molecule^{-1} s^{-1}, $k_x = (605 \pm 141)$ s^{-1}, combined data: $k_{5.1} = (1.98 \pm 0.11) \times 10^{-12}$ cm^3 molecule^{-1} s^{-1}, $k_x = (-4 \pm 63)$ s^{-1}. Uncertainties are 1σ.

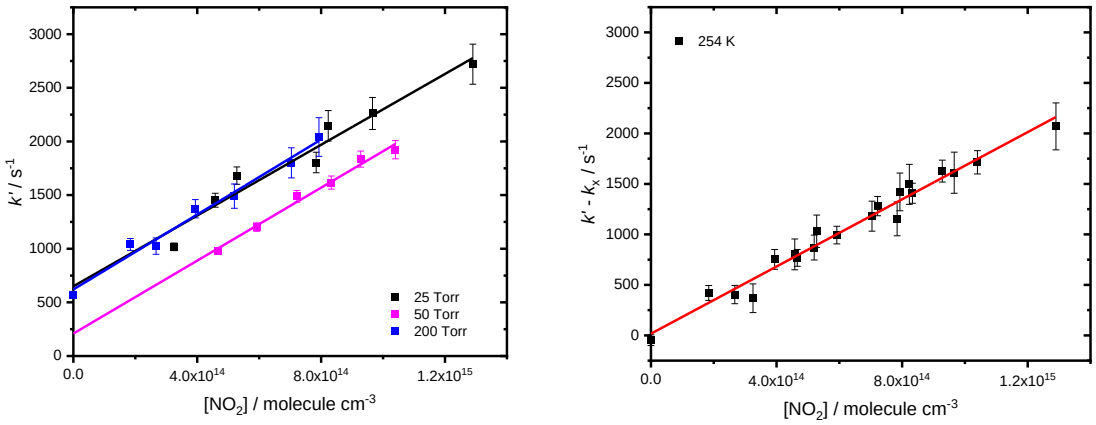

Figure 5.26. Left: Pseudo-first-order losses for CH_2OO as a function of NO_2 concentration for experiments carried out at 254 K. Right: Pseudo-first-order losses after the k_x values for each data set have been subtracted. The red line represents an unweighted linear fit to the data. 25 Torr (black): $k_{5.1} = (1.65 \pm 0.17) \times 10^{-12}$ cm^3 molecule^{-1} s^{-1}, $k_x = (650 \pm 138)$ s^{-1}, 50 Torr (pink): $k_{5.1} = (1.70 \pm 0.10) \times 10^{-12}$ cm^3 molecule^{-1} s^{-1}, $k_x = (209 \pm 78)$ s^{-1}, 200 Torr (blue): $k_{5.1} = (1.75 \pm 0.10) \times 10^{-12}$ cm^3 molecule^{-1} s^{-1}, $k_x = (620 \pm 49)$ s^{-1}, combined data: $k_{5.1} = (1.66 \pm 0.06) \times 10^{-12}$ cm^3 molecule^{-1} s^{-1}, $k_x = (17 \pm 46)$ s^{-1}. Uncertainties are 1σ.

Bimolecular plots obtained before the intercept was subtracted are shown in Appendix 5 for all other temperatures.

Rate coefficients at each temperature are summarised in Table 5.4, where the uncertainties represent a combination of the statistical error and the systematic errors resulting from uncertainties in gas flow rates and in the concentration of NO_2.

Temperature / K	Pressure / Torr	$k_{5.1}$ / 10^{-12} cm^3 molecule^{-1} s^{-1}
242	25	1.96 ± 0.34
	50	1.95 ± 0.24
	200	2.03 ± 0.31
254	25	1.65 ± 0.24
	50	1.70 ± 0.20
	200	1.75 ± 0.20
277	50	1.31 ± 0.19
298	25	1.19 ± 0.14
	50	1.11 ± 0.14
	100	1.24 ± 0.15
	200	1.39 ± 0.15
	300	1.28 ± 0.15
318	50	0.94 ± 0.13
335	50	0.77 ± 0.10
353	50	0.58 ± 0.08

Table 5.4. Bimolecular rate coefficients for R5.1 obtained in this work at pressures between 25 and 300 Torr and temperatures between 242 and 353 K. The uncertainties represent a combination of the statistical error and the systematic errors resulting from uncertainties in gas flow rates and in the concentration of NO_2.

Results show that the reaction between CH_2OO and NO_2 exhibits a negative temperature dependence between 242 and 353 K. A comparison of fits to the data is shown in Figure 5.27, which compares fitting the data with the Arrhenius equation (further details in Chapter 2) and fitting the data using the power law form, AT^n, to determine the best description of the temperature dependence.

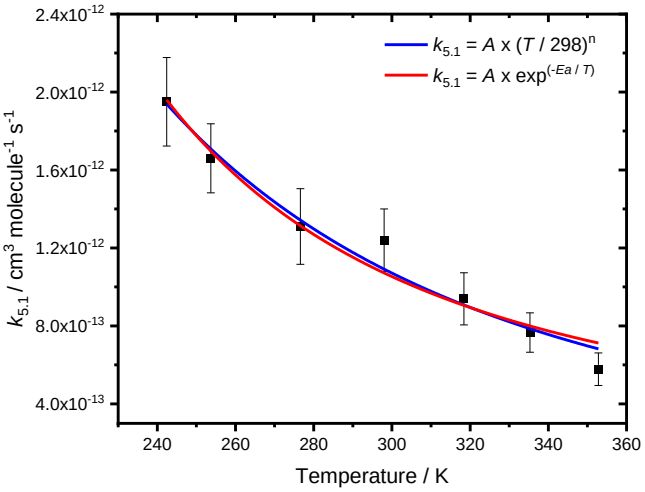

Figure 5.27. A plot of the bimolecular rate coefficients for $CH_2OO + NO_2$ as a function of temperature for the results obtained in this work at pressures between 25 and 200 Torr and temperatures between 242 and 353 K. Errors represent a combination of the statistical error and the systematic errors resulting from uncertainties in gas flow rates and in the concentration of NO_2. The blue line represents a fit to the equation $k_{5.1} = (1.07 \pm 0.02) \times 10^{-12} \times (T/298)^{-(2.9 \pm 0.2)}$ cm^3 molecule^{-1} s^{-1} with $R^2 = 0.97$ and the red line represents a fit to the equation $k_{5.1} = (7.71 \pm 2.08) \times 10^{-14} \times exp(-784/T)$ cm^3 molecule^{-1} s^{-1} with $R^2 = 0.96$.

Fitting the data with the Arrhenius equation gave: $k_{5.1} = (7.71 \pm 2.08) \times 10^{-14} \times exp(-784/T)$ cm^3 molecule^{-1} s^{-1} with $R^2 = 0.96$ and fitting with AT^n gave: $k_{5.1} = (1.07 \pm 0.02) \times 10^{-12} \times (T/298)^{-(2.9 \pm 0.2)}$ cm^3 molecule^{-1} s^{-1} with $R^2 = 0.97$. The data were well described by both equations (as seen in Figure 5.28) however, fitting with AT^n gave an R^2 value closer to 1 and so it was concluded that this fit provides the best description of the data. There have been no previous experimental investigations of the temperature dependence of this reaction however, the same theoretical study by Vereecken and Nguyen[12] predicted a small positive dependence. Figure 5.28 shows a comparison of the temperature dependence of $k_{5.1}$ derived from the experimental results obtained in this work and the calculations performed by Vereecken and Nguyen.

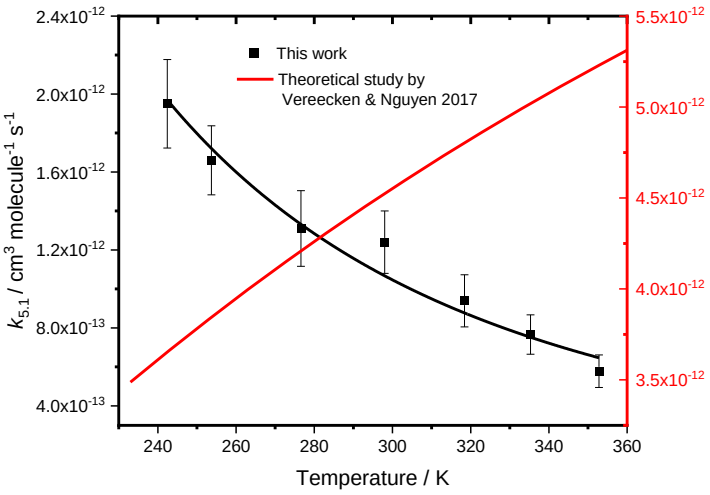

Figure 5.28. A plot of $k_{5.1}$ as a function of temperature for the results obtained in this work and the theoretical results obtained in the work of Vereecken and Nguyen[12] using the equation $k = 1.15 \times 10^{-11} \, exp(-298/T)$ cm^{-3} molecule^{-1} s^{-1}.

5.5.3 Theoretical Calculations

The Master Equation Solver for Multi-Energy well Reactions (MESMER) was used by Dr Robin Shannon and Dr Daniel Stone to explore the sensitivity of calculated rate coefficients to the potential energy surface for R5.1. MESMER uses an energy-grained master equation approach described in Chapter 2, and can be used to optimise potential energy surfaces and transition state energies to fit to experimental results. Figure 5.29 shows the potential energy surface employed in MESMER in this work, which considers only those reaction channels expected to contribute to the overall reaction under atmospheric conditions.

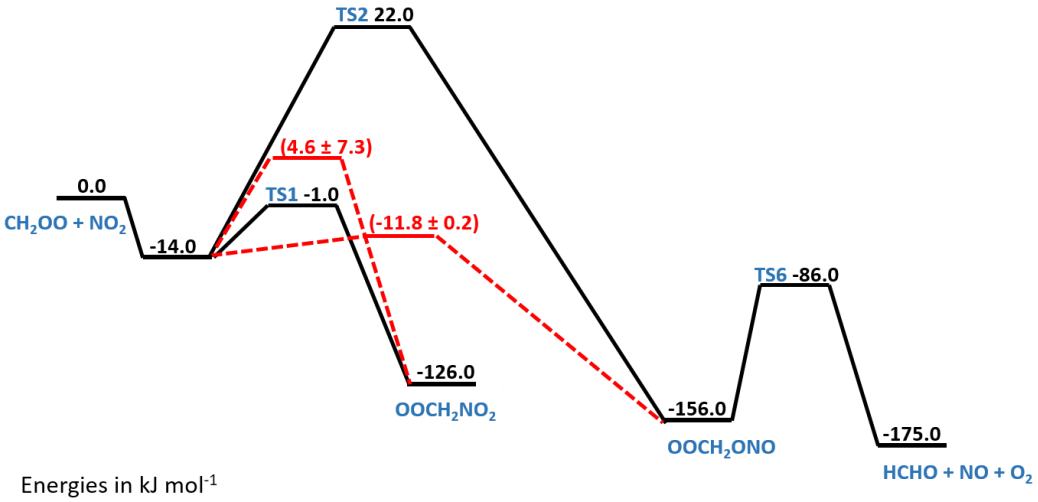

Figure 5.29. Simplified potential energy surface for the reaction between $CH_2OO + NO_2$ based on the results reported by Vereecken and Nguyen. Solid lines and values in black show the surface reported by Vereecken and Nguyen.[12] Dashed lines and values in red show the result obtained by fitting the barrier heights for TS1 and TS2 to the experimental observations made in this work using MESMER.

Geometries, vibrational frequencies, and rotational constants required as inputs for each species considered were obtained from calculations performed at the M06-2X/cc-pVTZ level of theory in Gaussian09 using the optimised geometries reported by Vereecken and Nguyen as the initial structure for each species. Hindered rotation potentials for the transition states were obtained from M06-2X/6-31+G** relaxed scans along the relevant dihedral coordinates. Hindered rotor state densities were calculated in MESMER using the methodology described in previous work.[21] It should be noted that the intention of the electronic structure and hindered rotor calculations was not to attempt improvements to the work of Vereecken and Nguyen, as the calculations were performed at a lower level of theory, but to provide appropriate inputs with a physical basis for the MESMER calculations. Previous calculations indicated substantial multi-reference character in the entrance channel transition states. Furthermore the energies in the region of TS1 and TS2 (Figure 5.29) were shown to be unusually sensitive to the size of the active space used. As such, considerable uncertainty remains regarding this portion of the potential energy surface.

Rate coefficients were calculated in MESMER using a rigid rotor-harmonic oscillator approximation for all but the hindered modes, which were assumed to be separable. Lennard-Jones parameters used to describe collisions with the bath gas were estimated from work by Vereecken *et al.*,[22] with collisional energy transfer described by an exponential down model in which the average energy transferred in a downward direction on collision was represented by the parameter $\langle \Delta E \rangle_{down}$. For calculations reported in this work, a value of 250 cm^{-1} was

used for $\langle \Delta E \rangle_{down}$ which was approximated as being independent of temperature owing to the relatively narrow range of temperatures considered. It is noted that neither the experiments nor the preliminary MESMER calculations suggest any pressure dependence in this system and the calculated rates are therefore insensitive to the collisional energy transfer parameters. The input file for MESMER is provided in Appendix 7.

MESMER calculations were fit to the experimentally determined values for $k_{5.1}$ by varying the barrier heights of TS1 and TS2. In these calculations the energy of TS2 needed to be lowered considerably from 22 to -11.8 ± 0.2 kJ mol^{-1} in order to fit the experimental data. The fits were found to be less sensitive to the value of TS1 returning a fitted value of 4.6 ± 7.3 kJ mol^{-1}. Figure 5.30 shows the comparison between the experimental measurements for $k_{5.1}$ and MESMER fit. At 298 K, the MESMER fit gave $k_{5.1} = 1.1 \times 10^{-12}$ cm^3 molecule^{-1} s^{-1}, in good agreement with the experimental value of $(1.26 \pm 0.11) \times 10^{-12}$ cm^3 molecule^{-1} s^{-1} obtained in this work, and there is no significant pressure dependence in the MESMER result in agreement with the experimental results.

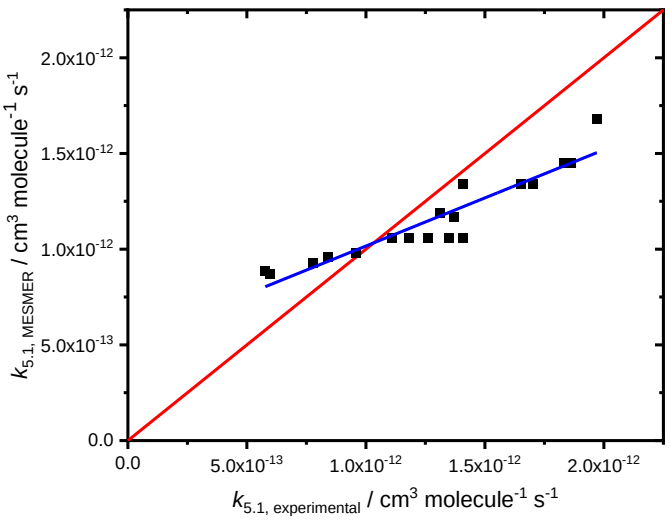

Figure 5.30. Comparison of MESMER fit results and observed values for $k_{5.1}$. The best fit to the trend is given by $k_{5.1,MESMER} = (0.50 \pm 0.04) \times k_{5.1,experimental} + (5.14 \pm 0.62) \times 10^{-13}$ cm^3 molecule^{-1} s^{-1} ($r^2 = 0.87$) and is shown by the solid blue line. The 1:1 line is shown by the solid red line.

The fit agrees well at 298 K and, in contrast to the result reported by Vereecken and Nguyen, is able to reproduce the negative temperature dependence in general terms. Clearly there is substantial uncertainty regarding the energy of TS2 due to the aforementioned multi-reference effects although this has been partially circumvented through fitting this barrier to the experimental data. However, given the submerged nature of TS2 in the fitted model

determined in this work, the theoretical rate coefficients are particularly sensitive to potential inaccuracies in the geometry and thus the vibrational frequencies of TS2 and the lack of fully considering the coupling between hindered rotational modes in the current model.

The MESMER calculations indicate that the reaction between CH_2OO + NO_2 proceeds primarily via TS1, leading to production of the adduct bound via a C-N bond ($O_2CH_2NO_2$ in Figure 5.29) with a 90 % yield at 298 K and 760 Torr. The channel producing HCHO, NO, and O_2 is expected to contribute 10 % of the reaction products at 298 K and 760 Torr, with no significant dependence of product yields on temperature or pressure on the timescales of the reaction. These results are in line with the work of Caravan *et al.*,[9] in which a mass signal consistent with adduct formation was observed. However, earlier work, in which the kinetics of R5.1 were determined via observations of HCHO production indicated that CH_2OO was converted to HCHO with ~ 100 % yield. The kinetics of R5.1 determined through measurements of HCHO production are in good agreement with those determined in this work through direct measurements of CH_2OO, indicating the reliability of the HCHO measurements. In addition, the yields of CH_2OO from CH_2I + O_2 (R5.3) determined in earlier work carried out by Stone *et al.*[3] through measurements of HCHO produced via CH_2OO + NO_2 (R5.1), which assumed 100 % conversion of CH_2OO to HCHO, were in good agreement with the CH_2OO yields determined in a previous study by Stone *et al.*[23] via direct measurements of iodine atom production from R5.2 and R5.3 and of HCHO produced by reactions of CH_2OO with SO_2 and NO, and with results reported by other groups. There is thus an apparent inconsistency between the observed production of HCHO from R5.1 in the earlier work by Stone *et al.*, observations of adduct formation by Caravan *et al.*, and the results of the MESMER calculations reported in this work.

It is possible that the potential energy surface used in the MESMER calculations is incomplete owing to the challenges associated with the calculations described above, and that there is a reaction channel that produces HCHO as the dominant product, with the observed adduct formed as a minor product but at observable concentrations using the sensitive PIMS technique employed by Caravan *et al.* However, the differences could also be rationalised if the adduct $O_2CH_2NO_2$ observed by Caravan *et al.* is the main product, produced via TS1, but undergoes subsequent chemistry on rapid timescales to produce HCHO. Vereecken and Nguyen suggested that the adduct formed via TS1 is stable with respect to unimolecular decomposition but might be expected to react in a similar manner to a peroxy radical, generating OCH_2NO_2 in reactions with species such as NO or peroxy radicals, which would rapidly decompose to produce HCHO and NO_2. While NO is not present in the system, and earlier work suggests that the peroxy radical CH_2IO_2 produced in the system predominantly reacts with NO_2 to produce $CH_2IO_2NO_2$, a reaction of the $O_2CH_2NO_2$ adduct formed in R5.1

with NO_2 could lead to near-complete conversion of CH_2OO to HCHO, consistent with the kinetics and yields measured in earlier work by Stone *et al.*,[3] whilst also enabling observation of low adduct concentrations by the sensitive PIMS technique employed by Caravan *et al.*

5.5.4 Modelling of $O_2CH_2NO_2$

The production of the $O_2CH_2NO_2$ adduct was modelled using Equation 5.6 as a function of NO_2 concentration using the average rate coefficient determined in this work at 298 K ($k_{5.1}$ = (1.26 ± 0.11) × 10^{-12} cm^3 $molecule^{-1}$ s^{-1}) and a typical initial CH_2OO concentration of 1 × 10^{12} molecule cm^{-3}.

$$[O_2CH_2NO_2]_t = \frac{[CH_2OO]_0 k'_{CH_2OO+NO_2}}{(k'_{CH_2OO+NO_2} - k_{adduct-HCHO})} \left\{ exp^{(-k_{adduct-HCHO}t)} - exp^{(-k'_{CH_2OO+NO_2}t)} \right\} \quad \text{(Equation 5.6)}$$

The formation of HCHO from the $O_2CH_2NO_2$ adduct was modelled for a range of pseudo-first-order rate coefficients ($k_{adduct\text{-}HCHO}$). The modelled HCHO was fit to a pseudo-first-order growth (k_{fit}, Equation 5.7) and compared to $k_{5.1}[NO_2]$ as a function of $k_{adduct\text{-}HCHO}$.

$$[HCHO]_t = [CH_2OO]_0 - \left([CH_2OO]_0 \times exp^{-k_{fit}t}\right) \quad \text{(Equation 5.7)}$$

A ratio of k_{fit} / $k_{5.1}[NO_2]$ of ~ 1 (or 1 within experimental uncertainties) indicates that HCHO formation from the $O_2CH_2NO_2$ adduct is sufficiently rapid to give the correct CH_2OO + NO_2 kinetics from the observation of HCHO. Figure 5.31 shows a plot of k_{fit} / $k_{5.1}[NO_2]$ *vs* $k_{adduct\text{-}HCHO}$ which indicates that for an NO_2 concentration of 1 × 10^{14} molecule cm^{-3}, $k_{adduct\text{-}HCHO}$ needs to be greater than 400 s^{-1}, and for an NO_2 concentration of 1.5 × 10^{15} molecule cm^{-3}, $k_{adduct\text{-}HCHO}$ needs to be greater than 7500 s^{-1}. If the reaction taking place is between the $O_2CH_2NO_2$ adduct and NO_2, results indicate a rate coefficient of k = ~ 4 – 5 × 10^{-12} cm^3 $molecule^{-1}$ s^{-1}. A reaction between $O_2CH_2NO_2$ and NO_2 has the potential to lead to the formation of HCHO and NO_3, which could explain the observation of NO_3 in the work of Ouyang *et al.*[7] and reconcile the differences in the reaction products currently reported within the literature.

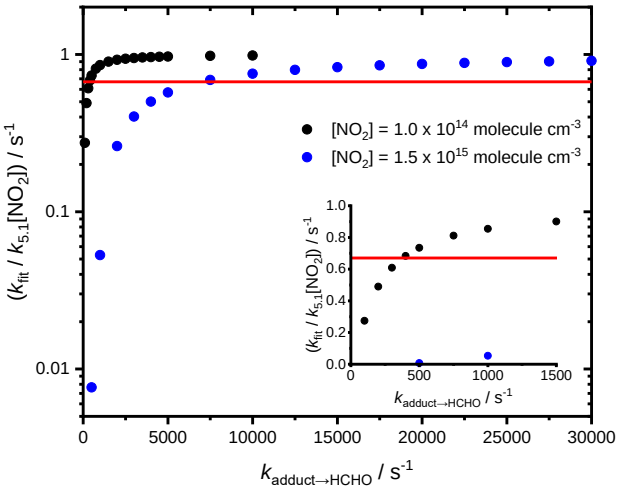

Figure 5.31. k_{fit} / $k_{5.1}[NO_2]$ *vs* $k_{adduct\text{-}HCHO}$, where $[NO_2]$ is equal to either 1×10^{14} molecule cm^{-3} (black) or 1.5×10^{15} molecule cm^{-3} (blue). The red line represents a ratio of 0.67, which indicates the point where HCHO formation from the adduct is fast enough to give the correct $CH_2OO + NO_2$ kinetics from observations of HCHO.[3]

5.6 Concluding Remarks

This work has measured the kinetics of the reaction between the simplest Criegee intermediate CH_2OO and NO_2 at temperatures between 242 and 353 K and pressures in the range 25 to 300 Torr. Experimental measurements show that the kinetics are independent of pressure, over the range investigated, with a mean value of $(1.26 \pm 0.11) \times 10^{-12}$ cm^3 molecule^{-1} s^{-1} at 298 K and a negative temperature dependence described by $(1.06 \pm 0.02) \times 10^{-12} \times (T/298)^{-(2.9\pm0.2)}$ cm^3 molecule^{-1} s^{-1}.

The experimentally determined negative temperature dependence of $k_{5.1}$ contrasts with an earlier theoretical prediction of a weak positive temperature dependence, which was impacted by the significant multi-reference character of the reaction. Calculations in this work using the Master Equation Solver for Multi-Energy well Reactions (MESMER) are able to reproduce a negative temperature dependence by reducing the calculated barrier heights for the reaction, but a significant discrepancy remains between measured and calculated rate coefficients.

Capabilities for accurate prediction of reaction kinetics are critical for many areas, including atmospheric chemistry, combustion, and astrochemistry, particularly when reactions of interest or conditions required present significant experimental challenges. The application of theoretical approaches to understand the chemistry of Criegee intermediates has gained significant attention in recent years owing to increased awareness of the potential role of Criegee intermediates in the atmosphere, and the use of theory has provided a basis for

understanding the behaviour and reactivity of Criegee intermediates. Notably, theory has also been used to help develop structure activity relationships (SARs) for Criegee intermediate reactions and reaction conditions that have yet to be studied experimentally. If the results of SARs and predictions based on theoretical approaches are to be used in numerical models to evaluate atmospheric composition for applications relating to air quality and climate, it is essential that such approaches are reliable. This work highlights a significant discrepancy between experimental measurements and theory, indicating a continued need for experimental measurements, both for direct application and for providing a means to test the validity of theoretical approaches, as well as care when applying theory, particularly when reaction systems have significant multi-reference character.

Uncertainties remain in the product yields of the reaction, but apparent discrepancies between observations of HCHO in previous work and the observation of an adduct between CH_2OO and NO_2 can be rationalised if the adduct reacts rapidly to produce HCHO. Further studies of product yields would be beneficial. The atmospheric implications are discussed in Chapter 8.

5.7 References

1. Welz, O., Savee, J.D., Osborn, D.L., Vasu, S.S., Percival, C.J., Shallcross, D.E. and Taatjes, C.A. Direct Kinetic Measurements of Criegee Intermediate (CH_2OO) Formed by Reaction of CH_2I with O_2. *Science.* 2012, **335**(6065), p.204.
2. Atkinson, R., Baulch, D.L., Cox, R.A., Crowley, J.N., Hampson, R.F., Hynes, R.G., Jenkin, M.E., Rossi, M.J., Troe, J. and Wallington, T.J. Evaluated kinetic and photochemical data for atmospheric chemistry: Volume IV – gas phase reactions of organic halogen species. *Atmos. Chem. Phys.* 2008, **8**(15), pp.4141-4496.
3. Stone, D., Blitz, M., Daubney, L., Howes, N.U.M. and Seakins, P. Kinetics of CH_2OO reactions with SO_2, NO_2, NO, H_2O and CH_3CHO as a function of pressure. *Physical Chemistry Chemical Physics.* 2014, **16**(3), pp.1139-1149.
4. Qiu, J. and Tonokura, K. Detection of the simplest Criegee intermediate CH_2OO in the ν4 band using a continuous wave quantum cascade laser and its kinetics with SO_2 and NO_2. *Chemical Physics Letters.* 2019, **737**, p.100019.
5. Luo, P.-L., Chung, C.-A. and Lee, Y.-P. Rate coefficient of the reaction CH_2OO + NO_2 probed with a quantum-cascade laser near 11 μm. *Physical Chemistry Chemical Physics.* 2019, **21**(32), pp.17578-17583.
6. Presto, A.A. and Donahue, N.M. Ozonolysis Fragment Quenching by Nitrate Formation: The Pressure Dependence of Prompt OH Radical Formation. *The Journal of Physical Chemistry A.* 2004, **108**(42), pp.9096-9104.

7. Ouyang, B., McLeod, M.W., Jones, R.L. and Bloss, W.J. NO_3 radical production from the reaction between the Criegee intermediate CH_2OO and NO_2. *Physical Chemistry Chemical Physics.* 2013, **15**(40), pp.17070-17075.

8. Lewis, T.R., Blitz, M.A., Heard, D.E. and Seakins, P.W. Direct evidence for a substantive reaction between the Criegee intermediate, CH_2OO, and the water vapour dimer. *Physical Chemistry Chemical Physics.* 2015, **17**(7), pp.4859-4863.

9. Caravan, R.L., Khan, M.A.H., Rotavera, B., Papajak, E., Antonov, I.O., Chen, M.-W., Au, K., Chao, W., Osborn, D.L., Lin, J.J.-M., Percival, C.J., Shallcross, D.E. and Taatjes, C.A. Products of Criegee intermediate reactions with NO_2: experimental measurements and tropospheric implications. *Faraday Discussions.* 2017, **200**(0), pp.313-330.

10. Chambers, R., Heard, A. and Wayne, R.J.T.J.o.P.C. Inorganic gas-phase reactions of the nitrate radical: iodine+ nitrate radical and iodine atom+ nitrate radical. 1992, **96**(8), pp.3321-3331.

11. Mir, Z.S., Lewis, T.R., Onel, L., Blitz, M.A., Seakins, P.W. and Stone, D. CH_2OO Criegee intermediate UV absorption cross-sections and kinetics of CH_2OO + CH_2OO and CH_2OO + I as a function of pressure. *Physical Chemistry Chemical Physics.* 2020, **22**(17), pp.9448-9459.

12. Vereecken, L. and Nguyen, H.M.T. Theoretical Study of the Reaction of Carbonyl Oxide with Nitrogen Dioxide: CH_2OO + NO_2. *International Journal of Chemical Kinetics.* 2017, **49**(10), pp.752-760.

13. Qiu, J. and Tonokura, K. Detection of the simplest Criegee intermediate CH_2OO in the ν4 band using a continuous wave quantum cascade laser and its kinetics with SO_2 and NO_2. *Chemical Physics Letters: X.* 2019, **2**, p.100019.

14. Harwood, M.H., Burkholder, J.B., Hunter, M., Fox, R.W. and Ravishankara, A.R. Absorption Cross Sections and Self-Reaction Kinetics of the IO Radical. *The Journal of Physical Chemistry A.* 1997, **101**(5), pp.853-863.

15. Atkinson, R., Baulch, D.L., Cox, R.A., Hampson, R.F., Jr., Kerr, J.A., Rossi, M.J. and Troe, J. Evaluated Kinetic and Photochemical Data for Atmospheric Chemistry: Supplement VIII, Halogen Species Evaluation for Atmospheric Chemistry. *Journal of Physical and Chemical Reference Data.* 2000, **29**(2), pp.167-266.

16. Himmelmann, S., Orphal, J., Bovensmann, H., Richter, A., Ladstätter-Weissenmayer, A. and Burrows, J.P. First observation of the OIO molecule by time-resolved flash photolysis absorption spectroscopy. *Chemical Physics Letters.* 1996, **251**(5), pp.330-334.

17. Atkinson, R., Baulch, D.L., Cox, R.A., Crowley, J.N., Hampson, R.F., Hynes, R.G., Jenkin, M.E., Rossi, M.J. and Troe, J. Evaluated kinetic and photochemical data for

atmospheric chemistry: Volume III - gas phase reactions of inorganic halogens. *Atmospheric Chemistry and Physics.* 2007, **7**(4), pp.981-1191.

18. Bröske, R. *Kinetische und spektroskopische Untersuchungen von Nitrylhalogeniden, Halogennitriten und Halogennitraten*. thesis, University of Wuppertal, Germany, 2000.
19. Spietz, P., Gómez Martín, J.C. and Burrows, J.P. Spectroscopic studies of the I_2/O_3 photochemistry: Part 2. Improved spectra of iodine oxides and analysis of the IO absorption spectrum. *Journal of Photochemistry and Photobiology A: Chemistry.* 2005, **176**(1), pp.50-67.
20. S.P. Sander, J.A., J.R. Burkholder. R.R. Freidl, D.M. Golden, R.E. Huie, C.E. Kolb, M.J. Kurylo, G.K. Moortgat, V.L. Orkin, P.H. Wine. Chemical Kinetics and Photochemical Data for Use in Atmospheric Studies, Evaluation Number 17. *JPL publication 10-6.* 2011.
21. Sharma, S., Raman, S. and Green, W.H. Intramolecular Hydrogen Migration in Alkylperoxy and Hydroperoxyalkylperoxy Radicals: Accurate Treatment of Hindered Rotors. *The Journal of Physical Chemistry A.* 2010, **114**(18), pp.5689-5701.
22. Vereecken, L., Harder, H. and Novelli, A. The reaction of Criegee intermediates with NO, RO_2, and SO_2, and their fate in the atmosphere. *Physical Chemistry Chemical Physics.* 2012, **14**(42), pp.14682-14695.
23. Stone, D., Blitz, M., Daubney, L., Ingham, T. and Seakins, P. CH_2OO Criegee biradical yields following photolysis of CH_2I_2 in O_2. *Physical Chemistry Chemical Physics.* 2013, **15**(44), pp.19119-19124.

Chapter 6

Kinetics of the Reactions of CH_2OO with Water as a Function of Temperature

Reactions with water vapour are expected to dominate the atmospheric chemistry of the simplest SCI, CH_2OO, but there is uncertainty over the role of the water monomers (H_2O, R6.1), water dimers ($(H_2O)_2$, R6.2), or potentially water trimers ($(H_2O)_3$, R6.3). There are currently a wide range of values reported for the kinetics of R6.1[1-5] and R6.2[4-8] and only one previous study to report the kinetics of R6.3.[5] There are also significant uncertainties regarding the products and product yields.[9-13]

$CH_2OO + H_2O \rightarrow$ Products (R6.1)

$CH_2OO + (H_2O)_2 \rightarrow$ Products (R6.2)

$CH_2OO + (H_2O)_3 \rightarrow$ Products (R6.3)

This chapter provides an overview of previous direct studies of the kinetics of CH_2OO in the presence of water vapour and gives results for a study of the temperature dependence of the reactions between CH_2OO and water vapour.

The results presented throughout this chapter have been submitted for publication in the *Environmental Science: Atmospheres* Journal. Lade, R.E., Blitz, M.A., Rowlingson, M., Evans, M.J., Seakins, P.W., Stone, D. Kinetics of the Reactions of the Criegee Intermediate CH_2OO with Water Vapour: Experimental Measurements as a Function of Temperature and Global Atmospheric Modelling. *Environmental Science: Atmospheres.* 2024.

6.1 Literature Studies

Welz *et al.*[1] produced CH_2OO following the 248 nm laser flash photolysis of CH_2I_2 and directly monitored its reaction with water vapour using tuneable VUV synchrotron PIMS at a total pressure of 4 Torr. Welz *et al.* observed no significant change in the decay of CH_2OO on addition of water vapour at concentrations up to 3.1×10^{16} molecule cm^{-3}, leading to the conclusion of an upper limit for $k_{6.1}$ of 4×10^{-15} cm^3 $molecule^{-1}$ s^{-1} at 298 K.

Photolytic production of CH_2OO was also used by Stone *et al.*[2] in a series of experiments monitoring the production of HCHO from CH_2OO reactions via LIF. No significant change in the rate of HCHO production was observed on addition of water vapour at concentrations up to 1.7×10^{17} molecule cm^{-3} at a total pressure of 200 Torr, with a small change in HCHO yield attributed to fluorescence quenching by water and results indicating an upper limit of 9×10^{-17} cm^3 $molecule^{-1}$ s^{-1} for $k_{6.1}$ at 295 K.

The effects of water vapour on CH_2OO chemistry have also been investigated in studies of ozonolysis reactions through the competition with the reaction of CH_2OO with SO_2.[6, 7] Berndt *et al.*[14] monitored the production of sulfuric acid, which is produced rapidly following the production of SO_3 via $CH_2OO + SO_2$,[15-17] during ethene ozonolysis experiments conducted in a flow tube at 293 K over a range of water vapour concentrations. A quadratic relationship was observed between the rate coefficient describing the loss of CH_2OO and the water monomer concentration, with a linear relationship demonstrated with the concentration of water dimers, $(H_2O)_2$, indicating that the dominant reaction of CH_2OO is with water dimers (R6.2) rather than water monomers (R6.1). Berndt *et al*. reported a value of $k_{6.2} = (1.07 \pm 0.04) \times 10^{-11}$ cm^3 molecule^{-1} s^{-1}. Later work by Berndt *et al*.[3] investigated the kinetics of CH_2OO reactions in the presence of water vapour using a free-jet flow system at 297 K by detecting H_2SO_4 formed following the reaction of CH_2OO with SO_2, and reported $k_{6.1} = (3.2 \pm 1.2) \times 10^{-16}$ cm^3 molecule^{-1} s^{-1}. Newland *et al.*[4] also investigated the impact of water vapour on $CH_2OO + SO_2$ by monitoring the consumption of SO_2 in ethene ozonolysis experiments at the EUPHORE atmospheric simulation chamber, with results also indicating a more rapid reaction of CH_2OO with water dimers than water monomers and giving $k_{6.1} = (1.2 \pm 0.4) \times 10^{-15}$ cm^3 molecule^{-1} s^{-1} and $k_{6.2} = (5.2 \pm 6.7) \times 10^{-13}$ cm^3 molecule^{-1} s^{-1} at 298 K using the current IUPAC recommendation of 3.7×10^{-11} cm^3 molecule^{-1} s^{-1} for the rate coefficient for the reaction of CH_2OO with SO_2.

Direct measurements of CH_2OO have also been made in the presence of excess water vapour using laser flash photolysis of $CH_2I_2/O_2/N_2/H_2O$ mixtures coupled with time-resolved broadband UV absorption spectroscopy.[13, 18] Results from several studies have now demonstrated a quadratic dependence of the pseudo-first-order rate coefficient describing the loss of CH_2OO on the water monomer concentration[13, 18-20] thus also indicating that the reaction of CH_2OO with water dimers dominates over reaction with water monomers. Lewis *et al*.[19] reported a rate coefficient for reaction of CH_2OO with water dimers of $(4.0 \pm 1.2) \times 10^{-12}$ cm^3 molecule^{-1} s^{-1} at 294 K, with no significant dependence on pressure in the range 50 to 400 Torr. Chao *et al.*[18] reported a value for $k_{6.2}$ of $(6.5 \pm 0.8) \times 10^{-12}$ cm^3 molecule^{-1} s^{-1} at 298 K that also showed no significant dependence on pressure between 100 and 500 Torr.

The temperature dependence of $k_{6.2}$ was subsequently investigated by Smith *et al.*[20] using UV absorption spectroscopy between 283 and 324 K, with results giving $k_{6.2} = (7.4 \pm 0.6) \times 10^{-12}$ cm^3 molecule^{-1} s^{-1} at 298 K, in agreement with the work of Chao *et al.*,[18] and a negative temperature dependence.[21] Further experiments have been performed using UV absorption spectroscopy by Wu *et al*.[5] at temperatures between 290 and 346 K, which led to the conclusion that observed kinetics of CH_2OO removal in the presence

of water vapour result from a combination of reactions with water monomers, dimers, and trimers. Experiments by Wu *et al.* were carried out at higher relative humidities than those employed in other studies, reaching close to 100 % at each temperature investigated, and Wu *et al.* reported that the measurements at the highest relative humidity correspond to reaction with the water trimer, with experiments at low relative humidity providing information relating to the reaction with the water monomer. Wu *et al.* reported a positive temperature dependence for the reaction of CH_2OO with the water monomer, and a negative temperature dependence for the reaction of CH_2OO with water dimers that is in broad agreement with the behaviour observed by Smith *et al*. The reaction with water trimers also displayed a negative temperature dependence, with results indicating that water trimers could play an important role at high relative humidities at temperatures of 298 K and below but becoming insignificant at higher temperatures.

There is a growing consensus that the chemistry of CH_2OO in the presence of water vapour is rapid, with a significant role for a reaction with water dimers, which, despite low water dimer concentrations ($[H_2O] = 3.8 \times 10^{17}$ molecule cm^{-3} and $[(H_2O)_2] = 3.0 \times 10^{14}$ molecule cm^{-3} for a relative humidity of 50 % at 298 K) compared to water monomers in the atmosphere, is likely to dominate atmospheric losses of CH_2OO. Although the study by Welz *et al.*[1] did not observe any evidence for the reaction between CH_2OO and water dimers, the water dimer concentrations at the low pressure (4 Torr) used by Welz *et al.* would have limited the impact of the reaction. The HCHO LIF experiments performed by Stone *et al.*[2] did enable the use of higher water vapour concentrations, and thus significant water dimer concentrations, however, the impact of water vapour on production of HCHO may have been limited if HCHO is not a direct product of CH_2OO reactions with water vapour, and the reduction in HCHO signal which was attributed to quenching may have resulted from the production of other products. Product studies in ozonolysis reactions have reported the formation of HCHO, among other potential products,[11, 22] but more recent time-resolved product measurements using laser flash photolysis of CH_2I_2/O_2 in the presence of water vapour have observed production of hydroxymethyl hydroperoxide ($HOCH_2OOH$, HMHP) by rotational spectroscopy[23] and PIMS,[13] with the PIMS study indicating HMHP as the dominant product of R6.1 and R6.2.[13] Theory[24-34] has also indicated that HMHP is a major product of R6.1 and R6.2, and supports the experimental results which suggest the dominant reaction is with water dimers. Subsequent chemistry of HMHP can lead to the production of formic acid (HCOOH), H_2O_2, and HCHO, which has been investigated by Nguyen *et al.*[11] using measurements made in an atmospheric simulation chamber at 295 K and 1 atm at relative humidities between 4 and 76 %. Measurements of HCHO, OH and HO_2 were made in the chamber using LIF,[35] while hydroperoxides (such as HMHP) and acids (such as HCOOH) were measured by chemical

ionisation mass spectrometry (CIMS). At relative humidities below ~ 40 %, HMHP was observed to be the dominant product, followed by HCOOH and H_2O_2. However, at relative humidities above ~ 40 %, Nguyen *et al.* observed a significant decrease in the yield of HMHP, accompanied by an increase in the yield of HCOOH. Modelling of the observed yields for HMHP and HCOOH led to the conclusion that R6.1 leads to production of 73 % HMHP, 21 % HCOOH + H_2O, and 6 % HCHO + H_2O_2, while R6.2 leads to production of 54 % HCOOH + H_2O, 40 % HMHP, and 6 % HCHO + H_2O_2. The product distribution reported by Nguyen *et al.* forms the basis for current mechanism adopted in the global atmospheric chemistry transport model (CTM) GEOS-Chem.

There is general agreement regarding the atmospheric significance of CH_2OO reactions involving water, but there are discrepancies in product distributions and measured kinetics at room temperature, and the temperature dependence of the kinetics has only been investigated over a relatively narrow temperature range. In this work we report the results of experiments performed using laser flash photolysis of $CH_2I_2/O_2/N_2/H_2O$ mixtures coupled with time-resolved broadband UV absorption spectroscopy at temperatures in the range 262 to 353 K at 760 Torr.

6.2 Experimental

The kinetics of CH_2OO loss in the presence of water vapour have been studied as a function of temperature between 262 and 353 K at 760 Torr, using the experimental apparatus described in Chapter 3.

Water vapour was added to the system by passing a known flow of N_2 gas through a bubbler containing deionised water held in a water bath at 70 ^{o}C. The concentration of water vapour was measured at the exit of the reaction cell by a relative humidity (RH) probe (Michell Instruments PCMini52) that was calibrated against a dew point hygrometer (Buck Research Instruments, CR-4 chilled mirror hygrometer) (see Appendix 2). Experiments were performed under pseudo-first-order conditions, with the lowest water dimer concentration at least five times greater than the concentration of CH_2OO. Initial concentrations were: $[H_2O] = (0 – 5.5) \times 10^{17}$ molecule cm^{-3}, $[CH_2I_2] = (3.8 – 6.4) \times 10^{13}$ molecule cm^{-3}, $[O_2] = (1.2 – 2.7) \times 10^{18}$ molecule cm^{-3} and $[CH_2OO]_0 = (2.0 – 8.3) \times 10^{11}$ molecule cm^{-3}.

The pulse repetition rate was set at 0.075 Hz to ensure there was enough time for a fresh gas mixture to be introduced to the reaction cell before the laser fired again. The effective pathlength for these experiments was determined to be $l = (595 \pm 53)$ cm. More details of the experimental procedure are given in Chapter 3.

6.3 Results and Discussion

Figure 6.1 shows a typical absorbance spectrum observed following photolysis, which contains contributions from CH_2OO, the CH_2I_2 precursor and iodine monoxide (IO) radicals.

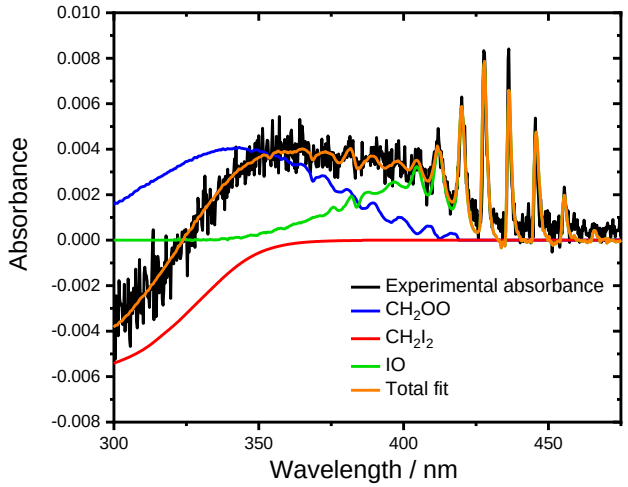

Figure 6.1. Observed absorbance (black), total fit (orange) and individual contributions of CH_2OO,[36] CH_2I_2[37] and IO[38] obtained by performing a least squares fit of reference cross-sections to the observed absorbance at t = 1 ms after photolysis at p = 760 Torr, T = 298 K, and $[CH_2I_2]_0 = 4.1 \times 10^{13}$ molecule cm^{-3}. $[CH_2OO]_t = 6.4 \times 10^{11}$ molecule cm^{-3}, $\Delta[CH_2I_2]_t = -3.8 \times 10^{12}$ molecule cm^{-3} and $[IO]_t = 7.3 \times 10^{11}$ molecule cm^{-3}.

Figures 6.2 and 6.3 show typical concentration-time profiles for both CH_2I_2 and IO obtained in this work.

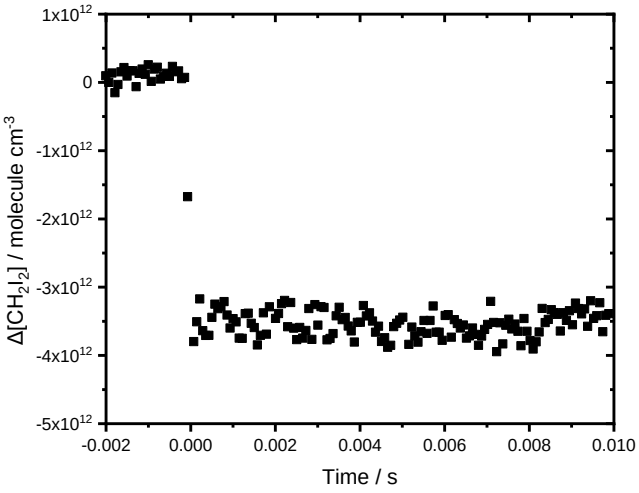

Figure 6.2. Concentration-time profile for CH_2I_2 for an experiment at 760 Torr and 298 K. For these data, $[H_2O] = 0$, $[CH_2I_2]_0 = 4.1 \times 10^{13}$ molecule cm^{-3} and $\Delta[CH_2I_2] = -3.5 \times 10^{12}$ molecule cm^{-3}.

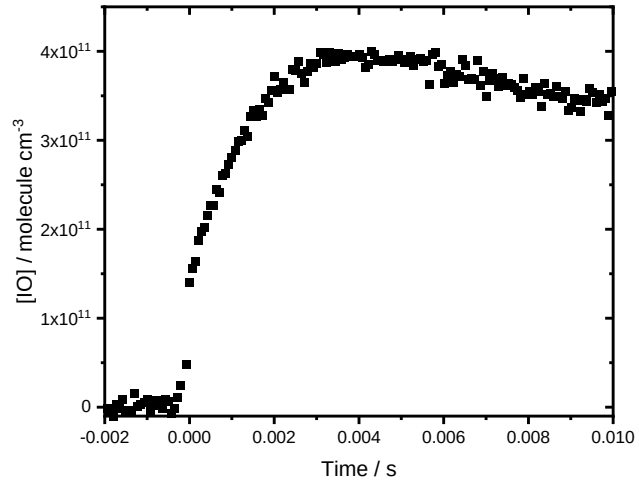

Figure 6.3. Concentration-time profile for IO for an experiment at 760 Torr and 298 K. For these data, $[H_2O] = 0$ and $[CH_2I_2]_0 = 4.1 \times 10^{13}$ molecule cm^{-3}.

Figure 6.4 shows typical concentration-time profiles for CH_2OO for a range of water vapour concentrations, demonstrating a more rapid loss of CH_2OO as the water vapour concentration is increased. Experiments were performed under pseudo-first-order conditions, with water vapour concentrations in excess over CH_2OO and the temporal behaviour of CH_2OO thus described by Equation 6.1.

$$[CH_2OO]_t = [CH_2OO]_0 exp^{-k't}$$ (Equation 6.1)

where k' represents the sum of the rate coefficients describing the loss of CH_2OO (Equation 6.2):

$$k' = k_x + k'_{6.1} + k'_{6.2} + k'_{6.3}$$ (Equation 6.2)

The rate coefficient k_x represents the loss of CH_2OO in the absence of water, $k'_{6.1}$ represents the loss of CH_2OO as a result of its reaction with the water monomer (Equation 6.3), $k'_{6.2}$ represents the loss of CH_2OO due to its reaction with the water dimer (Equation 6.4) and $k'_{6.3}$ represents the loss of CH_2OO due to its reaction with the water trimer (Equation 6.5):

$$k'_{6.1} = k_{6.1}[H_2O]$$ (Equation 6.3)

$$k'_{6.2} = k_{6.2}[(H_2O)_2]$$ (Equation 6.4)

$$k'_{6.3} = k_{6.3}[(H_2O)_3]$$ (Equation 6.5)

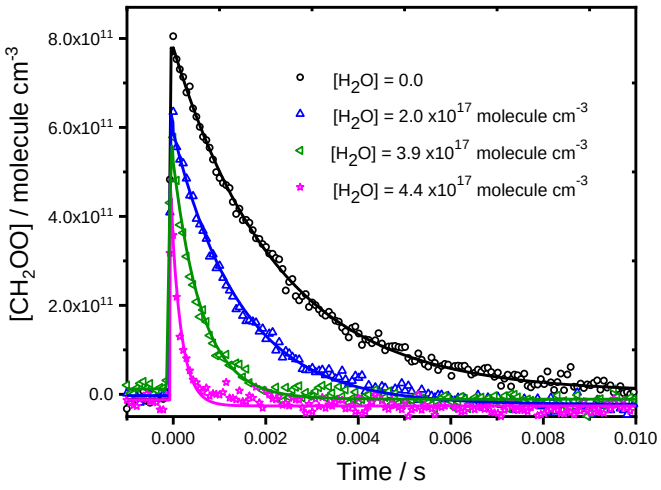

Figure 6.4. Concentration – time profiles showing the CH_2OO decay, in the presence and absence of water vapour, at p = 760 Torr and T = 298 K. Solid lines represent an unweighted fit to Equation 6.1 convoluted with the instrument response function. For $[H_2O]$ = 0, the fit gave $[CH_2OO]_0$ = 8.3 × 10^{11} molecule cm^{-3} and k' = (313 ± 7) s^{-1}; for $[H_2O]$ = 2.0 × 10^{17} molecule cm^{-3}, the fit gave $[CH_2OO]_0$ = 6.6 × 10^{11} molecule cm^{-3} and k' = (1247 ± 37) s^{-1}; for $[H_2O]$ = 3.9 × 10^{17} molecule cm^{-3}, the fit gave $[CH_2OO]_0$ = 5.8 × 10^{11} molecule cm^{-3} and k' = (2669 ± 120) s^{-1} and for $[H_2O]$ = 4.4 × 10^{17} molecule cm^{-3}, the fit gave $[CH_2OO]_0$ = 5.7 × 10^{11} molecule cm^{-3} and k' = (3722 ± 245) s^{-1}. Instrument response parameters were: t_c = – (8.80 ± 0.32) × 10^{-5} s and w = (2.85 ± 0.45) × 10^{-5} (further details regarding the instrument response function are given in Section 3.3.4.1). Uncertainties are 1σ.

Figure 6.5 compares fitting a typical concentration-time profile for CH_2OO with the first-order model and the mixed first- and second-order model. Results show less than 5 % difference between the first-order component obtained from each fit, and we concluded that the data were well-described by pseudo-first-order kinetics.

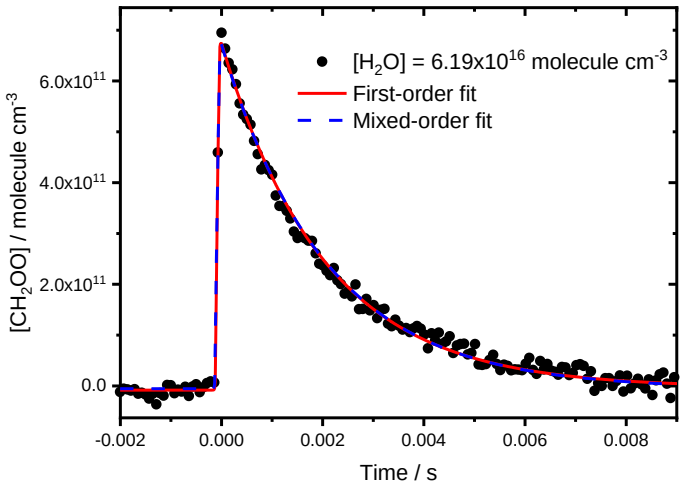

Figure 6.5. Comparison between a first-order fit (red) and mixed-order fit (blue) for data at 324 K and 760 Torr. The first-order fit gave: k' = (728 ± 14) s^{-1}, $[CH_2OO]_0 = (7.05 \pm 0.07) \times 10^{11}$ molecule cm^{-3}, t_c = – (8.80 ± 0.32) × 10^{-5} s and $w = (2.85 \pm 0.45) \times 10^{-5}$ s. The mixed-order fit gave: k' = (703 ± 10) s^{-1}, $k'' = (9.18 \pm 0.33) \times 10^{-11}$ cm^3 $molecule^{-1}$ s^{-1}, $[CH_2OO]_0 = (7.20 \pm 0.22) \times 10^{11}$ molecule cm^{-3}, t_c = – (1.10 ± 0.13) × 10^{-4} s and $w = (3.30 \pm 0.75) \times 10^{-5}$ s. Uncertainties are 1σ.

The observed pseudo-first-order rate coefficients, k', obtained by fitting with Equation 6.1, display a non-linear dependence on the water vapour concentration, as shown in Figure 6.6. Fits to Equation 6.2 for data obtained at 298 K were insensitive to $k_{6.1}$ and $k_{6.3}$ indicating that losses of CH_2OO owing to reaction with water monomers and trimers were insignificant under the conditions employed in this work. Subsequent fits to the data were performed to determine k_x and $k_{6.2}$, with $k_{6.1}$ and $k_{6.3}$ set to zero.

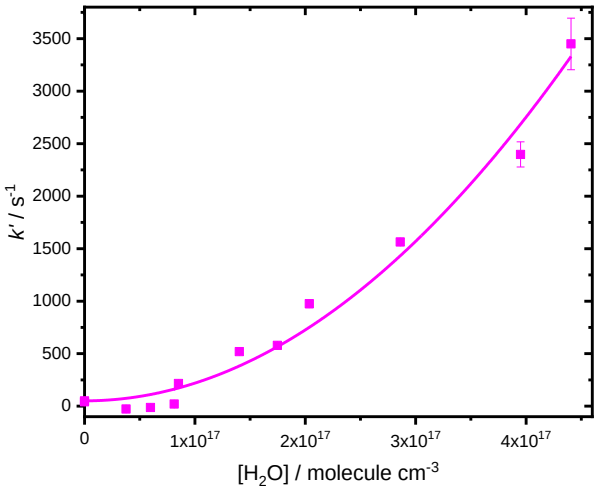

Figure 6.6. Pseudo-first-order rate coefficients as a function of water monomer concentration for experiments carried out at 298 K. The solid line represents an unweighted fit to Equation 6.2 with $k_{6.1}$ and $k_{6.3}$ set to zero. The error bars represent the error in the exponential fit to Equation 6.1. The fit gave $k_{6.2}K_{eq} = (1.69 \pm 0.07) \times 10^{-32}$ cm^6 molecule^{-2} s^{-1} and $k_x = (51 \pm 54)$ s^{-1}.

Similar behaviour has been observed in previous work,[14, 18, 19, 39] with the non-linear dependence attributed to reaction of CH_2OO with water dimers (R6.2) dominating over the reaction of CH_2OO with water monomers (R6.1) and water trimers (R6.3), which leads to a quadratic dependence of k' on the water monomer concentration owing to the equilibrium between the water monomer and dimer (R6.4, Equations 6.6 & 6.7):

$2\ H_2O \rightleftharpoons (H_2O)_2$ (R6.4)

$$K_{eq} = \frac{[(H_2O)_2]}{[H_2O]^2}$$ (Equation 6.6)

$$[(H_2O)_2] = K_{eq}\,[H_2O]^2$$ (Equation 6.7)

(i.e. At 298 K, $K_{eq} = 0.501$ bar^{-1}.[40] For RH = 50%, $[H_2O] = 0.016$ bar and $[(H_2O)_2]$ is calculated to be 1.25×10^{-5} bar, which is equivalent to 3.02×10^{14} molecule cm^{-3}).

Equation 6.2 can thus be described explicitly in terms of water monomer, dimer and trimer concentrations (Equations 6.2-6.5), or in terms of water monomer concentrations and the equilibrium constant for dimer and trimer formation (Equations 6.8-6.9).

$$k'_{6.2} = k_{6.2}K_{eq}[H_2O]^2 \quad \text{(Equation 6.8)}$$

$$k'_{6.3} = k_{6.3}K_{eq}[H_2O]^3 \quad \text{(Equation 6.9)}$$

where $k_{6.2}K_{eq}$ and $k_{6.3}K_{eq}$ can be used as effective rate coefficients which removes the need for explicit calculation of the water dimer and trimer concentrations, and allows for simpler parameterisation of the kinetics for use in atmospheric models.

Figure 6.7 represents the data in terms of the linear dependence on the water dimer concentration (Equations 6.2 and 6.4).

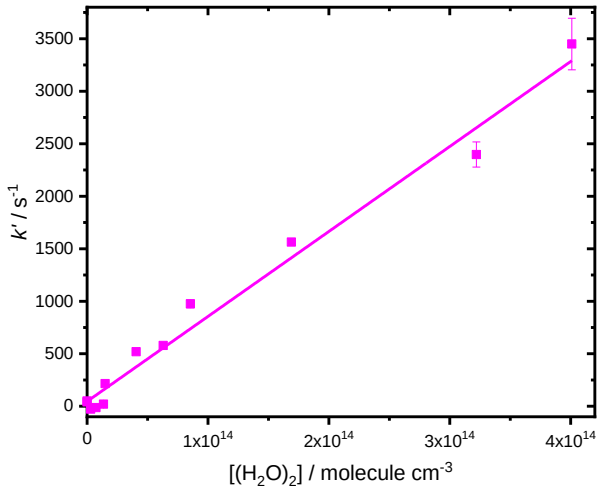

Figure 6.7. Pseudo-first-order rate coefficients as a function of water dimer concentration for experiments carried out at 298 K. The solid line represents an unweighted fit to Equation 6.4. The error bars represent the error in the exponential fit to Equation 6.1. The fit gave $k_{6.2} = (8.09 \pm 0.63) \times 10^{-12}$ cm^3 molecule^{-1} s^{-1} and $k_x = (46 \pm 148)$ s^{-1}.

Where dimer concentrations are given in this work, and used to describe the kinetics of R6.2 in terms of dimer concentrations (i.e. Figure 6.7), the equilibrium constant for water dimer formation reported by Ruscic *et al.*[40] has been used. When comparing previous experimental investigations of this reaction, it is noted that some studies[14, 19] utilise K_{eq} values reported by Scribano *et al.*,[41] whereas others,[5, 18, 20] use K_{eq} values reported by Ruscic *et al.*[40]

Table 6.1 compares the K_{eq} values reported by Scribano *et al.* and Ruscic *et al.* for a range of temperatures and demonstrates the differences in calculated water dimer concentrations using the different values for K_{eq}. The differences in calculated water dimer concentrations impact calculated values for CH_2OO kinetics with water dimers if the kinetics are described in terms of the water dimer concentration directly (i.e. using *rate* = $k_{6.2}[CH_2OO][(H_2O)_2]$), leading to errors of up to 25 % if the reference for K_{eq} is not consistent with that used in this work.

When describing the kinetics of the reaction of CH_2OO with water dimers in terms of water monomer concentrations (i.e. using $rate = k_{6.2}K_{eq}[CH_2OO][H_2O]^2$), values for $k_{6.2}K_{eq}$ reported in this work can be used directly, without need to calculate K_{eq} separately, thereby reducing the potential for introducing errors in the calculated kinetics.

T / K	[H_2O] / molecule cm^{-3}	K_{eq} / bar^{-1} (Scribano *et al.* [41])	[$(H_2O)_2$] / molecule cm^{-3}	k' / s^{-1}	K_{eq} / bar^{-1} (Ruscic *et al.*[40])	[$(H_2O)_2$] / molecule cm^{-3}	k' / s^{-1}	k'_{Ruscic} / $k'_{Scribano}$
262	7.23×10^{16}	0.1471	2.78×10^{13}	803	0.1194	2.25×10^{13}	650	0.81
298	7.63×10^{17}	0.0519	1.24×10^{15}	11767	0.0501	1.20×10^{15}	11388	0.97
353	9.80×10^{18}	0.0150	7.02×10^{16}	188136	0.0187	8.75×10^{16}	234500	1.25

Table 6.1. A comparison of the Equilibrium constant, K_{eq}, values reported by Scribano *et al.*[41] and Ruscic *et al.*[40] for water dimer formation at 262, 298 and 353 K, and impacts on calculated water dimer concentrations and pseudo-first-order losses for CH_2OO resulting from reaction with water dimers when described explicitly in terms of water dimer concentrations (i.e. $k' = k_{6.2}[(H_2O)_2]$, using values for $k_{6.2}$ determined at each temperature in this work).

Experiments were repeated at temperatures between 262 and 353 K with results showing a quadratic dependence of k' on the water monomer concentration across all temperatures (Figure 6.8).

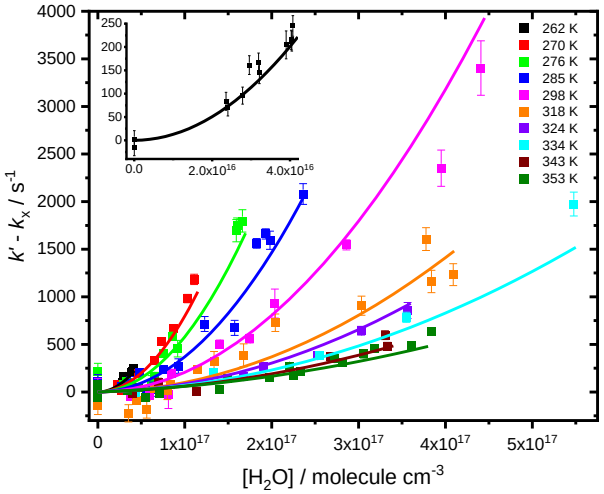

Figure 6.8. Pseudo-first-order rate coefficients as a function of water monomer concentration for experiments carried out at 760 Torr and temperatures between 262 and 353 K. The solid lines represent an unweighted fit to Equation 6.2, with $k_{6.3}$ set to zero. The error bars represent the error in the exponential fit to Equation 6.1. The inset shows data from experiments carried out at 262 K for clarity.

Global fits to Equation 6.2 were performed over all relative humidities and temperatures studied in this work, enabling $k_{6.1}$ to be better defined from data obtained at higher temperatures. Fits were insensitive to $k_{6.3}$ indicating that losses of CH_2OO owing to reaction with water trimers were insignificant under the conditions employed in this work. Subsequent fits to the data were performed to determine k_x, $k_{6.1}$ and $k_{6.2}$, with $k_{6.3}$ set to zero. The final fits (shown in Figure 6.8) gave $k_{6.1} = (3.15 \pm 1.06) \times 10^{-13}\ exp(-(2405 \pm 265)/T)$ cm^3 molecule^{-1} s^{-1} and $k_{6.2}K_{eq} = (2.78 \pm 0.28) \times 10^{-38}\ exp((4012 \pm 400)/T)$ cm^6 molecule^{-2} s^{-1}, where uncertainties represent a combination of the statistical error and the systematic errors resulting from uncertainties in relative humidity measurements and gas flow rates. The uncertainty in the equilibrium constant, K_{eq}, taken from Ruscic *et al.*[40] ranges between 2.7 and 3.6 % for the temperature range studied in this work. The RH probe used to determine the water vapour concentration had been calibrated using a hygrometer, which gave an uncertainty in the RH readings of 7.9 %. The flow of gases to the reaction cell were controlled using three calibrated MFCs, which gave a combined uncertainty of 5.5 %. The overall uncertainties were determined by propagating the errors in K_{eq}, the RH values and the gas flows and an overall systematic error of 10 % was determined for values of $k_{6.1}$ and $k_{6.2}K_{eq}$ to account for the

uncertainties in the water monomer concentration and a 14 % systematic error on values of $k_{6.2}$ to account for the additional uncertainty of K_{eq}.

Results for $k_{6.2}K_{eq}$ correspond to $k_{6.2} = (2.85 \pm 0.40) \times 10^{-15}\ exp((2417 \pm 338)/T)$ cm^3 molecule^{-1} s^{-1} using the temperature-dependent equilibrium constants for water dimer formation, and associated uncertainties, reported by Ruscic *et al.*, and results are consistent with suggestions made in previous work[4, 13, 14, 18-20] that the dominant loss of CH_2OO in the presence of water vapour occurs via reaction with water dimers (R6.2). The reaction of CH_2OO with water monomers (R6.1) was a minor contribution to the total loss of CH_2OO for all conditions employed in this work. The kinetics of R6.1 were thus less well defined than those for R6.2, which represented the major contribution to the total CH_2OO loss at high relative humidities at all temperatures, and results for $k_{6.1}$ should be considered as estimates owing to the challenges associated with separating the impacts of k_x and $k_{6.1}$.

Kinetics of CH_2OO reactions in the presence of water vapour have been investigated by Wu *et al.*[5] in experiments performed between 290 and 346 K using UV absorption spectroscopy, which demonstrated evidence for a reaction between CH_2OO and water trimers, $(H_2O)_3$. Wu *et al.* described the total pseudo-first-order loss of CH_2OO using Equation 6.10 and investigated the behaviour of $(k'\text{-}k_x)[H_2O]^{-2}$ (Equation 6.11).

$$(k'\text{-}k_x) = k_{6.1}[H_2O] + k_{6.2}[H_2O]^2 + k_{6.3}[H_2O]^3 \qquad \text{(Equation 6.10)}$$

$$(k'\text{-}k_x)\,[H_2O]^{-2} = k_{6.1}[H_2O]^{-1} + k_{6.2} + k_{6.3}[H_2O] \qquad \text{(Equation 6.11)}$$

where k' and k_x represent the pseudo-first-order rate coefficients describing the loss of CH_2OO in the presence and absence of water vapour, respectively, $k_{6.1}$ represents the reaction with the water monomer, $k_{6.2}$ represents the reaction with the water dimer, $k_{6.3}$ represents the reaction with the water trimer and $[H_2O]$ is the water monomer concentration.

If the loss of CH_2OO were dominated by reaction with water dimers, $(k'\text{-}k_x)[H_2O]^{-2}$ would not be expected to display any dependence on $[H_2O]$, while contributions from monomer reactions would show a negative dependence of $(k'\text{-}k_x)[H_2O]^{-2}$ on $[H_2O]$ at low $[H_2O]$, and contributions from trimer reactions would show a positive dependence of $(k'\text{-}k_x)[H_2O]^{-2}$ on $[H_2O]$ at high $[H_2O]$. Results obtained by Wu *et al.* are shown in Figure 6.9, which indicated that there is a contribution to the loss of CH_2OO from reaction with water trimers at 298 K that becomes more significant at lower temperatures.

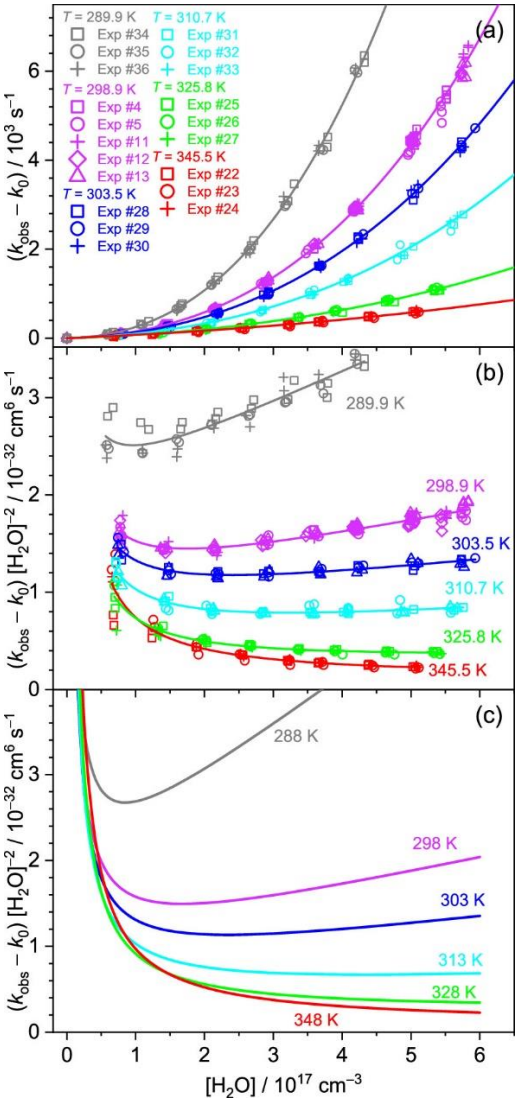

Figure 6.9. Experimental (a and b) and theoretical (c) results obtained by Wu *et al.*[5] The solid lines in (a) represent fits to Equation 6.2 and the solid lines in (b) represent fits to Equation 6.11. Copied from Wu *et al.*[5]

Figure 6.10 shows the dependence of $(k'-k_x)[H_2O]^{-2}$ on $[H_2O]$ for data obtained at the lowest (262 K) and highest (353 K) temperature studied in this work and at 298 K, where the dashed blue lines represent Equation 6.11. Values for rate coefficients were obtained from the parameterisation reported by Wu *et al.* The data obtained in this work indicate that there is no significant contribution from a reaction with the water trimer under the conditions studied. To fully investigate the potential role of the water trimer in the atmospheric removal of CH_2OO, further experiments need to be carried out under higher water vapour concentrations, as with the work of Wu *et al.*, where this reaction will be more significant and the relationship between k' and $k_{6.3}[H_2O]$ would be more evident on the bimolecular plot.

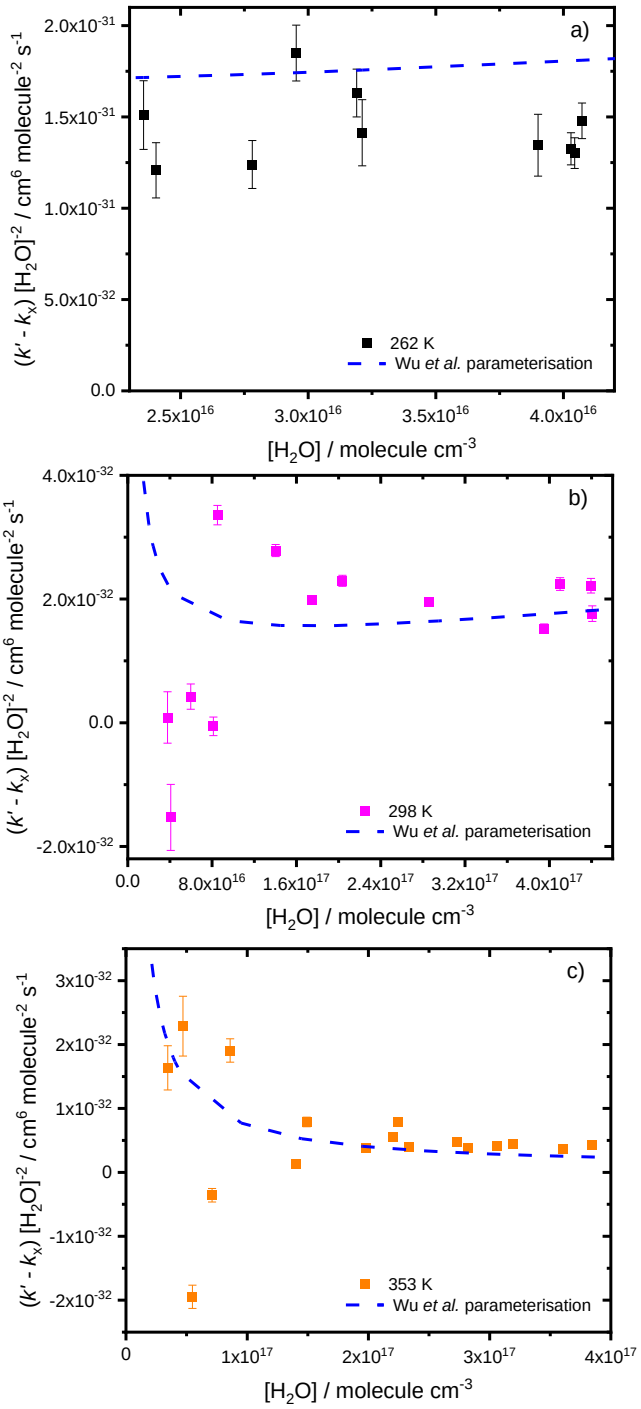

Figure 6.10. Dependence of $(k'-k_x)[H_2O]^{-2}$ on $[H_2O]$ for data obtained in this work at a) 262 K, b) 298 K and c) 353 K. The blue dashed lines represents Equation 6.11, where $k_{6.1}$, $k_{6.2}$ and $k_{6.3}$ were obtained from the work of Wu *et al.*[5] Results at all other temperatures investigated in this work are shown in Appendix 8.

Figure 6.11 compares the results for $k_{6.1}$ obtained in this study with measurements, upper limits based on experimental observations, and theoretical calculations reported in previous work, with experimental results at ~ 298 K summarised in Table 6.2.

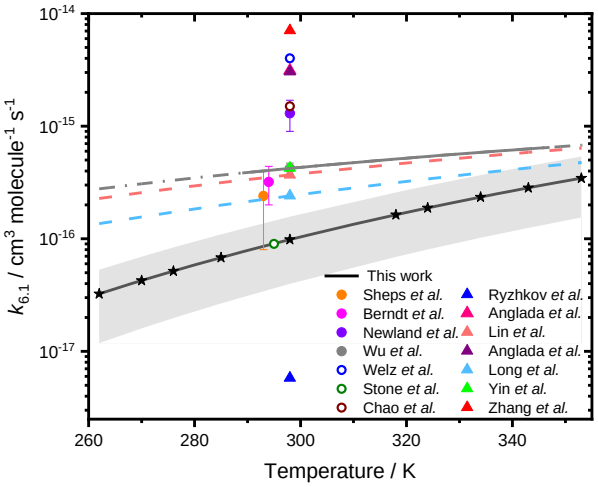

Figure 6.11. $k_{6.1}$ as a function of temperature. The fit to results obtained in this work are shown by the solid black line, with uncertainties determined from a combination of the statistical error and the systematic errors resulting from uncertainties in gas flow rates and in the concentration of [H_2O] shown by the shaded region. Stars represent the temperatures at which measurements were made. Results from previous studies are also included, where filled circles represent experimentally measured rate coefficients,[3-5, 13] hollow circles represent experimentally determined upper limits,[1, 2, 18] and triangles represent rate coefficients calculated from theory.[24-28, 31, 34] The solid grey line shows the data reported by Wu *et al.*,[5] with the dashed grey line showing the extrapolation of the data reported by Wu *et al.* over the temperature range investigated in this work. The coral and light blue dashed lines are the parameterisations calculated by Lin *et al.*[28] and Long *et al.*,[31] respectively.

T / K	p / Torr	Experimental technique	$k_{6.1}$ / 10^{-17} cm^3 molecule^{-1} s^{-1}	Reference
298	4	LFP / PIMS	≤ 400	Welz *et al.*[1]
295	200	LFP / LIF	≤ 9	Stone *et al.*[2]
297	760	Ozonolysis / CI-APi-TOF-MS	32 ± 12	Berndt *et al.*[3]
298	50 - 400	LFP / UV abs	≤ 150	Chao *et al.*[18]
298	760	RR. Ethene Ozonolysis	130 ± 40	Newland *et al.*[4]
293	30 - 100	LFP / UV abs	24 ± 16	Sheps *et al.*[13]
298	300	LFP / UV abs	42 ± 5	Wu *et al.* [5]
298	760	LFP / UV abs	9.8 ± 5.9	This work

Table 6.2. Comparison between $k_{6.1}$ values obtained at room temperature in this work and in previous literature.[1-5, 13, 18] LFP = laser flash photolysis, PIMS = photo-ionisation mass spectrometry, CI-APi-TOF-MS = Chemical ionisation-atmospheric pressure interface-time-of-flight mass spectrometry, RR = relative rate study.

Results for $k_{6.1}$ obtained in this work are systematically lower than those measured previously, but are consistent with the prediction of a positive barrier to reaction,[24-32] and are in agreement with calculated values of $k_{.6.1}$ reported by Long *et al.*[33] at temperatures above 324 K, where results obtained in this work are more reliable. Previous direct experimental measurements of $k_{6.1}$[3, 5, 13] at ~ 298 K range between $(2.4 \pm 1.6) \times 10^{-16}$ cm^3 molecule^{-1} s^{-1} [13] and $(4.2 \pm 1.6) \times 10^{-16}$ cm^3 molecule^{-1} s^{-1},[5] compared to the value of $(9.8 \pm 5.9) \times 10^{-17}$ cm^3 molecule^{-1} s^{-1} indicated in this work, while theory predicts values between 5.8×10^{-18} cm^3 molecule^{-1} s^{-1} [24] and 7.08×10^{-15} cm^3 molecule^{-1} s^{-1}.[34] The temperature dependence for $k_{6.1}$ indicated in this work is more significant than the temperature dependence reported by Wu *et al.*, but while there are significant uncertainties in $k_{6.1}$, the kinetics of R6.2 are well defined from the fits shown in Figure 6.6.

Figure 6.12 shows the temperature dependence of $k_{6.2}K_{eq}$, which is in good agreement with previous measurements[14, 18, 39] over the temperature ranges in common, with this work extending the temperature range over which the kinetics have been investigated. At 298 K, this work indicates $k_{6.2}K_{eq} = (1.96 \pm 0.51) \times 10^{-32}$ cm^6 molecule^{-2} s^{-1}, which corresponds to $k_{6.2} = (9.52 \pm 2.49) \times 10^{-12}$ cm^3 molecule^{-1} s^{-1} using the temperature-dependent equilibrium constants for water dimer formation reported by Ruscic *et al*. Table 6.3 compares results for $k_{6.2}$ and $k_{6.2}K_{eq,dimer}$ obtained at 298 K in this work with those reported previously, with good agreement between the results reported here and the results of Berndt *et al.*,[14] Smith *et al.*,[20] Chao *et al.*[18] and Sheps *et al.*[13]

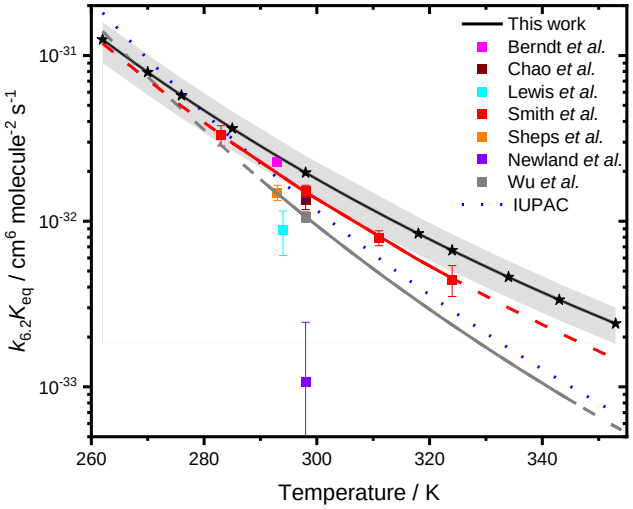

Figure 6.12. $k_{6.2}K_{eq}$ as a function of temperature obtained in this work. The fit to results obtained in this work are shown by the solid black line, with uncertainties determined from a combination of the statistical error and the systematic errors resulting from uncertainties in gas flow rates and in the concentration of [H_2O] shown by the shaded region. Stars represent the temperatures at which measurements were made. The solid grey line shows the data reported by Wu *et al.*,[5] with the dashed grey line showing the extrapolation of the data reported by Wu *et al.* over the temperature range investigated in this work. The red solid line represents a fit to the data reported by Smith *et al.*,[39] with the dashed red line showing the extrapolation of the data reported by Smith *et al.* over the temperature range investigated in this work. The blue dotted line represents the current IUPAC recommendation,[42] which is based on the data reported by Smith *et al.*

T / K	p / Torr	Experimental technique	$k_{6.2}$ / 10^{-12} cm^3 $molecule^{-1}$ s^{-1}	$k_{6.2}K_{eq}$ / 10^{-32} cm^6 $molecule^{-2}$ s^{-1}	Reference
293	760	IfT-LFT (H_2SO_4) measurements	10.7 ± 0.40	2.28 ± 0.09	Berndt *et al.*[14]
298	100 – 500	LFP / UV abs	6.5 ± 0.8	1.34 ± 0.17	Chao *et al.* [18]
294	50 – 400	LFP / UV abs	4.0 ± 1.2	0.89 ± 0.27	Lewis *et al.*[19]
298	200 – 600	LFP / UV abs	7.4 ± 0.6	1.53 ± 0.12	Smith *et al.*[20]
293	30 – 100	LFP / UV abs	6.6 ± 0.7	1.49 ± 0.16	Sheps *et al.*[13]
298	760	RR. Ethene Ozonolysis	0.52 ± 0.67	0.11 ± 0.14	Newland *et al.*[4]
298	300	LFP / UV abs	5.17 ± 0.40	1.07 ± 0.08	Wu *et al.*[5]
298	760	LFP / UV abs	9.52 ± 2.49	1.96 ± 0.51	This work

Table 6.3. Comparison between the $k_{6.2}$ values obtained at room temperature in this work and in previous literature.[4, 13, 14, 18-20] LFP = laser flash photolysis, IfT-LFT = Institute for Tropospheric Research – Laminar Flow Tube, RR = relative rate study. $k_{6.2}K_{eq}$ have been calculated using the K_{eq} values reported by Ruscic *et al.*[40]

The value for $k_{6.2}K_{eq}$ reported by Wu *et al.*[5] at 298 K is a factor of ~ 1.8 lower than that reported here, but there is good agreement in the total pseudo-first-order rate coefficients as a function of water monomer concentration observed in this work and reported by Wu *et al*. Figure 6.13 compares the total pseudo-first-order losses observed in this work at 262, 298 and 353 K and the work of Wu *et al*. as well as the individual contributions of $k_{6.1}$ and $k_{6.2}K_{eq}$ from this work and $k_{6.1}$, $k_{6.2}K_{eq}$ and $k_{6.3}$ from Wu *et al*. Comparisons between the pseudo-first-order losses observed in this work and in the work of Wu *et al.* at all other temperatures are shown in Appendix 9.

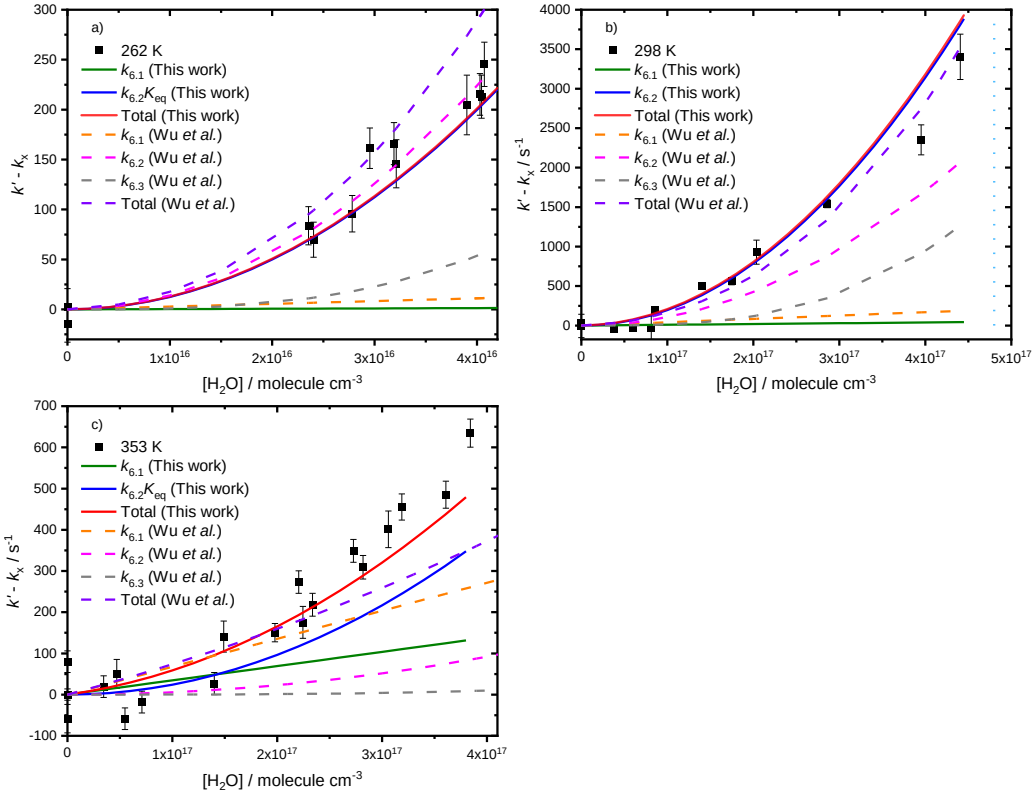

Figure 6.13. Pseudo-first-order losses as a function of H_2O concentration for experiments at a) 262K, b) 298 K and c) 353 K. Black points represent the experimental data, the green and blue solid lines represent losses due to reaction with the water monomer and the water dimer and the solid red line represents the total loss. The results of Wu *et al.*[5] are also included in the plot, where the orange, pink and grey dashed lines represent reactions with the water monomer, dimer and trimer, and the purple dashed line represents the total loss. The light blue dotted line on b) represents [H_2O] = 4.8×10^{17} molecule cm^{-3}, the point at which Wu *et al.* report the reaction with the water trimer becomes significant at 298 K.

Although Wu *et al*. reported an impact of a reaction between CH_2OO and water trimers, it was noted that there was little impact of the trimer reaction for water monomer concentrations below 4.8×10^{17} molecule cm^{-3} at 298 K, which is higher than the highest water concentrations used in this work at 298 K, and the differences in kinetics for R6.2 between the results of Wu *et al*. and other studies, including this work, are impacted by differences in kinetics for R6.1 as well as contributions from R6.3. Rate coefficients reported by Newland *et al.*[4] for R6.2 at 298 K are notably lower than those reported elsewhere, but experiments were carried out over a relatively narrow range of relative humidities (1.5 to 20%), leading to low water dimer concentrations and relatively limited impact of the dimer reaction. Lewis *et al.*[19] also reported lower values than those obtained in this work and in other studies using flash photolysis with UV absorption,[13, 18, 20] potentially resulting from overestimation of the water

vapour, and thus water dimer, concentrations, which were based on flow rates and vapour pressure and assumed 100 % saturation of the gas flow with water vapour. Results reported here, and in other studies using flash photolysis with UV absorption,[5, 18, 20] measured the relative humidity of the gas flow, providing greater certainty in the water vapour and dimer concentrations.

The negative temperature dependence observed for $k_{6.2}K_{eq}$ is in agreement with previous experimental[5, 20] and theoretical[24, 25] work. Rate coefficients obtained in this work are in agreement with those reported by Smith *et al.*[20] over the common temperature ranges, but there are some discrepancies between the measurements made at the highest temperature employed in this work and extrapolation of the results reported by Smith *et al*. and Wu *et al*., as shown in Figure 6.12.

Observations of a negative temperature dependence for the kinetics of R6.2, and of the dominance of R6.2 over R6.1, are consistent with theoretical studies of R6.1 and R6.2.[24, 25, 27, 28] Calculations of the potential energy surfaces for R6.1 and R6.2, summarised in Table 6.4,[24-33] indicate that both reactions proceed via the formation of pre-reaction complexes which then undergo rearrangement to form HMHP as the dominant product of both reactions. For R6.1, rearrangement of the pre-reaction complex to HMHP involves a transition state which is higher in energy than the initial reactants (i.e. there is an overall positive barrier to reaction). In contrast, the pre-reaction complex for R6.2 is more stable than that for R6.1 by a factor of ~ 2 (Table 6.4, Figure 6.14), and the subsequent transition state to product formation is lower in energy than the initial reactants. The difference in barrier heights leads to the dominance of R6.2 over R6.1, and the submerged barrier for R6.2 leads to the observed negative temperature dependence.

Method	PRC R6.1 / kJ mol^{-1}	TS R6.1 / kJ mol^{-1}	PRC R6.2 / kJ mol^{-1}	TS R6.2 / kJ mol^{-1}	$k_{6.1}$ / cm^3 molecule^{-1} s^{-1}	$k_{6.2}$ / cm^3 molecule^{-1} s^{-1}	Ref.
CCSD(T)/6-311G(d,p)	-30.1	9.6	-	-	-	-	[29]
CCSD(T)/6-311+G(2d,2p)	-32.6	7.9	-	-	-	-	[30]
CCSD(T)/6-311+G(2d,2p) CTST	-30.9	14.2	-65.7	-36.8	5.8×10^{-18}	1.1×10^{-12}	[24]
CCSD(T)/aug-cc-pVTZ C/VTST	-26.0	8.5	-	-	3.12×10^{-15}	-	[26]
W3X-L//CCSD(T)-F12a/TZ-F12 MP-CVT/SCT	-26.2	14.7	-	-	2.41×10^{-16}	-	[31]
CCSD(T)/ aug-cc-PVTZ VTST	-25.7	6.3	-44.8	-35.5	3.05×10^{-15}	1.67×10^{-10}	[25]
CCSD(T)//M06-2X/6-311+G(2d,2p) CTST	-28.5	11.2	-63.7	-45.3	-	6.71×10^{-12}	[32]
QCISD(T)/CBS// 6-311+G(2d,2p) VPT2	-27.3	11.8	-46.2	-27.3	3.7×10^{-16}	5.4×10^{-12}	[28]
B3LYP/6-311+G(2d,2p) VPT2	-26.4	12.8	-42.4	-24.6	4.26×10^{-16}	2.91×10^{-12}	[27]
CCSD(T)/6-311+G(3df, 2dp) CTST	-25.9	14.2	-32.0	-8.4	7.08×10^{-15}	1.15×10^{-12}	[34]
W3X-L//CCSD(T)- F12a/cc-pVDZ-F12 [a] W3X-L//CCSD(T)-F12a/cc-pVTZ-F12 [b] CUS	-	-	-45.5	-22.9	-	6.73×10^{-12}	[33]

Table 6.4. Theoretical calculations of the PES for R6.1 and R6.2 and, where available, calculations of the reaction kinetics. Where multiple reaction pathways for R6.1 and R6.2 were given, the lowest energy pathway was chosen. PRC = pre-reaction complex, TS = transition state, CTST = conventional transition state theory, VTST = variational transition state theory, VPT2 = vibrational second order perturbation theory, MP-CVT/SCT = Multipath variational transition state theory with small-curvature tunneling, CUS = canonical unified statistical theory. [a] Level of theory used to optimise geometries and energies for reactant, PRCs, and products. [b] Level of theory used to optimise geometries and energies for transition state.

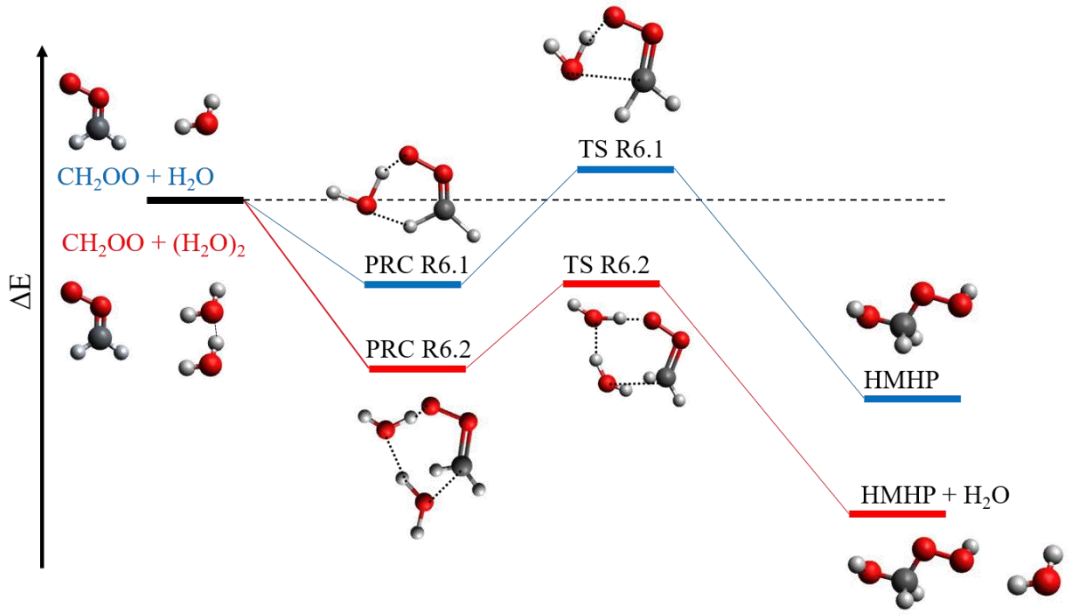

Figure 6.14. Schematic potential energy surface for the reactions of CH_2OO with H_2O (blue) and $(H_2O)_2$ (red). PRC = pre-reaction complex, TS = transition state, HMHP = hydroxymethyl hydroperoxide.

6.4 Concluding Remarks

The kinetics of the reactions of the simplest Criegee intermediate, CH_2OO, with water vapour have been investigated using laser flash photolysis coupled with time-resolved broadband UV absorption spectroscopy at temperatures between 262 and 353 K at a total pressure of 760 Torr. The reaction of CH_2OO with water monomers (R6.1) represents a minor contribution to the total loss of CH_2OO under the conditions employed in this work, with an estimated value for $k_{6.1}$ of $(9.8 \pm 5.9) \times 10^{-17}$ cm^3 molecule^{-1} s^{-1} at 298 K and a temperature dependence described by $k_{6.1} = (3.15 \pm 1.06) \times 10^{-13} \exp(-(2405 \pm 265)/T)$ cm^3 molecule^{-1} s^{-1}. The results show that the reaction with water dimers (R6.2) dominates the loss of CH_2OO, with $k_{6.2} = (9.52 \pm 2.49) \times 10^{-12}$ cm^3 molecule^{-1} s^{-1} at 298 K, with a temperature dependence described by $k_{6.2} = (2.85 \pm 0.40) \times 10^{-15} \exp((2417 \pm 338)/T)$ cm^3 molecule^{-1} s^{-1}, where use of $k_{6.2}$ requires use of the water dimer concentration to determine the rate of reaction. The kinetics of R6.2 can also be expressed in terms of the product $k_{6.2}K_{eq}$, allowing calculation of the rate of reaction in terms of the square of the water monomer concentration rather than the water dimer concentration, giving $k_{6.2}K_{eq} = (1.96 \pm 0.51) \times 10^{-32}$ cm^6 molecule^{-2} s^{-1} at 298 K and a temperature dependence described by $k_{6.2}K_{eq} = (2.78 \pm 0.28) \times 10^{-38} \exp((4012 \pm 400)/T)$ cm^6 molecule^{-2} s^{-1}. No significant impact of a reaction between CH_2OO and water trimers was observed in this work. The kinetic results are consistent with theoretical studies which predict the existence of a positive barrier to reaction for R6.1 and a submerged barrier for R6.2. The atmospheric implications of the results are discussed in Chapter 8.

6.5 References

1. Welz, O., Savee, J.D., Osborn, D.L., Vasu, S.S., Percival, C.J., Shallcross, D.E. and Taatjes, C.A. Direct Kinetic Measurements of Criegee Intermediate (CH_2OO) Formed by Reaction of CH_2I with O_2. *Science.* 2012, **335**(6065), p.204.
2. Stone, D., Blitz, M., Daubney, L., Howes, N.U.M. and Seakins, P. Kinetics of CH_2OO reactions with SO_2, NO_2, NO, H_2O and CH_3CHO as a function of pressure. *Physical Chemistry Chemical Physics.* 2014, **16**(3), pp.1139-1149.
3. Berndt, T., Kaethner, R., Voigtländer, J., Stratmann, F., Pfeifle, M., Reichle, P., Sipilä, M., Kulmala, M. and Olzmann, M. Kinetics of the unimolecular reaction of CH_2OO and the bimolecular reactions with the water monomer, acetaldehyde and acetone under atmospheric conditions. *Physical Chemistry Chemical Physics.* 2015, **17**(30), pp.19862-19873.
4. Newland, M.J., Rickard, A.R., Alam, M.S., Vereecken, L., Muñoz, A., Ródenas, M. and Bloss, W.J. Kinetics of stabilised Criegee intermediates derived from alkene ozonolysis: reactions with SO_2, H_2O and decomposition under boundary layer conditions. *Physical Chemistry Chemical Physics.* 2015, **17**(6), pp.4076-4088.
5. Wu, Y.-J., Takahashi, K. and Lin, J.J.-M. Kinetics of the Simplest Criegee Intermediate Reaction with Water Vapor: Revisit and Isotope Effect. *The Journal of Physical Chemistry A.* 2023, **127**(39), pp.9059-8072.
6. Suto, M., Manzanares, E.R. and Lee, L.C. Detection of sulfuric acid aerosols by ultraviolet scattering. *Environmental Science & Technology.* 1985, **19**(9), pp.815-820.
7. Becker, K.H., Bechara, J. and Brockmann, K.J. Studies on the formation of H_2O_2 in the ozonolysis of alkenes. *Atmospheric Environment. Part A. General Topics.* 1993, **27**(1), pp.57-61.
8. Leather, K.E., McGillen, M.R., Cooke, M.C., Utembe, S.R., Archibald, A.T., Jenkin, M.E., Derwent, R.G., Shallcross, D.E. and Percival, C.J. Acid-yield measurements of the gas-phase ozonolysis of ethene as a function of humidity using Chemical Ionisation Mass Spectrometry (CIMS). *Atmos. Chem. Phys.* 2012, **12**(1), pp.469-479.
9. Hasson, A.S., Orzechowska, G. and Paulson, S.E. Production of stabilized Criegee intermediates and peroxides in the gas phase ozonolysis of alkenes: 1. Ethene, trans-2-butene, and 2,3-dimethyl-2-butene. *Journal of Geophysical Research: Atmospheres.* 2001, **106**(D24), pp.34131-34142.
10. Orzechowska, G.E. and Paulson, S.E. Photochemical Sources of Organic Acids. 1. Reaction of Ozone with Isoprene, Propene, and 2-Butenes under Dry and Humid Conditions Using SPME. *The Journal of Physical Chemistry A.* 2005, **109**(24), pp.5358-5365.

11. Nguyen, T.B., Tyndall, G.S., Crounse, J.D., Teng, A.P., Bates, K.H., Schwantes, R.H., Coggon, M.M., Zhang, L., Feiner, P., Milller, D.O., Skog, K.M., Rivera-Rios, J.C., Dorris, M., Olson, K.F., Koss, A., Wild, R.J., Brown, S.S., Goldstein, A.H., de Gouw, J.A., Brune, W.H., Keutsch, F.N., Seinfeld, J.H. and Wennberg, P.O. Atmospheric fates of Criegee intermediates in the ozonolysis of isoprene. *Physical Chemistry Chemical Physics.* 2016, **18**(15), pp.10241-10254.

12. Millet, D.B., Baasandorj, M., Farmer, D.K., Thornton, J.A., Baumann, K., Brophy, P., Chaliyakunnel, S., de Gouw, J.A., Graus, M., Hu, L., Koss, A., Lee, B.H., Lopez-Hilfiker, F.D., Neuman, J.A., Paulot, F., Peischl, J., Pollack, I.B., Ryerson, T.B., Warneke, C., Williams, B.J. and Xu, J. A large and ubiquitous source of atmospheric formic acid. *Atmospheric Chemistry and Physics.* 2015, **15**(11), pp.6283-6304.

13. Sheps, L., Rotavera, B., Eskola, A.J., Osborn, D.L., Taatjes, C.A., Au, K., Shallcross, D.E., Khan, M.A.H. and Percival, C.J. The reaction of Criegee intermediate CH_2OO with water dimer: primary products and atmospheric impact. *Physical Chemistry Chemical Physics.* 2017, **19**(33), pp.21970-21979.

14. Berndt, T., Voigtländer, J., Stratmann, F., Junninen, H., Mauldin III, R.L., Sipilä, M., Kulmala, M. and Herrmann, H. Competing atmospheric reactions of CH_2OO with SO_2 and water vapour. *Physical Chemistry Chemical Physics.* 2014, **16**(36), pp.19130-19136.

15. Vereecken, L., Harder, H. and Novelli, A. The reaction of Criegee intermediates with NO, RO_2, and SO_2, and their fate in the atmosphere. *Physical Chemistry Chemical Physics.* 2012, **14**(42), pp.14682-14695.

16. Kuwata, K.T., Guinn, E.J., Hermes, M.R., Fernandez, J.A., Mathison, J.M. and Huang, K. A Computational Re-examination of the Criegee Intermediate–Sulfur Dioxide Reaction. *The Journal of Physical Chemistry A.* 2015, **119**(41), pp.10316-10335.

17. Wang, Y.-Y., Dash, M.R., Chung, C.-Y. and Lee, Y.-P. Detection of transient infrared absorption of SO_3 and 1,3,2-dioxathietane-2,2-dioxide [cyc-$(CH_2)O(SO_2)O$] in the reaction CH_2OO+SO_2. *The Journal of Chemical Physics.* 2018, **148**(6), p.064301.

18. Chao, W., Hsieh, J.-T., Chang, C.-H. and Lin, J.J.-M. Direct kinetic measurement of the reaction of the simplest Criegee intermediate with water vapor. *Science.* 2015, **347**(6223), p.751.

19. Lewis, T.R., Blitz, M.A., Heard, D.E. and Seakins, P.W. Direct evidence for a substantive reaction between the Criegee intermediate, CH_2OO, and the water vapour dimer. *Physical Chemistry Chemical Physics.* 2015, **17**(7), pp.4859-4863.

20. Smith, M.C., Chang, C.-H., Chao, W., Lin, L.-C., Takahashi, K., Boering, K.A. and Lin, J.J.-M. Strong Negative Temperature Dependence of the Simplest Criegee

Intermediate CH_2OO Reaction with Water Dimer. *The Journal of Physical Chemistry Letters.* 2015, **6**(14), pp.2708-2713.

21. Cox, R.A., Ammann, M., Crowley, J.N., Herrmann, H., Jenkin, M.E., McNeill, V.F., Mellouki, A., Troe, J. and Wallington, T.J. Evaluated kinetic and photochemical data for atmospheric chemistry: Volume VII – Criegee intermediates. *Atmospheric Chemistry and Physics.* 2020, **20**(21), pp.13497-13519.
22. Becker, K.H., Brockmann, K.J. and Bechara, J. Production of hydrogen peroxide in forest air by reaction of ozone with terpenes. *Nature.* 1990, **346**(6281), pp.256-258.
23. Nakajima, M. and Endo, Y. Observation of hydroxymethyl hydroperoxide in a reaction system containing CH_2OO and water vapor through pure rotational spectroscopy. *The Journal of Chemical Physics.* 2015, **143**(16), p.164307.
24. Ryzhkov, A.B. and Ariya, P.A. A theoretical study of the reactions of parent and substituted Criegee intermediates with water and the water dimer. *Physical Chemistry Chemical Physics.* 2004, **6**(21), pp.5042-5050.
25. Anglada, J.M. and Solé, A. Impact of the water dimer on the atmospheric reactivity of carbonyl oxides. *Physical Chemistry Chemical Physics.* 2016, **18**(26), pp.17698-17712.
26. Anglada, J.M., González, J. and Torrent-Sucarrat, M. Effects of the substituents on the reactivity of carbonyl oxides. A theoretical study on the reaction of substituted carbonyl oxides with water. *Physical Chemistry Chemical Physics.* 2011, **13**(28), pp.13034-13045.
27. Yin, C. and Takahashi, K. Effect of unsaturated substituents in the reaction of Criegee intermediates with water vapor. *Physical Chemistry Chemical Physics.* 2018, **20**(30), pp.20217-20227.
28. Lin, L.-C., Chang, H.-T., Chang, C.-H., Chao, W., Smith, M.C., Chang, C.-H., Lin, J. and Takahashi, K. Competition between H_2O and $(H_2O)_2$ reactions with CH_2OO/CH_3CHOO. *Physical Chemistry Chemical Physics.* 2016, **18**(6), pp.4557-4568.
29. Aplincourt, P. and Ruiz-López, M.F. Theoretical Investigation of Reaction Mechanisms for Carboxylic Acid Formation in the Atmosphere. *Journal of the American Chemical Society.* 2000, **122**(37), pp.8990-8997.
30. Crehuet, R., Anglada, J.M. and Bofill, J.M. Tropospheric Formation of Hydroxymethyl Hydroperoxide, Formic Acid, H_2O_2, and OH from Carbonyl Oxide in the Presence of Water Vapor: A Theoretical Study of the Reaction Mechanism. *Chemistry – A European Journal.* 2001, **7**(10), pp.2227-2235.

31. Long, B., Bao, J.L. and Truhlar, D.G. Atmospheric Chemistry of Criegee Intermediates: Unimolecular Reactions and Reactions with Water. *Journal of the American Chemical Society.* 2016, **138**(43), pp.14409-14422.

32. Chen, L., Wang, W., Zhou, L., Wang, W., Liu, F., Li, C. and Lü, J. Role of water clusters in the reaction of the simplest Criegee intermediate CH_2OO with water vapour. *Theoretical Chemistry Accounts.* 2016, **135**(11), p.252.

33. Long, B., Wang, Y., Xia, Y., He, X., Bao, J.L. and Truhlar, D.G. Atmospheric Kinetics: Bimolecular Reactions of Carbonyl Oxide by a Triple-Level Strategy. *Journal of the American Chemical Society.* 2021, **143**(22), pp.8402-8413.

34. Zhang, T., Lan, X., Wang, R., Roy, S., Qiao, Z., Lu, Y. and Wang, Z. The catalytic effects of H_2CO_3, CH_3COOH, HCOOH and H_2O on the addition reaction of $CH_2OO + H_2O \rightarrow CH_2(OH)OOH$. *Molecular Physics.* 2018, **116**(14), pp.1783-1794.

35. Nguyen, T.B., Crounse, J.D., Schwantes, R.H., Teng, A.P., Bates, K.H., Zhang, X., St. Clair, J.M., Brune, W.H., Tyndall, G.S., Keutsch, F.N., Seinfeld, J.H. and Wennberg, P.O. Overview of the Focused Isoprene eXperiment at the California Institute of Technology (FIXCIT): mechanistic chamber studies on the oxidation of biogenic compounds. *Atmos. Chem. Phys.* 2014, **14**(24), pp.13531-13549.

36. Mir, Z.S., Lewis, T.R., Onel, L., Blitz, M.A., Seakins, P.W. and Stone, D. CH_2OO Criegee intermediate UV absorption cross-sections and kinetics of $CH_2OO + CH_2OO$ and CH_2OO + I as a function of pressure. *Physical Chemistry Chemical Physics.* 2020, **22**(17), pp.9448-9459.

37. S.P. Sander, J.A., J.R. Burkholder. R.R. Freidl, D.M. Golden, R.E. Huie, C.E. Kolb, M.J. Kurylo, G.K. Moortgat, V.L. Orkin, P.H. Wine. Chemical Kinetics and Photochemical Data for Use in Atmospheric Studies, Evaluation Number 17. *JPL publication 10-6.* 2011.

38. Harwood, M.H., Burkholder, J.B., Hunter, M., Fox, R.W. and Ravishankara, A.R. Absorption Cross Sections and Self-Reaction Kinetics of the IO Radical. *The Journal of Physical Chemistry A.* 1997, **101**(5), pp.853-863.

39. Smith, M.C., Chang, C.-H., Chao, W., Lin, L.-C., Takahashi, K., Boering, K.A. and Lin, J.J.-M. Strong Negative Temperature Dependence of the Simplest Criegee Intermediate CH_2OO Reaction with Water Dimer. *The Journal of Physical Chemistry Letters.* 2015, **6**(14), pp.2708-2713.

40. Ruscic, B. Active Thermochemical Tables: Water and Water Dimer. *The Journal of Physical Chemistry A.* 2013, **117**(46), pp.11940-11953.

41. Scribano, Y., Goldman, N., Saykally, R.J. and Leforestier, C. Water Dimers in the Atmosphere III: Equilibrium Constant from a Flexible Potential. *The Journal of Physical Chemistry A.* 2006, **110**(16), pp.5411-5419.

42. Cox, R.A., Ammann, M., Crowley, J.N., Herrmann, H., Jenkin, M.E., McNeill, V.F., Mellouki, A., Troe, J. and Wallington, T.J. Evaluated kinetic and photochemical data for atmospheric chemistry: Volume VII – Criegee intermediates. *Atmospheric Chemistry and Physics.* 2020, **20**(21), pp.13497-13519.

Chapter 7

Kinetics of *syn*- and *anti*-CH_3CHOO Conformers with SO_2 as a Function of Temperature and Pressure

As discussed in Chapter σ, the SCI acetaldehyde oxide, CH_3CHOO, exists in two conformers, *syn*-CH_3CHOO and *anti*-CH_3CHOO, which are separated by a significant barrier to interconversion (~ 160 kJ mol^{-1})[1] and behave as distinct species under ambient conditions.[2,3] Significant conformer-dependence has been shown for the reactivity of CH_3CHOO with SO_2,[2, 3] with studies also showing distinct conformer-dependent reactivity for reactions of asymmetric CIs with H_2O[2-4] and acids[5] as well as differences in their decomposition rates.[6] CH_3CHOO is the simplest Criegee intermediate that exists as two conformers and can therefore be used as a prototype to characterise the reactions of the larger CIs, which requires rate coefficients to be well established across a range of conditions. This chapter summarises the previous experimental studies of the reactions of *syn*-CH_3CHOO and *anti*-CH_3CHOO with SO_2 and reports results of experiments performed in this work. Results are provided for a study of the kinetics of *syn*-CH_3CHOO and *anti*-CH_3CHOO with SO_2 at temperatures between 242 and 353 K and pressures between 10 and 600 Torr, determined using time-resolved broadband UV absorption spectroscopy.

The results presented throughout this chapter have been published in the *Journal of Physical Chemistry A*: Lade, R.E., Onel, L., Blitz, M.A., Seakins, P.W. and Stone, D. Kinetics of the Gas-Phase Reactions of *syn*- and *anti*-CH_3CHOO Criegee Intermediate Conformers with SO_2 as a Function of Temperature and Pressure. *The Journal of Physical Chemistry A.* 2024, **128**(14), pp.2815-2824.[7]

7.1 Previous Direct Studies

Taatjes *et al*.[2] studied the reactions of CH_3CHOO conformers with SO_2 (R7.1 and R7.2) using the LFP/PIMS technique at 298 K and 4 Torr in He, and were able to independently detect the two conformers using radiation at 10.2 eV to photo-ionise the *syn*-conformer and at 9.37 eV to photo-ionise the *anti*-conformer. Figure 7.1 shows a photo-ionisation spectrum obtained by Taatjes *et al.* following the reaction between CH_3CHI_2 and O_2. The low-energy end of the spectrum is dominated by the *anti*-conformer, which is also seen by the removal of signal in this region upon the addition of water, and the high-energy end of the spectrum is dominated by the *syn*-conformer.

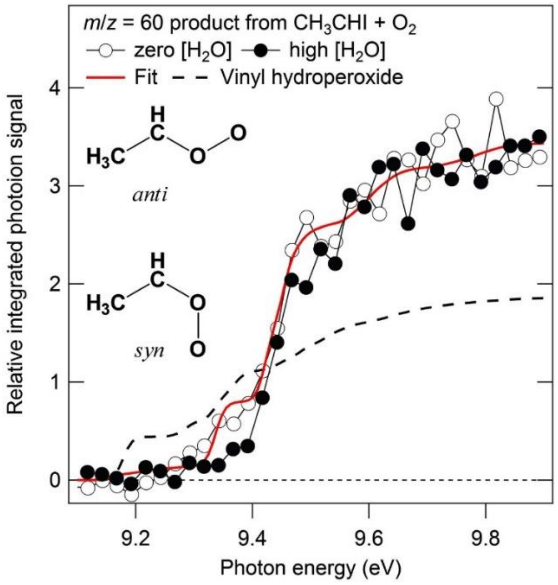

Figure 7.1. Photo-ionisation spectrum for the *m/z* = 60 product following the reaction of $CH_3CHI_2 + O_2$ in the presence (black solid circles) and absence (open circles) of water. The addition of water preferentially removes signal corresponding to the *anti*-conformer (between 9.3 and 9.4 eV). Copied from reference 2.[2]

syn-$CH_3CHOO + SO_2 \rightarrow$ Products (R7.1)

anti-$CH_3CHOO + SO_2 \rightarrow$ Products (R7.2)

Taatjes *et al.* reported the kinetics of the reaction between both conformers and SO_2 to display a significant conformer-dependence. Experiments were also carried out at higher ionisation energies (13 eV) allowing the SO_3 product to be directly observed. SO_3 was found to form with a rise time that correlates with the decay time of the Criegee intermediate, indicating that SO_3 is directly produced from the reaction between CH_3CHOO conformers and SO_2 under the experimental conditions of the study.

The rate coefficient for the reaction of *anti*-CH_3CHOO with SO_2 was found to be $k_{7.2} = (6.7 \pm 1.0) \times 10^{-11}$ cm^3 molecule^{-1} s^{-1}, which is greater than that found for the reaction of *syn*-CH_3CHOO with SO_2, which had a rate coefficient of $k_{7.1} = (2.4 \pm 0.3) \times 10^{-11}$ cm^3 molecule^{-1} s^{-1}. It has been postulated that the difference in reactivity may arise as a result of the geometrical differences between the conformers, where the *syn*-conformer may pose a greater steric hindrance than the *anti*-conformer. Calculations also place the *anti*-conformer ~ 15 kJ mol^{-1} higher in energy than the *syn*-conformer.[2] In addition to measurements of the conformer-dependent kinetics, the experiments performed by Taatjes *et al.* provided information regarding the relative yield of each conformer, with results indicating a *syn*:*anti* ratio of 0.9:0.1 from the reaction of CH_3CHI with O_2 at 4 Torr and 298 K. Subsequent experiments using the PIMS technique by Howes *et al.*[8] at a fixed ionisation

energy of 10.5 eV (to photo-ionise the *syn*-conformer) gave a value for $k_{7.1}$ of $(1.7 \pm 0.3) \times 10^{-11}$ cm^3 molecule^{-1} s^{-1} at 295 K and total pressures between 1 and 2.5 Torr in N_2, with measurements indicating production of acetaldehyde (CH_3CHO) from R7.1 at a yield of (0.86 ± 0.11) at 2 Torr.[8] The reaction of *syn*-CH_3CHOO with SO_2 has also been investigated by monitoring the kinetics of OH radical production from the decomposition of *syn*-CH_3CHOO occurring in competition with R7.1, giving $k_{7.1} = (2.5 \pm 0.2) \times 10^{-11}$ cm^3 molecule^{-1} s^{-1} at 298 K and 10 Torr in Ar.[9]

Experiments using laser flash photolysis of CH_3CHI_2/O_2 mixtures with broadband UV absorption spectroscopy have also indicated that R7.1 and R7.2 are rapid.[3 10] A rate coefficient of $k = (2.0 \pm 0.3) \times 10^{-11}$ cm^3 molecule^{-1} s^{-1} at 295 K and pressures between 7.5 and 500 Torr of N_2 was reported from experiments in which the conformer-specific contributions to the total absorbance were not resolved.[10] However, the result is expected to be dominated by *syn*-CH_3CHOO on the basis of results from the earlier PIMS experiments[2] which indicated that *syn*-CH_3CHOO represents 90 % of the total CH_3CHOO produced using the photolytic method. Conformer-specific measurements using broadband UV absorption spectroscopy have been achieved in experiments performed at 293 K and a total pressure of 10 Torr in He, giving $k_{7.1} = (2.9 \pm 0.3) \times 10^{-11}$ cm^3 molecule^{-1} s^{-1} and $k_{7.2} = (2.2 \pm 0.2) \times 10^{-10}$ cm^3 molecule^{-1} s^{-1}.[3] The conformer-specific UV experiments indicated that *syn*-CH_3CHOO is the dominant conformer produced,[3] in agreement with the earlier PIMS experiments,[2] although a lower yield of 70 % was reported, which may result from the different experimental conditions or uncertainties in the UV absorption cross-sections, particularly for *anti*-CH_3CHOO.[3]

Table 7.1 summarises previous measurements of the kinetics of CH_3CHOO conformers with SO_2. It is evident from the literature that a limited range of pressures and temperatures have been used to investigate the kinetics of these reactions and so the reactions between larger Criegee intermediates and SO_2 cannot be fully characterised under atmospheric conditions from previous work. Investigating these reactions over a range of temperatures and pressures is crucial to determine what impact they may have within the atmosphere, which is the focus of the work presented throughout this chapter.

Reference	Method	Photolysis λ / nm	T / K	p / Torr	Bath Gas	$[CH_3CHI_2]$ / 10^{13} molecule cm^{-3}	$[SO_2]$ / 10^{13} molecule cm^{-3}	$k_{7.1}$ / 10^{-11} cm^3 $molecule^{-1}$ s^{-1}	$k_{7.2}$ / 10^{-10} cm^3 $molecule^{-1}$ s^{-1}
Taatjes *et al.*[2]	LFP/PIMS	351	298	4	He		0.7 – 5	2.4 ± 0.3	0.67 ± 0.10
Smith *et al.*[10]	LFP/UV abs	248	295	7.5 – 500	N_2	1300	155 – 600	[a]2.0 ± 0.3	-
Sheps *et al.*[3]	LFP/UV abs	266	293	10	He	1.5	0.8 – 4.8	2.9 ± 0.3	2.2 ± 0.2
Howes *et al.*[8]	LFP/PIMS	248	295	1 – 2.5	N_2	1 – 10	2 – 9	1.7 ± 0.3	-
Zhou *et al.*[9]	LFP/LIF	248	298	10	Ar	1.9 -10.4	0.3 – 2.2	2.5 ± 0.2	-

Table 7.1. Summary of literature results for $k_{7.1}$ and $k_{7.2}$. LFP = Laser flash photolysis, PIMS = Photo-ionisation mass spectrometry, LIF = laser-induced fluorescence. [a] The value reported by Smith *et al.* is not entirely conformer-specific, however the result is expected to be dominated by *syn*-CH_3CHOO.

7.2 Experimental

Experiments to investigate the kinetics of $CH_3CHOO + SO_2$ in this work were performed at pressures between 10 and 600 Torr, and temperatures between 242 and 353 K using the experimental set-up described in Chapter 3, where reactions R7.3 – R7.6 were initiated within the cell using LFP at λ = 248 nm and the concentrations of both *syn*-CH_3CHOO and *anti*-CH_3CHOO were monitored using time-resolved broadband UV absorption spectroscopy.

$CH_3CHI_2 + h\nu$ (λ = 248 nm) → $CH_3CHI + I$ (R7.3)

$CH_3CHI + O_2 \rightarrow CH_3CHIOO^*$ (R7.4)

$CH_3CHIOO^* + M \rightarrow CH_3CHIO_2 + M$ (R7.5)

$CH_3CHIOO^* \rightarrow$ *syn*-$CH_3CHOO + I$ (R7.6a)

$CH_3CHIOO^* \rightarrow$ *anti*-$CH_3CHOO + I$ (R7.6b)

Experiments were performed under pseudo-first-order conditions, with the concentrations of SO_2 in excess over initial CH_3CHOO concentrations. Concentrations were varied in the range $[CH_3CHI_2] = (1.6 – 3.5) \times 10^{13}$ molecule cm^{-3}, $[O_2] = (0.6 - 20) \times 10^{17}$ molecule cm^{-3}, and $[SO_2] = (0.4 – 5.0) \times 10^{13}$ molecule cm^{-3}, with typical initial CH_3CHOO concentrations on the order of 10^{11} molecule cm^{-3}. Low precursor concentrations were maintained throughout in order to minimise the impact of reactions between the precursor and CH_3CHOO, which has been observed in previous work in this laboratory,[11] and to maintain low initial Criegee concentrations to minimise the effects of Criegee-Criegee and other potential Criegee-radical reactions.

The total flow rate through the cell was set to an equivalent of 1200 standard cm^3 per minute (sccm) at 50 Torr and adjusted with pressure to maintain a constant residence time in the cell of ~ 2.6 s. The laser fluence typically ranged between 20 – 35 mJ cm^{-2}. The pulse repetition rate remained at 0.33 Hz to ensure a fresh gas mixture entered the reaction cell after each laser pulse, with intensity data typically averaged over 300 laser shots. The effective pathlength for the initial experiments was determined to be (471 ± 50) cm.

Initial experiments were carried out at 50 Torr and 298 K, to obtain the kinetics for both *syn*- and *anti*-CH_3CHOO. Initially the kinetics for *anti*-CH_3CHOO were not easily obtained. The next section of this chapter will describe the problems encountered when extracting data for the *anti*-conformer, the different methods of analysis performed and changes to the initial experimental conditions, which allowed for the simultaneous extraction of the kinetics for both the *syn*- and *anti*-conformers.

Changes made to the initial experimental conditions were as follows:

The initial concentration of CH_3CHI_2 was increased from (1.6 – 3.5) × 10^{13} molecule cm^{-3} to (2.8 – 6.0) × 10^{13} molecule cm^{-3}, resulting in initial CH_3CHOO concentrations increasing from 10^{11} to 10^{12} molecule cm^{-3}. Two more spectral mirrors were added to the multi-pass set-up, increasing the effective pathlength from (471 ± 50) cm to (595 ± 53) cm. The laser fluence was increased, with typical values ranging between 40 – 60 mJ cm^{-2}, and the data were averaged over 500 laser shots, rather than 300. All other experimental conditions remained the same as above.

Experiments were performed as a function of pressure and temperature.

7.3 Analysis

Figure 7.2 shows typical absorbance spectra obtained at different times following the photolysis of CH_3CHI_2, which was used to obtain the concentration of each species present at each time point during the reaction by fitting reference absorption cross-sections to the observed absorbance, as described in Chapter 3. It should be noted that Sheps *et al.* were unable to directly determine the UV absorption cross-sections for *anti*-CH_3CHOO, but estimated the values to be similar to the cross-sections obtained for *syn*-CH_3CHOO, based on the initial concentration of *anti*-CH_3CHOO in their experiments. Sheps *et al.*[3] report a peak cross-section for *anti*-CH_3CHOO at ~ 360 nm of 1.2 × 10^{-17} cm^2, which is the same as the peak UV cross-section for *syn*-CH_3CHOO at 323 nm. Reference spectra were fit for CH_3CHI_2,[12] *syn*-CH_3CHOO,[3] *anti*-CH_3CHOO[3] and IO[13] and concentration-time profiles were obtained. Typical concentration-time profiles are shown in Figures 7.3 – 7.6.

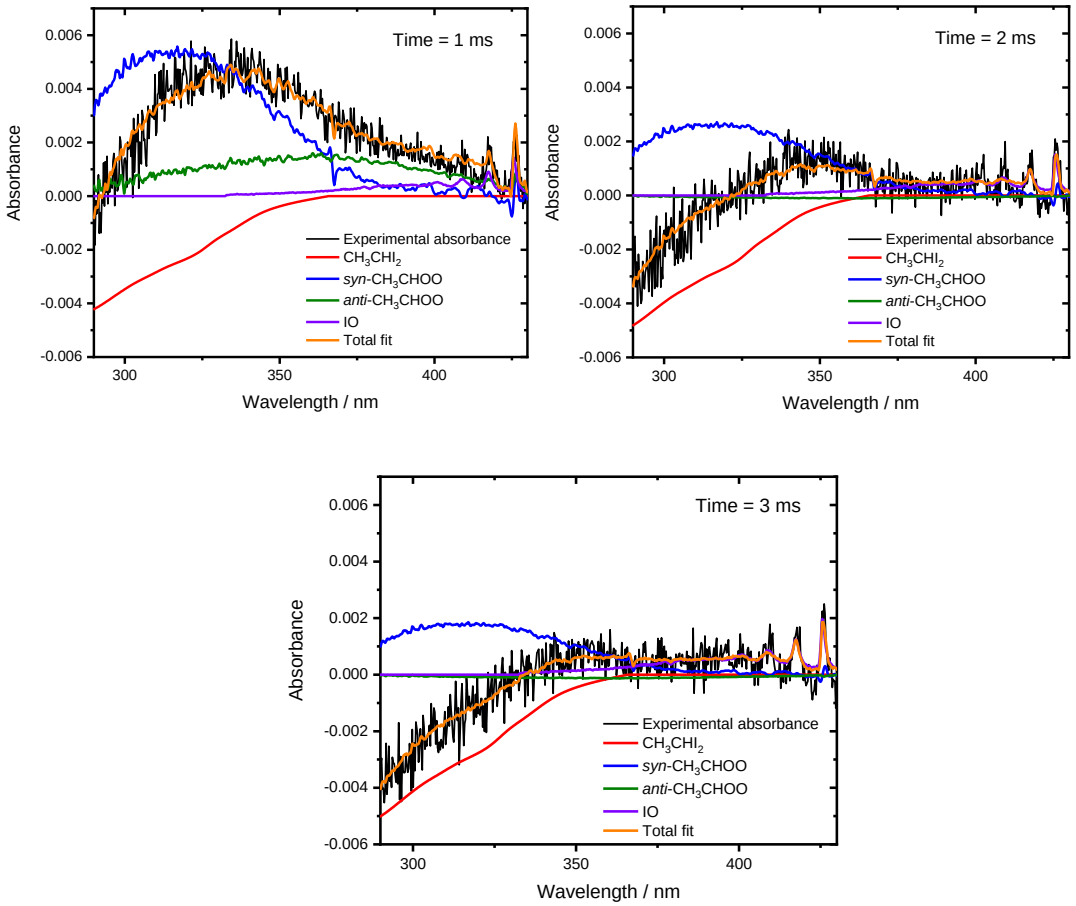

Figure 7.2. Plots outlining how the experimental absorbance evolves as the reaction progresses (shown for 1 ms, 2 ms, and 3 ms after photolysis). Observed absorbance (black), total fit (orange) and the individual contributions from *syn*-CH_3CHOO[3] (blue), *anti*-CH_3CHOO[3] (green), CH_3CHI_2[12] (red), and IO[13] (purple).

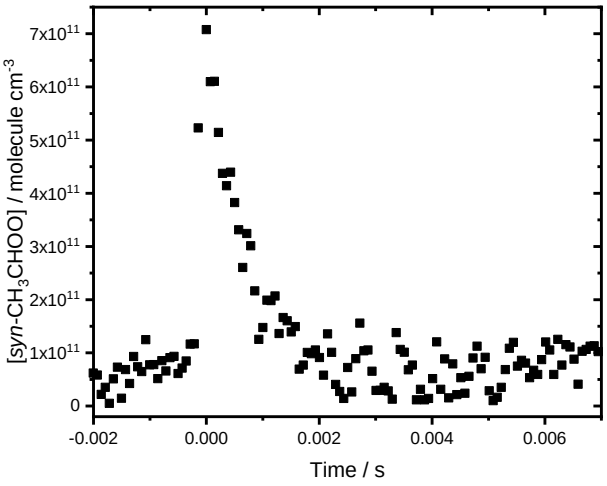

Figure 7.3. Concentration-time profile for *syn*-CH_3CHOO at 298 K and 50 Torr. $[CH_3CHI_2]_0 = 1.9 \times 10^{13}$ molecule cm^{-3}, $[SO_2] = 3.01 \times 10^{13}$ molecule cm^{-3}.

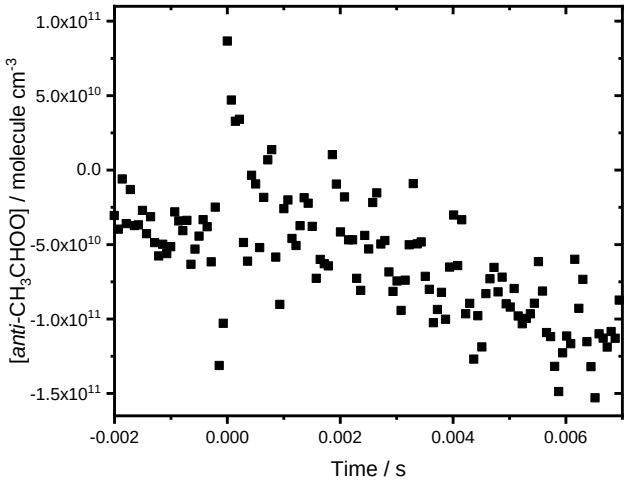

Figure 7.4. Concentration-time profile for *anti*-CH_3CHOO at 298 K and 50 Torr. $[CH_3CHI_2]_0 = 1.9 \times 10^{13}$ molecule cm^{-3}, $[SO_2] = 3.01 \times 10^{13}$ molecule cm^{-3}.

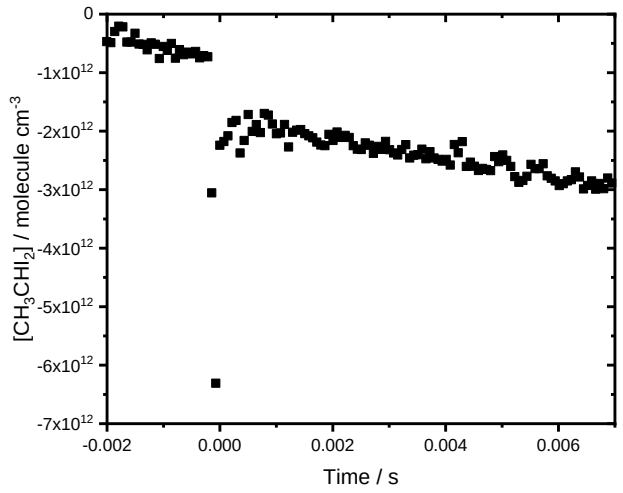

Figure 7.5. Concentration-time profile for CH_3CHI_2 at 298 K and 50 Torr which exhibits a negative absorbance owing to depletion on photolysis. $[CH_3CHI_2]_0 = 1.9 \times 10^{13}$ molecule cm^{-3}, $[SO_2] = 3.01 \times 10^{13}$ molecule cm^{-3}.

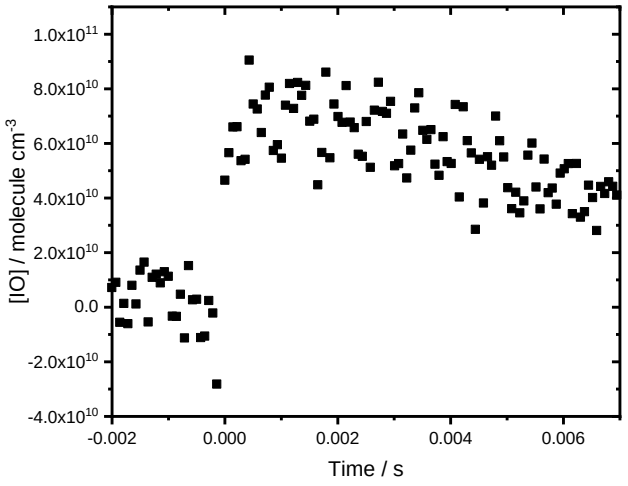

Figure 7.6. Concentration-time profile for IO at 298 K and 50 Torr. $[CH_3CHI_2]_0 = 1.9 \times 10^{13}$ molecule cm^{-3}, $[SO_2] = 3.01 \times 10^{13}$ molecule cm^{-3}.

As experiments were conducted under pseudo-first-order conditions with respect to SO_2, the change in the concentration of CH_2OO can be described using Equation 7.1.

$$[\mathrm{CH_3CHOO}]_t = [\mathrm{CH_3CHOO}]_0 \times (exp^{-k't}) \qquad \text{(Equation 7.1)}$$

where $[\mathrm{CH_3CHOO}]_t$ is the concentration of *syn*- or *anti*-CH_3CHOO at time *t*, $[\mathrm{CH_3CHOO}]_0$ is the initial concentration of the Criegee intermediate conformer, and k' is the rate coefficient describing the sum of first-order losses of the CH_3CHOO conformers and is given by

$k' = k_x + k_{7.1}[SO_2]$ for *syn*-CH_3CHOO and $k' = k_x + k_{7.2}[SO_2]$ for *anti*-CH_3CHOO, where k_x represents losses of *syn*- or *anti*-CH_3CHOO via any reaction or process other than reaction with SO_2. Previous work[6] has shown that unimolecular decomposition and bimolecular reactions with the CH_3CHI_2 precursor contribute significantly to k_x for both *syn*- and *anti*-CH_3CHOO (R7.7 – R7.11), with potential additional contributions from reactions with iodine atoms, IO, or Criegee-Criegee chemistry as well as diffusion out of the probe region.

syn-$CH_3CHOO + CH_3CHI_2 \rightarrow$ Products (R7.7)

anti-$CH_3CHOO + CH_3CHI_2 \rightarrow$ Products (R7.8)

syn-CH_3CHOO + *syn*-$CH_3CHOO \rightarrow$ Products (R7.9)

syn-CH_3CHOO + *anti*-$CH_3CHOO \rightarrow$ Products (R7.10)

anti-CH_3CHOO + *anti*-$CH_3CHOO \rightarrow$ Products (R7.11)

The data were fit with an equation which incorporates an instrument response function (IRF) in Equation 7.1, to account for the simultaneous illumination of multiple rows on the CCD followed by row-by-row shifting (further details regarding the IRF are given in Chapter 3).

Figure 7.7 shows a typical concentration-time profile obtained for *syn*-CH_3CHOO in the presence of SO_2, fit with Equation 7.1 convoluted with the IRF.

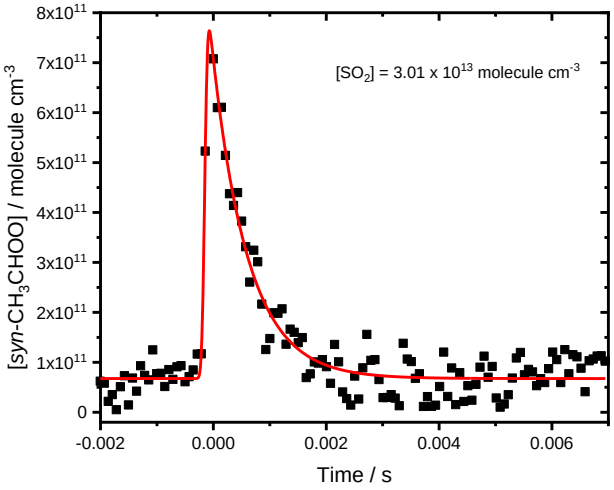

Figure 7.7. A plot of *syn*-[CH_3CHOO] as a function of time for experiments at 298 K and 50 Torr, for $[CH_3CHI_2]_0 = 1.9 \times 10^{13}$ molecule cm^{-3} and $[SO_2] = 3.01 \times 10^{13}$ molecule cm^{-3}. $k' = (1586 \pm 89)$ s^{-1}, $w = (4.09 \pm 0.86) \times 10^{-5}$ s, $t_c = -(1.53 \pm 0.05) \times 10^{-4}$ s, $[CH_3CHOO]_0 = (8.13 \pm 0.33) \times 10^{11}$ molecule cm^{-3}. The solid red line represents a fit to Equation 7.1 convoluted with the IRF. Uncertainties are 1σ.

Values for the bimolecular rate coefficients for R7.1 were obtained by plotting the individual k' values against the concentration of SO_2 as shown in Figure 7.8.

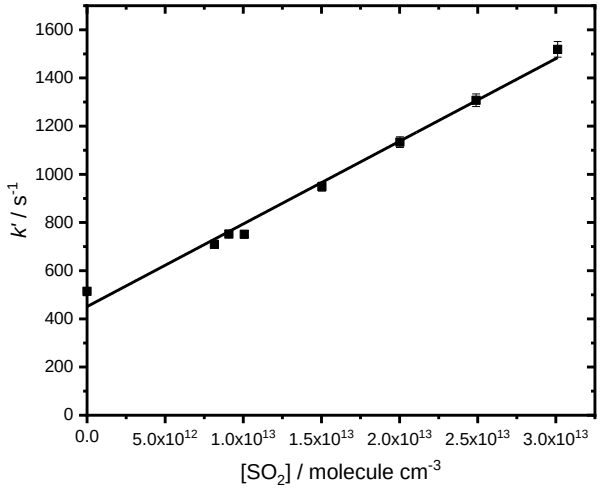

Figure 7.8. A plot of the observed rate coefficient k' as a function of $[SO_2]$ for *syn*-$[CH_3CHOO]$ at 298 K and 50 Torr, where the solid line represents an unweighted linear fit to the data, with a gradient of $(3.59 \pm 0.12) \times 10^{-11}$ cm^3 molecule^{-1} s^{-1} and intercept of (401 ± 13) s^{-1} for $[CH_3CHI_2]_0 = 1.9 \times 10^{13}$ molecule cm^{-3}. Uncertainties are 1σ.

The concentration-time profiles obtained for *anti*-CH_3CHOO (Figure 7.4) typically showed a decreasing baseline signal following photolysis, resulting in negative values for the absorbance and thus concentration. This was observed under a range of experimental conditions, for experiments both with and without SO_2 added to the system. As the data obtained for the *syn*-conformer from these experiments were of good quality and gave bimolecular rate coefficients that agreed well with previous literature studies, numerous different methods of analysis were tested to see if the data for the *anti*-conformer from these experiments could be extracted. These methods involved applying a baseline correction directly to the *anti*-conformer, fixing the concentration of CH_3CHI_2, and averaging the absorbance data between 340 – 400 nm to simultaneously extract the kinetics of both conformers. A description of each method of analysis is given below.

7.3.1 Applying a Baseline Correction

To account for the decline in the baseline signal observed for the *anti*-conformer following photolysis, a baseline correction was applied where a straight line was fit through the data points corresponding to the baseline (any points between 0-3 ms were removed prior to this fitting as this is the time region where we expect the chemistry to be taking place) followed by subtraction of the baseline from the signal. Figure 7.9 shows an example of the determination of the baseline.

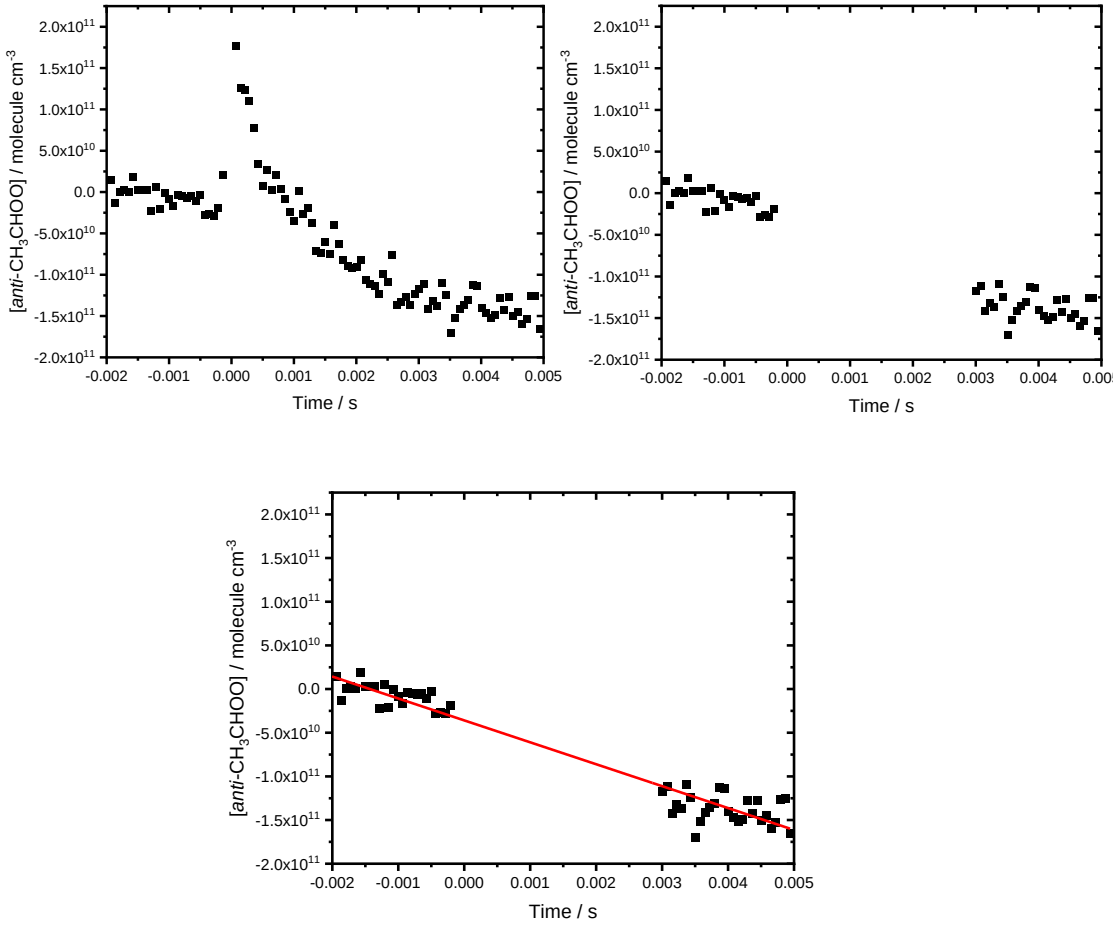

Figure 7.9. Example plots outlining how the baseline correction was applied to the *anti*-data. The gradient -(8.1 ± 0.4) × 10^{12} molecule cm^{-3} s^{-1} and intercept -(3.5 ± 0.2) × 10^{10} molecule cm^{-3} were subtracted from the overall *anti*-signal.

Figure 7.10 shows a comparison of the *anti*-data before the baseline correction had been applied (black points) and after the baseline correction was applied (red points).

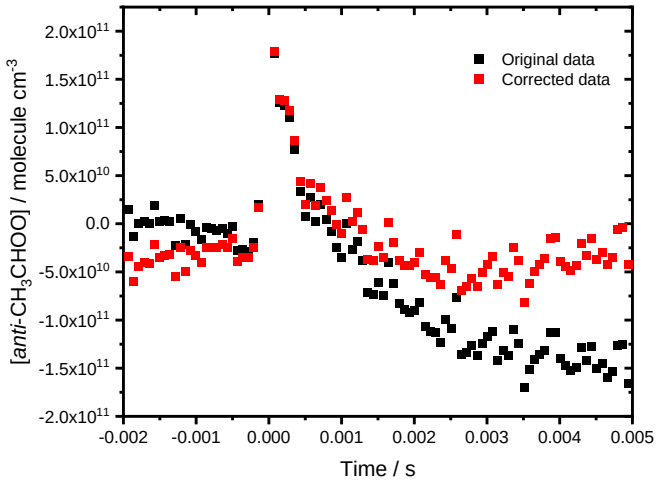

Figure 7.10. A plot of *anti*-[CH_3CHOO] as a function of time for [SO_2] = 9.10 × 10^{12} molecule cm^{-3} and [CH_3CHI_2]$_0$ = 1.9 × 10^{13} molecule cm^{-3} at 298 K and 50 Torr. The black points represent the data before the baseline correction was applied and the red points represent the data after the baseline correction was applied.

After the baseline correction was applied to the data, concentration-time profiles were analysed using Equation 7.1. An example fit to a concentration-time profile is shown in Figure 7.11.

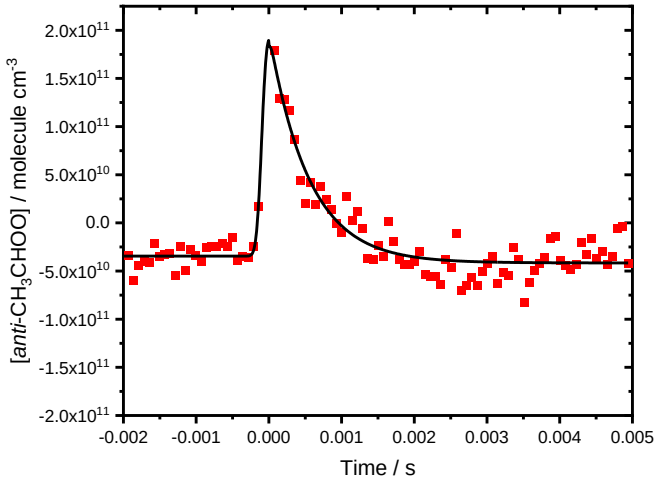

Figure 7.11. A plot of *anti*-[CH_3CHOO] as a function of time for [SO_2] = 9.10 × 10^{12} molecule cm^{-3} and [CH_3CHI_2]$_0$ = 1.9 × 10^{13} molecule cm^{-3} at 298 K and 50 Torr, after the baseline correction was applied. k' = (1827 ± 165) s^{-1}, *anti*-[CH_3CHOO]$_0$ = (1.83 ± 0.28) × 10^{11} molecule cm^{-3}. Uncertainties are 1σ.

A value for the bimolecular rate coefficient, $k_{7.2}$, was obtained by plotting the individual k' values, obtained from the concentration-time profiles, against the concentration of SO_2. Figure 7.12 shows a bimolecular plot for *anti*-CH_3CHOO after the data were analysed using the baseline correction method described above.

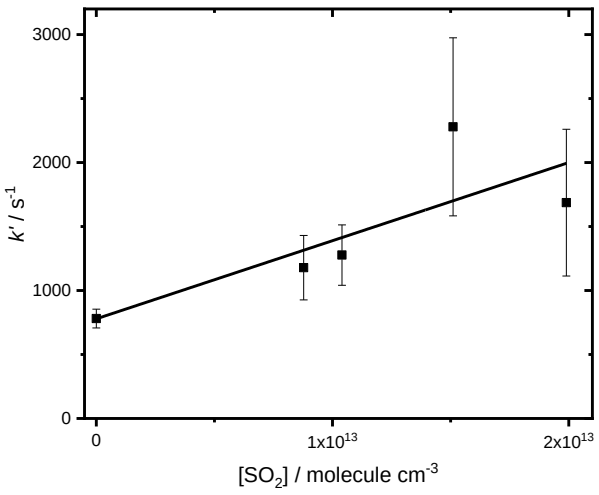

Figure 7.12. A plot of the observed rate coefficient, k', as a function of SO_2 concentration for *anti*-CH_3CHOO at 298 K and 50 Torr, where the black line represents an unweighted linear fit to the data, giving a gradient of $(6.11 \pm 2.64) \times 10^{-11}$ cm^3 molecule^{-1} s^{-1} and intercept of (779 ± 336) s^{-1}. Uncertainties are 1σ.

There were still some issues with extracting the *anti*-data from the overall absorbance, which contributes to the large error bars present on the bimolecular plot, and therefore nearly a 50 % error in the bimolecular rate coefficient, which were not observed for the *syn*-data. As the CH_3CHOO system requires four different reference spectra to be fit to the absorbance, CH_3CHI_2, *syn*-CH_3CHOO, *anti*-CH_3CHOO and IO, it can be challenging for the spectral fit to distinguish between the different species, particularly when the concentration, and absorbance, of one species (i.e. *anti*-CH_3CHOO) is low, and so further data analysis was required.

7.3.2 Constraining the Change in CH_3CHI_2 Concentration

When the *anti*-absorbance signal is low, issues arise extracting its concentration from the measured absorbance. Figure 7.13 shows absorbance spectra obtained at different time points following photolysis, where the signal corresponding to the *anti*-conformer is shown to be negative, and the signal corresponding to CH_3CHI_2 significantly changes between spectra, which is expected to remain at a constant value following photolysis. Figure 7.14 shows an example concentration-time profile for *anti*-CH_3CHOO where the concentration of *anti*-CH_3CHOO is low and there is a gradual decrease in the baseline, which significantly reduces the quality of the fit to obtain kinetics.

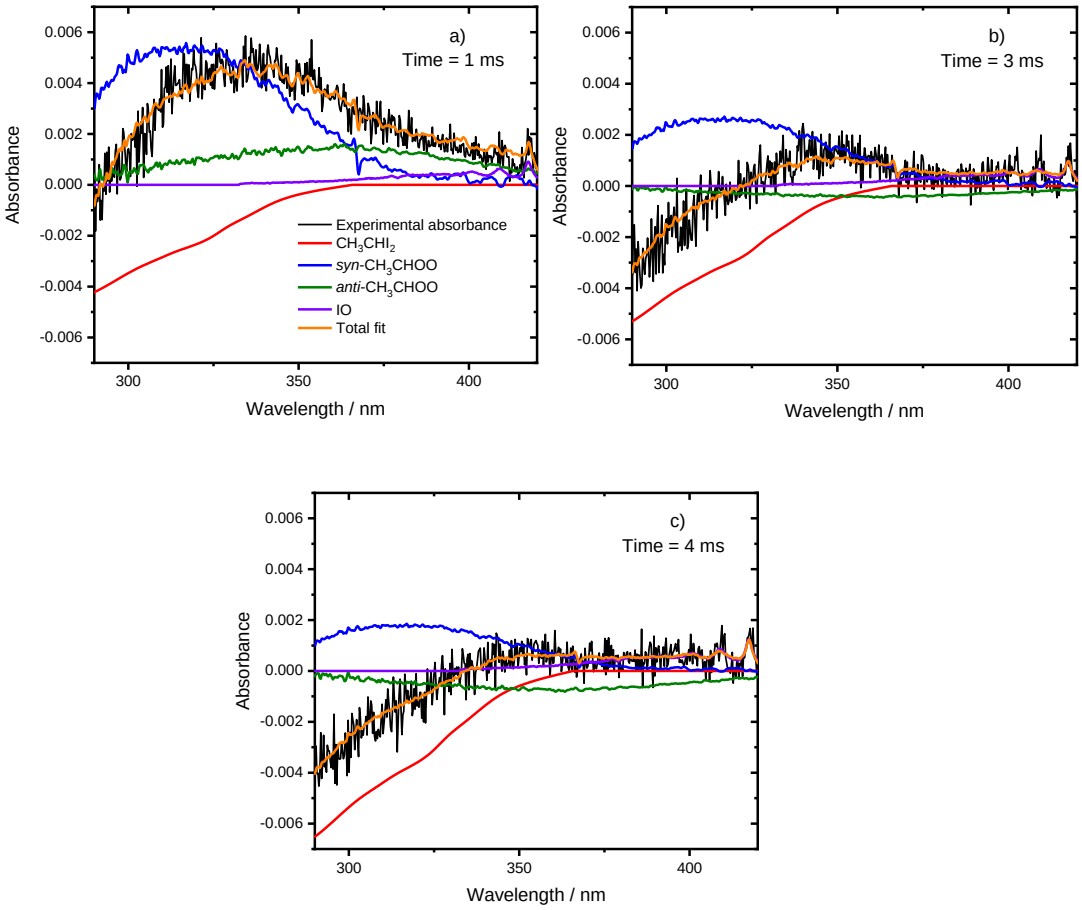

Figure 7.13. Observed absorbance (black), total fit (orange), and the individual contributions from *syn*-CH_3CHOO,[3] (blue) *anti*-CH_3CHOO,[3] (green) CH_3CHI_2,[12] (red) and IO[13] (purple) determined by fitting reference spectra to the observed absorbance using the Beer-Lambert law. For these data, T = 298 K, p = 50 Torr, t = a) 1, b) 3 and c) 4 ms post-photolysis, $[CH_3CHI_2]_0 = 1.7 \times 10^{13}$ molecule cm^{-3}.

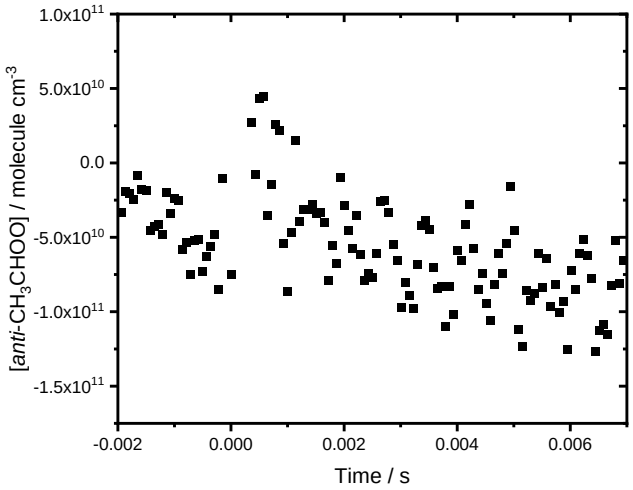

Figure 7.14. Concentration-time profile for *anti*-CH_3CHOO used to demonstrate a low signal for the *anti*-conformer. $[CH_3CHI_2]_0 = 1.7 \times 10^{13}$ molecule cm^{-3} and $[SO_2] = 0$, at 298 K and 50 Torr.

As the spectral fitting procedure involves four different reference spectra, it is plausible that the fit could be overestimating the contribution of one species and in-turn underestimating the contribution of *anti*-CH_3CHOO. As the absorption spectrum of IO is structured and well-defined in the region between 420 – 450 nm, the concentrations of IO are retrieved well by the fits and it is unlikely that this will influence the contribution from the Criegee intermediate. However, the absorption spectrum for CH_3CHI_2 is relatively broad and expands over the same wavelength region as the Criegee intermediate, meaning it would be possible for the spectral fit to assign the contribution of *anti*-CH_3CHOO as the contribution from CH_3CHI_2. Figure 7.15 shows a typical concentration-time profile for CH_3CHI_2 obtained in these experiments, which shows some noise and a steady decrease in signal following photolysis, which should remain constant on the timescale of the experiment. Such effects are likely to cause issues when extracting the absorbance data from the other contributing species, particularly *anti*-CH_3CHOO which is present in low yields in the system.

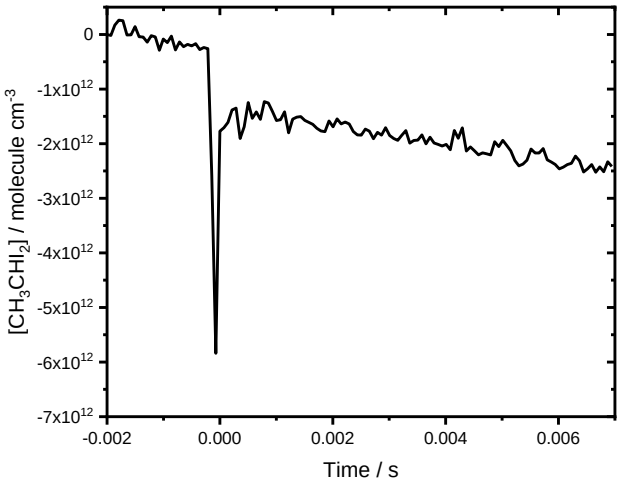

Figure 7.15. Concentration-time profile for CH_3CHI_2 following the photolysis of CH_3CHI_2. $[CH_3CHI_2]_0 = 1.7 \times 10^{13}$ molecule cm^{-3} and $[SO_2] = 0$, at 298 K and 50 Torr.

To attempt to resolve this issue, fits to the spectra were performed in which the pre-photolysis precursor concentration was fixed to zero and the post-photolysis precursor concentration was fixed to the average value determined in the initial fits at times between 1 and 4 ms. An example of this is shown in Figure 7.16 below, where the black line represents the experimentally observed precursor concentration and the blue line represents both the pre- and post-photolysis concentrations that have been given a fixed value.

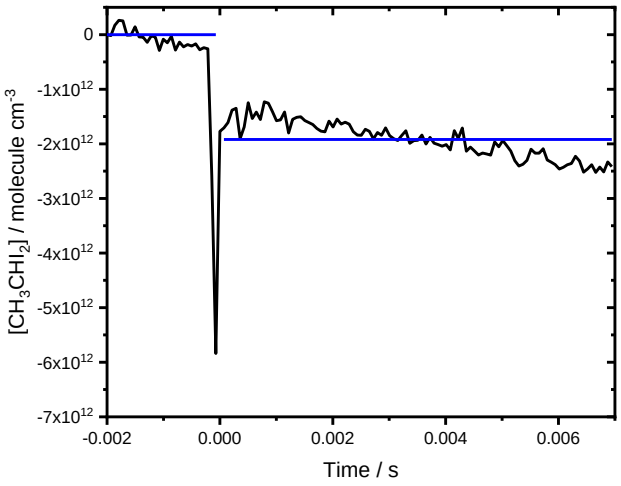

Figure 7.16. Concentration-time profile for CH_3CHI_2, where the black line represents the experimentally observed precursor concentration and the blue line represents the pre- and post-photolysis precursor concentrations that have been fixed. For these data, the change in concentration of CH_3CHI_2 was fixed to -1.92×10^{12} molecule cm^{-3}.

Figure 7.17 below shows a comparison of the concentration-time profiles obtained for *anti*-CH_3CHOO from fits to the spectra in which the precursor contribution to the absorbance was unconstrained and in which the precursor contribution to the absorbance was constrained to a constant value determined from the average precursor concentration obtained between 1 and 4 ms following photolysis in the unconstrained fit.

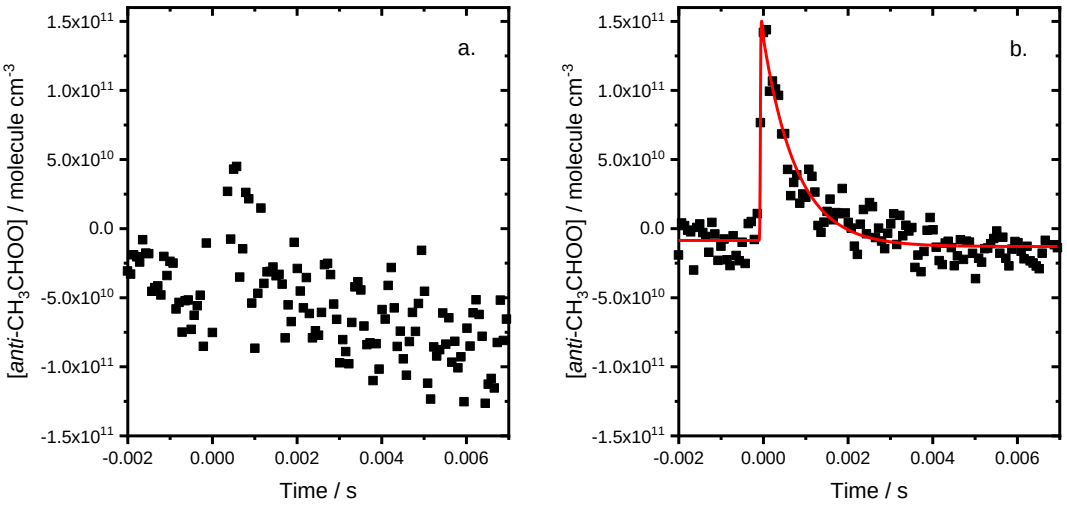

Figure 7.17. Comparison of concentration-time profiles for *anti*-CH_3CHOO before the precursor concentration was fixed (a) and after the precursor concentration had been fixed (b) where the red line on the right plot represents a fit to Equation 7.1.

The concentration time profiles for *anti*-CH_3CHOO were then analysed using Equation 7.1 convoluted with the IRF and a value for the bimolecular rate coefficient, $k_{7.2}$, was obtained in the same way as described above. Figure 7.18 below shows a comparison of the bimolecular plots obtained for R7.2 when the baseline correction was applied, as described above, (black points, as shown above in Figure 7.12) and the bimolecular plot obtained after the precursor concentration was fixed (pink points). Figure 7.18 highlights that fixing the precursor concentration allows more data points to be included in the bimolecular plot for *anti*-CH_3CHOO as a result of the better quality fits of Equation 7.1 to the *anti*-data.

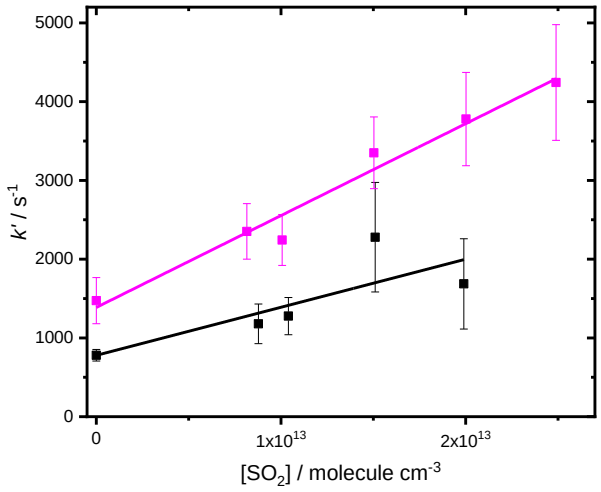

Figure 7.18. A comparison of the bimolecular plots obtained for *anti*-CH_3CHOO + SO_2 at 298 K and 50 Torr for data before the precursor concentration was fixed (black) and after the precursor concentration was fixed (pink). The black line represents an unweighted linear fit to the data before the precursor was fixed, with a gradient of $(6.11 \pm 2.64) \times 10^{-11}$ cm^3 $molecule^{-1}$ s^{-1} and intercept of (779 ± 336) s^{-1} and the pink line represents an unweighted linear fit to the data, with a gradient of $(1.17 \pm 0.10) \times 10^{-10}$ cm^3 $molecule^{-1}$ s^{-1} and intercept of (1387 ± 153) s^{-1}. Uncertainties are 1σ.

Constraining the post-photolysis precursor concentration allowed the *anti*-signal to be better identified from the baseline signal, as shown in Figure 7.17 but also resulted in bimolecular plots containing large error bars, higher values for *k'* when compared to the corresponding *k'* values when the precursor concentration had not been fixed, as well as a significantly higher value for the intercept. Analysis of the *anti*-data is challenging owing to low yields and high reactivity, and while the analysis in which the precursor concentration is constrained in the spectral fit does offer some advantages, there are still large uncertainties in the result. Analysing the data using this method also influenced the data previously obtained for the *syn*-conformer. Figure 7.19 shows a comparison of the bimolecular plots obtained for the reaction of *syn*-CH_3CHOO with SO_2 when the post-photolysis precursor concentration was unconstrained (black points, results as described above) and when the precursor concentration had been constrained (pink points).

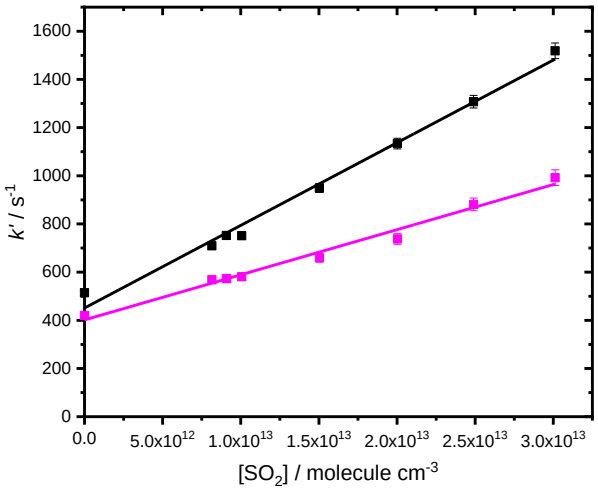

Figure 7.19. Comparison of the bimolecular plots for the reaction of *syn*-CH_3CHOO with SO_2 before and after the precursor had been fixed. The black points represent the values before the precursor was fixed, with a gradient of $(3.59 \pm 0.12) \times 10^{-11}$ cm^3 $molecule^{-1}$ s^{-1} and intercept of (401 ± 13) s^{-1} and the pink points represent the data after the precursor had been fixed, with a gradient of $(1.94 \pm 0.17) \times 10^{-11}$ cm^3 $molecule^{-1}$ s^{-1} and intercept of (387 ± 22) s^{-1}. Uncertainties are 1σ.

Constraining the change in the concentration of CH_3CHI_2 enabled signal corresponding to the *anti*-conformer to be better identified when compared to the previous analysis. However, this method of analysis resulted in a ~ 50 % change in the rate coefficient obtained for $k_{7.1}$. While the signal corresponding to the *anti*-conformer is lower than that of the *syn*-conformer and is more likely to be influenced by any changes in the baseline signal, fixing the concentration of CH_3CHI_2 would still influence the kinetics obtained for the *syn*-conformer as there is still an overlap between the absorption cross-sections of each species. To ensure reliable data is being obtained for each conformer, the method of analysis would need to avoid any data manipulation, such as taking the average absorbance between a given wavelength range, and simultaneously extracting the kinetics for each conformer.

7.3.3 Averaging the Absorbance Data

An alternative method presented in the literature was used by Sheps *et al.*,[3] to analyse the data from similar time-resolved broadband UV experiments, in which the kinetics are obtained by fitting to the average absorbance within a given wavelength range, rather than fitting to reference spectra to obtain concentration-time profiles. This analysis gives a single profile for the average absorbance as a function of time, which demonstrates a biexponential decay (Equation 7.2) with a fast component corresponding to the *anti*-conformer and a slow component corresponding to the *syn*-conformer. Figure 7.20 shows an absorption signal obtained by Sheps *et al.* and a kinetic model that is made up of two independent components, each with a single exponential rise and decay.

$$A_t = A_{0,\text{syn}}\left(exp^{-k'_{syn}t}\right) + A_{0,\text{anti}}\left(exp^{-k'_{anti}t}\right) \qquad \text{(Equation 7.2)}$$

where A_t is the absorbance at time t, $A_{0,syn}$ is the initial absorbance pertaining to *syn*-CH_3CHOO, $A_{0,anti}$ is the initial absorbance pertaining to *anti*-CH_3CHOO, k'_{syn} is the pseudo-first-order rate coefficient corresponding to *syn*-CH_3CHOO and k'_{anti} is the pseudo-first-order rate coefficient corresponding to *anti*-CH_3CHOO.

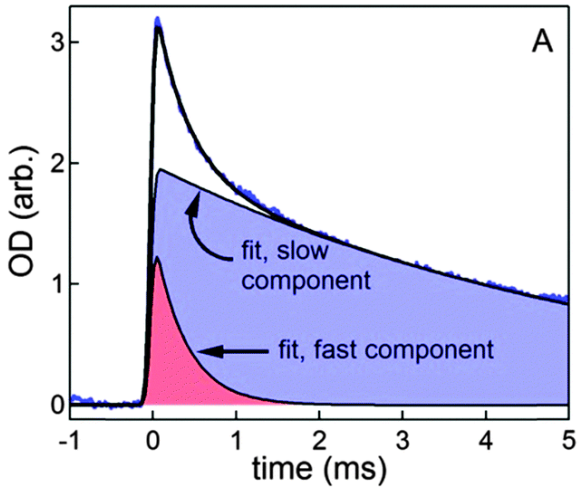

Figure 7.20. Absorption signals obtained by Sheps *et al.*, where the data was averaged between 320 and 400 nm. The thick black line shows a fit to the two components in the model, which are outlined by the blue and pink shaded areas. Copied from reference 3.[3]

Figure 7.21 shows example plots obtained in this work, where the absorbance was averaged between 340 and 400 nm. Each decay profile was fit with an equation that combined the parameters for the exponential decay (Equation 7.2) with the instrument response function.

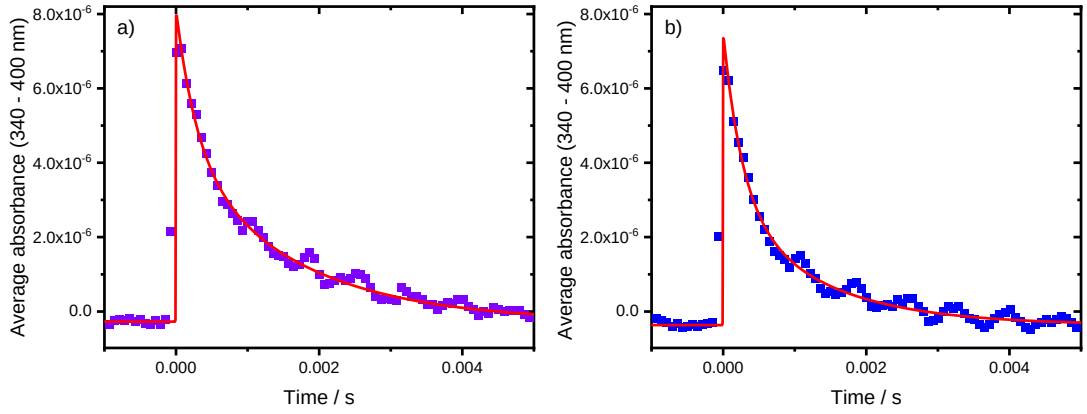

Figure 7.21. Biexponential decay for an experiment at 298 K and 50 Torr for (a) $[SO_2] = 1.00 \times 10^{13}$ molecule cm^{-3} and (b) $[SO_2] = 2.00 \times 10^{13}$ molecule cm^{-3}, where the red line represents a fit to Equation 7.2 convoluted with the IRF. The fit gave: (a) $A_{0,syn} = (3.8 \pm 2.5) \times 10^{-6}$, $k'_{syn} = (629 \pm 65)$ s^{-1}, $A_{0,anti} = (4.6 \pm 0.8) \times 10^{-6}$, $k'_{anti} = (3432 \pm 771)$ s^{-1}, (b) $A_{0,syn} = (3.3 \pm 0.9) \times 10^{-6}$, $k'_{syn} = (788 \pm 135)$ s^{-1}, $A_{0,anti} = (4.6 \pm 3.2) \times 10^{-6}$, $k'_{anti} = (3706 \pm 838)$ s^{-1}. Uncertainties are 1σ.

The pseudo-first-order rate coefficients obtained for *anti*-CH_3CHOO from experiments carried out at 298 K and 50 Torr are shown as a function of SO_2 concentration in Figure 7.22 below.

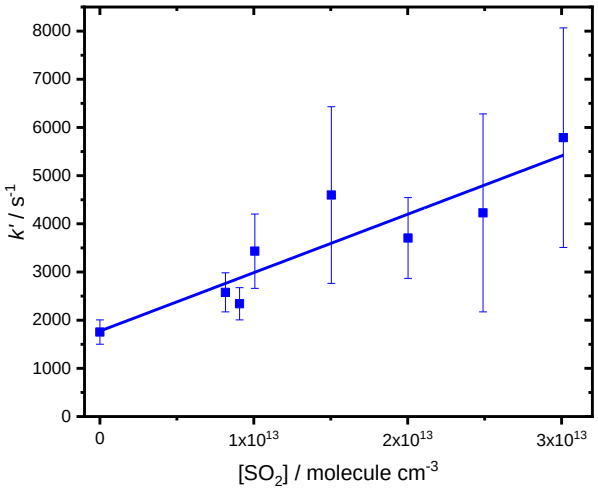

Figure 7.22. Bimolecular plot for *anti*-CH_3CHOO obtained after averaging the absorbance data between 340 and 400 nm. The blue line represents an unweighted linear fit to the data, with a gradient of $(1.21 \pm 0.23) \times 10^{-10}$ cm^3 molecule^{-1} s^{-1} and intercept of (774 ± 402) s^{-1}. Uncertainties are 1σ.

As with constraining the precursor concentration, this method of analysis allowed the signal corresponding to the *anti*-conformer to be better identified, resulting in an increased number of data points on the bimolecular plot, when compared to the more basic analysis, in which only a baseline correction had been applied. However, this method also led to data points containing large error bars, an even higher value for the intercept compared to the other methods, as well as a fraction of the data points being above the limit of detection of the camera (4000-5000 s^{-1}), making them unreliable. Figure 7.23 compares the bimolecular plots for the three different methods of analysis for the *anti*-data.

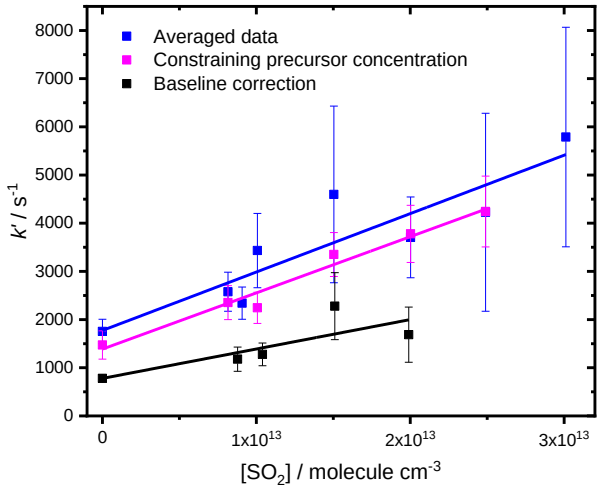

Figure 7.23. A comparison of the bimolecular plots obtained for *anti*-CH_3CHOO + SO_2 at 298 K and 50 Torr for data when the baseline correction was applied (black), after the precursor concentration was fixed (pink) and from averaging the absorbance data between 340 and 400 nm (blue). The black line represents an unweighted linear fit to the data before the precursor was fixed, with a gradient of (6.11 ± 2.64) × 10^{-11} cm^3 $molecule^{-1}$ s^{-1} and intercept of (779 ± 336) s^{-1}, the pink line represents an unweighted linear fit to the data, with a gradient of (1.17 ± 0.10) × 10^{-10} cm^3 $molecule^{-1}$ s^{-1} and intercept of (1387 ± 153) s^{-1} and the blue line represents an unweighted linear fit to the data, with a gradient of (1.21 ± 0.23) × 10^{-10} cm^3 $molecule^{-1}$ s^{-1} and intercept of (774 ± 402) s^{-1}. Uncertainties are 1σ.

Three methods of analysis were investigated as a means of accurately assigning a fraction of the decrease in absorbance as a function of time to the reaction of *anti*-CH_3CHOO with SO_2, enabling conformer dependent kinetics to be determined. While the first two methods of analysis, applying a baseline correction and fixing the precursor concentration, involved some level of data manipulation, the third method, averaging the absorbance data, was simply an alternate method of analysis that has been suggested within the literature. It can be seen from the results above that both constraining the precursor concentration and taking the average

absorbance between 340 and 400 nm enabled the *anti*-signal to be better identified from the overall absorbance and thus more data points for the *anti*-conformer to be determined and resulted in rate coefficients that were within the statistical error of each other. However, these methods of analysis resulted in pseudo-first-order rate coefficients that were significantly higher than those determined by application of a baseline correction, and with extremely large error bars. The three methods of analysis were not producing reliable results so the experimental conditions were taken into consideration.

7.3.4 Changing the Experimental Conditions

Initial experiments were carried out at 298 K and 50 Torr, where the initial concentration of CH_2CHI_2 was in the range (1-2) × 10^{13} molecule cm^{-3}. Whilst simply increasing the precursor concentration would offer some benefits, such that the signal for both *syn*- and *anti*-conformers would be increased, this would also increase the likelihood of the Criegee self-reaction, or the reaction between Criegee intermediates and the precursor, impacting results. A second option was to increase the laser fluence, which again would increase the concentrations of the Criegee intermediate conformers and potentially enable them to be extracted from the overall absorbance more easily. Increasing the laser fluence would subsequently also increase the radical concentration in the reaction cell and result in Criegee-radical reactions being more significant. It was clear that the overall absorbance would have to be increased to increase the signal-to-noise, without impacting the chemistry taking place in the reaction cell. To do this, a number of improvements were made to the experimental set-up. Firstly, the total effective pathlength of light was increased by increasing the number of passes of light through the reaction cell from seven to nine by the addition of two Al mirrors, each of 12 mm diameter (further details given in Chapter 3). The total absorbance is directly proportional to the concentration, absorption cross-section and pathlength and so increasing the pathlength would increase the absorbance without the need for changes to the initial conditions. The addition of the two extra passes increased the pathlength from (471 ± 50) cm to (595 ± 53) cm, which was determined using the method outlined in Appendix 4. Following this, the alignment of the probe beam through the reaction cell was optimised and the cell windows were also cleaned, ensuring the maximum amount of light available could reach the detector. These improvements, alongside minor adjustments to both the initial concentrations and laser fluence, resulted in better sensitivity and a significant improvement in the signal-to-noise ratio, which enabled the two conformers to be better identified from the observed absorbance and thus the conformer specific kinetics of the reaction between CH_3CHOO and SO_2 to be determined. Figure 7.24 shows typical absorbance spectra at different time points following photolysis obtained after the adjustments to the experimental set-up, where the signal corresponding to the *anti*-conformer is no longer shown as a negative absorbance.

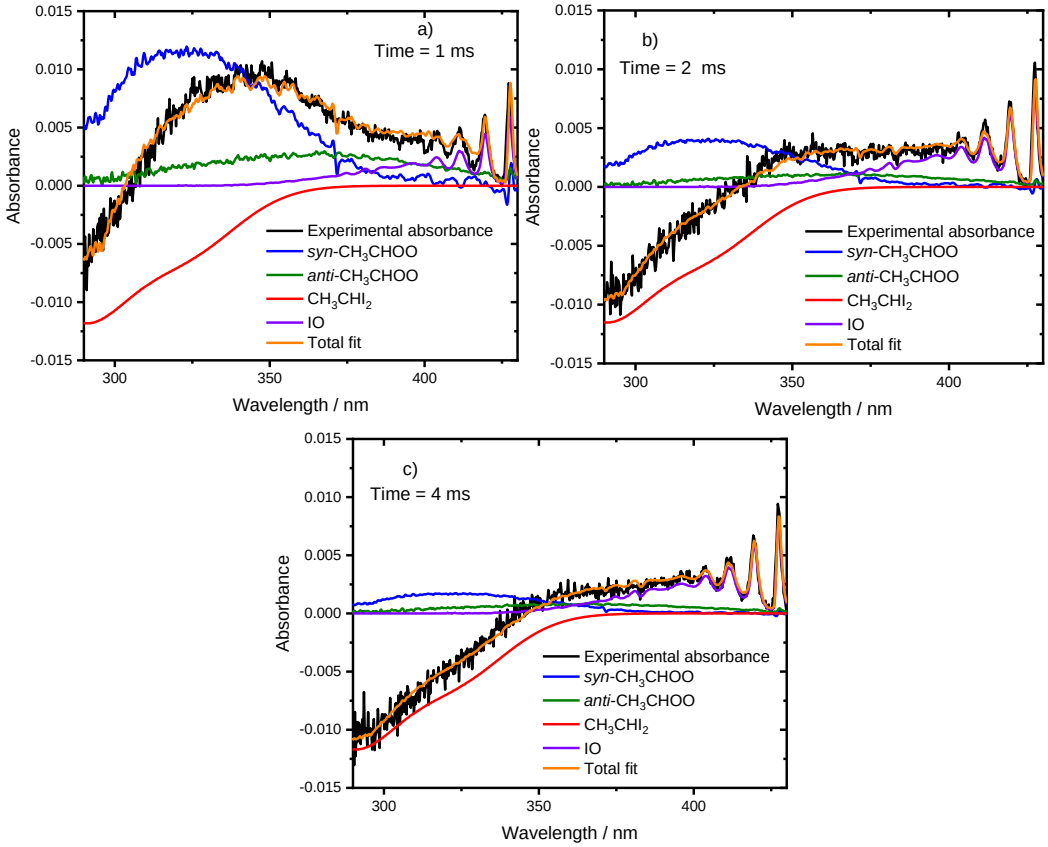

Figure 7.24. Observed absorbance (black), total fit (orange), and the individual contributions from *syn*-CH_3CHOO[3] (blue), *anti*-CH_3CHOO[3] (green), CH_3CHI_2[12] (red), and IO[13] (purple) determined by fitting reference spectra to the observed absorbance using the Beer-Lambert law. For these data, T = 353 K, p = 10 Torr, t = 1, 2 and 4 ms post-photolysis, $[CH_3CHI_2]_0 = 6.0 \times 10^{13}$ molecule cm^{-3}.

Typical concentration-time profiles for CH_3CHI_2 obtained after changes were made to the initial experimental conditions are shown in Figures 7.25 and 7.26 for experiments carried out under different experimental conditions. The plots show a negative change due to the depletion of CH_3CHI_2 upon photolysis, followed by an effectively constant concentration. From these data it is evident that the baseline issues described previously were no longer observed within the analysis and it was therefore concluded that the contribution from each species obtained from the fits to the spectra were reliable.

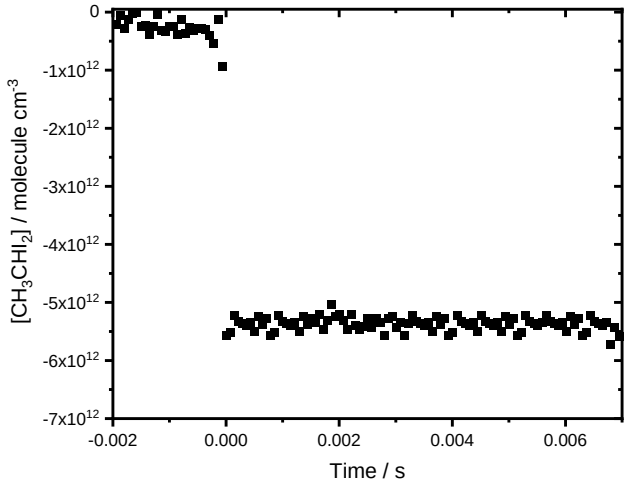

Figure 7.25. Concentration-time profile for CH_3CHI_2. T = 353 K, p = 10 Torr, $[CH_3CHI_2]_0 = 6.0 \times 10^{13}$ molecule cm^{-3} and $\Delta[CH_3CHI_2] = -5.5 \times 10^{12}$ molecule cm^{-3}.

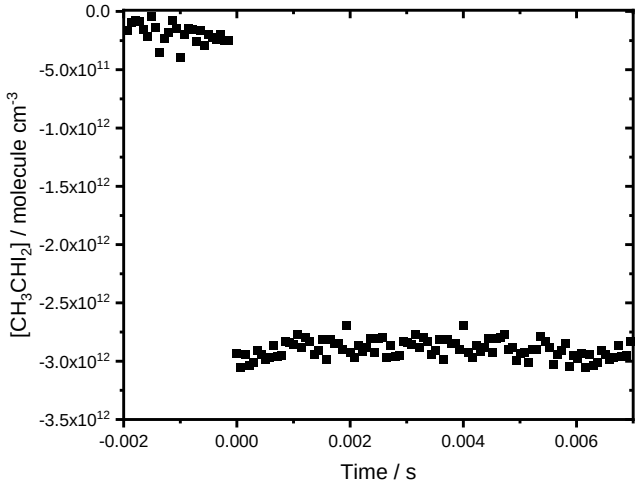

Figure 7.26. Concentration-time profile for CH_3CHI_2. T = 298 K, p = 10 Torr, $[CH_3CHI_2]_0 = 4.1 \times 10^{13}$ molecule cm^{-3} and $\Delta[CH_3CHI_2] = -2.8 \times 10^{12}$ molecule cm^{-3}.

Data obtained after the experimental conditions were optimised were also analysed using the method of averaging the absorbance data between 340 and 400 nm. Figure 7.27 shows time profiles for *syn*- and *anti*-CH_3CHOO obtained by fitting reference spectra to the observed absorbance between 290 and 450 nm as well as a plot of the averaged absorbance between 340 and 400 nm against time for the same dataset.

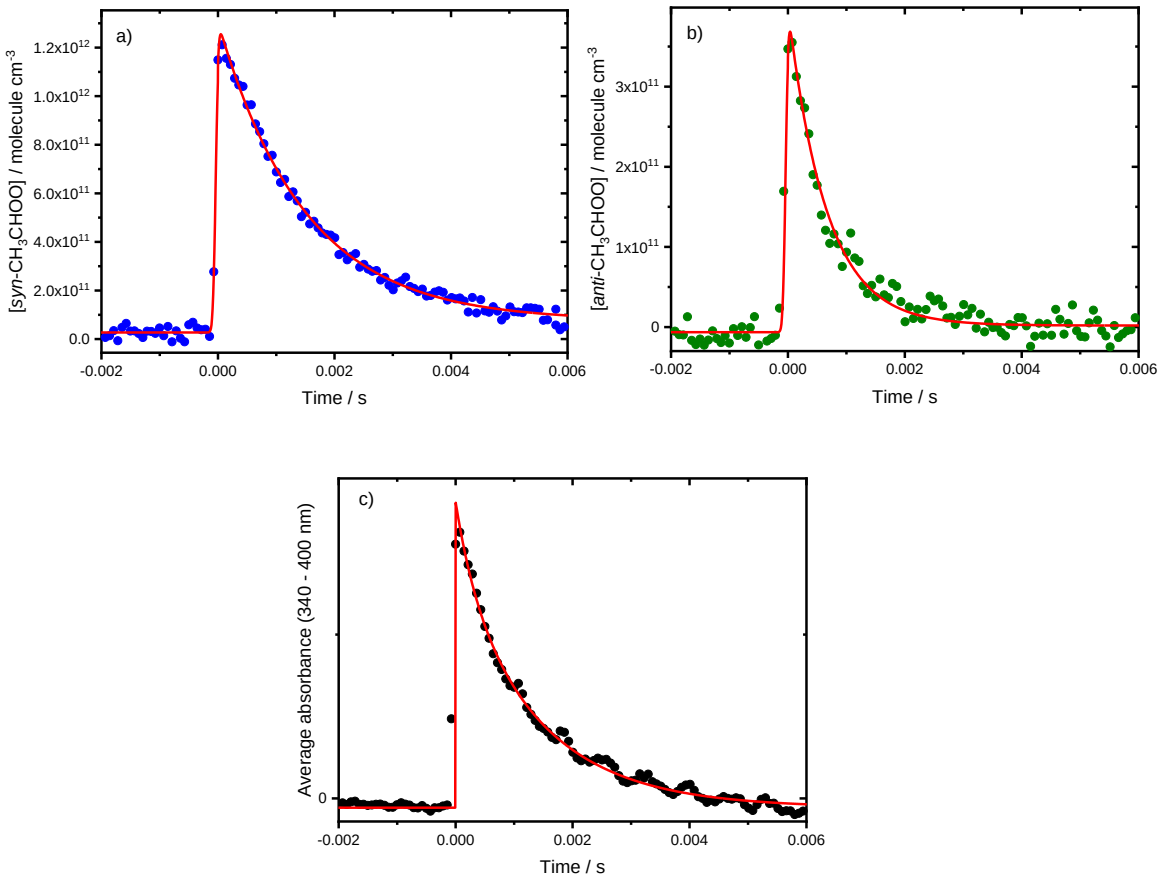

Figure 7.27. Time profiles for (a) *syn*-CH_3CHOO, (b) *anti*-CH_3CHOO and (c) the averaged absorbance signal between 340 and 400 nm for experiments at T = 289 K and p = 10 Torr. Solid red lines represent fits to Equation 7.1 convoluted with the IRF for (a) and (b) and Equation 7.2 convoluted with the IRF for (c). The fits to Equation 7.1 gave: (a) k'_{syn} = (674 ± 11) s^{-1}, (b) k'_{anti} = (1532 ± 63) s^{-1} and fits to Equation 7.2 gave: (c) k'_{syn} = (708 ± 66) s^{-1}, and k'_{anti} = (2639 ± 1135) s^{-1}.

Figure 7.28 compares pseudo-first-order rate coefficients as a function of SO_2 concentration for *syn*- and *anti*-CH_3CHOO obtained using the two methods.

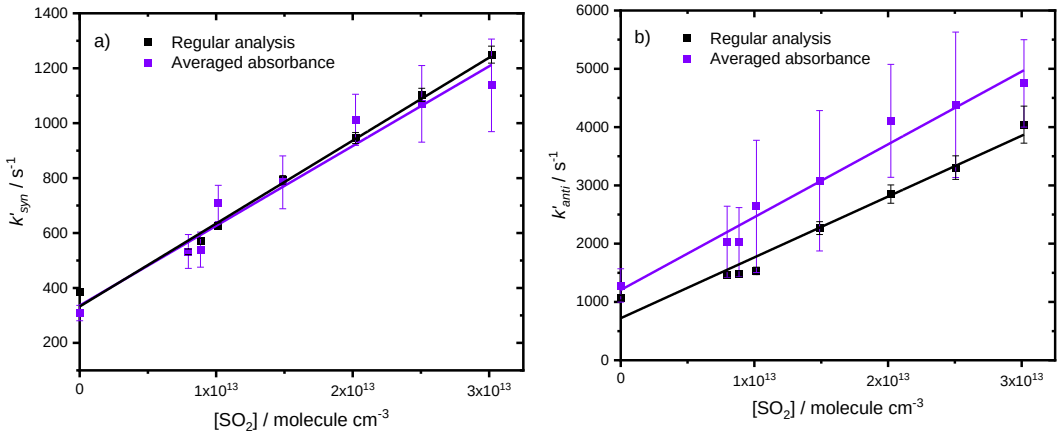

Figure 7.28. Pseudo-first-order rate coefficients as a function of SO_2 concentration obtained from experiments at T = 289 K and p = 10 Torr for (a) *syn*-CH_3CHOO and (b) *anti*-CH_3CHOO for the regular analysis (black) and the analysis where absorbance data is averaged between 340 – 400 nm (purple). Solid lines represent an unweighted linear fit to the data. For *syn*-CH_3CHOO, the regular analysis gave: $k_{7.1}$ = (3.02 ± 0.12) × 10^{-11} cm^3 $molecule^{-1}$ s^{-1} and k_x = (332 ± 21) s^{-1} and the averaging analysis gave: $k_{7.1}$ = (2.90 ± 0.24) × 10^{-11} cm^3 $molecule^{-1}$ s^{-1} and k_x = (336 ± 42) s^{-1}. For *anti*-CH_3CHOO, the regular analysis gave: $k_{7.2}$ = (1.04 ± 0.08) × 10^{-10} cm^3 $molecule^{-1}$ s^{-1} and k_x = (721 ± 135) s^{-1} and the averaging analysis gave: $k_{7.2}$ = (1.25 ± 0.24) × 10^{-10} cm^3 $molecule^{-1}$ s^{-1} and k_x = (1205 ± 157) s^{-1}. Uncertainties are 1σ.

Rate coefficients for R7.1 and R7.2 obtained by averaging the absorbance data between 340 and 400 nm ($k_{7.1}$ = (2.90 ± 0.24) × 10^{-11} cm^3 $molecule^{-1}$ s^{-1} and $k_{7.2}$ = (1.25 ± 0.24) × 10^{-10} cm^3 $molecule^{-1}$ s^{-1}) are within the error of rate coefficients obtained using the regular method of analysis ($k_{7.1}$ = (3.02 ± 0.12) × 10^{-11} cm^3 $molecule^{-1}$ s^{-1} and $k_{7.2}$ = (1.04 ± 0.08) × 10^{-10} cm^3 $molecule^{-1}$ s^{-1}). Values for the intercept, k_x, for the *syn*-conformer are also very similar however, there is a significant difference in the k_x values obtained for the *anti*-conformer from the two methods of analysis. It is clear in Figure 7.28 that the pseudo-first-order rate coefficients obtained from averaging the absorbance data have considerably larger errors than pseudo-first-order rate coefficients obtained in the regular analysis, particularly for the *anti*-conformer, which may be a reason for the difference in k_x values observed. The errors associated with the *anti*-conformer may result from a combination of the *anti*-conformer being present in lower concentrations when compared to the *syn*-conformer and the reaction of the *anti*-conformer being ~ 10 times faster than the reaction of the *syn*-conformer. Both of which are likely to make fitting the data more difficult, and therefore more uncertain. Nonetheless, the rate coefficients obtained for the two methods of analysis agree well for each conformer for experiments carried out after changes were made to the experimental conditions, which was not the case for data obtained prior to these changes.

7.4 Results and Discussion

Figure 7.29 shows concentration-time profiles for *syn*- and *anti*-CH_3CHOO in the presence of SO_2.

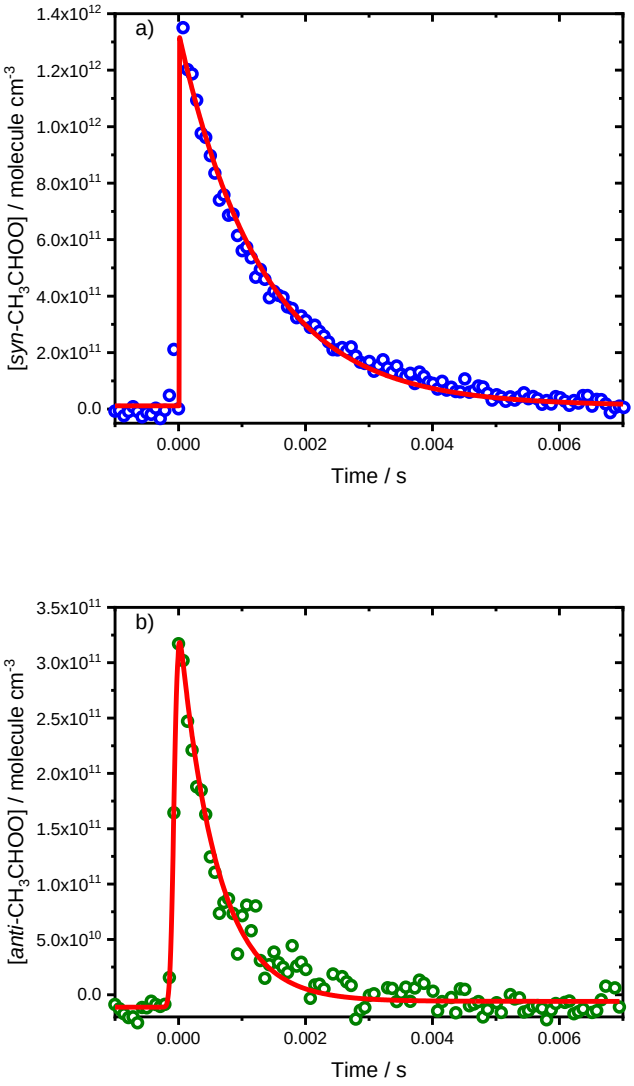

Figure 7.29. Observed concentration-time profiles for a) *syn*-CH_3CHOO and b) *anti*-CH_3CHOO. For these data, T = 298 K, p = 50 Torr, $[SO_2] = 1.1 \times 10^{13}$ molecule cm^{-3} and $[CH_3CHI_2]_0 = 2.8 \times 10^{13}$ molecule cm^{-3}. The fits to Equation 7.1 (solid line) gave an initial concentration of $(1.31 \pm 0.03) \times 10^{12}$ molecule cm^{-3} and $k' = (765 \pm 15)$ s^{-1} for *syn*-CH_3CHOO and an initial concentration of $(3.39 \pm 0.02) \times 10^{11}$ molecule cm^{-3} and $k' = (2280 \pm 218)$ s^{-1} for *anti*-CH_3CHOO. Instrument response parameters were: $w = (2.99 \pm 0.10) \times 10^{-5}$ s and $t_c = -(4.80 \pm 0.09) \times 10^{-5}$ s for both conformers. Uncertainties are 1σ.

The rate coefficients $k_{7.1}$ and $k_{7.2}$ were determined from the dependence of the pseudo-first-order losses on the concentration of SO_2, with typical results shown in Figure 7.30.

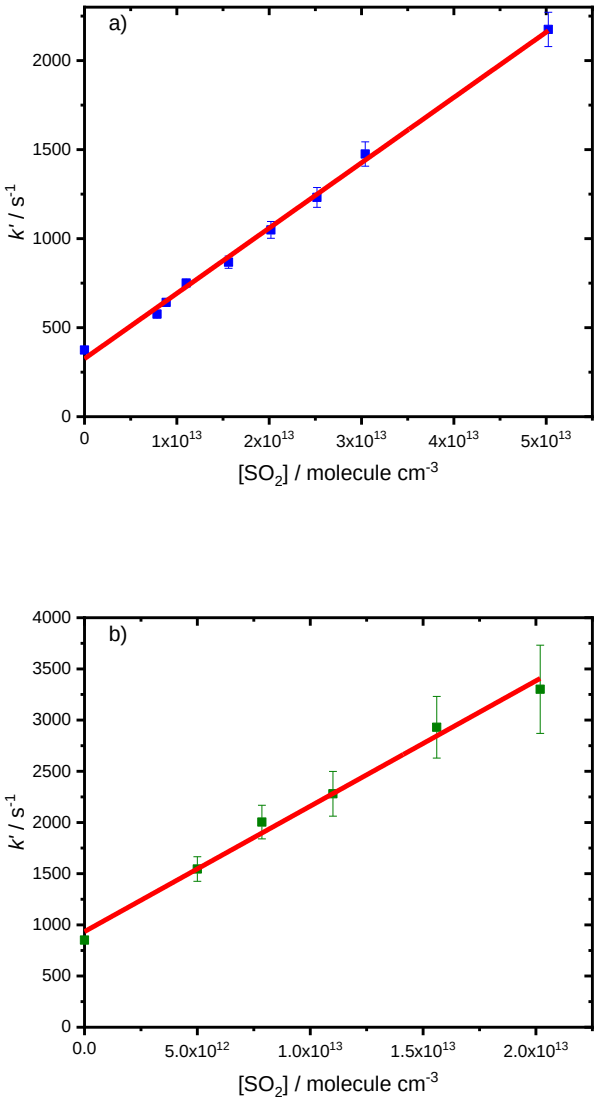

Figure 7.30. Dependence of k' on $[SO_2]$ at T = 298 K and p = 50 Torr for a) *syn*-CH_3CHOO and b) *anti*-CH_3CHOO. Fits to the data gave $k_{7.1} = (3.67 \pm 0.07) \times 10^{-11}$ cm^3 molecule^{-1} s^{-1}, with an intercept k_x of (326 ± 18) s^{-1}, and $k_{7.2} = (1.22 \pm 0.10) \times 10^{-10}$ cm^3 molecule^{-1} s^{-1}, with an intercept k_x of (934 ± 70) s^{-1}. Uncertainties are 1σ.

At 298 K, results gave $k_{7.1} = (3.67 \pm 0.07) \times 10^{-11}$ cm^3 molecule^{-1} s^{-1} which is in good agreement with the value obtained in this work for $k_{7.1}$ prior to the adjustments to the experimental set-up ($(3.59 \pm 0.12) \times 10^{-11}$ cm^3 molecule^{-1} s^{-1}) and with the value obtained for $k_{7.1}$ by averaging the absorbance signal between 340 and 400 nm ($(3.37 \pm 1.17) \times 10^{-11}$ cm^3 molecule^{-1} s^{-1}). Results also gave $k_{7.2} = (1.22 \pm 0.10) \times 10^{-10}$ cm^3 molecule^{-1} s^{-1}, this value compares well with values previously obtained for $k_{7.2}$ in this work through analysis where the concentration of CH_3CHI_2 was fixed ($(1.17 \pm 0.10) \times 10^{-10}$ cm^3 molecule^{-1} s^{-1}) and through analysis where the absorbance data was averaged between 340 and 400 nm ($(1.21 \pm 0.23) \times 10^{-10}$ cm^3 molecule^{-1}

s^{-1}). Comparison of results obtained for $k_{7.1}$ and $k_{7.2}$ with results obtained from averaging the absorbance data between 340 and 400 nm provides further evidence that the results obtained following the changes made to the experimental set-up are reliable.

The potential for the contribution of second-order behaviour was also investigated, where the decay of CH_3CHOO is described by a mixed first- and second-order model. Figure 7.31 shows a comparison between the first-order and mixed-order fits to typical concentration-time profiles for *syn*- and *anti*-CH_3CHOO, which indicates there were no significant differences between the first-order component obtained when describing the kinetics using a first-order model and when describing the kinetics using a mixed-order model. Figure 7.32 compares rate coefficients for reactions of *syn*- and *anti*-CH_3CHOO with SO_2 obtained from the first-order fits to those obtained from the mixed-order fits. Results show less than 5 % difference between the rate coefficients obtained when kinetics were described using the first-order and mixed-order models and values obtained for the intercept, k_x, between the two fits were within their error limits. We therefore concluded that data were well described by pseudo-first-order kinetics.

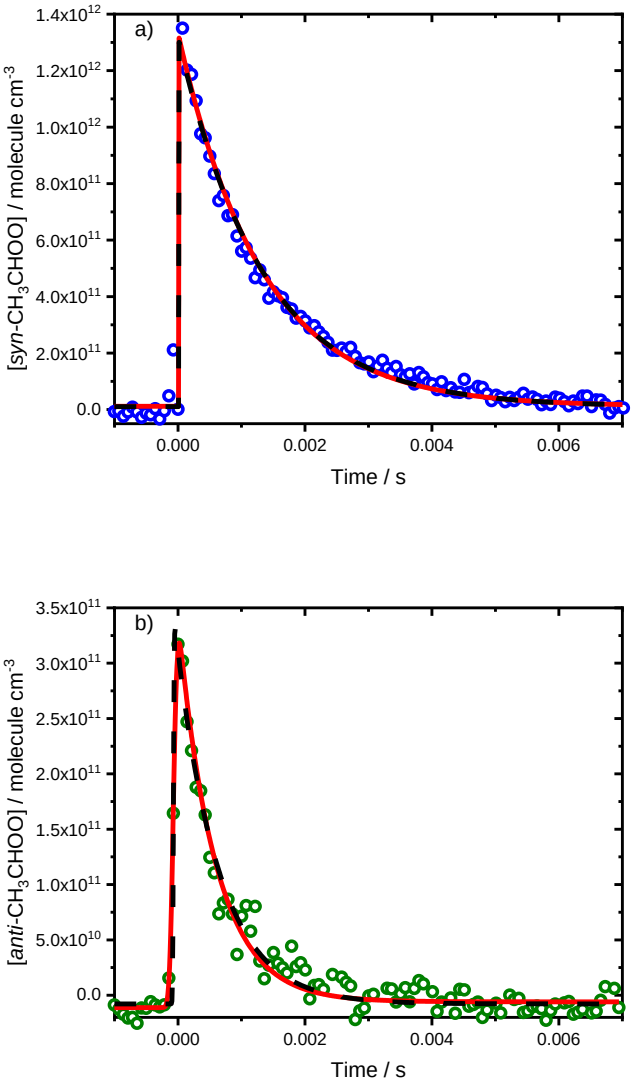

Figure 7.31. Comparison between first-order (solid red lines) and mixed-order (dashed black lines) for typical concentration-time profiles for a) *syn*-CH_3CHOO and b) *anti*-CH_3CHOO. The first-order fit to the *syn*-CH_3CHOO data gave k' = (765 ± 15) s^{-1} and $[CH_3CHOO]_0$ = (1.31 ± 0.03) × 10^{12} molecule cm^{-3} and the mixed-order fit gave k' = (754 ± 15) s^{-1}, k'' = (7.66 ± 0.34) × 10^{-11} cm^3 $molecule^{-1}$ s^{-1} and $[CH_3CHOO]_0$ = (1.35 ± 0.07) × 10^{12} molecule cm^{-3}. The first order fit to the *anti*-CH_3CHOO gave k' = (2280 ± 220) s^{-1} and $[CH_3CHOO]_0$ = (3.39 ± 0.02) × 10^{11} molecule cm^{-3} and the mixed-order fit gave k' = (2147 ± 93) s^{-1}, k'' = (2.55 ± 0.16) × 10^{-10} cm^3 $molecule^{-1}$ s^{-1} and $[CH_3CHOO]_0$ = (3.47 ± 0.04) × 10^{11} molecule cm^{-3}. Uncertainties are 1σ.

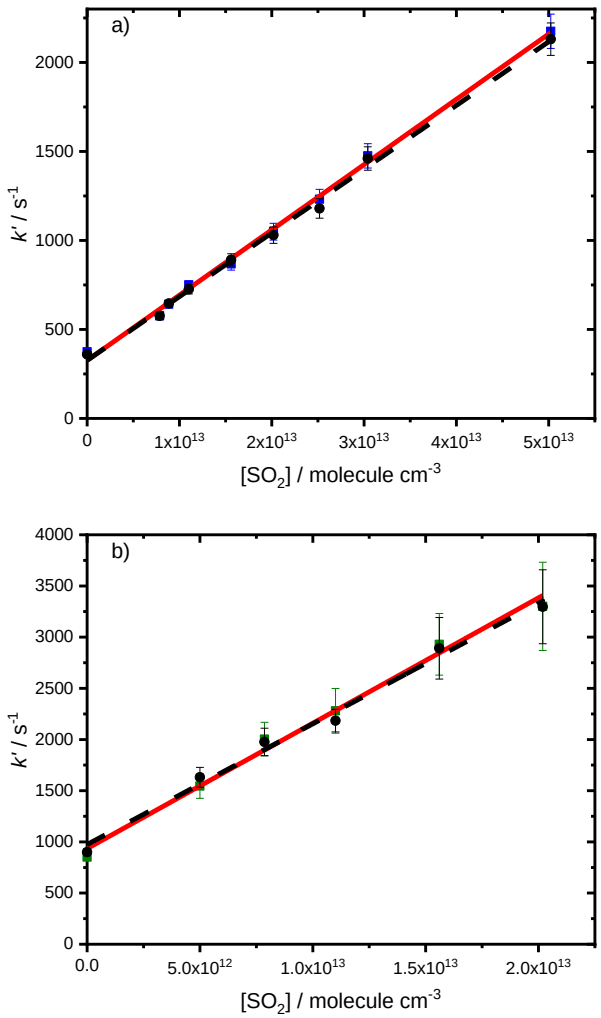

Figure 7.32. Dependence of k' on [SO_2] at T = 298 K and p = 50 Torr obtained for first-order fits (solid lines) and mixed-order fits (dashed lines) for a) *syn*-CH_3CHOO and b) *anti*-CH_3CHOO. Fits to the data for *syn*-CH_3CHOO gave $k_{7.1}$ (first-order, blue data) = (3.67 ± 0.07) × 10^{-11} cm^3 $molecule^{-1}$ s^{-1}, with an intercept k_x of (326 ± 18) s^{-1} and $k_{7.1}$ (mixed-order, black data) = (3.58 ± 0.07) × 10^{-11} cm^3 $molecule^{-1}$ s^{-1}, with an intercept k_x of (330 ± 9) s^{-1}. Fits to the data for *anti*-CH_3CHOO gave $k_{7.2}$ (first-order, green data) = (1.22 ± 0.10) × 10^{-10} cm^3 $molecule^{-1}$ s^{-1}, with an intercept k_x of (934 ± 70) s^{-1} and $k_{7.2}$ (mixed-order, black data) = (1.17 ± 0.06) × 10^{-10} cm^3 $molecule^{-1}$ s^{-1}, with an intercept k_x of (974 ± 67) s^{-1}. Uncertainties are 1σ.

Experiments were repeated at 298 K and pressures between 10 and 600 Torr with results showing an increase in $k_{7.1}$ from (3.02 ± 0.32) × 10^{-11} cm^3 $molecule^{-1}$ s^{-1} at 10 Torr to (4.66 ± 0.52) × 10^{-11} cm^3 $molecule^{-1}$ s^{-1} at 600 Torr (Figure 7.33), where the uncertainties represent a combination of the statistical error and the systematic errors resulting from uncertainties in gas flow rates and in the concentration of SO_2.

The data were fit with Equations 7.3 and 7.4, which describe a chemical activation mechanism with a non-zero rate coefficient at zero pressure,[14] to described the observed pressure dependence of R7.1 (further details regarding the chemical activation mechanism are given in Chapter 2). Figure 7.33 shows a potential energy surface describing the chemical activation and association pathways.

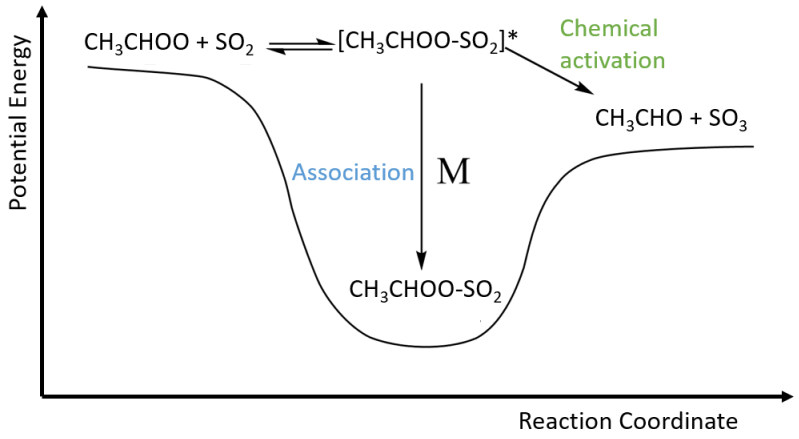

Figure 7.33. Schematic potential energy surface for the reaction between CH_3CHOO and SO_2 to produce excited $[CH_3CHOO\text{-}SO_2]^*$ and the possible reaction pathways following excitation. A further description of the chemical activation mechanism is given in Chapter 2, section 2.2.2.2.

Equation 7.4 is a variation of Equation 7.3 that includes a broadening factor, *F*, as described by the Troe fall-off form in Chapter 2 (Section 2.2.2.5).

$$k_{7.1} = k_{int} + \frac{(k_\infty - k_{int})k_0[M]}{(k_0[M]) + k_\infty} \qquad \text{(Equation 7.3)}$$

$$k_{7.1} = k_{int} + \frac{(k_\infty - k_{int})k_0[M]}{(k_0[M]) + k_\infty} F \qquad \text{(Equation 7.4)}$$

where k_{int} represents the rate coefficient at zero pressure, k_0 is the low-pressure limiting rate coefficient and k_∞ is the high-pressure limiting rate coefficient, and are given by Equations 7.5-7.7:

$$k_{int} = A_{int} \times \left(\frac{T}{298}\right)^{n_{int}} \qquad \text{(Equation 7.5)}$$

$$k_0 = A_0 \times \left(\frac{T}{298}\right)^{n_0} \qquad \text{(Equation 7.6)}$$

$$k_\infty = A_\infty \times \left(\frac{T}{298}\right)^{n_\infty} \qquad \text{(Equation 7.7)}$$

A comparison between fits to Equations 7.3 and 7.4 for data at 298 K is shown in Figure 7.34. The comparison plots at all other temperatures are shown in Appendix 11.

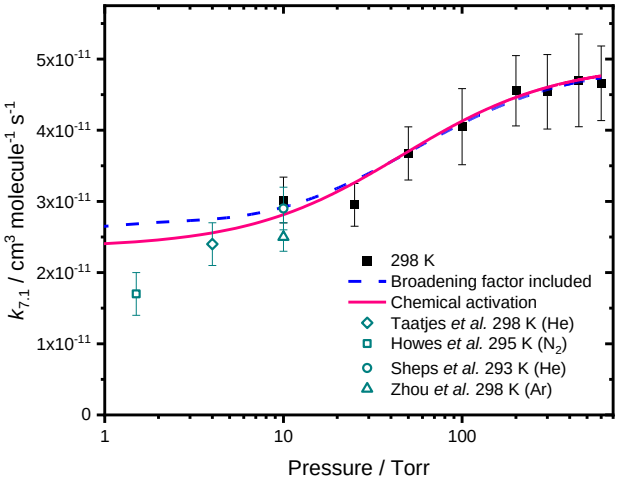

Figure 7.34. Comparison of the fit to Equations 7.3 and 7.4 for data at 298 K and pressures between 10 and 600 Torr. Results from previous studies at ~ 298 K are also shown.[2 8 3 9] The fit result for Equation 7.3 gave: A_{int} = (2.35 ± 0.39) × 10^{-11} cm^3 $molecule^{-1}$ s^{-1}, n_{int} = (0.61 ± 0.79), A_0 = (3.29 ± 1.30) × 10^{-29} cm^3 $molecule^{-1}$ s^{-1}, n_0 = -(9.52 ± 1.78), A_∞ = (4.95 ± 0.51) × 10^{-11} cm^3 $molecule^{-1}$ s^{-1}, n_∞ = -(2.52 ± 0.29) and the fit result for Equation 7.4 gave: A_{int} = (2.39 ± 0.28) × 10^{-11} cm^3 $molecule^{-1}$ s^{-1}, n_{int} = (0.19 ± 0.72), A_0 = (6.07 ± 4.74) × 10^{-29} cm^3 $molecule^{-1}$ s^{-1}, n_0 = -(10.13 ± 1.81), A_∞ = (8.98 ± 7.22) × 10^{-11} cm^3 $molecule^{-1}$ s^{-1}, n_∞ = -(3.34 ± 0.71).

Fitting the data with Equation 7.3 gave A_{int} = (2.35 ± 0.39) × 10^{-11} cm^3 $molecule^{-1}$ s^{-1}, n_{int} = (0.61 ± 0.79), A_0 = (3.29 ± 1.30) × 10^{-29} cm^3 $molecule^{-1}$ s^{-1}, n_0 = -(9.52 ± 1.78), A_∞ = (4.95 ± 0.51) × 10^{-11} cm^3 $molecule^{-1}$ s^{-1}, n_∞ = -(2.52 ± 0.29) and fitting the data with Equation 7.4 gave A_{int} = (2.39 ± 0.28) × 10^{-11} cm^3 $molecule^{-1}$ s^{-1}, n_{int} = (0.19 ± 0.72), A_0 = (6.07 ± 4.74) × 10^{-29} cm^3 $molecule^{-1}$ s^{-1}, n_0 = -(10.13 ± 1.81), A_∞ = (8.98 ± 7.22) × 10^{-11} cm^3 $molecule^{-1}$ s^{-1}, n_∞ = - (3.34 ± 0.71). The inclusion of the broadening factor to Equation 7.9 did not improve the quality of the fit to the data and therefore was not included in the final fit.

The pressure dependence observed in this work at 298 K (Figure 7.34) reconciles discrepancies between values for $k_{7.1}$ reported at room temperature in previous work at pressures below 10 Torr.[2, 8,3,9] While kinetics reported by Smith *et al.*[10] at 295 K over the pressure range 7.5 to 500 Torr are in broad agreement with low pressure values for $k_{7.1}$ reported in this work and in previous work, Smith *et al.* were unable to distinguish between the *syn*-

and *anti*-conformers and so the rate coefficient reported will contain contributions from the reactivity of both *syn*-CH_3CHOO and *anti*-CH_3CHOO.

Figure 7.35 shows the results for $k_{7.1}$ under all conditions studied in this work. Results demonstrate an increase in $k_{7.1}$ from 10 Torr to 600 Torr across all temperatures studied and an overall negative temperature dependence.

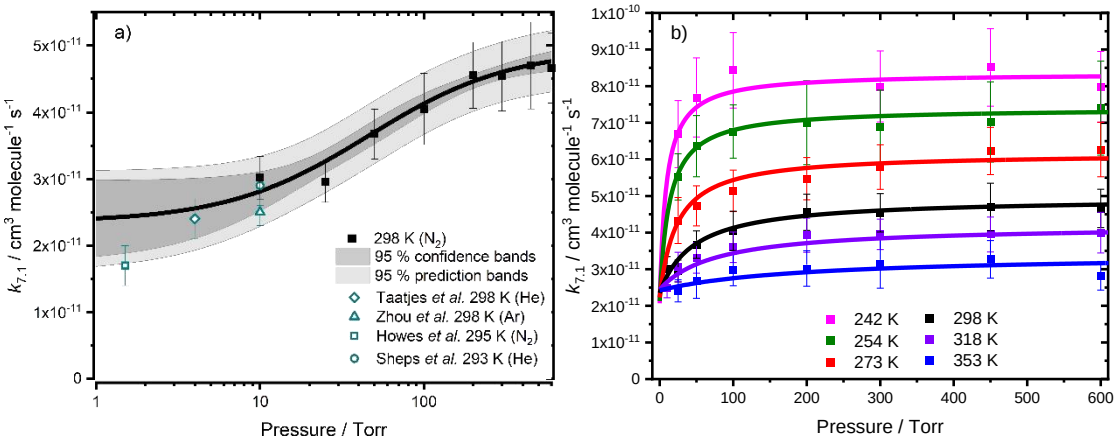

Figure 7.35. Effects of pressure on $k_{7.1}$ at (a) 298 K and (b) all temperatures studied in this work. Previous reports for $k_{7.1}$ are also shown.[2,3,8,9] Solid lines represent a fit to Equation 7.3. Error bars represent a combination of the statistical error and the systematic errors resulting from uncertainties in gas flow rates and in the concentration of SO_2.

The negative temperature dependence observed in this work is indicative of the barrierless addition of SO_2 to the Criegee intermediate, similar to that of CH_2OO + SO_2 (Chapter 4). The reaction proceeds via the formation of a secondary ozonide (SOZ) which can either become stabilised or decompose to produce CH_3CHO and SO_3. Figure 7.36 shows the structures of the SOZ and the transition state that leads to the formation of CH_3CHO and SO_3 reported by Zhao *et al.*[15]

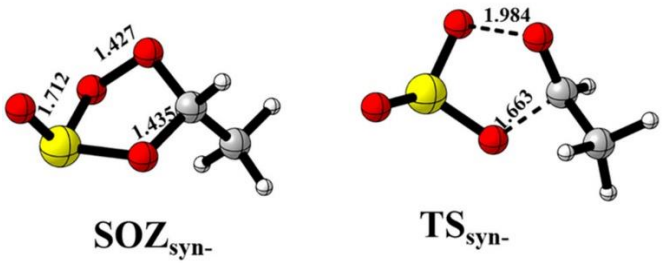

Figure 7.36. The structures of the secondary ozonide (SOZ) and the transition state (TS) formed in the reaction between *syn*-CH_3CHOO and SO_2. Copied from reference 15.[15]

The fit of Equation 7.3 allowed rate coefficients for the formation of the SOZ (association) and the formation of $CH_3CHO + SO_3$ (chemical activation) to be determined as a function of pressure using Equations 7.8 and 7.9.

$$Assocation = \frac{k_\infty k_0[\mathrm{M}]}{k_0[\mathrm{M}] + k_\infty} \quad \text{(Equation 7.8)}$$

$$Chemical\ activation = k_{int}\left(\frac{1 - k_0[\mathrm{M}]}{k_0[\mathrm{M}] + k_\infty}\right) \quad \text{(Equation 7.9)}$$

The total rate coefficient at a given pressure is the sum of association and chemical activation, which gave a value for $k_{7.1}$ of $(4.80 \pm 0.46) \times 10^{-11}$ cm^3 s^{-1} at 298 K and 760 Torr. The fraction corresponding to association and chemical activation can thus be calculated, with results suggesting a yield greater than 99 % for the SOZ at 298 K and 760 Torr (Figure 7.37), limiting production of SO_3 and potentially of sulfuric acid in the atmosphere.

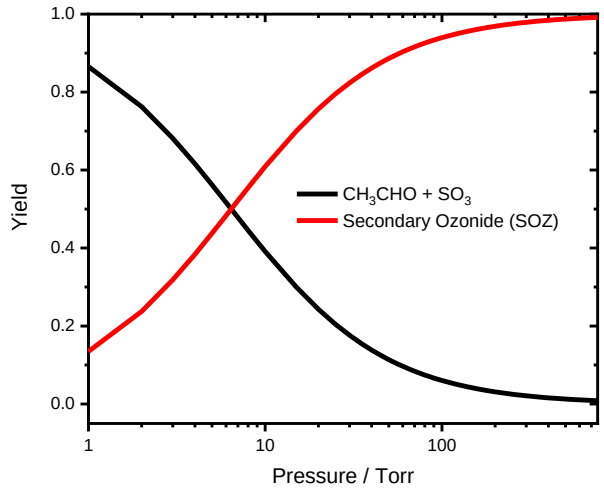

Figure 7.37. The yield of the SOZ and $CH_3CHO + SO_3$ as a function of pressure, calculated using Equations 7.3 and 7.5-7.7.

The reaction between *syn*-CH_3CHOO and SO_2 has been investigated by Manonmani *et al.*[16] using theoretical approaches, which indicate a barrierless reaction with a 98 % yield of acetaldehyde (CH_3CHO) + SO_3 at 298 K and 200 Torr of He and a rate coefficient for $CH_3CHO + SO_3$ production of 4.49×10^{-11} cm^3 molecule^{-1} s^{-1} at 298 K. However, the possible impacts of pressure were not fully discussed and the reaction of *anti*-$CH_3CHOO + SO_2$ was not considered. The calculations by Manonmani *et al.* have predicted a positive temperature dependence for the reactions of CH_2OO, *syn*-CH_3CHOO and $(CH_3)_2CHOO$ with SO_2, despite the reactions being barrierless and in contrast to the negative temperature dependence shown

in this work for *syn*-CH_3CHOO + SO_2, our previous work for CH_2OO + SO_2[17] (outlined in Chapter 4) and experimental results for $(CH_3)_2CHOO$ + SO_2.[18] Figure 7.38 shows a comparison between the temperature dependent results for CH_2OO, *syn*-CH_3CHOO and $(CH_3)_2CHOO$ with SO_2 reported by Manonmani *et al.* and the temperature dependent results of CH_2OO + SO_2 from our previous work,[17] *syn*-CH_3CHOO + SO_2 reported here, and $(CH_3)_2CHOO$ + SO_2 using the IUPAC recommendation for the temperature dependence[19] (which is based on the work of Smith *et al.*[18]).

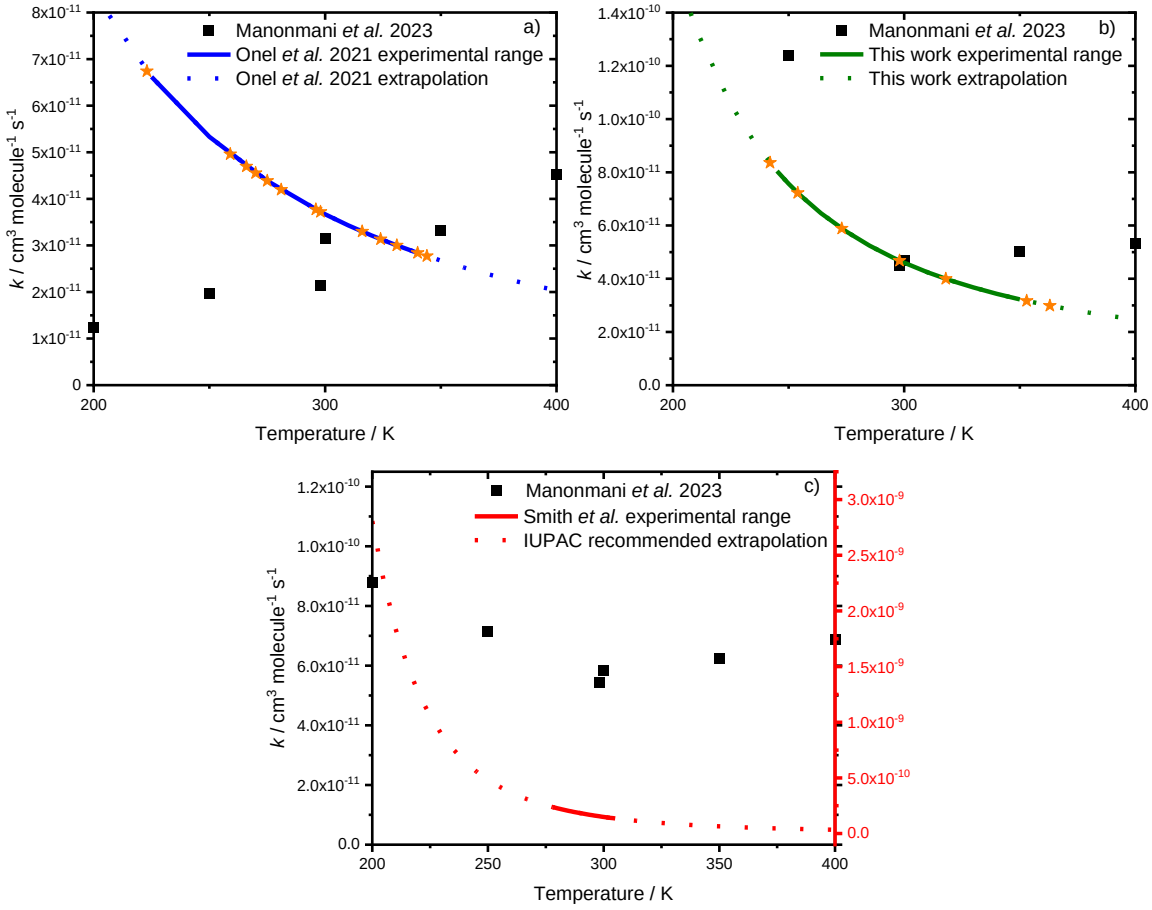

Figure 7.38. Comparison of rate coefficients as a function of temperature for a) CH_2OO + SO_2 reported by Manonmani *et al.* and Onel *et al.*,[17] b) *syn*-CH_3CHOO + SO_2 reported by Manonmani *et al.* and the results of this work and c) $(CH_3)_2CHOO$ + SO_2 reported by Manonmani *et al.* and the IUPAC recommended parameterisation.[19] The solid lines represent the experimental temperature range investigated in each study and the dotted lines are an extrapolation of the data to temperatures between 200 and 400 K. The orange stars in a) and b) represent the temperatures where experiments were carried out. The black squares represent rate coefficients calculated by Manonmani *et al*. using canonical variational transition state theory (CVT) with small curvature tunnelling correction (SCT).

Where potential impacts of pressure have been considered in detail in theoretical studies of SCI + SO_2 reactions, there is agreement with the lack of observed pressure dependence in the

kinetics for $CH_2OO + SO_2$ under atmospheric conditions,[19,20,21,22] but there are differences in the predicted pressure dependence of the reaction between $(CH_3)_2COO$ and SO_2.[21,22] Vereecken *et al.* suggested that > 80 % of the SOZ formed by $(CH_3)_2COO + SO_2$ undergoes prompt decomposition to acetone ($CH_3C(O)CH_3$) and SO_3 at 298 K and a pressure of 4 Torr, while > 97 % of the SOZ is collisionally stabilised at 298 K and 760 Torr, with the difference compared to $CH_2OO + SO_2$ attributed to the greater number of degrees of freedom in the SOZ formed via $(CH_3)_2COO + SO_2$, which would also be relevant to the comparison between the SOZ formed via $CH_2OO + SO_2$ and those from reactions of CH_3CHOO conformers with SO_2. However, Kuwata *et al.* calculated a different potential energy surface for the reaction between $(CH_3)_2COO$ and SO_2 to that reported by Vereecken *et al.*, and thus a different mechanism for the reaction, with calculations predicting no significant collisional stabilisation of the SOZ at pressures below 10^4 Torr at 298 K and SO_3 yields greater than 96 % at 298 K and pressures from 1 Torr to 760 Torr. The pressure dependence observed for $k_{7.1}$ in this work indicates significant stabilisation of the SOZ, with an expected yield greater than 99 % at 298 K and 760 Torr (Figure 7.37), agreeing well with Vereecken *et al.* Although formation of the SOZ will inhibit SO_3, the subsequent fate of the SOZ is uncertain and there may still be a contribution to the atmospheric production of SO_3 and therefore H_2SO_4. Experimental measurements of the kinetics for $(CH_3)_2COO + SO_2$ have indicated significant pressure dependence and a negative temperature dependence under atmospheric conditions,[23,18,24] similar to observations in this work for the reaction between *syn*-$CH_3CHOO + SO_2$. Differences between theoretical approaches and between experiment and theory indicate that the application of theory to the prediction of SCI kinetics remains a challenge. Potential explanations for the discrepancy between theory and experiment have been discussed in more detail in Chapter 5 of this thesis.

In contrast to the results for $k_{7.1}$, no significant dependence of $k_{7.2}$ on temperature and pressure was observed. At 298 K, results gave a mean value for $k_{7.2}$ of $(1.15 \pm 0.16) \times 10^{-10}$ cm^3 molecule^{-1} s^{-1} between 10 and 600 Torr, with results over all temperatures and pressures giving a mean value of $(1.18 \pm 0.21) \times 10^{-10}$ cm^3 molecule^{-1} s^{-1}. Results for $k_{7.2}$ are shown in Figure 7.39 for data at 298 K and Figure 7.40 for data at each temperature.

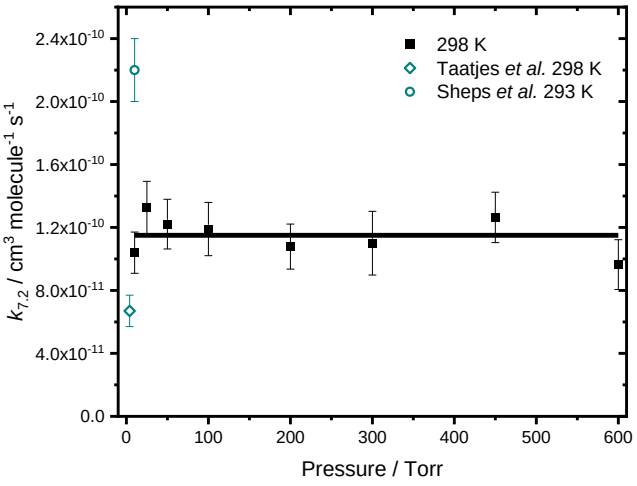

Figure 7.39. Effects of pressure on $k_{7.2}$ at 298 K. The solid line shows the mean value for $k_{7.2}$ at 298 K ((1.15 ± 0.16) × 10^{-10} cm^3 molecule^{-1} s^{-1}). Previous results reported for $k_{7.2}$ are also shown.[2, 3] Error bars represent a combination of the statistical error and the systematic errors resulting from uncertainties in gas flow rates and in the concentration of SO_2.

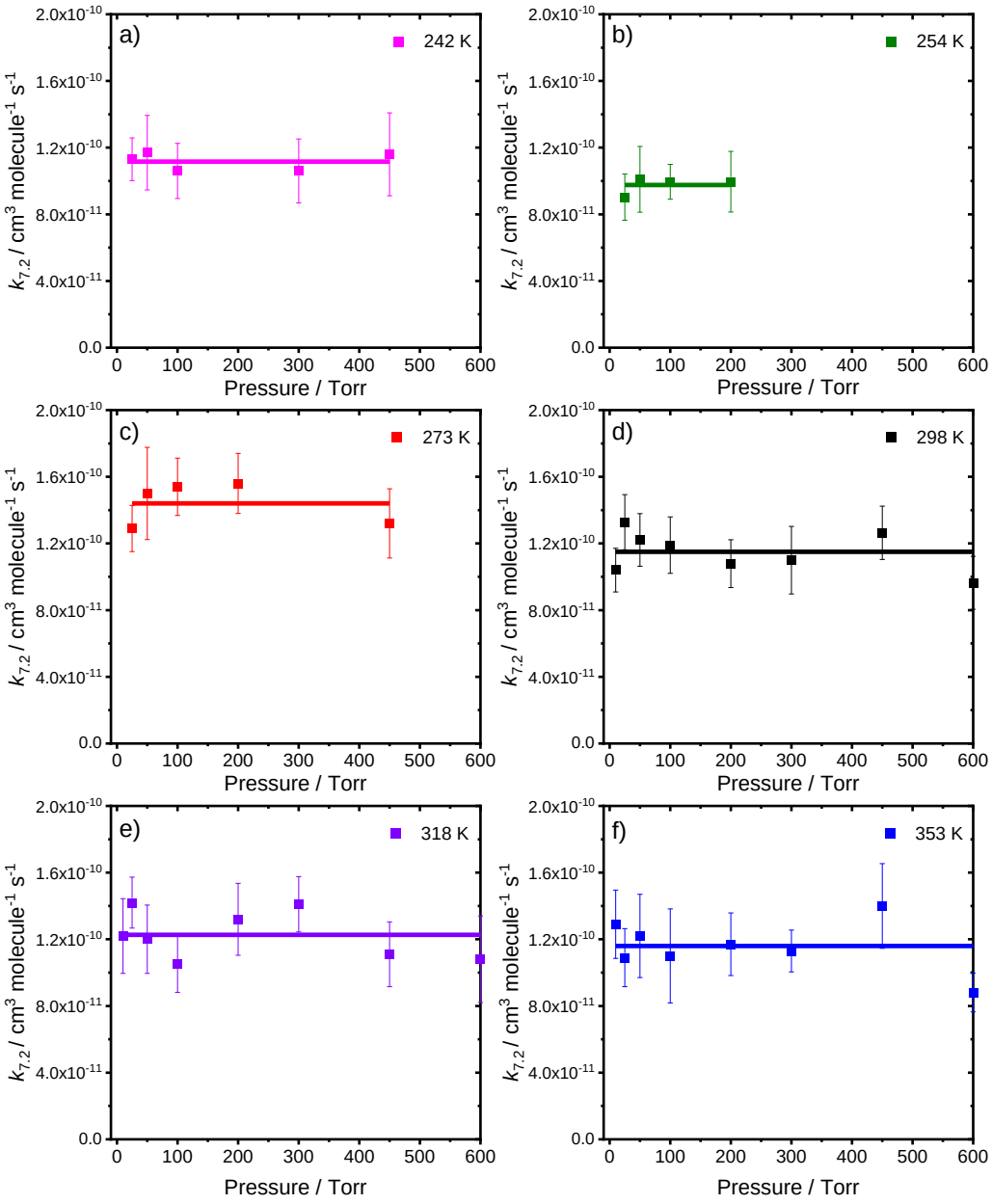

Figure 7.40. Effect of pressure on $k_{7.2}$ at each temperature, where solid lines represent the average value for the rate coefficient across each temperature. a) T = 242 K, $k_{7.2}$ = (1.12 ± 0.19) × 10^{-10} cm^3 molecule^{-1} s^{-1}; b) T = 254 K, $k_{7.2}$ = (0.98 ± 0.16) × 10^{-10} cm^3 molecule^{-1} s^{-1}; c) T = 273 K, $k_{7.2}$ = (1.47 ± 0.20) × 10^{-10} cm^3 molecule^{-1} s^{-1}; d) T = 298 K, $k_{7.2}$ = (1.15 ± 0.16) × 10^{-10} cm^3 molecule^{-1} s^{-1}; e) T = 318 K, $k_{7.2}$ = (1.23 ± 0.20) × 10^{-10} cm^3 molecule^{-1} s^{-1} and f) T = 353 K, $k_{7.2}$ = (1.16 ± 0.20) × 10^{-10} cm^3 molecule^{-1} s^{-1}.

The kinetics of R7.2 have been reported in two previous studies[2,3] at room temperature. Taatjes *et al.*[2] performed experiments at 4 Torr using the PIMS technique, and reported a value for $k_{7.2}$ of (6.7 ± 1.0) × 10^{-11} cm^3 molecule^{-1} s^{-1}, while Sheps *et al.*[3] performed experiments at 10 Torr using cavity-enhanced UV absorption spectroscopy and reported a value for

$k_{7.2}$ of $(2.2 \pm 0.2) \times 10^{-10}$ molecule^{-1} cm^3 s^{-1}. Differences between the studies reflect the challenges associated with measuring such rapid kinetics, with the lack of dependence of $k_{7.2}$ on temperature and pressure observed in this work potentially indicating that the kinetics for R7.2 are controlled by collision-limited or capture-limited kinetics. The difference in behaviour between the *syn*- and *anti*-conformers is potentially influenced by lower steric hindrance for the *anti*-conformer, coupled with the higher ground state energy for *anti*-CH_3CHOO by ~ 15 kJ mol^{-1} [1] compared to *syn*-CH_3CHOO and a higher dipole moment for *anti*-CH_3CHOO than *syn*-CH_3CHOO (5.53 D compared to 4.69 D, calculated at the B3LYP/AVTZ level of theory[25]).

Figure 7.41 compares the experimental results for $k_{7.2}$ with estimated values using a collision model (Equation 7.10) and a capture model (Equation 7.11).

$$k_{\mathrm{col}} = \pi(\mathrm{r_{CI}} + r_{\mathrm{SO_2}})^2 \sqrt{\frac{8k_{\mathrm{B}}T}{\pi\mu}} \qquad \text{(Equation 7.10)}$$

where $r_{\mathrm{CI}}$and $r_{\mathrm{SO_2}}$are the effective radii of *anti*-CH_3CHOO[26] and SO_2[27], respectively, k_{B} is the Boltzmann constant, T is the temperature, and μ is the reduced mass. The effective radius for *anti*-CH_3CHOO was assumed to be the same as that reported in the literature for *syn*-CH_3CHOO.[26]

$$k_{\mathrm{capt}} = C\sqrt{\frac{\pi}{\mu}}(D_{\mathrm{CI}}D_{\mathrm{SO_2}})^{\frac{2}{3}}(k_{\mathrm{B}}T)^{-\frac{1}{6}} \qquad \text{(Equation 7.11)}$$

where C is a constant (4.08 for the case of isotropic capture),[25,28] and D_{CI} and $D_{\mathrm{SO_2}}$ are the dipole moments of *anti*-CH_3CHOO[25] and SO_2,[29] respectively.

The experimental results for $k_{7.2}$ obtained in this work are lower than the estimated rate coefficients using either the collision model or the capture model, with experimental values a factor of ~ 2 lower than those calculated from collision theory, and a factor of ~ 6 lower than those calculated from capture theory. However, the calculated values do offer some insight to the kinetics and suggest that R7.2 is close to the collision limit.

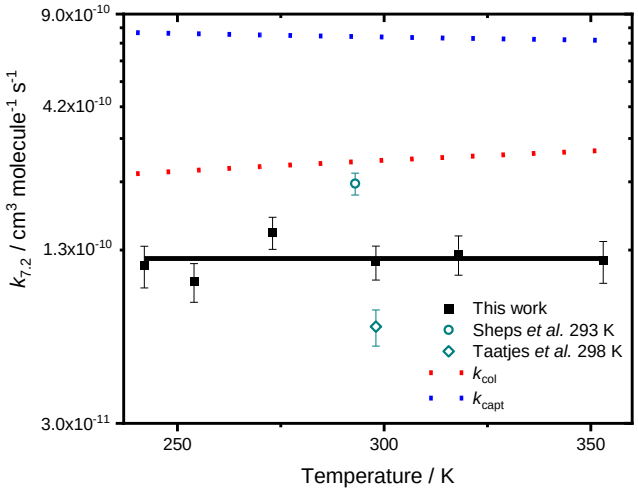

Figure 7.41. Mean value for $k_{7.2}$ determined at each temperature. The solid line represents the mean value for $k_{7.2}$ over all conditions investigated in this work is $(1.18 \pm 0.21) \times 10^{-10}$ cm^3 molecule^{-1} s^{-1}. Previous results reported for $k_{7.2}$ and rate coefficients calculated using collision theory (k_{col}, red dashed line) and capture theory (k_{capt}, blue dashed line) are also shown. Error bars represent a combination of the statistical error and the systematic errors resulting from uncertainties in gas flow rates and in the concentration of SO_2.

Results obtained for $k_{7.1}$ and $k_{7.2}$ at each temperature and pressure are summarised in Table 7.2. Results show that, under all conditions investigated in this work, the reaction between *anti*-CH_3CHOO and SO_2 is significantly faster than that of *syn*-CH_3CHOO and SO_2. The difference in behaviour between the *syn*- and *anti*-conformers is potentially influenced by lower steric hindrance for the *anti*-conformer, coupled with the higher ground state energy for *anti*-CH_3CHOO by ~ 15 kJ mol^{-1} [1] compared to *syn*-CH_3CHOO. The results of this chapter can be used to characterise the reactions of larger asymmetric Criegee intermediates that may not be easily produced within the laboratory.

T / K	p / Torr	$k_{7.1}$ / 10^{-11} cm^3 molecule^{-1} s^{-1}	$k_{7.2}$ / 10^{-10} cm^3 molecule^{-1} s^{-1}
242	25	6.69 ± 0.92	1.13 ± 0.13
	50	7.69 ± 1.08	1.17 ± 0.22
	100	8.43 ± 1.03	1.06 ± 0.17
	300	7.99 ± 0.97	1.06 ± 0.19
	450	8.51 ± 1.06	1.16 ± 0.25
	600	7.98 ± 0.97	-
254	25	5.52 ± 0.63	0.90 ± 0.14
	50	6.36 ± 0.83	1.01 ± 0.20
	100	6.76 ± 0.73	1.00 ± 0.10
	200	7.00 ± 1.14	1.00 ± 0.18
	300	6.88 ± 1.02	-
	450	7.02 ± 1.09	-
	600	7.4 ± 1.28	-
273	25	4.33 ± 0.63	1.29 ± 0.14
	50	4.73 ± 0.55	1.50 ± 0.28
	100	5.14 ± 0.57	1.54 ± 0.17
	200	5.47 ± 0.58	1.56 ± 0.18
	300	5.79 ± 0.61	-
	450	6.23 ± 0.64	1.32 ± 0.21
	600	6.27 ± 0.74	-
298	10	3.02 ± 0.32	1.04 ± 0.13
	25	3.00 ± 0.30	1.33 ± 0.17
	50	3.67 ± 0.37	1.22 ± 0.16
	100	4.05 ± 0.54	1.19 ± 0.17
	200	4.55 ± 0.49	1.08 ± 0.14
	300	4.54 ± 0.52	1.10 ± 0.20
	450	4.70 ± 0.65	1.26 ± 0.16
	600	4.66 ± 0.52	0.96 ± 0.16
318	10	2.50 ± 0.48	1.22 ± 0.22
	25	3.06 ± 0.41	1.42 ± 0.15
	50	3.31 ± 0.42	1.20 ± 0.21
	100	3.60 ± 0.42	1.05 ± 0.17
	200	3.93 ± 0.47	1.32 ± 0.22
	300	3.95 ± 0.42	1.41 ± 0.17
	450	3.95 ± 0.48	1.11 ± 0.20
	600	4.00 ± 0.56	1.08 ± 0.26
353	10	-	1.29 ± 0.20
	25	2.41 ± 0.30	1.09 ± 0.17
	50	2.67 ± 0.47	1.22 ± 0.25
	100	2.98 ± 0.43	1.10 ± 0.28
	200	3.02 ± 0.48	1.17 ± 0.19
	300	3.15 ± 0.67	1.13 ± 0.13
	450	3.27 ± 0.51	1.40 ± 0.25
	600	2.82 ± 0.39	0.88 ± 0.12

Table 7.2. Results obtained in this work for $k_{7.1}$ and $k_{7.2}$ at each temperature and pressure.

7.5 Concluding Remarks

The kinetics of *syn*- and *anti*-CH_3CHOO reactions with SO_2 have been investigated in the temperature range 242 to 353 K at pressures between 10 and 600 Torr using laser flash photolysis of $CH_3CHI_2/O_2/N_2/SO_2$ gas mixtures coupled with time-resolved broadband UV absorption spectroscopy.

Results for *syn*-CH_3CHOO + SO_2 show that the kinetics are pressure dependent, with a negative dependence on temperature. The kinetics can be parameterised by a model that indicates a role for chemical activation which gives a rate coefficient of $k_{7.1} = (4.80 \pm 0.46) \times 10^{-11}$ cm^3 molecule^{-1} s^{-1} at 298 K and 760 Torr. The observed pressure dependence reconciles apparent discrepancies in previous measurements of *syn*-CH_3CHOO + SO_2 kinetics made at ~ 298 K but at different pressures, and indicates significant collisional stabilisation of the secondary ozonide formed in the reaction under atmospheric conditions, with an expected yield of the secondary ozonide greater than 99 % at 298 K and 760 Torr.

Kinetics of the reaction between *anti*-CH_3CHOO and SO_2 display no significant dependence on temperature or pressure over the ranges investigated. Results give a mean value for $k_{7.2}$ of $(1.15 \pm 0.16) \times 10^{-10}$ cm^3 molecule^{-1} s^{-1} at 298 K and $(1.18 \pm 0.21) \times 10^{-10}$ cm^3 molecule^{-1} s^{-1} over all conditions studied in this work. The atmospheric implications of the results presented throughout this chapter are discussed in detail in Chapter 8.

7.6 References

1. Kuwata, K.T., Hermes, M.R., Carlson, M.J. and Zogg, C.K. Computational Studies of the Isomerization and Hydration Reactions of Acetaldehyde Oxide and Methyl Vinyl Carbonyl Oxide. *The Journal of Physical Chemistry A.* 2010, **114**(34), pp.9192-9204.
2. Taatjes, C.A., Welz, O., Eskola, A.J., Savee, J.D., Scheer, A.M., Shallcross, D.E., Rotavera, B., Lee, E.P.F., Dyke, J.M., Mok, D.K.W., Osborn, D.L. and Percival, C.J. Direct Measurements of Conformer-Dependent Reactivity of the Criegee Intermediate CH_3CHOO. *Science.* 2013, **340**(6129), p.177.
3. Sheps, L., Scully, A.M. and Au, K. UV absorption probing of the conformer-dependent reactivity of a Criegee intermediate CH_3CHOO. *Physical Chemistry Chemical Physics.* 2014, **16**(48), pp.26701-26706.
4. Anglada, J.M., González, J. and Torrent-Sucarrat, M. Effects of the substituents on the reactivity of carbonyl oxides. A theoretical study on the reaction of substituted

carbonyl oxides with water. *Physical Chemistry Chemical Physics*. 2011, **13**(28), pp.13034-13045.

5. Welz, O., Eskola, A.J., Sheps, L., Rotavera, B., Savee, J.D., Scheer, A.M., Osborn, D.L., Lowe, D., Murray Booth, A., Xiao, P., Anwar H. Khan, M., Percival, C.J., Shallcross, D.E. and Taatjes, C.A. Rate Coefficients of C1 and C2 Criegee Intermediate Reactions with Formic and Acetic Acid Near the Collision Limit: Direct Kinetics Measurements and Atmospheric Implications. *Angewandte Chemie International Edition*. 2014, **53**(18), pp.4547-4550.
6. Robinson, C., Onel, L., Newman, J., Lade, R., Au, K., Sheps, L., Heard, D.E., Seakins, P.W., Blitz, M.A. and Stone, D. Unimolecular Kinetics of Stabilized CH_3CHOO Criegee Intermediates: syn-CH_3CHOO Decomposition and anti-CH_3CHOO Isomerization. *The Journal of Physical Chemistry A*. 2022, **126**(39), pp.6984-6994.
7. Lade, R.E., Onel, L., Blitz, M.A., Seakins, P.W. and Stone, D. Kinetics of the Gas-Phase Reactions of *syn*- and *anti*-CH_3CHOO Criegee Intermediate Conformers with SO_2 as a Function of Temperature and Pressure. *The Journal of Physical Chemistry A*. 2024, **128**(14), pp.2815-2824.
8. Howes, N.U.M., Mir, Z.S., Blitz, M.A., Hardman, S., Lewis, T.R., Stone, D. and Seakins, P.W. Kinetic studies of C1 and C2 Criegee intermediates with SO_2 using laser flash photolysis coupled with photoionization mass spectrometry and time resolved UV absorption spectroscopy. *Physical Chemistry Chemical Physics*. 2018, **20**(34), pp.22218-22227.
9. Zhou, X., Liu, Y., Dong, W. and Yang, X. Unimolecular Reaction Rate Measurement of *syn*-CH_3CHOO. *The Journal of Physical Chemistry Letters*. 2019, **10**(17), pp.4817-4821.
10. Smith, M.C., Ting, W.-L., Chang, C.-H., Takahashi, K., Boering, K.A. and Lin, J.J.-M. UV absorption spectrum of the C2 Criegee intermediate CH_3CHOO. *The Journal of Chemical Physics*. 2014, **141**(7), p.074302.
11. Robinson, O., Lade, Newman, Heard, Seakins, Blitz, Stone. *Decomposition Kinetics of syn-CH_3CHOO as a function of temperature and pressure, in preparation*. Unpublished, 2021.
12. S.P. Sander, J.A., J.R. Burkholder. R.R. Freidl, D.M. Golden, R.E. Huie, C.E. Kolb, M.J. Kurylo, G.K. Moortgat, V.L. Orkin, P.H. Wine. Chemical Kinetics and Photochemical Data for Use in Atmospheric Studies, Evaluation Number 17. *JPL publication 10-6*. 2011.
13. Harwood, M.H., Burkholder, J.B., Hunter, M., Fox, R.W. and Ravishankara, A.R. Absorption Cross Sections and Self-Reaction Kinetics of the IO Radical. *The Journal of Physical Chemistry A*. 1997, **101**(5), pp.853-863.

14. Tyndall, G.S., Orlando, J.J., Wallington, T.J. and Hurley, M.D. Pressure dependence of the rate coefficients and product yields for the reaction of CH_3CO radicals with O_2. *International Journal of Chemical Kinetics.* 1997, **29**(9), pp.655-663.

15. Zhao, H., Wang, S., Lu, C., Tang, Y. and Guan, J. Theoretical investigations on the reactions of criegee intermediates with SO_2 to form SO_3. *Journal of Physical Organic Chemistry.* 2022, **35**(9), p.e4394.

16. Manonmani, G., Sandhiya, L. and Senthilkumar, K. Reaction of Criegee Intermediates with SO_2─A Possible Route for Sulfurous Acid Formation in the Atmosphere. *ACS Earth and Space Chemistry.* 2023, **7**(10), pp.1890-1904.

17. Onel, L., Lade, R., Mortiboy, J., Blitz, M.A., Seakins, P.W., Heard, D.E. and Stone, D. Kinetics of the gas phase reaction of the Criegee intermediate CH_2OO with SO_2 as a function of temperature. *Physical Chemistry Chemical Physics.* 2021, **23**(35), pp.19415-19423.

18. Smith, M.C., Chao, W., Takahashi, K., Boering, K.A. and Lin, J.J.-M. Unimolecular Decomposition Rate of the Criegee Intermediate $(CH_3)_2COO$ Measured Directly with UV Absorption Spectroscopy. *The Journal of Physical Chemistry A.* 2016, **120**(27), pp.4789-4798.

19. Cox, R.A., Ammann, M., Crowley, J.N., Herrmann, H., Jenkin, M.E., McNeill, V.F., Mellouki, A., Troe, J. and Wallington, T.J. Evaluated kinetic and photochemical data for atmospheric chemistry: Volume VII – Criegee intermediates. *Atmospheric Chemistry and Physics.* 2020, **20**(21), pp.13497-13519.

20. Stone, D., Blitz, M., Daubney, L., Howes, N.U.M. and Seakins, P. Kinetics of CH_2OO reactions with SO_2, NO_2, NO, H_2O and CH_3CHO as a function of pressure. *Physical Chemistry Chemical Physics.* 2014, **16**(3), pp.1139-1149.

21. Vereecken, L., Harder, H. and Novelli, A. The reaction of Criegee intermediates with NO, RO_2, and SO_2, and their fate in the atmosphere. *Physical Chemistry Chemical Physics.* 2012, **14**(42), pp.14682-14695.

22. Kuwata, K.T., Guinn, E.J., Hermes, M.R., Fernandez, J.A., Mathison, J.M. and Huang, K. A Computational Re-examination of the Criegee Intermediate–Sulfur Dioxide Reaction. *The Journal of Physical Chemistry A.* 2015, **119**(41), pp.10316-10335.

23. Chhantyal-Pun, R., Welz, O., Savee, J.D., Eskola, A.J., Lee, E.P.F., Blacker, L., Hill, H.R., Ashcroft, M., Khan, M.A.H., Lloyd-Jones, G.C., Evans, L., Rotavera, B., Huang, H., Osborn, D.L., Mok, D.K.W., Dyke, J.M., Shallcross, D.E., Percival, C.J., Orr-Ewing, A.J. and Taatjes, C.A. Direct Measurements of Unimolecular and Bimolecular Reaction Kinetics of the Criegee Intermediate $(CH_3)_2COO$. *The Journal of Physical Chemistry A.* 2017, **121**(1), pp.4-15.

24. Huang, H.-L., Chao, W. and Lin, J.J.-M. Kinetics of a Criegee intermediate that would survive high humidity and may oxidize atmospheric SO_2. *Proceedings of the National Academy of Sciences.* 2015, **112**(35), pp.10857-10862.

25. Chhantyal-Pun, R., Rotavera, B., McGillen, M.R., Khan, M.A.H., Eskola, A.J., Caravan, R.L., Blacker, L., Tew, D.P., Osborn, D.L., Percival, C.J., Taatjes, C.A., Shallcross, D.E. and Orr-Ewing, A.J. Criegee Intermediate Reactions with Carboxylic Acids: A Potential Source of Secondary Organic Aerosol in the Atmosphere. *ACS Earth and Space Chemistry.* 2018, **2**(8), pp.833-842.

26. Takahashi, K. Theoretical analysis on reactions between *syn*-methyl Criegee intermediate and amino alcohols. *Journal of the Chinese Chemical Society.* 2022, **69**(1), pp.184-192.

27. P.J. Linstrom, W.G.M. *NIST Chemistry WebBook.* National Institute of Standards and Technology, Gaithersburg MD.

28. Maergoiz, A.I., Nikitin, E.E., Troe, J. and Ushakov, V.G. Classical trajectory and adiabatic channel study of the transition from adiabatic to sudden capture dynamics. III. Dipole–dipole capture. *The Journal of Chemical Physics.* 1996, **105**(15), pp.6277-6284.

29. Patel, D., Margolese, D. and Dykea, T.R. Electric dipole moment of SO_2 in ground and excited vibrational states. *The Journal of Chemical Physics.* 2008, **70**(6), pp.2740-2747.

Chapter 8
Atmospheric Implications

8.1 Atmospheric Implications

In this work, reactions of the simplest Criegee intermediate, CH_2OO, with SO_2, NO_2 and water vapour, and the reactions of CH_3CHOO conformers with SO_2 have been investigated under conditions relevant to those of the troposphere to widen our understanding of the impacts that Criegee intermediates have on atmospheric composition and thus air quality. The following sections used output from the global 3D atmospheric chemistry transport model (CTM) GEOS-Chem (version 14.2.2[1]) and the rate coefficients obtained in this work to determine the atmospheric fates of CH_2OO, *syn*-CH_3CHOO and *anti*-CH_3CHOO. Simulations were performed by Dr Matthew Rowlinson and Professor Mathew Evans at the University of York and the results, along with the results presented in Chapter 6 of this thesis, have been submitted for publication in the *Environmental Science: Atmospheres* Journal.

The model was run for 2 years (2018-2019) driven by MERRA-2 meteorology[2] with a $4.0° \times 4.5°$ spatial resolution and 72 vertical levels. The first year was considered as model spin up and discarded. The model contains a detailed VOC oxidation chemistry[3] including Criegee intermediate reactions.[4] Biogenic emissions of VOCs were taken from MEGANv2.1,[5] biomass burning emissions from GFED4s,[6] while anthropogenic emissions use the Community Emissions Data System (CEDS).[7]

8.1.1 Model Simulations for CH_2OO Chemistry using results obtained in Chapter 6

Model simulations were performed to determine the atmospheric implications of the results obtained in Chapter 6. Simulations were performed with the base chemistry and then with two sets of updates. The Criegee intermediate chemistry in the base model was described in 2015[8] and subsequently updated by Bates *et al.*[3] in 2021 to the current CH_2OO chemistry in the base model as shown in Table 8.1. The first update represents the state of current understanding, and involves updates to the rate coefficients for the reactions of CH_2OO with H_2O, $(H_2O)_2$, and NO_2 to the values currently recommended by IUPAC,[9] and to the rate coefficients of reactions with O_3, reported by Onel *et al.*[10] and SO_2, reported in Chapter 4 of this thesis.[11] In the first update the reactions of CH_2OO with NO or CO have been removed as the kinetics of these reactions are highly uncertain, and the reactions are not expected to represent significant losses for CH_2OO. The second update to the model changes the rate coefficient for reactions R6.1 ($CH_2OO + H_2O$) and R6.2 ($CH_2OO + (H_2O)_2$) from those currently recommended by IUPAC to those determined in the experiments described in Chapter 6. Comparisons between

the temperature-dependent rate coefficients for $CH_2OO + H_2O$ and $CH_2OO + (H_2O)_2$ in the three model simulations are shown in Figure 8.1. The complete set of CH_2OO chemistry used in the model is described in Table 8.1.

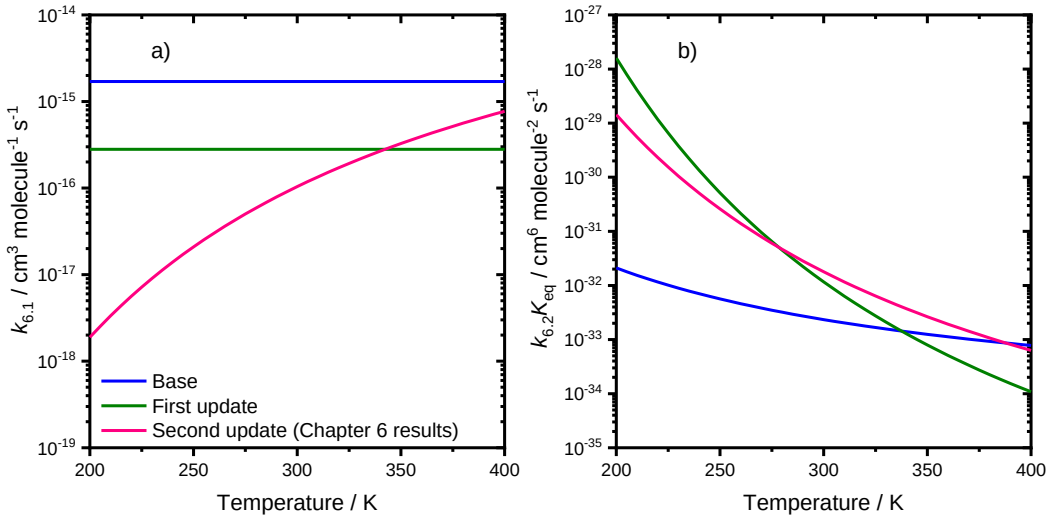

Figure 8.1. Comparison of rate coefficients used in GEOS-Chem for reactions of CH_2OO with (a) the water monomer and (b) the water dimer at temperatures between 200 and 400 K. Parameterisations are given in Table 8.1.

Reaction	Products	Base	First update	Second update
		Rate coefficient / cm^3 $molecule^{-1}$ s^{-1} (second-order reactions) or cm^6 $molecule^{-2}$ s^{-1} (third-order reactions)	**Rate coefficient / cm^3 $molecule^{-1}$ s^{-1} (second-order reactions) or cm^6 $molecule^{-2}$ s^{-1} (third-order reactions)**	**Rate coefficient / cm^3 $molecule^{-1}$ s^{-1} (second-order reactions) or cm^6 $molecule^{-2}$ s^{-1} (third-order reactions)**
$CH_2OO + H_2O$	0.73 HMHP + 0.21 HCOOH + 0.21 H_2O + 0.06 HCHO + 0.06 H_2O_2	1.7×10^{-15} (ref.[12])	2.8×10^{-16} (ref.[9])	**3.15×10^{-13} exp(–2405/*T*)**
$CH_2OO + H_2O + H_2O$	0.40 HMHP + 0.54 HCOOH + 0.54 H_2O + 0.06 HCHO + 0.06 H_2O_2	$2.88\times10^{-35}\times\exp(1319/T)$ (ref. [12])	$7.35 \times 10^{-18}\times\exp(4076/T)$ (ref. [9])	**2.78×10^{-38} exp(4012/*T*)**
$CH_2OO + O_3$	HCHO + $2O_2$	1.4×10^{-12} (ref.[13])	3.60×10^{-13} (ref.[10])	3.60×10^{-13} (ref.[14])
$CH_2OO + SO_2$	HCHO + SO_3	3.70×10^{-11} (ref.[13])	**$3.72 \times 10^{-11}\times(T/298)^{-2.05}$ (ref.[11])**	**$3.72 \times 10^{-11}\times(T/298)^{-2.05}$ (ref.[11])**
$CH_2OO + NO_2$	HCHO + NO_3	1.00×10^{-15} (ref.[4])	3.00×10^{-12} (ref.[9])	3.00×10^{-12} (ref.[9])
$CH_2OO + NO$	HCHO + NO_2	1.00×10^{-14} (ref.[4])	-	-
$CH_2OO + CO$	HCHO + CO_2	1.20×10^{-15} (ref.[4])	-	-

Table 8.1. Summary of reactions, products, rate coefficients and percentage losses for CH_2OO reactions used in the three model simulations. The bold values are rate coefficients that have been determined as part of this thesis.

Kinetics for the reaction of CH_2OO with water dimers in the base GEOS-Chem mechanism were estimated from the relative rates of CH_2OO reactions with SO_2 and water monomers, with a temperature dependence estimated from the temperature dependence of the equilibrium between water monomers and dimers, as described in previous work.[3, 12, 15] Rate coefficients for R6.2 measured in this work and other direct studies[16-21] are typically two orders of magnitude greater than those estimated in the simulations for the base case, leading to significant changes in the behaviour of CH_2OO in the model.

Figure 8.2 shows the impact of the changes made in the first update, compared to the base model run, on annual mean surface layer concentrations for CH_2OO and several key atmospheric species. The model shows significant decreases in CH_2OO in most locations, with mean surface layer concentrations decreased by 64.2 % compared to the base model run owing to the faster kinetics for $CH_2OO + (H_2O)_2$ used in the updated model. However, there are some regional differences to the global mean trend, with hot and dry regions over areas including Australia and parts of Africa and the Middle East displaying significant increases in the concentration of CH_2OO. In these regions, the impacts of updates to $k_{6.2}K_{eq}$ are limited as a result of low water dimer concentrations owing to low water monomer concentrations and the temperature dependence of the equilibrium between H_2O and $(H_2O)_2$, with the observed impact dominated by the decreased values for $k_{6.1}$ used in the updated model.

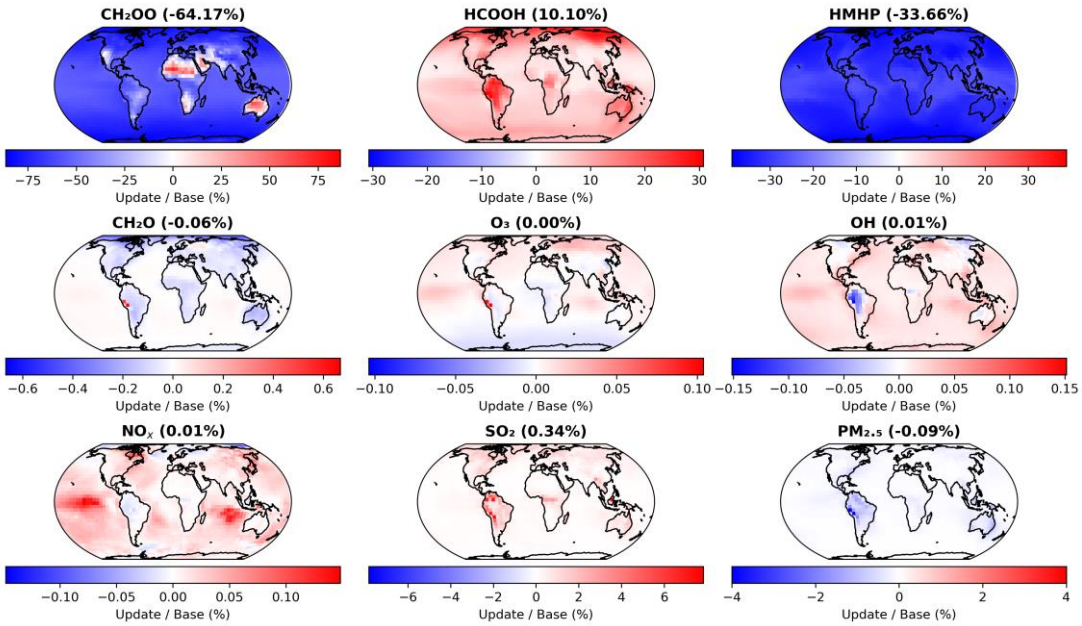

Figure 8.2. Impacts of changes made in the first set of GEOS-Chem updates, compared to the base model run, on annual mean surface layer concentrations for CH_2OO and several key atmospheric species. The first set of model updates incorporate current IUPAC recommendations for $k_{6.1}$ and $k_{6.2}K_{eq}$, as well as updates to rate coefficients for reactions of CH_2OO with O_3, SO_2, and NO_2 (see Table 8.1 for details).

The first set of model updates also affect concentrations of products formed in CH_2OO reactions with H_2O and $(H_2O)_2$, which are based on the work of Nguyen *et al.*[12] and thus consider the yields of products on longer timescales than the initial production of HMHP from the elementary reactions R6.1 and R6.2. In the first set of model updates, the annual mean surface layer concentration for HCOOH is increased by 10.1 %, while that for HMHP is decreased by 33.7 % owing to an increase in importance of the dimer reaction, which favours production of HCOOH over HMHP. Concentrations of other key atmospheric species display smaller changes, with SO_2 showing regional surface layer increases of over 6 % but an overall annual mean surface layer change of 0.3 %, and $PM_{2.5}$ showing decreases of up to 4 % regionally but with a decrease in the overall annual mean surface layer of 0.1 %.

The impacts of the second set of model updates, which make use of the results obtained in Chapter 6 of this work, are shown in Figure 8.3. Further decreases in CH_2OO concentrations are observed, with a reduction in the annual mean surface layer concentration of 3.7 % compared to that obtained in the model run using the first set of updates, with little regional variation, and 61.8 % compared to the base model run. However, changes to other species are more limited, with an increase in HCOOH of only 0.4 % and a decrease in HMHP of only 3.0 % compared to the overall annual mean surface concentrations obtained in the model run

using the first set of updates. Species such as SO_2 and $PM_{2.5}$ display little difference compared to the results obtained with the first set of model updates.

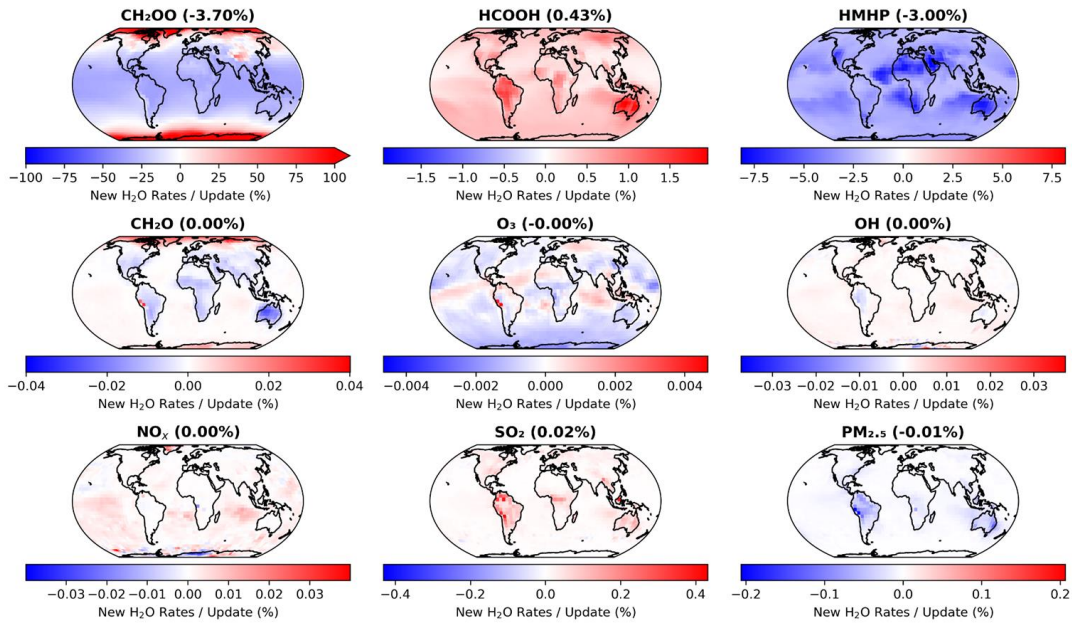

Figure 8.3. Impacts of changes made in the second set of GEOS-Chem updates, compared to the results obtained with the first set of updates, on annual mean surface layer concentrations for CH_2OO and several key atmospheric species. The second set of model updates make use of the results obtained in this work for $k_{6.1}$ and $k_{6.2}K_{eq}$ (see Table 8.1 for details).

Output from the second set of model updates for pressure, temperature and the concentrations of NO_2, SO_2 and water monomers/dimers was then used to determine the atmospheric implications of all of the results presented throughout this thesis by determining the losses of CH_2OO, *syn*-CH_3CHOO and *anti*-CH_3CHOO by decomposition or bimolecular reactions with SO_2, NO_2 and water monomers and dimers.

The loss of CH_2OO is described by R8.1-R8.5:

$$CH_2OO + H_2O \rightarrow \text{Loss} \quad \text{(R8.1)}$$

$$CH_2OO + (H_2O)_2 \rightarrow \text{Loss} \quad \text{(R8.2)}$$

$$CH_2OO + SO_2 \rightarrow \text{Loss} \quad \text{(R8.3)}$$

$$CH_2OO + NO_2 \rightarrow \text{Loss} \quad \text{(R8.4)}$$

$$CH_2OO \xrightarrow{dec} \text{Loss} \quad \text{(R8.5)}$$

The pseudo-first-order rate coefficient describing the total loss of CH_2OO was then calculated using Equation 8.1:

$$k_{tot} = k'_{8.1} + k'_{8.2} + k'_{8.3} + k'_{8.4} + k_{8.5}$$ (Equation 8.1)

where $k'_{8.1} = k_{8.1}[H_2O]$, $k'_{8.2} = k_{8.2}[(H_2O)_2]$, $k'_{8.3} = k_{8.3}[SO_2]$ and $k'_{8.4} = k_{8.4}[NO_2]$

The fractional loss of CH_2OO with H_2O was then calculated using Equation 8.2:

$$\text{Fractional loss by } H_2O = \frac{k'_{8.1}}{k_{tot}}$$ Equation 8.2

Fractional losses for R8.2-R8.5 are calculated in the same way. Calculations for the fractional losses of *syn*- and *anti*-CH_3CHOO are determined in the same way as CH_2OO.

The temperature profile of the surface layer is shown in Figure 8.4 and concentrations of water monomers, water dimers, SO_2 and NO_2 are shown in Figure 8.5.

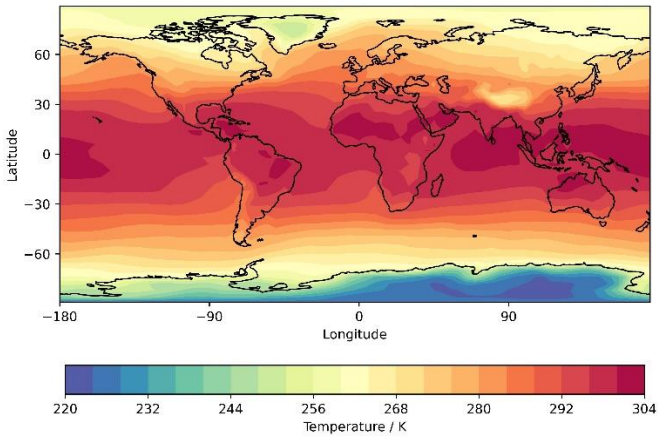

Figure 8.4. Temperature profile of the surface layer.

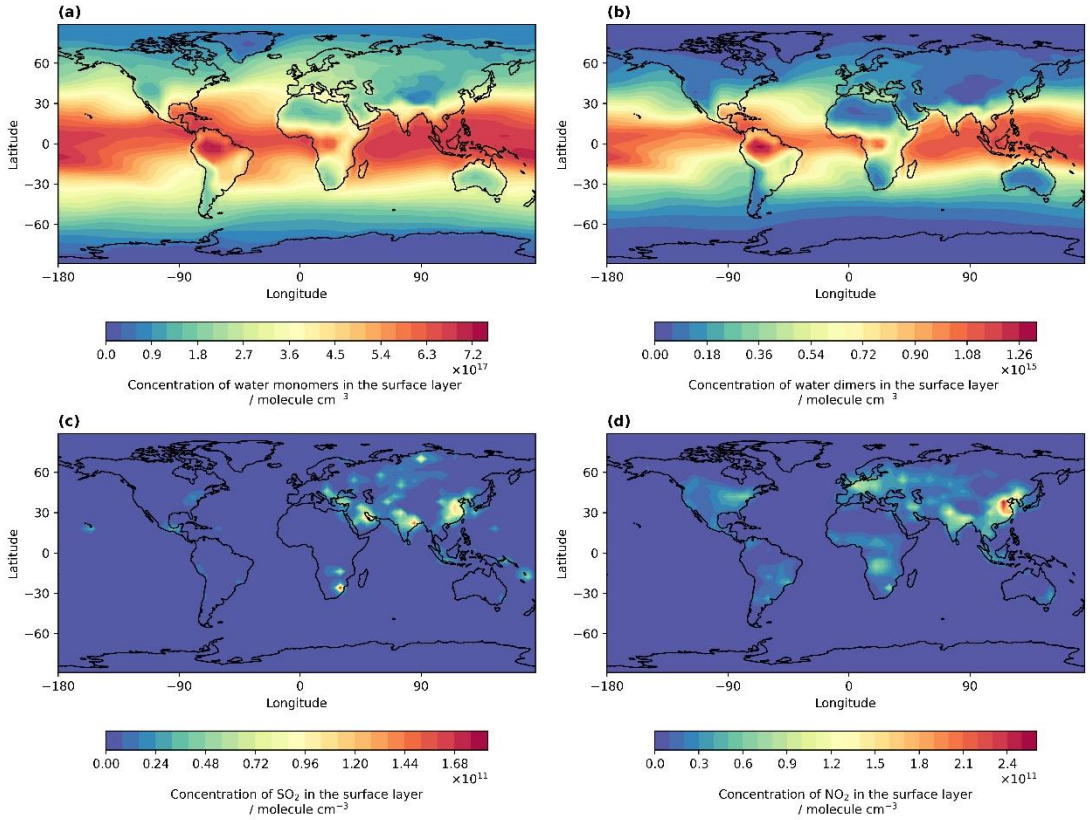

Figure 8.5. Concentrations of a) water monomers, b) water dimers, c) SO_2 and d) NO_2 in the surface layer.

8.1.2 Atmospheric Losses of CH_2OO

The percentage losses of CH_2OO due to decomposition, reaction with NO_2, SO_2 and water vapour in the surface layer were determined using temperature (Figure 8.4) and species concentration (Figure 8.5) outputs from the updated GEOS-Chem simulation and the rate coefficients reported in this work for the reactions between CH_2OO and NO_2, SO_2[11] and water vapour, and the literature value reported for CH_2OO decomposition.[22]

Figure 8.6 shows the percentage loss of CH_2OO due to decomposition, reaction with NO_2, SO_2 and water vapour, in the surface layer of the model using temperature (Figure 8.4) and concentration (Figure 8.5) outputs from the updated GEOS-chem simulation and rate coefficients determined in this work for the reactions between CH_2OO and NO_2, SO_2[11] and water monomers/dimers, and the literature value reported for CH_2OO decomposition.[22]

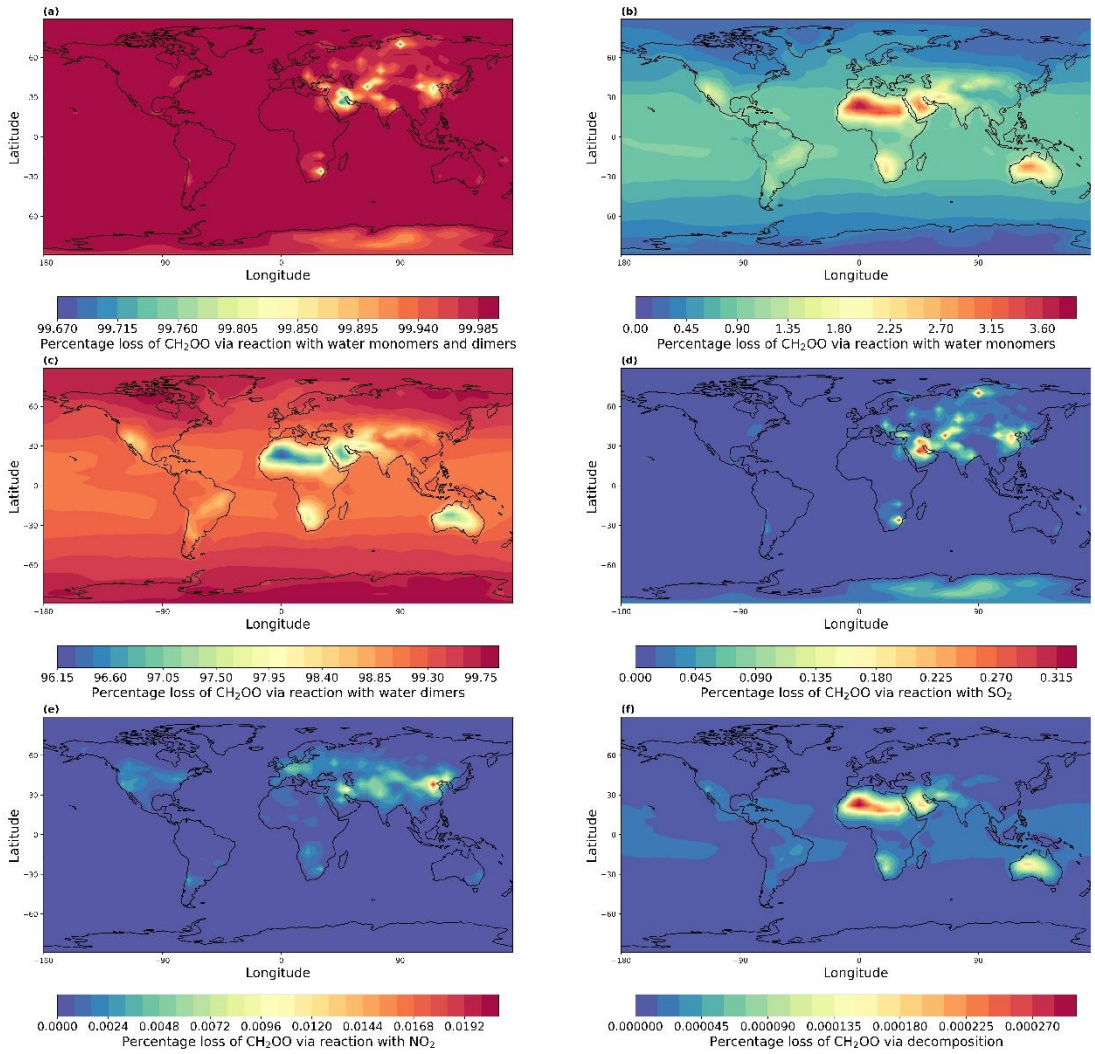

Figure 8.6. Percentage losses of CH_2OO via reaction with a) water monomers and dimers combined, b) water monomers, c) water dimers, d) SO_2 e) NO_2 and f) thermal decomposition.

Figure 8.7 shows mixing ratios of CH_2OO obtained for the second set of model updates. The annual surface layer CH_2OO peaks at 1.5×10^{-2} parts per quadrillion (ppq), with an annual mean of 3.5×10^{-4} ppq. Mixing ratios of CH_2OO are highest over landmasses where the emissions of unsaturated VOCs into the atmosphere are highest, and lowest over remote oceanic regions. Vertically, the highest mixing ratios (1.9×10^{-2} ppq) are seen in the tropical upper troposphere, where convective lifting brings unsaturated VOCs into contact with high O_3 concentrations in a region with low concentrations of water vapour. The mean lifetime of CH_2OO in the updated model is 0.45 s, varying from 9.8×10^{-4} s in the surface layer to > 2 s in the upper troposphere owing to changes in water concentrations.

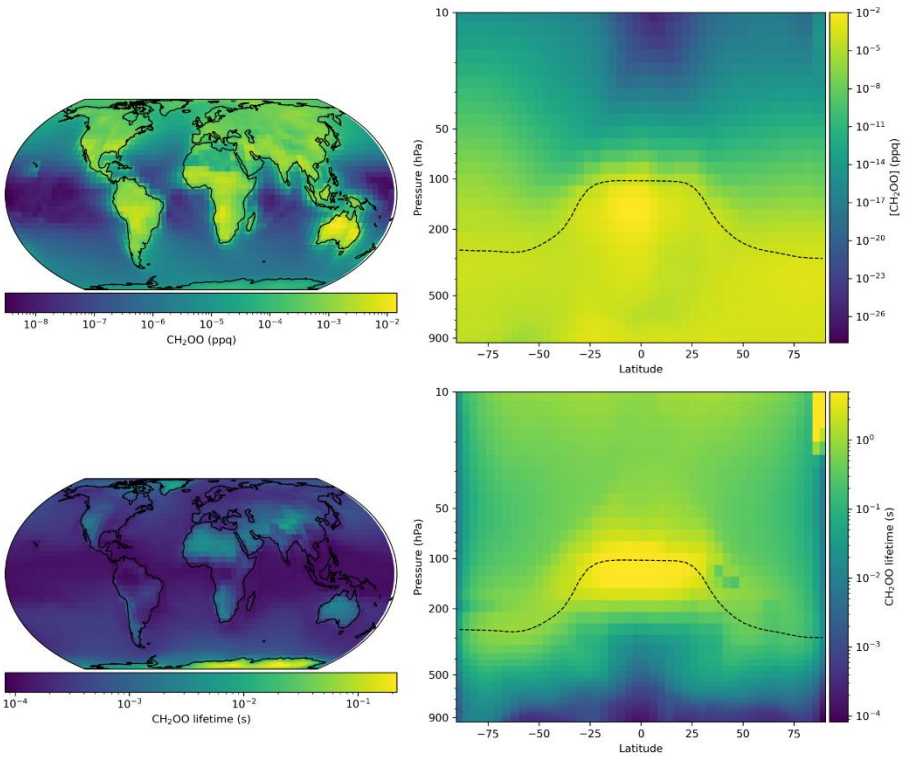

Figure 8.7. CH_2OO surface and zonal distributions (top panel) and lifetime (bottom panel) for GEOS-Chem simulations using the second set of model updates, which make used of results obtained in this work for $k_{6.1}$ and $k_{6.2}K_{eq}$ (see Table 8.1 for details). The black dotted line represents the tropopause.

In the updated model, the annual mean global loss of CH_2OO in the troposphere is dominated by the reaction with water dimers, which represents 98.3 % of the total CH_2OO loss, with a further 0.8 % of the total loss occurring through reaction with water monomers. Reactions of CH_2OO with species other than water account for less than 1 % of the total loss, other than in a few regions, primarily northern Eurasia, where this reaches up to 4 %. The updated simulations restrict the importance of non-water reactions significantly, although there may be more localised impacts which are not realised in this work owing to the spatial resolution of the simulations.

8.1.3 Atmospheric Losses of *syn*-CH_3CHOO

Figure 8.8 shows the percentage loss of *syn*-CH_3CHOO due to decomposition, reaction with NO_2, SO_2 and water monomers, in the surface layer of the model using the rate coefficients reported in this work for the reactions between *syn*-CH_3CHOO and SO_2[23] and the literature value reported for *syn*-CH_3CHOO decomposition[24] and the reactions of *syn*-CH_3CHOO with NO_2[25] and water monomers.[26]

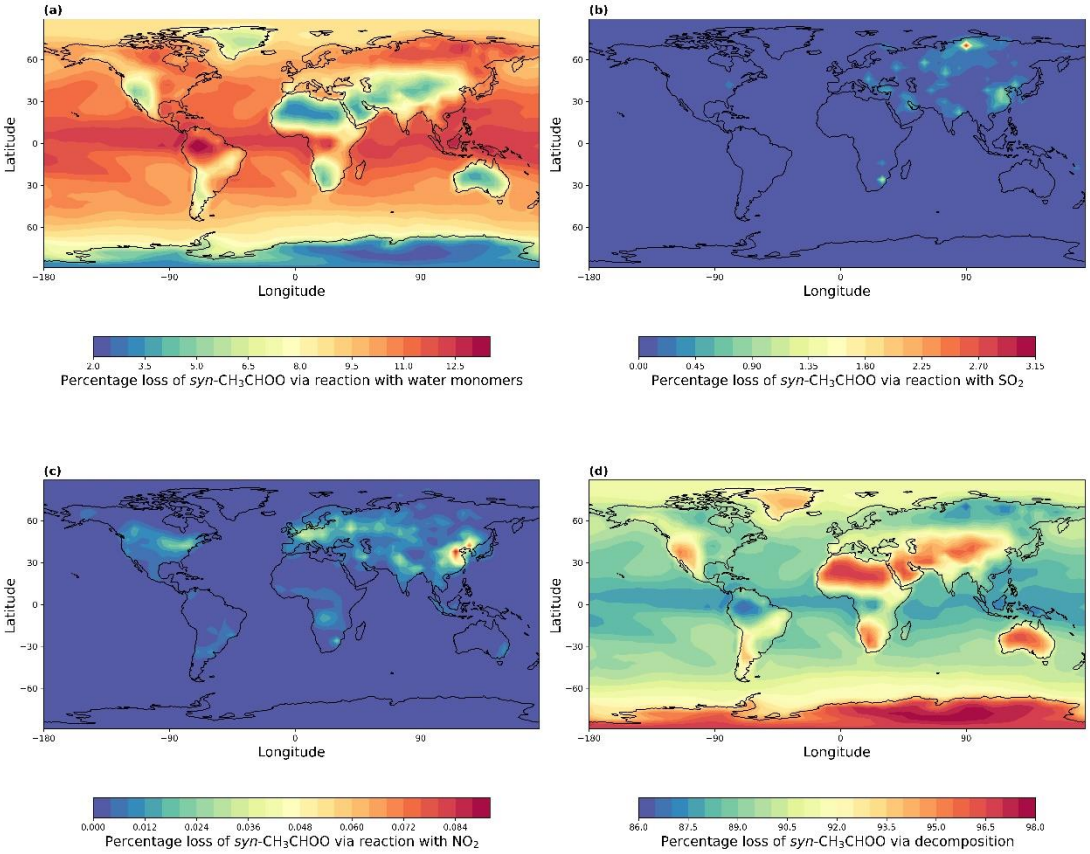

Figure 8.8. Percentage losses of *syn*-CH_3CHOO via reaction with a) water monomers b) SO_2 c) NO_2 and d) thermal decomposition.

Decomposition is expected to dominate the atmospheric loss of *syn*-CH_3CHOO, which is facilitated by a 1,4-Hydrogen transfer from the methly group to its terminal oxygen. This H-atom transfer results in the production of vinyl hydroperoxide, which may subsequently decompose to produce OH radicals, meaning that the decomposition of *syn*-CH_3CHOO has the potential to influence the oxidising capacity of the troposphere in areas of low sunlight and at night-time, when photolytic sources of OH are low.[24] Reaction with water monomers is currently expected to be the next significant loss *syn*-CH_3CHOO in the troposphere, which potentially makes up for 13 % of its loss in some areas. However, the rate coefficient for this reaction remains uncertain, with only an upper limit currently reported at 298 K.[26] There are also currently no experimental studies to investigate the reaction between *syn*-CH_3CHOO and water dimers, which may be more important than reaction with the water monomer. The reaction between *syn*-CH_3CHOO and SO_2 may be competitive with decomposition and its reaction with water vapour in areas with high SO_2 concentrations and lower humidities, with results showing this reaction may constitue up to 3 % of its atmospheric loss in some areas of China and Russia.

8.1.4 Atmospheric Losses of *anti*-CH_3CHOO

Figure 8.9 shows the percentage loss of *anti*-CH_3CHOO due to decomposition, reaction with NO_2, SO_2 and water monomers, in the surface layer of the model using the rate coefficients reported in this work for the reaction between *anti*-CH_3CHOO and SO_2[23] and the literature value reported for *anti*-CH_3CHOO decomposition[24] and the reactions of *anti*-CH_3CHOO with NO_2[25] and water vapour.[27]

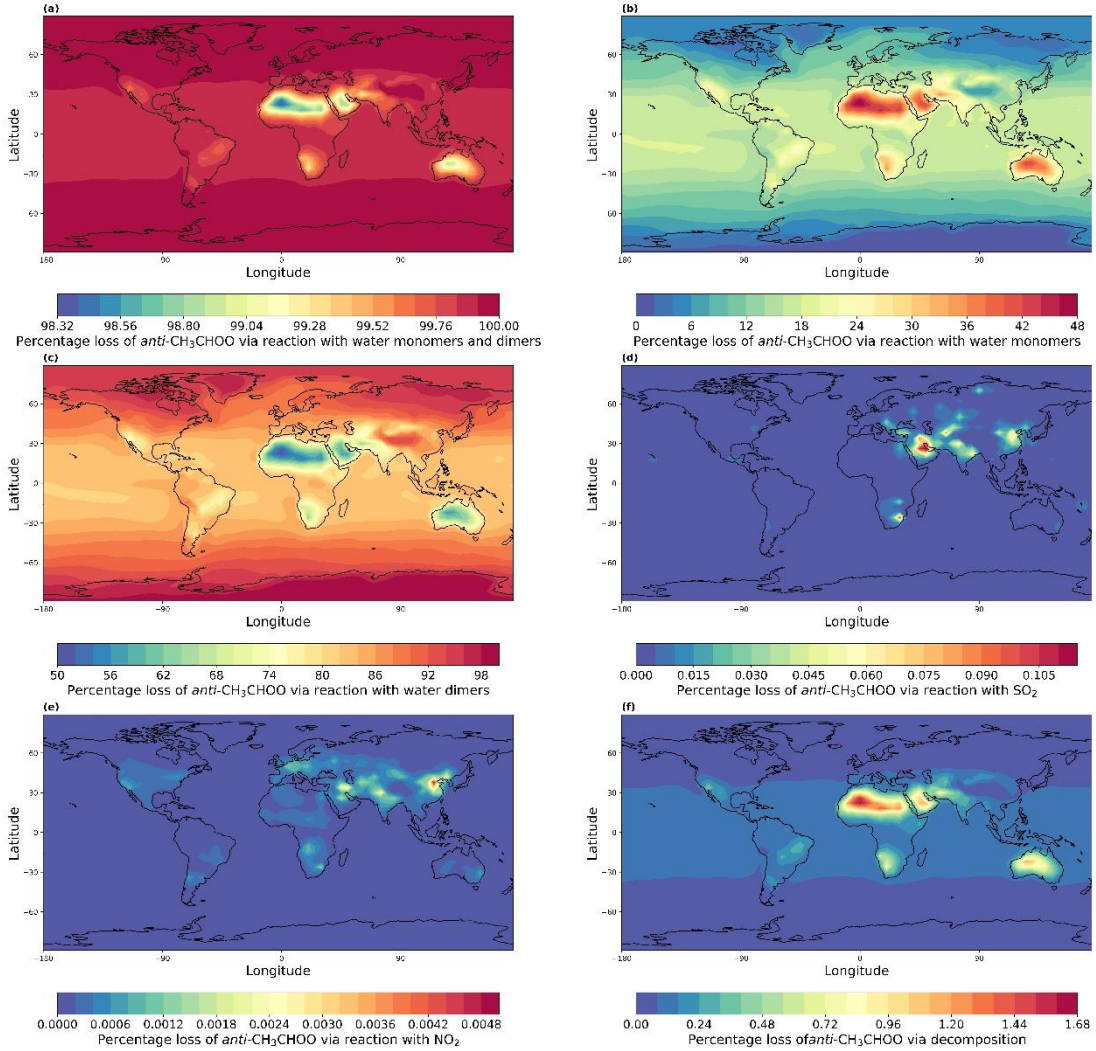

Figure 8.9. Percentage losses of *anti*-CH_3CHOO via reaction with a) water monomers and dimers combined, b) water monomers, c) water dimers, d) SO_2 e) NO_2 and f) thermal decomposition.

As with CH_2OO, the atmospheric loss of *anti*-CH_3CHOO is expected to be through its reaction with water dimers, with the reaction between *anti*-CH_3CHOO and water monomers becoming more significant in areas of higher temperatures, due to the lower water dimer concentrations. However, the reactions between *anti*-CH_3CHOO and water monomers and dimers have only been investigated over a relatively narrow temperature range,[28] and current IUPAC

recommendations[9] do not extend beyond 298 K, so the rate coefficients for these reactions currently remain uncertain. Decomposition is less significant for *anti*-CH_3CHOO than for *syn*-CH_3CHOO as the 1,4-H transfer mechanism is hindered by the restricted rotation around the carbon-oxygen double bond and so *anti*-CH_3CHOO is unlikely to be a significant source of OH in the atmosphere. While the rate coefficient for *anti*-$CH_3CHOO + SO_2$ is significantly faster than reactions of *anti*-CH_3CHOO with water monomers and dimers, it constitutes less than 1 % of the atmospheric loss of *anti*-CH_3CHOO, due to the lower concentrations of SO_2 in the atmosphere, so production of SO_3 via this reaction may be limited.

The reactions of CH_3CHOO conformers can be used as a proxy to characterise the reactions of larger Criegee intermediates. Results presented throughout this thesis suggest that, for Criegee intermediates with a methyl group in the *syn*-position, thermal decomposition is likely to be the dominant loss process in the troposphere. For Criegee intermediates with a methyl group in the *anti*-position, where the 1,4-H transfer mechanism is hindered, the reactions with water monomers and dimers are likely to dominate.

8.2 Summary

The reactions with water dimers dominates the atmospheric losses of CH_2OO and *anti*-CH_3CHOO. As described in Chaper 6, there have been both theoretical and experimental investigations into the products of the reaction between CH_2OO and water vapour. The current mechanism used within the GEOS-Chem model is based on the work of Nguyen *et al.*[12] which suggests that the reaction between CH_2OO and water monomers leads to production of 74 % hydroxymethly hydroperoxde (HMHP), 21 % $HCOOH + H_2O$, and 6 % $HCHO + H_2O_2$, while reaction with water dimers leads to production of 54 % $HCOOH + H_2O$, 40 % HMHP, and 6 % $HCHO + H_2O_2$. There is also evidence that a hydroperoxide is the major product of the reaction between *anti*-CH_3CHOO and water vapour[29] however, there have been a limited number of studies to investigate this reaction and therefore the products remain uncertain. To gain a full understanding of the atmospheric implications of the reactions between Criegee intermediates and water vapour, time-resolved experiments to monitor the reaction products should be conducted across a range of temperatures and relative humidities.

The atmospheric loss of *syn*-CH_3CHOO is dominated by decomposition, which is likely to be a significant source of OH radicals under low-light conditions. However, there are currently no experimental measurements of the kinetics of *syn*-CH_3CHOO with water dimers, which may decrease the role of decomposition, particularly in areas where water dimer concentrations are higher. The uncertainty in the reaction rates and products of *syn*- and *anti*-CH_3CHOO with water and water dimers limits the full assessment of the atmospheric

implications of other reactions for these Criegee intermediates and should therefore be the subject of further research into Criegee intermediates.

While the reactions between Criegee intermediates and SO_2 tend to have relatively large rate coefficients (10^{-10}-10^{-11} cm^3 $molecule^{-1}$ s^{-1}), atmospheric concentrations of SO_2 remain low, making these reactions insignificant in most regions globally. However, in areas where SO_2 concentrations may be higher i.e. where coal and oil are used to produce electricity, these reactions may become more important. It is known that a major product of the reaction between CH_2OO and SO_2 is SO_3,[30, 31] and the atmospheric fate of the SOZ produced from CH_3CHOO is uncertain, but may decompose to SO_3, meaning H_2SO_4 production in these areas may be significant and potentially result in damage to ecosystems via acid rain or negative impacts on human health.

The reaction between all three Criegee intermediates and NO_2 shows little atmospheric significance, with losses being limited to less than 1 % across the globe, due to the low atmospheric NO_2 concentrations alongside relatively low rate coefficients. However, in ozonolysis chamber experiments, concentrations of NO_2 may be much higher than tropospheric concentrations and chamber studies may also take place without the addition of water, and under these conditions, the reactions between Criegee intermediates and NO_2 will be significant. As previously described, the products of the reaction between CH_2OO and NO_2 currently remain unknown, and it is therefore difficult to provide an accurate assessment of the atmospheric implications of the reaction at present. It had previously been suggested that the major products from this reaction were HCHO and the nitrate radical, NO_3, which would therefore influence the overall oxidising capacity of the troposphere. Many literature studies, including the work presented in Chapter 5, have been unable to detect either NO_3 or NO as direct reaction products, and there have been previous studies reporting the formation of HCHO[32] as well as a Criegee-NO_2 adduct.[33] Modelling presented in Chapter 5 suggests the potential formation of HCHO as a result of a reaction between a Criegee-NO_2 adduct and NO_2, which may reconcile differences currently reported within the literature.[33, 34] Future work should include further investigation into the products of this reaction to enable a full assessment of the atmospheric implications.

8.3 References

1. Bey, I., Jacob, D.J., Yantosca, R.M., Logan, J.A., Field, B.D., Fiore, A.M., Li, Q., Liu, H.Y., Mickley, L.J. and Schultz, M.G. Global modeling of tropospheric chemistry with assimilated meteorology: Model description and evaluation. 2001, **106**(D19), pp.23073-23095.
2. Gelaro, R., McCarty, W., Suárez, M.J., Todling, R., Molod, A., Takacs, L., Randles, C.A., Darmenov, A., Bosilovich, M.G., Reichle, R., Wargan, K., Coy, L., Cullather, R., Draper, C., Akella, S., Buchard, V., Conaty, A., da Silva, A.M., Gu, W., Kim, G.-K., Koster, R., Lucchesi, R., Merkova, D., Nielsen, J.E., Partyka, G., Pawson, S., Putman, W., Rienecker, M., Schubert, S.D., Sienkiewicz, M. and Zhao, B. The Modern-Era Retrospective Analysis for Research and Applications, Version 2 (MERRA-2). *Journal of Climate.* 2017, **30**(14), pp.5419-5454.
3. Bates, K.H., Jacob, D.J., Li, K., Ivatt, P.D., Evans, M.J., Yan, Y. and Lin, J. Development and evaluation of a new compact mechanism for aromatic oxidation in atmospheric models. *Atmospheric Chemistry and Physics.* 2021, **21**(24), pp.18351-18374.
4. Millet, D.B., Baasandorj, M., Farmer, D.K., Thornton, J.A., Baumann, K., Brophy, P., Chaliyakunnel, S., de Gouw, J.A., Graus, M., Hu, L., Koss, A., Lee, B.H., Lopez-Hilfiker, F.D., Neuman, J.A., Paulot, F., Peischl, J., Pollack, I.B., Ryerson, T.B., Warneke, C., Williams, B.J. and Xu, J. A large and ubiquitous source of atmospheric formic acid. *Atmospheric Chemistry and Physics.* 2015, **15**(11), pp.6283-6304.
5. Guenther, A.B., Jiang, X., Heald, C.L., Sakulyanontvittaya, T., Duhl, T., Emmons, L.K. and Wang, X. The Model of Emissions of Gases and Aerosols from Nature version 2.1 (MEGAN2.1): an extended and updated framework for modeling biogenic emissions. *Geoscientific Model Development.* 2012, **5**(6), pp.1471-1492.
6. van der Werf, G.R., Randerson, J.T., Giglio, L., van Leeuwen, T.T., Chen, Y., Rogers, B.M., Mu, M., van Marle, M.J.E., Morton, D.C., Collatz, G.J., Yokelson, R.J. and Kasibhatla, P.S. Global fire emissions estimates during 1997–2016. *Earth System Science Data.* 2017, **9**(2), pp.697-720.
7. Hoesly, R.M., Smith, S.J., Feng, L., Klimont, Z., Janssens-Maenhout, G., Pitkanen, T., Seibert, J.J., Vu, L., Andres, R.J., Bolt, R.M., Bond, T.C., Dawidowski, L., Kholod, N., Kurokawa, J.I., Li, M., Liu, L., Lu, Z., Moura, M.C.P., O'Rourke, P.R. and Zhang, Q. Historical (1750–2014) anthropogenic emissions of reactive gases and aerosols from the Community Emissions Data System (CEDS). *Geoscientific Model Development.* 2018, **11**(1), pp.369-408.

8. Jenkin, M.E., Young, J.C. and Rickard, A.R. The MCM v3.3.1 degradation scheme for isoprene. *Atmospheric Chemistry and Physics.* 2015, **15**(20), pp.11433-11459.

9. Cox, R.A., Ammann, M., Crowley, J.N., Herrmann, H., Jenkin, M.E., McNeill, V.F., Mellouki, A., Troe, J. and Wallington, T.J. Evaluated kinetic and photochemical data for atmospheric chemistry: Volume VII – Criegee intermediates. *Atmospheric Chemistry and Physics.* 2020, **20**(21), pp.13497-13519.

10. Onel, L., Blitz, M., Seakins, P., Heard, D. and Stone, D. Kinetics of the Gas Phase Reactions of the Criegee Intermediate CH_2OO with O_3 and IO. *The Journal of Physical Chemistry A.* 2020, **124**(31), pp.6287-6293.

11. Onel, L., Lade, R., Mortiboy, J., Blitz, M.A., Seakins, P.W., Heard, D.E. and Stone, D. Kinetics of the gas phase reaction of the Criegee intermediate CH_2OO with SO_2 as a function of temperature. *Physical Chemistry Chemical Physics.* 2021, **23**(35), pp.19415-19423.

12. Nguyen, T.B., Tyndall, G.S., Crounse, J.D., Teng, A.P., Bates, K.H., Schwantes, R.H., Coggon, M.M., Zhang, L., Feiner, P., Millller, D.O., Skog, K.M., Rivera-Rios, J.C., Dorris, M., Olson, K.F., Koss, A., Wild, R.J., Brown, S.S., Goldstein, A.H., de Gouw, J.A., Brune, W.H., Keutsch, F.N., Seinfeld, J.H. and Wennberg, P.O. Atmospheric fates of Criegee intermediates in the ozonolysis of isoprene. *Physical Chemistry Chemical Physics.* 2016, **18**(15), pp.10241-10254.

13. Bates, K.H. and Jacob, D.J. A new model mechanism for atmospheric oxidation of isoprene: global effects on oxidants, nitrogen oxides, organic products, and secondary organic aerosol. *Atmospheric Chemistry and Physics.* 2019, **19**(14), pp.9613-9640.

14. Mir, Z.S., Lewis, T.R., Onel, L., Blitz, M.A., Seakins, P.W. and Stone, D. CH_2OO Criegee intermediate UV absorption cross-sections and kinetics of CH_2OO + CH_2OO and CH_2OO + I as a function of pressure. *Physical Chemistry Chemical Physics.* 2020, **22**(17), pp.9448-9459.

15. Wennberg, P.O., Bates, K.H., Crounse, J.D., Dodson, L.G., McVay, R.C., Mertens, L.A., Nguyen, T.B., Praske, E., Schwantes, R.H., Smarte, M.D., St Clair, J.M., Teng, A.P., Zhang, X. and Seinfeld, J.H. Gas-Phase Reactions of Isoprene and Its Major Oxidation Products. *Chemical Reviews.* 2018, **118**(7), pp.3337-3390.

16. Berndt, T., Voigtländer, J., Stratmann, F., Junninen, H., Mauldin III, R.L., Sipilä, M., Kulmala, M. and Herrmann, H. Competing atmospheric reactions of CH_2OO with SO_2 and water vapour. *Physical Chemistry Chemical Physics.* 2014, **16**(36), pp.19130-19136.

17. Chao, W., Hsieh, J.-T., Chang, C.-H. and Lin, J.J.-M. Direct kinetic measurement of the reaction of the simplest Criegee intermediate with water vapor. *Science.* 2015, **347**(6223), p.751.

18. Lewis, T.R., Blitz, M.A., Heard, D.E. and Seakins, P.W. Direct evidence for a substantive reaction between the Criegee intermediate, CH_2OO, and the water vapour dimer. *Physical Chemistry Chemical Physics.* 2015, **17**(7), pp.4859-4863.

19. Smith, M.C., Chang, C.-H., Chao, W., Lin, L.-C., Takahashi, K., Boering, K.A. and Lin, J.J.-M. Strong Negative Temperature Dependence of the Simplest Criegee Intermediate CH_2OO Reaction with Water Dimer. *The Journal of Physical Chemistry Letters.* 2015, **6**(14), pp.2708-2713.

20. Sheps, L., Rotavera, B., Eskola, A.J., Osborn, D.L., Taatjes, C.A., Au, K., Shallcross, D.E., Khan, M.A.H. and Percival, C.J. The reaction of Criegee intermediate CH_2OO with water dimer: primary products and atmospheric impact. *Physical Chemistry Chemical Physics.* 2017, **19**(33), pp.21970-21979.

21. Wu, Y.-J., Takahashi, K. and Lin, J.J.-M. Kinetics of the Simplest Criegee Intermediate Reaction with Water Vapor: Revisit and Isotope Effect. *The Journal of Physical Chemistry A.* 2023, **127**(39), pp.9059-8072.

22. Stone, D., Au, K., Sime, S., Medeiros, D.J., Blitz, M., Seakins, P.W., Decker, Z. and Sheps, L. Unimolecular decomposition kinetics of the stabilised Criegee intermediates CH_2OO and CD_2OO. *Physical Chemistry Chemical Physics.* 2018, **20**(38), pp.24940-24954.

23. Lade, R.E., Onel, L., Blitz, M.A., Seakins, P.W. and Stone, D. Kinetics of the Gas-Phase Reactions of *syn*- and *anti*-CH_3CHOO Criegee Intermediate Conformers with SO_2 as a Function of Temperature and Pressure. *The Journal of Physical Chemistry A.* 2024, **128**(14), pp.2815-2824.

24. Robinson, C., Onel, L., Newman, J., Lade, R., Au, K., Sheps, L., Heard, D.E., Seakins, P.W., Blitz, M.A. and Stone, D. Unimolecular Kinetics of Stabilized CH_3CHOO Criegee Intermediates: syn-CH_3CHOO Decomposition and anti-CH_3CHOO Isomerization. *The Journal of Physical Chemistry A.* 2022, **126**(39), pp.6984-6994.

25. Taatjes, C.A., Welz, O., Eskola, A.J., Savee, J.D., Scheer, A.M., Shallcross, D.E., Rotavera, B., Lee, E.P.F., Dyke, J.M., Mok, D.K.W., Osborn, D.L. and Percival, C.J. Direct Measurements of Conformer-Dependent Reactivity of the Criegee Intermediate CH_3CHOO. *Science.* 2013, **340**(6129), p.177.

26. Sheps, L., Scully, A.M. and Au, K. UV absorption probing of the conformer-dependent reactivity of a Criegee intermediate CH_3CHOO. *Physical Chemistry Chemical Physics.* 2014, **16**(48), pp.26701-26706.

27. Lin, L.-C., Chao, W., Chang, C.-H., Takahashi, K. and Lin, J.J.-M. Temperature dependence of the reaction of anti-CH_3CHOO with water vapor. *Physical Chemistry Chemical Physics.* 2016, **18**(40), pp.28189-28197.

28. Lin, L.-C., Chang, H.-T., Chang, C.-H., Chao, W., Smith, M.C., Chang, C.-H., Lin, J. and Takahashi, K. Competition between H_2O and $(H_2O)_2$ reactions with CH_2OO/CH_3CHOO. *Physical Chemistry Chemical Physics.* 2016, **18**(6), pp.4557-4568.

29. Cabezas, C. and Endo, Y. The reactivity of the Criegee intermediate CH_3CHOO with water probed by FTMW spectroscopy. *The Journal of Chemical Physics.* 2018, **148**(1), p.014308.

30. Wang, Y.-Y., Dash, M.R., Chung, C.-Y. and Lee, Y.-P. Detection of transient infrared absorption of SO_3 and 1,3,2-dioxathietane-2,2-dioxide [cyc-$(CH_2)O(SO_2)O$] in the reaction CH_2OO+SO_2. *The Journal of Chemical Physics.* 2018, **148**(6), p.064301.

31. Mir, Z.S., Jamieson, M., Greenall, N.R., Seakins, P.W., Blitz, M.A. and Stone, D. Identification, monitoring, and reaction kinetics of reactive trace species using time-resolved mid-infrared quantum cascade laser absorption spectroscopy: development, characterisation, and initial results for the CH_2OO Criegee intermediate. *Atmospheric Measurement Techniques.* 2022, **15**(9), pp.2875-2887.

32. Stone, D., Blitz, M., Daubney, L., Howes, N.U.M. and Seakins, P. Kinetics of CH_2OO reactions with SO_2, NO_2, NO, H_2O and CH_3CHO as a function of pressure. *Physical Chemistry Chemical Physics.* 2014, **16**(3), pp.1139-1149.

33. Caravan, R.L., Khan, M.A.H., Rotavera, B., Papajak, E., Antonov, I.O., Chen, M.-W., Au, K., Chao, W., Osborn, D.L., Lin, J.J.-M., Percival, C.J., Shallcross, D.E. and Taatjes, C.A. Products of Criegee intermediate reactions with NO_2: experimental measurements and tropospheric implications. *Faraday Discussions.* 2017, **200**(0), pp.313-330.

34. Ouyang, B., McLeod, M.W., Jones, R.L. and Bloss, W.J. NO_3 radical production from the reaction between the Criegee intermediate CH_2OO and NO_2. *Physical Chemistry Chemical Physics.* 2013, **15**(40), pp.17070-17075.

Chapter 9
Conclusions and Future Work

The kinetics of reactions between CH_2OO and CH_3CHOO conformers with atmospherically relevant trace species have been investigated in this work under a range of conditions relevant to the troposphere using laser flash photolysis coupled to time-resolved broadband UV absorption spectroscopy.

Results show that the reaction with water vapour dominates the atmospheric loss of CH_2OO under all conditions relevant to the troposphere, with loss via reaction with the water dimer dominating over the water monomer. Kinetics of the reactions between CH_2OO and water vapour were investigated at 760 Torr and temperatures between 262 and 353 K, with results providing an estimated value for $k_{6.1}$ of $(9.8 \pm 5.9) \times 10^{-17}$ cm^3 molecule^{-1} s^{-1} at 298 K and a temperature dependence described by $k_{6.1} = (3.15 \pm 1.06) \times 10^{-13} \exp(-(2405 \pm 265)/T)$ cm^3 molecule^{-1} s^{-1} and a rate coefficient for the reaction with the water dimer of $k_{6.2} = (9.52 \pm 2.49) \times 10^{-12}$ cm^3 molecule^{-1} s^{-1} at 298 K, with a temperature dependence described by $k_{6.2} = (2.85 \pm 0.40) \times 10^{-15} \exp((2417 \pm 338)/T)$ cm^3 molecule^{-1} s^{-1}. Atmospheric modelling of these results suggests that, while reaction with the water dimer is dominant, reaction with the water monomer will become more significant in areas with higher temperatures, where the reaction between CH_2OO and H_2O becomes faster and concentrations of the water dimer are reduced. There is agreement between theory and experiment that HMHP is an initial product of the reactions between water monomers and water dimers with CH_2OO however, there is currently uncertainty regarding its fate which therefore limits a full assessment into the atmospheric implications of these reactions. Future work should therefore look to monitor the production and possible fates of HMHP as a function of time to provide a better understanding of the impacts of these reactions.

The reaction between CH_2OO and SO_2 has also been investigated as a function of temperature with the results giving a rate coefficient of $(3.60 \pm 0.10) \times 10^{-11}$ cm^3 molecule^{-1} s^{-1} at 298 K and a negative temperature dependence that is well described by $k_{4.1} = (3.72 \pm 0.01) \times 10^{-11} (T/298)^{-(2.05 \pm 0.02)}$ cm^3 molecule^{-1} s^{-1}. Modelling of the results has shown that this reaction may become dominant over the reaction with water vapour in areas where SO_2 concentrations are higher and where relative humidites are lower. The characteristics of this reaction have now been well established, with previous work showing that it is independent of pressure between 1.5 and 450 Torr and both theoretical and experimental studies showing that the major reaction products are HCHO and SO_3.

Investigation into the reaction between CH_2OO and NO_2 has shown that this represents less than 0.1 % of the overall loss of CH_2OO in the troposphere, with results giving a pressure independent rate coefficient of $(1.26 \pm 0.11) \times 10^{-12}$ cm^3 molecule^{-1} s^{-1} at 298 K and a negative temperature dependence described by $(1.06 \pm 0.02) \times 10^{-12} \times (T/298)^{-(2.9\pm0.2)}$ cm^3 molecule^{-1} s^{-1}. However, this work has highlighted significant discrepancies between experimental measurements and theoretical calculations, which are likely a result of the difficulties in characterising the entrance channels due to substantial multi-reference effects. The application of theoretical approaches to understand the chemistry of Criegee intermediates has developed significantly in recent years and is often used to develop structure activity relationships for Criegee intermediate reactions and reaction conditions that have yet to be studied experimentally. If the results of predictions based on theoretical approaches are to be used in numerical models to evaluate atmospheric composition for applications relating to air quality and climate, it is essential that such approaches are reliable. This work highlights a continued need for experimental measurements, both for direct application and for providing a means to test the validity of theoretical approaches, as well as care when applying theory, particularly when reaction systems have significant multi-reference character.

Reactions between CH_3CHOO conformers and SO_2 were investigated as a function of temperature (242 – 353 K) and pressure (10 – 600 Torr). Results for *syn*-CH_3CHOO + SO_2 show that the kinetics are pressure dependent and exert a negative dependence on temperature, with a rate coefficient of $k_{7.1} = (4.80 \pm 0.46) \times 10^{-11}$ cm^3 molecule^{-1} s^{-1} at 298 K and 760 Torr. Atmospheric modelling has shown that this reaction may be competitive with unimolecular decomposition and reaction with water vapour in areas where SO_2 concentrations are higher and water concentrations are lower. The observed pressure dependence indicates significant collisional stabilisation of the SOZ formed in the reaction under atmospheric conditions, with an expected yield of the SOZ greater than 99 % at 298 K and 760 Torr. However, there is currently uncertainty regarding the atmospheric fate of the SOZ, which has the potential to decompose, resulting in the formation of SO_3 and thus H_2SO_4. Future work into this reaction should look to monitor the fate of the SOZ over time to enable a complete assessment of the atmospheric impacts of this reaction. Kinetics of the reaction between *anti*-CH_3CHOO and SO_2 display no significant dependence on temperature or pressure over the ranges investigated. Results give a mean value for $k_{7.2}$ of $(1.15 \pm 0.16) \times 10^{-10}$ cm^3 molecule^{-1} s^{-1} at 298 K and $(1.18 \pm 0.21) \times 10^{-10}$ cm^3 molecule^{-1} s^{-1} over all conditions studied in this work. To determine the atmospheric implications of the reactions of CH_3CHOO conformers with SO_2, future work should focus on investigating the kinetics of the reactions between CH_3CHOO conformers and water monomers and water dimers. Current work suggests that the reaction with water vapour represents nearly 100 % of the loss of *anti*-CH_3CHOO however, the

reactions with water monomers and dimers have only been investigated over a relatively narrow temperature range (288-328 K) and the current IUPAC recommendation does not exceed 298 K. There are also currently no studies into the reaction of *syn*-CH_3CHOO with the water dimer, and only an upper limit for its reaction with the water monomer. Following this, future work should also look to monitor the production and fate of the reaction products to determine the overall impact on atmospheric composition and air quality.

Appendices

Appendix 1. Mass Flow Controller Calibrations

The MFCs used throughout experimental work were calibrated by flowing varying amounts of N_2 through the MFC and measuring the flow of bubbles along a burette of known volume. This could be carried out manually, where the movement of the bubble through the burette was timed using a stop watch, or digitally using a flowmeter. A calibration plot was then produced from the set and measured flows (Figure A.1 below).

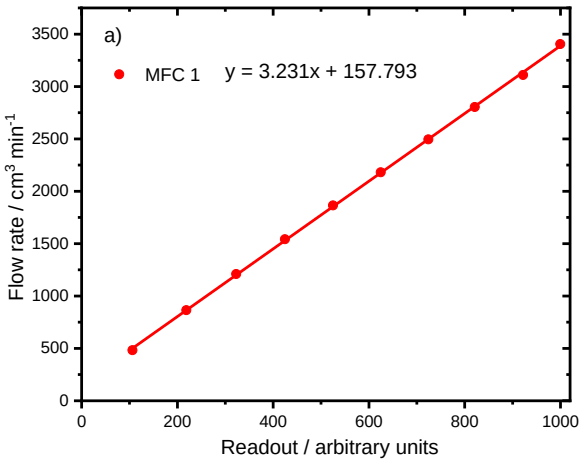

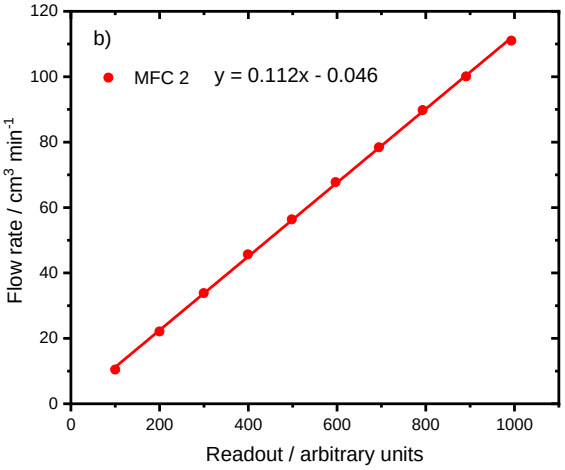

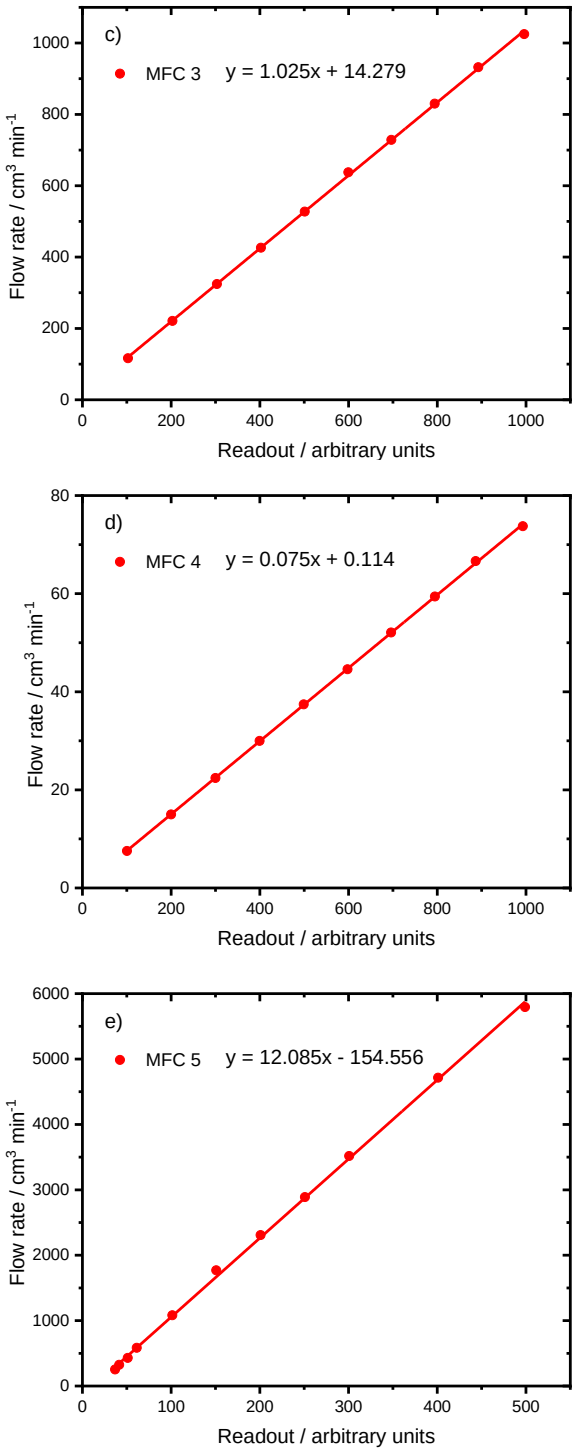

Figure A.1. MFC calibration data for MFC 1 (a) – MFC 5 (e). Each fit gave: a) intercept = (157.793 ± 10.469), gradient = (3.231 ± 0.016), R^2 = 0.9998. b) Intercept = - (0.046 ± 0.400), gradient = (0.112 ± 0.006), R^2 = 0.9997. c) Intercept = (14.279 ± 3.512), gradient = (1.025 ± 0.006), R^2 = 0.9997. d) Intercept = (0.114 ± 0.150), gradient = (0.075 ± 0.002), R^2 = 0.9999. e) Intercept = - (154.556 ± 22.194), gradient = (12.085 ± 0.096), R^2 = 0.9994.

Appendix 2. Hygrometer Calibration and Measuring Potential Water Vapour Losses in the System

Water was introduced into the reaction system by passing a flow of N_2 through a bubbler containing deionised water and then combined with the N_2/O_2 in a gas manifold using calibrated mass flow controllers (MFCs). The water vapour concentration was measured using relative humidity (RH) probes that were calibrated against a dew point hygrometer (Buck Research Instruments, CR-4 chilled mirror hygrometer) for RH between 0 and 95 % (Figure A.2).

Experiments involving two calibrated RH probes (RH1 and RH2) were carried out to ensure that no water vapour was being lost throughout the experimental apparatus. The first probe (RH1) was placed at the exit of the reaction cell at all times (where RH measurements were made for the experiments), and the second probe (RH2) was initially placed at the end of the gas mixing manifold, and then moved to the entrance of the reaction cell. For each position of RH2, the flow through the water bubbler was increased and decreased, whilst maintaining a total flow through the cell of 3.7 standard litres per minute and comparisons between RH1 and RH2 were made. Under all flow conditions, RH readings from RH1 and RH2 were within the reported error value (0.2 % RH) from each other.

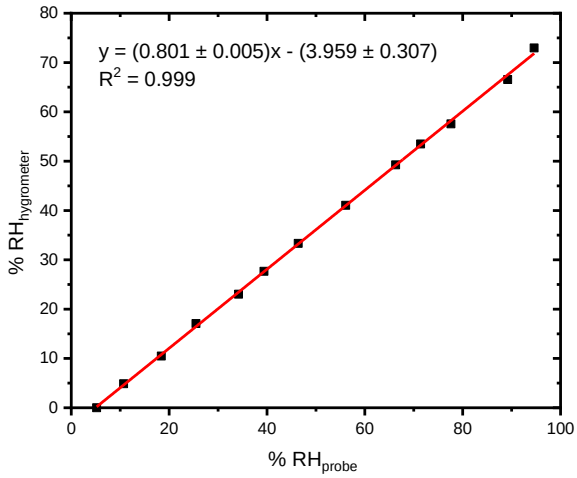

Figure A.2. Calibration plot of the relative humidity (RH) measured with the RH probe used for experiments against the RH measured using a dew point hygrometer. The red line represents a linear fit to the data and gave: gradient = 0.801 ± 0.005, intercept = 3.959 ± 0.307 and R^2 = 0.999.

Appendix 3. Determination of the Reaction Temperature

The reaction cell was heated or cooled by circulating a thermofluid (HUBE6479 DW-THERM) from a thermoregulator (Huber Unistat 360) through the outer jacket of the reaction cell. The temperature of a flow of N_2 gas, under a range of conditions for total flow and pressure as used in kinetics experiments, was measured in the centre of the reaction cell at 5 cm intervals along the length of the cell by a K-type thermocouple inserted into the cell through a flange which replaced one of the cell windows and ensured a sealed system. The range of temperatures and pressures investigated were 243–363 K and 12–760 Torr, to provide a temperature calibration for the range of conditions used in kinetics experiments.

At each temperature and pressure, a plot of the thermocouple position against temperature was produced, an example of which can be seen in Figure A.3.

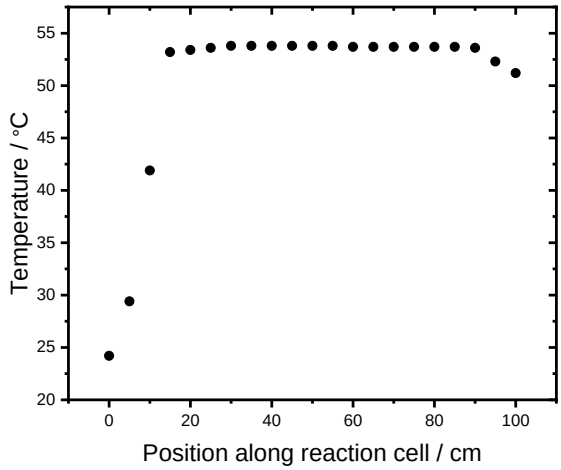

Figure A.3. An example plot of the thermocouple position / cm against the measured temperature from the thermocouple / ºC for measurements taken at 328 ºC and 85 Torr. A position of 0 cm corresponds to the end of the cell where the gas enters through an inlet tube.

As shown in Figure A.3, the temperature across the reaction cell remains relatively constant throughout the majority of the reaction cell. However, it can be seen that the gas needs to travel some distance (approximately 15 cm) from the gas inlet tube until the temperature is established, from which the temperature remains relatively constant until the final 5 cm, a region of the reaction cell that is not encapsulated by the heating jacket, where the temperature drops slightly as the gases approach the outlet tube. As there are regions at either end of the reaction chamber that differ in temperature to the rest of the cell, the average temperature throughout the reaction cell was calculated.

The average temperature across the reaction cell at each temperature and pressure was determined by integrating the curve of the plot of thermocouple position against temperature (Figures A.3). The total area under the curve of the plot, determined by integration, was then divided by the furthest position along the reaction cell (100 cm) to give a value for the average temperature throughout the reaction cell.

A summary table of the calibrated temperature at each set temperature and pressure is given below.

Temperature (Huber) / ^{o}C	Pressure / Torr	Temperature (Thermocouple) / ^{o}C
-30	25	-19.78
	100	-18.33
	150	-17.04
	250	-16.17
	500	-15.34
	760	-15.04
-10	25	-5.21
	100	-3.67
	150	-2.96
	250	-2.36
	500	-1.97
	760	-1.55
-14	85	-8.60
-3	85	1.40
8	85	10.70
10	25	12.18
	50	12.22
	100	12.43
	150	12.60
	250	12.60
	500	13.01
	760	13.06
40	25	37.29
	50	37.02
	100	36.64
	150	36.24
	250	36.21
	500	35.88
	760	35.52
45	12	41.80
	35	41.50
	65	40.90
	80	40.70
	160	39.90
	300	39.60
	725	38.90
50	25	45.92
	50	45.45
	100	45.01
	150	44.68

	200	44.51
	250	44.23
	500	43.53
	760	43.13
55	85	51.00
60	25	54.55
	50	53.95
	100	52.94
	150	51.81
	200	51.35
	250	51.31
	500	50.46
	760	50.03
65	12	59.60
	35	58.90
	65	58.20
	85	58.00
	90	57.90
	150	57.60
	300	56.60
70	25	63.29
	50	62.34
	100	61.47
	150	61.41
	200	61.31
	250	60.58
	500	60.17
	760	60.15
75	85	67.30
80	25	72.19
	50	71.02
	100	70.29
	150	69.52
	250	69.30
	500	68.36
	760	68.11
90	12	81.20
	65	79.30
	90	79.20
	150	77.80
	300	77.20

Table A.1. A summary table of the results obtained from the temperature calibration experiments.

Appendix 4. Calculating the Effective Pathlength

The optical multipass arrangement used in this work includes either 8 or 10 Al mirrors which allows the UV light to be multi-passed 7 or 9 times through the reaction cell. The effective path length is the length of overlap between the photolysis beam (aligned such that it travels along the centre of the reaction cell) and the multipass beam. The effective path length was measured from the calculated depletion of CH_2I_2, $\Delta[CH_2I_2]_{calculated}$, for a typical laser fluence of 20 mJ cm^{-2} (RA.1) and $\Delta[CH_2I_2]_{experimental} \times l$ from the absorbance spectra obtained from a photolytic experiment. $\Delta[CH_2I_2]_{calculated}$ is calculated using Equation A.1.

$$CH_2I_2 + h\nu \rightarrow CH_2I \qquad \text{(RA.1)}$$

$$\Delta[CH_2I_2]_{calculated} = number\ of\ photons \times \sigma_{CH2I2,298\,nm} \times [CH_2I_2]_0 \qquad \text{(Equation A.1)}$$

where $\sigma_{CH2I2,298\,nm}$ is the absorption cross-section of CH_2I_2 at 248 nm (1.6×10^{-18} cm^2 $molecule^{-1}$)[52] and $[CH_2I_2]_0$ is the concentration of CH_2I_2 prior to photolysis measured in separate experiments.

The number of photons is calculated from the energy of a single photon (Equation A.2) and the typical laser fluence, *f*. (Equation A.3)

$$E_{photon} = \frac{h\,c}{\lambda} \qquad \text{(Equation A.2)}$$

$$number\ of\ photons = \frac{f}{E_{photon}} \qquad \text{(Equation A.3)}$$

$\Delta[CH_2I_2]_{experimental} \times l$ was obtained from fitting the observed absorbance with reference spectra for CH_2I_2[47] (further details given in section 3.3.3). A typical plot of $\Delta[CH_2I_2] \times l$ as a function of time is shown in Figure A.4.

The path length was then calculated using Equation A.4.

$$l = \frac{\Delta[CH_2I_2]_{experimental}}{\Delta[CH_2I_2]_{calculated}} \qquad \text{(Equation A.4)}$$

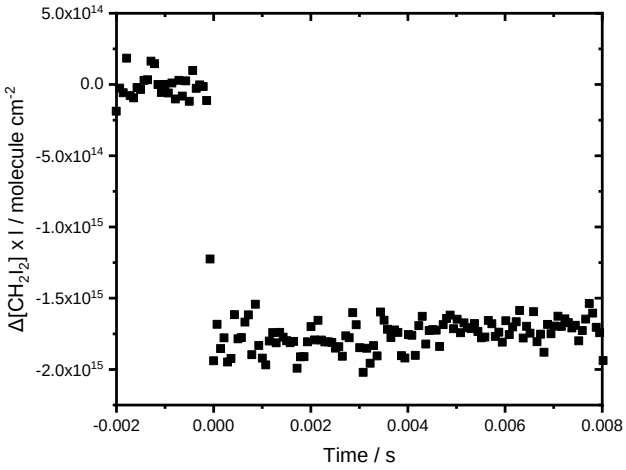

Figure A.4. A typical profile of $\Delta[CH_2I_2] \times l$ as a function of time for $[CH_2I_2]_0 = 8.1 \times 10^{13}$ molecule cm^{-3} at 298 K and 50 Torr. The data points at t<0 correspond to pre-photolysis data points.

Appendix 5. Bimolecular Plots for the Reaction between CH_2OO and NO_2

Bimolecular plots presented in Chapter 5 for the temperature dependence of R5.1 are shown with the value for the intercept, k_x, removed at each temperature for clarity on the combined plot. Results before the subtraction of k_x are shown in Chapter 5 for 242 and 254 K to show results of the investigation into the pressure dependence of R5.1 at these temperatures. Figures A.5-A.9 show the bimolecular plots obtained for R5.1 at 277 K and above before k_x had been subtracted.

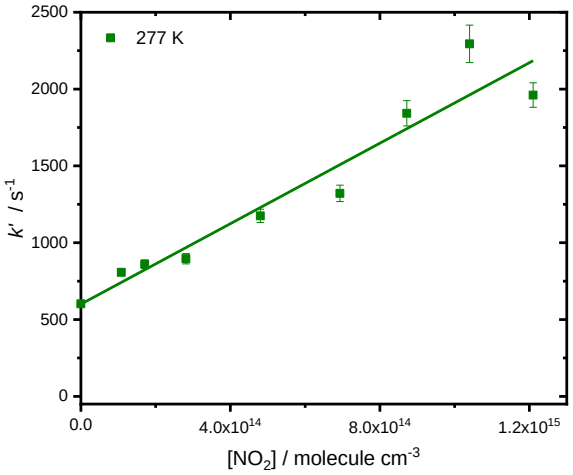

Figure A.5. Bimolecular plot for the reaction between CH_2OO and NO_2 at 277 K and 50 Torr. The solid line represents an unweighted linear fit and gives $k_{5.1} = (1.31 \pm 0.14) \times 10^{-12}$ cm^3 molecule^{-1} s^{-1} and an intercept of $k_x = (600 \pm 97)$ s^{-1}. Uncertainties are 1σ.

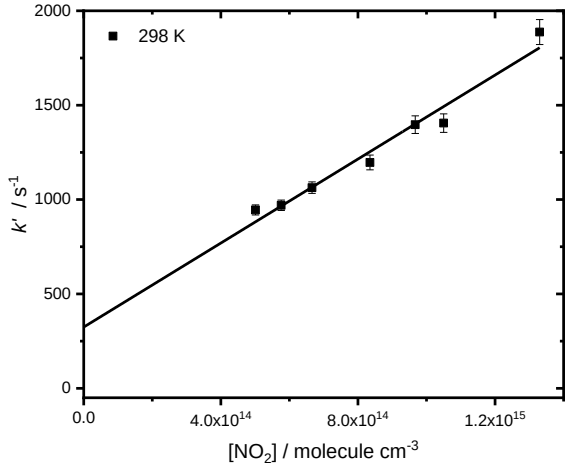

Figure A.6. Bimolecular plot for the reaction between CH_2OO and NO_2 at 298 K and 50 Torr. The solid line represents an unweighted linear fit and gives $k_{5.1} = (1.11 \pm 0.09) \times 10^{-12}$ cm^3 molecule^{-1} s^{-1} and an intercept of $k_x = (324 \pm 82)$ s^{-1}. Uncertainties are 1σ.

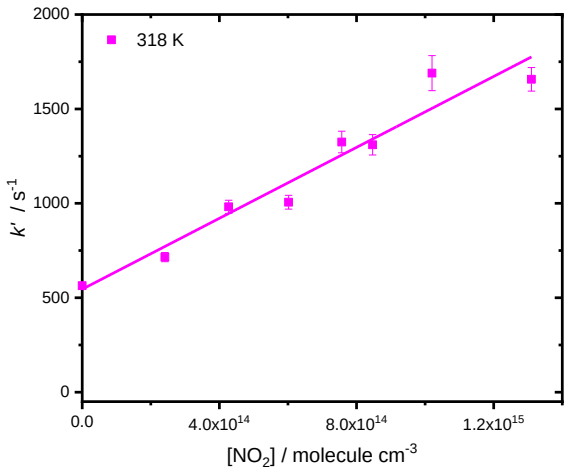

Figure A.7. Bimolecular plot for the reaction between CH_2OO and NO_2 at 318 K and 50 Torr. The solid line represents an unweighted linear fit and gives $k_{5.1} = (9.39 \pm 0.96) \times 10^{-13}$ cm^3 molecule^{-1} s^{-1} and an intercept of $k_x = (545 \pm 73)$ s^{-1}. Uncertainties are 1σ.

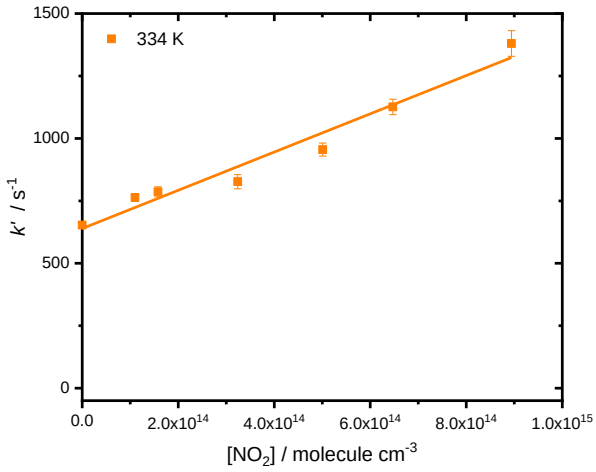

Figure A.8. Bimolecular plot for the reaction between CH_2OO and NO_2 at 334 K and 50 Torr. The solid line represents an unweighted linear fit and gives $k_{5.1} = (7.66 \pm 0.67) \times 10^{-13}$ cm^3 molecule^{-1} s^{-1} and an intercept of $k_x = (639 \pm 32)$ s^{-1}. Uncertainties are 1σ.

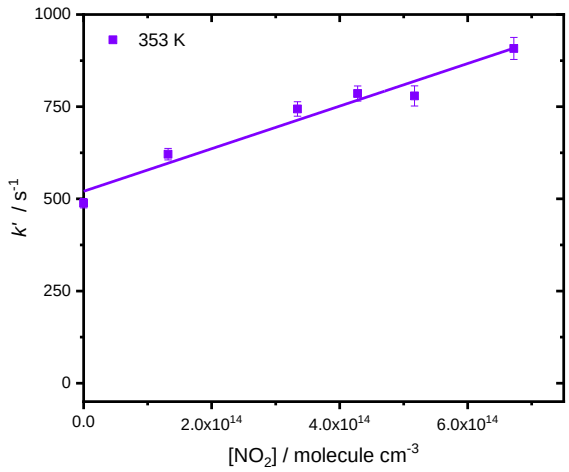

Figure A.9. Bimolecular plot for the reaction between CH_2OO and NO_2 at 353 K and 50 Torr. The solid line represents an unweighted linear fit and gives $k_{5.1} = (5.78 \pm 0.60) \times 10^{-13}$ cm^3 molecule^{-1} s^{-1} and an intercept of $k_x = (521 \pm 25)$ s^{-1}. Uncertainties are 1σ.

Appendix 6. Experimental Data Obtained for the Reaction between CH_2OO and NO_2

Temperature / K	Pressure / Torr	$[CH_2I_2]$ / 10^{13} molecule cm^{-3}	$[NO_2]$ / 10^{14} molecule cm^{-3}	k' / s^{-1}
242	25	5.3	0	761 ± 29
			1.9	1503 ± 78
			4.7	2026 ± 116
			5.7	2020 ± 126
			7.3	2620 ± 200
			9.8	2692 ± 239
242	50	6.1	0	761 ± 19
			2.6	1417 ± 89
			3.5	1512 ± 95
			4.8	1561 ± 91
			6.2	1965 ± 122
			7.3	2225 ± 172
			8.1	2431 ± 181
242	200	7.1	0	461 ± 21
			1.5	1000 ± 102
			3.6	1574 ± 202
			6.7	1747 ± 299
			10.8	2837 ± 429
254	25	5.4	3.3	1018 ± 35
			4.6	1452 ± 65
			5.3	1682 ± 81
			7.8	1804 ± 95
			8.2	2146 ± 142
			9.7	2261 ± 150
			12.9	2720 ± 187
254	50	4.6	4.7	977 ± 29
			5.9	1202 ± 39
			7.2	1489 ± 55
			8.3	1616 ± 61
			9.3	1836 ± 75
			10.4	1923 ± 85
254	200	5.6	0	573 ± 20
			1.8	1040 ± 56
			2.7	1024 ± 76
			3.9	1373 ± 85
			5.2	1490 ± 113
			7.0	1801 ± 140
			7.9	2041 ± 180
277	50	4.0	0	603 ± 14
			1.1	807 ± 21
			1.7	860 ± 28
			2.8	896 ± 33

			4.8	1175 ± 43
			6.9	1321 ± 54
			8.7	1843 ± 82
			10.4	2294 ± 122
			12.1	1961 ± 80
298	25	6.1	0	608 ± 11
			4.5	985 ± 22
			6.1	1116 ± 27
			10.6	1740 ± 53
			12.3	2022 ± 71
			14.3	2242 ± 86
298	50	5.9	5.0	945 ± 27
			5.8	970 ± 28
			6.7	1063 ± 30
			8.4	1197 ± 39
			9.7	1397 ± 47
			10.5	1405 ± 49
			13.3	1887 ± 66
298	100	5.5	0	557 ± 13
			0.9	666 ± 18
			1.5	764 ± 22
			2.4	814 ± 28
			3.3	885 ± 27
			5.0	1062 ± 38
			6.5	1271 ± 44
			8.1	1642 ± 62
			10.6	1853 ± 70
298	200	6.3	0	579 ± 14
			8.8	695 ± 27
			2.2	875 ± 45
			4.7	1169 ± 68
			6.4	1410 ± 81
			8.0	1725 ± 95
298	300	6.1	0	574 ± 16
			2.1	844 ± 39
			2.9	1069 ± 45
			4.5	1270 ± 65
			6.1	1393 ± 68
			9.8	1836 ± 85
318	50	4.8	0	564 ± 15
			2.4	715 ± 24
			4.3	982 ± 35
			6.0	1006 ± 37
			7.6	1325 ± 57
			8.5	1310 ± 54
			10.2	1690 ± 93

			13.1	1657 ± 62
335	50	7.5	0	653 ± 12
			1.1	763 ± 15
			1.6	786 ± 20
			3.2	827 ± 28
			5.0	955 ± 26
			6.5	1126 ± 31
			8.9	1380 ± 51
353	50	5.7	0	488 ± 13
			1.3	621 ± 16
			3.3	744 ± 20
			4.3	786 ± 20
			5.2	779 ± 27
			6.7	908 ± 30

Table A.2. Experimental data obtained for experiments to investigate the kinetics of CH_2OO and NO_2 between 25 and 200 Torr and 242 and 353 K

Appendix 7. MESMER Input for the Reaction between CH_2OO and NO_2

```
?xml version="1.0" encoding="utf-8" ?>
<?xml-stylesheet type='text/xsl' href='../../mesmer2.xsl' media='other'?>
<?xml-stylesheet type='text/xsl' href='../../mesmer1.xsl' media='screen'?>
<me:mesmer xmlns="http://www.xml-cml.org/schema" xmlns:me="http://www.chem.leeds.ac.uk/mesmer"
xmlns:xsi="http://www.w3.org/2001/XMLSchema-instance" xmlns:cml="http://www.xml-cml.org/schema">
<me:title>CH2OO + NO2</me:title>
<moleculeList>
 <molecule id="CH2OO">
   <propertyList>
   <property title="Energy" dictRef="me:ZPE">
   <scalar units="kJ/mol">0</scalar>
   </property>
   <property title="Vibrational Frequencies" dictRef="me:vibFreqs">
    <array units="cm-1"> 537.7503 697.5723 1022.3957 1261.0787 1630.8711 3141.7356</array>
   </property>
   <property title="Rotational Constants" dictRef="me:rotConsts">
    <array units="GHz"> 81.19793 12.6778 10.96568 </array>
   </property>
  <property dictRef="me:frequenciesScaleFactor">
   <scalar>1</scalar>
  </property>
  <property dictRef="me:symmetryNumber">
   <scalar>1</scalar>
  </property>
  <property dictRef="me:MW">
   <scalar units="amu">46</scalar>
  </property>
  <property dictRef="me:spinMultiplicity">
   <scalar>1</scalar>
  </property>
  <property dictRef="me:symmetryNumber">
   <scalar>2</scalar>
  </property>
```

```
</propertyList>
<bondRef>b1</bondRef>
<me:HinderedRotorPotential format="analytical" units="kJ/mol">
<me:PotentialPoint index="0" coefficient="0.1"/>
<me:PotentialPoint index="2" coefficient="0.1"/>
</me:HinderedRotorPotential>
<me:DOSCMethod name="ClassicalRotors"/>
<me:energyTransferModel xsi:type="me:ExponentialDown">
<me:deltaEDown units="cm-1">250</me:deltaEDown>
</me:energyTransferModel>
</molecule>
   <molecule id="NO2">
  <propertyList>
  <property title="Energy" dictRef="me:ZPE">
  <scalar units="kJ/mol">0</scalar>
  </property>
  <property title="Vibrational Frequencies" dictRef="me:vibFreqs">
   <array units="cm-1"> 783.454 1465.3073 1775.7005</array>
  </property>
  <property title="Rotational Constants" dictRef="me:rotConsts">
   <array units="GHz">254.03982 13.29059 12.62984</array>
  </property>
 <property dictRef="me:frequenciesScaleFactor">
  <scalar>1</scalar>
 </property>
 <property dictRef="me:symmetryNumber">
  <scalar>2</scalar>
 </property>
 <property dictRef="me:MW">
  <scalar units="amu">46</scalar>
 </property>
 <property dictRef="me:spinMultiplicity">
  <scalar>2</scalar>
 </property>
</propertyList>
```

```
<me:DOSCMethod name="ClassicalRotors"/>
<me:energyTransferModel xsi:type="me:ExponentialDown">
<me:deltaEDown units="cm-1">250</me:deltaEDown>
</me:energyTransferModel>
 </molecule>
  <molecule id="prc">
  <propertyList>
  <property title="Energy" dictRef="me:ZPE">
  <scalar units="kJ/mol">-14</scalar>
  </property>
  <property title="Vibrational Frequencies" dictRef="me:vibFreqs">
          <array units="cm-1">36.5724 107.5697 110.1268 162.9850 194.5654 210.5406 540.5284 699.1192 781.9472 920.7260 1053.4548 1261.2692 1439.7321 1450.9565
1642.9652 1768.4335 3142.5373 3290.3128</array>
  </property>
  <property title="Rotational Constants" dictRef="me:rotConsts">
   <array units="GHz">7.45177 2.19286 1.79541</array>
  </property>
 <property dictRef="me:frequenciesScaleFactor">
  <scalar>1</scalar>
 </property>
 <property dictRef="me:symmetryNumber">
  <scalar>2</scalar>
 </property>
 <property dictRef="me:MW">
  <scalar units="amu">92</scalar>
 </property>
 <property dictRef="me:spinMultiplicity">
  <scalar>2</scalar>
 </property>
</propertyList>
<me:DOSCMethod name="ClassicalRotors"/>
<me:energyTransferModel xsi:type="me:ExponentialDown">
<me:deltaEDown units="cm-1">250</me:deltaEDown>
</me:energyTransferModel>
 </molecule>
```

<molecule xmlns="http://www.xml-cml.org/schema" spinMultiplicity="2" id="TS1">
<atomArray>
<atom id="a1" elementType="C" hydrogenCount="2" x3="-1.003917" y3="1.152438" z3="-0.189718"/>
<atom id="a2" elementType="N" hydrogenCount="0" x3="1.242808" y3="-0.023190" z3="-0.079844"/>
<atom id="a3" elementType="O" hydrogenCount="0" x3="-1.615194 " y3="0.058976" z3="-0.391825"/>
<atom id="a4" elementType="H" hydrogenCount="0" x3="-0.733346" y3="1.418446" z3="0.827089"/>
<atom id="a5" elementType="H" hydrogenCount="0" x3="-0.892113" y3="1.787891" z3="-1.059485"/>
<atom id="a6" elementType="O" hydrogenCount="0" x3="2.125785" y3="0.598784" z3="0.428986"/>
<atom id="a7" elementType="O" hydrogenCount="0" x3="1.127361" y3="-1.146678" z3="-0.442632"/>
<atom id="a8" elementType="O" hydrogenCount="0" x3="-1.769288" y3="-0.755912" z3="0.646671"/>
</atomArray>
<bondArray>
<bond atomRefs2="a5 a1" order="1"/>
<bond atomRefs2="a7 a2" order="1"/>
<bond atomRefs2="a3 a1" order="1" id="b2"/>
<bond atomRefs2="a3 a8" order="1"/>
<bond atomRefs2="a1 a4" order="1"/>
<bond atomRefs2="a2 a6" order="2"/>
<bond atomRefs2="a1 a2" order="1" id="b1"/>
</bondArray>
<propertyList>
<property dictRef="me:ZPE">
<scalar units="kJ/mol">-1</scalar>
</property>
<property dictRef="me:spinMultiplicity">
<scalar units="cm-1">2</scalar>
</property>
<property dictRef="me:hessian">
<matrix matrixType="squareSymmetricLT" rows="24" units="Hartree/Bohr2">0.15381251 0.21562422 0.61189263 0.05319560 -0.07616602 0.73371541 0.04238448
0.01528405 0.01818776 0.51820900 -0.03855624 -0.01838975 -0.01167084 0.22025323 0.82974498 0.00240617 0.00118233 -0.00470393 0.26654700 0.33312803
0.22556779 -0.08462447 -0.14382306 -0.04588697 -0.03438209 0.02600126 -0.00150979 0.15071756 -0.08228321 -0.28765038 -0.04849821 -0.03845621 0.04307148
0.00054316 0.16891633 0.41466328 -0.05749329 -0.07664634 -0.15516902 -0.00738563 -0.00400902 -0.00224592 0.05154372 -0.04511899 0.38744641 -0.04792106 -
0.01637439 -0.05855182 -0.00552243 0.00675368 0.00369509 0.00309886 -0.02912857 -0.02331122 0.04958694 -0.02744105 -0.07098306 -0.04775631 0.00491096 -
0.00366241 -0.00151234 -0.01677909 -0.00395199 -0.02967260 0.03080040 0.06582182 -0.06648500 -0.05541819 -0.33185310 -0.00091386 0.00023480 0.00073267 -

0.00964460 -0.00968773 -0.00057514 0.07728046 0.06748773 0.33823662 -0.03248895 -0.02351019 0.01736121 -0.00089379 0.00229957 -0.00125032 -0.01180781 -
0.01900625 0.02085896 0.00522730 0.00379304 -0.00418339 0.03266137 -0.03050764 -0.14774954 0.13639283 0.00003869 0.00004651 0.00052787 -0.00535095 -
0.02949153 0.02795390 0.00046921 0.00915339 -0.00639787 0.03966780 0.16572648 0.02105537 0.14592870 -0.26375159 0.00045365 -0.00140539 0.00062495
0.00343685 -0.00169681 0.01054542 0.00391475 0.01314566 -0.00524399 -0.02659280 -0.15392516 0.25344993 -0.01071746 -0.00590222 -0.00712006 -0.44060181 -
0.18742073 -0.23106705 0.00398965 0.00935635 0.00233797 0.00032867 -0.00055222 0.00047556 -0.00021681 0.00043321 0.00008956 0.44373364 0.00756744
0.00445099 0.00121590 -0.19433642 -0.19132726 -0.13403607 -0.00509915 -0.00933328 0.00241055 -0.00129497 0.00055297 0.00026834 -0.00065530 -0.00000762
0.00031342 0.27285079 0.27270427 0.00048117 -0.00054084 0.00028237 -0.23565928 -0.13041227 -0.14160159 -0.00136029 -0.00168300 0.00142526 -0.00109175
0.00038981 -0.00012480 0.00005576 0.00014757 -0.00003300 0.26065639 0.19168240 0.16656399 -0.00654699 -0.00150895 -0.00186148 -0.08538346 -0.02553564 -
0.03886937 0.00371822 0.00767685 0.00017379 0.00000769 -0.00019599 0.00007175 0.00004550 0.00006179 0.00012963 0.00505978 -0.07968902 -0.02275193
0.08427215 0.01425925 0.00353956 0.00315676 -0.01693593 -0.64324305 -0.19716993 -0.01091980 -0.01760997 0.00475047 -0.00092808 0.00025781 -0.00021240 -
0.00032159 -0.00063446 0.00026928 -0.08727189 -0.08120220 -0.06106087 0.10088066 0.73066783 -0.00060020 -0.00062141 0.00176126 -0.03221923 -0.20082689 -
0.07978250 -0.00034909 -0.00022408 0.00109803 -0.00043229 0.00000319 -0.00027395 0.00010808 -0.00021019 -0.00028021 -0.02797783 -0.05808858 -0.02593340
0.06106959 0.25882757 0.10487495 -0.01389806 -0.03978945 0.02467576 0.00619010 -0.00379513 0.00004828 -0.03070992 -0.01707529 0.01327570 -0.00480597
0.00546395 0.00339906 0.00747318 -0.00481210 -0.00248700 -0.00157566 0.00065663 -0.00033006 -0.00117290 0.00123737 0.00040096 0.03849924 -0.05866278 -
0.09511044 0.04332590 0.00924163 -0.01624050 -0.00266305 -0.01294554 -0.10969760 0.12033204 0.00970271 0.00281146 0.00372531 -0.00226707 0.00295677 -
0.00262969 -0.00149328 0.00416212 0.00147720 -0.00168969 0.00822448 0.00114039 0.05811403 0.20289372 0.04744019 0.06228177 0.01971860 -0.00901040
0.01496159 0.00140854 0.00377016 0.10636567 -0.24252505 -0.00150322 -0.00208515 -0.00089831 -0.00635749 -0.00448895 0.00468848 0.00260545 -0.00376596 -
0.00057884 0.00203802 -0.00856087 -0.00146417 -0.03898270 -0.16470810 0.21965075</matrix>
    </property>
        <property dictRef="me:frequenciesScaleFactor">
  <scalar>1</scalar>
 </property>
 <property dictRef="me:symmetryNumber">
  <scalar>0.5</scalar>
 </property>
   </propertyList>
   <me:ExtraDOSCMethod xsi:type="me:HinderedRotorQM1D">
   <bondRef>b1</bondRef>
   <me:HinderedRotorPotential format="numerical" units="kJ/mol" expansionSize="5" UseSineTerms="yes">
   <me:PotentialPoint angle="248.5855594211199" potential="0.0"/>
   <me:PotentialPoint angle="258.5855571532413" potential="-0.3074250037316233"/>
   <me:PotentialPoint angle="268.5855366907492" potential="2.081837428268045"/>
   <me:PotentialPoint angle="278.58563041603844" potential="1.8680377416312695"/>
   <me:PotentialPoint angle="288.5855738053534" potential="3.6515816543251276"/>
   <me:PotentialPoint angle="298.5856162644453" potential="3.444172433926724"/>

<me:PotentialPoint angle="308.58561515315205" potential="4.380081664770842"/>
<me:PotentialPoint angle="318.5855834188542" potential="4.663218171102926"/>
<me:PotentialPoint angle="328.58560609450524" potential="5.236824204795994"/>
<me:PotentialPoint angle="338.5855585295781" potential="5.474274391890503 5"/>
<me:PotentialPoint angle="348.58557104072804" potential="5.801955125527456"/>
<me:PotentialPoint angle="358.58563776103233" potential="5.5344298399286345"/>
<me:PotentialPoint angle="8.585606428559894" potential="5.627831989550032"/>
<me:PotentialPoint angle="18.585599933685764" potential="4.944432812277228"/>
<me:PotentialPoint angle="28.585575406094982" potential="4.447213064879179"/>
<me:PotentialPoint angle="38.58556385112812" potential="3.8234967452008277"/>
<me:PotentialPoint angle="48.58553145446165" potential="3.712582513107918"/>
<me:PotentialPoint angle="58.585634436852324" potential="3.3098938803886995"/>
<me:PotentialPoint angle="68.58558967985303" potential="3.310051410458982"/>
<me:PotentialPoint angle="78.58561773016976" potential="3.6096813055919483"/>
<me:PotentialPoint angle="88.58558223533208" potential="3.9024166389135644"/>
<me:PotentialPoint angle="98.58554224513662" potential="4.279858466936275"/>
<me:PotentialPoint angle="108.58559187554616" potential="4.91619556338992"/>
<me:PotentialPoint angle="118.585598283927" potential="5.08559542556759"/>
<me:PotentialPoint angle="128.58554183367966" potential="5.769020857987925"/>
<me:PotentialPoint angle="138.58555333191993" potential="5.865111519233324"/>
<me:PotentialPoint angle="148.5855703441631" potential="6.274521430837922"/>
<me:PotentialPoint angle="158.5856310233686" potential="6.29852374875918"/>
<me:PotentialPoint angle="168.58553053554928" potential="6.362000453518704"/>
<me:PotentialPoint angle="178.58552938839125" potential="5.965904450509697"/>
<me:PotentialPoint angle="188.58560256439029" potential="5.713139723753557"/>
<me:PotentialPoint angle="198.5855153228107" potential="5.039615050307475"/>
<me:PotentialPoint angle="208.5855422933186" potential="4.33666902827099"/>
<me:PotentialPoint angle="218.58559376284984" potential="3.6047926254104823"/>
<me:PotentialPoint angle="228.58556474491886" potential="3.322918983991258"/>
<me:PotentialPoint angle="238.58557168711116" potential="2.9312364461366087"/>
        <me:PotentialPoint angle="248.5855594211199" potential="0.0"/>
</me:HinderedRotorPotential>
   <me:CalculateInternalRotorInertia phaseDifference="0"/>
        </me:ExtraDOSCMethod>
<me:ExtraDOSCMethod xsi:type="me:HinderedRotorQM1D">

<bondRef>b2</bondRef>
<me:HinderedRotorPotential format="numerical" units="kJ/mol" expansionSize="5" UseSineTerms="yes">
<me:PotentialPoint angle="180.06190490758095" potential="0.0"/>
<me:PotentialPoint angle="190.044722276271" potential="2.4982994323363528"/>
<me:PotentialPoint angle="200.03827004334136" potential="11.179897310910746"/>
<me:PotentialPoint angle="210.02945230627256" potential="22.671107990317978"/>
<me:PotentialPoint angle="220.02414503525938" potential="37.70558271103073"/>
<me:PotentialPoint angle="230.01938296330889" potential="52.8639652619604"/>
<me:PotentialPoint angle="240.00247485399134" potential="68.09128555678762"/>
<me:PotentialPoint angle="249.99257320982653" potential="84.17656137258746"/>
<me:PotentialPoint angle="259.9836705487136" potential="94.92069663188886"/>
<me:PotentialPoint angle="269.93984102914084" potential="101.33588970825076"/>
<me:PotentialPoint angle="279.9066356208051" potential="140.44818624504842"/>
<me:PotentialPoint angle="289.9186883899843" potential="100.82336592371576"/>
<me:PotentialPoint angle="299.7837979915119" potential="92.451892062556"/>
<me:PotentialPoint angle="309.8606198437122" potential="84.16671574895736"/>
<me:PotentialPoint angle="319.9562614691991" potential="69.41514123964589"/>
<me:PotentialPoint angle="329.9944425696477" potential="51.95761915715411"/>
<me:PotentialPoint angle="340.0163431077207" potential="32.19037940504495"/>
<me:PotentialPoint angle="350.11842151706276" potential="14.388134471024387"/>
<me:PotentialPoint angle="359.98489061611974" potential="5.89952131791506"/>
<me:PotentialPoint angle="10.017465177183205" potential="5.636112815584056"/>
<me:PotentialPoint angle="19.909713382055045" potential="9.558105179923587"/>
<me:PotentialPoint angle="29.873802371287187" potential="19.387088408577256"/>
<me:PotentialPoint angle="39.76610806530279" potential="29.341969595989212"/>
<me:PotentialPoint angle="49.76770879694637" potential="46.630183708737604"/>
<me:PotentialPoint angle="59.651033141073626" potential="58.11923885287251"/>
<me:PotentialPoint angle="69.73623792863934" potential="83.51781826233491"/>
<me:PotentialPoint angle="79.59574587801504" potential="94.34493243740872"/>
<me:PotentialPoint angle="89.76456298471722" potential="124.74152848136146"/>
<me:PotentialPoint angle="99.73325052948476" potential="136.08461372193415"/>
<me:PotentialPoint angle="109.90128118337367" potential="164.91038645943627"/>
<me:PotentialPoint angle="119.82913861897711" potential="203.10235610604286"/>
<me:PotentialPoint angle="129.97234960883713" potential="145.3130007807631"/>
<me:PotentialPoint angle="139.83909835872578" potential="90.39699751138687"/>

```
    <me:PotentialPoint angle="150.06942348741296" potential="55.944970709620975"/>
    <me:PotentialPoint angle="160.0054974525835" potential="28.663075775722973"/>
    <me:PotentialPoint angle="170.05741769494665" potential="16.4671573638916"/>
            <me:PotentialPoint angle="180.06190490758095" potential="0.0"/>
    </me:HinderedRotorPotential>
       <me:CalculateInternalRotorInertia phaseDifference="0"/>
            </me:ExtraDOSCMethod>
</molecule>
      <molecule id="OOCH2NO2">
   <propertyList>
   <property title="Energy" dictRef="me:ZPE">
   <scalar units="kJ/mol">-126</scalar>
   </property>
   <property title="Vibrational Frequencies" dictRef="me:vibFreqs">
    <array units="cm-1">36.5724 107.5697 110.1268 162.985 194.5654 210.5406 540.5284 699.1192 781.9472 920.726 1053.4548 1261.2692 1439.7321 1450.9565
1642.9652 1768.4335 3142.5373 3290.3128</array>
   </property>
   <property title="Rotational Constants" dictRef="me:rotConsts">
    <array units="GHz">7.45177 2.19286 1.79541</array>
   </property>
   <property title="Symmetry Number" dictRef="me:symmetryNumber">
    <scalar>1 </scalar>
   </property>
   <property dictRef="me:MW">
         <scalar units="amu">92</scalar>
       </property>
  </propertyList>
 <me:energyTransferModel xsi:type="me:ExponentialDown">
 <me:deltaEDown units="cm-1">250</me:deltaEDown>
 </me:energyTransferModel>
   <me:DOSCMethod>ClassicalRotors</me:DOSCMethod>
  </molecule>
<molecule xmlns="http://www.xml-cml.org/schema" spinMultiplicity="2" id="TS2">
    <atomArray>
    <atom id="a1" elementType="O" hydrogenCount="0" x3="-1.613939" y3="-0.989516" z3="0.079091"/>
```

<atom id="a2" elementType="N" hydrogenCount="0" x3="-1.720811 " y3="0.103536" z3="-0.386590"/>
<atom id="a3" elementType="O" hydrogenCount="0" x3="-0.996380" y3="1.056539" z3="-0.201391"/>
<atom id="a4" elementType="C" hydrogenCount="2" x3="0.780755" y3="0.336925" z3="0.978924"/>
<atom id="a5" elementType="O" hydrogenCount="0" x3="1.296591" y3="-0.522811" z3="0.178315"/>
<atom id="a6" elementType="O" hydrogenCount="0" x3="2.068039" y3="-0.046472" z3="-0.790128"/>
<atom id="a7" elementType="H" hydrogenCount="0" x3="1.118099" y3="1.364405" z3="0.914316"/>
<atom id="a8" elementType="H" hydrogenCount="0" x3="0.208562" y3="-0.092621" z3="1.791174"/>
</atomArray>
<bondArray>
<bond atomRefs2="a6 a5" order="1"/>
<bond atomRefs2="a2 a3" order="1" id="b2"/>
<bond atomRefs2="a2 a1" order="2"/>
<bond atomRefs2="a5 a4" order="1" id="b3"/>
<bond atomRefs2="a7 a4" order="1"/>
<bond atomRefs2="a4 a8" order="1"/>
<bond atomRefs2="a4 a3" order="1" id="b1"/>
</bondArray>
<propertyList>
<property dictRef="me:ZPE">
<scalar units="kJ/mol">22</scalar>
</property>
<property dictRef="me:spinMultiplicity">
<scalar units="cm-1">2</scalar>
</property>
<property dictRef="me:symmetryNumber">
<scalar>0.5</scalar>
</property>
<property dictRef="me:hessian">
<matrix matrixType="squareSymmetricLT" rows="24" units="Hartree/Bohr2">
0.04661739 -0.00640040 0.69936346 0.02888721 -0.29273861 0.15289532 -0.04329753 0.05840762 -0.04614379 0.26617225 0.07287077 -0.54403608 0.27351344
0.16094486 0.89500642 -0.05189992 0.26633569 -0.16541329 0.11478925 -0.24219284 0.21518452 -0.02025449 -0.05407480 0.00260790 -0.16547078 -0.21963257 -
0.02421781 0.15134499 -0.06150167 -0.15431269 0.02419714 -0.23032263 -0.36196975 -0.03049127 0.28516398 0.53311487 0.00697709 0.02659389 0.00685635 -
0.02366126 -0.02155464 -0.03180880 -0.00982879 0.00050099 0.01545154 0.03569090 0.00314843 0.02353188 -0.09380013 -0.02025098 -0.05590109 0.08193907
0.00228174 0.05137118 0.26782433 -0.02664841 0.00034085 -0.02149493 0.06455838 0.01988008 0.03724746 -0.07217499 -0.01943061 -0.03727332 0.15350571
0.66256357 0.00654736 0.00100974 -0.00389620 -0.02211408 -0.00863693 -0.00105752 0.02007345 0.00223700 0.00055608 -0.30578811 0.02816839 0.53021205 -

0.02171262 0.00343584 -0.01192214 0.04525320 0.00228277 0.02367444 -0.04543679 0.00446262 -0.01942236 -0.05823906 0.03563000 0.08940204 0.20884146
0.02048704 -0.00029763 0.01542552 -0.05044515 -0.00926219 -0.03007145 0.05824932 -0.00003012 0.03209267 0.01162276 -0.26789159 -0.13135589 0.01034213
0.40382765 0.02264363 -0.00413324 0.01851837 -0.05329721 -0.00316718 -0.03350648 0.04378118 0.00648780 0.02546626 0.03925599 -0.08837622 -0.17130053 -
0.21338659 0.03673970 0.34856193 0.00756094 -0.00329934 0.00636627 -0.01603842 0.00157449 -0.01093139 0.01311509 0.00033673 0.00638101 -0.04844662
0.02742698 0.05772413 -0.12005930 -0.07691419 0.12633197 0.15623656 0.00077570 0.00003191 0.00025572 -0.00223665 -0.00055985 -0.00016077 -0.00114539
0.00175890 -0.00235856 0.01919353 0.03164231 -0.02030210 -0.07446996 -0.10784276 0.08935592 0.05382633 0.07400868 -0.01161680 0.00399354 -0.00890715
0.02624880 -0.00103162 0.01568881 -0.01964135 -0.00233959 -0.00865578 0.07446989 -0.03236651 -0.07188173 0.12228646 0.09025490 -0.18075960 -0.18349240 -
0.06354952 0.25134101 -0.00177082 0.00117880 -0.00138267 0.00280469 -0.00016098 0.00146928 -0.00995243 -0.00240926 -0.00464136 -0.07220248 -0.10962017
0.02273978 0.01290544 0.02292201 0.01423505 -0.00203962 0.00101805 -0.00767324 0.06852395 0.00012687 0.00008798 0.00008987 0.00043932 -0.00006337
0.00047099 0.00229795 0.00146328 0.00081654 -0.09542666 -0.31877509 0.03025900 -0.00137081 -0.03042725 -0.00927962 -0.00327037 0.00294567 0.00680991
0.09623124 0.34297490 -0.00138056 0.00009822 -0.00031867 0.00383959 0.00195029 0.00112474 -0.01061059 -0.00244657 -0.00467553 0.03473206 0.03231629 -
0.05915232 -0.00121965 -0.02132878 0.01246356 -0.00485292 0.00074331 -0.00108019 -0.02377745 -0.02715234 0.04599880 -0.00283376 -0.00239615 -0.00194465
0.00437671 0.00237164 0.00301724 -0.00528466 0.00198849 -0.00717551 -0.11276601 -0.07267750 0.13141542 -0.02155232 0.00373609 0.02043597 0.00967137
0.00303840 -0.00058137 0.00173127 0.00097246 0.00326952 0.12665741 0.00029012 -0.00117780 0.00075185 -0.00134574 0.00100474 -0.00113781 0.00131650 -
0.00059388 0.00118243 -0.07407453 -0.10832953 0.09862081 0.01968740 0.01192388 -0.02762718 0.00031936 -0.00198486 -0.00177110 -0.00915968 0.00179387
0.01581958 0.06296657 0.09736357 -0.00015800 -0.00115923 0.00026527 0.00033869 0.00111948 -0.00021199 -0.00216399 0.00185449 -0.00319011 0.13832819
0.08177885 -0.22347984 0.01058779 0.00824334 -0.01944350 0.00247332 -0.00398400 0.00425463 -0.00096939 -0.00201435 0.00563960 -0.14843661 -0.08583858
0.23616595
        </matrix>
   </property>
        <property dictRef="me:frequenciesScaleFactor">
  <scalar>1</scalar>
 </property>
   </propertyList>
   <me:ExtraDOSCMethod xsi:type="me:HinderedRotorQM1D">
   <bondRef>b1</bondRef>
   <me:HinderedRotorPotential format="numerical" units="kJ/mol" expansionSize="10" UseSineTerms="yes">
   <me:PotentialPoint angle="61.649766455425265" potential="0.0"/>
   <me:PotentialPoint angle="71.6497707355341" potential="-1.5225771251134574"/>
   <me:PotentialPoint angle="81.64981698124777" potential="2.461686839815229"/>
   <me:PotentialPoint angle="91.64982834465461" potential="1.9290307241026312"/>
   <me:PotentialPoint angle="101.6498698023692" potential="4.822058274177834"/>
   <me:PotentialPoint angle="111.64979727250011" potential="4.222958638914861"/>
   <me:PotentialPoint angle="121.64981409364079" potential="6.258631907403469"/>
   <me:PotentialPoint angle="131.64983239527146" potential="5.435133443796076"/>

<me:PotentialPoint angle="141.6497842969692" potential="7.060462122433819"/>
<me:PotentialPoint angle="151.64977578474034" potential="6.231946329004131"/>
<me:PotentialPoint angle="161.64985364344676" potential="7.669643676257692"/>
<me:PotentialPoint angle="171.64981579668685" potential="6.830809669103473"/>
<me:PotentialPoint angle="181.6498198240206" potential="7.891532527166419"/>
<me:PotentialPoint angle="191.64977760844127" potential="6.8944596567889675"/>
<me:PotentialPoint angle="201.64972534807634" potential="7.551015726057813"/>
<me:PotentialPoint angle="211.64977285991506" potential="6.5665216244524345"/>
<me:PotentialPoint angle="221.6497953057978" potential="6.907553023775108"/>
<me:PotentialPoint angle="231.6498348029502" potential="5.482174520730041"/>
<me:PotentialPoint angle="241.6497605517806" potential="5.985805738018826"/>
<me:PotentialPoint angle="251.6497928386061" potential="5.0816466744290665"/>
<me:PotentialPoint angle="261.6497889511581" potential="6.2623968737898394"/>
<me:PotentialPoint angle="271.64981946416157" potential="6.511575168231502"/>
<me:PotentialPoint angle="281.64985655251365" potential="9.631514150067233"/>
<me:PotentialPoint angle="291.64977712033397" potential="12.151586850523017"/>
<me:PotentialPoint angle="301.64982001090914" potential="18.556656000437215"/>
<me:PotentialPoint angle="311.6497697104546" potential="22.09848914446775"/>
<me:PotentialPoint angle="321.6498452735534" potential="27.274328243685886"/>
<me:PotentialPoint angle="331.6497865731461" potential="24.808942075120285"/>
<me:PotentialPoint angle="341.64979271678453" potential="23.57524342427496"/>
<me:PotentialPoint angle="351.6497759283049" potential="17.33919869014062"/>
<me:PotentialPoint angle="1.6498750614656263" potential="14.450203907908872"/>
<me:PotentialPoint angle="11.649726334443015" potential="10.30183571355883"/>
<me:PotentialPoint angle="21.64981925854016" potential="9.27679339563474"/>
<me:PotentialPoint angle="31.64985430340482" potential="7.317579927737825"/>
<me:PotentialPoint angle="41.64979827459801" potential="7.082621339592151"/>
<me:PotentialPoint angle="51.6498432309229" potential="6.2676531239412725"/>
<me:PotentialPoint angle="61.649766455425265" potential="0.0"/>
</me:HinderedRotorPotential>
<me:CalculateInternalRotorInertia phaseDifference="0"/>
</me:ExtraDOSCMethod>
<me:ExtraDOSCMethod xsi:type="me:HinderedRotorQM1D">
<bondRef>b2</bondRef>
<me:HinderedRotorPotential format="numerical" units="kJ/mol" expansionSize="10" UseSineTerms="yes">

<me:PotentialPoint angle="6.63406438354096" potential="0.0"/>
<me:PotentialPoint angle="16.63915864335284" potential="-1.0431818949291483"/>
<me:PotentialPoint angle="26.647779690473328" potential="4.6127665704116225"/>
<me:PotentialPoint angle="36.651223368819124" potential="7.0494455262087286"/>
<me:PotentialPoint angle="46.648055570040924" potential="13.895926802651957"/>
<me:PotentialPoint angle="56.64713306107582" potential="17.24709616310429"/>
<me:PotentialPoint angle="66.6413765649965" potential="23.537307580118068"/>
<me:PotentialPoint angle="76.63800559297037" potential="25.075356774381362"/>
<me:PotentialPoint angle="86.62719768838669" potential="29.463855791138485"/>
<me:PotentialPoint angle="96.62130497491349" potential="29.69955214462243"/>
<me:PotentialPoint angle="106.61387783671614" potential="32.44572762318421"/>
<me:PotentialPoint angle="116.61509190647261" potential="31.516067081829533"/>
<me:PotentialPoint angle="126.61707337868596" potential="32.38918748870492"/>
<me:PotentialPoint angle="136.61913696912336" potential="30.93268106202595"/>
<me:PotentialPoint angle="146.62695422650555" potential="30.918534869910218"/>
<me:PotentialPoint angle="156.6289701290035" potential="29.31992064998485"/>
<me:PotentialPoint angle="166.63101065538245" potential="29.18253613030538"/>
<me:PotentialPoint angle="176.63331784293433" potential="28.02628971892409"/>
<me:PotentialPoint angle="186.6335693844957" potential="28.260106214671396"/>
<me:PotentialPoint angle="196.63315420633253" potential="27.777127177803777"/>
<me:PotentialPoint angle="206.63370184198402" potential="28.666024211794138"/>
<me:PotentialPoint angle="216.63438526689652" potential="28.93558163428679"/>
<me:PotentialPoint angle="226.63757766086908" potential="29.975767834112048"/>
<me:PotentialPoint angle="236.65386617221534" potential="29.844708143384196"/>
<me:PotentialPoint angle="246.65174551279995" potential="30.689050448709168"/>
<me:PotentialPoint angle="256.64424094109125" potential="29.57719598489348"/>
<me:PotentialPoint angle="266.6468642664007" potential="29.49859902798198"/>
<me:PotentialPoint angle="276.6378585031653" potential="27.434662255691364"/>
<me:PotentialPoint angle="286.6387133843822" potential="26.646012048819102"/>
<me:PotentialPoint angle="296.63066928756757" potential="23.79759436310269"/>
<me:PotentialPoint angle="306.6346430595059" potential="21.828125693951733"/>
<me:PotentialPoint angle="316.6311143787251" potential="18.088836598210037"/>
<me:PotentialPoint angle="326.63491466478735" potential="15.41187191568315"/>
<me:PotentialPoint angle="336.6332128842909" potential="11.595647804089822"/>
<me:PotentialPoint angle="346.6344203982221" potential="9.13276898744516"/>

```
<me:PotentialPoint angle="356.63348582669806" potential="6.622436890611425"/>
        <me:PotentialPoint angle="6.63406438354096" potential="0.0"/>
</me:HinderedRotorPotential>
   <me:CalculateInternalRotorInertia phaseDifference="0"/>
        </me:ExtraDOSCMethod>
<me:ExtraDOSCMethod xsi:type="me:HinderedRotorQM1D">
<bondRef>b3</bondRef>
<me:HinderedRotorPotential format="numerical" units="kJ/mol" expansionSize="10" UseSineTerms="yes">
<me:PotentialPoint angle="350.38144916049134" potential="0.0"/>
<me:PotentialPoint angle="0.48638838561308434" potential="0.2631407013395801"/>
<me:PotentialPoint angle="10.59312102516287" potential="9.902284553041682"/>
<me:PotentialPoint angle="20.662910184438896" potential="17.77590592193883"/>
<me:PotentialPoint angle="30.62156428212205" potential="33.67800062755123"/>
<me:PotentialPoint angle="40.71952448118727" potential="46.61297093308531"/>
<me:PotentialPoint angle="50.651433024580605" potential="64.51283456920646"/>
<me:PotentialPoint angle="60.74469442875526" potential="78.04294263059273"/>
<me:PotentialPoint angle="70.7100821489505" potential="90.79811872076243"/>
<me:PotentialPoint angle="80.5058010920952" potential="98.1927124292124"/>
<me:PotentialPoint angle="91.17771763534085" potential="93.94599564396776"/>
<me:PotentialPoint angle="100.62865340092534" potential="94.88420218683314"/>
<me:PotentialPoint angle="110.54800223093844" potential="84.44689069199376"/>
<me:PotentialPoint angle="120.39377880464025" potential="67.23360571346711"/>
<me:PotentialPoint angle="130.38993579860747" potential="51.576548888580874"/>
<me:PotentialPoint angle="140.42066147780946" potential="38.292153461952694"/>
<me:PotentialPoint angle="150.43375821392527" potential="27.163112079142593"/>
<me:PotentialPoint angle="160.45793613168723" potential="19.955926534719765"/>
<me:PotentialPoint angle="170.45941752001337" potential="13.74368195515126"/>
<me:PotentialPoint angle="180.44028300619527" potential="13.435899883275852"/>
<me:PotentialPoint angle="190.457196396965" potential="13.566074780886993"/>
<me:PotentialPoint angle="200.42313154596295" potential="21.286303958506323"/>
<me:PotentialPoint angle="210.47742847255276" potential="30.91149065445643"/>
<me:PotentialPoint angle="220.4087365534245" potential="48.50401067745406"/>
<me:PotentialPoint angle="230.46870073485064" potential="68.65872954274528"/>
<me:PotentialPoint angle="240.42065703642862" potential="90.4376218674006"/>
<me:PotentialPoint angle="250.44291747230412" potential="111.25706735660788"/>
```

```
    <me:PotentialPoint angle="260.44877245861153" potential="124.62050607532728"/>
    <me:PotentialPoint angle="270.9246548232789" potential="127.43577157706022"/>
    <me:PotentialPoint angle="280.6970084126812" potential="113.79398788860999"/>
    <me:PotentialPoint angle="290.68790008252427" potential="90.45137423428241"/>
    <me:PotentialPoint angle="300.52552283566996" potential="70.39567083667498"/>
    <me:PotentialPoint angle="310.50083944757324" potential="50.6281685346039"/>
    <me:PotentialPoint angle="320.4399471796961" potential="36.082540842471644"/>
    <me:PotentialPoint angle="330.5009704301126" potential="25.715217291377485"/>
    <me:PotentialPoint angle="340.7609824740177" potential="17.815894906641915"/>
            <me:PotentialPoint angle="350.38144916049134" potential="0.0"/>
    </me:HinderedRotorPotential>
       <me:CalculateInternalRotorInertia phaseDifference="0"/>
            </me:ExtraDOSCMethod>
</molecule>
      <molecule id="OOCH2ONO">
   <propertyList>
   <property title="Energy" dictRef="me:ZPE">
   <scalar units="kJ/mol">-156</scalar>
   </property>
   <property title="Vibrational Frequencies" dictRef="me:vibFreqs">
    <array units="cm-1">36.5724 107.5697 110.1268 162.985 194.5654 210.5406 540.5284 699.1192 781.9472 920.726 1053.4548 1261.2692 1439.7321 1450.9565
1642.9652 1768.4335 3142.5373 3290.3128</array>
   </property>
   <property title="Rotational Constants" dictRef="me:rotConsts">
    <array units="GHz">7.45177 2.19286 1.79541</array>
   </property>
   <property title="Symmetry Number" dictRef="me:symmetryNumber">
    <scalar>1 </scalar>
   </property>
   <property dictRef="me:MW">
         <scalar units="amu">92</scalar>
       </property>
  </propertyList>
 <me:energyTransferModel xsi:type="me:ExponentialDown">
 <me:deltaEDown units="cm-1">250</me:deltaEDown>
```

```
 </me:energyTransferModel>
   <me:DOSCMethod>ClassicalRotors</me:DOSCMethod>
 </molecule>
 <molecule id="TS6">
<propertyList>
 <property dictRef="me:ZPE">
  <scalar units="kJ/mol">-86</scalar>
 </property>
 <property dictRef="me:rotConsts">
  <array units="GHz"> 5.5119500 3.3180200 2.2246400 </array>
 </property>
 <property dictRef="me:vibFreqs">
  <array units="cm-1"> 128.2076 164.4839 177.3422 301.3451 345.3390 419.2101 499.9614 541.4747 836.4649 1127.2150 1238.2106 1342.1804 1465.5587 1623.9678
2022.4283 3019.7531 3111.5250 </array>
 </property>
 <property title="ImaginaryFrequency" dictRef="me:imFreqs">
  <array units="cm-1"> 532.2821 </array>
 </property>
 <property dictRef="me:frequenciesScaleFactor">
  <scalar>1</scalar>
 </property>
 <property dictRef="me:symmetryNumber">
  <scalar>1</scalar>
 </property>
 <property dictRef="me:MW">
  <scalar units="amu">92</scalar>
 </property>
 <property dictRef="me:spinMultiplicity">
  <scalar>3</scalar>
 </property>
</propertyList>
<me:DOSCMethod name="ClassicalRotors"/>
</molecule>
   <molecule id="HCHO">
  <propertyList>
```

```
 <property title="Energy" dictRef="me:ZPE">
 <scalar units="kJ/mol">-75</scalar>
 </property>
 <property title="Vibrational Frequencies" dictRef="me:vibFreqs">
  <array units="cm-1">1213.6323 1273.5787 1540.0681 1870.2951 2945.3436 3015.4336</array>
 </property>
 <property title="Rotational Constants" dictRef="me:rotConsts">
  <array units="GHz">284.78174 39.46619 34.66252</array>
 </property>
 <property title="Symmetry Number" dictRef="me:symmetryNumber">
  <scalar>1 </scalar>
 </property>
 <property dictRef="me:MW">
       <scalar units="amu">30</scalar>
     </property>
</propertyList>
<me:energyTransferModel xsi:type="me:ExponentialDown">
<me:deltaEDown units="cm-1">250</me:deltaEDown>
</me:energyTransferModel>
 <me:DOSCMethod>ClassicalRotors</me:DOSCMethod>
</molecule>
    <molecule id="NO">
 <propertyList>
 <property title="Energy" dictRef="me:ZPE">
 <scalar units="kJ/mol">-50</scalar>
 </property>
 <property title="Vibrational Frequencies" dictRef="me:vibFreqs">
  <array units="cm-1"> 2066.0389</array>
 </property>
 <property title="Rotational Constants" dictRef="me:rotConsts">
  <array units="GHz">0 52.5361972 52.5361972</array>
 </property>
 <property title="Symmetry Number" dictRef="me:symmetryNumber">
  <scalar>1 </scalar>
 </property>
```

```
  <property dictRef="me:MW">
        <scalar units="amu">30</scalar>
       </property>
 </propertyList>
<me:energyTransferModel xsi:type="me:ExponentialDown">
<me:deltaEDown units="cm-1">250</me:deltaEDown>
</me:energyTransferModel>
  <me:DOSCMethod>ClassicalRotors</me:DOSCMethod>
 </molecule>
 <molecule id="O2">
  <propertyList>
  <property title="Energy" dictRef="me:ZPE">
  <scalar units="kJ/mol">-50</scalar>
  </property>
  <property title="Vibrational Frequencies" dictRef="me:vibFreqs">
   <array units="cm-1">1754.4088</array>
  </property>
  <property title="Rotational Constants" dictRef="me:rotConsts">
   <array units="GHz">0 44.6349128 44.6349128</array>
  </property>
  <property title="Symmetry Number" dictRef="me:symmetryNumber">
   <scalar>1 </scalar>
  </property>
  <property dictRef="me:MW">
        <scalar units="amu">32</scalar>
       </property>
 </propertyList>
<me:energyTransferModel xsi:type="me:ExponentialDown">
<me:deltaEDown units="cm-1">250</me:deltaEDown>
</me:energyTransferModel>
  <me:DOSCMethod>ClassicalRotors</me:DOSCMethod>
 </molecule>
<molecule id="N2">
 <atom elementType="N"/>
 <propertyList>
```

```
  <property dictRef="me:epsilon">
   <scalar>48.0</scalar>
  </property>
  <property dictRef="me:sigma">
   <scalar>3.9</scalar>
  </property>
  <property dictRef="me:MW">
   <scalar units="amu">28.0</scalar>
  </property>
 </propertyList>
</molecule>
</moleculeList>
<reactionList>
            <reaction id="R1">
    <reactantList>
     <reactant>
      <molecule ref="CH2OO" role="deficientReactant"/>
     </reactant>
     <reactant>
      <molecule ref="NO2" role="excessReactant"/>
     </reactant>
    </reactantList>
    <productList>
     <product>
      <molecule ref="prc" role="modelled"/>
     </product>
    </productList>
    <me:MCRCMethod xsi:type="me:MesmerILT">
       <me:preExponential units="cm3molecule-1s-1">3.e-10</me:preExponential>
       <me:activationEnergy  units="cm-1">0.0</me:activationEnergy>
       <me:nInfinity>0</me:nInfinity>
     </me:MCRCMethod>
            <me:excessReactantConc>1.0E16</me:excessReactantConc>
    </reaction>
 <reaction id="R2">
```

```
<reactantList>
    <reactant>
     <molecule ref="prc" role="modelled"/>
    </reactant>
</reactantList>
  <me:transitionState>
 <molecule ref="TS1" me:type="transitionState" />
</me:transitionState>
<productList>
 <product>
  <molecule ref="OOCH2NO2" role="modelled"/>
 </product>
</productList>
<me:MCRCMethod name="SimpleRRKM"/>
</reaction>
   <reaction id="R3">
<reactantList>
    <reactant>
     <molecule ref="prc" role="modelled"/>
    </reactant>
</reactantList>
  <me:transitionState>
 <molecule ref="TS2" me:type="transitionState" />
</me:transitionState>
<productList>
 <product>
  <molecule ref="OOCH2ONO" role="modelled"/>
 </product>
</productList>
<me:MCRCMethod name="SimpleRRKM"/>
</reaction>
   <reaction id="R4">
<reactantList>
 <reactant>
  <molecule ref="OOCH2ONO" role="modelled"/>
```

```
  </reactant>
 </reactantList>
 <productList>
  <product>
   <molecule ref="HCHO" role="sink"/>
  </product>
    <product>
   <molecule ref="NO" role="sink"/>
  </product>
    <product>
   <molecule ref="O2" role="modelled"/>
  </product>
 </productList>
    <me:transitionState>
  <molecule ref="TS6" role="transitionState"/>
 </me:transitionState>
          <me:MCRCMethod name="SimpleRRKM"/>
</reaction>
</reactionList>
<me:conditions>
 <me:bathGas>N2</me:bathGas>
 <me:PTs>
          <me:PTpair units="Torr" P= "50" T="223" precision="dd"> <me:bathGas>N2</me:bathGas><me:experimentalEigenvalue EigenvalueID="3" error="1.97E3"   >
          1.97E4   </me:experimentalEigenvalue> </me:PTpair>
          <me:PTpair units="Torr" P= "25" T="242" precision="dd"> <me:bathGas>N2</me:bathGas><me:experimentalEigenvalue EigenvalueID="3" error="1.83E3"   >
          1.83E4   </me:experimentalEigenvalue> </me:PTpair>
          <me:PTpair units="Torr" P= "50" T="242" precision="dd"> <me:bathGas>N2</me:bathGas><me:experimentalEigenvalue EigenvalueID="3" error="1.85E3"   >
          1.85E4   </me:experimentalEigenvalue> </me:PTpair>
          <me:PTpair units="Torr" P= "200" T="242" precision="dd"> <me:bathGas>N2</me:bathGas><me:experimentalEigenvalue EigenvalueID="3" error="1.86E3" >
          1.86E4   </me:experimentalEigenvalue> </me:PTpair>
          <me:PTpair units="Torr" P= "25" T="254" precision="dd"> <me:bathGas>N2</me:bathGas><me:experimentalEigenvalue EigenvalueID="3" error="1.65E3"   >
          1.65E4   </me:experimentalEigenvalue> </me:PTpair>
          <me:PTpair units="Torr" P= "50" T="254" precision="dd"> <me:bathGas>N2</me:bathGas><me:experimentalEigenvalue EigenvalueID="3" error="1.70E3"   >
          1.70E4   </me:experimentalEigenvalue> </me:PTpair>
```

```
 <me:PTpair units="Torr" P= "200" T="254" precision="dd"> <me:bathGas>N2</me:bathGas><me:experimentalEigenvalue EigenvalueID="3" error="1.41E3" >
1.41E4   </me:experimentalEigenvalue> </me:PTpair>
 <me:PTpair units="Torr" P= "50" T="273" precision="dd"> <me:bathGas>N2</me:bathGas><me:experimentalEigenvalue EigenvalueID="3" error="1.31E3"   >
1.31E4   </me:experimentalEigenvalue> </me:PTpair>
 <me:PTpair units="Torr" P= "50" T="277" precision="dd"> <me:bathGas>N2</me:bathGas><me:experimentalEigenvalue EigenvalueID="3" error="1.37E3"   >
1.37E4   </me:experimentalEigenvalue> </me:PTpair>
 <me:PTpair units="Torr" P= "25" T="298" precision="dd"> <me:bathGas>N2</me:bathGas><me:experimentalEigenvalue EigenvalueID="3" error="1.35E3"   >
1.35E4   </me:experimentalEigenvalue> </me:PTpair>
 <me:PTpair units="Torr" P= "50" T="298" precision="dd"> <me:bathGas>N2</me:bathGas><me:experimentalEigenvalue EigenvalueID="3" error="1.11E3"   >
1.11E4   </me:experimentalEigenvalue> </me:PTpair>
 <me:PTpair units="Torr" P= "100" T="298" precision="dd"> <me:bathGas>N2</me:bathGas><me:experimentalEigenvalue EigenvalueID="3" error="1.26E3" >
1.26E4   </me:experimentalEigenvalue> </me:PTpair>
 <me:PTpair units="Torr" P= "200" T="298" precision="dd"> <me:bathGas>N2</me:bathGas><me:experimentalEigenvalue EigenvalueID="3" error="1.41E3" >
1.41E4   </me:experimentalEigenvalue> </me:PTpair>
 <me:PTpair units="Torr" P= "300" T="298" precision="dd"> <me:bathGas>N2</me:bathGas><me:experimentalEigenvalue EigenvalueID="3" error="1.18E3" >
1.18E4   </me:experimentalEigenvalue> </me:PTpair>
 <me:PTpair units="Torr" P= "50" T="318" precision="dd"> <me:bathGas>N2</me:bathGas><me:experimentalEigenvalue EigenvalueID="3" error="9.57E2"   >
9.57E3   </me:experimentalEigenvalue> </me:PTpair>
 <me:PTpair units="Torr" P= "50" T="323" precision="dd"> <me:bathGas>N2</me:bathGas><me:experimentalEigenvalue EigenvalueID="3" error="8.39E2"   >
8.39E3   </me:experimentalEigenvalue> </me:PTpair>
 <me:PTpair units="Torr" P= "50" T="335" precision="dd"> <me:bathGas>N2</me:bathGas><me:experimentalEigenvalue EigenvalueID="3" error="7.79E2"   >
7.79E3   </me:experimentalEigenvalue> </me:PTpair>
 <me:PTpair units="Torr" P= "50" T="353" precision="dd"> <me:bathGas>N2</me:bathGas><me:experimentalEigenvalue EigenvalueID="3" error="5.77E2"   >
5.77E3   </me:experimentalEigenvalue> </me:PTpair>
 <me:PTpair units="Torr" P= "50" T="363" precision="dd"> <me:bathGas>N2</me:bathGas><me:experimentalEigenvalue EigenvalueID="3" error="5.98E2"   >
5.98E3   </me:experimentalEigenvalue> </me:PTpair>

 </me:PTs>
</me:conditions>
<me:modelParameters>
 <me:grainSize units="cm-1">50</me:grainSize>
 <me:energyAboveTheTopHill>25.0</me:energyAboveTheTopHill>
</me:modelParameters>
<me:control>
<me:testDOS />
```

<me:printSpeciesProfile />
<me:testRateConstant />
<me:printGrainDOS />
<me:printGrainkfE />
<me:printGrainkbE />
<me:eigenvalues>0</me:eigenvalues>
</me:control>
</me:mesmer>

Appendix 8. Investigating the Potential for a Reaction between CH_2OO and Water Trimers

Figure A.10 shows the dependence of $(k'\text{-}k_x)[H_2O]^{-2}$ on $[H_2O]$, where the dashed blue lines represent the equation $(k' - k_x)[H_2O]^{-2} = k_{6.1}[H_2O]^{-1} + k_{6.2} + k_{6.3}[H_2O]$, with rate coefficients for $k_{6.1}$, $k_{6.2}$ and $k_{6.3}$ representing reaction with the water monomer, dimer and trimer respectively. Values for rate coefficients were obtained from the parameterisation reported by Wu *et al.* The data obtained in this work indicate that there is no significant contribution from a reaction with the water trimer under the conditions studied in this work. Plots for data at 262 K, 298 K and 353 K are shown in Chapter 6.

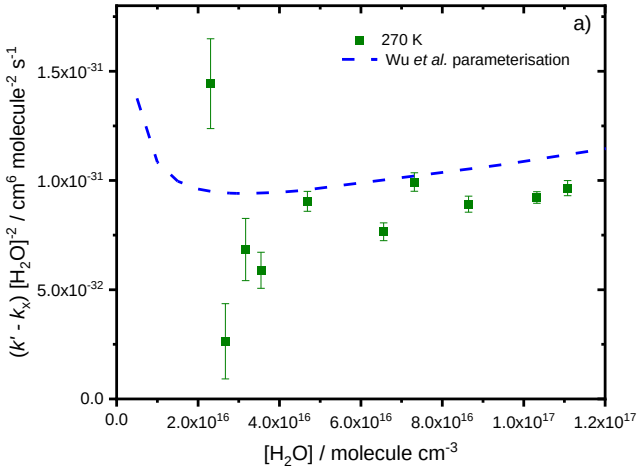

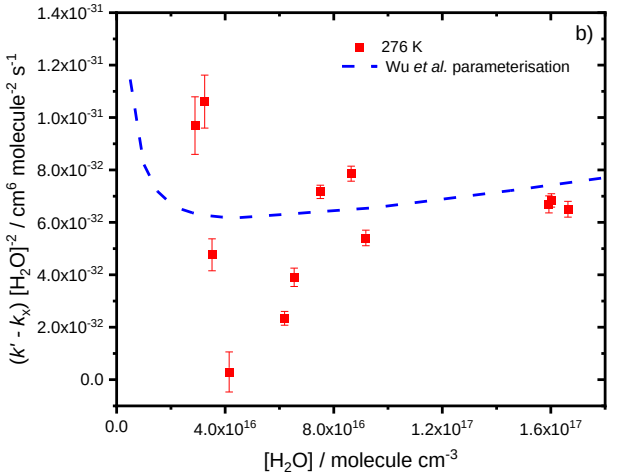

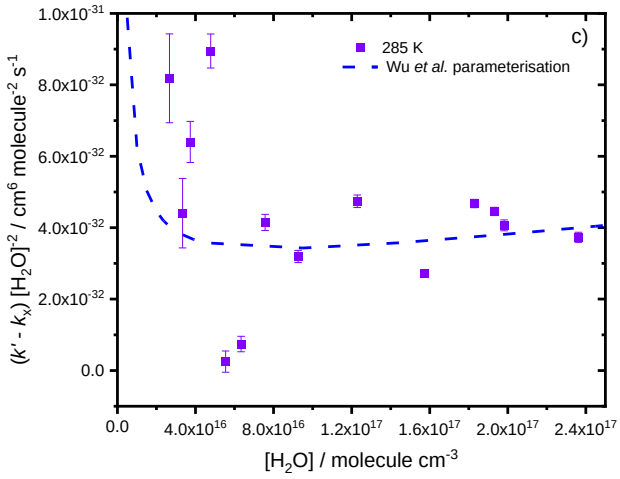
c)
285 K
Wu et al. parameterisation
(k' - kx) [H2O]-2 / cm6 molecule-2 s-1
[H2O] / molecule cm-3
1.0x10-31
8.0x10-32
6.0x10-32
4.0x10-32
2.0x10-32
0.0
0.0
4.0x1016
8.0x1016
1.2x1017
1.6x1017
2.0x1017
2.4x1017

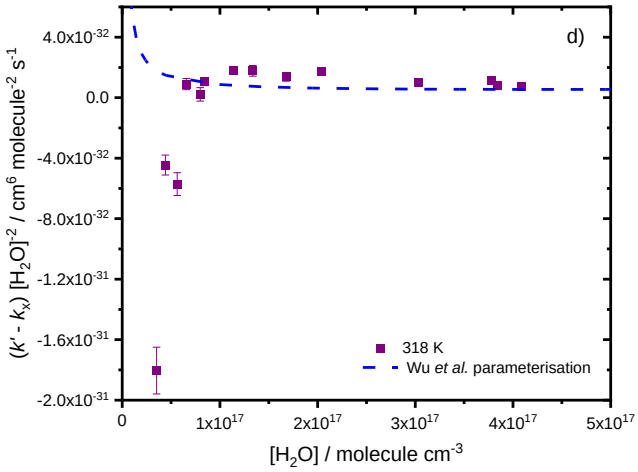
d)
318 K
Wu et al. parameterisation
(k' - kx) [H2O]-2 / cm6 molecule-2 s-1
[H2O] / molecule cm-3
4.0x10-32
0.0
-4.0x10-32
-8.0x10-32
-1.2x10-31
-1.6x10-31
-2.0x10-31
0
1x1017
2x1017
3x1017
4x1017
5x1017

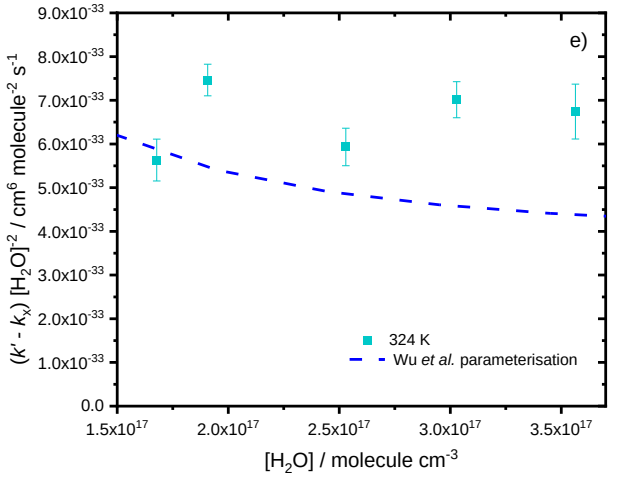
e)
324 K
Wu et al. parameterisation
(k' - kx) [H2O]-2 / cm6 molecule-2 s-1
[H2O] / molecule cm-3
9.0x10-33
8.0x10-33
7.0x10-33
6.0x10-33
5.0x10-33
4.0x10-33
3.0x10-33
2.0x10-33
1.0x10-33
0.0
1.5x1017
2.0x1017
2.5x1017
3.0x1017
3.5x1017

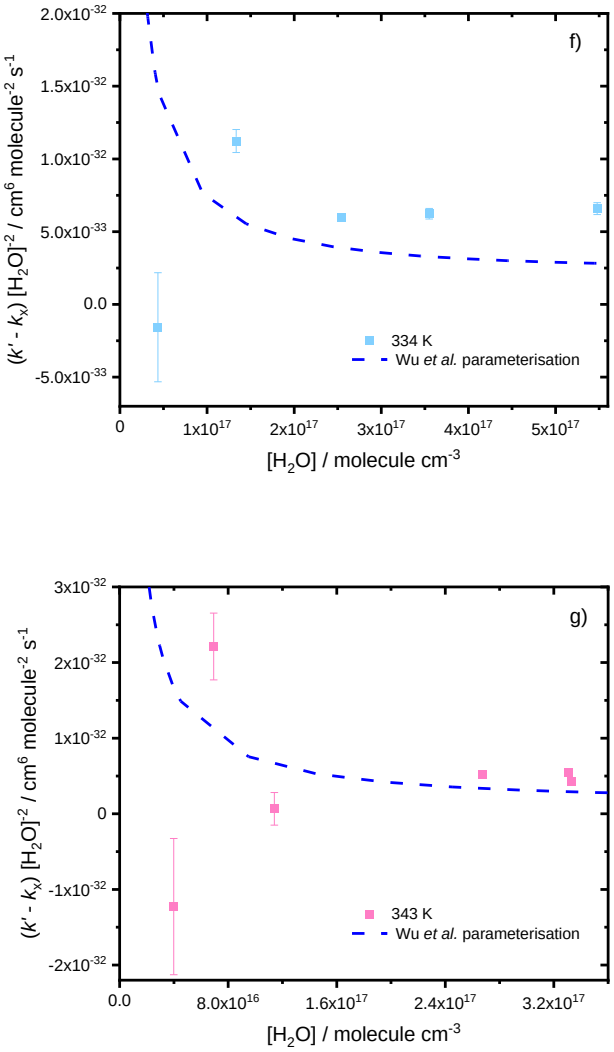

Figure A.10. Dependence of $(k'\text{-}k_x)[H_2O]^{-2}$ on $[H_2O]$ for data obtained in this work at temperatures between 270 and 343 K. The blue dashed line represents the equation $(k' - k_x)[H_2O]^{-2} = k_{6.1}[H_2O]^{-1} + k_{6.2} + k_{6.3}[H_2O]$, where $k_{6.1}$, $k_{6.2}$ and $k_{6.3}$ were obtained from the work of Wu *et al.*[23] Results at 262, 298 and 353 K are shown in Chapter 6.

Appendix 9. Comparison of Pseudo-First-Order Losses of CH_2OO in the Presence of Water Vapour with Literature

There is good agreement in the total pseudo-first-order rate coefficients as a function of water monomer concentration observed in this work and reported by Wu *et al*. Figure A.11 compares the total pseudo-first-order losses observed in this work at temperatures between 270 and 343 K and the work of Wu *et al*. as well as the individual contributions of $k_{6.1}$ and $k_{6.2}K_{eq}$ from this work and $k_{6.1}$, $k_{6.2}K_{eq}$ and $k_{6.3}$ from Wu *et al*. Comparisons between the pseudo-first-order losses observed in this work and in the work of Wu *et al*. at 262, 298 and 353 K are shown in Chapter 6.

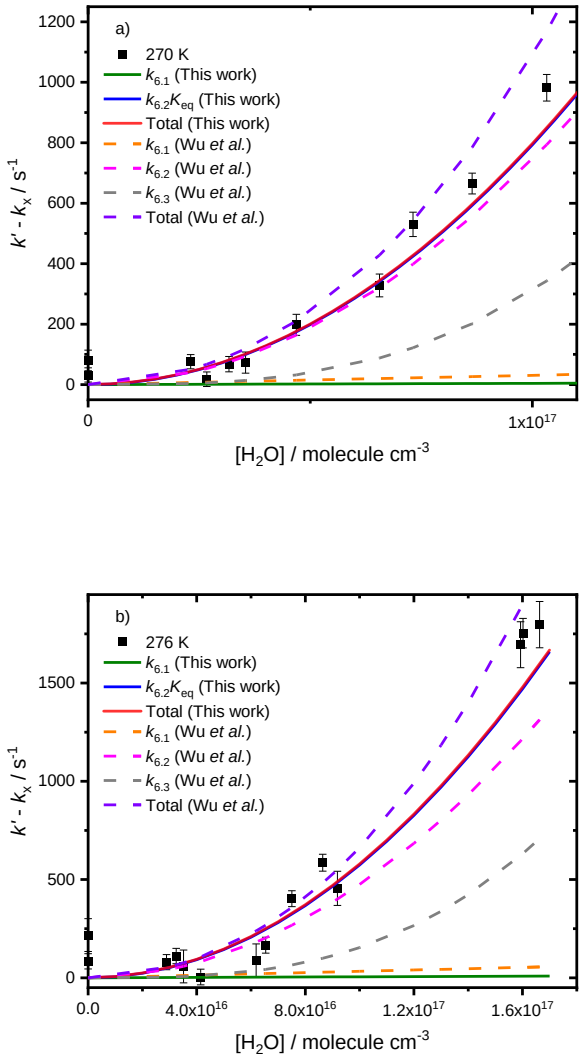

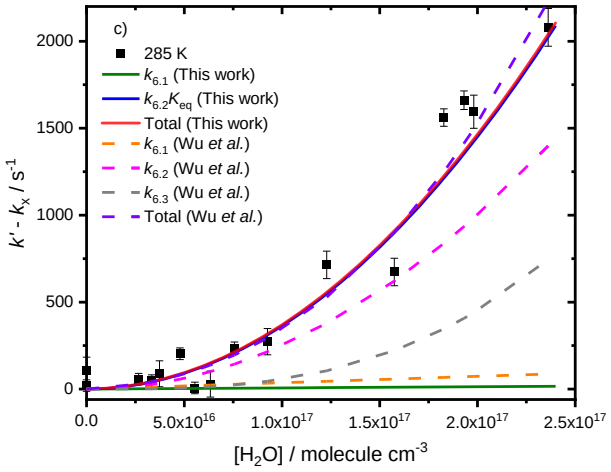
c)
285 K
$k_{6.1}$ (This work)
$k_{6.2}K_{eq}$ (This work)
Total (This work)
$k_{6.1}$ (Wu *et al.*)
$k_{6.2}$ (Wu *et al.*)
$k_{6.3}$ (Wu *et al.*)
Total (Wu *et al.*)
$k' - k_x$ / s^{-1}
[H$_2$O] / molecule cm^{-3}

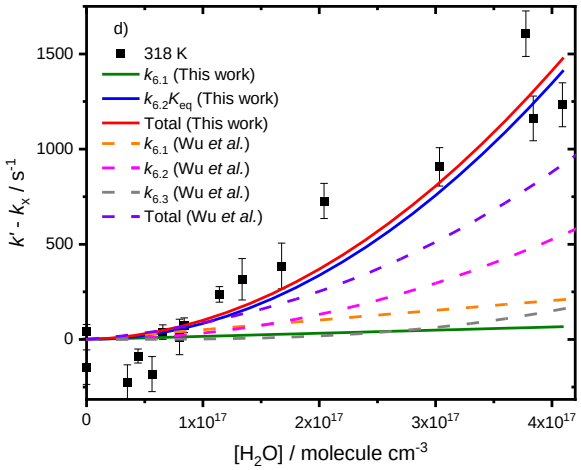
d)
318 K
$k_{6.1}$ (This work)
$k_{6.2}K_{eq}$ (This work)
Total (This work)
$k_{6.1}$ (Wu *et al.*)
$k_{6.2}$ (Wu *et al.*)
$k_{6.3}$ (Wu *et al.*)
Total (Wu *et al.*)
$k' - k_x$ / s^{-1}
[H$_2$O] / molecule cm^{-3}

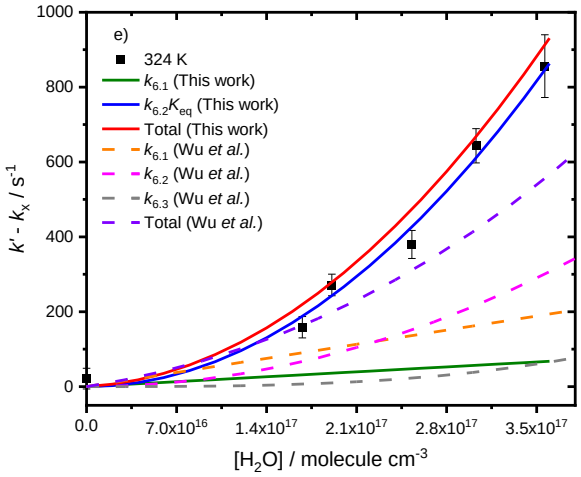
e)
324 K
$k_{6.1}$ (This work)
$k_{6.2}K_{eq}$ (This work)
Total (This work)
$k_{6.1}$ (Wu *et al.*)
$k_{6.2}$ (Wu *et al.*)
$k_{6.3}$ (Wu *et al.*)
Total (Wu *et al.*)
$k' - k_x$ / s^{-1}
[H$_2$O] / molecule cm^{-3}

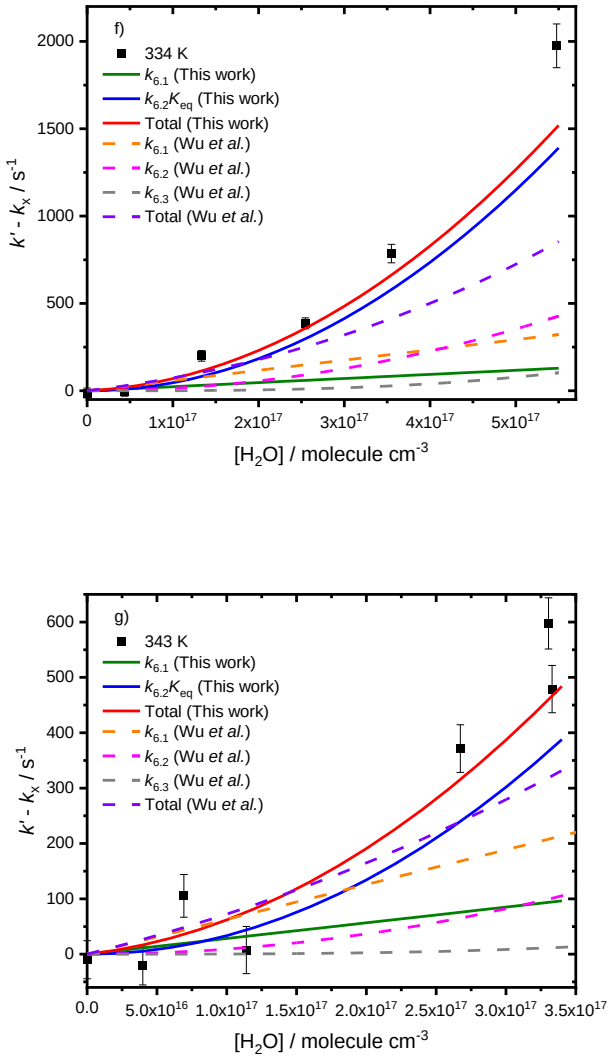

Figure A.11. Pseudo-first-order losses as a function of H_2O concentration for experiments at 262 - 353 K. Black points represent the experimental data, the green and blue solid lines represent losses due to reaction with the water monomer and the water dimer and the solid red line represents the total loss. The results of Wu *et al.* are also included in the plot, where the orange, pink and grey dashed lines represent reactions with the water monomer, dimer and trimer, and the purple dashed line represents the total loss. Comparisons for data at 262, 298 and 353 K are shown in Chapter 6.

Appendix 10. Experimental Data for the Reaction between CH_2OO and Water Vapour

T / K	$[CH_2I_2]_0$ / 10^{13} molecule cm^{-3}	$[H_2O]$ / 10^{16} molecule cm^{-3}	$[(H_2O)_2]$ / 10^{13} molecule cm^{-3}	k' / s^{-1}	$k' - k_x$ / s^{-1}
262	5.8	0	0	483 ± 10	3 ± 18
		2.40	0.25	550 ± 9	70 ± 17
		2.78	0.34	576 ± 10	96 ± 18
		2.95	0.38	641 ± 13	161 ± 20
		3.21	0.45	626 ± 19	146 ± 24
		3.90	0.66	685 ± 26	205 ± 30
		4.07	0.72	725 ± 16	245 ± 22
262	5.7	0	0	573 ± 7	-15 ± 18
		2.35	0.24	672 ± 10	84 ± 19
		3.19	0.44	754 ± 13	166 ± 21
		4.03	0.70	803 ± 14	215 ± 21
		4.04	0.71	801 ± 14	213 ± 21
270	5.8	0	0	470 ± 6	80 ± 34
		3.54	0.45	463 ± 10	73 ± 35
		4.69	0.79	588 ± 10	198 ± 35
		6.56	1.55	718 ± 17	328 ± 38
		7.31	1.93	920 ± 23	530 ± 40
		10.3	3.84	1372 ± 28	982 ± 44
		11.1	4.42	1573 ± 42	1183 ± 54
270	5.8	0	0	342 ± 11	32 ± 24
		2.31	0.19	386 ± 11	76 ± 24
		2.67	0.26	328 ± 12	18 ± 24
		3.17	0.32	378 ± 14	68 ± 25
		8.64	2.69	975 ± 27	665 ± 34
276	5.9	0	0	620 ± 7	217 ± 83
		3.51	0.39	461 ± 8	58 ± 83
		6.19	1.21	492 ± 10	89 ± 84
		9.18	2.67	858 ± 25	455 ± 87
		15.9	8.02	2098 ± 82	1695 ± 117
		16.6	8.74	2200 ± 83	1797 ± 118
276	6.1	0	0	316 ± 10	84 ± 39
		2.89	0.26	312 ± 9	80 ± 39
		3.24	0.33	343 ± 11	111 ± 39
		4.15	0.54	236 ± 13	4 ± 40
		6.54	1.35	398 ± 15	166 ± 40
		7.51	1.78	635 ± 14	403 ± 40
		8.64	2.36	818 ± 21	586 ± 43
		16.0	8.12	1986 ± 65	1754 ± 75
285	6.2	0	0	572 ± 6	109 ± 74
		3.73	0.37	551 ± 8	88 ± 75
		6.33	1.06	492 ± 9	29 ± 75
		9.26	2.26	736 ± 15	273 ± 76
		12.3	3.97	1177 ± 27	714 ± 79
		15.7	6.53	1137 ± 27	674 ± 79
		19.8	10.3	2058 ± 60	1595 ± 95
		23.6	14.7	2543 ± 79	2080 ± 109
285	6.3	0	0	225 ± 9	20 ± 33
		2.67	0.18	262 ± 9	57 ± 33
		3.34	0.29	253 ± 11	48 ± 34

		4.78	0.60	408 ± 11	203 ± 34
		5.54	0.81	212 ± 9	7 ± 33
		7.57	1.51	441 ± 13	236 ± 34
		18.3	8.80	1766 ± 39	1561 ± 50
		19.3	9.82	1866 ± 43	1661 ± 54
298	4.1	0	0	522 ± 5	32 ± 41
		3.77	0.29	445 ± 6	-45 ± 41
		5.97	0.74	459 ± 7	-31 ± 41
		8.51	1.49	687 ± 11	197 ± 42
		14.0	4.06	991 ± 19	501 ± 45
		17.5	6.30	1051 ± 20	561 ± 45
		28.6	16.9	2035 ± 34	1545 ± 53
298	6.4	0	0	313 ± 7	-5 ± 148
		8.12	0.14	292 ± 10	-26 ± 148
		20.4	0.86	1247 ± 37	929 ± 152
		39.5	0.32	2669 ± 120	2351 ± 190
		44.1	0.40	3722 ± 245	3404 ± 286
318	4.2	0	0	496 ± 18	-146 ± 91
		3.52	0.18	418 ± 19	-224 ± 91
		5.63	0.47	460 ± 24	-182 ± 92
		7.99	0.95	654 ± 29	-13 ± 93
		13.4	2.64	958 ± 63	316 ± 109
		16.8	4.16	1028 ± 81	386 ± 120
		20.4	6.17	1370 ± 25	728 ± 92
		30.3	13.6	1549 ± 48	907 ± 101
		38.4	21.8	1803 ± 77	1161 ± 117
		40.9	24.7	1875 ± 74	1233 ± 116
318	3.8	0	0	585 ± 9	43 ± 36
		4.42	0.29	455 ± 13	-87 ± 37
		6.56	0.64	581 ± 16	39 ± 38
		8.40	1.04	616 ± 18	74 ± 39
		11.4	1.93	779 ± 22	237 ± 41
		37.8	21.1	2148 ± 114	1606 ± 119
324	4.1	0	0	590 ± 11	21 ± 28
		16.8	3.8	728 ± 14	159 ± 29
		19.1	4.92	841 ± 13	272 ± 29
		25.3	8.65	949 ± 27	380 ± 37
		30.3	12.4	1212 ± 38	643 ± 46
		35.6	17.2	1425 ± 80	856 ± 84
334	4.2	0	0	465 ± 8	-13 ± 28
		4.37	0.22	475 ± 7	-3 ± 28
		13.3	2.08	678 ± 14	200 ± 30
		25.5	7.59	864 ± 16	386 ± 31
		35.5	14.7	1263 ± 46	785 ± 53
		54.8	35.1	2453 ± 122	1975 ± 125
343	4.8	0	0	385 ± 12	-10 ± 34
		3.98	0.17	375 ± 14	-20 ± 35
		6.93	0.50	500 ± 21	105 ± 39
		11.4	1.35	402 ± 28	8 ± 43
		26.7	7.40	766 ± 28	371 ± 43
		33.0	11.3	992 ± 33	597 ± 46
		33.3	11.5	874 ± 28	479 ± 43
353	4.8	0	0	532 ± 4	80 ± 26

		3.44	0.11	471 ± 4	19 ± 26
		5.48	0.27	394 ± 5	-58 ± 26
		7.11	0.46	434 ± 5	-18 ± 26
		14.0	1.79	479 ± 7	27 ± 27
		22.1	4.44	725 ± 9	273 ± 27
		27.3	6.79	801 ± 10	349 ± 28
		31.9	9.28	907 ± 19	455 ± 32
		36.1	11.9	937 ± 20	485 ± 33
		38.4	13.5	1087 ± 22	635 ± 34
353	5.1	0	0	468 ± 13	0 ± 14
		19.8	3.57	618 ± 22	150 ± 22
		23.4	4.98	686 ± 28	218 ± 28
		28.2	7.25	777 ± 28	309 ± 29
353	5.5	0	0	502 ± 8	-58 ± 35
		4.70	0.20	611 ± 10	51 ± 35
		14.9	2.03	701 ± 17	141 ± 38
		22.5	4.60	735 ± 20	175 ± 39
		30.6	8.55	961 ± 29	401 ± 44

Table A.3. Experimental data obtained in this work for the reaction between CH_2OO and water vapour. All experiments were carried out at a total pressure of 760 Torr.

Appendix 11. A Comparison between Fits to the Data Obtained for *syn*-CH_3CHOO with SO_2

The data were fit with two different equations to describe the observed pressure dependence (Chapter 7). Figure A.12 shows a comparison between fits to both equations for temperatures between 242 and 353 K.

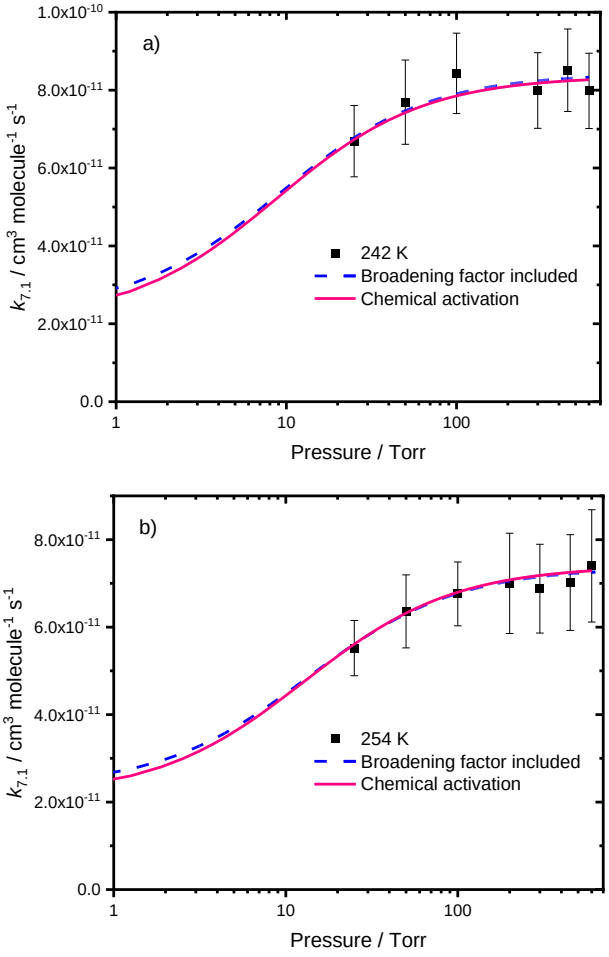

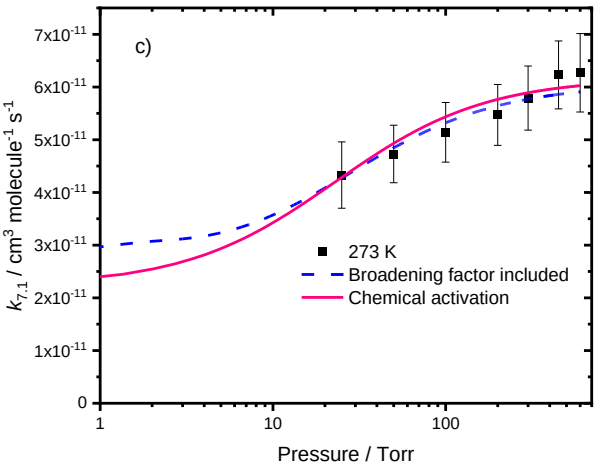
c)
$k_{7,1}$ / cm^3 molecule^{-1} s^{-1}
7x10^{-11}
6x10^{-11}
5x10^{-11}
4x10^{-11}
3x10^{-11}
2x10^{-11}
1x10^{-11}
0
1
10
100
Pressure / Torr
273 K
Broadening factor included
Chemical activation

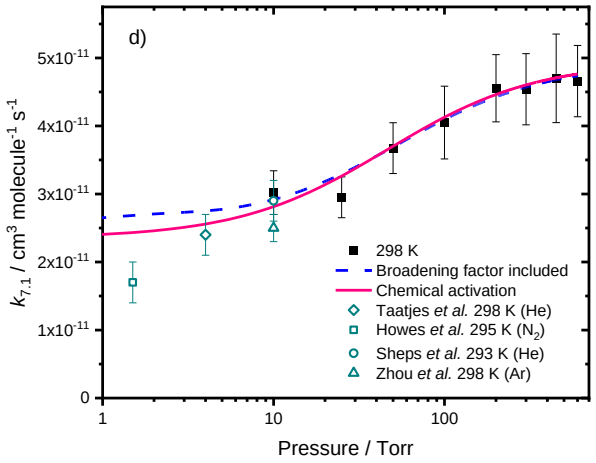
d)
$k_{7,1}$ / cm^3 molecule^{-1} s^{-1}
5x10^{-11}
4x10^{-11}
3x10^{-11}
2x10^{-11}
1x10^{-11}
0
1
10
100
Pressure / Torr
298 K
Broadening factor included
Chemical activation
Taatjes *et al.* 298 K (He)
Howes *et al.* 295 K (N_2)
Sheps *et al.* 293 K (He)
Zhou *et al.* 298 K (Ar)

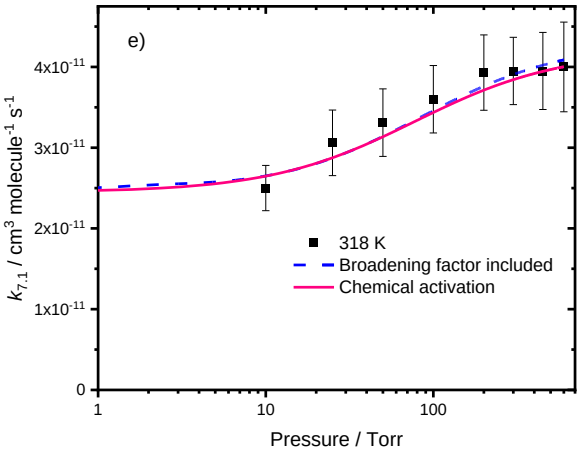
e)
$k_{7,1}$ / cm^3 molecule^{-1} s^{-1}
4x10^{-11}
3x10^{-11}
2x10^{-11}
1x10^{-11}
0
1
10
100
Pressure / Torr
318 K
Broadening factor included
Chemical activation

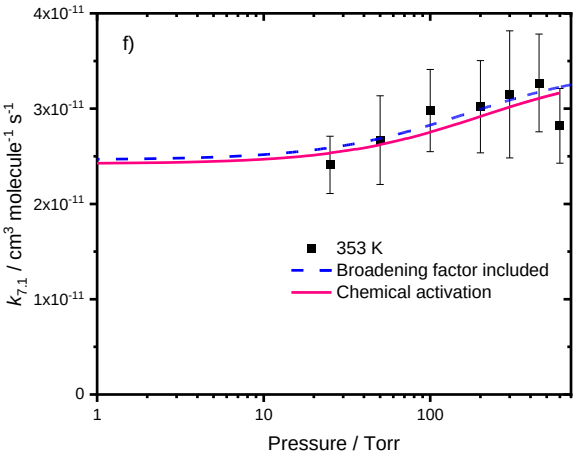

Figure A.12. Comparison of the fit to Equations 7.9 and 7.13 for $k_{7.1}$ at T = 242 - 353 K and p = 10 - 600 Torr. Both equations were fit globally to each temperature and pressure investigated. Results from previous studies at ~ 298 K are also shown.[2 7 3 8] The fit result for Equation 7.9 gave: A_{int} = (2.35 ± 0.39) × 10^{-11} cm^3 $molecule^{-1}$ s^{-1}, n_{int} = (0.61 ± 0.79), A_0 = (3.29 ± 1.30) × 10^{-29} cm^3 $molecule^{-1}$ s^{-1}, n_0 = -(9.52 ± 1.78), A_∞ = (4.95 ± 0.51) × 10^{-11} cm^3 $molecule^{-1}$ s^{-1}, n_∞ = -(2.52 ± 0.29) and the fit result for Equation 7.13 gave: A_{int} = (2.39 ± 0.28) × 10^{-11} cm^3 $molecule^{-1}$ s^{-1}, n_{int} = (0.19 ± 0.72), A_0 = (6.07 ± 4.74) × 10^{-29} cm^3 $molecule^{-1}$ s^{-1}, n_0 = -(10.13 ± 1.81), A_∞ = (8.98 ± 7.22) × 10^{-11} cm^3 $molecule^{-1}$ s^{-1}, n_∞ = -(3.34 ± 0.71).

Appendix 12. Experimental Data for the Reaction between CH_3CHOO and SO_2

T / K	Pressure / Torr	$[SO_2]$ / 10^{12} molecule cm^{-3}	$k'_{7.1}$ / s^{-1}	$k'_{7.2}$ / s^{-1}
242	25	0	790 ± 18	1454 ± 86
		5.8	1228 ± 24	2274 ± 130
		6.7	-	2165 ± 180
		7.5	1103 ± 31	2209 ± 178
		18	2048 ± 221	-
		22	2176 ± 126	3924 ± 575
	50	0	958 ± 13	2077 ± 89
		6.7	1234 ± 20	2910 ± 161
		7.5	-	2587 ± 385
		8.3	1393 ± 26	3225 ± 240
		11	1496 ± 47	3313 ± 413
		18	2282 ± 63	-
		22	2542 ± 66	-
	100	0	-	2031 ± 97
		6.7	1178 ± 23	2675 ± 172
		8.3	1198 ± 27	2758 ± 221
		13	-	3279 ± 583
		18	2037 ± 77	-
		22	2439 ± 23	-
	300	0	-	1062 ± 42
		5.9	957 ± 48	1651 ± 164
		6.7	1228 ± 30	1630 ± 82
		8.3	1322 ± 48	2296 ±210
		9.4	1258 ± 66	2414 ± 286
		11	1449 ± 69	-
		18	2159 ± 107	3566 ± 584
		26	2599 ± 97	3545 ± 465
	450	0	-	1419 ± 128
		7.1	1246 ± 29	2259 ± 196
		8.8	1587 ± 49	2427 ± 282
		9.9	1515 ± 46	2254 ± 282
		12	1638 ± 60	2981 ± 435
		19	2307 ± 94	-
		23	2697 ± 104	-
	600	0	970 ± 34	-
		7.1	1480 ± 50	-
		9	1475 ± 56	-
		14	1824 ± 54	-
		31	3425 ± 211	-
254	25	0	489 ± 18	886 ± 51
		8.5	808 ± 39	1895 ± 185

		11	1028 ± 52	2382 ± 278
		14	1225 ± 62	-
		31	2173 ± 127	3797 ± 822
	50	0	407 ± 18	343 ± 10
		8.5	-	585 ± 44
		12	848 ± 71	-
		14	1180 ± 79	1414 ± 159
		27	2108 ± 173	2954 ± 492
		31	2300 ± 165	-
	100	0	327 ± 15	1098 ± 62
		8.7	814 ± 29	1697 ± 141
		12	1004 ± 41	2211 ± 249
		14	1176 ± 48	2430 ± 266
		23	1962 ± 98	3331 ± 549
		28	2117 ± 106	3755 ± 618
		32	2430 ± 115	4240 ± 668
	200	0	593 ± 24	406 ± 31
		8.7	755 ± 41	1301 ± 159
		12	932 ± 83	-
		14	1090 ± 82	1246 ± 159
		23	2378 ± 208	-
		28	2470 ± 195	-
		32	2546 ± 152	3646 ± 727
	300	0	755 ± 28	-
		23	2187 ± 167	-
		27	2705 ± 160	-
	450	0	1162 ± 47	-
		9.6	1343 ± 59	-
		13	1410 ± 99	-
		16	1628 ± 103	-
		26	2624 ± 198	-
		31	3026 ± 210	-
		36	3415 ± 180	-
	600	0	641 ± 28	-
		10	918 ± 64	-
		17	1669 ± 141	-
		28	2250 ± 234	-
		33	3116 ± 272	-
273	25	0	653 ± 7	1691 ± 43
		6.6	893 ± 9	2488 ± 72
		7.3	834 ± 11	2627 ± 92
		8.6	861 ± 14	2813 ± 131
		17	1250 ± 31	-
		22	1616 ± 40	-

	50	0	417 ± 14	1536 ± 89
		6.1	557 ± 15	2206 ± 130
		6.7	636 ± 18	2421 ± 139
		7.6	640 ± 19	2884 ± 192
		7.9	647 ± 18	-
		10	1380 ± 49	-
		11	851 ± 24	3174 ± 201
		15	1047 ± 31	-
		24	1431 ± 47	-
	100	0	-	1208 ± 57
		6.6	537 ± 15	2169 ± 109
		7.3	641 ± 16	2382 ± 118
		8.3	567 ± 19	-
		8.6	654 ± 22	2528 ± 164
		12	866 ± 23	-
		17	1085 ± 41	-
		26	1549 ± 43	-
	200	0	-	1397 ± 66
		7.5	587 ± 24	2714 ± 330
		8.5	641 ± 26	2707 ± 330
		8.8	-	2742 ± 215
		13	906 ± 33	3392 ± 480
		17	1158 ± 40	-
		23	1423 ± 74	-
	300	0	453 ± 19	-
		6.7	795 ± 14	-
		7.4	793 ± 20	-
		13	1136 ± 38	-
		17	1345 ± 37	-
		23	1729 ± 62	-
		27	1992 ± 57	-
	450	0	-	1258 ± 70
		7.4	-	1849 ± 115
		8.3	811 ± 30	2206 ± 182
		9.7	870 ± 50	2529 ± 424
		14	1157 ± 60	-
		19	1444 ± 100	3715 ± 838
		25	1879 ± 119	-
	600	0	622 ± 27	-
		8.9	1048 ± 32	-
		15	1424 ± 82	-
		21	1736 ± 79	-
		32	2618 ± 228	-
298	10	0	384 ± 7	1071 ± 37

		8.9	570 ± 10	1477 ± 58
		10	625 ± 12	1532 ± 63
		15	794 ± 16	2267 ± 110
		20	946 ± 20	2851 ± 157
		25	1103 ± 24	3304 ± 202
		30	1249 ± 31	4042 ± 318
		8	532 ± 10	1465 ± 56
	25	8.9	665 ± 20	1086 ± 54
		10	723 ± 21	1358 ± 75
		15	856 ± 29	1729 ± 128
		20	1012 ± 32	2391 ± 178
		24	1166 ± 43	3261 ± 353
		30	1286 ± 44	-
		40	1581 ± 49	-
	50	0	374 ± 7	851 ± 35
		5	-	1546 ± 120
		7.9	576 ± 21	2004 ± 164
		8.8	642 ± 14	-
		11	765 ± 15	2280 ± 218
		16	868 ± 35	2930 ± 301
		20	1049 ± 47	3301 ± 431
		25	1231 ± 56	-
		30	1475 ± 68	-
		50	2175 ± 96	-
	100	0	470 ± 11	941 ± 47
		9	618 ± 17	-
		10	678 ± 19	1864 ± 124
		15	924 ± 27	-
		20	1139 ± 33	3306 ± 397
		25	1442 ± 46	1863 ± 121
		30	1568 ± 44	-
	200	8.2	725 ± 17	1353 ± 84
		8.9	786 ± 17	1314 ± 79
		10	847 ± 17	1550 ± 95
		15	1085 ± 24	2074 ± 158
		20	1336 ± 29	2329 ± 294
		25	1558 ± 38	3240 ± 345
		30	1692 ± 37	-
	300	0	601 ± 15	1363 ± 281
		9	876 ± 25	2138 ± 396
		10	928 ± 24	2329 ± 390
		12	1009 ± 29	2978 ± 565
		15	1159 ± 33	2812 ± 565
		20	1426 ± 33	4095 ± 712

		25	1734 ± 56	3745 ± 1013
		30	1855 ± 48	-
	450	0	652 ± 15	-
		8.1	-	1464 ± 163
		8.9	844 ± 24	1377 ± 158
		10	875 ± 24	1770 ± 210
		15	1112 ± 34	2209 ± 287
		20	1438 ± 41	2931 ± 442
		25	1806 ± 60	-
		30	1899 ± 52	-
	600	8.9	858 ± 39	1540 ± 395
		9.9	854 ± 34	1707 ± 372
		12	981 ± 44	2077 ± 419
		15	1181 ± 50	2531 ± 504
		20	1377 ± 55	2419 ± 471
		25	1658 ± 85	2956 ± 685
		30	1785 ± 73	3909 ± 832
318	10	0	710 ± 10	1121 ± 40
		9.5	898 ± 12	1641 ± 61
		11	991 ± 21	-
		13	1015 ± 20	2614 ± 152
		15	1030 ± 25	2209 ± 138
		17	1138 ± 24	-
		24	1299 ± 31	3276 ± 330
		33	1597 ± 37	5263 ± 439
		41	1665 ± 32	-
	25	0	647 ± 22	590 ± 31
		7	745 ± 26	1409 ± 74
		7.9	720 ± 22	-
		9.2	914 ± 26	1771 ± 90
		10	810 ± 26	1837 ± 101
		15	1047 ± 34	2362 ± 146
		21	1229 ± 34	3566 ± 236
		31	1510 ± 42	-
	50	0	-	322 ± 22
		7.1	668 ± 26	918 ± 55
		8	617 ± 23	990 ± 69
		9.3	808 ± 30	2111 ± 155
		10	849 ± 31	1941 ± 132
		15	960 ± 35	2429 ± 208
		21	1168 ± 43	-
		26	1224 ± 45	-
		31	1490 ± 54	3942 ± 347
	100	0	-	1497 ± 60

		6.8	1015 ± 34	1926 ± 126
		7.9	1048 ± 45	-
		9.2	1043 ± 50	-
		11	1127 ± 54	2059 ± 168
		15	1269 ± 57	2985 ± 261
		20	1430 ± 62	-
		25	1701 ± 82	4048 ± 465
	200	0	775 ± 15	669 ± 32
		6.8	-	1316 ± 50
		7.9	1043 ± 32	1608 ± 100
		8.6	1081 ± 39	-
		9.4	1156 ± 35	1648 ± 95
		14	-	2511 ± 146
		18	1420 ± 53	-
		23	1753 ± 69	-
		27	1794 ± 42	-
	300	0	692 ± 18	458 ± 29
		7.5	1065 ± 34	1304 ± 87
		9.2	1102 ± 35	1764 ± 139
		10	1118 ± 31	-
		15	1323 ± 40	2425 ± 184
		21	1521 ± 49	3409 ± 318
		25	1732 ± 74	-
	450	0	-	1635 ± 81
		7.4	1096 ± 19	-
		8.7	1289 ± 32	2268 ± 114
		9.4	1271 ± 38	2662 ± 166
		10	1354 ± 40	3097 ± 214
		15	1513 ± 39	2890 ± 165
		20	1667 ± 54	-
		25	1953 ± 71	4472 ± 370
		30	2042 ± 47	-
	600	0	913 ± 25	1286 ± 81
		6.7	-	1715 ± 146
		7.3	972 ± 26	-
		8.1	1064 ± 45	1691 ± 106
		9	1221 ± 68	1887 ± 154
		15	1500 ± 84	2972 ± 286
		20	1643 ± 77	-
		30	2006 ± 83	-
353	10	0	-	238 ± 26
		4	-	751 ± 39
		4.7	-	818 ± 42
		5.3	-	820 ± 47

		5.9	-	1079 ± 61
	25	0	1190 ± 43	0
		5.5	1263 ± 42	595 ± 27
		6.3	1368 ± 46	781 ± 35
		7	1305 ± 45	751 ± 35
		7.9	1377 ± 47	974 ± 46
		8.9	1335 ± 46	796 ± 37
		11	1445 ± 52	941 ± 46
		19	1618 ± 57	2099 ± 125
		22	1715 ± 59	-
	50	0	1545 ± 70	472 ± 26
		5.8	1522 ± 67	-
		6.6	1642 ± 78	922 ± 45
		7.4	1696 ± 81	-
		8.3	1627 ± 83	1418 ± 92
		9.4	1870 ± 95	1456 ± 102
		11	1803 ± 97	1910 ± 155
		20	2012 ± 100	-
		24	2115 ± 100	-
	100	0	1560 ± 52	641 ± 43
		6.1	1711 ± 74	1144 ± 73
		7.1	1840 ± 82	2001 ± 132
		8.2	1734 ± 77	1541 ± 96
		9	1738 ± 79	1804 ± 120
		10	1763 ± 81	2424 ± 165
		14	1804 ± 79	-
		19	2094 ± 98	2633 ± 173
		23	2375 ± 112	-
	200	0	1464 ± 43	889 ± 33
		6.4	1619 ± 83	1146 ± 80
		8.4	1763 ± 89	1377 ± 103
		9.1	-	1782 ± 142
		10	-	1723 ± 134
		14	1865 ± 103	2403 ± 190
		19	1898 ± 82	2965 ± 189
		27	2351 ± 155	-
	300	0	1854 ± 103	518 ± 42
		5.6	-	1047 ± 106
		7.1	1918 ± 114	-
		8	2022 ± 131	1303 ± 100
		9	-	1401 ± 86
		11	2072 ± 119	-
		19	2441 ± 122	2661 ± 197
	450	6.4	-	1695 ± 108

		7.2	-	1825 ± 100
		8.1	2101 ± 89	1955 ± 110
		9.1	2191 ± 99	-
		10	2237 ± 110	2027 ± 140
		14	2360 ± 108	2785 ± 206
		19	2486 ± 131	-
	600	6.7	2029 ± 149	1058 ± 106
		7.6	1957 ± 80	1312 ± 90
		8.5	-	1163 ± 52
		9.6	2032 ± 84	1393 ± 78
		11	2088 ± 86	-
		16	2261 ± 97	-
		23	2423 ± 119	2521 ± 211

Table A.4. Experimental data obtained for experiments to investigate the kinetics of CH_3CHOO and SO_2 between 10 and 600 Torr and 242 and 353 K.